



# **FINAL REPORT**

**Final Report  
WY2501F**

**TPF-5(391)**

## **COMPREHENSIVE FIELD TEST AND GEOTECHNICAL INVESTIGATION PROGRAM FOR DEVELOPMENT OF LRFD RECOMMENDATIONS OF DRIVEN PILES ON INTERMEDIATE GEOMATERIALS**

Prepared by:

Kam Ng, Ph.D., P.E., Professor  
Nafis Bin Masud, Ph.D. Graduate  
Opeyemi E. Oluwatuyi, Ph.D. Graduate  
Shaun S. Wulff, Ph.D., Professor

Department of Civil & Architectural Engineering and Construction Management  
Department of Mathematics & Statistics  
University of Wyoming  
1000 E. University Avenue  
Laramie, Wyoming 82071

July 2025



## **DISCLAIMER Notice**

This document was disseminated under the sponsorship of the Wyoming Department of Transportation (WYDOT) in the interest of information exchange. WYDOT assumes no liability for the use of the information contained in this document. WYDOT does not endorse products or manufacturers. Trademarks or manufacturers' names appear in this report only because they were considered essential to the objective of the document.

### **Quality Assurance Statement**

WYDOT provides high-quality information to serve Government, industry, and the public in a manner that promotes public understanding. Standards and policies were used to ensure and maximize the quality, objectivity, utility, and integrity of its information. WYDOT periodically reviews quality issues and adjusts its programs and processes to ensure continuous quality improvement. Further, if the report contains either confidential information or, if any information in the report was subject to copyright, patent, or trademark requirements, the report must contain additional disclaimers that may be obtained through the Research Center.

### **Creative Commons**

#### **Copyrighted works**

This report was covered under a Creative Commons, [CC BY-SA](#) license and when using any information from this report, whether it was from the finalized report or an unpublished draft, ensure you adhere to the following:

Attribution — You must give appropriate credit, provide a link to the license, and indicate if changes were made. You may do so in any reasonable manner but not in any way that suggests the licensor endorses you or your use.

ShareAlike — If you remix, transform, or build upon the material, you must distribute your contributions under the same license as the original.

No additional restrictions — You may not apply legal terms or technological measures that legally restrict others from doing anything the license permits.

You do not have to comply with the license for elements of the material in the public domain or where your use was permitted by an applicable exception or limitation.

No warranties were given. The license may not give you all of the permissions necessary for your intended use. For example, other rights such as publicity, privacy, or moral rights may limit how you use the material.

#### **Non-copyrightable work generated by Artificial Intelligence**

For all work in this report that was generated using an artificial intelligence tool and that cannot be copyrighted, and which will be available on any public domain, Author waives all rights to that portion of the work generated by artificial intelligence under copyright laws. Others may copy, modify, and distribute the specified artificial intelligence generated work without permission. Authors make no warranties about the work, and disclaim all liabilities for all use of that work. When using or citing the work, you should not imply endorsement by the author, contractor, or WYDOT.

## **Copyright and Proprietary Information**

No copyrighted material, except that which falls under the Doctrine of Fair Use, may be incorporated into a report without permission from the copyright owner, if the copyright owner requires such. Prior use of the material in a WYDOT or governmental publication does not necessarily constitute permission to use it in a later publication.

- **Courtesy** — Acknowledgment or credit will be given by footnote, bibliographic reference, or a statement in the text for use of material contributed or assistance provided even when a copyright notice was not applicable.
- **Caveat for Unpublished Work** — Some material may be protected under common law or equity even though no copyright notice was displayed on the material. Credit will be given and permission will be obtained as appropriate.

**Proprietary Information** — To avoid restrictions on the availability of reports, proprietary information will not be included in reports unless it was critical to the understanding of a report and prior approval was received from WYDOT and the contractor. Reports containing such proprietary information will contain a statement on the Technical Report Documentation Page restricting availability and a notice on how to request a copy of the material.

## **No Generative Artificial Intelligence Training**

Without any way limiting the author or other copyright owner's exclusive right under copyright, the owner of this report, which includes the authors, contractor and WYDOT, does not consent to the content being used or downloaded for the purposes of developing, training, or operating any artificial intelligence (AI) tool or model, or other machine learning systems operated by any generative artificial intelligence (GAI) model, which could include but was not limited to machine learning (ML) tools, large language models (LLM), generative adversarial networks (GAN), open AI programs (OpenAI), generative pre-trained transformers (GPT), or their sublicensees. Any use of this publication to train generative AI technologies or their sublicenses was expressly prohibited. The owner of this report reserve all rights to license uses of this work and any artificial intelligence tool that was capable of generating works must obtain the owner's specific and express permission to generate any works using data and information from this report.



## TECHNICAL REPORT DOCUMENTATION PAGE

1. Report No. WY-2501F	2. Government Accession No.	3. Recipient's Catalog No.	
4. Title and Subtitle Comprehensive field load test and geotechnical investigation program for development of LRFD recommendations of driven piles on intermediate geomaterials		5. Report Date July 2025	
		6. Performing Organization Code:	
7. Author(s) Kam W. Ng (0000-0001-5099-5454), Nafis Bin Masud (0000-0003-0740-6655), Opeyemi E. Oluwatuyi (0000-0002-0499-6998) Shaun S. Wulff (0000-0002-5695-4925)		8. Performing Organization Report No.	
9. Performing Organization Name and Address Department of Civil and Architectural Engineering and Construction Management University of Wyoming 1000 E. University Avenue, Dept. 3295 Laramie, WY 82071-2000		10. Work Unit No.	
		11. Contract or Grant No. RS05219 <a href="https://ror.org/00pqdc111">https://ror.org/00pqdc111</a>	
12. Sponsoring Agency Name and Address Wyoming Department of Transportation 5300 Bishop Blvd. Cheyenne, WY 82009-3340 WYDOT Research Center (307) 777-4182		13. Type of Report and Period Final Report	
		14. Sponsoring Agency Code WYDOT	
15. Supplementary Notes WYDOT Project Champion: Bridge Program and Geology Program. All restrictions for this report are set out on the <u>Disclaimer page</u> .			
16. Abstract Pile foundations were often driven into intermediate geomaterials (IGM) to support heavy civil infrastructures like bridges due to shallow bedrock stratigraphy. Thus, the pile foundations of this region must rely on the resistance contributed from the IGM layers. However, IGM is a transitional geomaterial between soil and rock, that needs to be better defined for the design and construction of driven piles. AASHTO suggests applying the same static analysis (SA) methods developed for piles driven in soil to IGM. However, past studies concluded that SA methods developed for soil resulted in an inconsistent and conservative estimation of geotechnical resistance and considerable variation between the predicted resistances and measured resistances determined from the signal-matching technique using the CAsE Pile Wave Analysis Program (CAPWAP). Thus, there is a need to improve the current practice of driven pile design and construction in IGM by establishing representative engineering properties of IGM, by improving SA and construction control methods, and developing more efficient LRFD recommendations. Such recommendations were necessary for reliable and economical design and construction of driven piles. This research aims to improve the efficiency of driven piles in IGM, increasing the system reliability of civil infrastructures, especially bridge structures. The objectives of this proposed research were to classify IGM, determine IGM properties, improve pile resistance estimations in IGM by advanced SA methods, understand the time-dependent pile resistances in IGM, validate the performance of dynamic analysis methods through a static load test program, and recommend changes and improvements to current pile design and construction practices.			
17. Key Words driven piles, intermediate geomaterials, LRFD, machine learning, static analysis method, pile setup, Wyoming		18. Distribution Statement This document is available through the National Transportation Library and the Wyoming State Library. Copyright ©2019. All rights reserved, State of Wyoming, Wyoming Department of Transportation, and the University of Wyoming.	
19. Security Classif. (of this report) Unclassified	20. Security Classif. (of this page) Unclassified	21. No. of Pages: 308	22. Price

# SI\* (MODERN METRIC) CONVERSION FACTORS

## APPROXIMATE CONVERSIONS TO SI UNITS

Symbol	When You Know	Multiply By	To Find	Symbol
<b>LENGTH</b>				
in	inches	25.4	millimeters	mm
ft	feet	0.305	meters	m
yd	yards	0.914	meters	m
mi	miles	1.61	kilometers	km
<b>AREA</b>				
in <sup>2</sup>	square inches	645.2	square millimeters	mm <sup>2</sup>
ft <sup>2</sup>	square feet	0.093	square meters	m <sup>2</sup>
yd <sup>2</sup>	square yard	0.836	square meters	m <sup>2</sup>
ac	acres	0.405	hectares	ha
mi <sup>2</sup>	square miles	2.59	square kilometers	km <sup>2</sup>
<b>VOLUME</b>				
fl oz	fluid ounces	29.57	milliliters	mL
gal	gallons	3.785	liters	L
ft <sup>3</sup>	cubic feet	0.028	cubic meters	m <sup>3</sup>
yd <sup>3</sup>	cubic yards	0.765	cubic meters	m <sup>3</sup>
NOTE: volumes greater than 1000 L shall be shown in m <sup>3</sup>				
<b>MASS</b>				
oz	ounces	28.35	grams	g
lb	pounds	0.454	kilograms	kg
T	short tons (2000 lb)	0.907	megagrams (or "metric ton")	Mg (or "t")
<b>TEMPERATURE (exact degrees)</b>				
°F	Fahrenheit	5 (F-32)/9 or (F-32)/1.8	Celsius	°C
<b>ILLUMINATION</b>				
fc	foot-candles	10.76	lux	lx
fl	foot-Lamberts	3.426	candela/m <sup>2</sup>	cd/m <sup>2</sup>
<b>FORCE and PRESSURE or STRESS</b>				
lbf	poundforce	4.45	newtons	N
lbf/in <sup>2</sup>	poundforce per square inch	6.89	kilopascals	kPa

## APPROXIMATE CONVERSIONS FROM SI UNITS

Symbol	When You Know	Multiply By	To Find	Symbol
<b>LENGTH</b>				
mm	millimeters	0.039	inches	in
m	meters	3.28	feet	ft
m	meters	1.09	yards	yd
km	kilometers	0.621	miles	mi
<b>AREA</b>				
mm <sup>2</sup>	square millimeters	0.0016	square inches	in <sup>2</sup>
m <sup>2</sup>	square meters	10.764	square feet	ft <sup>2</sup>
m <sup>2</sup>	square meters	1.195	square yards	yd <sup>2</sup>
ha	hectares	2.47	acres	ac
km <sup>2</sup>	square kilometers	0.386	square miles	mi <sup>2</sup>
<b>VOLUME</b>				
mL	milliliters	0.034	fluid ounces	fl oz
L	liters	0.264	gallons	gal
m <sup>3</sup>	cubic meters	35.314	cubic feet	ft <sup>3</sup>
m <sup>3</sup>	cubic meters	1.307	cubic yards	yd <sup>3</sup>
<b>MASS</b>				
g	grams	0.035	ounces	oz
kg	kilograms	2.202	pounds	lb
Mg (or "t")	megagrams (or "metric ton")	1.103	short tons (2000 lb)	T
<b>TEMPERATURE (exact degrees)</b>				
°C	Celsius	1.8C+32	Fahrenheit	°F
<b>ILLUMINATION</b>				
lx	lux	0.0929	foot-candles	fc
cd/m <sup>2</sup>	candela/m <sup>2</sup>	0.2919	foot-Lamberts	fl
<b>FORCE and PRESSURE or STRESS</b>				
N	newtons	0.225	poundforce	lbf
kPa	kilopascals	0.145	poundforce per square inch	lbf/in <sup>2</sup>

## TABLE OF CONTENTS

<b>CHAPTER 1: INTRODUCTION.....</b>	<b>1</b>
1.1 Background.....	1
1.2 Problem Statement.....	2
1.2.1 Review of Driven Pile in IGM .....	2
1.2.2 Determination of Axial Pile Resistances.....	3
1.2.3 Static Analysis Method (SA method).....	3
1.2.4 Pile driving analyzer (PDA) & case pile wave analysis program (CAPWAP).....	4
1.2.5 Static Pile Load Test.....	4
1.2.6 LRFD calibration of resistance factors on driven piles .....	5
1.3 Report Objectives.....	6
1.4 Report Plan.....	6
1.5 Report Focus and Organization .....	7
<b>CHAPTER 2: PILE DATA COLLECTION AND ELECTRONIC DATABASE.....</b>	<b>9</b>
2.1 Introduction.....	9
2.1.1 WyoPile .....	9
2.1.2 Historical Pile Load Test Data .....	9
2.2 Database Overview .....	12
2.3 User Manual for the Electronic Database .....	14
<b>CHAPTER 3: EVALUATION OF STATIC LOAD TEST SYSTEMS FOR DRIVEN PILES IN INTERMEDIATE GEOMATERIALS.....</b>	<b>26</b>
3.1 Introduction.....	26
3.2 Site Description and Subsurface Condition .....	28
3.3 Site Description and Subsurface Condition .....	33
3.3.1 Independent Static Pile Load System (IndeSPLS).....	33
3.3.2 Integrated Static Pile Load System (InteSPLS).....	35
3.3.3 Innovative Static Pile Load System (InnoSPLS).....	36
3.4 Test Pile Preparation .....	39

3.4.1	Strain Gauge Installation.....	39
3.4.2	Strain Gauge Protection .....	39
3.5	Static Load Test Setup .....	40
3.6	Data Acquisition System.....	42
3.7	Static Load Test Results.....	43
3.8	Pile Resistance from Dynamic Load Testing and Analysis.....	52
3.9	Comparison of Dynamic and Static Load Test Results .....	56
3.10	Summary and Conclusions .....	58
<b>CHAPTER 4: DRIVEN PILES IN FINE GRAINED SOIL BASED INTERMEDIATE GEOMATERIALS .....</b>		<b>61</b>
4.1	Introduction.....	61
4.2	Overview of Pile Load Test Data.....	63
4.3	Proposed Classification Criteria for Fine Grained Soil Based IGM.....	67
4.4	Development of New Static Analysis Methods .....	69
4.4.1	Unit Shaft Resistance for Fine-Grained Soil Based IGM .....	72
4.4.2	Unit End Bearing for Fine-Grained Soil-Based IGM.....	73
4.5	Validation of Proposed Static Analysis Methods .....	74
4.5.1	Unit Shaft Resistance .....	74
4.5.2	Unit End Bearing.....	77
4.6	Calibration of LRFD Resistance Factors .....	79
4.7	Resistance and Efficiency Factors .....	83
4.8	Change in Pile Resistances .....	84
4.8.1	Change in Unit Shaft Resistance .....	84
4.8.2	Change in Unit End Bearing.....	85
4.9	Summary and Conclusions .....	88
<b>CHAPTER 5: DRIVEN PILE RESISTANCES IN COARSE GRAINED SOIL BASED INTERMEDIATE GEOMATERIALS.....</b>		<b>90</b>
5.1	Introduction.....	90
5.2	Pile load Test Data .....	92
5.3	Proposed Classification for Coarse Grained Soil-Based IGM.....	93

5.4 Development of New Static Analysis Methods .....	98
5.4.1 Prediction of Unit Shaft Resistance for Coarse-Grained Soil-Based IGMs .....	98
5.4.2 Prediction of Unit End Bearing for Coarse-Grained Soil-Based IGM.....	100
5.5 Validation of Proposed Static Analysis Methods .....	101
5.5.1 Unit Shaft Resistance .....	101
5.5.2 Unit End Bearing.....	106
5.6 Change in Pile Resistances .....	108
5.6.1 Change in Unit Shaft Resistance .....	108
5.6.2 Change in Unit End Bearing.....	110
5.7 LRFD Recommendations.....	110
5.8 Resistance and Efficiency Factors .....	111
5.9 Summary and Conclusions .....	111
<b>CHAPTER 6: DRIVEN PILE RESISTANCES IN ROCK BASED INTERMEDIATE GEOMATERIALS .....</b>	<b>113</b>
6.1 Introduction.....	113
6.2 Existing SA Methods for Prediction of Driven Pile Resistances in R-IGMs .....	115
6.3 Overview of Pile Load Test Data.....	117
6.4 New Static Analysis Methods for Resistance Prediction.....	117
6.4.1 Siltstone .....	123
6.4.2 Claystone .....	125
6.4.3 Mudstone .....	127
6.4.4 Sandstone.....	128
6.4.5 Granite .....	129
6.5 Validation of Proposed SA Methods .....	130
6.5.1 Unit Shaft Resistance .....	130
6.5.2 Unit End Bearing.....	131
6.6 Calibration of LRFD Resistance Factors .....	132
6.7 Resistance and Efficiency factor.....	133
6.8 Changes in Driven Pile Resistances.....	133
6.8.1 Unit Shaft Resistance .....	134

6.8.2 Unit End Bearing.....	140
6.9 Summary and Conclusions .....	140
<b>CHAPTER 7: DRIVEN PILES IN ROCK-BASED SHALES .....</b>	<b>142</b>
7.1 Introduction.....	142
7.2 Usable Pile Data.....	143
7.3 Shale Classification and Properties.....	144
7.3.1 Shale Classification .....	144
7.3.2 Shale Properties .....	150
7.3.3 Stress Strain Behaviors.....	151
7.3.4 Young's Modulus of Shale.....	154
7.3.5 Unconfined Compressive Strength of Shale.....	154
7.4 Development of Static Analysis Methods.....	156
7.4.1 Unit Shaft Resistance Prediction .....	156
7.4.2 Unit End Bearing Prediction .....	159
7.5 Validation of Proposed Static Analysis Methods .....	161
7.5.1 Unit Shaft Resistance Prediction .....	161
7.5.2 Unit End Bearing Prediction .....	162
7.6 Validation of Proposed Static Analysis Methods .....	165
7.7 Change in Pile Resistance in Shale .....	166
7.7.1 Change in Unit Shaft Resistance .....	166
7.7.2 Change in Unit End Bearing.....	173
7.8 Summary and conclusions .....	176
<b>CHAPTER 8: IMPROVED WAVE EQUATION ANALYSIS OF DRIVEN STEEL PILES IN INTERMEDIATE GEOMATERIALS .....</b>	<b>179</b>
8.1 Introduction.....	179
8.2 Existing Wave Equation Analysis of Pile Driving .....	180
8.3 Test Pile Data.....	183
8.4 WEAP Procedures for Bearing Graph Analysis .....	183
8.4.1 WEAP SAD Method .....	183
8.4.2 WEAP UWD Method.....	194

8.4.3 WEAP SAR Method.....	194
8.4.4 WEAP UWR Method.....	197
8.5 Back-Calculation Procedure .....	198
8.5.1 Soil Based IGM .....	198
8.5.2 Rock Based IGM .....	203
<b>8.6 Bearing Graph Analysis Results.....</b>	<b>208</b>
8.6.1 Soil Based IGM .....	208
8.6.2 Rock based IGM.....	210
<b>8.7 Validation.....</b>	<b>214</b>
8.7.1 Soil Based IGM .....	214
8.7.2 Rock Based IGM .....	218
8.8 LRFD Resistance Factors .....	225
8.8.1 Soil Based IGM .....	225
8.8.2 Rock Based IGM .....	226
<b>8.9 Summary and Conclusions .....</b>	<b>230</b>
<b>CHAPTER 9: MACHINE LEARNING BASED ECONOMIC IMPACT ANALYSIS FOR STEEL PILES DRIVEN IN INTERMEDIATE GEOMATERIALS .....</b>	<b>232</b>
9.1 Introduction.....	232
9.2 Historical Pile Load Test Data.....	233
9.3 Economic Impact Assessment .....	235
9.3.1 Methodology and Test Pile Example.....	235
9.3.2 Comparative Study of the Difference in Steel Pile Weight.....	239
9.4 Prediction of Difference in Steel Weight with Machine Learning Algorithms .....	241
9.4.1 Random Forest (RF) .....	242
9.4.2 Neural Network (NNET).....	243
9.4.3 Support Vector Machine (SVM) .....	243
9.4.4 Hyperparameter Tuning.....	243
9.4.5 Prediction Performance .....	245
9.4.6 Optimization .....	245
9.5 Summary and Conclusions .....	251

<b>CHAPTER 10: VARIABILITY ANALYSIS .....</b>	<b>253</b>
10.1 Introduction.....	253
10.2 Geological Uncertainty and Inherent Variability in Site Investigation .....	255
10.2.1 Geological Uncertainty in Site Investigation .....	255
10.2.2 Inherent Variability in Site Investigation .....	256
10.3 Methodology .....	257
10.3.1 Geological Uncertainty.....	257
10.3.2 Inherent Variability .....	259
10.3.3 Optimal Site Investigation Plan.....	262
10.4 Site Investigation Plans.....	265
10.4.1 Current Site Investigation Plan.....	265
10.4.2 Actual Site Investigation Plan .....	267
10.4.3 Optimal Site Investigation Plan.....	270
10.5 Pile foundation design.....	271
10.5.1 End-bearing resistance prediction (Geotechnical-structural uncertainties).....	271
10.5.2 Pile design using CSIP .....	272
10.5.3 Pile design using OSIP .....	272
10.5.4 Load and resistance factor design (LRFD) calibration.....	274
10.6 Cost-Benefit and Break-Even Analysis .....	278
10.6.1 Cost-Benefit Analysis.....	278
10.6.2 Break-even analysis.....	280
10.7 Practical Recommendations for Future Projects.....	281
<b>CHAPTER 11: SUMMARY, CONCLUSIONS AND RECOMMENDATIONS .....</b>	<b>283</b>
11.1 Summary .....	283
11.2 Conclusions.....	283
11.3 Recommendations.....	285
11.3.1 Classification of IGM.....	285
11.3.2 Proposed Prediction Equations and LRFD recommendations .....	285
11.3.3 Improved WEAP analysis and LRFD resistance factors.....	289
11.3.3 Economic Impact Analysis.....	290



11.4 Future Studies .....	290
<b>REFERENCES.....</b>	<b>291</b>
<b>APPENDIX.....</b>	<b>306</b>

## LIST TO FIGURES

Figure 2.1. Breakdown of the 223 Usable Test Piles Collected from the Seven States. ....	10
Figure 2.2. Breakdown of the 223 Usable Test Piles Collected According to Pile Type. ....	11
Figure 2.3. Breakdown of the 207 Usable Test Piles Collected According to Known IGMs. ....	11
Figure 2.4. Partial Screenshot of MontanaPile Showing the “Pile Load Test Records” Table. ...	12
Figure 2.5. Partial Screenshot of The MontanaPile Showing The “Average Subsurface Profile” Table. ....	13
Figure 2.6. Partial Screenshot of the MontanaPile Showing the “Nominal Unit Shaft Resistance” Table. ....	13
Figure 2.7. Partial screenshot of the MontanaPile showing the “Nominal Unit End Bearing” Table. .....	14
Figure 2.8. Partial Screenshot of the Desktop Showing All Database Files Stored on the Hard Drive of the Computer. ....	15
Figure 2.9. Partial Screenshot of MontanaPile Representing the Home Screen and Navigation Pane. ....	15
Figure 2.10. Partial screenshot of MontanaPile representing the “Pile Load Test Records” form for ID 1. ....	16
Figure 2.11. Partial Screenshot of MontanaPile Representing the “Pile Load Test Records” for Future Pile Load Test Input. ....	17
Figure 2.12. Partial Screenshot of MontanaPile Representing the “Montana Counties” Table. ..	18
Figure 2.13. Partial Screenshot of MontanaPile Representing the “Pile Type” Table. ....	19
Figure 2.14. Partial Screenshot of MontanaPile Representing the “Dynamic Test and Analysis Results” Tab in a New “Pile Load Test Records” Form. ....	22
Figure 2.15. Partial Screenshot of MontanaPile Representing the “Static Load Test Results” Tab in a New “Pile Load Test Records” Form. ....	24
Figure 2.16. Partial Screenshot of MontanaPile Representing the “Usable Test Piles” Table. ....	25
Figure 3.1. Subsurface profiles and SPT N-values at a) TP1 at Adair County, IA, b) TP2 at Wapello County, IA, c) TP3 at McKenzie County, ND, d) TP4 at Sumner County, KS, e) TP5 at Sedgwick County, KS, f) TP6 at Laramie County, WY, g) TP7 at Sweetwater County, WY,	

h) TP8 at Delta County, CO, i) TP9 at Arapahoe County CO, j) TP10 at EL Paso County, CO, and k)TP11 at Jefferson and Denver Counties, CO.....	32
Figure 3.2. Static pile load systems for IndeSPLS on TP1 in Adair County, IA.....	35
Figure 3.3. Static Pile Load System: a) InteSPLS on TP2 in Sweetwater County, WY, b) Main Reaction Beam System, c) Assembly of Spreader Beam, Main Reaction and 1.75-in Diameter HS Treated Bar, and d) A Treated Bar and Anchor Block of the InteSPLS.....	36
Figure 3.4. InnoSPLS on TP3 in Delta County, CO: a) Schematic Drawing and Elevation View of the Piles and Abutment Cap, and b) Configuration and Cross-Sectional Views of the Pile Hat. ....	38
Figure 3.5. Different Stages of InnoSPLS: a) Pile Driving, b) Pulling Strain Gauge Cables from TP3, c) Casted Abutment Cap, d) Cables Come Through PVC Pipe, e) Girders Placement, f) Deck Placement, and g) Concrete Pouring of the Deck.....	39
Figure 3.6. Equation. Micro Strain Calculation from Sensor Readings. ....	39
Figure 3.7. Equation. Stress Calculation from Strain. ....	40
Figure 3.8. Test Pile Instrumentation: a) Strain Gauge Welded on the Web Face of the Pile, b) Protection of Strain Gauge Cables with Aluminum Foils, c) Protection of Strain Gauges and Cables with Aluminum Tapes and Membranes, and d) Protection Using Steel Angles with Tapered Steel Angles Near the Pile Tip.....	40
Figure 3.9. Instruments and Equipment Used in the SLT: a) Hydraulic Jack, b) Hydraulic Pump, c) Digital Pressure Reading, d) Load Cell, e) Linear Position Transducers to Measure Test Pile Displacement, f) String Potentiometer to Measure the Upward Displacement of Reaction Piles, g) Linear Position Transducers on Reference Beams Supported by Two Ladders at the Test Pile, and h) String Potentiometer on Wooden Beam Supported by the Ladder at the Reaction or Production Pile. ....	41
Figure 3.10. Data Acquisition System: a) Multiplexer, b) 16-Channels in the Multiplexer, c) Data Logger Box, d) VW Analog Converter, e) USB Flash Drive, and f) Computer System to Collect the Readings During Testing. ....	42
Figure 3.11. Load Displacement Response: a) TP1, b) TP2 , c) TP3, d) TP4, e) TP5, f) TP6, g) TP7, h) TP8, i) TP9, j) TP10, k) TP11, and extrapolated load displacement response of l) TP8, m) TP9, n) TP10 and o) TP11.....	46

Figure 3.12. Axial load distribution along the length of piles: a) TP1, b) TP2 c) TP3, d) TP4, e) TP5, f) TP6, g) TP7, h) TP8, i) TP9, j) TP10, k) TP11. ....	52
Figure 3.13. Comparison of Total Resistance, Shaft Resistance, and End Bearing: a) TP1, b) TP2 c) TP3, d) TP4, e) TP5, f) TP6, g) TP7, h) TP8, i) TP9, j) TP10, k) TP11. ....	55
Figure 4.1. Comparison of COV and Maximum $s_u$ for the Existing $\alpha$ -method. ....	68
Figure 4.2. Proposed Classification for Fine Grained Soil-Based Geomaterial in a Flowchart. ..	69
Figure 4.3. Plot of Unit Shaft Resistance from CAPWAP Versus $s_u$ for (a) ML-IGM, (b) CL-IGM, and (c) CH-IGM. ....	71
Figure 4.4. Equation. Unit Shaft Resistance Prediction for a) ML-IGM, b) CL-IGM and c) CH-IGM. ....	72
Figure 4.5. Equation. Unit End Bearing Prediction for FG-IGM. ....	73
Figure 4.6. Plot of Unit End Bearing from CAPWAP Versus Undrained Shear Strength and a Ratio of Pile Diameter to Pile Penetration $s_u * D/D_B$ for Fine Grained Soil Based IGM. ....	73
Figure 4.7. Comparison Between Unit Shaft Resistances from CAPWAP And Predicted Unit Shaft Resistances Using (A) Proposed SA Methods, and the (B) Existing $\alpha$ -Method. The Mean and Coefficient of Variation of The Resistance Bias were also included. ....	78
Figure 4.8. Comparison Between Unit End Bearing from CAPWAP And Predicted Unit End Bearing Using the (A) Proposed SA Method and (B) Existing $\alpha$ -Method. ....	79
Figure 4.9. Resistance factor estimation based on the FOSM method .....	80
Figure 4.10. Equation. Setup Factor A Prediction. ....	84
Figure 4.11. (a) A Plot of Percent Change in Unit Shaft Resistance Against A Duration After The EOD In A Logarithmic Scale and (b) The Comparison Of Pile Setup Factor for $q_s$ and Undrained Shear Strength of FG-IGM. ....	86
Figure 4.12. (a) A Plot of Percent Change in Unit End Bearing Against A Duration After The EOD In A Logarithmic Scale and (B) The Comparison of Pile Setup Factor For $q_b$ and Undrained Shear Strength Of FG-IGM. ....	87
Figure 5.1. Comparison of COV and Maximum SPT N-Value of Each Consecutive Pile Dataset Based on the Existing $\beta$ -Method. ....	97
Figure 5.2. SH-28 Lemhi River Bridge Project Core Samples Indicate a) CG-IGM Starting From 12.5 ft, b) CG-IGM, and c) CG-IGM Terminated at 50 ft Overlaying the Bedrock. ....	97

Figure 5.3. Equation. Unit shaft resistance prediction for CG-IGM. ....	99
Figure 5.4. Relationship Between Unit Shaft Resistance from CAPWAP and $\sigma'_v N_{160}$ for a) H-piles in CG-IGM b) Pipe Piles in CG-IGM. ....	100
Figure 5.5. Equation. Unit end bearing prediction equation for CG-IGM. ....	100
Figure 5.6. Relationship Between Unit End Bearing from CAPWAP and ratio of $(N_1)_{60}$ to $\sigma'_v$ for Coarse-Grained Soil-Based IGMs. ....	101
Figure 5.7. Comparison Between Unit Shaft Resistances from CAPWAP and Predicted Unit Shaft Resistances using (a) the Proposed SA Methods and (b) the Existing $\beta$ -Method.....	102
Figure 5.8. Comparison Between Unit End Bearing from CAPWAP and Predicted Unit End Bearing using the (a) Proposed SA Method and (b) Existing $\beta$ -Method.....	107
Figure 5.9. A Plot of Percent Change in Unit Shaft Resistance in CG-IGMs Against a Duration After The EOD.....	109
Figure 5.10. Plot of Percent Change in Unit End Bearing in CG-IGMs Against a Duration After the EOD. ....	109
Figure 6.1. Equation. Unit Shaft Resistance Prediction Equation for Siltstone Based on Unconfined Compressive Strength. ....	123
Figure 6.2. Equation. Unit Shaft Resistance Prediction Equation for Siltstone Based on Corrected SPT N Value. ....	123
Figure 6.3: Equation. Unit End Bearing Prediction Equation for siltstone. ....	123
Figure 6.4. Relationship Between Unit Shaft Resistance from CAPWAP and a) Unconfined Compressive Strength and b) Corrected SPT N-Value of Siltstone. ....	124
Figure 6.5. Relationship Between Unit End Bearing from CAPWAP and the ratio of SPT N-value to Total Pile Penetration to Siltstone. ....	125
Figure 6.6. Equation. Unit Shaft Resistance Prediction Equation for Claystone. ....	125
Figure 6.7. Equation. Unit End Bearing Prediction Equation for Claystone.....	126
Figure 6.8. Relationship Between Unit Shaft Resistance from CAPWAP and Unconfined Compressive Strength of Claystone.....	126
Figure 6.9. Unit End Bearing from CAPWAP Versus Unconfined Compressive Strength.....	126
Figure 6.10. Equation. Unit Shaft Resistance Prediction Equation for Mudstone. ....	127

Figure 6.11. Relationship Between Unit Shaft Resistance from CAPWAP Versus the Combined Average SPT N-Value and Effective Vertical Stress at Mid-Depth of Mudstone Layers..	127
Figure 6.12. Equation. Unit Shaft Resistance Prediction Equation for Sandstone based on Unconfined Compressive Strength. ....	128
Figure 6.13. Equation. Unit Shaft Resistance Prediction Equation for Sandstone based on Unconfined Compressive Strength and Corrected SPT N-values. ....	128
Figure 6.14. Relationship Between Unit Shaft Resistance from CAPWAP and (a) Unconfined Compressive Strength for Sandstone Layers, (b) Product of Average Unconfined Compressive Strength and Corrected SPT N-value ( $(N_1)_{60}$ ).....	129
Figure 6.16. Equation. Unit Shaft Resistance Prediction Equation for granite. ....	129
Figure 6.17. Relationship Between Unit Shaft Resistances from CAPWAP and SPT N-Values of Granite.....	130
Figure 6.18. Comparison of $q_s$ from CAPWAP and Predicted $q_s$ based on Separate Test Piles Driven into Siltstone, Sandstone, Claystone, and Granite. ....	131
Figure 6.19. Comparison of $q_b$ from CAPWAP and Predicted $q_b$ based on Separate Test Piles Driven into Siltstone and Claystone. ....	132
Figure 6.20. Change in a) unit shaft resistance b) unit end bearing observed in different geomaterials at 24 hours after the EOD. ....	139
Figure 7.1. Stress–Strain Curves of (a) Soil-Based Shale, (b) Soft & Highly Weathered Shale, (c) Moderately Hard & Weathered shale, (d) Hard & Slightly Weathered Shale at their respective void ratios, e.....	153
Figure 7.2. Equation. Prediction Equation of Young’s Modulus for Shale.....	154
Figure 7.3. Relationships for (a) Young’s Modulus Based on the Ratio of Unconfined Compressive Strength $q_u$ to water content $\omega$ , (b) $q_u$ based on $\omega$ , and (c) $q_u$ based on SPT N-value. ....	155
Figure 7.4: Equation. Prediction Equation of Unconfined Compressive strength for shale.....	155
Figure 7.5. Equation. Prediction Equation of Unconfined Compressive Strength Based on SPT N Value. ....	156
Figure 7.6. The Unit Shaft Resistance of Piles Driven in: (a) Soil-Based Shale, (b) Soft & Highly Weathered Shale, (c) Moderately Hard & Weathered Shale, (d) Hard & Slightly Weathered Shale.....	158

Figure 7.7. Equation. Unit Shaft Resistance Prediction for a) SS Shale, b) HW Shale, c) MW Shale, and d) SW Shale.....	159
Figure 7.8. Equation. Unit End Bearing Prediction Equation for a) SS-HW Shale and b) MW-SW Shale.....	160
Figure 7.9. Relationship between unconfined compressive strength and unit end bearing of piles driven into: (a) soil based, soft & highly weathered shale, (b) moderately hard to hard & weathered to slightly weathered shale. ....	161
Figure 7.10. Comparison of Unit Pile Resistances from CAPWAP with (a) Predicted Unit Shaft Resistances, and (b) Unit End Bearing. ....	172
Figure 7.11. Percent change in the unit shaft resistance with time in logarithmic scale: (a) SS shale, (b) HW shale, (c) MW shale, (d) SW shale. ....	175
Figure 7.12. Percent change in the unit end bearing with time in logarithmic scale: (a) SS shale, (b) HW shale, (c) MW shale, (d) SW shale. ....	176
Figure 8.1. A Flowchart Showing the Input Procedures for Four WEAP Methods. ....	198
Figure 8.2. Equation. Predicting Damping Value for FG-IGM as Bearing Layer.....	200
Figure 8.3. Relationship Between Back-Calculated Damping Factor and the Product of Undrained Shear Strength and Slenderness Ratio. ....	200
Figure 8.4. Equation. Predicting Damping Value for CG-IGM as Bearing Layer. ....	201
Figure 8.5. Relationship Between Back-Calculated Damping Factor the Ratio of Pile Penetration to Corrected SPT N- Value. ....	202
Figure 8.6. Flowchart to Classify the Subsurface Conditions I, II, and III.....	203
Figure 8.7. Equation. Back Calculated Damping Factors for All R-IGM Except Shale for Subsurface Condition IV.....	203
Figure 8.8. Back-Calculated Damping Factors for Rock-Based IGMs Except Shale for Subsurface Condition IV with Respect to Slenderness Ratio and Rated Hammer Energy. ....	204
Figure 8.9. Back-Calculated Damping Factors for Rock-Based IGMs Except Shale for Subsurface Condition V with Respect to Slenderness Ratio and Rated hammer energy. ....	205
Figure 8.10. A flowchart to determine subsurface conditions IV and V. ....	206
Figure 8.11. Relationship of Back-Calculated Damping Factors for Shale with Unconfined Compressive Strength. ....	207

Figure 8.12. Relationship of Back-Calculated Damping Factors for Shale with Pile Penetration Length. ....	207
Figure 8.13. Comparison of Measured Pile Resistances from CAPWAP and Predicted Pile Resistance from WEAP for the 25 H- and 9 Pipe piles as Training Data Using (a) WEAP-SAD method, (b) WEAP-UWR method, (c) WEAP-UWD method, and (d) WEAP-SAR method.....	209
Figure 8.14. Comparison of WEAP Predicted Pile Resistance with that from CAPWAP for 72 H and 23 Pipe Training Pile Data (a) WEAP-SAD, (b) WEAP-UWR, (c) WEAP-UWD, and (d) WEAP-SAR method. ....	211
Figure 8.15. Comparison of measured pile resistances from CAPWAP and predicted pile resistances for the 22 separate pile data from (a) WEAP-SA-R, (b) WEAP-UW-R, (c) WEAP-UW-D, and (d) WEAP-SA-D method. ....	215
Figure 8.16. Comparison of Pile Resistances from Static Load Tests and CAPWAP with the Predicted Pile Resistances from WEAP Methods for the 16 Validation Test Piles Using (a) WEAP-SAD, (b) WEAP-UWR, (c) WEAP-UWD, and (d) WEAP-SAR method.....	219
Figure 9.1. Map of the Total Number of Test Piles and Total Pile Penetration Ranges in Seven US States. ....	234
Figure 9.2. Map Showing the Bearing IGM Layers For Different Test Piles and Range Of Pile Penetration in IGM in Seven US States.....	234
Figure 9.3. A Flow Chart Showing the Methodology for Economic Impact Assessment.....	237
Figure 9.4. Subsurface Profile and Geomaterial Properties for the Test Pile from the Cherry Creek Bridge on Highway 1806 in North Dakota. ....	238
Figure 9.5. Plots of Average Difference in Steel Weight based on (a) States, (b) Pile Types, and (c) Bearing IGM types with No. of Piles in Each Parenthesis. ....	240
Figure 9.6. Equations. Predictors of the Difference in Steel Weight Involving Percentage of IGM a) Length, b) Shaft, and c) End .....	241
Figure 9.7. Pairwise Relationships Among the Variables Based on 149 Test Piles.....	242
Figure 9.8. Equation. Computation of LOOCV RMSE.....	244
Figure 9.9. Equations. Prediction accuracy measures given by a) RMSE, b) MAD and c) Pseudo R <sup>2</sup> . ....	245



Figure 9.10 Contour Plots for the Optimized Values Using SVM a) percent Length was Optimized and Fixed at 31.5 percent, b) percent End was Optimized and Fixed at 36.3 percent, and c) percent Shaft was Optimized and Fixed at 43 percent.....	247
Figure 9.11. Contour Plot to predict the Difference in Steel Weight in Terms of percent Shaft, percent End and a) 10 percent Length, b) 20 percent Length c) 30 percent Length d) 40 percent Length e) 50 percent Length f) 60 percent Length g) 70 percent Length h) 80 percent Length i) 90 percent Length, and j) 100 percent Length in IGM. ....	249
Figure 9.12. Plot of the Predicted Values for SVM Based on the Test Data Versus the Observed Predicted Values from the Contour Plot Which was Originally Developed from the Training Data. ....	250
Figure 10.1. Equation. The Transition Probability. ....	257
Figure 10.2. Equation. Transition Probability Matrix. ....	258
Figure 10.3. Equation. Conditional Probability Matrix. ....	258
Figure 10.4. Equation. Information Entropy to Quantify Geological Uncertainty. ....	259
Figure 10.5. Equation. Covariance Matrix.....	260
Figure 10.6. Equation. Exponential Correlation Matrix. ....	260
Figure 10.7. Equation. Spatial Correlation Structure.....	260
Figure 10.8. Equation. Unsampld Location Prediction Equation. ....	261
Figure 10.9. Equation. Standard Deviation Prediction Equation.....	261
Figure 10.10. Flowchart of An Optimal Site Investigation Plan for Pile Design Considering Both Geological and Property Uncertainties. ....	263
Figure 10.11. Pictorial Explanation of Subsequent Recommended Borehole Selection for OSIP (Plus Sign Implies Combination and Not Summation).....	264
Figure 10.12. Pictorial Explanation of Actual and Recommended Boreholes that Determine the Optimal Number of Boreholes.....	264
Figure 10.13. Equation. Total resistance Prediction Equation.....	266
Figure 10.14. Current Site Investigation Plan used in pile design for a bridge site in Kansas, USA. ....	267
Figure 10.15. Simulated geological profile for the bridge site in Kansas, USA.....	269
Figure 10.16. Simulated geomaterial property for the bridge site in Kansas, USA. ....	269

Figure 10.17. Geostatistical Simulation of the Geomaterial Property at the Pile Location for the Design. ....	270
Figure 10.18. Equation. Unit End Bearing Prediction for Shale. ....	271
Figure 10.19. Incorporating OSIP and Geostatistical Simulation into Pile Design.....	273
Figure 10.20. Equation. Bias Prediction Equation.....	276
Figure 10.21. Resistance bias distribution comparing CSIP and OSIP incorporated into pile design. ....	277
Figure 10.22. Equation. The Probability of Failure. ....	277
Figure 10.23. Equation. The reliability Index.....	277
Figure 10.24. Equation. The Reliability Index. ....	279
Figure 10.25. Equation. The reliability index. ....	281
Figure 10.26. Relationship Between Average Savings and Cost of Additional Site Investigation Based Upon The 22 Test Piles Driven into Weathered Shale.....	281
Figure 11.1. Flowchart for Classification of Different IGM for Driven Pile Design .....	285

## LIST OF TABLES

Table 3.1 Test Pile and Bearing Layer Properties of Different SLT Systems.....	33
Table 4.1 Summary of 51 Driven Piles in Fine Grained Soil Based IGM.....	64
Table 4.2 Summary of 33 Separate Test Piles Driven into Fine Grained Soil Based IGM.....	75
Table 4.3. Normality Results of The Proposed Static Analysis Methods and Existing $\alpha$ -Method for the Estimation of Unit Shaft Resistance and Unit End Bearing in the Fine Grained Soil-Based IGM.....	81
Table 4.4. LRFD Resistance Factors and Efficiency Factors of the Proposed Static Analysis Methods and Existing $\alpha$ -Method for the Estimation of Unit Shaft Resistance and Unit End Bearing in Fine Grained Soil-Based IGM.....	82
Table 5.1 Summary of 30 Driven Piles in Coarse Grained Soil-Based IGM. ....	95
Table 5.2 Summary of 24 Separate Test Piles Driven into Coarse Grained Soil-Based IGM. ..	103
Table 5.3 Normality Results of the Proposed Static Analysis Methods and Existing $\beta$ -method for the Estimation of Unit Shaft Resistance and Unit End Bearing in Coarse-Grained Soil-Based IGM.....	104
Table 5.4 LRFD Resistance Factors and Efficiency Factors of The Proposed Static Analysis Methods and Existing $\beta$ -Method for the Estimation of Unit Shaft Resistance and Unit End Bearing in Coarse-Grained Soil-Based IGM. ....	105
Table 6.1. Existing Static Analysis Methods for the Estimation of Pile Resistances in Weak Rocks or Rock-Based IGM. ....	118
Table 6.2. Summary of 39 Driven Piles in Rock Based IGM.....	120
Table 6.3. Summary of 19 Independent Test Piles Driven into Rock-Based IGM .....	135
Table 6.4. Summary of Normality Results of the Resistance Biases Associated with Proposed Static Analysis Methods for Prediction of Unit Shaft Resistance and Unit End Bearing in Rock Based IGM.....	137
Table 6.5. LRFD Resistance Factors and Efficiency Factors of the Proposed Static Analysis Methods for the Prediction of Unit Shaft Resistance and Unit End Bearing in Rock Based IGM.....	138
Table 7.1. Summary of Usable Driven Piles in Shales from Kansas.....	146

Table 7.2. Range, Mean, and Standard Deviation of Mechanical Properties of Shales. ....	149
Table 7.3. Summary of Separate Test Pile Data Used in the Validation Study.....	163
Table 7.4. Summary of Setup Factors for Driven Piles in Shales.....	168
Table 7.5. Normality Test Results for the Proposed Static Analysis Methods for the Estimation of Unit Shaft Resistance and Unit End Bearing in Shales. ....	170
Table 7.6 LRFD Resistance Factors and Efficiency Factors of the Proposed Static Analysis Methods for the Estimation of Unit Shaft Resistance and Unit End Bearing in Shales. ....	171
Table 8.1. Summary of Smith Parameters for Soils and Rocks from Previous Studies. ....	182
Table 8.2. Summary of Historical Test Pile Data and Relevant Information for Soil Based IGM. .....	184
Table 8.3. Summary of Historical Test Pile Data and Relevant Information for Rock Based IGM. .....	187
Table 8.4. Proposed Static Analysis Methods for Predicting Unit Resistances in IGM.....	196
Table 8.5. Back-Calculated Quake and Damping Parameters for Subsurface Conditions I, II, and III.....	212
Table 8.6 Back-Calculated Quake and Damping Parameters for Subsurface Conditions IV and V. .....	213
Table 8.7 Summary of Independent Separate Test Pile Data and Relevant End of Driving (EOD) Information for Validation. ....	216
Table 8.8. Summary of Independent Test Pile Data and Relevant Information for Validation of WEAP methods.....	220
Table 8.9. Results from the Shapiro-Wilk and Anderson-Darling Tests for Soil Based IGM. ..	223
Table 8.10. Calibrated Resistance Factors for WEAP Analysis on driven piles in Soil-Based IGM. .....	224
Table 8.11 Results from the Shapiro-Wilk Test and Anderson-Darling Test.....	228
Table 8.12. Calibrated Resistance Factors for WEAP Analysis on Piles in Rock-Based IGM..	229
Table 9.1. Calculation of Difference in Steel Weight for a HP12×53 Test Pile in ND. ....	239
Table 9.2. Different Factors for the Exploration of Machine Learning Algorithms.....	244
Table 10.1. The Three Forms of Sips Used in Pile Design.....	265
Table 10.2. Summary of Test Pile Data and End-Bearing in Weathered Shale. ....	275

Table 10.3. LRFD Calibration for End-Bearing H-Piles Driven into Weathered Shale.....	278
Table 10.4. Cost-Benefit Analysis of Using OSIP and Geostatistical Simulation in Pile Design. .....	280
Table 11.1 Proposed Prediction Equations and LRFD Recommendations for Driven Piles in Soil Based IGM .....	286
Table 11.2. Proposed Prediction Equations and LRFD Recommendations for Driven Piles in Rock Based IGM .....	287
Table 11.3 Back calculated quake and damping parameters for subsurface conditions I, II, III, IV, and V .....	289
Table 11.4. Recommended Resistance and Efficiency Factors for WEAP analysis .....	290

## LIST OF ABBREVIATIONS

$s_u$ = Undrained Shear Strength

$q_u$  = Unconfined Compressive Strength

$\phi$ = Resistance Factor

$P_a$ = Atmospheric Pressure

$q_s$  = Unit shaft resistance

$(N_1)_{60}$  or  $N_{60}$  = Corrected SPT N values

$D$ = Pile dimension or diameter

$D_B$ = Total Pile penetration length

$\hat{\beta}$  =vector of estimated coefficient values

$\hat{\sigma}^2 = \text{RSE}^2$  =estimated variance

$i$  =observation,

$n$  =number of observations

$p$  =number of predictors

$y_i$  = observed response for observation  $i$

$\hat{y}_i$ = predicted response for observation  $i$

$\lambda_R, \lambda_D$  and  $\lambda_L$  = Mean Biases (list separately with description)

$\gamma_D$  and  $\gamma_L$  = Load factors (list separately with description)

$\bar{x}$ = Mean resistance bias

$\beta_T$ =Target Reliability index

$q_{s-t_o}$ =Initial Unit Shaft Resistance

$q_{s-t}$ = Unit Shaft Resistance after  $t$  Days

$R^2$  = Pseudo  $R^2$

$t_o$  =initial time

$t$ = Duration after End of Driving

$A$ = Pile Setup Factor

AASHTO = American Association of State Highway and Transportation Officials

AD = Anderson-Darling

AIC= Akaike Information Criterion

ASD = Allowable Stress Design  
ASTM = American Society for Testing and Materials  
BIC= Bayesian Information Criteria  
BOR = Beginning of Restrike  
CAPWAP = CAsE Pile Wave Analysis Program  
CDOT = Colorado Department of Transportation  
CG-IGM = Coarse Grained Soil Based Intermediate Geomaterials  
COV= Coefficient of Variation  
CSIP = Current Site Investigation Plan  
CV= Cross-Validation  
FG-IGM = Fine Grained Soil Based Intermediate Geomaterials  
FHWA = Federal Highway Administration  
FOSM = First Order Second Moment  
FORM = First Order Reliability Method  
IADOT = Iowa Department of Transportation  
IGM = Intermediate Geomaterials  
IndeSPLS = Independent Static Pile Load System  
InnoSPLS = Innovative Static Pile Load System  
ITD = Idaho Transportation Department  
InteSPLS = Integrated Static Pile Load System  
KDOT = Kansas Department of Transportation  
LOOCV = Leave One Out Cross Validation  
LRFD = Load and Resistance Factor Design  
MAD = Mean Absolute Deviation  
MDT = Montana Department of Transportation  
ML = Machine Learning  
MPP = Most Probable Point  
MSE= Mean Squared Error  
MSPT = Modified Standard Penetration Test  
NDDOT = North Dakota Department of Transportation

NGI = Norwegian Geotechnical Institute  
NNET = Neural Network  
OSIP = Optimal Site Investigation Plan  
PDA = Pile Driving Analyzer  
RF = Random Forest  
R-IGM = Rock Based Intermediate Geomaterials  
RMR = Rock Mass Rating  
RMSE = Root Mean Square Error  
RP = Reaction Piles  
RQD = Rock Quality Designation  
RSE= Residual Standard Error  
SA = Static Analysis  
SLT = Static Load Testing  
SPT = Standard Penetration Test  
SVM = Support Vector Machine  
SW = Sharpio-Wilk  
TP = Test Piles  
USCS = Unified Soil Classification System  
VW = Vibrating Wire  
WEAP = Wave Equation Analysis of Pile Driving  
WisDOT = Wisconsin Department of Transportation  
WSDOT = Washington Department of Transportation  
WYDOT = Wyoming Department of Transportation



## CHAPTER 1: INTRODUCTION

### 1.1 Background

Due to relatively shallow bedrock stratigraphy in the Rocky Mountain region and in some states in the Appalachian region, pile foundations were often driven on and into rock to support structures like bridges. The pile foundation must rely on the resistance contributed from the rock-bearing layer to attain the increasing demand in capacity from structures and to satisfy the Load and Resistance Factor Design (LRFD) strength limit state. However, this rock-bearing layer usually has high natural variability and the associated engineering characteristics may not be fully characterized. Furthermore, Intermediate GeoMaterial (IGM), also known as soft rock, is a transitional geomaterial between soil and hard rock, that is not well defined for the design and construction of driven piles. This variability creates challenges in identifying, sampling, and quantifying of IGM materials (Long and Anderson 2017). The American Association of State Highway and Transportation Officials (AASHTO 2020) acknowledges that there are currently no acceptable approaches to differentiate soft rock from hard rock for the design of driven piles. Local experience with driving piles on soft rocks is often applied to define its quality. However, limited test results were available to describe the characteristics and engineering properties of IGM (Adhikari et al. 2020).

Reliable static analysis methods have not yet been developed to estimate the pile resistance in IGM. AASHTO (2020) suggests that piles driven on soft rock should be treated in the same manner as soil. However, a past research study based on 15 steel H-piles driven in IGMs in Wyoming concluded that static analysis methods originally developed for soil provided inconsistent and conservative geotechnical resistance estimations (Ng and Sullivan 2017a). The pile load tests conducted by Long (2016) found large differences between estimated and measured pile resistances. The limitation on the estimation of pile resistances creates challenges during the pile design stage.

The resistances of piles driven in IGM are currently determined using dynamic analysis or static load tests during construction. AASHTO (2020) recommends that piles be driven based on locally developed criteria to prevent pile damage. The Wisconsin Department of Transportation

(WisDOT) revealed that steel H-piles have been found to either run longer than the design length or be damaged during driving when a higher pile driving criterion was established (Long and Anderson 2017). WisDOT acknowledged that there were still unknowns with both the design and construction of steel H-piles in IGM. In Wyoming, pile driving was terminated when a target nominal pile resistance was achieved at the planned depth, as determined from the Wave Equation Analysis Method (WEAP) on all production piles. The Pile Driving Analyzer (PDA), with subsequent signal matching analysis using the CAsE Pile Wave Analysis Program (CAPWAP), was used as a construction control method on about two percent of the production piles. PA/CAPWAP tests are recommended in bridge projects experiencing relatively high load demand and soft rock bearing. For bridge projects with piles driven in IGM in Wyoming from 2012 and 2015, the performance of some production piles was considered reliability in accordance with the LRFD strength limit state recommended by AASHTO (Ng and Sullivan 2017b).

These limitations exaggerate the uncertainty of the subsurface condition, or the discrepancy between estimated and measured pile resistances, which increases the difficulty in establishing criteria to differentiate IGM from hard rocks. These factors can reduce the accuracy of pile resistance estimation, result in lower LRFD resistance factors, and eventually increase the construction cost.

## **1.2 Problem Statement**

### ***1.2.1 Review of Driven Pile in IGM***

AASHTO (2020) suggests using the existing static analysis method for predicting driven pile resistances in IGM. Structural capacity has been considered the limiting capacity for the pile driving in hard rocks. However, the driven pile resistances may be underestimated if IGMs are treated as soil. Ng and Sullivan (2017a) showed that the calculated resistance biases (i.e., ratio of measured to estimated pile capacity) of 15 steel H-piles driven in IGMs in Wyoming varied from 2 to 21. This comparison highlights the existing gap in the design methodologies of driven piles in IGM. Most deep foundation studies in IGM have focused on drilled shafts and minimal literature were found on the driven piles (O'Neill et.al 1999). Mokwa and Brooks (2008)

investigated the capacity of piles driven into IGM in Montana and demonstrated that considerable differences exist between predicted capacities using conventional methods and measured capacities with CAPWAP. The pile capacities were predicted using dynamic formulas like the Federal Highway Administration (FHWA) Gates driving formula, Washington Department of Transportation (WSDOT) Gates driving formula, an empirical method used by the Colorado Department of Transportation (CDOT), and computer programs like DRIVEN and GRLWEAP (Mokwa and Brooks 2008). Mokwa and Brooks (2008) also acknowledged that the challenge associated with the accurate prediction of the pile capacity in IGM was attributed to the difficulties with obtaining representative IGM samples. In the absence of quality samples, representative material properties were difficult to determine.

### ***1.2.2 Determination of Axial Pile Resistances***

Total axial capacity is the sum of shaft resistance and end bearing experienced by a pile. Axial pile capacity is determined by using various static analysis methods during the design stage to estimate a pile length. The dynamic techniques are used for the verification of the designed pile capacity. Along with verifying pile capacity, dynamic methods can be used for pile construction control, detection of pile damage, evaluation of driving hammer performance, assessment of soil resistance distribution, determination of dynamic soil parameters, and evaluation of time-dependent pile capacity. Different methods are now being routinely used and have been incorporated into a standard specification for deep pile foundations by the American Society for Testing and Materials (ASTM D4945-2008). The most prevalent dynamic analysis methods are PDA and CAPWAP.

### ***1.2.3 Static Analysis Method (SA method)***

Static analysis methods are very important for driven pile design. There are five available Static Analysis (SA) methods for predicting the total axial capacity of driven piles in soil (AASHTO 2020). They are usually used to determine the most cost-effective pile type and estimate the contact lengths in the design phase. The  $\alpha$ -method (Tomlinson 1980) is suitable for predicting pile resistance in cohesive soil, and the main soil parameter is an undrained shear strength. The  $\beta$ -method (Esrig et al. 1981) is used to estimate the pile resistance in cohesionless soil and

layered soil, where the main parameters are friction angle of soil and vertical effective stress. The Nordlund (Nordlund 1979) method is an effective stress analysis method that is used to estimate both shaft resistance and end bearing of a pile in cohesionless soil. The Standard Penetration Test (SPT) method (Mayerhof 1976) uses in-situ SPT N values to calculate the pile resistance. The Lambda method calculates only the shaft resistance of a pile using undrained shear strength and overburden effective vertical stress.

#### ***1.2.4 Pile driving analyzer (PDA) & case pile wave analysis program (CAPWAP)***

The PDA is a data acquisition system that uses the Case Method developed at the Case Western Reserve University to estimate total pile capacity, investigates soil resistance as a function of time, assesses soil resistance distribution, evaluates pile integrity, and assesses driving system performance. The measurement of pile strains and accelerations used in the Case Method is fulfilled by a pair of transducers and accelerometers fitted near a pile top. PDA converts the strain to force and acceleration to velocity generated at every hammer impact on the test pile during pile driving as a function of time. The PDA force and velocity records are inputted into the CAPWAP to determine the static shaft resistance and end bearing, the load settlement curve, and the dynamic soil parameters (i.e., quake and damping factors). CAPWAP is a signal matching technique that adjusts the soil static resistance at each soil segment, soil quake, the Smith damping factor ( $J_s$ ), and the Case damping factor ( $J_c$ ) until the computed signal matches the measured signal from PDA. Nowadays, the dynamic analysis method is popular for driven pile capacity estimation due to time requirements and cost-effectiveness, but the static load test is still warranted to validate the dynamic load test results, particularly for IGM. Another drawback is that pile capacities determined from the signal matching technique analysis heavily depends on the assumptions made by the user analyzing the test results (Verbeek et al. 2015).

#### ***1.2.5 Static Pile Load Test***

The Static Load Test (SLT) provides the most reliable relationship of load settlement response of a pile foundation. These test results can also provide information on side shear resistance along the pile shaft and end bearing at the pile toe. After applying the appropriate resistance factor of 0.8, as suggested by AASHTO (2020), an engineer can determine whether the capacity and

deflection are adequate to support the structure. The static load test can also ensure improved pile performance and can be used to validate the dynamic load test results. Though this method is time consuming and costly, SLT is warranted for driven piles in IGM to ensure proper recommendations and guidelines. Adhikari et al. (2020) compare CAPWAP and SLT test results of 25 driven piles in IGM resulted in a means bias of 1.01. However, reported SLT test results for 7 test piles of Wisconsin, by Long (2016), only provide the total ultimate capacity of the driven piles, and the ultimate capacities were determined based on Davisson criterion. For the test piles, neither unit shaft resistance of each geomaterial layer, nor unit end bearing was reported. Among them, the load settlement response of one test pile did not cross the Davisson line, and the ultimate capacity of the load cell was taken as the ultimate capacity of the pile (Long 2016). Davisson was a gradual failure method, and other pile failure methods have been used. For example, the plunging failure method includes the Chin Kodner method, De court extrapolation method, and 80 percent Brinch Hanson method. The settlement-based method includes 5 percent of pile width to diameter, 10 percent of pile width to diameter, and 1-inch displacement. More extensive research is necessary to determine which failure criteria were suitable for driven piles in IGM.

#### ***1.2.6 LRFD calibration of resistance factors on driven piles***

The geological, design, and construction uncertainties can be incorporated in the calibration of LRFD resistance factors for a particular target reliability index. Different probability-based methods like FOSM, First Order Reliability Method (FORM), and MCS have been used to calculate LRFD resistance factors. FOSM is one of the analytical methods used to calculate the probability of failure. The limit state function was expanded using Taylor series where only the first-order terms were retained. Taylor series was used to approximate the function as the sum of terms involving derivatives of that function at a single point. As only first-order terms of Taylor series expansion are retained in FOSM, the process is called the linearization of the function at the point considered. In FOSM, linearization is carried out at the mean values of the random variables involved in the limit state function. On the other hand, in FORM, linearization is carried out at some design points called the most probable point (MPP) lying on the failure surface instead of the mean values. To find the MPP, the variables are first transformed into

standard normal variables (having mean zero and unit standard deviation). While changing the variables into standard normal variables, the probability density functions, and the cumulative distributions of the actual normal distributions are kept equal. Then, the point on the failure surface is located using optimization techniques such that it lies at the shortest distance from the origin. Iterations are generally adopted for finding MPP, and the shortest distance from the basis of the standard normal variation to the MPP was the reliability index. MCS is the technique used to generate random numbers according to the distribution of the random variables, which facilitates the calculation of the probability of failure and the reliability index. MCS does not require the location of the design point, and rather the data need to be fit in the region of the design point (Allen, 2005).

### **1.3 Report Objectives**

The overall goal of the report was to develop a comprehensive field load test program and LRFD recommendations for driven piles into intermediate geomaterials to reduce construction and improve reliability. The main objectives of this research were to:

- Develop the classification criteria for IGM for driven pile design.
- Develop new static analysis methods to predict the resistance of piles driven to different intermediate geomaterials.
- Determine static pile responses in IGM and evaluate the performance of dynamic analysis methods through a static pile load test program.
- Predict driven pile resistance based on cavity expansion theory.
- Calibrate LRFD resistance and efficiency factors of piles driven into different intermediate geomaterials, accounting for design and construction uncertainties.
- Evaluate the change in pile resistances with time for efficient pile design.
- Improve the prediction of economic performance using machine learning algorithms to mitigate the existing challenges with piles driven in IGM.

### **1.4 Report Plan**

The report objectives were accomplished by completing 10 tasks. The first task was to develop the electronic database of IGM for driven pile design. The second task was to evaluate different

static pile loads for driven piles in IGM. The third research task was to develop classification of IGM. The fourth task was to evaluate the static pile load for driven piles in IGM. The fifth task was to develop new static analysis methods and LRFD recommendations for soil-based IGM. The sixth task was to develop new static analysis methods for different rock based IGM. The seventh task was to improve the Wave Equation Analysis of pile driving for IGM. The eighth task was to assess the economic impact of driven piles in IGM. The ninth task was to consider site variability and uncertainty for driven pile design. The tenth task was to provide engineers with recommendations for driven pile design in IGM.

### **1.5 Report Focus and Organization**

This report consists of ten chapters. The name and a brief overview of each chapter are presented below.

- Chapter 1 of this report presents background information and the relevant literature to build the required body of knowledge and understand the different aspects of this study.
- Chapter 2 describes the pile data collection and electronic database consisting of collected data from seven state DOTs: Wyoming, Colorado, Montana, Kansas, Idaho, Iowa, North Dakota.
- Chapter 3 evaluates the three different static pile load systems: independent, integrated, and innovative for driven piles in intermediate geomaterials. It also provides test pile instrumentation, data collection, and residual driving force analysis. The comparison with the dynamic load test results with static load test will help engineers to select the acceptable static pile load system for driven piles in intermediate geomaterials.
- Chapter 4 describes the design of driven piles for fine grained intermediate geomaterials: classification of fine-grained soil based IGM (FG-IGM) from fine grained geomaterials, statistical analysis and development of new static analysis methods for different FG-IGM, validation of proposed static analysis methods, development of LRFD resistance factors, and changes in driven resistances with time.

- Chapter 5 shows resistance response and design recommendations for driven piles in coarse grained IGM (CG-IGM): the methodology and statistical analysis to classify the CG-IGM, development of new static analysis methods, resistances for driven pile design. The efficient design methodologies were provided with newly calibrated LRFD resistance factors and changes in pile resistances.
- Chapter 6 describes the reliability-based design improvement and prediction of steel driven pile resistances in rock-based intermediate geomaterials.
- Chapter 7 describes the driven pile design in shale considering weathering effects.
- Chapter 8 demonstrates the procedure of improved wave equation analysis of pile driving and developing new damping parameters for driven piles in IGM.
- Chapter 9 demonstrates the machine learning based economic impact analysis for piles driven in intermediate geomaterials based on proposed static analysis methods developed in Chapters 2, 3, and 4 for different intermediate geomaterials. It also provides guidelines to enhance the pile performance in IGM for future bridge projects.
- Chapter 10 provides the site variability and uncertainty for driven pile design and design in IGM.
- Chapter 11 provides conclusions and recommendations regarding the objectives of this research.



## **CHAPTER 2: PILE DATA COLLECTION AND ELECTRONIC DATABASE**

### **2.1 Introduction**

Pile data were collected for developing foundation design. The accuracy and cost-effectiveness of a design were dependent on sample size and data reliability. However, data collection for geotechnical and structural analyses can be expensive and time-consuming (Machairas et al., 2018). Another challenge was to have the data collected in available databases in an organized and easily accessible format to be used as an information source for design, research, and development. Other desirable features of an electronic database include high quality and complete data, system flexibility, user-friendly interface, maintenance, and online accessibility (Abu-Hejleh et al., 2015). There have been attempts to organize pile load test data using electronic database systems. An example is the WyoPile briefly discussed below.

#### ***2.1.1 WyoPile***

The database, WyoPile (Ng et al. 2019), was developed using the dynamic load tests of 45 test piles provided by the Wyoming Department of Transportation (WYDOT) from 17 bridge projects and 1 building project. This database collected information on site location, subsurface conditions, pile type and location, hammer information, pile driving information, and pile resistance from a dynamic load test. The database was created as a part of a research study to develop static analysis methods for piles driven in IGM, and regional-specific LRFD resistance factor calibration.

#### ***2.1.2 Historical Pile Load Test Data***

Like the WyoPile database developed for dynamic load test of driven H-piles from Wyoming, a comprehensive database was developed in this study for other transportation agencies: CDOT, Montana Department of Transportation (MDT), North Dakota Department of Transportation (NDDOT), Idaho Transportation Department (ITD), Iowa Department of Transportation (IADOT), and Kansas Department of Transportation (KDOT). Additional test piles from WYDOT were added to the WyoPile database. Information on driven test piles from the corresponding states was also collected. In general, the collected information consisted of

hardcopy Portable Document Format (PDF) reports as well as digital reports set out as EXCEL spreadsheets. The complete information for a pile load test included the project plan, pile information, driving records, hammer information, load test results (end of initial driving (EOD), beginning of restrike (BOR), and subsurface information (geotechnical reports or boring logs). Test piles with complete information were considered usable, whereas those with incomplete information were rendered as non-usable. The pile penetration depths in the load test reports were matched with the subsurface information using the pile bottom elevation and cutoff elevation from the design plan of the construction project.

A total of 393 test piles were collected from the 7 state DOTs. A total of 223 test piles were usable. The breakdown of these usable piles by DOT is shown in Figure 2.1. Of the 223 usable test piles, 207 were driven in IGM and the breakdown is shown in Figure 2.3. The most common IGM was shale. In addition, a few test piles were driven into granite, breccia, granodiorite, and quartzite.

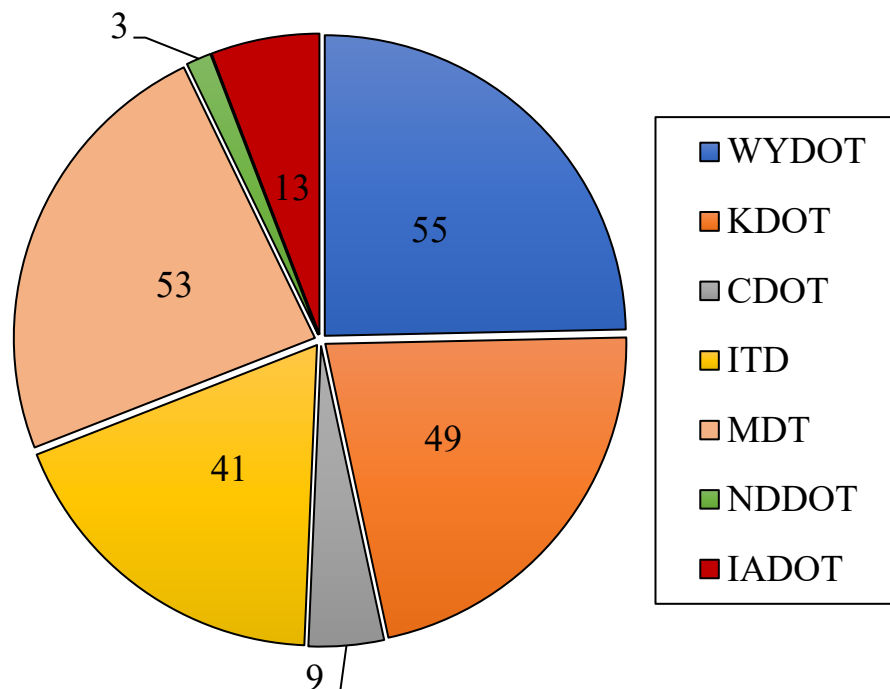


**Figure 2.1. Breakdown of the 223 Usable Test Piles Collected from the Seven States.**

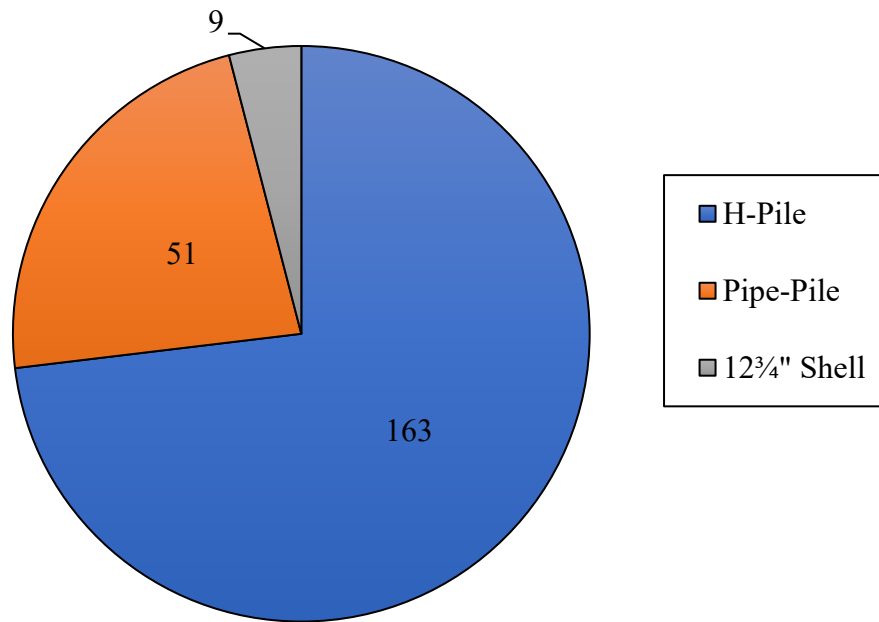


**Figure 2.2. Breakdown of the 223 Usable Test Piles Collected According to Pile Type.**

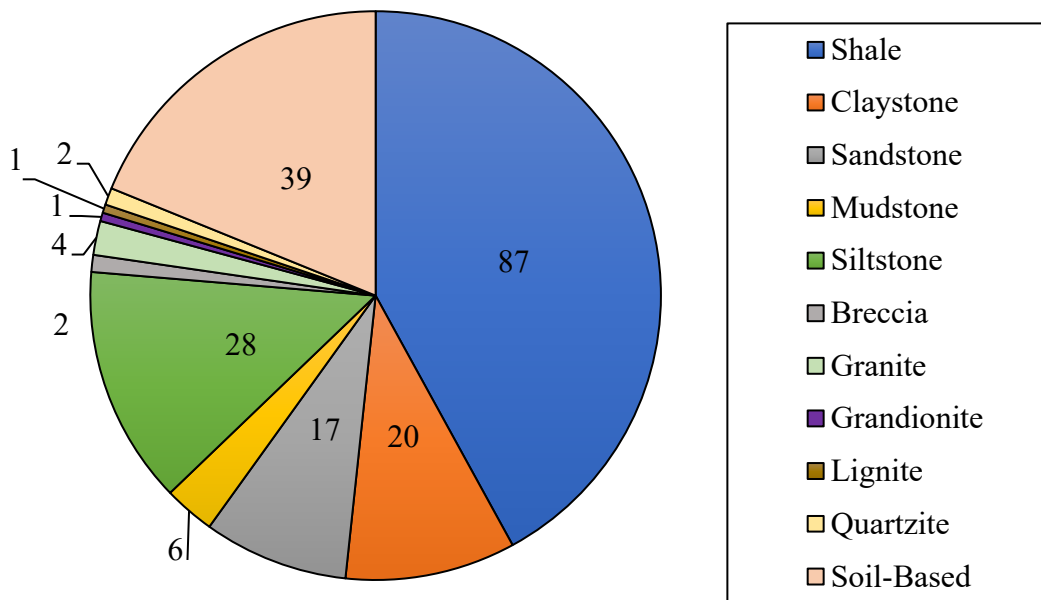


**Figure 2.3. Breakdown of the 207 Usable Test Piles Collected According to Known IGMs.**

## 2.2 Database Overview

Microsoft<sup>TM</sup> Access (Access) provides a user-friendly and easy-to-use tool for creating the database. The Access database and the user manual are described in this chapter using the database created for the Montana Department of Transportation (MDT), which is known as MontanaPile. The organization and the use of the database was propagated similarly across the database created for other state transportation agencies. The database consists of four major sections to describe the test pile records: pile test records, average subsurface profile, nominal unit shaft resistance, and nominal unit end bearing. Figure 2.4 shows a partial screenshot of the MontanaPile to represent the layout of the “Pile Load Test Records”. The “Pile Load Test Records” consist of the general information regarding the driven test piles such as pile id, project number, state, county, project name or bridge/structure, pile location, LRFD factored design load, pile type, date of driving, pile elevation, and driving information such as hammer type, stroke height, blow count, CAPWAP measured capacity at each EOD, and subsequent restrikes. The test pile reports, and subsurface information reports are attached to this section for detailed inspection.

ID	Project Number	State	County	Bridge/Structure	Pile Location	LRFD Factored load	Pile Type	Date Driven
1	STPB 44303(2)	MT	Rosebud	Bridge Over Butte Creek	Bent 1, Pile 4	457	conical point	8/6/20
2	STPB 9003(50)	MT	Blaine	Milk River - 4 KM West Of Zurich	Bent 1, Pile 1	560	P with 0.5" w	6/19/20
3	STPB 9003(50)	MT	Blaine	Milk River - 4 KM West Of Zurich	Bent 2, Pile 6	500	le fit cut shoe	5/22/20
4	STPB 9003(50)	MT	Blaine	Milk River - 4 KM West Of Zurich	Bent 3, Pile 1	560	le fit cut shoe	4/17/20
5	BR 81-1(11)34	MT	Fergus	Bridge Over Warm Spring Creek	Bent 1	1057	P with 0.75" w	8/15/20
6	BR 81-1(11)34	MT	Fergus	Bridge Over Warm Spring Creek	Bent 2	1057	P with 0.75" w	8/20/20
7	BR 253-1(11)4	MT	Prairie	Bridge Over Cherry Creek	Bent 1, Pile 2	674	P with 0.5" w	

**Figure 2.4. Partial Screenshot of MontanaPile Showing the “Pile Load Test Records” Table.**

The next section of the database consists of the average subsurface profile. Figure 2.5 shows a partial screenshot of the MontanaPile showing the “Average Subsurface Profile” Table. In this section, the subsurface profile obtained from the respective boring logs are shown as individual layers. The section includes layer number, pile id (record id), geomaterial type, descriptions provided in the boring logs or geotechnical reports, the thickness of the individual geomaterial layers, and relevant geomaterial properties such as SPT N-value (i.e., SPT hammer blow count in the last 12 inches),  $q_u$ ,  $s_u$ , cohesion, friction angle, RQD for rock geomaterial. These subsurface layers were extracted from the nearest boring logs by matching the pile top and toe elevations from the driving information provided in the dynamic load test reports. The dynamic load test

results were used to match the pile resistances measured to the individual geomaterial layers to determine the unit shaft resistance and unit end bearing of those layers.

Average Subsurface Profile								
Record ID	State	Layer	Geomaterial	Description	Thickness (ft)	SPT N	qu (ksf)	Su (ksf)
1	MT	1	Sandy Lean CLAY (CL)	stiff, dry, brown, Occasional Orange stain	1.74	7		2.473
1	MT	2	Poorly Graded Gravel With Sand (GP)	medium dense, dry, tan, fine to coarse grained, r	3.5	27		
1	MT	3	Poorly graded SAND with gravel (SP)	medium dense, dry to wet, tan, fine to coar	13.899	13		
1	MT	4	CLAYSTONE	gray, very soft field hardness	5.8	79	10.656	
1	MT	5	CLAYSTONE	gray, very soft field hardness	3.4		15.84	
2	MT	1	SAND (SM)	very loose to loose dry to wet, tan, fine, grai	18.3	6		
2	MT	2	Fat CLAY (CH)	medium, stiff, moist, brown	5.5	7		2.473
2	MT	3	Silty, Clayey SAND (SC-SM)	Loose, moist to wet. Brown	10	6		
2	MT	4	Sandy SILT (ML)	fine to medium dense, wet, gray to tan, fine	20.5	17		4.684
2	MT	5	Sandy Lean CLAY (CL)	Very stiff, moist, brown	15	21		5.453
2	MT	6	Sandy CLAYSTONE	medium, medium bedded, soft field hardness, o	7	100	56.34	
2	MT	7	SANDSTONE	medium, medium bedded, thickly bedded, medium field h	4	167		
2	MT	8	Sandy CLAYSTONE	medium, medium bedded, soft field hardness, C	1.9		163.1	
3	MT	1	Sandy Lean CLAY (CL)	Medium stiff to stiff, wet, gray	14.099	13		3.861
3	MT	2	Poorly graded SAND (SC)	medium, dense, wet, brown	10.5	12		
3	MT	3	Silty SAND with Gravel (SM)	medium dense to dense, wet, gray	22	25		
3	MT	4	Sandy CLAYSTONE	medium, medium bedded, very soft to medium fi	3.7		56.304	

**Figure 2.5. Partial Screenshot of The MontanaPile Showing The “Average Subsurface Profile” Table.**

The measured CAPWAP resistances were then updated for the database in the “Nominal Unit Shaft Resistance” and “Nominal Unit End Bearing” sections represented by the partial screenshots of MontanaPile, in Figures 2.6 and 2.7, respectively.

Average Subsurface Profile								
Nominal Unit Shaft Resistance								
Pile Rec ID	Layer	State	Geomaterial	Thickness (ft)	CAPWAP(ksf)	Remarks		
1	1	MT	Sandy Lean CLAY (CL)	1.74	0.28			
1	2	MT	Poorly Graded Gravel With Sand (GP)	3.5	0.28			
1	3	MT	Poorly graded SAND with gravel (SP)	13.9	0.64			
1	4	MT	CLAYSTONE	5.8	1.15			
1	5	MT	CLAYSTONE	3.4	1.27			
2	1	MT	SAND (SM)	18.3	0.12			
2	2	MT	Fat CLAY (CH)	5.5	0.25			
2	3	MT	Silty, Clayey SAND (SC-SM)	10	0.1			
2	4	MT	Sandy SILT (ML)	20.5	0.1			
2	5	MT	Sandy Lean CLAY (CL)	15	0.59			
2	6	MT	Sandy CLAYSTONE	7	2.28			
2	7	MT	SANDSTONE	4	3.6			
2	8	MT	Sandy CLAYSTONE	1.9	3.6			

**Figure 2.6. Partial Screenshot of the MontanaPile Showing the “Nominal Unit Shaft Resistance” Table.**

Record ID	State	Bearing Layer Geomaterial	CAPWAP(ksf)	C
1	MT	CLAYSTONE	369	
2	MT	Sandy CLAYSTONE	245.75	
3	MT	Sandy CLAYSTONE	368.1	

**Figure 2.7. Partial screenshot of the MontanaPile showing the “Nominal Unit End Bearing” Table.**

### 2.3 User Manual for the Electronic Database

The user manual provides detailed step-by-step information on how to access and use the electronic database for each of the seven states, namely WyoPile for WYDOT, IowaPile for IADOT, IdahoPile for IDT, NorthDakotaPile for NDDOT, ColoradoPile for CDOT, and KanasPile for KDOT. Access must be installed on a computer to use one of these databases. The database can be accessed by opening the database files from any location on the computer, such as the desktop, hard drive, USB flash drive, or network drive. As an example, the database files are shown in the partial screenshot in Figure 2.8. The database was designed such that the home screen of the database always shows the “Pile Load Test List” form and navigation pane window, that acts as the access point of all other tables and forms. Figure 2.9 shows the home screen for the database along with different tables, forms, and queries attached to the database. Each table, form, or query can be accessed individually by double clicking the respective “object” in the navigation pane. All the general information was stored and can be accessed from the “Pile Load Test List” form. Additional information was stored in specific tables and forms. To view the detailed information of the individual test pile, “ID” can be clicked to open the “Pile Load Test Records” form. The “Pile Load Test Records” form for “ID 1” was shown in Figure 2.10. All the information such as “Subsurface Profile”, “Nominal Shaft Resistance”, “Nominal Unit End bearing”, “Driving Information”, “Dynamic Test Analysis Result”, and “Static Load Test Result” can be accessed as individual tabs as shown in Figure 2.11.



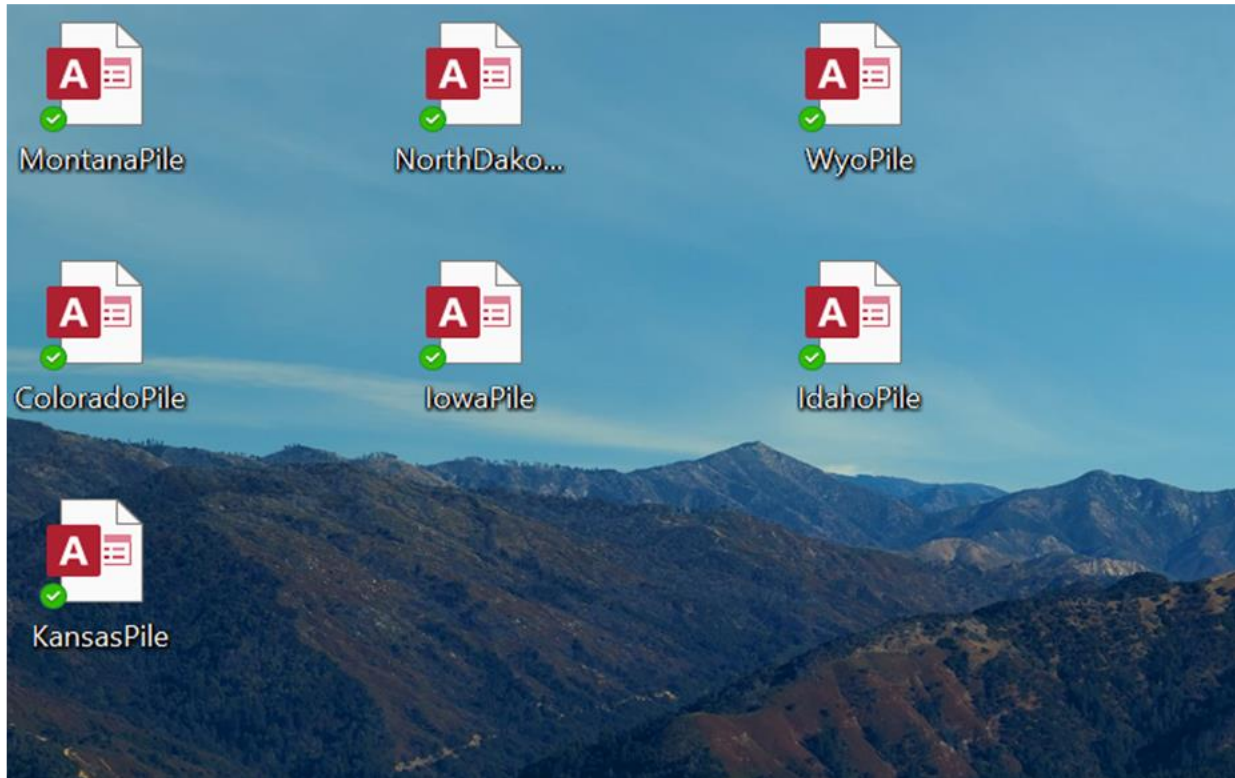


**Figure 2.8. Partial Screenshot of the Desktop Showing All Database Files Stored on the Hard Drive of the Computer.**

ID	County	Project Number	Pile Type	Design Load (kip)	Date Driven	Pile Toe Elevation	Pile embedment at EOD (ft)
1	Rosebud	STPB 44303(2)	16" steel pipe pile with conical point with 0.5" wall thickness	457	8/6/2015	2460.1	28.34
2	Blaine	STPB 9003(50)	16" steel OEP with 0.5" wall thickness	560	6/19/2018	2305.7	82.2
3	Blaine	STPB 9003(50)	16" steel OEP with inside fit cut shoe with 0.5" wall thickness	500	5/22/2018	2311.6	50.3
4	Blaine	STPB 9003(50)	16" steel OEP with inside fit cut shoe with 0.5" wall thickness	560	4/17/2018	2312.6	76.2
5	Fergus	BR 81-1(11)34	24" steel CEP with 0.75" wall thickness	1057	8/15/2007	3560.4	46.3
6	Fergus	BR 81-1(11)34	24" steel CEP with 0.75" wall thickness	1057	8/20/2007	3569.5	35.3
7	Prairie	BR 253-1(11)34	20" steel OEP with 0.5" wall thickness	674			
8	Prairie	BR 253-1(11)34	24" steel CEP with 0.75" wall thickness	832	3/21/2007	2251.31	57.97
9	Musselshell	STPB 9033(27)	16" steel OEP with inside fit cut shoe with 0.5" wall thickness	455	7/11/2017	2896.5	32.7
10	Lewis & Clark	IM-NHPB 15-4(128)192	HP 14 X 117				
11	Lewis & Clark	IM-NHPB 15-4(128)192	16" steel pipe pile with conical point with 0.5" wall thickness				
12	Lewis & Clark	IM-NHPB 15-4(128)192	16" steel pipe pile with conical point with 0.5" wall thickness				
13	Lewis & Clark	IM-NHPB 15-4(128)192	16" steel pipe pile with conical point with 0.5" wall thickness				
14	Lewis & Clark	IM-NHPB 15-4(128)192	16" steel pipe pile with conical point with 0.5" wall thickness				
15	Lewis & Clark	IM-NHPB 15-4(128)192	16" steel pipe pile with conical point with 0.5" wall thickness	700	6/6/2016	3927	29.47
16	Lewis & Clark	IM-NHPB 15-4(128)192	16" steel pipe pile with conical point with 0.5" wall thickness	670	5/3/2016	3905.2	32.16
17	Lewis & Clark	IM-NHPB 15-4(128)192	16" steel pipe pile with conical point with 0.5" wall thickness	650	5/11/2016	3912.4	48.47
18	Lewis & Clark	IM-NHPB 15-4(128)192	16" steel pipe pile with conical point with 0.5" wall thickness	700	3/27/2017	3927.5	29
19	Lewis & Clark	IM-NHPB 15-4(128)192	16" steel pipe pile with conical point with 0.5" wall thickness	700	3/27/2017	3928.5	27.98
20	Lewis & Clark	IM-NHPB 15-4(128)192	16" steel pipe pile with conical point with 0.5" wall thickness	670	5/9/2017	3909.9	27.5
21	Lewis & Clark	IM-NHPB 15-4(128)192	16" steel pipe pile with conical point with 0.5" wall thickness	650	4/10/2017	3912.8	48.2
22	Golden Valley	BR 9019(12)	16" steel OEP with inside fit cut shoe with 0.5" wall thickness	638	12/14/2011	3459.9	27.5
23	Valley	BR 9053(104)	20" steel OEP with 0.5" wall thickness	610	9/13/2013	2413.8	45
24	Valley	BR 9053(104)	20" steel OEP with 0.5" wall thickness	370	9/18/2013	2422.1	41
25	Valley	STPB 31-1(18)39	16" steel OEP with 0.5" wall thickness	315	11/7/2017	2834.6	47.3
26	Valley	STPB 31-1(18)39	20" steel OEP with 0.5" wall thickness	455	11/7/2017	2833.2	46.2
27	Fallon	STPS 336-1(3)0	HP 12 X 74		4/5/2016	3084.7	34.5
28	Fallon	STPS 336-1(3)0	HP 12 X 74		8/8/2016	3044.5	57
29	Judith Basin	BR 9023(12)	HP 12 X 84		5/25/2006	3867.45	
30	Rosebud	STPIP 14-6(11)207	16" steel pipe pile with umb nosed conical point with 0.5" wall thickness	640	10/24/2018	2832.5	42.2
31	Rosebud	STPIP 14-6(11)207	16" steel OEP with inside fit cut shoe with 0.5" wall thickness	415	3/18/2019	2811.6	25

**Figure 2.9. Partial Screenshot of MontanaPile Representing the Home Screen and Navigation Pane.**

File Load Test Records

UNIVERSITY of WYOMING

MONTANA MDTA DEPARTMENT OF TRANSPORTATION

## Pile Load Test Record Form

All Record Data Entered? ☒

[Print](#) [Close](#)

ID:  Project No.

County:  State:

Bridge/Structure:

Pile Location:

1. Pile Size..... 16" steel pipe pile with conical point with 0.5" wall thickness

2. Date Driven..... 8/6/2015

3. LRFD Pile Load (kips)..... 457

4. ASD Load (kip).....

5. Type of Hammer Used..... Delmag D19-32/42

6. Pile Embedment at EOD (ft)..... 28.34

7. Elevation at the Top of the Test Pile (ft)..... 2488.44

8. Elevation at the Bottom Tip of the Test Pile (ft)..... 2460.1

Subsurface Profile Nominal Unit Shaft Resistance (ksf) Nominal Unit Endbearing (ksf) Driving Information Dynamic Test and Analysis Results Stati

Average Subsurface Profile

Layer	Geomaterial	Description	AAI
1	Sandy Lean CLAY (CL)	Medium stiff, dry, brown, Occasional Orange staining noted	
2	Poorly Graded Gravel With Sand (GP)	Medium dense, dry, tan, fine to coarse grained, rounded	
3	Poorly graded SAND with gravel (SP)	Medium dense, dry to medium dense, dry to wet, tan, fine to coarse grained	
4	CLAYSTONE	gray, very soft field hardness	
5	CLAYSTONE	gray, very soft field hardness	

Record: 1 of 5

9. Ground Surface Elevation (ft)..... 2495.7

10. Water Table Elevation (ft)..... 2469.7

Record Comments:

Attachments (1):  
[Montana Test File R](#)

Attachments (2):

**Figure 2.10. Partial screenshot of MontanaPile representing the “Pile Load Test Records” form for ID 1.**

The main form also includes a “New Pile Load Test” tab, which is shown in Figure 2.9, and which can be clicked to access an input form for future pile load tests. All information input on that form automatically spreads over the tables and forms across the database. A sample of this form is presented as a partial screenshot in Figure 2.10. There was an option to print the pile test record using a “Print” tab in each “Pile Load Test Record” form, as shown in Figure 2.11. It is recommended to print the data in a landscape paper layout. Also, disclaimers for all the databases were in the “Disclaimer” tab at the right-hand top of the “Pile Load Test List” form, which was shown in Figure 2.9.



The screenshot shows the 'Pile Load Test Record Form' interface. At the top, there are logos for the University of Wyoming and Montana MDTA Department of Transportation. A red banner at the top right says 'Pile Load Test Record Form'. Below this, a status bar indicates 'All Record Data Entered?' with a blue icon. The form contains several input fields and sections:

- Form Fields:**
  - ID: [New]
  - Project No. [ ]
  - County: [ ] State: [ ]
  - Bridge/Structure: [ ]
  - Pile Location: [ ]
  - 1. Pile Size: [ ]
  - 2. Date Driven: [ ]
  - 3. LRFD Pile Load (kips): [ ]
  - 4. ASD Load (kip): [ ]
  - 5. Type of Hammer Used: [ ]
  - 6. Pile Embedment at EOD (ft): [ ]
  - 7. Elevation at the Top of the Test Pile (ft): [ ]
  - 8. Elevation at the Bottom Tip of the Test Pile (ft): [ ]
  - 9. Ground Surface Elevation (ft): [ ]
  - 10. Water Table Elevation (ft): [ ]
- Subsurface Profile Section:**
  - Tabs: Subsurface Profile | Nominal Unit Shaft Resistance (ksf) | Nominal Unit Endbearing (ksf) | Driving Information | Dynamic Test and Analysis Results | Status
  - Table: Average Subsurface Profile

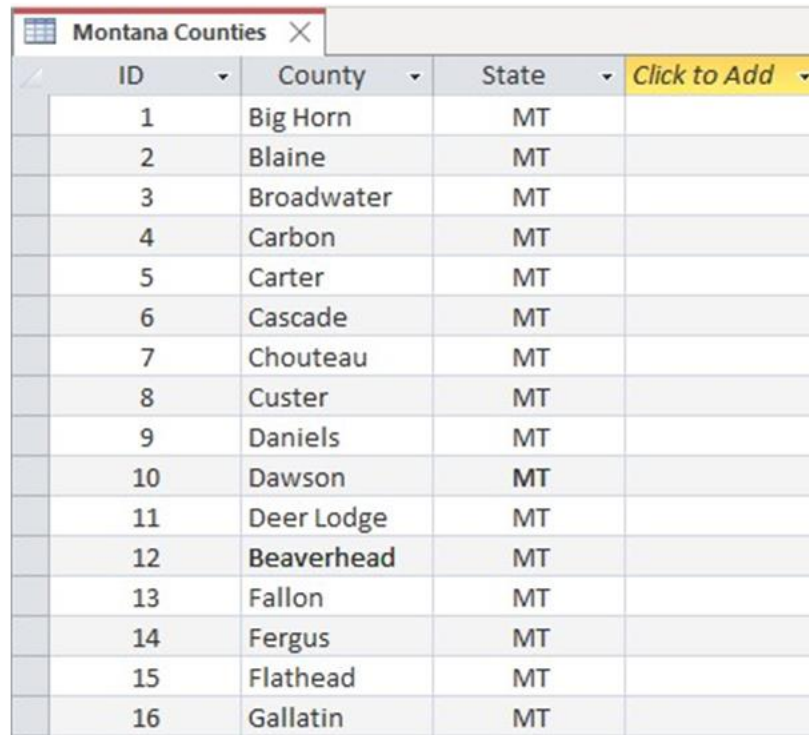
Layer	Geomaterial	Description	AASHTO
*			
  - Record: 1 of 1 | No Filter | Search [ ]
- Record Comments:** [ ]
- Attachments:**
  - Attachments (1): [ ]
  - Attachments (2): [ ]

**Figure 2.11. Partial Screenshot of MontanaPile Representing the “Pile Load Test Records” for Future Pile Load Test Input.**

The “Pile Load Test Records” form asks for information on the test pile. Some of the fields that can be filled out for a new test pile record are listed and explained below.

- **All Record Data Entered:** This field allows an input of “Yes” or “No” corresponding to whether all the information has been entered or not. If all the fields in the form are completed, then the tick mark will appear automatically.
- **ID:** This was a unique number assigned automatically to the test pile record by Access within each database. The “ID” could be the same for different test pile records in separate databases. This field does not need to be entered in the “Pile Load Test Record” form as inputs from other fields will automatically assign a value.

- **Project No.:** This field identifies the project number assigned by the respective DOT.
- **County:** This field identifies the county where the project was located. This field can be filled out using a drop-down menu consisting of all the counties in the respective state. The respective counties are assigned in a table titled “State Counties”. For example, the Montana counties are shown in the partial screenshot in Figure 2.12.

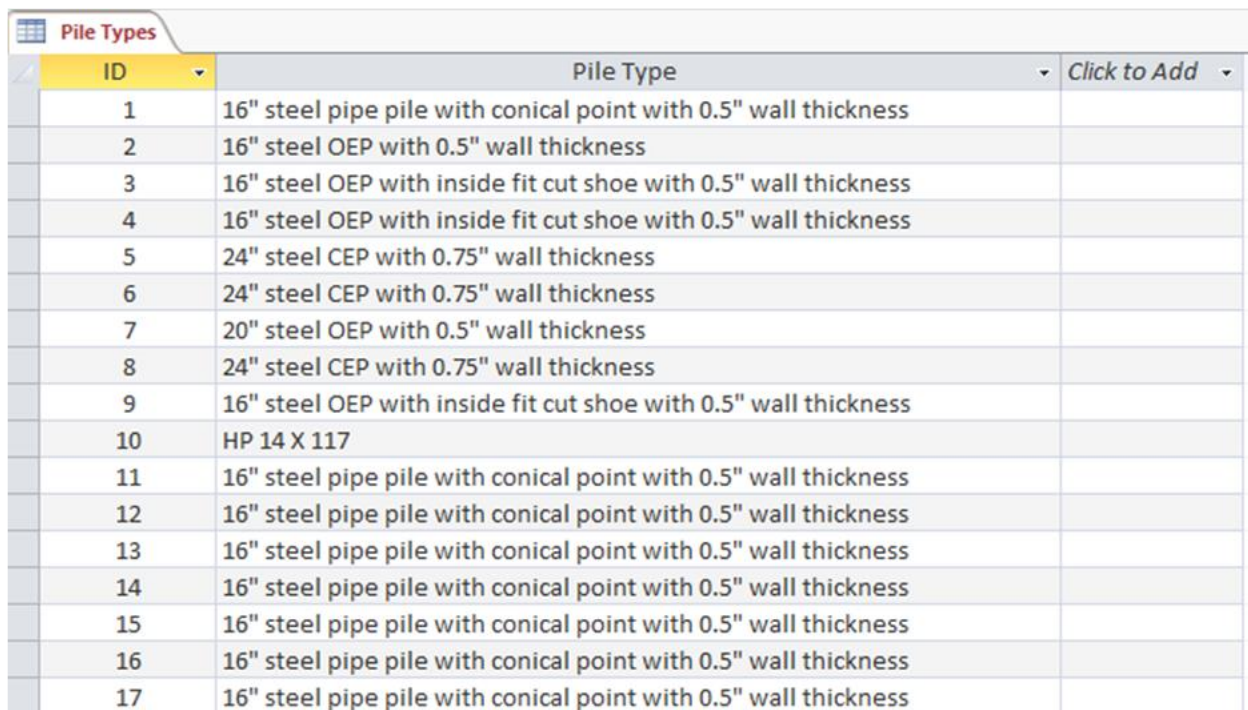


ID	County	State	Click to Add
1	Big Horn	MT	
2	Blaine	MT	
3	Broadwater	MT	
4	Carbon	MT	
5	Carter	MT	
6	Cascade	MT	
7	Chouteau	MT	
8	Custer	MT	
9	Daniels	MT	
10	Dawson	MT	
11	Deer Lodge	MT	
12	Beaverhead	MT	
13	Fallon	MT	
14	Fergus	MT	
15	Flathead	MT	
16	Gallatin	MT	

**Figure 2.12. Partial Screenshot of MontanaPile Representing the “Montana Counties” Table.**

- **State:** This field asks for the state where the project was implemented using a drop-down menu.
- **Bridge/Structure:** This field allows manual input of the name assigned to the bridge or any other structure.
- **Pile Location:** This field allows input of the pile location. The pile location is the identification of the test pile using the pile number in the bent/abutment/pier of the bridge, such as Bent 1, Pile 4.

- **Pile Size:** This field utilizes a drop-down menu for the selection of the test pile size. Most of the test piles type and sizes are already stored in a table titled “Pile Types” in each database. If the user wants to add pile type and size, then the table “Pile Types” can be accessed by double clicking the title in the navigation pane and manually inputting the information on the table. A partial screenshot of the table is shown in Figure 2.13



ID	Pile Type	Click to Add
1	16" steel pipe pile with conical point with 0.5" wall thickness	
2	16" steel OEP with 0.5" wall thickness	
3	16" steel OEP with inside fit cut shoe with 0.5" wall thickness	
4	16" steel OEP with inside fit cut shoe with 0.5" wall thickness	
5	24" steel CEP with 0.75" wall thickness	
6	24" steel CEP with 0.75" wall thickness	
7	20" steel OEP with 0.5" wall thickness	
8	24" steel CEP with 0.75" wall thickness	
9	16" steel OEP with inside fit cut shoe with 0.5" wall thickness	
10	HP 14 X 117	
11	16" steel pipe pile with conical point with 0.5" wall thickness	
12	16" steel pipe pile with conical point with 0.5" wall thickness	
13	16" steel pipe pile with conical point with 0.5" wall thickness	
14	16" steel pipe pile with conical point with 0.5" wall thickness	
15	16" steel pipe pile with conical point with 0.5" wall thickness	
16	16" steel pipe pile with conical point with 0.5" wall thickness	
17	16" steel pipe pile with conical point with 0.5" wall thickness	

**Figure 2.13. Partial Screenshot of MontanaPile Representing the “Pile Type” Table.**

- **Date Driven:** The date when the pile was driven on the site.
- **LRFD Pile Load (kips):** This database field specifies the factored LRFD load needed to be supported by an individual pile. This load is the sum of all design loads for which any given pile in the structure is anticipated to support based on the superstructure loading evaluation.
- **ASD Load (kips):** This database field specifies the Allowable Stress Design (ASD) load needed to be supported by an individual pile, if the ASD criteria are implemented during the design process.

- **Type of Hammer Used:** This database field contains information about the type of hammer used for driving the test pile, such as MVE M-19, Delmag D36, and Delmag D16-32.
- **Pile embedment at EOD (ft):** This field identifies the pile embedment at the EOD.
- **Elevation at the Top of the Test Pile (ft):** The elevation of the top of the driven test pile to the mean sea level.
- **Record Comments:** Any additional comments on the pile test record can be entered in this field.
- **Attachments:** Six attachment fields are used to attach relevant reports and files. The attachment is created as a hyperlink that was stored in these fields.
- **Subsurface Profile Tab:** The information from the boring logs matched with the test pile records can be entered in this tab.
- **Layer:** This database field stores the number of layers from the top of the test pile.
- **Geomaterial:** This database field identifies the geomaterial type described by the boring logs.
- **Description:** This database field stores additional descriptions of the geomaterial including its composition, state, and coloring.
- **AASHTO Classification:** This field can be used to input the AASHTO classification of the geomaterial if provided in the geotechnical reports.
- **Thickness (ft):** A layer thickness can be identified based on different geomaterials or varying geomaterial properties of similar geomaterials.
- **SPT N:** Standard Penetration Test (SPT) value for the respective geomaterial in blows/ft.
- **$(N_1)_{60}$ :** Corrected SPT N-value for hammer efficiency, rod length, borehole diameter, and effective overburden pressure.
- **Unit Weight (pcf):** The unit weight of the geomaterial from field tests or predictions.
- **$q_u$  (ksf):** The unconfined compressive strength of the geomaterial from lab tests.
- **$s_u$  (ksf):** Undrained shear strength of the geomaterial from the lab tests or predictions.
- **Friction angle:** The friction angle of the coarse-grained geomaterials from lab tests or predictions.

- Rock quality designation as RQD (percent): The RQD value of the rock-based geomaterials from the boring logs and geotechnical reports.
- Ground Surface Elevation (ft): The elevation of the ground at the location of the driven pile to mean sea level obtained from the boring logs.
- Water Table Elevation (ft): The elevation of the groundwater level at the location of the driven pile to mean sea level obtained from the boring logs recorded during boring.
- CAPWAP (ksf): CAPWAP measured unit shaft resistance or unit end bearing for the respective geomaterial layer.
- Usable-Dynamic Test: Database field with an input of “Yes” or “No” corresponding to whether dynamic test results were available or not. This database field receives a checkmark when the PDA device was used to monitor the installation of the test pile, which must be instrumented with accelerometers and strain transducers near the pile head and assess bearing capacity at either the EOD or BOR conditions; otherwise, this database field was left unchecked.
- Driven Pile Length (ft): The total length of the driven pile in feet.
- Pile Cross-Sectional Area (in<sup>2</sup>): The cross-sectional area of the pile from the specifications.
- Pile Weight Per Linear ft (p/f): Weight of the pile per unit length from the specifications.
- Hammer Stroke (ft): Maximum stroke height of the hammer is entered in this field. This value can be found in the specification of the hammer provided by the manufacturer.
- Transferred Hammer Energy (ft-kip): This database field is used to enter the maximum transferred hammer energy specified by the manufacturer.
- Dynamic Test and Analysis Results: This is located on the fifth tab of the “Pile Load Test Record Form”, and holds information such as blow counts per foot, and pile capacity from WEAP, PDA, and CAPWAP for EOD as well as restrikes as shown in Figure 2.14.

The screenshot shows a web-based form titled "Pile Load Test Record Form" for the Montana Department of Transportation. The form is divided into several sections. At the top, there are logos for the University of Wyoming and the Montana Department of Transportation, along with a status indicator "All Record Data Entered?". Below this, there are buttons for "Print" and "Close". The main form area contains fields for "ID: (New)", "Project No.", "County:", "State:", "Bridge/Structure:", and "Pile Location:". A list of fields follows, numbered 1 through 8, including "Pile Size", "Date Driven", "LRFD Pile Load (kips)", "ASD Load (kip)", "Type of Hammer Used", "Pile Embedment at EOD (ft)", "Elevation at the Top of the Test Pile (ft)", and "Elevation at the Bottom Tip of the Test Pile (ft)". Below these fields is a tabbed interface with tabs for "Subsurface Profile", "Nominal Unit Shaft Resistance (ksf)", "Nominal Unit Endbearing (ksf)", "Driving Information", "Dynamic Test and Analysis Results", and "Statistics". The "Dynamic Test and Analysis Results" tab is currently selected. This tab contains checkboxes for "PDA Monitoring?", "EOD information?", and "Restrike Information?". Below these are sections for "EOD date and Information" and "First Restrike date and Information", each with fields for "Blows/ft", "WEAP Capacity (kips)", "PDA Capacity (kips)", "CAPWAP Capacity (kips)", "CAPWAP Shaft Resistance (kips)", and "CAPWAP End Bearing (kips)". There is also a "Record Comments" text area and a list of "Attachments" (1) through (5). At the bottom, there is a status bar showing "Record: 14 of 1" and a search bar.

**Figure 2.14. Partial Screenshot of MontanaPile Representing the “Dynamic Test and Analysis Results” Tab in a New “Pile Load Test Records” Form.**

- Transferred Hammer Energy (ft-kip): This database field is used to enter the maximum transferred hammer energy specified by the manufacturer.
- Dynamic Test and Analysis Results: This is located on the fifth tab of the “Pile Load Test Record Form” and holds information, such as blow counts per foot, and pile capacity from WEAP, PDA, and CAPWAP for EOD as well as restrikes as shown in Figure 2.14.
- Blows/ft: This database field is used to input the hammer blow count at EOD or BOR.
- WEAP Capacity (kips): The pile capacity as predicted by the WEAP is input in this field.

- PDA Capacity (kips): The pile capacity, as predicted by the PDA at EOD or BOR, is placed in this field.
- CAPWAP Capacity (kips): The total pile capacity, as predicted by the CAPWAP at EOR or BOR as the input, is placed in this database field.
- CAPWAP Shaft Resistance (kips): The shaft resistance of the driven pile as predicted by the CAPWAP at EOD or BOR as the input is placed in this database field.
- CAPWAP End Bearing (kips): The end bearing capacity of the driven pile, as predicted by the CAPWAP as the input, is placed in this database field.
- Static Load Test Results: This is located on the sixth tab of the “Pile Load Test Records” form, as shown in Figure 2.16, and contains information on static load testing such as the load, displacement, and Davison pile capacity.

Pile Load Test Records

UNIVERSITY of WYOMING

MONTANA MDTA DEPARTMENT OF TRANSPORTATION

**Pile Load Test Record Form**

All Record Data Entered? ☐

ID:  Project No.

County:  State:

Bridge/Structure:

Pile Location:

1. Pile Size.....

2. Date Driven.....

3. LRFD Pile Load (kips).....

4. ASD Load (kip).....

5. Type of Hammer Used.....

6. Pile Embedment at EOD (ft).....

7. Elevation at the Top of the Test Pile (ft).....

8. Elevation at the Bottom Tip of the Test Pile (ft).....

Nominal Unit Endbearing (ksf) Driving Information Dynamic Test and Analysis Results Static Load Test Results

Static Load Test Results

Load (Tons)	Gauge Reading (in)
*	

Record: 1 of 1 No Filter

37. Davisson Pile Capacity (kip).....

38. Reliable Static Load Test?..... ☐

39. Static Load Test?..... ☐

Record Comments:

Attachments (1):

Attachments (2):

Attachments (3):

Attachments (4):

**Figure 2.15. Partial Screenshot of MontanaPile Representing the “Static Load Test Results” Tab in a New “Pile Load Test Records” Form.**

- Load (Tons): This database field is used to input the load applied on the test pile during testing.
- Gauge Reading (in): This database field is used to enter the displacement recorded at the corresponding load (tons).
- Davisson Pile Capacity (kip): This database field is used to enter the pile capacity obtained from the static load test using the Davisson criterion.



In addition to the tables described previously, a built-in filter is set on the “Usable Test Piles” table that filters all the usable test pile records and provides a summary similar to the “Pile load Test Records” table. A partial screenshot of the “Usable Test Piles” is shown in Figure 2.16. This table facilitates easy access to the usable test piles without filtering the contents on the main “Pile Load Test Records” table or the “Pile Load Tests List” form.

Usable test piles						
ID	State	County	Bridge/Structure	Pile Location	Pile Type	LRFD Factored load (k)
1	MT	Rosebud	Bridge Over Butte Creek	Bent 1, Pile 4	16" steel pipe pile with conical point with 0.5" wall thickness	457
2	MT	Blaine	Milk River - 4 KM West Of Zurich	Bent 1, Pile 1	16" steel OEP with 0.5" wall thickness	560
3	MT	Blaine	Milk River - 4 KM West Of Zurich	Bent 2, Pile 6	16" steel OEP with inside fit cut shoe with 0.5" wall thickness	500
4	MT	Blaine	Milk River - 4 KM West Of Zurich	Bent 3, Pile 1	16" steel OEP with inside fit cut shoe with 0.5" wall thickness	560
5	MT	Fergus	Bridge Over Warm Spring Creek	Bent 1	24" steel CEP with 0.75" wall thickness	1057
6	MT	Fergus	Bridge Over Warm Spring Creek	Bent 2	24" steel CEP with 0.75" wall thickness	1057
8	MT	Prairie	Bridge Over Cherry Creek	Bent 3, Pile 4	24" steel CEP with 0.75" wall thickness	832
9	MT	Musselshell	Bridge Over Musselshell River	Bent 3, Pile 4	16" steel OEP with inside fit cut shoe with 0.5" wall thickness	455
15	MT	Lewis & Clai	Capitol Interchange/Cedar Interchange	Bent 1, Pile 1	16" steel pipe pile with conical point with 0.5" wall thickness	700
16	MT	Lewis & Clai	Capitol Interchange/Cedar Interchange	Bent 4, Pile 47	16" steel pipe pile with conical point with 0.5" wall thickness	670
17	MT	Lewis & Clai	Capitol Interchange/Cedar Interchange	Bent 5, Pile 8	16" steel pipe pile with conical point with 0.5" wall thickness	650
18	MT	Lewis & Clai	Capitol Interchange/Cedar Interchange	Bent 1, Pile 8	16" steel pipe pile with conical point with 0.5" wall thickness	700
19	MT	Lewis & Clai	Capitol Interchange/Cedar Interchange	Bent 1, Pile 2	16" steel pipe pile with conical point with 0.5" wall thickness	700
20	MT	Lewis & Clai	Capitol Interchange/Cedar Interchange	Bent 4, Pile 38	16" steel pipe pile with conical point with 0.5" wall thickness	670
21	MT	Lewis & Clai	Capitol Interchange/Cedar Interchange	Bent 5, Pile 11	16" steel pipe pile with conical point with 0.5" wall thickness	650
22	MT	Golden Valle	Bridge Over MusselShell River, Cushman	Bent 1, Pile 1	16" steel OEP with inside fit cut shoe with 0.5" wall thickness	638
23	MT	Valley	Bridge over Rock Creek	Bent 2, Pile 1	20" steel OEP with 0.5" wall thickness	610
24	MT	Valley	Bridge over Rock Creek	Bent 3, Pile 1	20" steel OEP with 0.5" wall thickness	370

**Figure 2.16. Partial Screenshot of MontanaPile Representing the “Usable Test Piles” Table.**

## CHAPTER 3: EVALUATION OF STATIC LOAD TEST SYSTEMS FOR DRIVEN PILES IN INTERMEDIATE GEOMATERIALS

### 3.1 Introduction

Due to the shallow underlying strata in the Rocky Mountain and Appalachian regions of the United States and Canada, pile foundations are frequently used to support transportation infrastructures like bridges. Thus, driven piles in these regions rely on resistance from the IGM or weak rock layer. IGM lays between those of hard soil and soft rock. The problem is that little is known about the design and construction of driven piles in IGM. Martin and Stacey (2018) and O'Neill and Reese (1999) define IGM as cohesive materials such as clay shales or mudstones, with undrained shear strength ( $s_u$ ) of 5 ksf to 50 ksf or non-cohesive material such as glacial till with corrected SPT N-value falling between 50 to 100 blows per feet. Because of a wide range of variability, many definitions and descriptions of IGM are available in the literature (Mokwa and Brooks 2008). Most of the available literature defined IGM based on unconfined compressive strength ( $q_u$ ) (Clark and Smith 1992; Marinos 1997; Akai 1997; De Freitas 1993). These definitions were not consistent due to different applications. A study of the driven pile in IGMs was carried out recently to differentiate IGMs from the soil and hard rock based on corrected SPT N-values ( $N_{160}$ ), rock mass rating (RMR), and  $q_u$  (Adhikari et al. 2020a). Another study classified the fine-grained soil-based IGM based on  $s_u > 2.7$  ksf (Masud et al. 2022a). AASHTOLRFD Bridge Design Specifications (2020) defines IGM as a transitional material between soil and rock in terms of strength and compressibility, such as residual soils, glacial tills, or very weak rock. AASHTO (2020) recommends treating IGM as soil in the estimation of geotechnical piles resistances for driven pile design. Thus, the design of driven piles in IGM is commonly conducted using current Static Analysis (SA) methods developed for soil. If IGM is treated as soil, construction concerns, such as early pile refusal and pile breakage, might occur due to a lack of suitable design approaches and static pile load test data (Ng et al 2015). The results of an investigation on fifteen steel piles driven into IGM in Wyoming by Ng and Sullivan (2017a) revealed that the current SA techniques designed for soils produced inconsistent and conservative predictions of geotechnical resistances. Pile resistances estimated using the signal matching method from CAPWAP vary with the resistances predicted using existing SA methods for driven piles in IGM (Mokwa and Brooks 2008).

Additionally, it has been observed that the pile resistances predicted for IGM using current SA approaches vary from those found by dynamic load testing (DLT) (Ng et al 2015; Ng and Sullivan 2017a; Ng and Sullivan 2017b). The prediction of pile resistances in soft rocks using 20 static pile load trials did not yield applicable prediction equations (Mokwa and Brooks 2008). Only a few SLTs on piles driven into IGM are published (Long 2016). Mokwa and Brooks (2008) conducted a study on piles driven into cohesive and cohesionless IGM from 9 bridge projects in Montana. DLTs were performed in these projects, but no SLTs were performed. The axial resistance of driven piles was predicted using existing methods: DRIVEN software, EAP, FHWA gates driving formula, WSDOT gates driving formula, and an empirical formula developed by CDOT. The comparison of pile resistance from the methods and CAPWAP revealed little or no correlations. In addition, no SA methods are developed to predict pile resistances in IGM.

In another study, 7 SLTs and 77 DLTs are conducted at 7 bridge locations in Brown County, Wisconsin (Long 2016). The SLTs were conducted in accordance with the ASTM D1143 (2007), and Davisson criterion (1972) was used to determine the ultimate pile resistance. These measured pile resistances are compared with that determined from PDA/CAPWAP. The CAPWAP based on BOR data underpredicted the measured pile resistances by 15 percent on average. In addition, SA methods were developed for predicting unit shaft resistance ( $q_s$ ) of fine-grained IGM as  $0.021N_{MSPT}$  for  $q_s$  less than 2 ksf, and unit end bearing ( $q_b$ ) of fine-grained IGM as  $0.935N_{MSPT}$  with large scatter of  $q_b$  to  $N_{MSPT}$ , and for  $q_b$  less than 200 ksf, where  $N_{MSPT}$  is defined as the N-value from modified SPT. With substantial scatter, the SA methods proposed for predicting  $q_s$  of coarse-grained IGM as  $0.9(N_{MSPT})^{0.25}$  for  $q_s$  less than 3 ksf and  $q_b$  as  $65(N_{MSPT})^{0.3}$  for  $q_b$  less than 300 ksf. Although the modified SPT may be a viable method, it has not been extensively utilized, and most historical geotechnical records contain only standard SPT values. In addition, LRFD guidelines are not developed since these SA methods are not assessed or validated with separate test pile data. On the other hand, a study by Masud et al. (2022b) developed SA methods and their corresponding LRFD resistance factors to predict the driven pile resistance in siltstone using dynamic load tests of 15 test piles.

Hence, it is difficult to comprehend the pile responses in IGM without having measurements from the SLT. DLT techniques are frequently used in current practice to assess the

effectiveness and acceptability of driven piles into IGM. However, a static load test was necessary to understand the load-displacement response and determine the load transfer mechanism from piles to IGM, even if dynamic techniques have technological and economic advantages. Considering these challenges, this study describes 11 different pile load systems for full-scale SLTs on steel H-piles driven in IGM implemented in 5 different states: Kansas, North Dakota, Iowa, Wyoming, and Colorado. The first SLT system was the Independent Static Pile Load System (IndeSPLS), which was designed for test piles (TP) 1 (TP1) to 5 (TP5) driven into shale and claystone in Iowa, Kansas, and North Dakota. The second system is the Integrated Static Pile Load System (InteSPLS) designed for test piles 6 (TP6) and 7 (TP7), which was driven into siltstone in Wyoming. The third system was the Innovative Static Pile Load System (InnoSPLS), which was designed for test piles 8 (TP8) to 11 (TP11) driven into shale, siltstone, and claystone in Colorado. This study presents test pile instrumentation, protection, data collecting, residual driving force on piles, SLT systems, and results from CAPWAP. The findings will help in choosing an acceptable SLT system for driven piles in IGM and to validate the findings from the DLT.

### **3.2 Site Description and Subsurface Condition**

The first test site for TP1 with four geotechnical investigation boreholes was a bridge replacement for Iowa (IA) Highway 92 across Marvel Creek close to Greenfield in Adair County, IA. The second test site for TP2 was located in the US 63 over the drainage ditch, 0.3 miles south of Ottumwa, in Wapello County, IA. The third test site for test pile 3 (TP3) is the reconstruction of Cheery Creek Bridge on Highway 1,806 approximately 3.25 miles north of the intersection with North Dakota Highway 23 on the edge of Watford City, ND. The fourth and fifth tests were located in Wichita, Kansas. The test site for test pile (TP4) was the reconstruction of the Highway K-55 bridge over the Arkansas River, in Sumner County, Kansas. The test site for TP5 was the construction of a new structure from westbound K-96 to northbound I-135 over North Hydraulic Street, built as part of the reconfiguration of the junction in north Wichita. The test site for TP6 in Wyoming is located at the north section of Pine Bluffs to Albin, Laramie County. Five test holes were drilled at this site, four near the abutments and one within the channel of Lodgepole Creek before the test pile installation. The second test site in Wyoming was for test pile TP7, with four boreholes, and was located at the I-80 interchange road over the Interchange Road, Rock Springs in Sweetwater County,

WY. The remaining 4 test sites for the Innovation Static Pile Load tests are located in Colorado. The first test site for test pile TP8, with two boreholes, was at a replacement bridge project of I-05-V over the Gunnison River in Delta County, CO. The second test site for TP9 is situated in Arapahoe County, Colorado, on Interstate 76 (I-76), where the new single structure E-17-GX will replace the existing bridge structures E-17-GV and E-17-GW. The third test site for test pile TP10 was at the replacement of bridge structure J-17-X with structure J-17-XA. The current bridge structure J-17-X allows for Rock Creek to pass under Colorado Highway 115 (CO115). The fourth test site for TP11 was at the replacement of the existing bridge that carries east and west bound I-70 over Harlan Street in Jefferson and Denver Counties, Colorado.

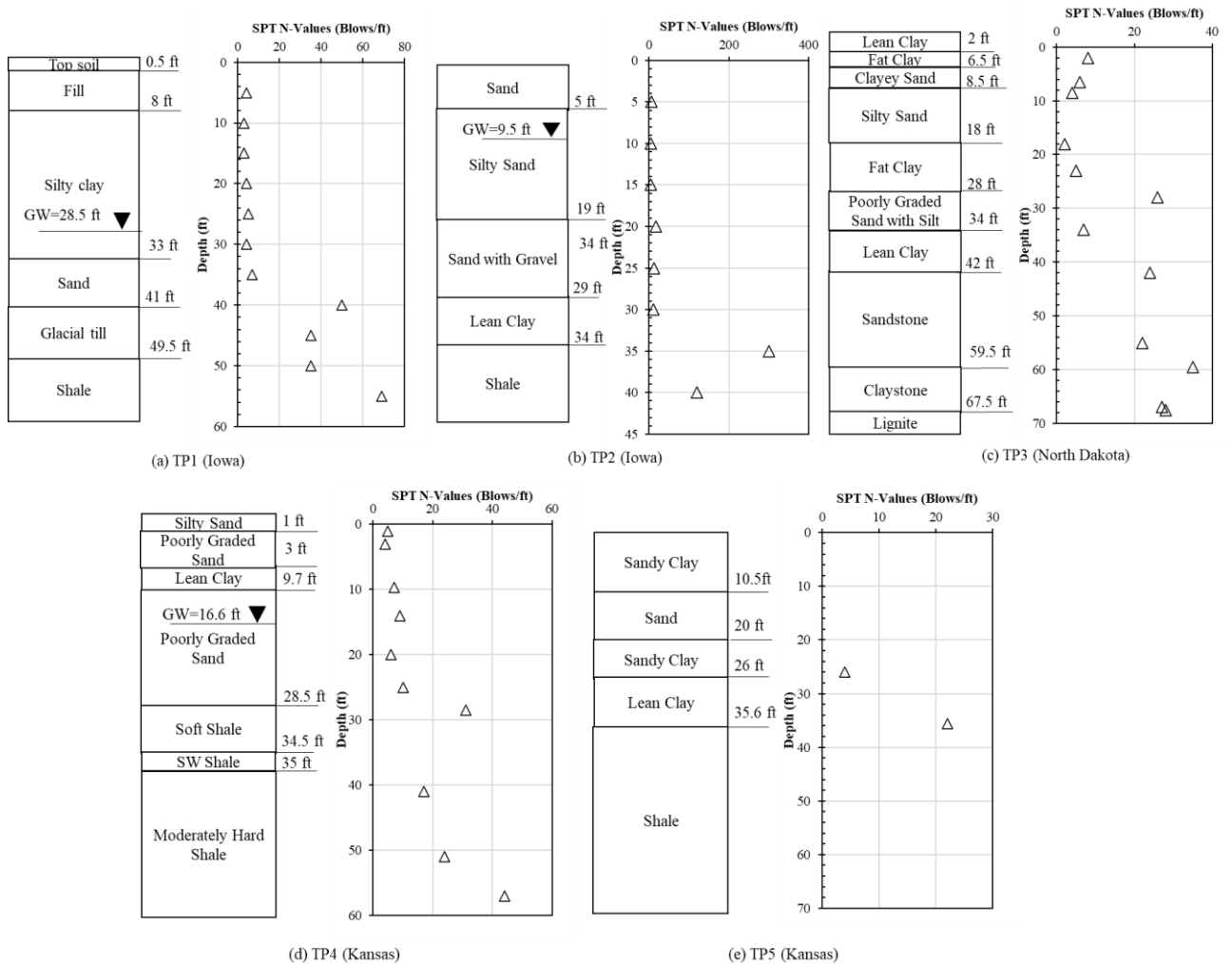
Figures 3.1a to 3.1k show the groundwater tables, SPT N-values and geotechnical subsurface profiles for the test piles (TP1 to TP11). TP1 is situated 15 ft north of the east abutment of the rebuilt IA Highway 92 bridge over Marvel Creek. This pile is not a part of the bridge foundation. Shale is located 49.5 ft beneath the soil surface, and the overburdened soil includes 33 ft of silty clay, 8 ft of sand, and 8.5 ft of glacial till (Figure 3.1a). The second test site for TP2 is located on US 63 over the drainage ditch, 0.3 miles south of Ottumwa, in Wapello County, Iowa. A total of six test holes were drilled at the site, and SPT profiles were obtained from each borehole prior to test pile installation. Figure 3.1b shows the SPT blow count and surface profile of the borehole report adjacent to the test pile. The subsurface profile consists of a 5 ft thick sand layer, followed by a 14 ft thick silty sand layer. The gravel is traced from 19 ft to 29 ft below the existing ground. The bedrock or shale layer is encountered 34 feet below the existing ground. The SPT N-values were reported at almost every 5 ft interval, and groundwater is encountered at 9.5 ft below the existing surface. TP3 shown in Figure 3.1c is an HP12×53 pile driven at multiple geomaterials layers, and the groundwater table is not encountered below the existing ground surface. Sandstone, claystone, and lignite bedrock starts at 42 ft, and the overburdened soil consists of 18.5 ft of clay, 9.5 ft of silty sand, and 6 ft poorly graded sand with silt.

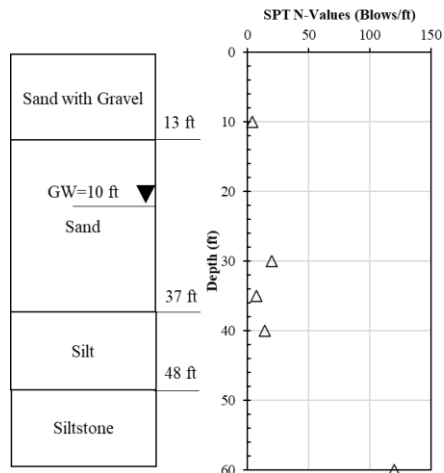
The test site for TP4 is situated in Sumner County, Kansas as a reconstruction of the Highway K-55 bridge over the Arkansas River. The overburdened soil comprised 1 ft of silty sand, 2 ft of poorly graded sand, 6.7 ft of lean clay, 18.8 ft of poorly graded sand, and 31.5 ft of Wellington formation, primarily consisting of 6 ft of soft shale, 0.5 ft of slightly weathered

shale, and 25 ft of moderately hard shale below the finished ground surface where the test pile is installed. The total pile penetration is 51 ft with 31.2 ft into the shale layer. Figure 3d shows the geotechnical subsurface profile and N-values from a standard penetration test. The site for TP5 (HP10×42) is the construction of a new structure from westbound K-96 to northbound I-135 over North Hydraulic Street built as part of the reconfiguration of the junction in north Wichita. The new structure is a 3-span continuous composite weathering steel welded plate girder span bridge along Ramp North. The bedrock at this site is soft shale of the upper permian wellington formation. Figure 3d shows the geotechnical subsurface profile and N-values from a standard penetration test.

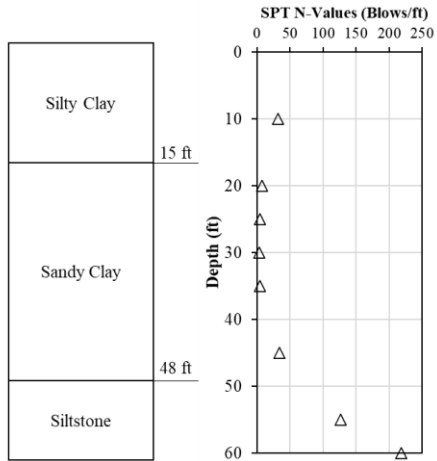
The test site in Wyoming for TP6 (HP10×42) is located at the north section of Pine Bluffs to Albin, Laramie County. Five test holes were drilled at this site, four near the abutments and one within the channel of Lodgepole creek before the test pile installation. Figure 3.1e shows the profiles of SPT blow counts and the description of each of the geomaterial layers in the profile from the bore log report closest to the test pile. The groundwater table was met at 22.5 ft below the existing ground surface. The subsurface profile at the site consisted of 13 ft of sand with gravel, followed by a 24 ft thick layer of sand, and an 11 ft thick layer of silt. The siltstone or bedrock was encountered at a depth of 48 feet below the ground surface. TP7 was an HP12×53 pile driven at the center of abutment 1 and the groundwater table was not encountered below the existing ground surface. Siltstone bedrock was encountered at 48 ft, and the overburdened soil consisted of 15 ft of sand with silt, 33 ft of sandy clay, and 15 ft of sand. TP8 was an HP14×89 pile that was a part of the bridge foundation system at abutment 4 in Colorado. The subsurface profile consisted of 6.85 ft of silty gravel with a sand fill layer, 8.5 ft of silty gravel with a sand layer, and a shale layer at 15.35 ft below the surface. TP9 test pile was close to borehole B1, and the three primary geologic units encountered in the exploration borings were embankment fill, native soils, and sedimentary bedrock. The 10.5 ft thick embankment fill is categorized as Lean Clay (CL). Native soils underlaid the CL and extended to depths 10.5 to 16.5 ft below the ground surface and overlaid the siltstone bedrock. No groundwater was observed at this test site location, and the total test pile penetration was 28.5 ft. TP10 is TP10 test pile was close to borehole B1, and the two primary geologic units encountered in the exploratory borings were native soils and sedimentary bedrock. Native soils underlaid the clayey gravel and silty sand and extended to depths up to 34 ft below the ground surface and overlaid the claystone bedrock. TP11 test pile was close

to borehole B3, the groundwater table was not encountered below the existing ground surface. The subsurface profile at the site consisted of 7 ft of native clay. The sandstone and claystone layers were encountered at depths of 7 ft and 12 ft below the ground surface, respectively.

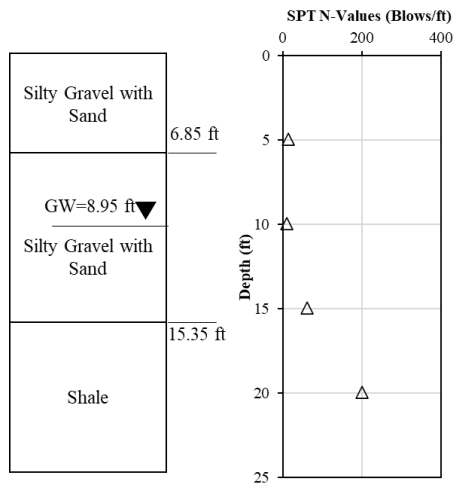




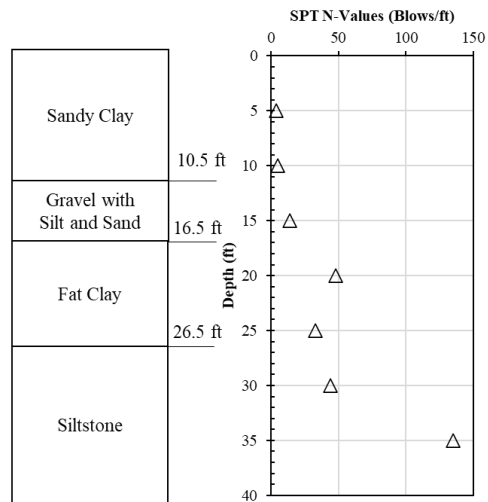
(f) TP6 (Wyoming)



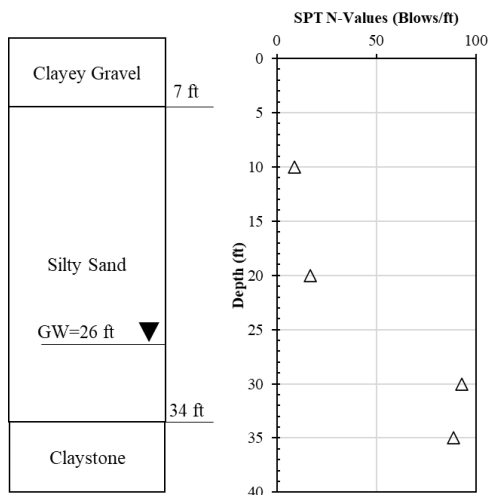
(g) TP7 (Wyoming)



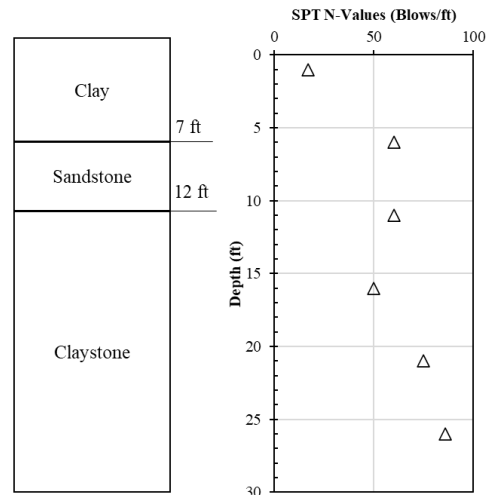
(h) TP8 (Colorado)



(i) TP9 (Colorado)



(j) TP10 (Colorado)



(k) TP11 (Colorado)

**Figure 3.1. Subsurface profiles and SPT N-values at a) TP1 at Adair County, IA, b) TP2 at Wapello County, IA, c) TP3 at McKenzie County, ND, d) TP4 at Sumner County,**



KS, e) TP5 at Sedgwick County, KS, f) TP6 at Laramie County, WY, g) TP7 at Sweetwater County, WY, h) TP8 at Delta County, CO, i) TP9 at Arapahoe County CO, j) TP10 at EL Paso County, CO, and k) TP11 at Jefferson and Denver Counties, CO.

### 3.3 Site Description and Subsurface Condition

This study was designed and conducted with three different static pile load systems: IndeSPLS, InteSPLS, and InnoSPLS. The test pile and bearing layer properties are shown in Table 3.1. These static pile load systems were described in the following sections. To describe the IndeSPLS, InteSPLS, and InnoSPLS static pile load systems TP1, TP7 and TP8 were selected.

**Table 3.1. Test Pile and Bearing Layer Properties of Different SLT Systems.**

Test Pile	SLT System	Pile Size	Pile length (ft)	Pile Penetration (ft)	Bearing Layer	$q_u$ (ksf)
TP1	IndeSPLS	HP10×57	60	56.1	Shale	9.36
TP2	IndeSPLS	HP10×42	42	36	Shale	-
TP3	IndeSPLS	HP12×53	80	67.5	Claystone	14.4
TP4	IndeSPLS	HP12×53	55	51	Shale	6.1
TP5	IndeSPLS	HP12×53	75	66.5	Shale	3.9
TP6	InteSPLS	HP10×42	60	57.2	Siltstone	22
TP7	InteSPLS	HP12×53	60	59.1	Siltstone	9.5
TP8	InnoSPLS	HP14×89	21	18.2	Shale	720
TP9	InnoSPLS	HP12×74	35	28.5	Siltstone	117
TP10	InnoSPLS	HP14×89	60	41	Claystone	16
TP11	InnoSPLS	HP14×89	40	24.5	Claystone	5.72

$q_u$ =Unconfined compressive strength of bearing layer.

#### 3.3.1 Independent Static Pile Load System (IndeSPLS)

For the IndeSPLS shown in Figure 3.2, TP1 in Adair County, IA, was installed at the center of the load frame along with four HP14×89 reaction piles (RP1 to RP4). The IndeSPLS was constructed about 15 ft to the west abutment. After driving the test pile, four reaction piles were installed with a clear distance of 7 ft to the test pile, which meets the minimum distance of 5 ft following the ASTM D1143 (2007). Two hold-down spreader beams were raised and positioned on top of the reaction piles (Figure 3.2). Each hold-down spreader beam was 10 ft long and constructed with two W12×79 sections. A 1.5-in thick steel plate was welded to the

top of the W12×79 sections and a 0.5-in thick steel plate was welded to the bottoms to increase the structural rigidity of the spreader beam. The 18-ft long main reaction beam (W40×183) was placed against the bottom of the spreader beams and over the test pile. The main reaction beam and the hold-down spreader beams were temporarily held in place using eight C-clamps. Next, the 1.25-in diameter full-threaded high-strength steel rod was dropped through the opening in each held-down spreader beam and along the flange face of each reaction pile. Each rod was secured and tightened to the 1.5-in thick bottom plate welded to the pile flange using rod nuts. The bottom plate was restrained from bending two 0.5-in thick vertical steel plates welded against the reaction pile flange. The axial load was applied on the TP1 using a hydraulic jack acting against the main reaction beam, and a load cell placed on the hydraulic jack measures the amount of axial force. The two hold-down beams resisted the axial load in the upward direction against the bottom of the main reaction beam. The spreader beams were again held-downed by the steel rods in tension. The steel rods were resisted by the uplift shaft resistances developed along the reaction piles. Considering a safety factor of two, the design load of the IndeSPLS for this project site is about 1,000 kips. In this IndeSPLS, the test pile and reaction piles were not part of the bridge foundation system and did not affect the bridge construction but did incur additional time and cost to the bridge project. In this system, the quick load test procedure A, in accordance with the ASTM D1143 (2007), was followed with 20 equal load increments and 10 load decrements. The load was applied until the geotechnical or structural capacity was obtained.

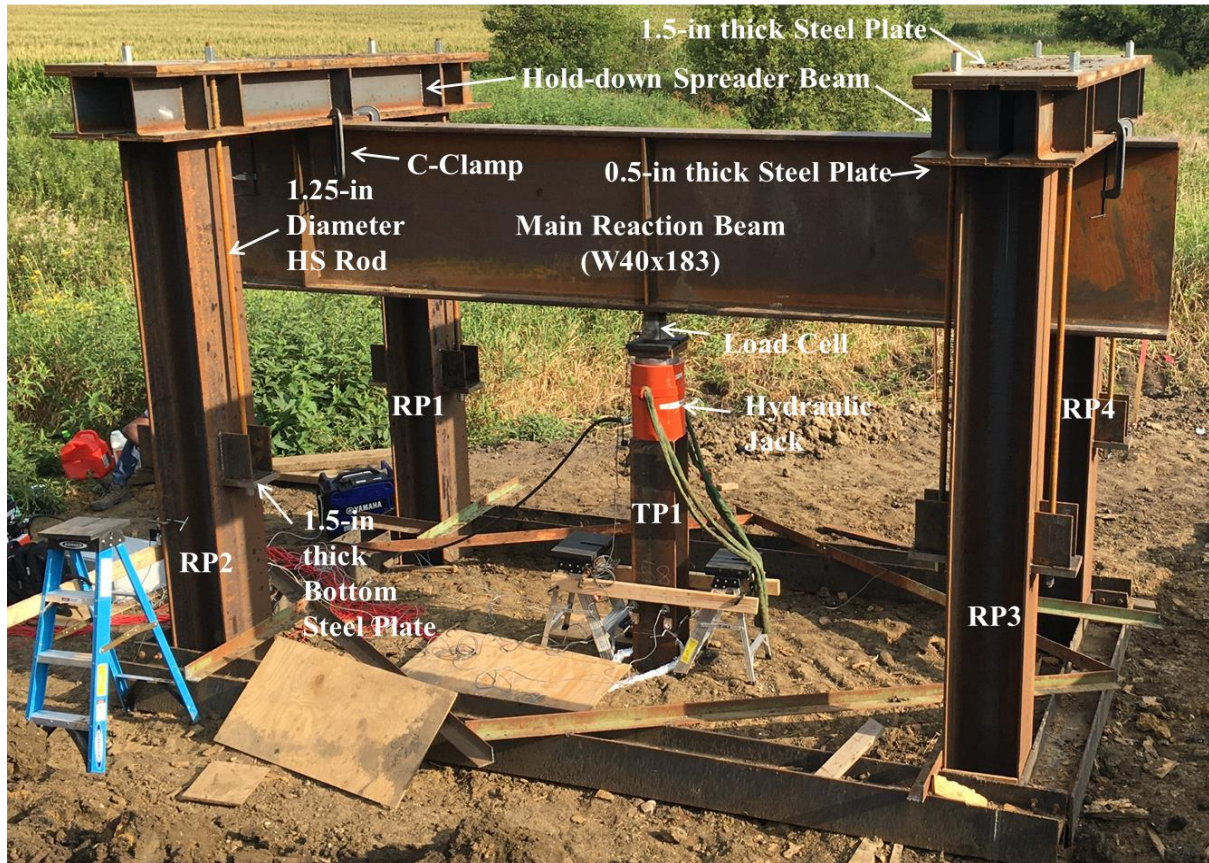


**Figure 3.2. Static pile load systems for InteSPLS on TP1 in Adair County, IA.**

### **3.3.2 Integrated Static Pile Load System (*InteSPLS*)**

InteSPLS was designed in which the test pile was not considered as a usable production pile of a foundation system of an abutment, while production piles of the same abutment served as reaction piles (Figure 3.3a). The InteSPLS consists of four HP12×53 production piles (P1 through P4) and the TP7 at abutment 1 of the bridge project site in Sweetwater County, WY. The distance between the production piles (P2 and P3) and the test pile was around 9 ft and 3 in which meets the minimum distance of 5 ft. Four hold-down spreader beams (Figure 3.3a) were then set on top of the main reaction beam system. The main reaction beam system consists of two 40-ft long W36×150 sections and a 21-ft long W36×150 section between the long sections (Figure 5.3b). They were raised and positioned over the production piles and TP7. P2 and P3 support the main reaction beam system for ease of construction. Each spreader beam was constructed with two C10×25 channels on which their top and bottom were welded with 0.5-in thick steel plates (Figure 3.3c). Each spreader beam was held-down by two 1.75-in diameter high-strength treated bars, which were fastened by an anchor block



welded to the flange face of the production pile (Figure 3.3d). A hydraulic jack placed on the TP7 was used to apply the axial load, which was measured using a load cell. Considering a safety factor of two, the design load of the InteSPLS for this project site was 775 kips. The load transfer mechanism of this system was the same as IndeSPLS. The test was carried out until the maximum structural or geotechnical capacity was attained. InteSPLS was less expensive than IndeSPLS because production piles were used as reaction piles. However, the SLT should be considered the critical path of the bridge construction schedule.

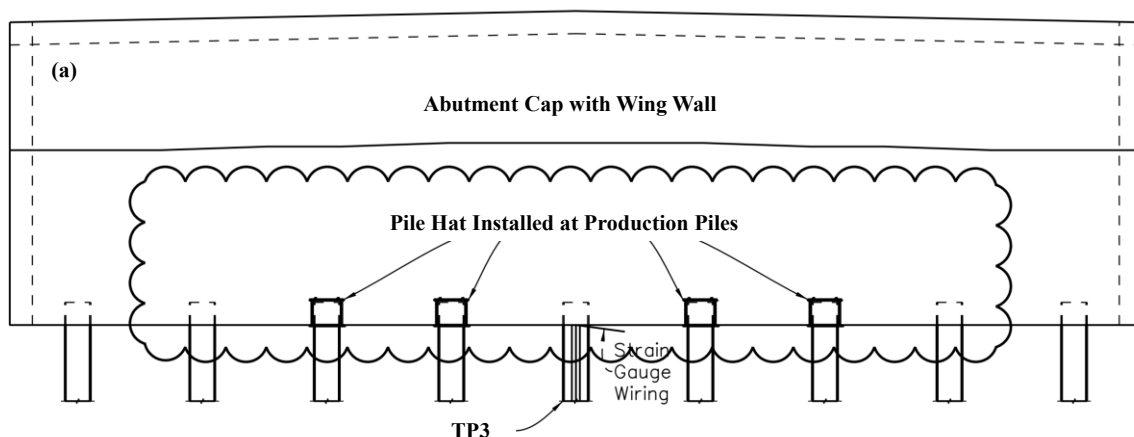


**Figure 3.3. Static Pile Load System: a) InteSPLS on TP7 in Sweetwater County, WY, b) Main Reaction Beam System, c) Assembly of Spreader Beam, Main Reaction and 1.75-in Diameter HS Treated Bar, and d) A Treated Bar and Anchor Block of the InteSPLS.**

### ***3.3.3 Innovative Static Pile Load System (InnoSPLS)***

InnoSPLS was designed and conducted on TP8 in Delta County, CO. In this system, no temporary loading frame and reaction piles were considered to save the additional labor and

frame setup costs. The test pile was part of the main foundation or bridge system. Load was applied to the test pile from the accumulated dead loads of the bridge structure: abutment cap, wing walls, girders, concrete deck, abutment stem, barriers, overlay, and utilities, as well as the live load when the bridge was open to traffic. Figure 3.4a shows the schematic diagram of the InnoSPLS with steel pile hats installed at the top of the four production piles adjacent to TP8. The remaining four production piles, with two at each end of the abutment cap, were concreted to maintain structural stability. The purpose of the pile hat was to create a gap between the production pile and the abutment cap so the accumulated structural and traffic loads can be transferred to the test pile. Figure 3.4b shows the configuration and cross-sectional views of the pile hat. The pile hat was constructed with four side steel plates, and a top steel plate welded together and rested on a  $\frac{3}{4}$ -in thick plywood cut into halves. To create a 1-in gap between the abutment cap and pile top, the pile hat and the plywood were placed on grade, and the two plywood halves must fit tightly around the pile perimeter to provide a full containment of concrete grout. Two No. 6 rebars were field welded to the top plate to integrate the pile hat into the abutment cap. A pressure grout tube was inserted through the top plate of the pile hat, and two backup pressure grout tubes were installed on one of the side plates to fill up the gap and void space inside the pile hat with 4,500 psi non-shrink grout upon conclusion of the SLT (Figure 3.4b).



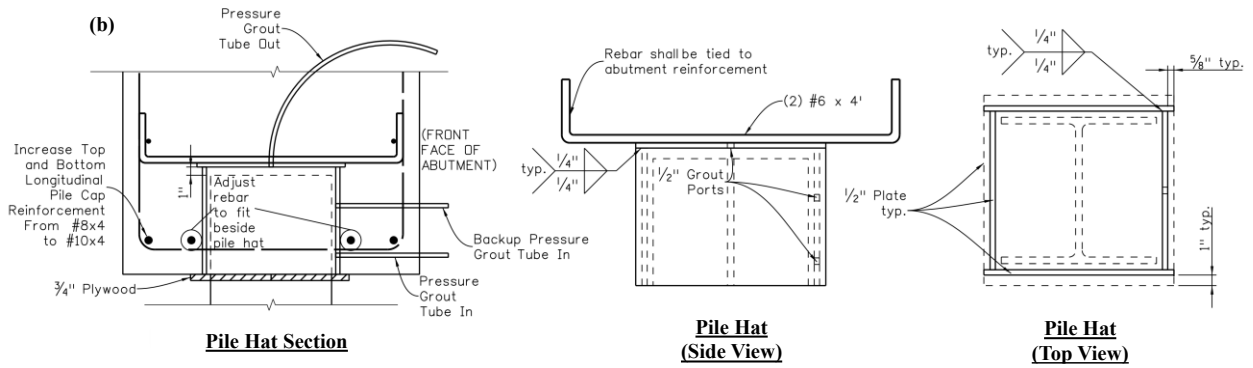


**Figure 3.4. InnoSPLS on TP8 in Delta County, CO: a) Schematic Drawing and Elevation View of the Piles and Abutment Cap, and b) Configuration and Cross-Sectional Views of the Pile Hat.**

Eventually, the design loads will evenly transfer to all the production piles. Figure 5.5 shows the various stages of InnoSPLS after pile driving (Figure 3.5a). The strain gauge cables were pulled out and wrapped with aluminum foils from TP8 (Figure 3.5b) to protect them from damage during abutment cap concreting. Figure 3.5c shows the concreted abutment cap in which the four production piles at both ends and TP3 were in direct contact with the cap. The cables of the strain gauges were pulled out through a PVC pipe (Figure 3.5d) once the abutment cap was concreted. Figures 3.5e to 3.5g show the different loading stages due to girder placement, deck placement, and concrete pouring of the deck. These different loading stages cause the TP8 to settle down from which axial loads and displacements of the test pile were calculated from the strain gauge readings.



**Figure 3.5. Different Stages of InnoSPLS: a) Pile Driving, b) Pulling Strain Gauge Cables from TP3, c) Casted Abutment Cap, d) Cables Come Through PVC Pipe, e) Girders Placement, f) Deck Placement, and g) Concrete Pouring of the Deck.**

### **3.4 Test Pile Preparation**

#### **3.4.1 Strain Gauge Installation**

All three test piles were instrumented with eight pairs of Geokon® vibrating-wire (VW) 4000A strain gauges along the pile length on both web faces to capture the load distribution and to bend during the SLT. The main reasons for choosing this VW strain gauge were for more extended stability, strong resistance to water incursion and lightning damage, and steady signal transmission over long cable lengths (Figure 3.8a). Before installing the mounting blocks, each web face at the gauge location was cleaned with a grinder to remove any rust and dirt. Next, the mounting blocks were set using a spacing jig, and the sides of the mounting blocks were welded by keeping the single set screw in the upper position (Figure 3.8a). The central tube of each VW strain gauge was inserted through a hose clamp and secured to the two mounting blocks shown in Figure 3.6a. Finally, a coil was fastened to the hose clamp at the middle central tube (Figure 3.8a). The strain gauge measures the change in sensor reading ( $\Delta R$ ), and the micro strain ( $\epsilon$ ) can be calculated using the equation shown in Figure 3.6, where  $G$  was the gauge factor = 4.062, and  $B$  was the batch factor = 0.96.

$$\epsilon = G \times B \times \Delta R$$

**Figure 3.6. Equation. Micro Strain Calculation from Sensor Readings.**

#### **3.4.2 Strain Gauge Protection**

The VW strain gauges and cables were shielded from the heat and spark of welding using aluminum foil (Figure 3.8b), aluminum tape, and aluminum-laminated rubber membrane (Figure 3.8c). The strain gauges and cables on each web face were eventually covered with a 3-in steel angle, which was welded to the test pile to avoid direct soil contact with pile installation. The steel angles were securely attached to the test pile with continuous 6-in long fillet welds at 24-in intervals (Figure 3.8d). The steel angles were tapered at the pile tip to minimize potential geomaterial disturbance during pile driving (Figure 3.8d). Pile stresses were calculated using the equation shown in Figure 3.7 based on the micro strains and the



modulus of elasticity ( $E$ ) of the steel pile before and after the end of the driving (EOD) and the beginning of the restrike (BOR) and during the SLT.

$$\sigma = \epsilon E = G \times B \times \Delta R \times E$$

**Figure 3.7. Equation. Stress Calculation from Strain.**

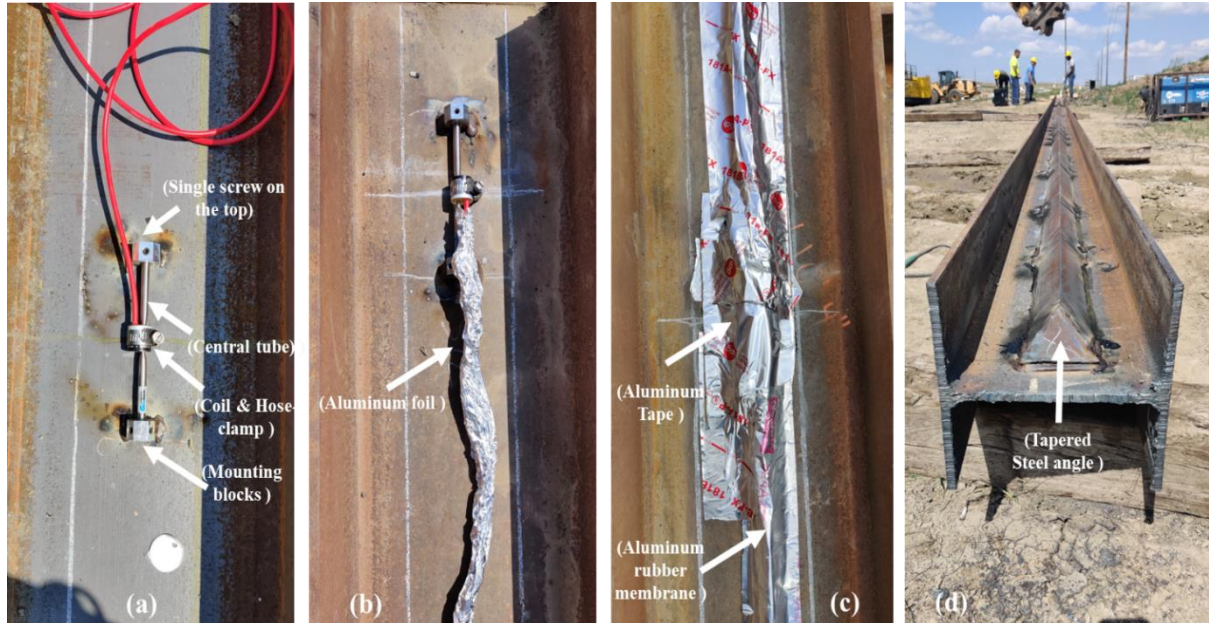


**Figure 3.8. Test Pile Instrumentation: a) Strain Gauge Welded on the Web Face of the Pile, b) Protection of Strain Gauge Cables with Aluminum Foils, c) Protection of Strain Gauges and Cables with Aluminum Tapes and Membranes, and d) Protection Using Steel Angles with Tapered Steel Angles Near the Pile Tip.**

### 3.5 Static Load Test Setup

A 355-ton Power Team<sup>TM</sup> hydraulic jack with a 10-in stroke was utilized to deliver an axial load to the test piles using the InteSPLS and IndeSPLS (Figure 3.9a). Pressure was applied to the jack using a Power Team<sup>TM</sup> double-acting gasoline-powered hydraulic pump with a maximum pressure output of 10,000 psi (Figure 3.9b). A Power Team<sup>TM</sup> digital pressure gauge with model DG9042 was attached to the pump to accurately measure the pressure (Figure 3.9c). A Honeywell load cell Model MPB, with a 500-ton capacity, was used to measure the applied load on the test pile (Figure 3.9d). The pressure created by the hydraulic pump was used to calibrate the load cell measurement before the SLT. Four JX-P420 series linear position transducers from UniMeasure, Inc., with a total stroke of 15 inches, were used



to measure the pile top displacement (Figure 3.9e). Two of the four linear position transducers were mounted, each horizontal wooden reference beam supported by two ladders without contacting the test pile, and each facing the web face of the pile (Figure 3.9g). Two SPD-12-3 string potentiometers, with a total stroke of 12.5 inches from Measurement Specialties, Inc., were mounted on independent wooden beams supported by ladders (Figure 3.9h) to measure upward displacements of either the reaction or production piles (Figure 3.9f).



**Figure 3.9. Instruments and Equipment Used in the SLT: a) Hydraulic Jack, b) Hydraulic Pump, c) Digital Pressure Reading, d) Load Cell, e) Linear Position Transducers to Measure Test Pile Displacement, f) String Potentiometer to Measure the Upward Displacement of Reaction Piles, g) Linear Position Transducers on Reference Beams Supported by Two Ladders at the Test Pile, and h) String Potentiometer on Wooden Beam Supported by the Ladder at the Reaction or Production Pile.**

### 3.6 Data Acquisition System

A 16-channel Geokon Model 8032 multiplexer was used to collect the strain gauge readings (Figure 3.10a). LabVIEW software was used to synchronize measurement time and give an orderly record to allow further data processing. The channel cycle was programmed through a mechanical relay that was positioned beneath the circuit board (Figure 3.10b) to provide readings for one sensor at a time. The VW sensors were all read by this multiplexer. The data logger system (Figures 3.10a and 3.10c) was used to convert the measured resonant frequency from the VW sensors into stresses using a Model 8020-59 VW-analog converter (Figure 3.10d). This converter stimulates the vibrating wire, measures the frequency over 500 times for each measurement, and generates a voltage output proportionate to the sensor reading. This procedure takes one to two seconds per sensor. The data collecting system (DAS) also comprises a power supply, hard drive, and on/off switch. All DAS measurements were stored via USB (Figure 3.10e) and monitored on a PC (Figure 3.10f) on which readings from the load cell and six displacement sensors were received.

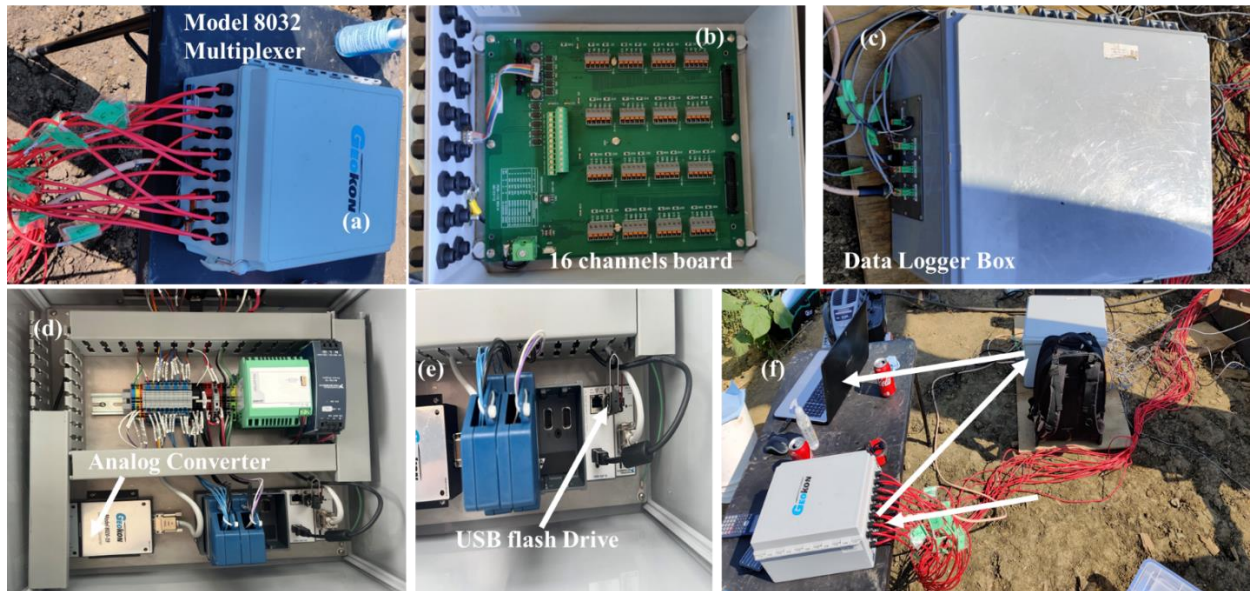


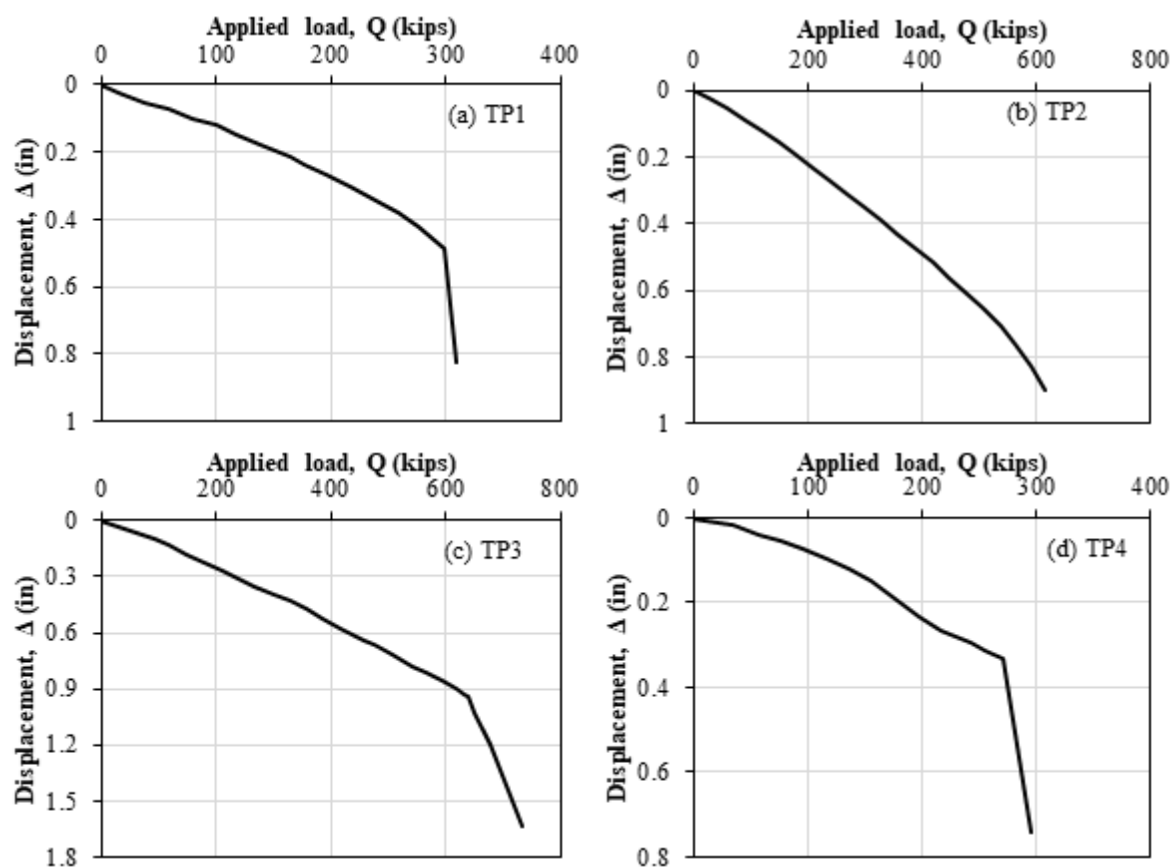
**Figure 3.10. Data Acquisition System: a) Multiplexer, b) 16-Channels in the Multiplexer, c) Data Logger Box, d) VW Analog Converter, e) USB Flash Drive, and f) Computer System to Collect the Readings During Testing.**

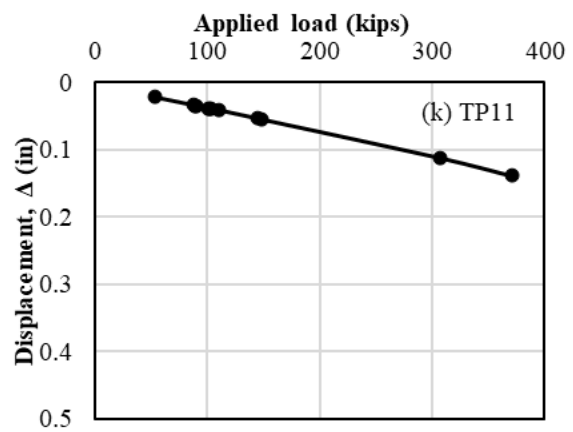
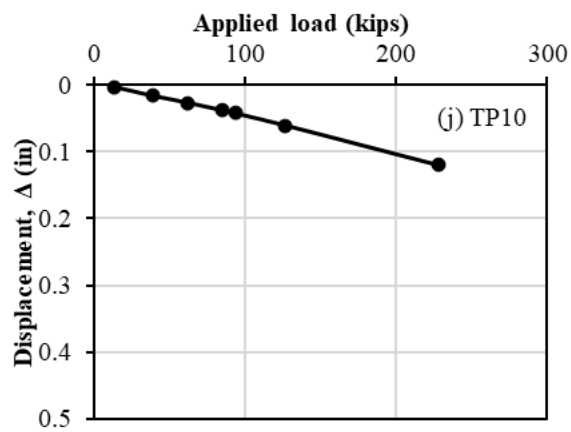
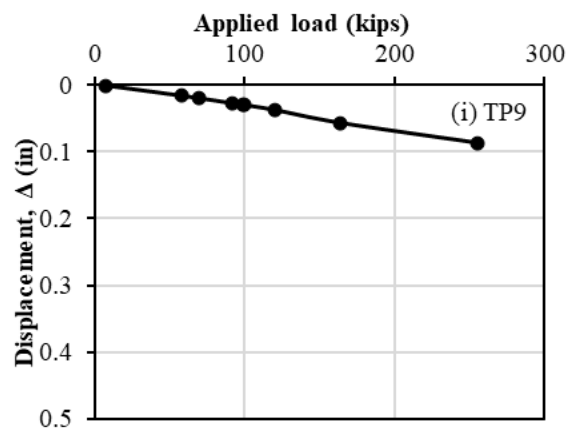
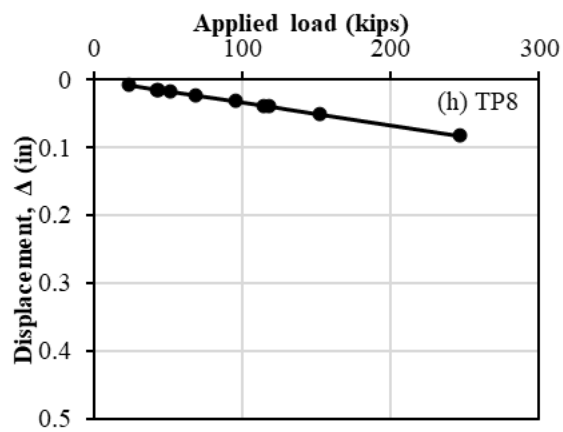
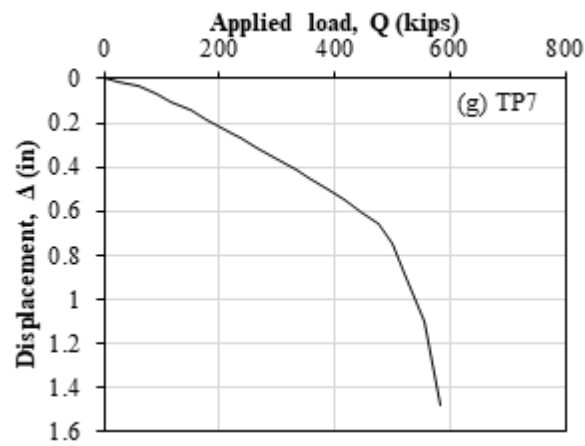
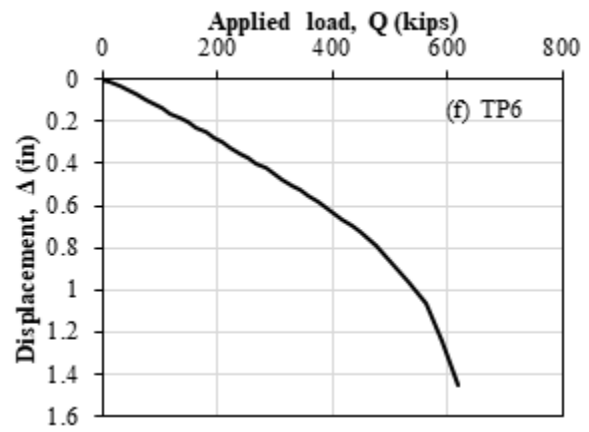
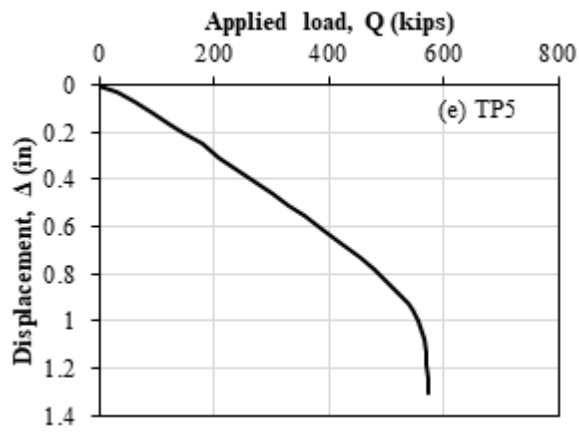
### 3.7 Static Load Test Results

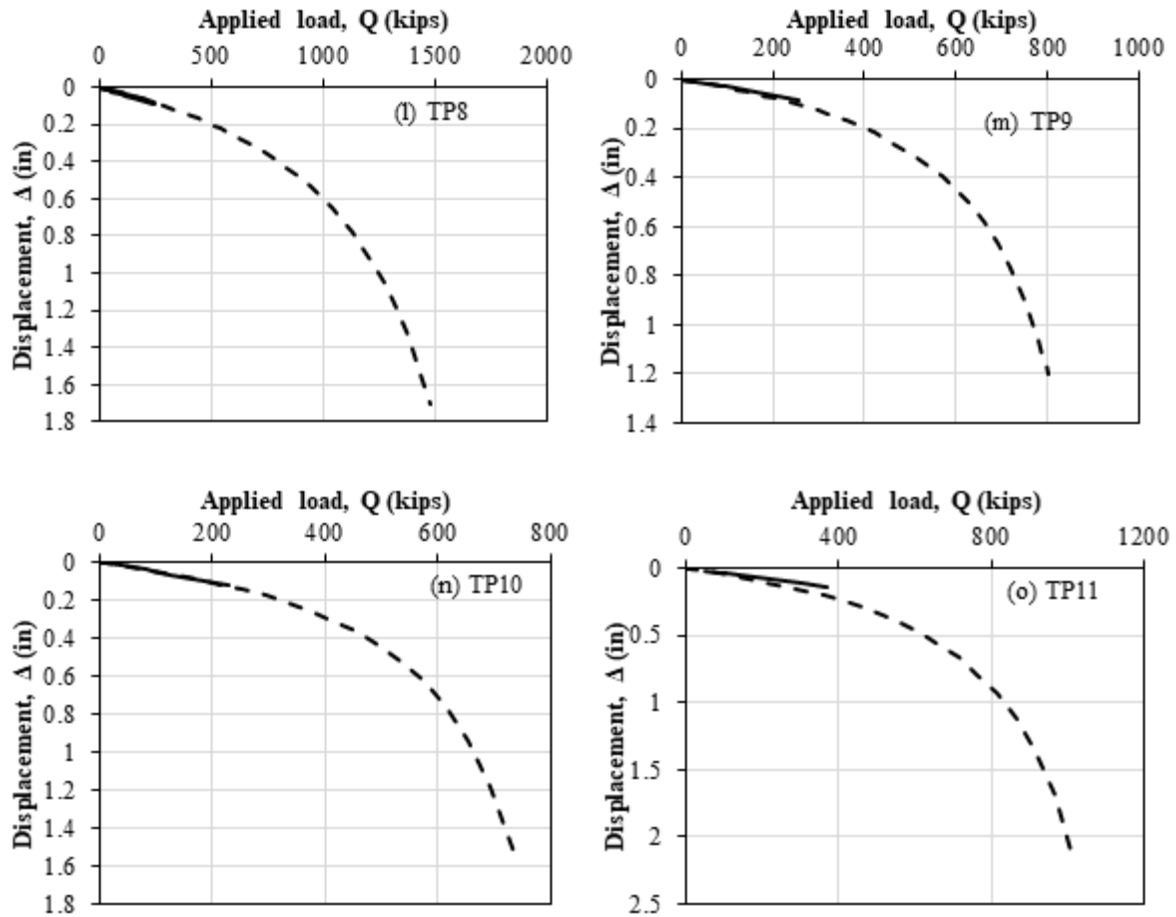
SLT was performed using the IndeSPLS on TP1 to TP5. The total pile penetration lengths were given in Table 3.1. The SLTs were performed on these test piles 1 to 3 days after end of driving (EOD). Figure 3.11a and Figure 3.11e show the pile top load-displacement responses obtained from IndeSPLS on TP1 to TP5. SLT on TP6 and TP7 using the InteSPLS was performed 2 days and 61 days after the EOD, and the total pile penetration length was 57.2 ft and 59.1 ft, respectively. Figure 3.11f and Figure 3.11g show the pile top load-displacement responses obtained from InteSPLS on TP6 and TP7. The load applied on the pile top increases linearly until the displacements reach about 0.43 inches for TP1, 0.7 in for TP2, 0.94 for TP3, 0.33 for TP4, and 0.92 for TP5. The load applied on the pile top increases linearly until the displacements reach about 0.7 inches for TP6 and 0.75 in for TP7. For TP8 to TP11 using the InnoSPLS in Colorado, the pile penetration length was 18.2 ft for TP8, 28.5 ft for TP9, 41 ft for TP10, and 24.5 ft for TP11. The loads on TP8 to TP11 increase from the construction of six structural components: abutment cap, wing walls, girders, deck panel, haunch, and concrete deck and live load (Figure 3.11h to Figure 3.11k). Figure 3.11h to Figure 3.11k shows that load increases linearly with the displacement, and the current pile top displacement was about 0.08 inches at 246 kips for TP8, 0.08 inches at 255 kips for TP9, 0.12 inches at 228 kips for TP10 and 0.13 inches at 371 kips for TP11 respectively. The linear trend suggests that TP8 to TP11 experience an elastic deformation of the steel pile, and the ultimate pile resistance has not been reached. An extrapolation method suggested by Paikowsky (1999) was adopted to predict the complete load-displacement response of TP8 to TP11 (Figure 3.11l to Figure 3.11o). The solid line represents the actual measured load-displacement response, and the dotted line corresponds to the extrapolated load-displacement response.

Based on gradual failure techniques, the ultimate pile resistances were determined based on Davisson (1972), De Beer yield load (YL) (1968), and Fuller and Hoy (1970) criteria. In addition, ultimate pile resistances were determined based on the following settlement-based failure criteria: 10 percent B (Bica et al. 2014), 5 percent B (Seo et al. 2009), and 1-in displacement. The equivalent diameter (B) of a steel H-pile was determined by converting its gross cross-sectional area (flange width  $\times$  depth) to an equivalent circular area for the 10 percent B and 5 percent B criteria (Seo et al. 2009). Figure 3.12 illustrates the distribution of

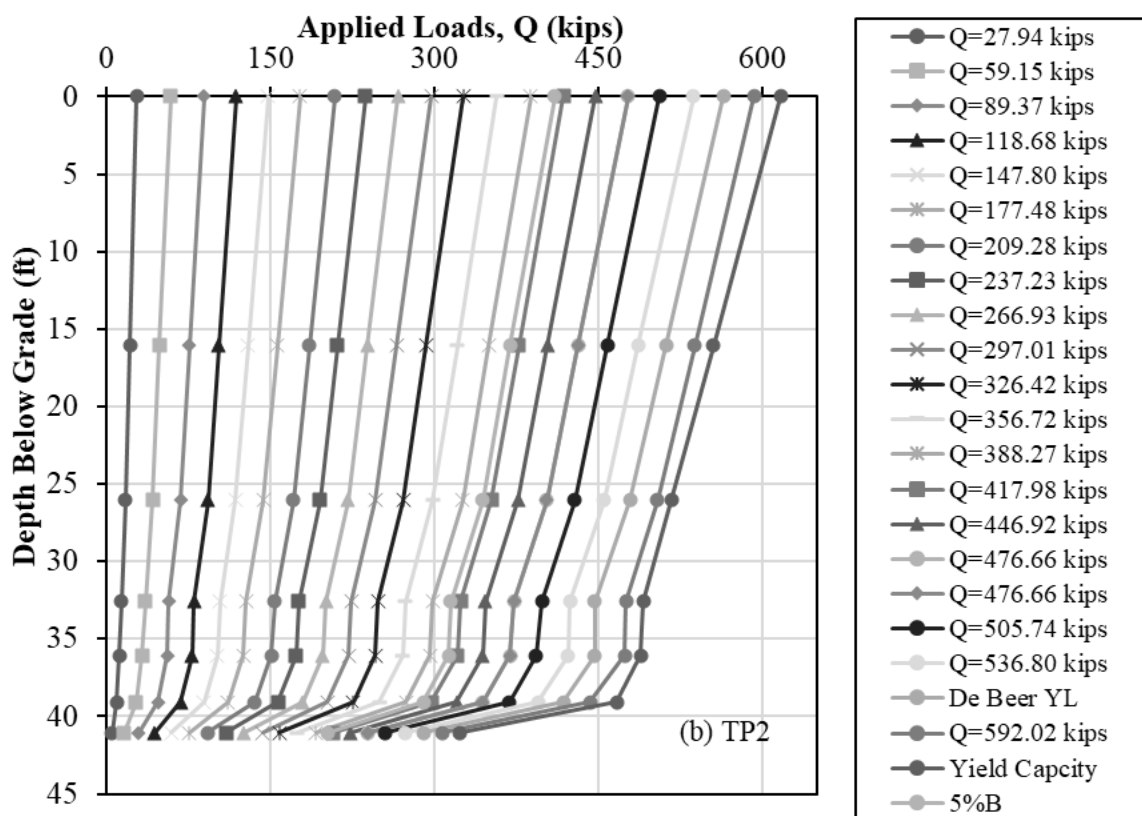
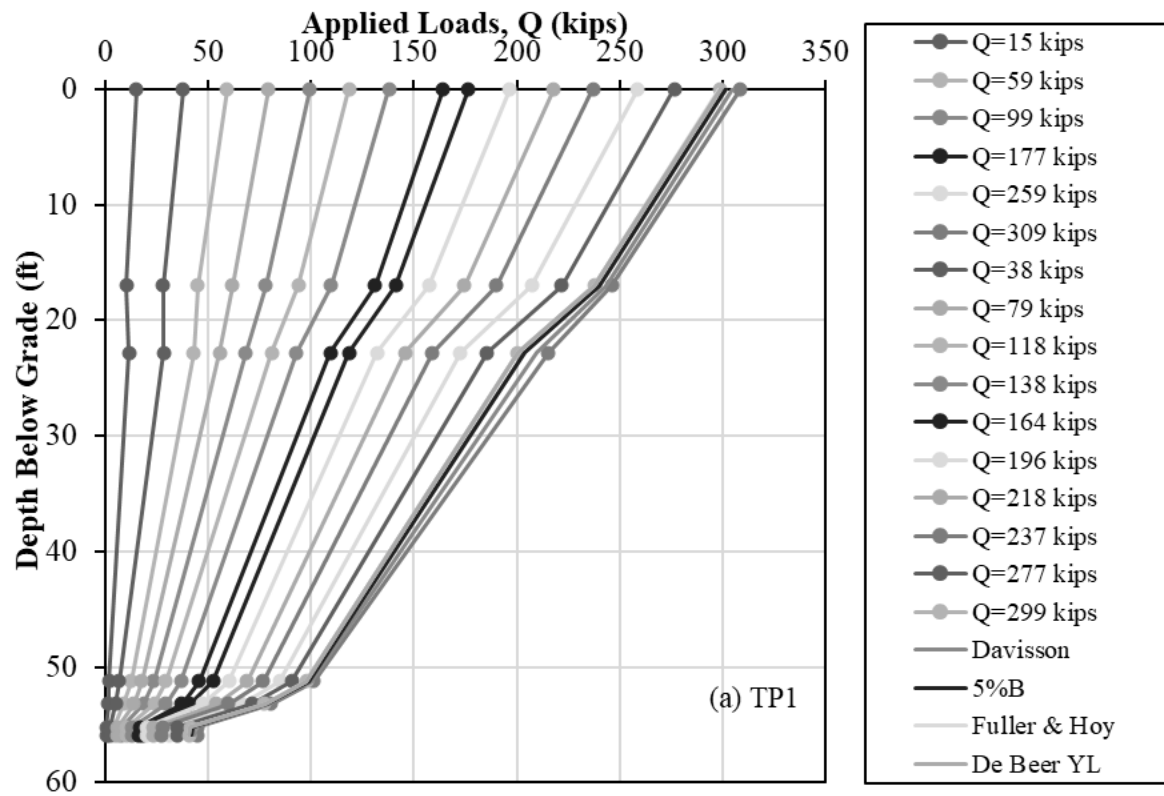
axial loads over the pile length for different applied loads. The axial load was calculated by multiplying the axial stress from the equation shown in Figure 3.7 by the cross-sectional area of the steel pile. The shaft resistance was the difference between the load at the pile head and the end bearing, which was the axial load at the pile toe. The highest ultimate resistances of 305 kips, 732.5 kips, 292 kips, 571 kips, 602 kips, and 561 kips for TP1, TP3, TP4, TP5, and TP6 (Figure 3.12a, Figure 3.12b, Figure 3.12d to Figure 3.12f), respectively, were determined based on the Davisson criteria. TP7 and TP8 to TP11 had the highest ultimate resistance obtained from the 10 percentB criteria, respectively (Figures 3.12g to 3.12k). For TP2 (Figure 3.12), the ultimate capacity was not achieved using the Davisson and 10 percentD criterion because pile failure occurred before geotechnical failure, and the yield capacity of the pile was governed for this case. Except for TP8 and TP2, all the TP show that the end bearing was less than 50 percent of the ultimate resistance on average, while the shaft resistance consists of more than 50 percent of the ultimate resistance for the four failure criteria.

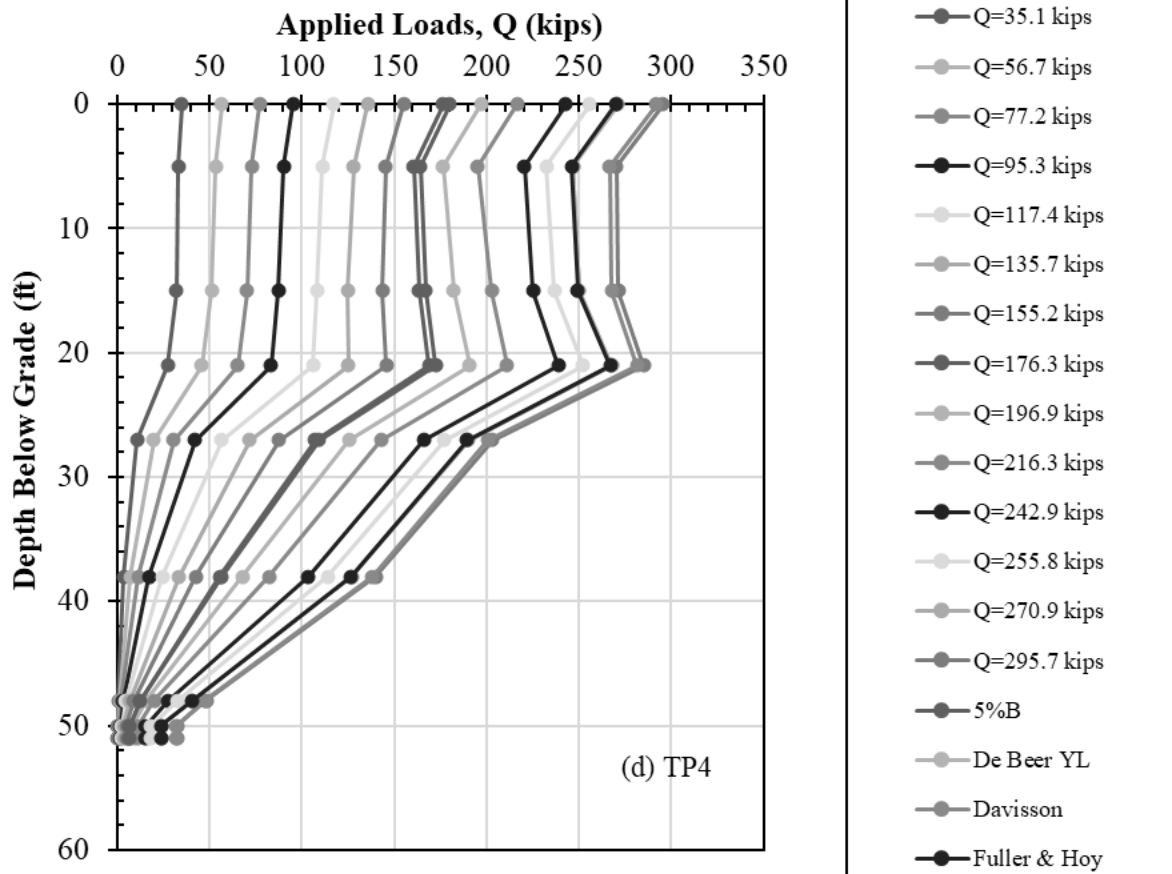
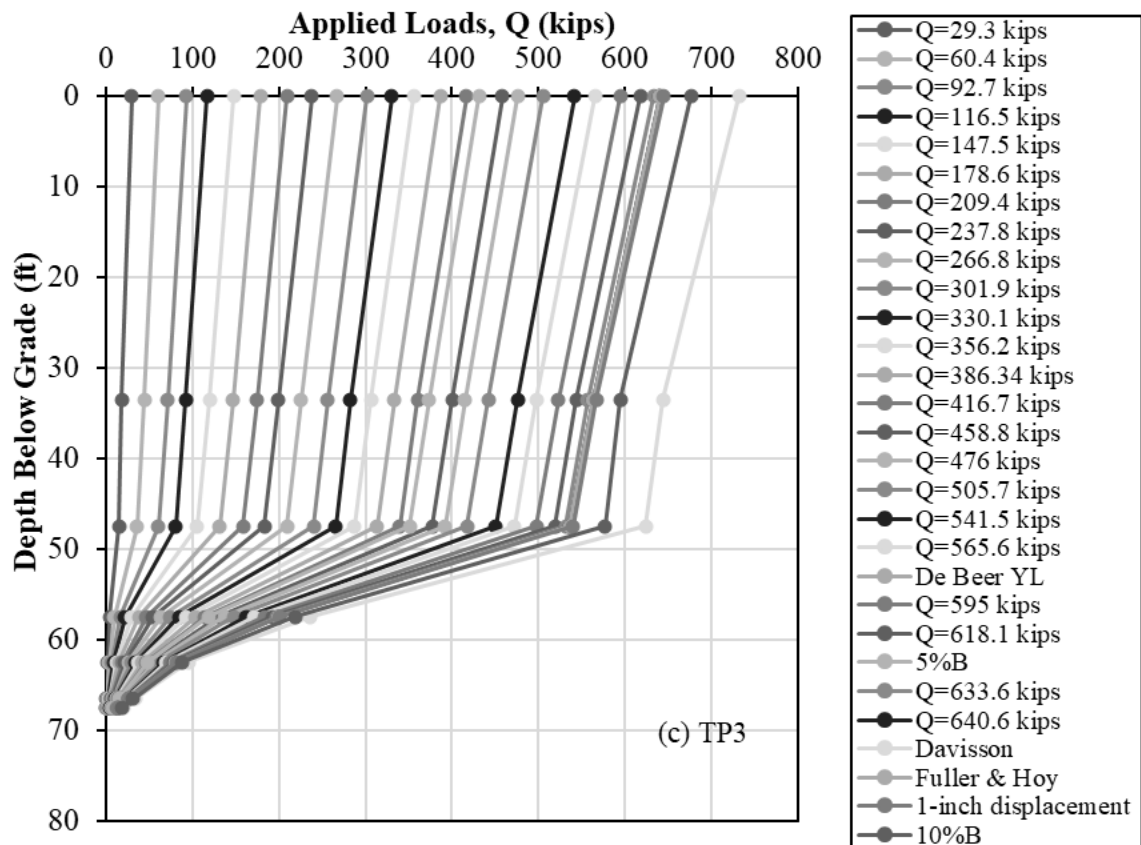




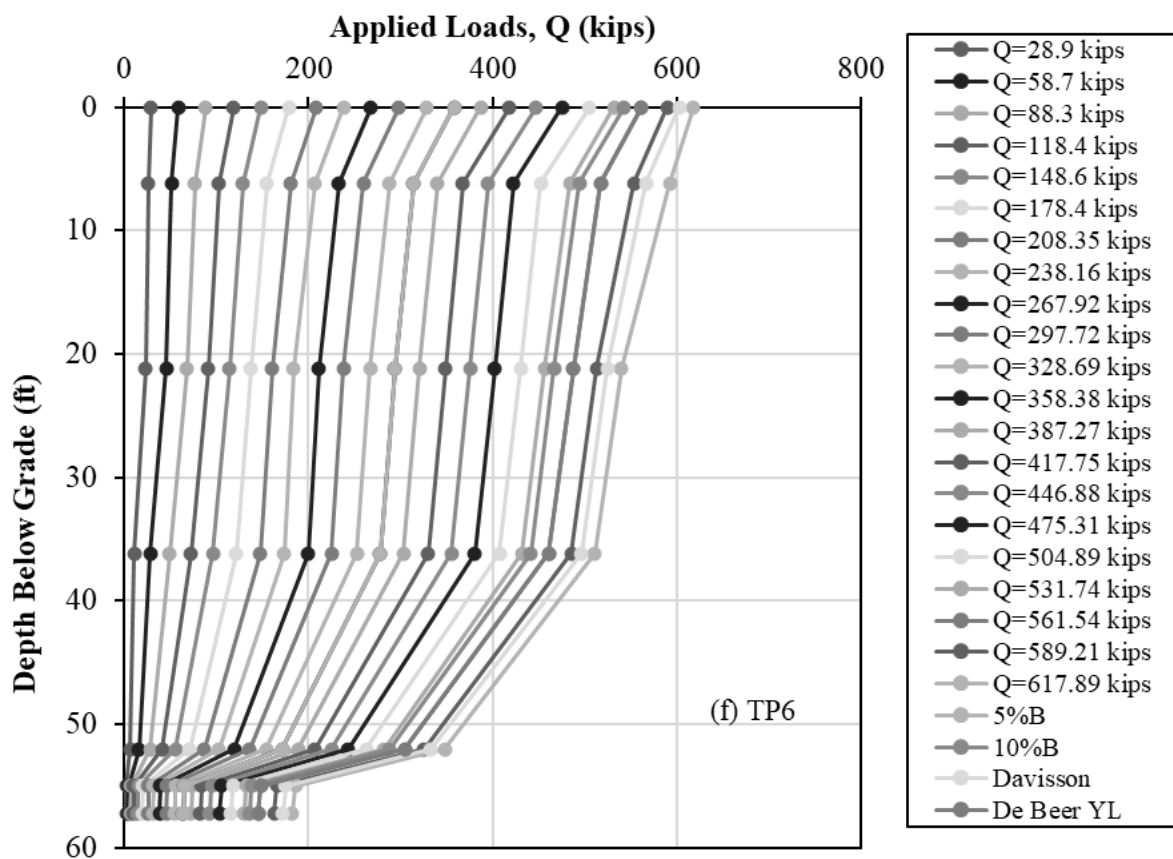
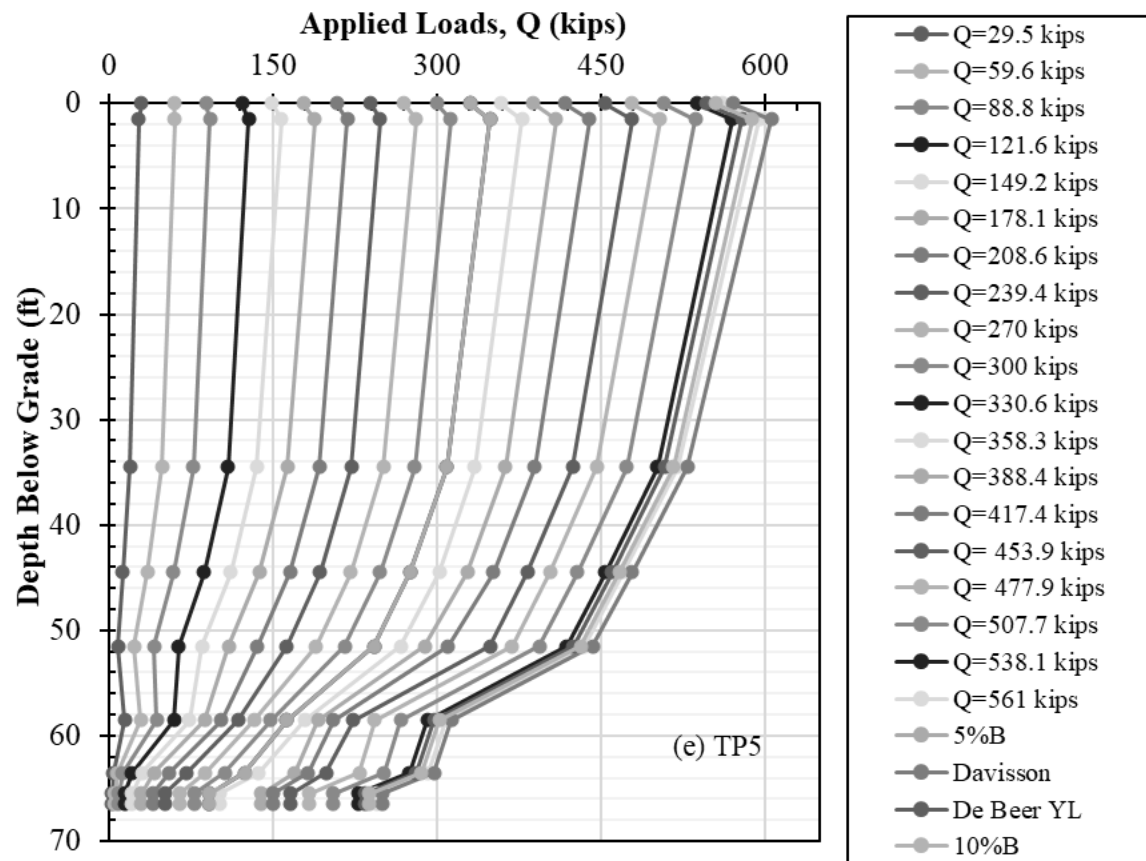


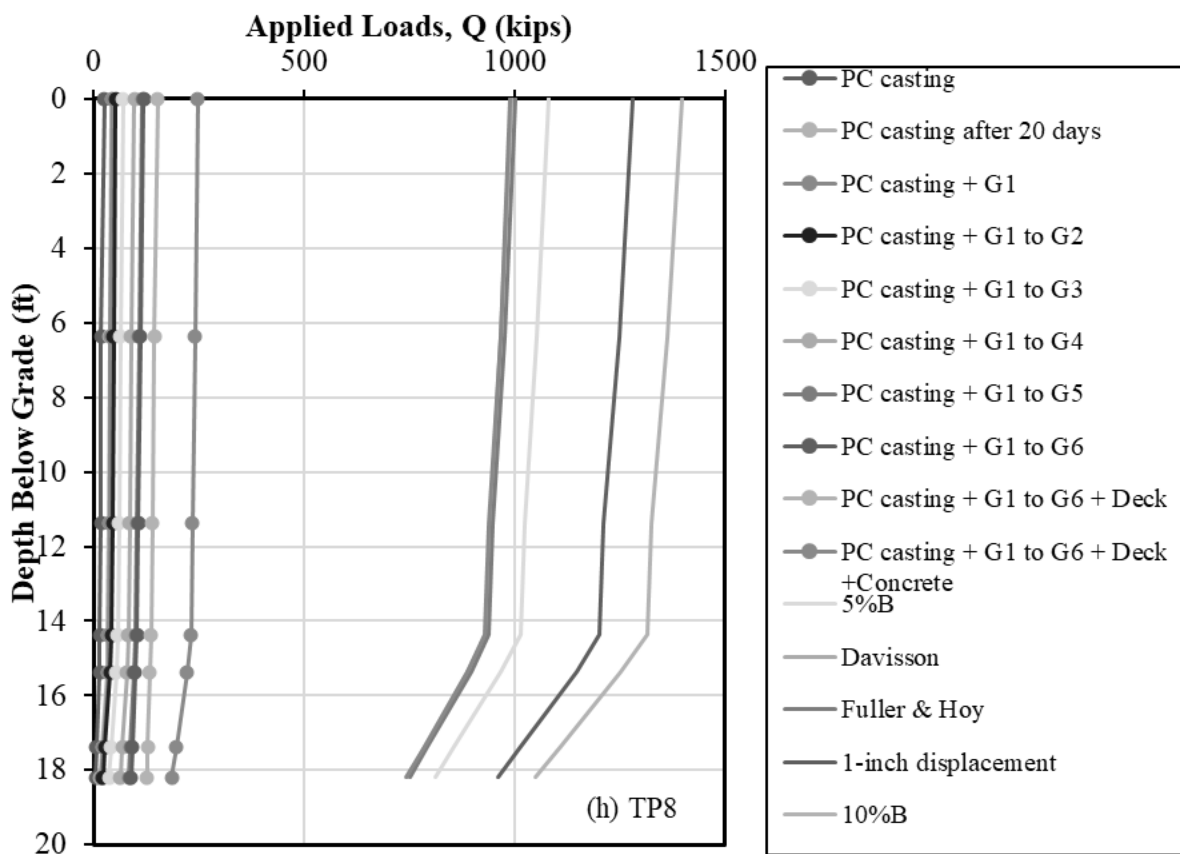
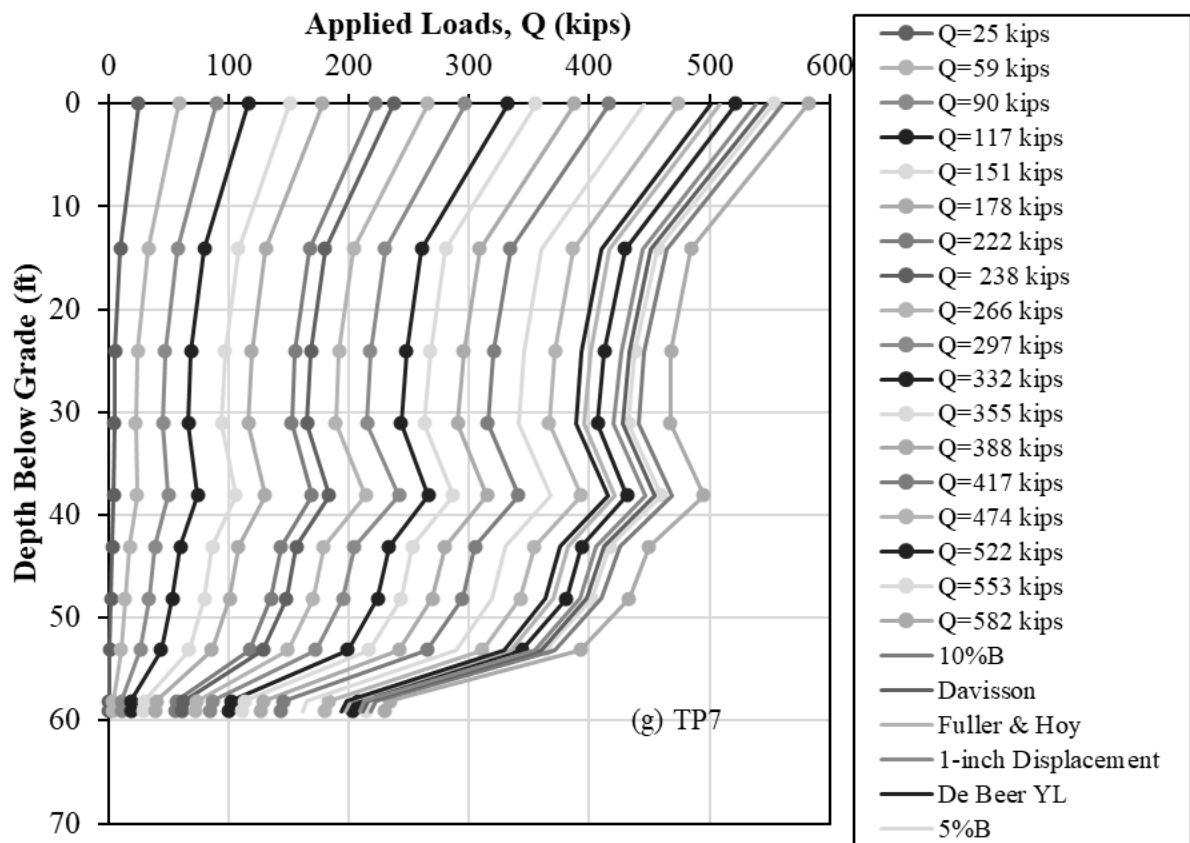
**Figure 3.11. Load Displacement Response: a) TP1, b) TP2, c) TP3, d) TP4, e) TP5, f) TP6, g) TP7, h) TP8, i) TP9, j) TP10, k) TP11, and extrapolated load displacement response of l) TP8, m) TP9, n) TP10 and o) TP11.**

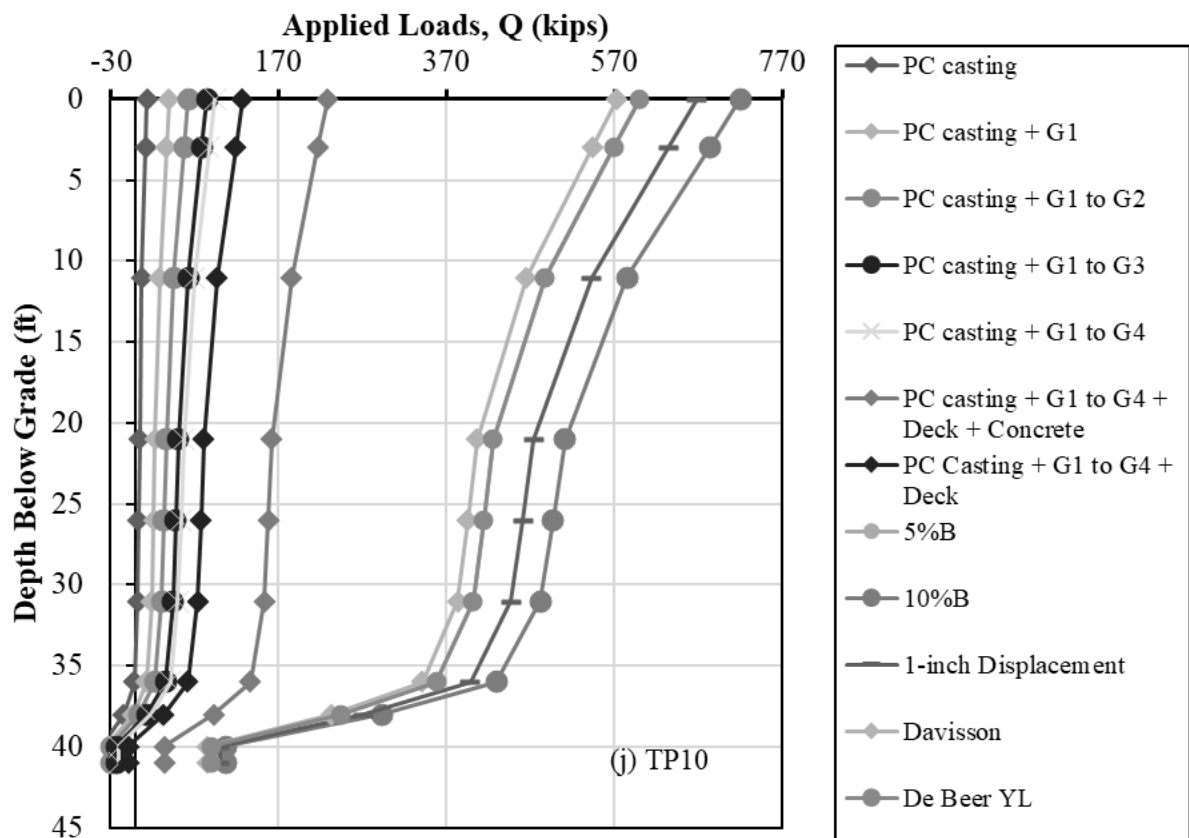
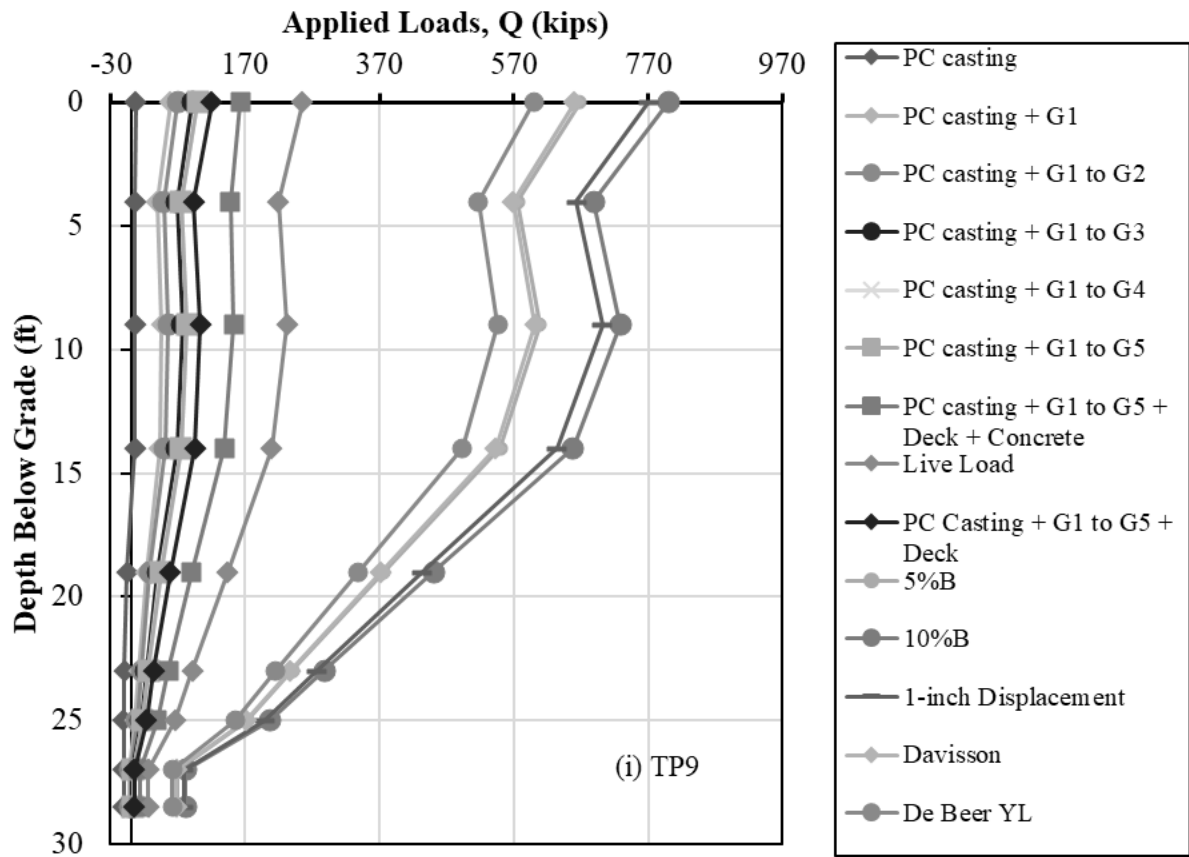












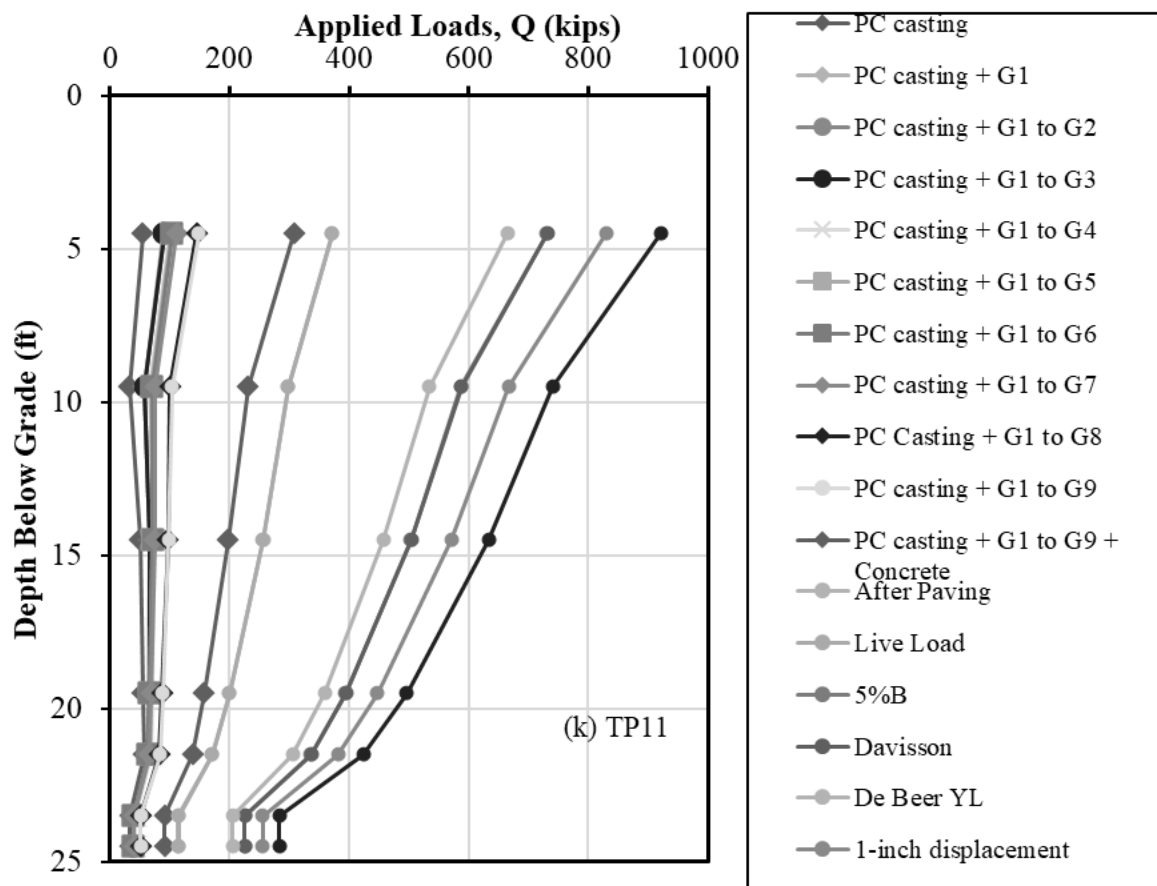
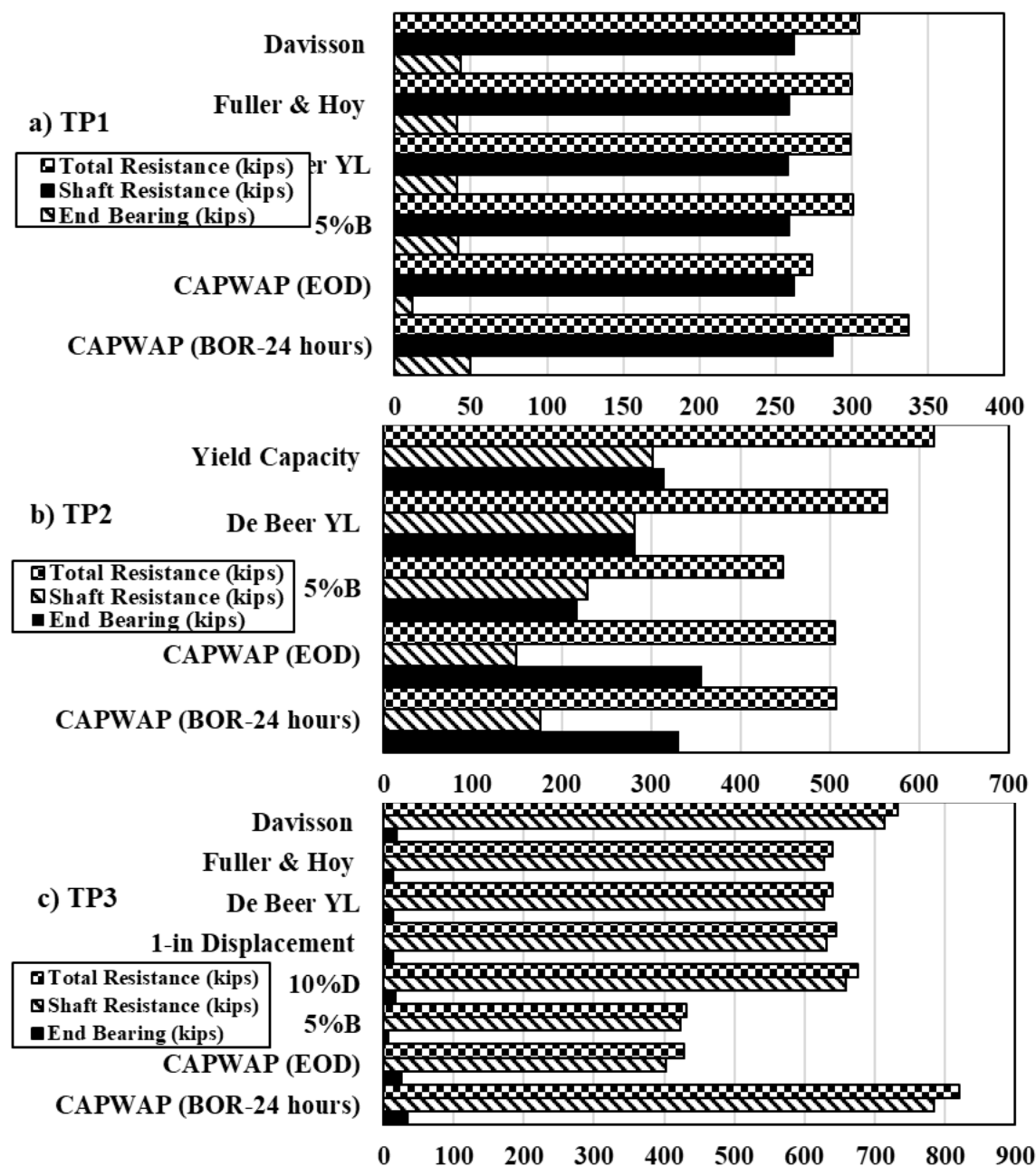


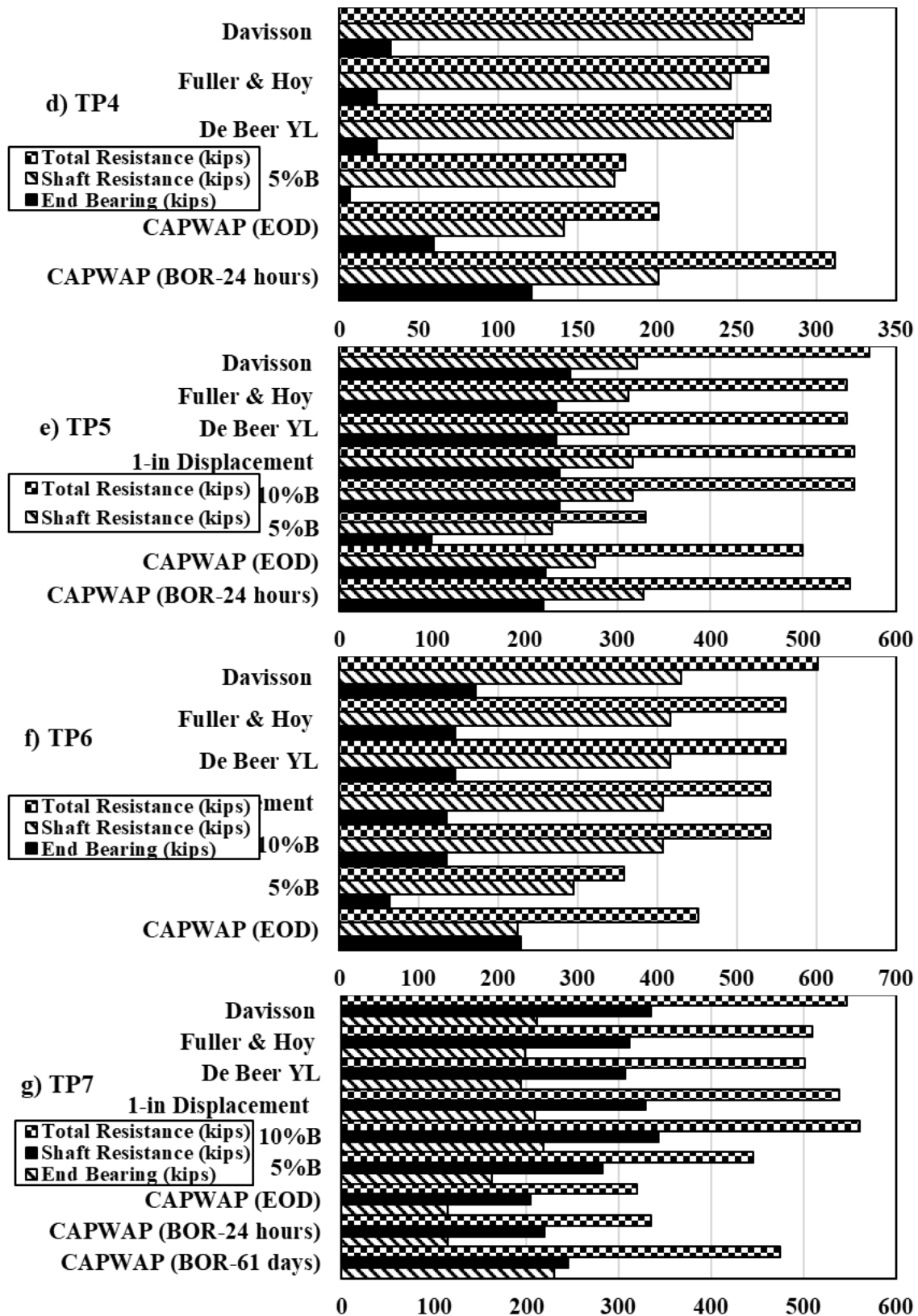
Figure 3.12. Axial load distribution along the length of piles: a) TP1, b) TP2 c) TP3, d) TP4, e) TP5, f) TP6, g) TP7, h) TP8, i) TP9, j) TP10, and k) TP11.

### 3.8 Pile Resistance from Dynamic Load Testing and Analysis

The PDA monitors all test piles during driving and subsequent restrikes. All the test piles restrike were performed 24 hours after the EOD. For TP7, restrikes were performed for 61 days after the EOD. The PDA data was used as input in the signal-matching analysis with CAPWAP to estimate the pile shaft resistance and end bearing. The estimated pile resistances from CAPWAP at the EOD and BOR for three test piles were presented in Figure 3.13. For TP1, a 23 percent increase in total pile resistance from 274 kips (CAWAP-EOD) to 337 kips (CAPWAP BOR-24 hours) was observed within 24 hours (Figure 3.13a). For TP2, a slight 0.3 percent increase in total pile resistance from 506 kips (CAWAP-EOD) to 507 kips (CAPWAP BOR-24 hours) was observed within 24 hours (Figure 3.13b). For TP3, a 96 percent increase in total pile resistance from 429 kips (CAWAP-EOD) to 820 kips (CAPWAP BOR-24 hours) was observed within 24 hours (Figure 3.13c). All test piles

experienced an increase in pile resistance with 24 hours. Furthermore, both shaft resistance and end bearing contributed to the increase in total resistance for all the test piles. For TP3, the highest contribution of 69 percent was observed from the shaft. For TP8, the highest contribution of 86 percent was observed for TP8.





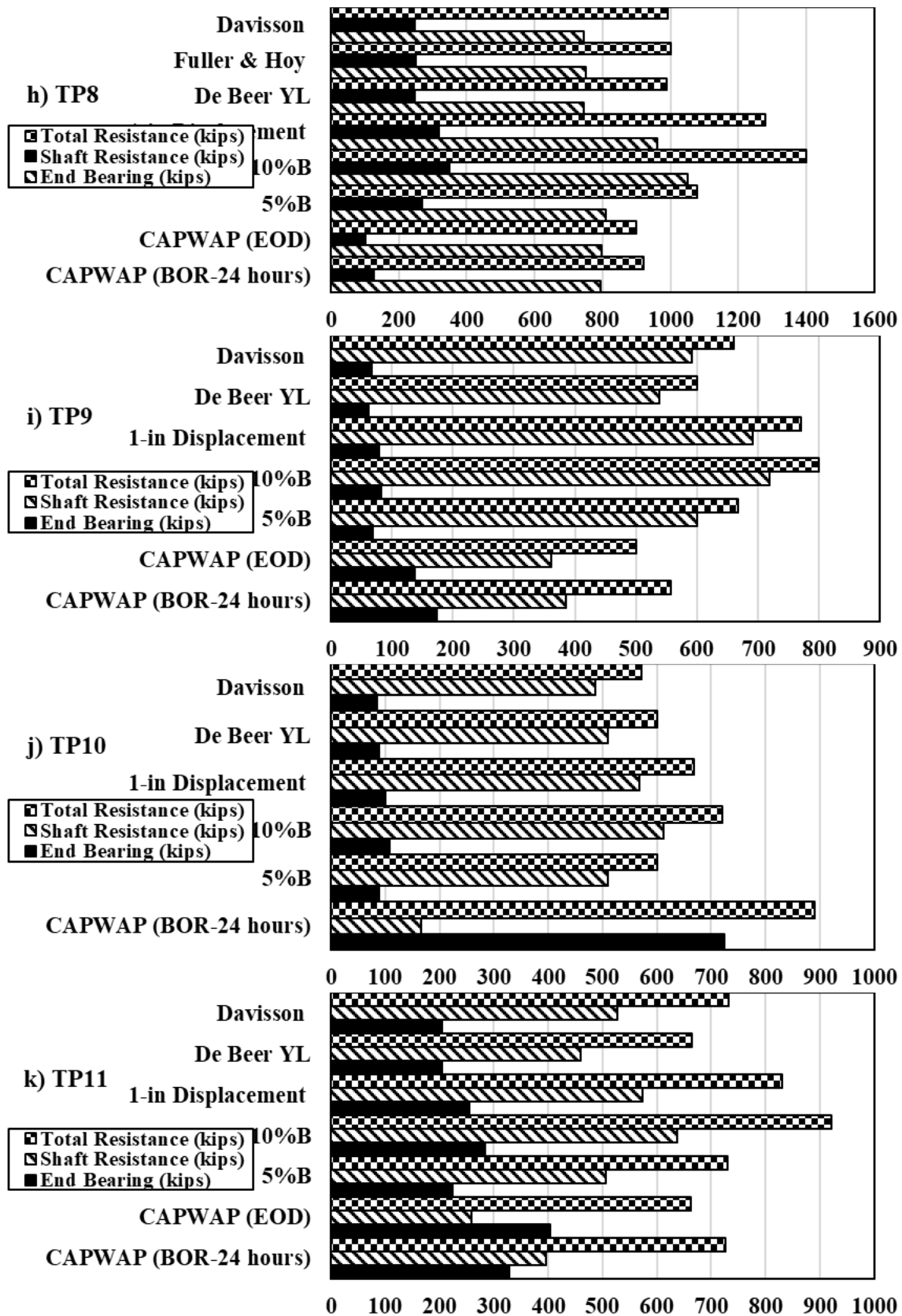


Figure 3.13. Comparison of Total Resistance, Shaft Resistance, and End Bearing: a) TP1, b) TP2 c) TP3, d) TP4, e) TP5, f) TP6, g) TP7, h) TP8, i) TP9, j) TP10, k) TP11.

### 3.9 Comparison of Dynamic and Static Load Test Results

For TP1, Figure 3.13a shows that the total resistance of 305 kips from the SLT based on Davisson criterion was 11 percent lower than that from the CAPWAP (BOR-24 hours), respectively. CAPWAP (BOR-24 hours) overpredicts the shaft resistance by about 10 percent compared with the shaft resistances from SLT based on Davisson, Fuller & Hoy, De Beer YL, and 5 percent B criteria. Compared with the end bearing from the SLT based on all criteria, CAPWAP (BOR-24 hours) also overpredicts the end bearing by about 20 percent.

For TP2, Figure 3.13b shows that the total resistance based on the De Beer YL criteria was 11.2 percent higher than that from CAPWAP (BOR-24 hours). For this test pile, the static load test reveals that the pile reaches the yield capacity before geotechnical failure occurs. The shaft resistance and end bearing based on yield capacity was 72 percent higher and 5 percent lower than that from CAPWAP (BOR- 24 hours).

For TP3 (Figure 3.13c), the total resistance of 732.45 kips from the SLT based on the Davisson criterion was 10.68 percent lower than that from the CAPWAP (BOR-24 hours). Additionally, CAPWAP (BOR-24 hours) overpredicts the shaft resistance by about 23.82 percent when compared with the shaft resistances from SLT based on the criteria of Davisson, Fuller & Hoy, De Beer YL, and 5 percent. Furthermore, when examining the end bearing values, CAPWAP (BOR-24 hours) also overpredicts the end bearing by approximately 48.32 percent compared to the SLT results across all criteria.

For TP4 (Figure 3.13d), the total resistance measured at 292.0 kips using the SLT method, based on Davisson's criterion, was 6.20 percent lower than the resistance calculated from the CAPWAP (BOR-24 hours) analysis. Furthermore, the CAPWAP method tends to overestimate shaft resistance by about 15.43 percent when compared to the SLT results derived from the Davisson, Fuller & Hoy, De Beer YL, and 5 percent criteria. Additionally, when looking at end bearing values, CAPWAP (BOR-24 hours) shows an overprediction of approximately 63.27 percent relative to the SLT findings across all evaluated criteria.

For TP5 (Figure 3.13e), the total resistance measured at 571.0 kips using the SLT method, based on Davisson criterion, was 3.76 percent greater than the corresponding value from CAPWAP (BOR-24 hours). In addition, CAPWAP tends to overestimate shaft resistance by around 10.67 percent when compared to the SLT results derived from the Davisson, Fuller &



Hoy, De Beer YL, and 5 percent criteria. Conversely, when evaluating end bearing values, CAPWAP (BOR-24 hours) underestimates the end bearing by approximately 0.57 percent in relation to the SLT findings across all criteria.

For TP6 (Figure 3.13f), the total resistance of 602.0 kips from the SLT based on the Davisson criterion was 33.19 percent higher than that from the CAPWAP (EOD). Additionally, CAPWAP (EOD) underpredicts the shaft resistance by about 73.74 percent compared with the shaft resistances from SLT based on the Davisson, Fuller & Hoy, De Beer YL, and 5 percent criteria. Furthermore, when examining the end bearing values, CAPWAP (EOD) also underpredicts the end bearing by approximately 35.71 percent compared to the SLT results across all criteria.

Figure 3.13g shows that the ultimate pile resistances of TP7 from the SLT based on the Davisson, De Beer YL, Fuller & Hoy, 10 percent B, and 1-in displacement criteria were higher than the total resistances from both CAPWAP and WEAP. Compared with the resistances from SLT based on the Davisson, De Beer YL, Fuller & Hoy, 5 percent B, 10 percent B, and 1-in displacement criteria, CAPWAP at 61-day restrike underpredicts the shaft resistance by about 37 percent, 25 percent, 27 percent, 16 percent, 40 percent, and 34 percent, respectively, while CAPWAP overpredicts the end bearing by around 8 percent, 16 percent, 14 percent, 30 percent, 5 percent, and 9 percent. The ultimate resistances from the WEAP at 61-day restrike were 44 percent, 32 percent, 34 percent, 17 percent, 47 percent, and 41 percent lower than that from the SLT based on the Davisson, De Beer YL, Fuller & Hoy, 5 percent B, 10 percent B, and 1-in displacement criteria, respectively.

Figure 3.13g shows that the predicted ultimate resistances of TP8 determined from the SLT were higher than the ultimate resistances determined from the dynamic analysis. For the Davisson, De Beer YL, Fuller & Hoy, 5 percent B, 10 percent B, and 1-in displacement criteria, WEAP underpredicts the pile resistances at 24-hour restrike by approximately 49 percent, 49 percent, 50 percent, 63 percent, 110 percent, and 93 percent, respectively. For the Davisson, De Beer YL, Fuller & Hoy, 5 percent B, percent B, and 1-in displacement criteria, CAPWAP underpredicts the shaft resistance at 24-hour restrike by approximately 97 percent, 98 percent, 95 percent, 115 percent, 178 percent, and 155 percent, respectively. Compared with the Davisson, De Beer YL, and Fuller & Hoy criteria, CAPWAP overpredicts the end bearing by about 6 percent, 7 percent, and 6 percent, respectively, but underpredicts the end

bearing by approximately 2 percent, 32 percent, and 21 percent when comparing with the 5 percent B, 10 percent B, and 1-in displacement, respectively.

For TP9, the total resistance of 660.0 kips from the SLT based on the Davisson criterion was 32.00 percent higher than that from the CAPWAP (BOR-24 hours). Additionally, CAPWAP (BOR-24 hours) underpredicts the shaft resistance by about 73.48 percent compared with the shaft resistances from SLT based on the criteria of Davisson, De Beer YL, 1-in Displacement, 10 percent B, and 5 percent B. Furthermore, when examining the end bearing values, CAPWAP (BOR-24 hours) also underpredicts the end bearing by approximately 30.73 percent compared to the SLT results across all criteria

For TP10, the total resistance recorded at 572.0 kips using the SLT method, based on the Davisson criterion, was 35.77 percent lower than the value obtained from the CAPWAP (BOR-24 hours) analysis. Furthermore, CAPWAP underestimates shaft resistance by approximately 225.03 percent when compared to the SLT results derived from the criteria of Davisson, De Beer YL, 1-in Displacement, 10 percent B, and 5 percent B. Additionally, in terms of end bearing values, CAPWAP (BOR-24 hours) also shows an underprediction of about 72.52 percent relative to the SLT findings across all evaluated criteria.

For TP11, the total resistance of 732.0 kips from the SLT based on the Davisson criterion was 0.91 percent higher than that from the CAPWAP (BOR-24 hours). Additionally, CAPWAP (BOR-24 hours) underpredicts the shaft resistance by about 36.34 percent compared with the shaft resistances from SLT based on the criteria of Davisson, De Beer YL, 1-in Displacement, 10 percent B, and 5 percent B. Furthermore, when examining the end bearing values, CAPWAP (BOR-24 hours) also underpredicts the end bearing by approximately - 17.17 percent compared to the SLT results across all criteria.

### **3.10 Summary and Conclusions**

Three static load test systems and dynamic analyses using PDA/CAPWAP and WEAP were conducted on three steel H-piles driven into IGMs in Iowa, Wyoming, and Colorado.

Vibrating wire strain gauges were installed to monitor the load distribution and residual driving forces along each test pile. This study yields the following conclusions.

- Three different SLT systems were described in this study. IndeSPLS was adopted on TP1 and TP2 in Iowa, TP3 in North Dakota, TP4 to TP5 in Kansas, where the test pile

and reaction piles were not part of the bridge foundations. The second was InteSPLS on TP6 and TP7 in Wyoming in which production piles of the main bridge foundation system serve as reaction piles, but the test pile was not part of the main bridge foundation system. SLT can be conducted using IndeSPLS and InteSPLS following the ASTM D1143 quick load test procedure. Load was applied until either geotechnical or structural failure was reached. IndeSPLS and InteSPLS were more costly and labor intensive, but the geotechnical or structural capacity of the test pile can be attained. IndeSPLS was not a critical path of bridge construction, and InteSPLS could increase the bridge construction duration.

- The third system was InnoSPLS, which was implemented on TP8 to TP11 in Colorado, and does not require a loading and reaction frame or reaction piles. The test pile was one of the production piles of the main bridge foundation system. The load was applied to the test pile from the dead and live loads of the superstructural bridge system. The test pile may not necessarily experience either geotechnical or structural failure considering the safety factor in the structural design of the bridge. The loading and unloading procedures in accordance with the ASTM standard cannot be followed, but InnoSPLS was more cost-effective than IndeSPLS and InteSPLS, and will not increase the construction duration. Data collection was required over the bridge construction duration.
- Six failure criteria, including Davisson, 10 percent B, 5 percent B, 1-in displacement, Fuller & Hoy, and De Beer's YL, were used to determine the ultimate failure resistances from the load-displacement response obtained from the SLT. The highest total resistances for TP1, TP3, TP4, TP5, TP7 and TP7 were 305 kips, 732.5 kips, 292 kips, 571 kips, and 602 kips based on the Davison criterion, respectively. For TP7, TP8, TP9, TP10 and TP11, the highest total resistances were 561 kips, 1398.8 kips, 800 kips, 720 kips, and 931 kips based on the 10 percent B criterion, respectively. Although TP3 has the highest resistance of 1,398 kips based on the 10 percent B criterion, this ultimate pile resistance was 7 percent higher than the pile structural capacity (HP 14×89) of 1,305 kips. Total ultimate resistances of TP2 determined based on the De Beer YL and 5 percent B criteria were 9 percent and 28 percent, respectively, less than the steel pile yield strength of 617 kips. For this test, pile structural capacity governs over geotechnical resistance.

- The ultimate resistances of TP1, TP3, TP4 and TP10 from the IndeSPLS and InnoSPLS based on all failure criteria were lower than that from CAPWAP at the 24-hour restrike. For TP7 and TP6, the ultimate pile resistances from the InteSPLS based on the Davisson, De Beer YL, Fuller & Hoy, 10 percent B, and 1-in displacement criteria were higher than the resistances from CAPWAP. The ultimate resistances of TP8 and TP9 from InnoSPLS were higher based on all six failure criteria than the total resistances determined from the dynamic analyses.

## CHAPTER 4: DRIVEN PILES IN FINE GRAINED SOIL BASED INTERMEDIATE GEOMATERIALS

### 4.1 Introduction

IGM has been defined as cohesive materials, such as clay shales or mudstones, with undrained shear strength ( $s_u$ ) varying from 5 ksf to 50 ksf or non-cohesive materials with corrected Standard Penetration Test (SPT) N-values falling between 50 and 100 blows per feet (Martin and Stacey 2018; O'Neill and Reese 1999). Most literature defines IGM based on unconfined compressive strength ( $q_u$ ) (Clarke and Smith 1992, Akai 1997, Marinos 1997, De Freitas 1993). Definitions of IGM vary as they were developed for different applications, such as drilled shafts and tunneling (Santi et al. 1997), and most transportation agencies do not have the criteria to define IGM for driven pile foundation. A study of driven piles in IGM has been recently completed to differentiate IGM based on corrected SPT N-value  $(N_1)_{60}$ , rock mass rating (RMR), and  $q_u$  (Adhikari et al. 2020c). The authors categorized the IGM into soil-based IGM and rock-based IGM. They recommended that if a soil-based geomaterial has  $(N_1)_{60}$  greater than 50, then it should be classified as a soil-based IGM. However, this recommendation was established based on data limited to one state involving steel H-piles and coarse-grained geomaterials. Hence, it was indispensable to expand the classification criteria to include fine-grained soil-based geomaterials.

With relatively high geological variability of IGM and different IGM definitions, higher uncertainties in deep foundation designs were expected, leading to many construction challenges (Mokwa and Brooks 2008). SA methods have been developed for the prediction of driven pile resistances in soil. AASHTO, LRFD Bridge Design Specifications (2020) recommends treating IGM in the same manner as soil for driven pile design. However, these existing SA methods cannot achieve the same target reliability for the prediction of pile resistances in IGM (Ng et al. 2015; Ng and Sullivan 2017a; Ng and Sullivan 2017b). Using 35 load test data of steel H-piles driven into IGM in Wyoming, a lower  $\phi$  of 0.09 was calibrated for the  $\alpha$ -method on IGM (Tomlinson 1980) compared to the AASHTO recommended value of 0.35 for soil to ensure the same target reliability index of 2.33 (Adhikari et al. 2020b). The economic study conducted revealed that the existing  $\alpha$ -method overpredicted the pile resistances in IGM, and a direct cost overrun was predicted with an additional average 0.835 lbs of steel per kips of applied load (Adhikari et al. 2020a). The

economic study revealed that the existing  $\alpha$ -method overpredicted the pile resistances in IGM, and a direct cost overrun is predicted with an additional average 0.835 lbs of steel per kips of applied load (Adhikari et al. 2020a). A different study was conducted by Long (2016) in Wisconsin to predict the resistances of only steel H-piles in fine-grained IGMs described as clay and silt based on an equivalent hammer blow count ( $N_{MSPT}$ ) obtained from a modified Standard Penetration Test (MSPT) that was originally developed for drilled shafts in shale and weak rocks (Stark et al. 2017). The study recommended predicting unit shaft resistance ( $q_s$ ) as  $0.021N_{MSPT}$  for a narrow range of  $q_s$  less than 2 ksf and unit end bearing ( $q_b$ ) as  $0.935N_{MSPT}$  with scatter of  $q_b$  to  $N_{MSPT}$  and for smaller  $q_b$  less than 200 ksf. These predictions were neither evaluated nor validated using separate test pile data, so that LRFD recommendations were not developed.

Furthermore, most studies were conducted on piles driven in rock-based IGM (Mokwa and Brooks 2008; Ng and Sullivan 2017a; Adhikari et al. 2018; Adhikari et al. 2020a; Adhikari et al. 2020b), and limited research has been conducted to develop LRFD recommendations for piles in fine-grained soil-based IGM (FG-IGM). Piles driven in fine-grained soils have exhibited an increase in pile resistance after the end of driving (EOD) as a function of time, which is known as pile setup (Ng et al. 2013a; Haque et al. 2017). Ng et al. (2013b) concluded that the amount of pile setup decreases in a denser fine-grained soil with a high SPT N-value, and the rate of pile setup decreases in fine-grained soil with a higher  $s_u$ . Past studies found that pile setup mostly occurred in the shaft resistance, but minimally in the end bearing (e.g., Ng and Sritharan 2016). However, similar studies have not been conducted to investigate the change in pile resistances in FG-IGM. It is not known if pile setup will occur in FG-IGMs that have higher N-value and  $s_u$ , whether  $q_s$  and  $q_b$  will exhibit different pile setups, and how the pile setups are affected by the  $s_u$  of FG-IGM.

To alleviate current limitations and to improve the understanding of pile responses in FG-IGM, 51 historical pile load test data from 25 bridge projects completed in four states were used to 1) develop a method to classify FG-IGM, 2) propose new SA methods to predict  $q_s$  and  $q_b$  of piles in FG-IGM, 3) establish LRFD recommendations for piles in FG-IGM, and 4) investigate the change in pile resistances after the EOD. The proposed SA methods were validated using 33 separate test piles from 3 different states. The performance of the proposed SA methods was evaluated in terms of efficiency factors and recommended LRFD resistance

factors ( $\phi$ ) using three probability-based methods. Changes in  $q_s$  and  $q_b$  from dynamic load tests at the EOD and beginning of restrikes (BOR) were determined and compared as a function of time and  $s_u$  of IGM.

#### 4.2 Overview of Pile Load Test Data

A total of 51 driven piles from 25 bridge projects in four states: Idaho, Montana, North Dakota, and Wyoming were compiled and analyzed. Table 4.1 summarizes the 51 test pile data that include pile type and size, general subsurface profile, total pile penetration ( $D_B$ ), driving hammer, type of FG-IGM,  $s_u$  of FG-IGM,  $q_s$  and  $q_b$  determined from PDA with subsequent signal matching using the CAPWAP, and pile hammer blow count taken at the EOD. Among the 51 test piles, 22 test piles were steel H-piles, and 29 were steel pipe piles (5 close-ended and 24 open-ended). Among 22 steel H piles, 19 test piles were in soil-based geomaterials and 3 test piles were in both soil and rock based geomaterials. Among 29 steel pipe piles, five test piles were in soil based geomaterials and 24 test piles were in both soil and rock based geomaterials. For the evaluation of  $q_b$ , only 14 test piles with pile tip embedding in the FG-IGM were included in the analysis. The classification for FG-IGM and development of new SA methods were conducted using the unit resistances determined from CAPWAP at the EOD as static load tests (SLT) were not conducted in the standard construction practice. Past studies have shown that CAPWAP results agree well with that measured from SLTs (Likins and Rausche 2004; Sakr 2013). A recent study comparing 25 pile resistances in IGM from SLTs and CAPWAP shows that the mean resistance bias of 1.077 was closer to unity and the coefficient of variation (COV) of the resistance bias of 0.121 for CAPWAP was relatively small (Adhikari et al. 2020a). Hence, in the absence of SLT measurements, it is reasonable to consider the pile resistance determined from CAPWAP as the measured resistance in this study.

**Table 4.1. Summary of 51 Driven Piles in Fine Grained Soil Based IGM.**

State	Project	Pile location	Pile	$D_B$ (ft)	Subsurface	FG-IGM	su (ksf)	$qs$ (ksf)	$qb$ (ksf)	Hammer	BC
ID	US-95 WR bridge	Pi-10 at P-1	HP 14×117	41.6	SBM	CH	8.44-15.94 <sup>#</sup>	3.61-4.68*	NA	Del. D19-42	590
ID	SH-51 SR bridge	Pi-1 at A-1	HP 14×117	68.9	SBM	ML	3.23-15.19 <sup>#</sup>	0.28-3.05*	200.37	ICE I-30v2	73
ID	SH-51 SR bridge	Pi at A-2	HP 14×117	68.9	SBM	ML & CL	9.37-13.63 <sup>#</sup>	1.31-3.36*	232.58	ICE I-30v2	52
ID	I-84B UPRR bridge	Pi-5 at A-2	HP 14×117	39.9	SBM	ML	9.07-12.00 <sup>#</sup>	1.23-3.85*	NA	ICE I-30v2	64
ID	I-84B UPRR bridge	Pi-5 at P-1	HP 14×117	23.8	SBM	ML	12.96	4.3	NA	ICE I-30v2	77
ID	I-84B UPRR bridge	Pi-12 at P-2	HP 14×117	35.9	SBM	ML	11.86	3.49	NA	ICE I-30v2	69
ID	RP road bridge	Pi-1 at A-1	18-in OEP	48	SBM & RB	ML	4.52	0.16	NA	ICE I-30v2	23
ID	RP road bridge	Pi-8 at A-2	18-in OEP	42.9	SBM & RB	ML	5.50	0.27	NA	ICE I-30v2	52
ID	SH-55 SR bridge	Pi-3 at P-1	HP 14×117	56.2	SBM	CH & CL	6.06-8.43 <sup>#</sup>	1.13-3.96*	119.42	Del. D19-42	1158
ID	SH-55 SR bridge	Pi-4 at A-1	HP 14×117	56.4	SBM	CH & CL	3.89-8.44 <sup>#</sup>	0.88-3.85*	137.67	Del. D19-42	420
ID	SH-55 SR bridge	Pi-2 at P-3	HP 14×117	35	SBM	ML & CL	14.16-16.07 <sup>#</sup>	2.61-4.35*	NA	Del. D19-42	72
ID	SH-55 SR bridge	Pi-1 at P-4	HP 14×117	20	SBM	CL	12.69-15.31 <sup>#</sup>	2.87-4.24*	397.14	Del. D19-42	333
ID	SH-55 SR bridge	Pi-1 at P-2	HP 14×117	48	SBM	CH & CL	7.79-12.41 <sup>#</sup>	3.61-3.96*	200.17	Del. D19-42	71
ID	SH-55 SR bridge	Pi-1 at P-5	HP 14×117	34	SBM	CL	7.78-9.83 <sup>#</sup>	1.35-3.92*	199.69	Del. D19-42	144
ID	SH-55 SR bridge	Pi-10 at A-2	HP 14×117	33.2	SBM	ML	10.72-14.68 <sup>#</sup>	1.83-3.87*	353.50	Del. D19-42	105
ND	Mamorial bridge	Pi-1 at P-10	HP 14×102	90	SBM	CH & CL	3.45-4.72 <sup>#</sup>	0.17-2.05*	NA	Del. D36	40
ND	Mamorial bridge	Pi-2 at P-10	HP 14×102	97	SBM	CH & CL	3.22-4.22 <sup>#</sup>	0.67-1.62*	NA	Del. D36	49
WY	PB-Parson street	Pi-5 at A-1	HP 12×53	87.9	SBM & RB	ML	4.24	0.31	NA	Del. D16-32	164



WY	PB-Muddy creek	Pi-1 at B-2	HP 12×53	35.3	SBM	ML & MH	2.7-4.72 <sup>#</sup>	0.57-1.40*	142.10	Del. D16-32	108
WY	PB-Beech street	Pi-3 at A-2	HP 12×53	46.4	SBM	ML	4.5	0.90	147.35	Del. D16-32	82
WY	PB-Muddy creek	Pi-1 at A-2	HP 12×53	53.6	SBM	ML	4.68	1.09	101.50	Del. D16-32	109
WY	PB-Beech street	Pi-1 at A-2	HP 12×53	44.7	SBM	ML	4.5	1.15	147.45	Del. D16-32	62
MT	MR-west of zurich	Pi-1 at B-1	16-in OEP	82.2	SBM & RB	ML	4.73-12.27 <sup>#</sup>	1.60-3.07	NA	ICE I-30	74
MT	MR-west of zurich	Pi-6 at B-2	16-in OEP	50.3	SBM & RB	CL	3.89	0.47	NA	ICE I-30	87
MT	MR-west of zurich	Pi-1 at B-3	16-in OEP	76.2	SBM & RB	CL	4.92	0.89	NA	ICE I-30	106
MT	Bridge over CC	Pi-4 at B-3	24-in OEP	58	SBM & RB	CH	2.75	0.35	NA	ICE I-36	135
MT	Capitol interchange	Pi-1 at B-1	16-in CEP	29.5	SBM & RB	CH	3.45	0.73	NA	ICE I-30	30
MT	Capitol interchange	Pi-8 at B-1	16-in CEP	29	SBM	CH	7.45	1.57	NA	ICE I-36	48
MT	Capitol interchange	Pi-2 at B-1	16-in CEP	28	SBM & RB	CH	3.67	1.20	NA	ICE I-30	60
MT	Capitol interchange	Pi-38 at B-4	16-in CEP	27.5	SBM	CH	4.73	1.87	NA	ICE I-30	44
MT	Bridge over RR	Pi-1 at B-3	20-in OEP	41	SBM & RB	CL	5.50	0.59	NA	ICE I-30	42
MT	Bridge over RR	Pi-1 at B-2	20-in OEP	45	SBM & RB	MH	6.59	2.02	NA	ICE I-30	73
MT	M FK porcupine	Pi-4 at B-1	16-in OEP	47.5	SBM	MH	4.73	0.85	27.71	ICE I-30	23
MT	M FK porcupine	Pi-2 at B-3	20-in OEP	46.2	SBM & RB	MH	4.32	1.65	NA	ICE I-30	35
MT	Bridge over HC	Pi-1 at B-1	16-in OEP	42.2	SBM & RB	CL	3.68	0.52	NA	APE D30-42	120
MT	Bridge over BNSF	Pi-5 at A-1	HP 14×117	68	SBM & RB	CH	4.52	1.74	NA	ICE I-30v2	96
MT	Bridge over BNSF	Pi-1 at A-4	HP 14×117	69.4	SBM & RB	CL	6.06	1.13	NA	ICE I-30v2	96
MT	Bridge over MR	Pi-1 at B-1	20-in OEP	91.5	SBM & RB	CL	4.11	0.27	NA	ICE I-36	172
MT	PC overflow	Pi at B-1	20-in OEP	82	SBM & RB	CL	4.72	0.45	NA	Del. D46-42	30

MT	Bridge over PC	Pi at B-3	20-in OEP	93.8	SBM & RB	CH	3.67	0.77	NA	Del. D46-42	31
MT	Bridge over PC	Pi at B-1	20-in OEP	91.8	SBM & RB	CH	3.22	0.28	NA	Del. D46-42	29
MT	Bridge over LCC	Pi-3 at B-1	20-in OEP	136.5	SBM	CH	6.94	2.02	57.43	ICE I-36	313
MT	Bridge over SC	Pi-4 at B-2	16-in CEP	32.5	SBM & RB	CH	3.90	0.47	NA	Del. D19-32	109
MT	Bridge over LMC	Pi-1 at B-1	16-in OEP	95	SBM & RB	CH	4.32	1.65	NA	APE D36-26	74
MT	Bridge over LMC	Pi-3 at B-2	16-in OEP	97.9	SBM & RB	CH	5.50	0.59	NA	APE D36-26	192
MT	Bridge over LMC	Pi-4 at B-4	16-in OEP	81	SBM	CH	4.72	0.57	NA	APE D36-26	107
MT	I-94 bridge BI	Pi-2 at B-3	16-in OEP	45.8	SBM & RB	CL	3.67	0.34	NA	ICE I-36	87
MT	I-94 bridge BI	Pi-4 at B-1	16-in OEP	52	SBM & RB	CL	3.67	0.35	NA	ICE I-36	40
MT	Bridge over Cr.	Pi-16 at B-1	16-in OEP	20.7	SBM & RB	CL	4.72	1.60	NA	ICE I-36	74
MT	Bridge over Cr.	Pi-2 at B-4	16-in OEP	20	SBM & RB	CL	4.93	1.62	NA	ICE I-36	44
MT	Bridge over Co.	Pi-3 at B-2	16-in OEP	36.8	SBM & RB	CL	12.27	3.22	NA	ICE I-30v2	80

ID=Idaho; ND=North Dakota; WY=Wyoming; MT=Montana; WR=Weiser River; SR= Snake River; RP=Robinson Park; BC=Butte Creek; MR=Milk River; CC=Cherry Creek; RR=Rock Reek; HC=Home Creek; PC=Porcupine Creek; LCC=Little Cottonwood Creek; SC=Sharpy Creek; BI=Broadus interchange; Cr.=Crooked Creek; Co.=Coral Creek; LMC=Little Muddy Creek; A=Abutment; Pi=Pile; P=Pier; B=Bent;  $D_B$ =Total pile penetration; CEP=Close ended pipe pile; OEP=Open ended pipe pile; SBM=Soil based (both coarse and fine) geomaterials; SBM & RB=Soil- and rock-based geomaterials; CH-IGM=High plasticity clay IGM; CL-IGM=Low plasticity clay IGM; MH-IGM=High plasticity silt IGM; ML-IGM=Low plasticity silt IGM;  $s_u$ =Undrained shear strength;  $q_s$ =Unit shaft resistance; #=Range of  $s_u$ ; \*=Range of  $q_s$ ;  $q_b$ =Unit end bearing; NA=Not applicable; Del.=Delmeg; ICE=International Construction Equipment; APE=American Pile Driving Equipment; BC=Hammer blow count at end of driving (bl/ft).

### 4.3 Proposed Classification Criteria for Fine Grained Soil Based IGM

The soil-based geomaterials of 51 test piles were first classified according to the Unified Soil Classification System (USCS). The  $\alpha$ -method (AASHTO 2020) was selected to distinguish FG-IGM from fine-grained soil as this method is currently and widely used in the estimation of driven pile resistances in fine-grained soil in terms of  $s_u$ . A total of 169 fine-grained layers of the 51 test piles, that have  $s_u$  values ranged from 0.61 ksf to 16.07 ksf, were identified for the  $q_s$  prediction using the  $\alpha$ -method. The  $s_u$  values were determined from laboratory tests, and some were predicted using the prediction equation ( $s_u/P_a = 0.29N^{0.72}$ ) that was chosen for a wider range of SPT N-values (Kulhawy and Mayne 1990). The uncertainty associated with this prediction equation for  $s_u$  have been accounted for in the LRFD calibration. The classification method was established by comparing the COV of  $q_s$  biases (ratio of  $q_s$  from CAPWAP to  $q_s$  from the  $\alpha$ -method) to  $s_u$ .

Fine-grained layers with  $s_u$  values ranging from 0.61 ksf to 16.07 ksf were reduced by excluding the layer with the maximum  $s_u$  value from each analysis cycle to produce the next datasets for subsequent analyses. The COV values of resistance biases were then determined for different datasets and compared with their respective maximum  $s_u$  values in Figure 4.1. To clarify the analysis process, the first dataset consisting of 169 fine-grained layers yielded a COV of 0.875, which was plotted against the maximum  $s_u$  of 16.07 ksf (Figure 4.1). In the next analysis cycle, the fine-grained layer with the  $s_u$  value of 16.07 ksf was eliminated from the dataset. Hence, the remaining 168 layers were used to yield a COV of 0.88, which was plotted against the new maximum  $s_u$  of 15.94 ksf. The analysis was repeated until the maximum  $s_u$  of the dataset reached 1.01 ksf as the boundary between FG-IGM and fine-grained soil was less likely to occur below 1.01 ksf. This was justified by the suggested  $s_u$  greater than 2.12 ksf for very stiff to hard fine-grained soil (Kulhawy and Mayne 1990), and the almost constant adhesion factor ( $\alpha$ ) of the  $\alpha$ -method for  $s_u$  exceeding about 3 ksf (AASHTO 2020). Furthermore, the decreasing COV values for  $s_u$  less than about 2.7 ksf agrees with the efficiency of the  $\alpha$ -method originally developed for fine-grained soil. Figure 4.1 shows two distinct groups of COV with the lower COV average of about 0.68 and the upper COV average of 0.95. The variation in COV values observed in the upper COV group for maximum  $s_u$  values ranging between 4 ksf and 5 ksf was attributed to the

presence of both steel H-piles and steel pipe piles used in the analysis. The transition from the lower COV to the upper COV group occurs at the maximum  $s_u$  of about 2.7 ksf. To facilitate the development of SA methods to improve the design efficiency of driven piles in FG-IGM, a  $s_u$  value of 2.7 ksf was recommended as the boundary separating FG-IGM from fine-grained soil. Figure 4.2 illustrates the proposed classification of fine-grained soil based geomaterials in a flow chart.

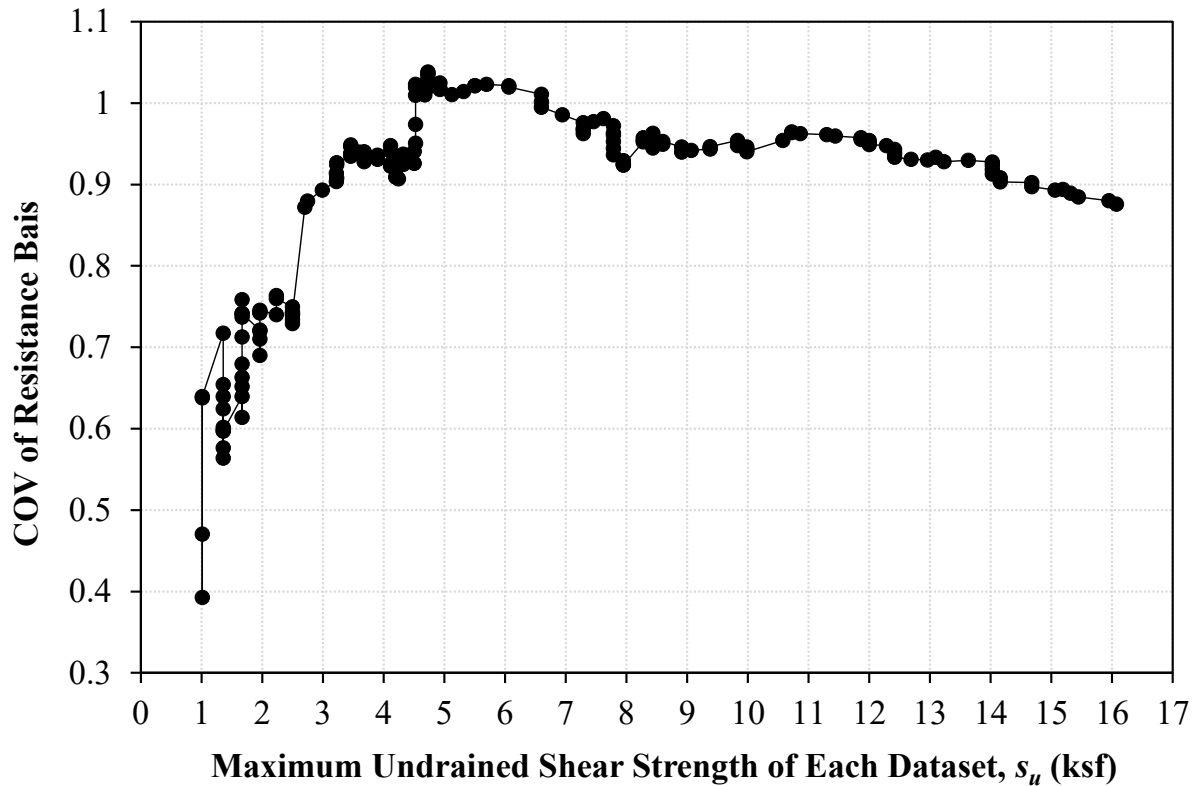


**Figure 4.1. Comparison of COV and Maximum  $s_u$  for the Existing  $\alpha$ -method.**

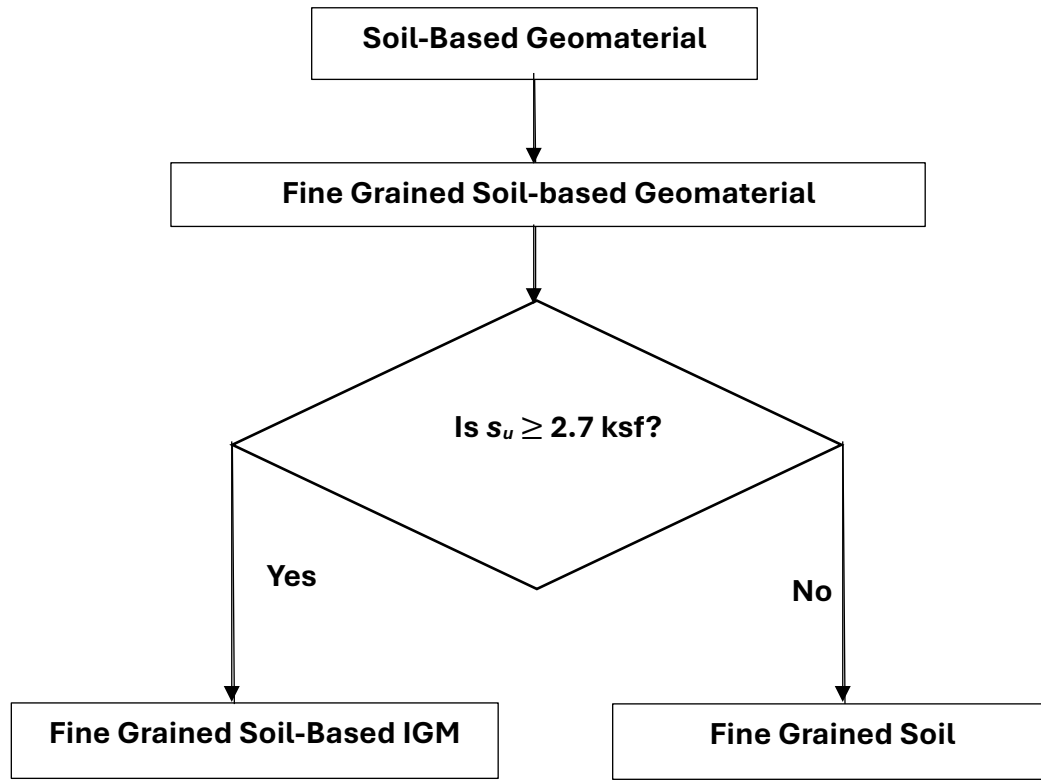


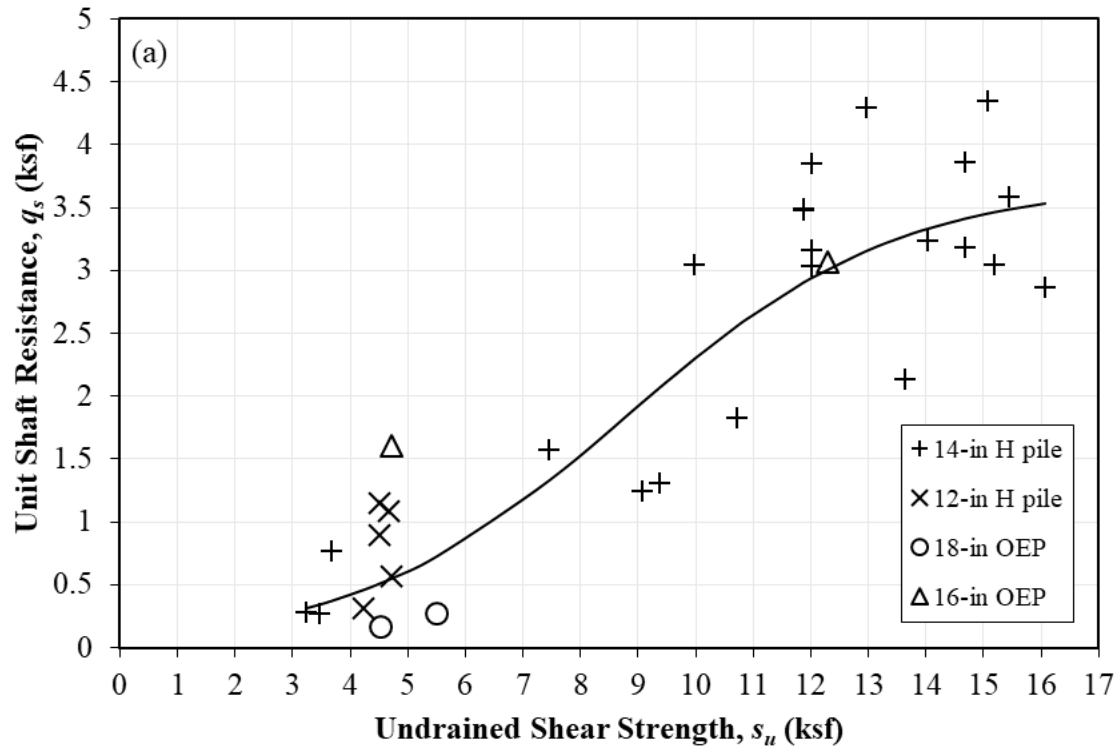
**Figure 4.2. Proposed Classification for Fine Grained Soil-Based Geomaterial in a Flowchart.**

#### **4.4 Development of New Static Analysis Methods**

New SA methods for the prediction of pile resistances in FG-IGM were developed for different subgroups to reduce uncertainties associated with fine-grained geomaterials and to improve the accuracy of pile resistance prediction. To develop more efficient SA methods for prediction of  $q_s$ , FG-IGM was divided into clay-based IGM and silt-based IGM based on grain size. The clay-based IGM was further divided into high plasticity clay-based IGM (CH-IGM) and low plasticity clay-based IGM (CL-IGM). For the silt-based IGM, only low plasticity silt-based IGM (ML-IGM) was considered in this study due to a small sample size of 4 in the high plasticity silt-based IGM (MH-IGM). The SA method for  $q_b$  was established using 14 piles with FG-IGM as the end-bearing layer. The  $q_b$  was calculated by dividing the end bearing from CAPWAP with a box area

of H-piles or a close-ended area of pipe piles as soil plugging was assumed from the predicted soil plug weight in the CAPWAP reports.

The proposed SA methods for  $q_s$  were developed by comparing the  $q_s$  at the EOD from CAPWAP with  $s_u$ . Figures 4.3a through 4.3c show an increasing nonlinear trend of  $q_s$  with respect to  $s_u$  for ML-IGM, CL-IGM, and CH-IGM, respectively



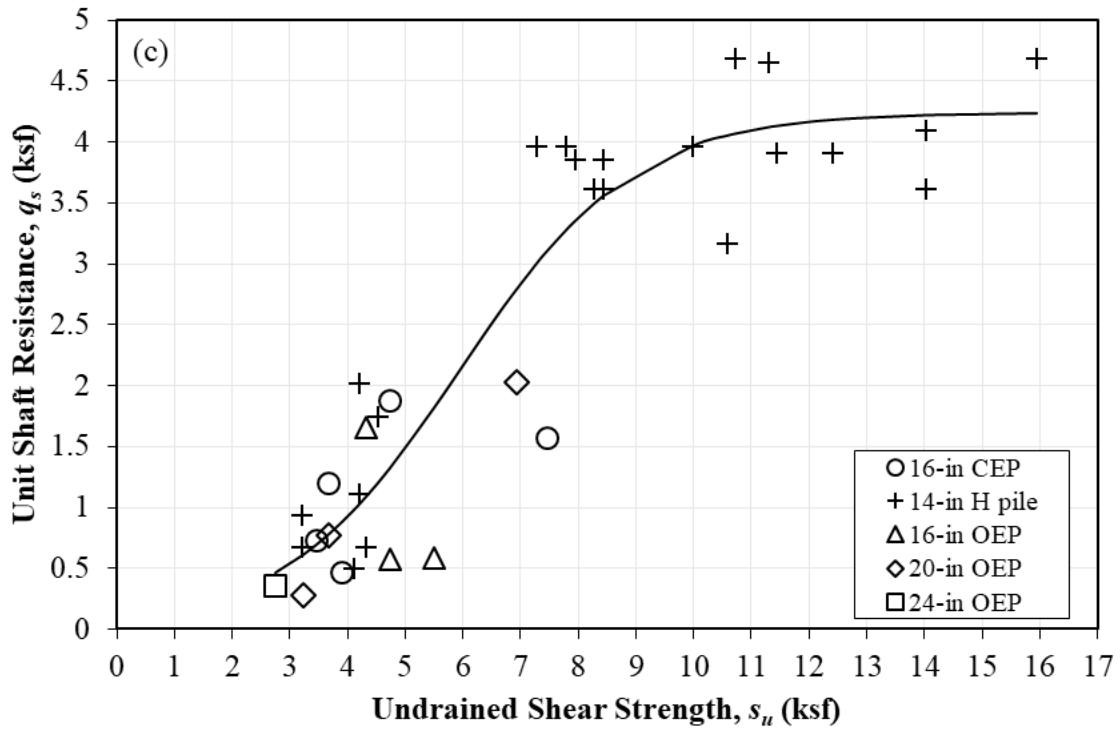
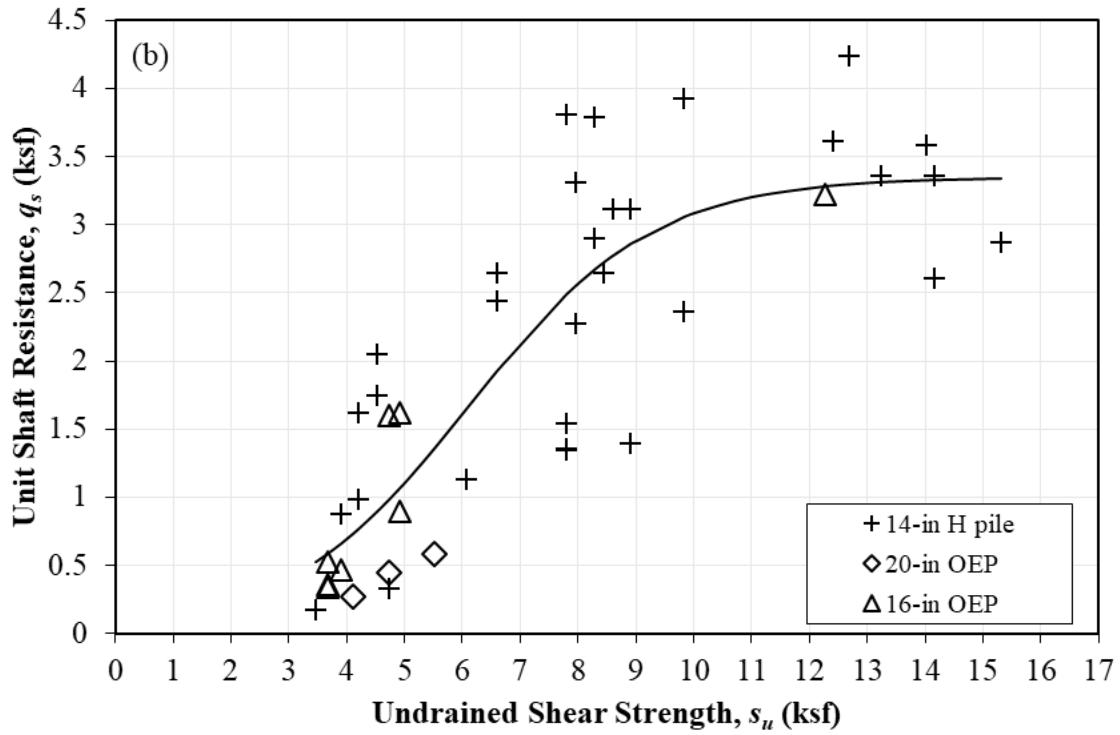


Figure 4.3. Plot of Unit Shaft Resistance from CAPWAP Versus  $s_u$  for (a) ML-IGM, (b) CL-IGM, and (c) CH-IGM.

#### 4.4.1 Unit Shaft Resistance for Fine-Grained Soil Based IGM

SA methods were developed for the prediction of  $q_s$  in FG-IGMs (ML-IGM, CL-IGM, CH-IGM) using  $q_s$  values from CAPWAP and the respective  $s_u$  values. The logistic model was recommended for the prediction of  $q_s$  in each of ML-IGM, CL-IGM, and CH-IGM. The respective prediction equations in terms of  $s_u$  and atmospheric pressure ( $P_a$ ) for ML-IGM, CL-IGM, and CH-IGM were given by the equations shown in Figure 4.4a to 4.5c, respectively.

$$\begin{aligned} \text{a) } \hat{q}_s &= \left[ \frac{1.80}{1 + 44e^{-0.89\frac{s_u}{P_a}}} \right] P_a \\ \text{b) } \hat{q}_s &= \left[ \frac{1.58}{1 + 47.6e^{-1.34\frac{s_u}{P_a}}} \right] P_a \\ \text{c) } \hat{q}_s &= \left[ \frac{2}{1 + 50.4e^{-1.4\frac{s_u}{P_a}}} \right] P_a \end{aligned}$$

**Figure 4.4. Equation. Unit Shaft Resistance Prediction for a) ML-IGM, b) CL-IGM and c) CH-IGM.**

It is important to note that the proposed predictions equations were applicable for  $q_s$  values ranging from 0.17 ksf to 4.68 ksf and  $s_u$  values ranging from 2.75 ksf to 16.07 ksf. Figure 4.3 shows the relationships between the  $s_u$  values and the  $q_s$  values from CAPWAP along with the prediction equations for ML-IGM in Figure 4.3a, CL-IGM in Figure 4.3b, and CH-IGM in Figure 4.3c. Figure 4.4a shows that  $q_s$  increases rapidly with the increase in  $s_u$ , and the increase in  $q_s$  reduces when the  $s_u$  is greater than about 10 ksf. Figures 4.3b and 4.3c show that the predicted  $q_s$  based on the proposed models have become almost constant when  $s_u$  exceeds about 10 ksf. The reducing rate of  $q_s$  at a higher  $s_u$  in all FG-IGM could be attributed to the plastic behavior of FG-IGM when an ultimate pile adhesion is reached.



#### 4.4.2 Unit End Bearing for Fine-Grained Soil-Based IGM

A SA method was developed to predict  $q_b$  of steel H- and pipe piles in FG-IGM. The reciprocal YD model was recommended for the  $q_b$  prediction. The resulting prediction equation is shown in Figure 4.5. The atmospheric pressure ( $P_a$ ) was included to account for the unit used in the  $q_b$  prediction. It is important to note that the proposed equation is applicable for  $q_b$  values ranging from 27.71 ksf to 397.14 ksf and the interaction term of  $s_u \times D/D_B$  for values ranging from 0.08 to 0.89. The proposed equation should be used with caution for  $q_b$  and  $s_u \times D/D_B$  values exceeding these ranges. Figure 4.6 shows a positive relationship between  $q_b$  from CAPWAP,  $s_u$  and  $D/D_B$ .

$$\hat{q}_b = \left[ \frac{\frac{s_u}{P_a} \times \frac{D}{D_B}}{0.001 + 0.0027 \frac{s_u}{P_a} \times \frac{D}{D_B}} \right] P_a$$

Figure 4.5. Equation. Unit End Bearing Prediction for FG-IGM.

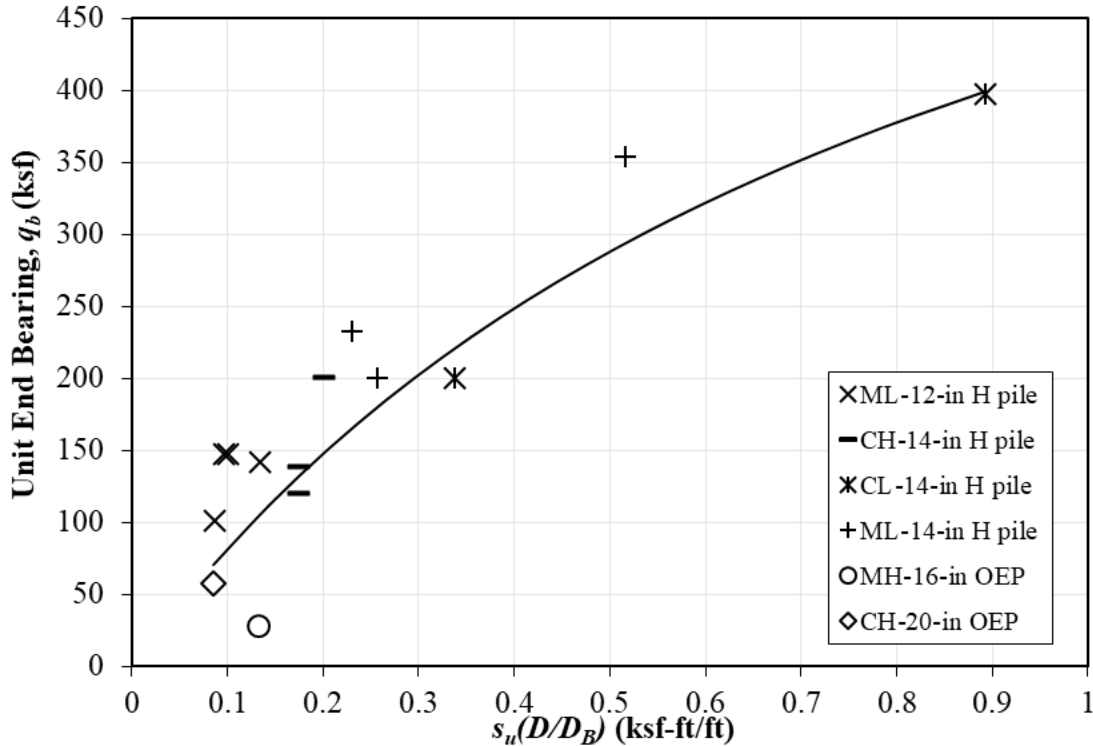


Figure 4.6. Plot of Unit End Bearing from CAPWAP Versus Undrained Shear Strength and a Ratio of Pile Diameter to Pile Penetration  $\left(s_u \frac{D}{D_B}\right)$  for Fine Grained Soil Based IGM.

## 4.5 Validation of Proposed Static Analysis Methods

### 4.5.1 Unit Shaft Resistance

Validation is conducted by comparing predicted  $q_s$  from the proposed SA methods given by the equations shown in Figure 4.4 with the  $q_s$  determined at the EOD from CAPWAP of 25 separate test piles from Kansas (8 test piles) and Illinois (17 test piles) (Long and Anderson 2012) as summarized in Table 4.2. The 25 test piles were four HP 10 piles, seven HP 12 piles, two HP 14 piles, and 12, 14-in diameter close-ended pipe (CEP) piles. From the 25 test piles, a total of 67 FG-IGM layers with  $q_s$  values from CAPWAP ranging from 0.15 ksf to 2.41 ksf were used in this study. To evaluate the performance of the proposed SA methods, comparisons were also conducted against the existing  $\alpha$ -method. Figure 4.7a and Figure 4.7b show that the proposed SA methods improve the  $q_s$  predictions that were closer along the line of equality (solid line). The statistical summaries (mean resistance bias and COV) inserted in Figure 4.7 asserts that the proposed SA methods with the average mean resistance bias of 0.91 provide a more accurate  $q_s$  prediction than the  $\alpha$ -method as the mean bias of 0.74 was lower. The proposed SA methods overpredict  $q_s$  by about 10 percent on average while the  $\alpha$ -method overpredicts the  $q_s$  by about 35 percent. The lower COV of 0.31 for the proposed SA methods compared to 0.56 for the  $\alpha$ -method suggests that the proposed SA methods provide a more consistent  $q_s$  prediction of piles driven in FG-IGM.

**Table 4.2. Summary of 33 Separate Test Piles Driven into Fine Grained Soil Based IGM**

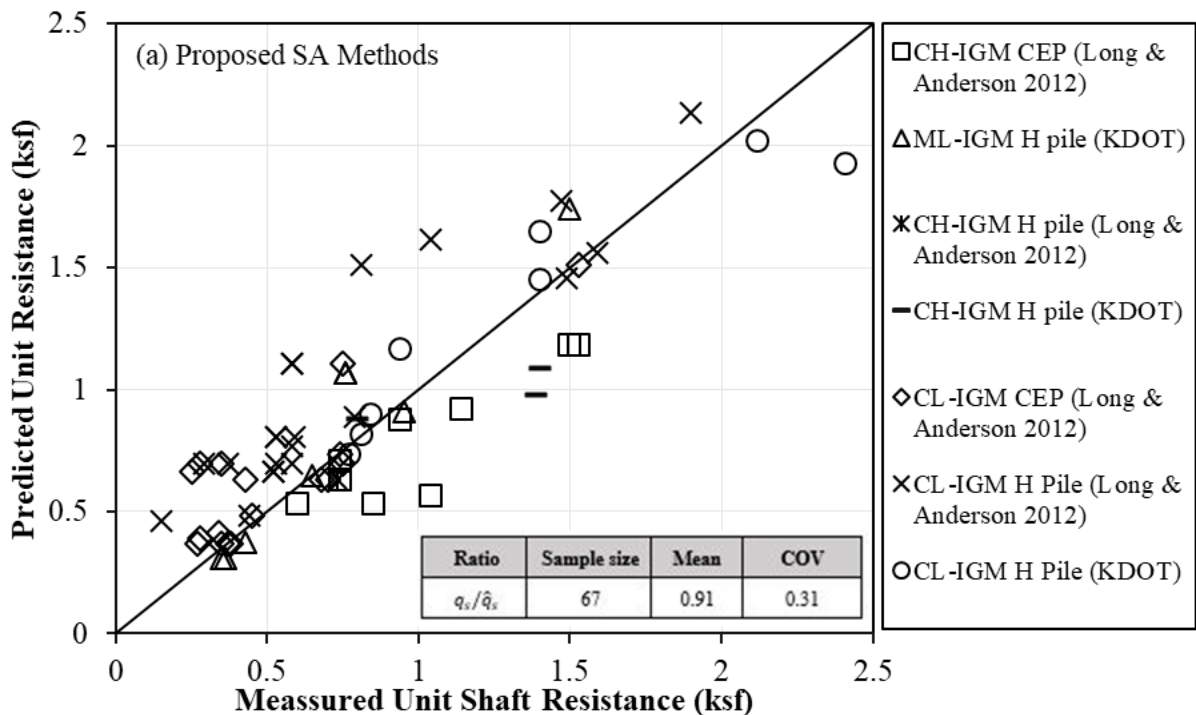
State	Project	Pile location	Pile	$D_B$ (ft)	Subsurface	FG-IGM	$s_u$ (ksf)	$q_s$ (ksf)	$q_b$ (ksf)	Hammer	BC
IL	Oquawka	Pi at EA	14-in CEP	57	SBM	Clay	3.0-3.2 <sup>#</sup>	0.6-0.85*	97.8	MKT DE-42	37
IL	Oquawka	Pi at WA	14-in CEP	62	SBM	Clay	4.5	1.5-1.53*	NA	MKT DE-42	172
IL	Oquawka	Pi at P	14-in CEP	51	SBM	Clay	2.8-3.3 <sup>#</sup>	0.38-0.45*	NA	MKT DE-42	68
IL	Godfrey	Pi at P-2	14-in CEP	39	SBM	Clay	2.8-4.8 <sup>#</sup>	0.27-0.74*	173.06	Del. D12-43	64
IL	Godfrey	Pi at WA	14-in CEP	66	SBM	Clay	2.8-4.0 <sup>#</sup>	0.4-1.04*	39.25	Del. D12-43	60
IL	Jacksonville	Pi at P-1	HP 12×53	39	SBM	Clay	4.0-7.0 <sup>#</sup>	0.58-1.90*	NA	Del. D12-43	194
IL	Jacksonville	Pi at P-2	HP 12×53	62	SBM	Clay	3.0-5.9 <sup>#</sup>	0.53-1.59*	17.77	Del. D12-43	172
IL	Greenville	Pi-3 at P-1	14-in CEP	28	SBM	Clay	3.8	0.43	NA	Del. D25-32	41
IL	Greenville	Pi-13 at P-1	14-in CEP	50	SBM	Clay	3.8	0.68	NA	Del. D25-32	37
IL	Greenville	Pi-12 at P-1	14-in CEP	23	SBM	Clay	3.8	0.7	NA	Del. D25-32	19
IL	Mahomet	Pi at P-2	HP 12×53	31.2	SBM	Clay	3.3	0.44-0.73	NA	Del. D30-32	49
IL	Plymouth	Pi at P-2	HP 14×102	43.2	SBM & RB	Clay	3.2	0.15	NA	Del. D19-32	403
IL	Plymouth	Pi at SA	HP 14×102	46	SBM & RB	Clay	4.0-4.3 <sup>#</sup>	0.29-0.59*	NA	Del. D19-32	85
IL	RCS Godfrey	TPi at SA	14-in CEP	40	SBM	Clay	3.9-5.8 <sup>#</sup>	0.94-1.54*	NA	Del. D19-32	80
IL	RCS Godfrey	Pi at NA	14-in CEP	38	SBM	Clay	2.8-3.0 <sup>#</sup>	0.34-0.37*	NA	Del. D19-32	128
IL	RCS Godfrey	PPi at SA	14-in CEP	40	SBM	Clay	3.9-5.0 <sup>#</sup>	0.25-0.75*	NA	Del. D19-32	65
IL	Stronghurst	Pi-1 at P-1	14-in CEP	69	SBM & RB	Clay	2.9	0.28	NA	Del. D19-42	38
KS	K-23 over PR	Pi at P-1	HP 12×63	50	SBM & RB	ML, CL	3.23-4.11 <sup>#</sup>	0.36-0.77*	NA	Del. D19-32	160
KS	K-4 over CCD	Pi at A-1	HP 10×42	79	SBM & RB	CL, CH	3.89-4.52 <sup>#</sup>	0.8-0.84*	NA	Del. D19-32	46
KS	MS over I-135	Pi at P-1	HP 10×42	84	SBM & RB	ML	4.0	0.65	NA	Del. D30-32	51
KS	K-14 over CC	Pi at P-2	HP 10×42	85	SBM	CL, CH, ML	4.32-6.77	0.76-1.5	22.33	Del. D19-42	25
KS	Int. of I-235 & 13 st.	Pi at P-2	HP 12×63	59	SBM & RB	CL	4.1	2.41	NA	Pil. D30-32	23
KS	Int. of I-235 & 13 st.	Pi at P-9	HP 12×63	59	SBM & RB	CL	3.46	2.12	NA	Pil. D30-32	25
KS	Int. of I-235 & 13 st.	Pi at P-5	HP 12×74	55	SBM & RB	CH	4.11	1.39	NA	Pil. D30-32	23
KS	K-14 over CC	Pi at P-6	HP 10×42	91	SBM & RB	ML, CL	3.2-6.24 <sup>#</sup>	0.35-0.95*	NA	Del. D19-42	13
WI	Int. of US41 & IH43	TPi-1 at P-5	HP 14×73	38	SBM	Clay	17.62	NA	300.72	Del. D25-32	NA
WI	Int. of US41 & IH43	Pi-1 at P-5	HP 14×73	35	SBM	Silt	13.25	NA	305.80	Del. D25-32	NA
WI	Int. of US41 & IH43	Pi-2 at P-5	HP 14×73	38.3	SBM	Clay	17.60	NA	295.65	Del. D25-32	NA

WI	Int. of US41 & IH43	Pi-1 at P-10	HP 14×73	53.8	SBM	Clay	10.02	NA	248.55	Del. D25-32	NA
WI	Int. of US41 & IH43	Pi-2 at P-10	HP 14×73	55	SBM	Clay	10.28	NA	255.80	Del. D25-32	NA
WI	Int. of US41 & IH43	TPi-1 at P-10	HP 14×73	54.5	SBM	Clay	10.69	NA	236.23	Del. D25-32	NA
WI	Int. of US41 & IH43	Pi-1 at P-1	HP 14×73	77	SBM	Clay	10.70	NA	100.72	Del. D25-32	NA
WI	Int. of US41 & IH43	SPi-1 at P-1	HP 14×73	74.8	SBM	Clay	17.62	NA	242.75	Del. D25-32	NA

IL=Illinois; KS=Kansas; WI=Wisconsin; PR=Pawnee River; CCD=Cow Creek drainage; MS=Maple treet; Int.=Interchange; St.=Street; CC=Cow creek; A=Abutment; Pi=Pile; P=Pier; B=Bent; TPi=Test pile; PPi=Production pile; EA=East abutment; WA=West abutment; NA=North abutment; SA=South abutment; D<sub>B</sub>=Total pile penetration; CEP=Close ended pipe pile; SBM=Soil based (both coarse and fine) geomaterials; SBM & RB=Soil- and rock-based geomaterials; CH-IGM=High plasticity clay IGM; CL-IGM=Low plasticity clay IGM; ML-IGM=Low plasticity silt IGM;  $s_u$ =Undrained shear strength;  $q_s$ =Unit shaft resistance; #=Range of  $s_u$ ; \*=Range of  $q_s$ ;  $q_b$ =Unit end bearing; NA=Not applicable; Del.=Delmeg; Pil.=Pileco; BC=Hammer blow count at end of driving (bl/ft).

#### 4.5.2 Unit End Bearing

The performance of the proposed SA method for  $q_b$  was similarly conducted using a separate dynamic pile load test conducted in Kansas from KDOT, eight pile load tests in Wisconsin from Long (2016), and four pile load tests in Illinois from Long and Anderson (2012) as summarized in Table 4.2. The total 13 test piles were one HP 10 pile, one HP 12 pile, eight HP 14 piles, and three 14-in diameter CEP piles. The  $q_b$  values determined from CAPWAP range from 17.77 ksf to 305.8 ksf. The comparisons of  $q_b$  values for the proposed SA method given by the equation shown in Figure 4.5 and the  $\alpha$ -method shown in Figure 4.8a and Figure 4.8b, respectively. Figure 4.8 reveals that the proposed SA method improves the  $q_b$  prediction as most data points lie closer along the line of equality. The mean bias of 1.15 suggests that the proposed SA methods underpredict the  $q_b$  by about 13 percent on average. On the other hand, the relatively high mean bias of 2.1 reveals that the existing  $\alpha$ -method underpredicts the  $q_b$  by about 52 percent on average. Furthermore, the lower COV of 0.37 for the proposed equation compared to the 0.48 for the  $\alpha$ -method suggests that the proposed equation provides a more consistent  $q_b$  prediction of piles driven in FG-IGM.



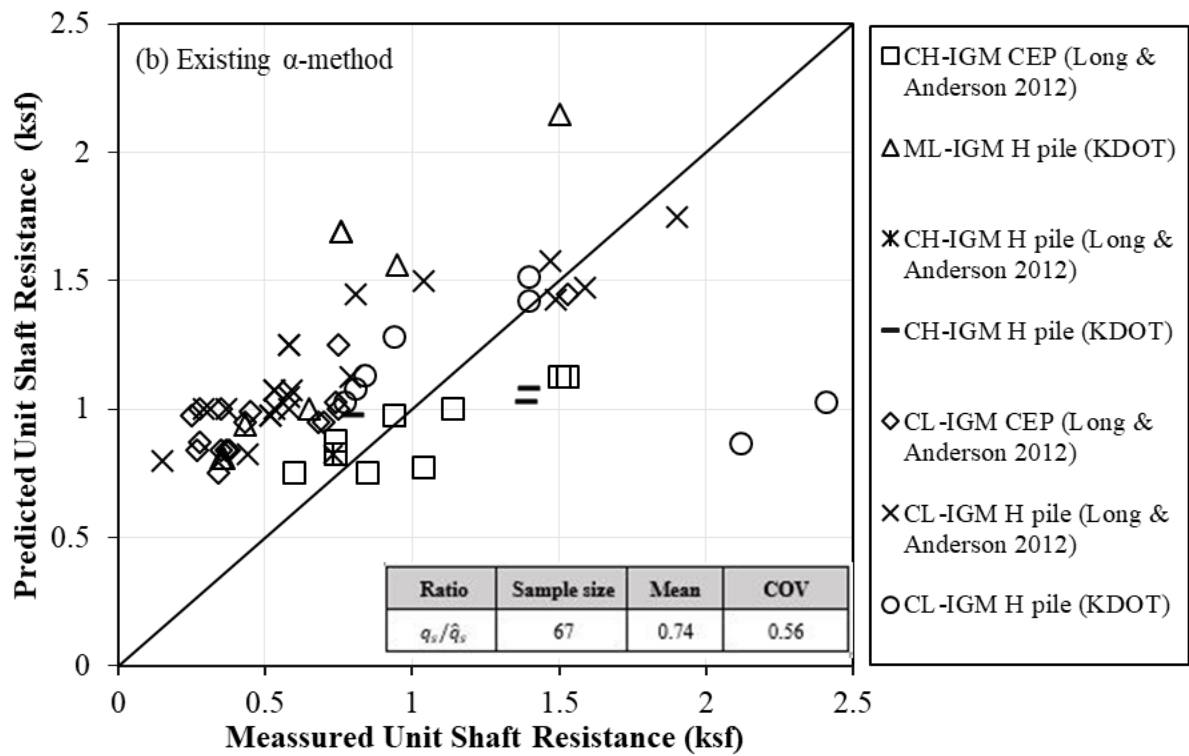
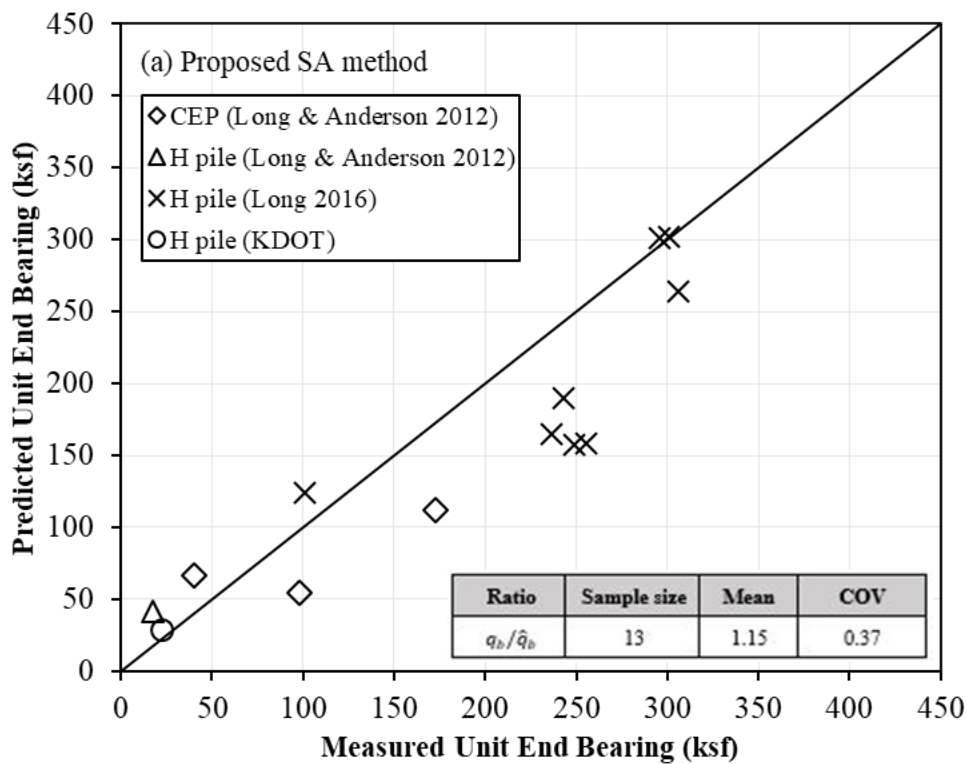
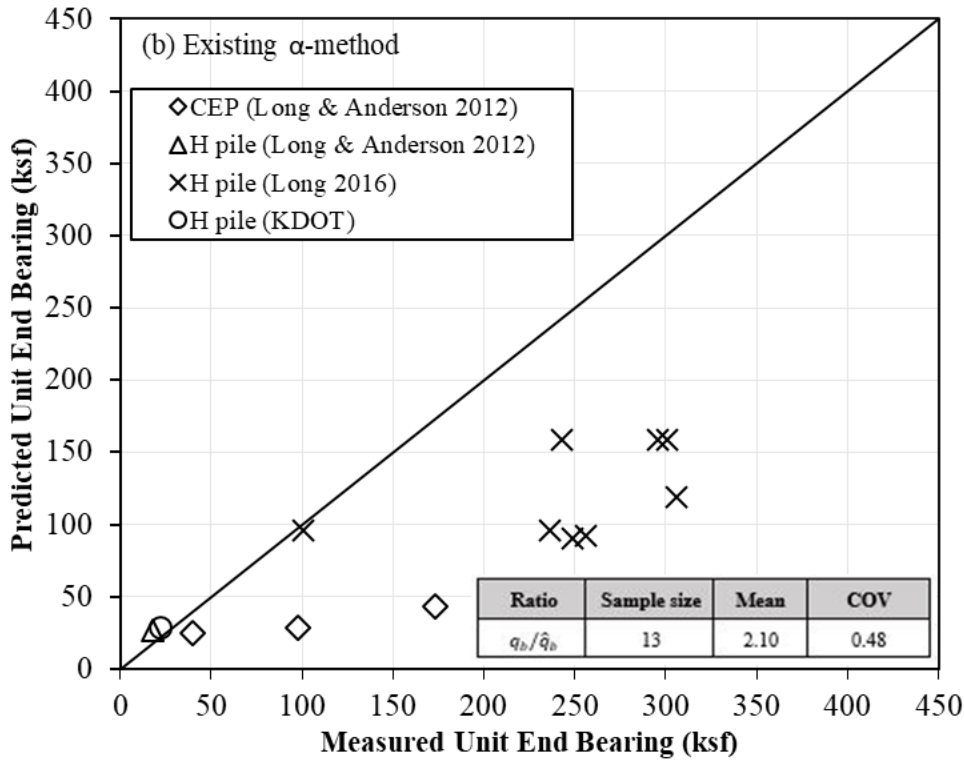


Figure 4.7. Comparison Between Unit Shaft Resistances from CAPWAP And Predicted Unit Shaft Resistances Using (a) Proposed SA Methods, and the (b) Existing  $\alpha$ -Method.

The Mean and Coefficient of Variation of The Resistance Bias were also included.





**Figure 4.8. Comparison Between Unit End Bearing from CAPWAP And Predicted Unit End Bearing Using the (a) Proposed SA Method and (b) Existing  $\alpha$ -Method. The Mean and Coefficient of Variation of The Resistance Bias were also included.**

#### 4.6 Calibration of LRFD Resistance Factors

The calibration of LRFD resistance factors was conducted using the FOSM, FORM, and MCS. The  $\phi$  values were determined at the target reliability indices ( $\beta_T$ ) of 2.33 for a redundant pile group and 3.00 for a non-redundant pile group (Paikowsky et al. 2004; AASHTO 2020). The calibration of  $\phi$  values required the statistical summaries: mean and COV, along with a best-fit distribution for all random variables involved in a limit state function (Allen et al. 2005). The random variables for this study were pile resistance ( $R$ ), dead load ( $Q_D$ ), and live load ( $Q_L$ ). Normality of the distribution of the resistance biases was assessed using the Shapiro-Wilk (SW) (1965) test and the Anderson-Darling (AD) (1952) test. The SW test is preferred over other normality tests due to its capability to detect non-normality (Mendes and Pala 2003). Both tests assess a null hypothesis that a sample (resistance bias) is taken from a population, which is normally distributed. If the responses in a sample come from a log-normal distribution, then the logarithm of the responses were assumed to follow a normal distribution. P-values from both SW and AD normality tests

were assessed using a level of significance ( $\alpha^*$ ) set at 0.05. The significance level indicated the Type I error associated with rejecting the null hypothesis when the null hypothesis was correct. If the p-value exceeds the level of significance, then the null hypothesis is not rejected, in which there is no evidence against the claim that appropriate responses (original or log) follow a normal distribution. For the FOSM method, the closed form equation shown in Figure 4.9, was used to calculate  $\phi$  in terms of mean biases ( $\lambda_R$ ,  $\lambda_D$ , and  $\lambda_L$ ), load factors ( $\gamma_D$  and  $\gamma_L$ ), and COV values for R,  $Q_D$  and  $Q_L$  (Barker et al., 1991). The statistical software program R (R Core Team 2016) was used to implement the 192 stepwise FORM utilizing the Rackwitz and Flessler (1978) algorithm. Similarly, MCS was conducted using the program R following the procedure described in Adhikari (2019). The efficiency of each proposed SA method was evaluated by an efficiency factor ( $\phi/\bar{x}$ ), which was defined as a ratio of  $\phi$  to the mean resistance bias ( $\bar{x}$ ) (McVay et al. 2000).

$$\phi = \frac{\lambda_R \left( \frac{\gamma_D Q_D}{Q_L} \right) \sqrt{\frac{(1 + COV_D^2 + COV_L^2)}{(1 + COV_R^2)}}}{\left( \frac{\lambda_D Q_D}{Q_L} + \lambda_L \right) \exp \left\{ \beta_T \sqrt{\ln[(1 + COV_R^2) + (1 + COV_D^2 + COV_L^2)]} \right\}}$$

**Figure 4.9. Equation. Resistance factor estimation based on the FOSM method**



**Table 4.3. Normality Results of The Proposed Static Analysis Methods and Existing  $\alpha$ -Method for the Estimation of Unit Shaft Resistance and Unit End Bearing in the Fine Grained Soil-Based IGM.**

For unit shaft resistance biases									
Steel pile type	SA method	Geo-material	Sample size	P-value for normality test		P-value for lognormality test		Loglikelihood	
				SW test	AD test	SW test	AD test	Normal	Lognormal
H & pipe pile	Fig. (4.4a)	ML-IGM	41	0.00	0.00	0.10	0.05	-29.82	-22.19
H & Pipe pile	Fig. (4.4b)	CL-IGM	92	0.00	0.01	0.18	0.08	-38.26	-31.66
H & pipe pile	Fig. (4.4c)	CH-IGM	43	0.41	0.12	0.26	0.11	-9.97	-10.7
H & Pipe pile	$\alpha$ -method	FG-IGM	176	0.00	0.00	0.35	0.65	-218.59	-178.15
For unit end bearing resistance biases									
H & pipe pile	Fig. (4.5)	FG-IGM	27	0.66	0.70	0.10	0.14	-12.11	-13.88
H & pipe pile	$\alpha$ -method	FG-IGM	27	0.24	0.22	0.07	0.05	-34.38	-35.01

SW=Shapiro-Wilk normality test; AD=Anderson-Darling normality test.

**Table 4.4. LRFD Resistance Factors and Efficiency Factors of the Proposed Static Analysis Methods and Existing  $\alpha$ -Method for the Estimation of Unit Shaft Resistance and Unit End Bearing in Fine Grained Soil-Based IGM.**

SA Method	IGM	Sample size (n)	Mean bias ( $\bar{x}$ )	COV bias (COV)	FOSM				FORM				MCS			
					$\beta_T=2.33$		$\beta_T=3.0$		$\beta_T=2.33$		$\beta_T=3.0$		$\beta_T=2.33$		$\beta_T=3.0$	
					$\varphi$	$\varphi/\bar{x}$	$\varphi$	$\varphi/\bar{x}$	$\varphi$	$\varphi/\bar{x}$	$\varphi$	$\varphi/\bar{x}$	$\varphi$	$\varphi/\bar{x}$	$\varphi$	$\varphi/\bar{x}$
Unit shaft resistance																
Fig. (4.4a)	ML-IGM	41	1.07	0.47	0.41	0.38	0.29	0.27	0.44	0.41	0.32	0.30	0.44	0.41	0.31	0.29
Fig. (4.4b)	CL-IGM	92	0.91	0.41	0.40	0.44	0.29	0.32	0.43	0.47	0.33	0.36	0.43	0.47	0.32	0.35
Fig. (4.4c)	CH-IGM	43	1.13	0.24	0.69	0.61	0.56	0.50	0.80	0.71	0.66	0.58	0.80	0.71	0.66	0.58
$\alpha$ -method	FG-IGM	176	1.26	0.66	0.31	0.24	0.21	0.16	0.34	0.27	0.22	0.17	0.34	0.27	0.21	0.17
Unit end bearing																
Fig. (4.5)	FG-IGM	27	1.07	0.36	0.52	0.49	0.40	0.37	0.57	0.53	0.44	0.41	0.57	0.53	0.43	0.40
$\alpha$ -method	FG-IGM	27	1.99	0.44	0.80	0.40	0.58	0.29	0.88	0.44	0.64	0.32	0.88	0.44	0.63	0.31

COV=Coefficient of variation;  $\phi$ =Resistance factor;  $\phi/\bar{x}$ =Efficiency factor;  $\beta_T$ =Target reliability index; FOSM=First order second moment; FORM=First order reliability method; MCS=Monte Carlo simulation.

#### 4.7 Resistance and Efficiency Factors

The normality results of the proposed SA methods summarized in Table 4.3 were determined with the training pile data used in the development of new SA methods and the testing pile data used in the validation. The normality results with p-values greater than 0.05 and smaller or comparable log-likelihood values indicate that the resistance biases were better fit with a log-normal distribution. In fact, the resistance biases of equations for ML-IGM and CL-IGM do not follow a normal distribution at the 0.05 level. The resistance and efficiency factors of the proposed SA methods for the  $q_s$  and  $q_b$  predictions in FG-IGM with a target  $\beta_T$  of 2.33 and 3.0 were calculated using both training and testing data as summarized in Table 4.3.

Resistance and efficiency factors determined from the more rigorous FORM and MCS methods were higher than that from FOSM. The  $\phi$  values for the  $q_s$  prediction based on the MCS and  $\beta_T$  of 2.33 were 0.43 for CL-IGM, 0.44 for ML-IGM, and 0.80 for CH-IGM. The relatively high  $\phi$  of 0.80 was attributed to the mean bias of 1.13 which was greater than one and a relatively small COV of 0.24. This indicates that the equation for CH-IGM provides a consistent  $q_s$  underprediction of piles in CH-IGM, which results in a relatively high  $\phi$  value to compensate for the underprediction, match the  $q_s$  values from CAPWAP, and achieve the same target  $\beta_T$ . Similarly, the calibration yields a  $\phi$  value of 0.57 for the  $q_b$  prediction in FG-IGM. Compared with the calibrated  $\phi$  values for  $\beta_T=2.33$ , all  $\phi$  values for  $\beta_T=3.00$  reduce by about 24 percent on average, which was comparable to the 20 percent recommended in the AASHTO (2020). The average efficiency factors based on the MCS method were 0.53 and 0.40 for  $\beta_T$  values of 2.33 and 3.00, respectively. These values were higher than the average efficiency factors of 0.45 and 0.33 calculated for the  $\alpha$ -method for soil and both steel H and pipe piles (Paikowsky et al. 2004).

A total of 176 FG-IGM layers were included in the assessment of  $q_s$  prediction using the  $\alpha$ -method. Due to the results in Table 4.3, the resistance biases of the  $\alpha$ -method were assumed to follow a log-normal distribution. The mean resistance bias of 1.26, and a relatively high COV of 0.66, suggest that the  $\alpha$ -method generally underpredicts  $q_s$  by about 21 percent, and any  $q_s$  prediction will possess a relatively high uncertainty. The mean resistance bias of 1.99 indicates that the  $\alpha$ -method underpredicts the  $q_b$  by about 50 percent on average. The mean resistance biases closer to unity, lower COV values, and higher efficiency factors indicate

that the proposed SA methods provide a more accurate and consistent prediction of  $q_s$  and  $q_b$  of steel H and pipe piles in FG-IGM.

## 4.8 Change in Pile Resistances

### 4.8.1 Change in Unit Shaft Resistance

A total of 69 FG-IGM layers from 25 test piles and 4 states: Wyoming, North Dakota, Kansas, and Illinois were included in this study to investigate the change in  $q_s$  over time. Among these 25 test piles, 15 test piles were steel H-piles, and 10 were 14-in CEP. The elapsed times ( $t$ ) from the EOD to BOR range from 15 minutes (0.0104 day) to 156 days. Figure 4.11 presents the percent change in  $q_{s-t}$  with respect to the  $q_{s-t_0}$ , which was determined at EOD from CAPWAP for clay-IGM and silt-IGM. The  $q_s$  generally increases with a logarithmic time (Figure 4.11a) as similarly observed in fine-grained soils (Ng et al. 2013b). A setup factor ( $A$ ) given by the equation shown in Figure 4.10 (Skov and Denver 1988) was determined by assuming the initial time ( $t_0$ ) at 0.0104 day to compare the rate of change in  $q_s$ . The inserted table in Figure 4.11a indicates that steel H-piles driven in clay-IGM, with an average  $A=0.28$ , have a higher pile setup rate than in silt-IGM, with an average  $A=0.20$ . Higher pile setup in clay-IGM could be attributed to the higher fine-grained particles in clay-IGM that delay the dissipation of excess pore water pressure and consolidation of FG-IGM induced during pile installation as similarly observed in fine-grained soils (Ng et al. 2013a; Haque et al. 2017). For clay-IGM, CEP piles with a larger cross-sectional area exhibit a higher pile setup rate with an average  $A=0.53$  compared to H-piles. A higher pile setup rate was expected from a larger pile size that creates greater radial displacement, disturbance, and remolding in the FG-IGM during the pile installation. If a 1-day pile restrike was performed, the  $q_s$  of H-piles and CEP piles in clay-IGM will increase on average by 56 percent and 105 percent, respectively (Figure 4.11a). A lower average 39 percent increase in  $q_s$  would be expected on H-piles in silt-IGM at 1 day after the EOD. Figure 4.11b shows that the pile setup factor generally decreases with an increase in  $s_u$  of FG-IGM. This agrees with the higher pile setup experienced in soft clays than compared to stiff clay (Long et al. 1999).

$$A = \frac{q_{s-t}/q_{s-t_0} - 1}{\log(t/t_0)}$$

**Figure 4.10. Equation. Setup Factor A Prediction.**

#### **4.8.2 Change in Unit End Bearing**

A total of 17 test piles from Wyoming, Wisconsin, Kansas, and Illinois, with both  $q_b$  determined at the EOD and BOR from CAPWAP, were used to investigate the change in  $q_b$  over time. Among these 17 test piles, 14 test piles were steel H-piles, and three were 14-in CEP. Thirteen test piles (10 H-piles and three 14-in CEP) were bearing on clay-IGM, and the remaining 4 H-piles were on silt-IGM. The elapsed times between the EOD and BOR range from 15 minutes (0.0104 day) to 156 days. Figure 4.12a shows that four H-piles in clay-IGM experience pile setup with percent increase in  $q_b$  varying from 5.3 percent to 345 percent while six H-piles experience a decrease in  $q_b$  (known as pile relaxation) with the percent change in  $q_b$  varying from -0.6 percent to -23 percent. The percent change in  $q_b$  of H-piles in silt IGM varies from -33 percent to 22 percent. For 14-in CEP in clay-IGM, two piles exhibit pile relaxation of -17 percent and -51 percent while one experiences pile setup of 202 percent. A logarithmic relationship between percent change in  $q_b$  and time was not observed, and in fact,  $q_b$  in silt-IGM decreases with time. Furthermore, the effect of pile type and size on the percent change in  $q_b$  was not apparent. Figure 4.11b showed that the pile setup factor decreased from positive to negative values as the  $s_u$  of FG-IGM increased from 2.8 ksf to 17.6 ksf. Piles driven onto FG-IGM with a  $s_u$  value greater than about 4 ksf will unlikely exhibit pile setup, and pile relaxation could occur in these cases. It is believed that pile relaxation could be attributed to the creation of a gap beneath a pile tip due to hard driving on stiffer FG-IGM and the development of negative excess pore water pressure due to the fracturing of stiff FG-IGM at the EOD.

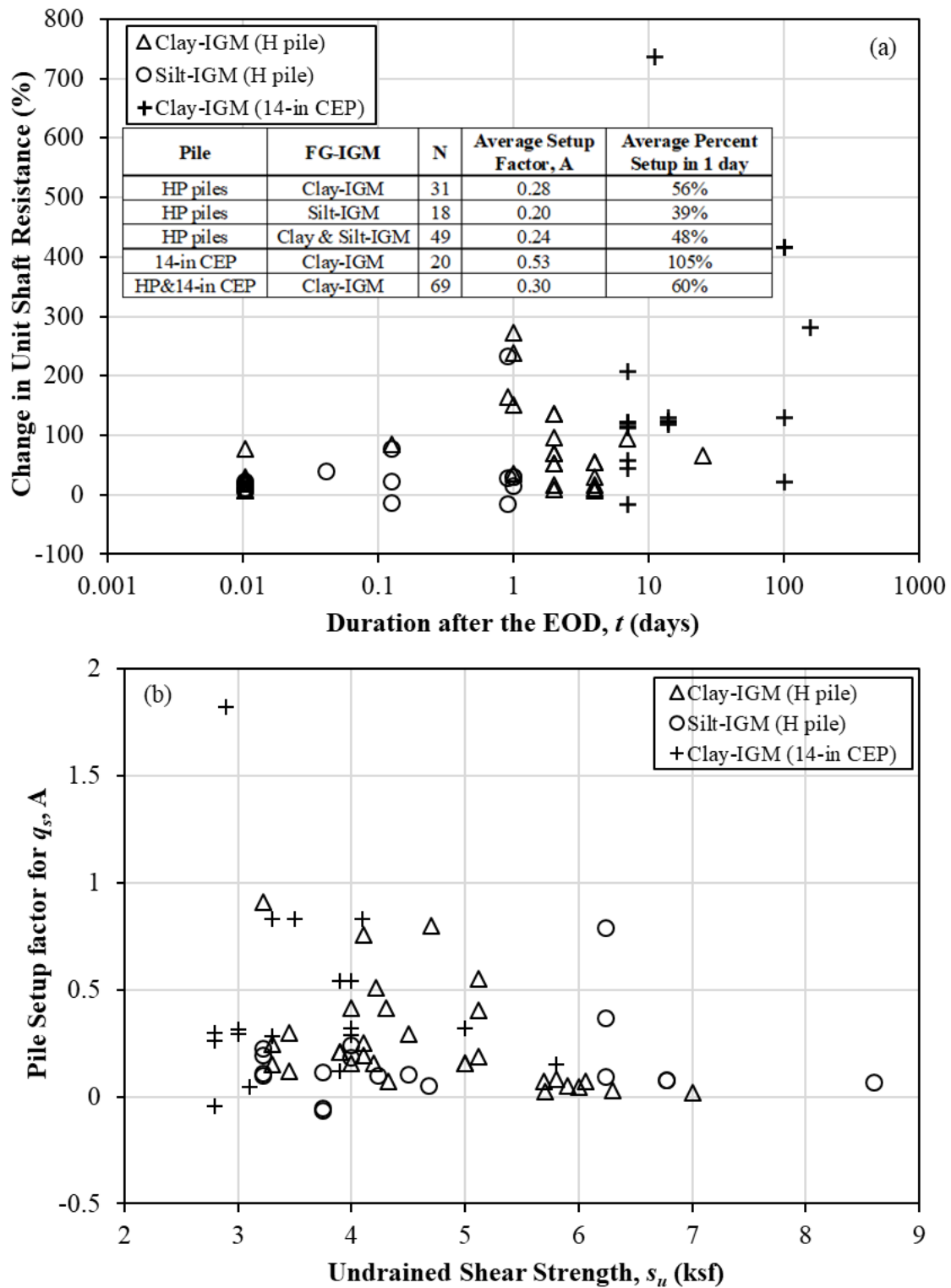


**Figure 4.11. (a) A Plot of Percent Change in Unit Shaft Resistance Against A Duration After The EOD In A Logarithmic Scale and (b) The Comparison Of Pile Setup Factor for  $q_s$  and Undrained Shear Strength of FG-IGM.**

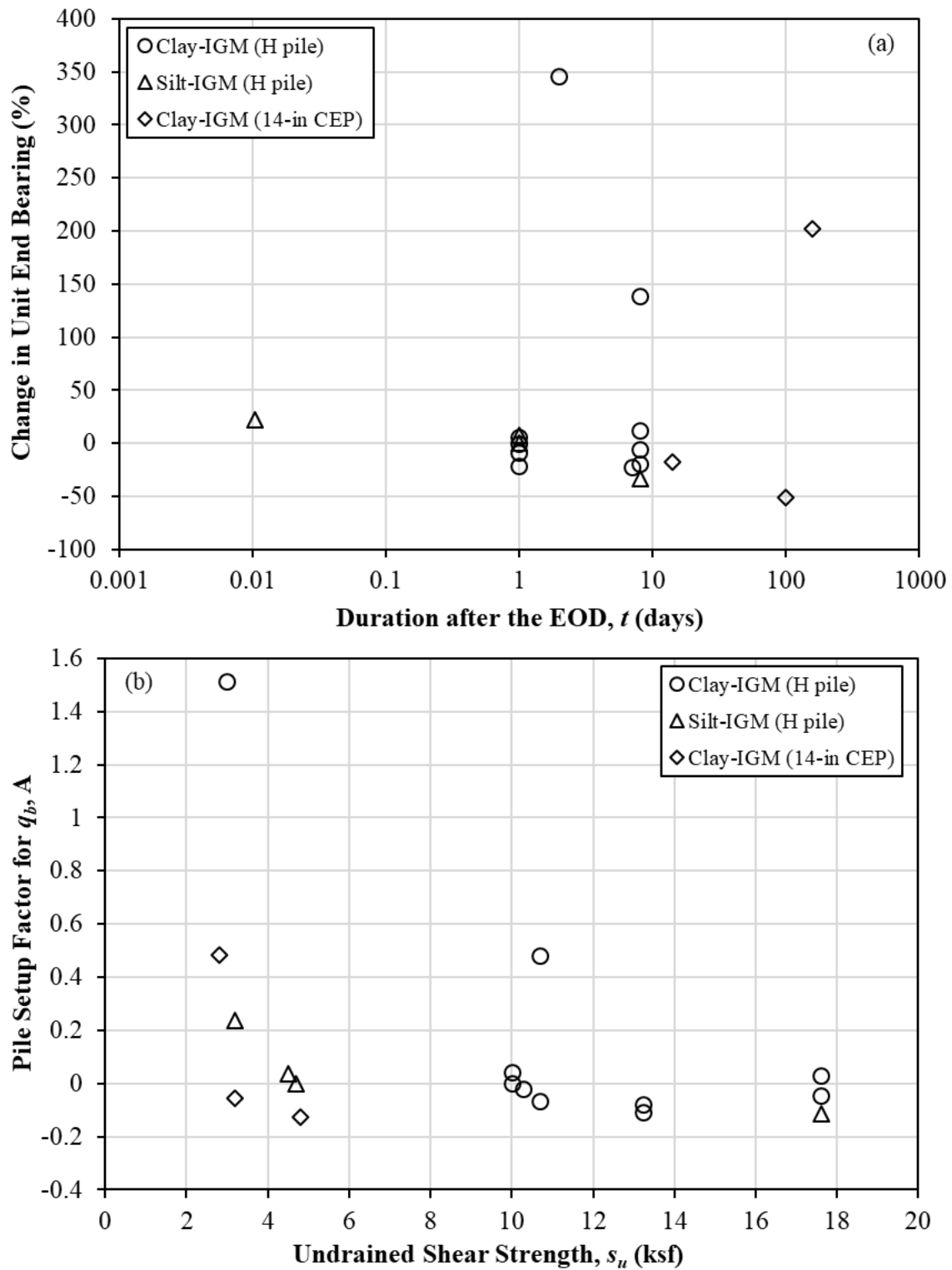


**Figure 4.12. (a) A Plot of Percent Change in Unit End Bearing Against A Duration After The EOD In A Logarithmic Scale and (b) The Comparison of Pile Setup Factor For  $q_b$  and Undrained Shear Strength Of FG-IGM.**

## 4.9 Summary and Conclusions

The design of driven steel H and pipe piles in FG-IGM was improved in this study through the proposed classification method for fine-grained geomaterials, the development of new SA methods to predict  $q_s$  and  $q_b$ , and the calibration of LRFD resistance factors to achieve the target design reliability using 51 pile load test data from 25 bridge projects in 4 states as a training data and 33 separate test pile data used for validation. In addition, the changes in  $q_s$  and  $q_b$  as a function of time and  $s_u$  were investigated. The study results in the following conclusions and recommendations:

- A classification method was proposed to differentiate fine-grain soil and FG-IGM. Fine-grained soil-based geomaterials with  $s_u \geq 2.7$  ksf were classified as FG-IGM so that the uncertainties associated with the design methods and characterization of IGM can be accounted for during pile design.
- To improve the estimation of  $q_s$  in FG-IGM, FG-IGM was categorized into silt-based IGM and clay-based IGM based on their grain size. Both silt-based IGM and clay-based IGM were further categorized based on plasticity to reduce uncertainties associated with IGM properties and increase the accuracy of  $q_s$  estimations. All FG-IGM types were included as training data to develop a new SA method for the estimation of  $q_b$ .
- The comparisons of  $q_s$  and  $s_u$  for all FG-IGM types show that  $q_s$  increased rapidly with and increase in  $s_u$ , and the increase in  $q_s$  reduces when the  $s_u$  was greater than about 10 ksf, especially in the clay-based IGM.
- The validation of the proposed SA methods using separate test pile data obtained from the literature and KDOT confirms the performance of the proposed SA methods in the estimation of  $q_s$  and  $q_b$ .
- The proposed SA methods with mean biases closer to unity, smaller COV of resistance biases, and higher efficiency factors provide a more accurate and consistent estimation of  $q_s$  and  $q_b$  of steel H and pipe piles in FG-IGM than the existing  $\alpha$ -method.
- Pile setup can be considered in the prediction of  $q_s$ . Higher pile setup in  $q_s$  was expected in clay-IGM and 14-in CEP piles. The pile setup factor decreases with the increased in  $s_u$  of FG-IGM. One day after the EOD, the  $q_s$  of steel H-piles increased on average by 56 percent and 39 percent in clay-IGM and silt-IGM, respectively or 48



percent in FG-IGM. The  $q_s$  of 14-in CEP increases on average by 105 percent in clay-IGM.

- It was recommended to neglect pile setup in the prediction of  $q_b$ . A construction control method should be included to determine any pile relaxation in FG-IGM, and pile restrike should be performed to close any potential gap below a pile tip.

## CHAPTER 5: DRIVEN PILE RESISTANCES IN COARSE GRAINED SOIL BASED INTERMEDIATE GEOMATERIALS

### 5.1 Introduction

Intermediate Geomaterial (IGM) is a transitional material that is harder than soil and softer than hard rock. IGM formation mechanisms can be divided into two kinds: 1) soil has been over-consolidated, cemented, or hardened to resemble rock-like characteristics or 2) rock formations that have been weakened due to weathering to resemble soil-like characteristics. Due to complex geological processes, IGM exhibits high inherent variability and geological uncertainty that could possess challenges in investigating, understanding and quantifying pile resistance responses. The lack of pile load test data and relevant research work further exacerbate the knowledge gap on pile responses in IGM and delay the advancement of driven pile design and construction in IGM. Coarse-grained geomaterials with Standard Penetration Test (SPT)  $N$ -values  $> 50$  blows/ft have been defined as “cohesionless” IGM (Mayne and Harris, 1993). SPT  $N$ -values ( $N_{60}$ ) ranging from 50 to 100 blows/ft have been utilized to determine IGMs in the design and construction of drilled shafts (Martin and Stacey 2018; O’Neill and Reese 1999). IGM definitions vary as they were created for different applications, such as drilled shafts and tunneling (Santi and Doyle 1997). Most transportation authorities have limited to no definitions of IGM in the design of driven piles (Adhikari 2019). Based on a past study relating pile resistances to measurable properties of IGM in Wyoming, IGM has been categorized into soil-based IGM and rock-based IGM, and the soil-based IGM is further classified into a coarse-grained soil-based IGM (CG-IGM) with  $(N_1)_{60} > 50$  blow/ft (Adhikari et al. 2020c).

Pile responses in dense coarse-grained soils have been investigated, and SA methods, such as the  $\beta$ -method (Esrig and Kirby 1979) and the Nordlund (1963) method, have been developed and implemented in current design practices. For example, a study conducted by O’Neill et al. (1991) found that the resistances of open and closed-ended pipe piles reduce as the interface friction angles ( $\delta$ ) of dense San Jacinto River sand with  $D_r=89$  percent decreases from 31.5 degrees to 29.4 degrees due to degradation of sand particles or particle breakage resulted from pile driving. Similarly, pile shaft resistances in cemented sand containing crushable particles were 20 percent less than those in crushable silica sands (McClelland 1974). Likewise, the degradation of cementation and crushing of cemented sand particles

results in a lower pile shaft resistance (Murff 1987; Ismael 1989; Kuwajima et al. 2009) and end bearing (White and Bolton 2004) than that in silica sand. However, it is not known if these similar pile resistance responses have been observed in CG-IGM.

Long (2016) used an equivalent hammer blow count ( $N_{MSPT}$ ) produced from a MSPT to develop prediction equations for unit shaft resistance ( $q_s$ ) < 2.92 ksf and unit end bearing ( $q_b$ ) < 292 ksf for steel H-piles in CG-IGM classified as sand, gravel, and boulder in Wisconsin. In Wisconsin, the modified SPT has not been extensively utilized, and most historical geotechnical records contain only standard SPT values. Furthermore, most studies have been conducted on piles driven in rock-based IGM (Mokwa and Brooks 2008; Ng and Sullivan 2017a; Adhikari et al. 2018; Adhikari et al. 2020a; Adhikari et al. 2020b; Islam et al. 2022a, Masud et al. 2022a, Masud et al. 2023a) and only one study on piles in fine-grained soil-based IGM was published (Masud et al. 2022b). Hence, it is indispensable to fill in the current knowledge gap and develop design recommendations for driven piles in CG-IGM.

Piles driven in coarse-grained soils have exhibited an increase in pile resistance (pile setup) or a decrease in pile resistance (pile relaxation) as a function of time (e.g., Axelsson 2002). Soil creep has been recognized as a strong mechanism for pile setup (Chow et al., 1998). Excess pore water pressure generated during pile installation could be another mechanism for pile setup (Finno et al. 1989; Koutsoftas 2002). Dense and well-graded sands exhibit a higher setup than loose and uniform sands (York et al., 1994). On the other hand, pile relaxation has been observed in dense to very dense fine sands (Long et al. 1999; Yang 1956; Yang, 1970). End bearing is more likely to experience relaxation than shaft resistance due to negative pore pressure and relief of high lateral ground stresses within dilatant materials (Sawant et al. 2013). Relaxation in a large group of piles is attributed to the cumulative effects of driving piles into the ground, causing the sand to be in a dense state and to dilate from subsequent driving (York et al. 1994). However, the time-dependent pile responses in CG-IGMs have not been explicitly investigated nor fully understood in past studies.

This chapter presents recent research advancement on 1) a classification approach for CG-IGM, 2) understanding the pile resistance responses in CG-IGM, 3) the development and validation of new SA methods for predicting  $q_s$  and  $q_b$  in CG-IGM, 4) understanding the time-dependent pile resistance responses, and 5) the development of LRFD recommendations for piles in CG-IGM.

## 5.2 Pile load Test Data

A total of 97 driven piles from 56 bridge projects in Idaho, Montana, North Dakota, and Wyoming were utilized to develop a classification procedure for CG-IGM. After establishing the classification criteria described in the next section, 30 test piles driven in CG-IGM layers and from 15 bridge projects (see Table 5.1) were used to better understand pile responses in CG-IGM and to develop new SA methods for  $q_s$  and  $q_b$ . These 30 test pile datasets contain pile type and size, general subsurface profile, total pile penetration ( $D_B$ ), driving hammer, CG-IGM type,  $\sigma'_v/(N_1)_{60}$  of CG-IGM,  $q_s$  and  $q_b$  determined from the Pile Driving Analyzer (PDA) with subsequent signal matching using the CAPWAP, and pile hammer blow count taken at the end of driving (EOD). Twenty-two test piles were steel H-piles, and the remaining were five close-ended pipe (CEP) piles, and three open-ended pipe (OEP) piles. Twenty-two test piles were driven in soil-based geomaterials, and eight test piles were driven in both soil and rock-based geomaterials. Only 16 test piles driven into CG-IGMs were used to study the effect of CG-IGM properties on  $q_b$  and to develop new SA method for  $q_b$ . Since static load tests (SLT) were not undertaken in typical construction practice, the unit resistances determined from CAPWAP at the EOD were used. In addition, pile restrikes and PDA testing with CAPWAP analysis at the BOR were performed at 0.125 to 18 days after the EOD to determine the time-dependent pile resistances.

Previous research has demonstrated that CAPWAP results were consistent with those obtained from SLTs (Likins and Rausche 2004; Sakr 2013). Using static and dynamic load test results of 25 piles in IGM by Adhikari et al. (2020a), the mean resistance bias (a ratio of pile resistance from SLT to resistance from CAPWAP of 1.077, and a coefficient of variation (COV) of the resistance bias of 0.121 was relatively small. A study by Verbeek et al. (2015) comparing 17 total pile resistances determined by seven operators using CAPWAP with the ultimate pile resistance of 1,007 kN from a SLT results in a  $\bar{x}$  of 0.971 and a relatively low COV of 0.121. Likewise, a similar study based on 19 predictions resulted in a comparable  $\bar{x}$  of 1.06 and a relatively low COV of 0.107 (Fellenius 1988). Referring to the five recently completed SLTs on steel H-piles in shale and siltstone (Islam et al., 2022b; Masud et al., 2022c; Masud et al., 2023a), the  $\bar{x}$  of 1.074 was determined closer to unity, and the COV of 0.119 was found to be relatively small. These comparisons consistently justify the use of pile resistances determined from CAPWAP in this study. These SLTs were conducted just the day

after the final pile restrike. Vibrating wire strain gauges installed along the test piles were used to record pile stresses before and after pile driving and after pile restrike (before SLTs). The incremental strain gauge readings from the final pile restrike to SLT were used to account for the residual stresses in the determination of pile resistance distribution from the SLTs. The residual stresses were determined and discussed in Masud et al. (2023b).

### 5.3 Proposed Classification for Coarse Grained Soil-Based IGM

The existing  $\beta$ -method was originally developed for predicting pile resistances in coarse-grained soil (Esrig and Kirby 1979). As the  $\beta$ -method neglects friction fatigue, which affects the shaft resistance prediction, and plugging that affects the end bearing prediction, much lower reliability in predicting pile resistances in IGM, other than coarse-grained soil, has been expected from the  $\beta$ -method. To distinguish CG-IGM from coarse-grained soil, the existing  $\beta$ -method was selected due to available soil parameters to evaluate the uncertainty in predicting the  $q_s$  in 309 coarse-grained strata of 97 test piles from 56 bridge sites. The SPT N-values of the coarse-grained strata obtained from boring records ranged from 1 blow/ft to 300 blows/ft. The COV of  $q_s$  biases (ratio of  $q_s$  from CAPWAP to  $q_s$  from the  $\beta$ -method) was compared against the corresponding maximum N-value of the pile data. The classification approach was established by comparing the COV of  $q_s$  biases using the  $\beta$ -method as a function of N-value. Coarse-grained layers with N-values ranging from 1 blow/ft to 300 blows/ft were reduced by excluding the layer with the maximum N-value from each analysis cycle to produce the next dataset for subsequent analyses. Figure 5.1 shows the COV of resistance biases for various datasets and compared to the corresponding maximum N-values. The first dataset, which consists of 309 coarse-grained layers, has a COV of 2.73 which was shown against the maximum N-value of 300 blows/ft to highlight the analysis procedure. The coarse-grained layer with the N-value of 300 blows/ft was excluded from the dataset in the next analysis cycle. As a result, the COV of the remaining 308 layers was 2.72, which was plotted against the new maximum N-value of 265 blows/ft. The analysis was repeated until the maximum N-value reaches 24 blows/ft because the boundary between CG-IGM and coarse-grained soil was less likely to occur below SPT N-value of 24 blows/ft. The proposed SPT N-value greater than 50 blows/ft for CG-IGMs agrees with the typical range of N-values for hard coarse-grained soils suggested by Kulhawy and Mayne (1990), but their study did not recommend an approach to distinguish between the coarse-grained soil and CG-IGM.

Furthermore, decreasing COV for N-values smaller than 58 blows/ft were consistent with the efficacy of the  $\beta$ -method originally intended for coarse-grained soil. Figure 5.1 depicts two distinct COV groups, with an average lower COV of 2.15 and an average upper COV of 2.65. The transition from the lower COV to the upper COV group occurs at the N-value of 58 blows/ft. Thus, coarse-grain geomaterials with N-value  $\geq 58$  blows/ft were classified as CG-IGM. The pile load test data were collected from four different states in this study, as shown in Table 5.1. Of all the 30 test piles that were driven into CG-IGM, the percent passing No. 200 sieve as the only common reported parameter for the CG-IGMs ranges from 0.2 percent to 11 percent. In particular, the geotechnical report of the SH-28 391 Lemhi River Bridge project in Idaho included photos of the CG-IGM starting from a depth of 12.5 ft shown in Figure 5.2a through some depths shown in Figure 5.2b before terminating at 50 ft shown in Figure 5.2c. The CG-IGM overlaid a bedrock as indicated by the red rectangle in Figure 5.2c.

**Table 5.1. Summary of 30 Driven Piles in Coarse Grained Soil-Based IGM**

State	Project	Pile location	Pile	$D_B$ (ft)	Subsurface	CG-IGM	$\sigma'_v/(N_1)_{60}$ (ksf-ft/bl)	$qs$ (ksf)	$qb$ (ksf)	Hammer	BC
ID	I-84B UPRR B	Pi-5 at A-2	HP 14×117	39.9	SBM	SM	0.006	0.36	NA	ICE I-30v2	64
ID	I-84B UPRR B	Pi-5 at A-1	HP 14×117	38	SBM	SP	0.06	2.56	167.36	ICE I-30v2	52
ID	SH-51 SR B	Pi-1 at A-1	HP 14×117	68.9	SBM	SP	0.02	0.7	NA	ICE I-30v2	73
ID	SH-51 SR B	Pi at A-2	HP 14×117	68.9	SBM	SP, SM, GM	0.003-0.04 <sup>#</sup>	0.15-2.13 <sup>*</sup>	NA	ICE I-30v2	52
ID	SH-28 391 LR B	Pi-2 at A-1	HP 14×89	41	SBM	GP-GM	0.009-0.03 <sup>#</sup>	0.26-2.17 <sup>*</sup>	188.36	Pileco 30-32	16
ID	SH-28 391 LR B	Pi-2 at A-2	HP 14×89	39.9	SBM	GW, GP-GM	0.002-0.02 <sup>#</sup>	0.13-0.62 <sup>*</sup>	NA	Pileco 30-32	17
ID	SH-28 411 LR B	Pi-2 at A-2	HP 14×89	65.2	SBM&RB	GW, GP-GM	0.003-0.02 <sup>#</sup>	0.22-1.1 <sup>*</sup>	NA	Diesel 30-32	241
ID	SH-28 416 LR B	Pi-1 at A-2	HP 14×89	56.5	SBM&RB	GP, GP-GM	0.001-0.05 <sup>#</sup>	0.16-3.04 <sup>*</sup>	NA	Diesel 30-32	17
ID	SH-28 416 LR B	Pi-1 at A-1	HP 14×89	56	SBM&RB	SW, GP-GM	0.014-0.06 <sup>#</sup>	0.29-2.59 <sup>*</sup>	NA	Diesel 30-32	17
ID	SH-28 436 LR B	Pi-1 at A-2	HP 14×89	29.5	SBM&RB	GW	0.001	0.21	NA	Diesel 30-32	100
ID	SH-28 436 LR B	Pi-2 at A-1	HP 14×89	38.7	SBM&RB	GW-GM, GP-GM	0.01-0.02 <sup>#</sup>	1.32-2.52 <sup>*</sup>	NA	Diesel 30-32	120
ID	SH-55 SR bridge	Pi-2 at P-3	HP 14×117	35	SBM	SM	0.03	2.0	248.37	Del. D36-32	72
ID	SH-55 PR bridge	Pi-1 at CP	30 in OEP	61	SBM&RB	GP	0.001	0.26	NA	APE D70-52	52
ID	SH-55 PR bridge	Pi-4 at CP	30 in OEP	51.8	SBM&RB	GP	0.002	0.49	NA	APE D70-52	61
ID	SH-55 PR bridge	Pi-4 at A-1	HP 12×74	56	SBM&RB	SP	0.013	0.71	NA	APE D30-42	60
ND	Mamorial bridge	Pi-1 at P-10	HP 14×102	90	SBM	SM & SC	0.06-0.07 <sup>#</sup>	1.83-2.59 <sup>*</sup>	206.76	Del. D36	40

ND	Mamorial bridge	Pi-2 at P-10	HP 14×102	97	SBM	SM & SC	0.07-0.08 <sup>#</sup>	2.55-2.81 <sup>*</sup>	196.99	Del. D36	49
MT	B over CR of YR	Pi at B-1	HP 14×89	32.6	SBM	Gravel	0.003	0.61	NA	ICE 80S	315
MT	B over LMC	Pi-4 at B-4	16 in OEP	75	SBM	SM	0.13	3.78	142.42	APE D36-26	107
MT	Capitol interchange	Pi-8 at B-1	16-in CEP	29	SBM	SC, GP	0.014-0.015 <sup>#</sup>	0.17-2.59 <sup>*</sup>	201.5	ICE I-30	48
MT	Capitol interchange	Pi-38 at B-4	16-in CEP	27.5	SBM	SC, GP	0.014-0.023 <sup>#</sup>	0.61-3.83 <sup>*</sup>	269.74	ICE I-30	44
MT	Capitol interchange	Pi-47 at B-4	16-in CEP	32.2	SBM	SC, GC	0.02-0.03 <sup>#</sup>	1.24-2.8 <sup>*</sup>	260.57	ICE I-30	37
MT	Capitol interchange	Pi-11 at B-5	16-in CEP	48.2	SBM	SC, SM & G	0.007-0.13 <sup>#</sup>	1.73-3.96 <sup>*</sup>	123.23	ICE I-30	74
MT	Capitol interchange	Pi-8 at B-5	16-in CEP	45.4	SBM	SC & G	0.009-0.03 <sup>#</sup>	1.82-3.52 <sup>*</sup>	NA	ICE I-36	32
WY	N Fork SoR	Pi-3 at A-2	HP 14×73	32	SBM	GW-GM	0.02	1.93	216.7	ICE I-42S	1125
WY	N Fork SoR	Pi-3 at A-1	HP 14×73	41	SBM	GW-GM	0.011	1.29	270.29	ICE I-42S	114
WY	Bridge over HC	Pi-3 at A-2	HP 12×53	19.5	SBM	SM, SP-SM	0.004-0.02 <sup>#</sup>	0.53-1.19 <sup>*</sup>	185	MKT DE-40	850
WY	Bridge over HC	Pi-3 at A-1	HP 12×53	36	SBM	SM	0.031	0.77	177	MKT DE-40	63
WY	Bridge over CF	Pi-1 at A-2	HP 14×73	45	SBM	SP-SM	0.003	0.44	260.83	MKT DE 40	96
WY	Bridge over EFC	Pi-5 at A-2	HP 14×73	40	SBM	GM, GW-GM	0.01-0.02 <sup>#</sup>	0.34-1.56 <sup>*</sup>	246.32	ICE I-42S	49

ID=Idaho; ND=North Dakota; WY=Wyoming; MT=Montana; SR= Snake River; LR=Lemhi river; SoR=Shoshone river; HC.=Hunter Creek; EFC.=Elle Fork Creek; CF=Clarks Fork; A=Abutment; Pi=Pile; P=Pier; B=Bent; D<sub>B</sub>=Total pile penetration; CEP=Close ended pipe pile; OEP=Open ended pipe pile; SBM=Soil based (both coarse and fine) geomaterials; SBM & RB=Soil- and rock-based geomaterials; SM=Silty sand; SC=Clayey Sand; GW=Well graded gravel; GP=Poorly graded gravel-IGM;  $q_s$ =Unit shaft resistance from signal matching technique; <sup>#</sup>=Range of  $\sigma'_v/(N_1)_{60}$ ; <sup>\*</sup>=Range of  $q_s$ ;  $q_b$ =Unit end bearing from signal matching technique; NA=Not applicable; Del.=Delmeg; ICE=International Construction Equipment; APE=American Pile Driving Equipment; BC=Hammer blow count at end of driving (bl/ft).



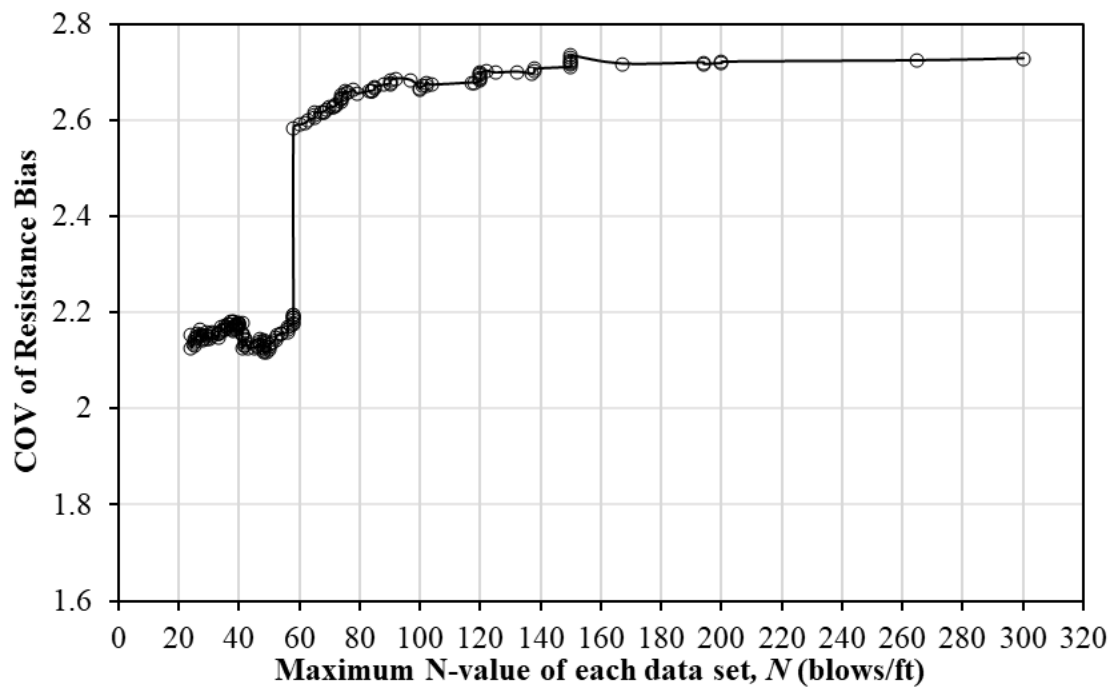


**Figure 5.1. Comparison of COV and Maximum SPT N-Value of Each Consecutive Pile Dataset Based on the Existing  $\beta$ -Method.**



**Figure 5.2. SH-28 Lemhi River Bridge Project Core Samples Indicate a) CG-IGM Starting From 12.5 ft, b) CG-IGM, and c) CG-IGM Terminated at 50 ft Overlaying the Bedrock.**

## 5.4 Development of New Static Analysis Methods

New SA methods for predicting pile resistances in CG-IGM at the EOD were developed for CG-IGMs. The time effect on pile resistances was discussed in the later section. These SA methods were developed to reduce uncertainties associated with different pile types: steel H pile and pipe pile. The SA method for  $q_b$  was developed using 16 piles driven into CG-IGMs as the end-bearing layer and for both steel H- and pipe piles. The  $q_b$  was calculated by dividing the end bearing from CAPWAP with a box area (flange width  $\times$  web depth) of H-piles or a close-ended area of pipe piles by assuming plugging as suggested from the predicted geomaterial plug weights ranging from 0.011 kips to 0.94 kips in CAPWAP reports.

The proposed SA methods for  $q_s$  were developed by comparing the  $q_s$  at the EOD from CAPWAP with the ratio of  $\sigma'_v$  to  $(N_1)_{60}$  taken at the middle of each shaft layer. These SA methods were developed based on the EOD so the change in pile resistances with time can be accounted for separately. Figures 5.3a and 5.4b show the increasing nonlinear trend of  $q_s$  and  $\sigma'_v/(N_1)_{60}$ . The proposed SA method for  $q_b$  prediction was developed by comparing  $q_b$  from CAPWAP with the ratio of  $(N_1)_{60}$ -value to  $\sigma'_v$  at the pile toe elevation (Figure 5.6).

### 5.4.1 Prediction of Unit Shaft Resistance for Coarse-Grained Soil-Based IGMs

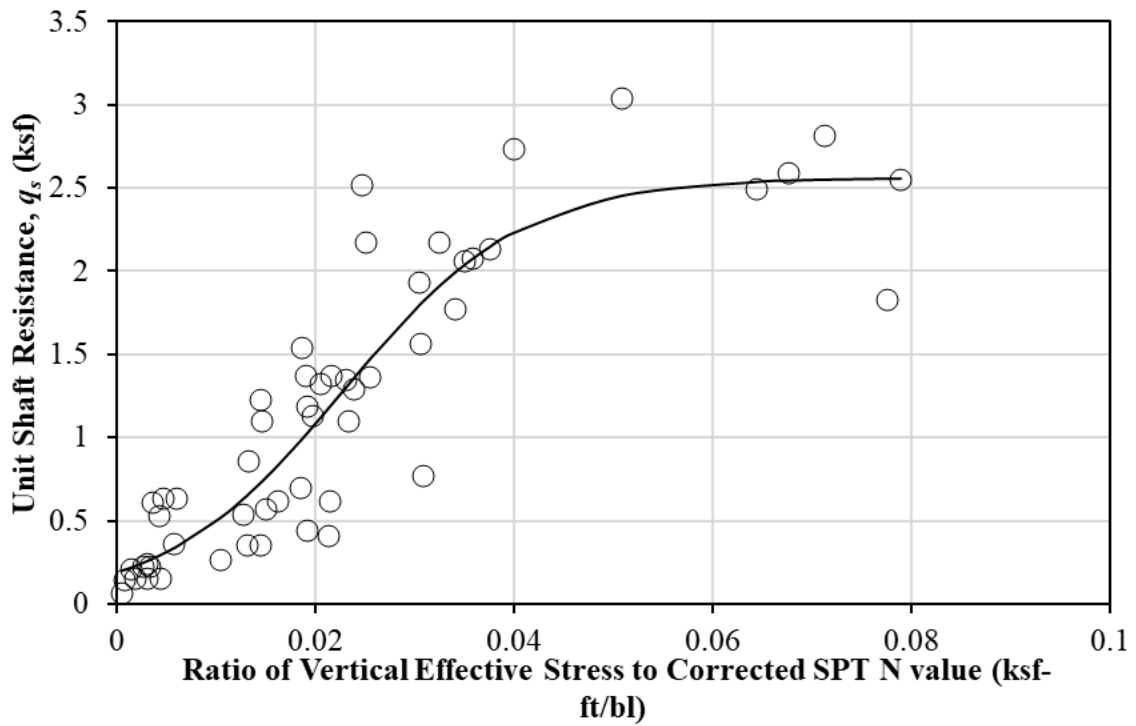
The proposed nonlinear SA equations for  $q_s$  and  $q_b$  were developed using the statistical software RStudio (R Core Team 2016). Model selection criteria play an important role in choosing among different nonlinear models (Gu et al. 2018). The same methodology to choose the best nonlinear model among the candidate models was explicitly described in Masud et al. (2022). For steel H-piles, the logistic model was recommended for  $q_s$  prediction. On the other hand, reciprocal yield density models were recommended for predicting the  $q_s$  of pipe piles in sand-based and gravel-based IGMs. The proposed equations for  $\hat{q}_s$  in terms of  $\sigma'_v/(N_1)_{60}$ , atmospheric pressure ( $P_a=2.12$  ksf) and 58 blows/ft to normalize the unit were used shown in Figure 5.3.

$$a) \hat{q}_s = \left[ \frac{1.21}{1 + 12.62e^{-4.06\left(\frac{\sigma'_v}{P_a} \frac{58}{(N_1)_{60}}\right)}} \right] P_a \text{ for H-piles in CG-IGM}$$

$$b) \hat{q}_s = \left[ \frac{\frac{\sigma'_v}{P_a} \frac{58}{(N_1)_{60}}}{0.105 + 0.52 \frac{\sigma'_v}{P_a} \frac{58}{(N_1)_{60}}} \right] P_a \quad \text{for pipe piles CG-IGM}$$

**Figure 5.3. Equation. Unit shaft resistance prediction for CG-IGM.**

It is important to note that the proposed equations were applicable for  $q_s$  values ranging from 0.13 ksf to 3.96 ksf and  $\sigma'_v/(N_1)_{60}$  values ranging from 0.00053 ksf-ft/blow to 0.13 ksf-ft/blow.



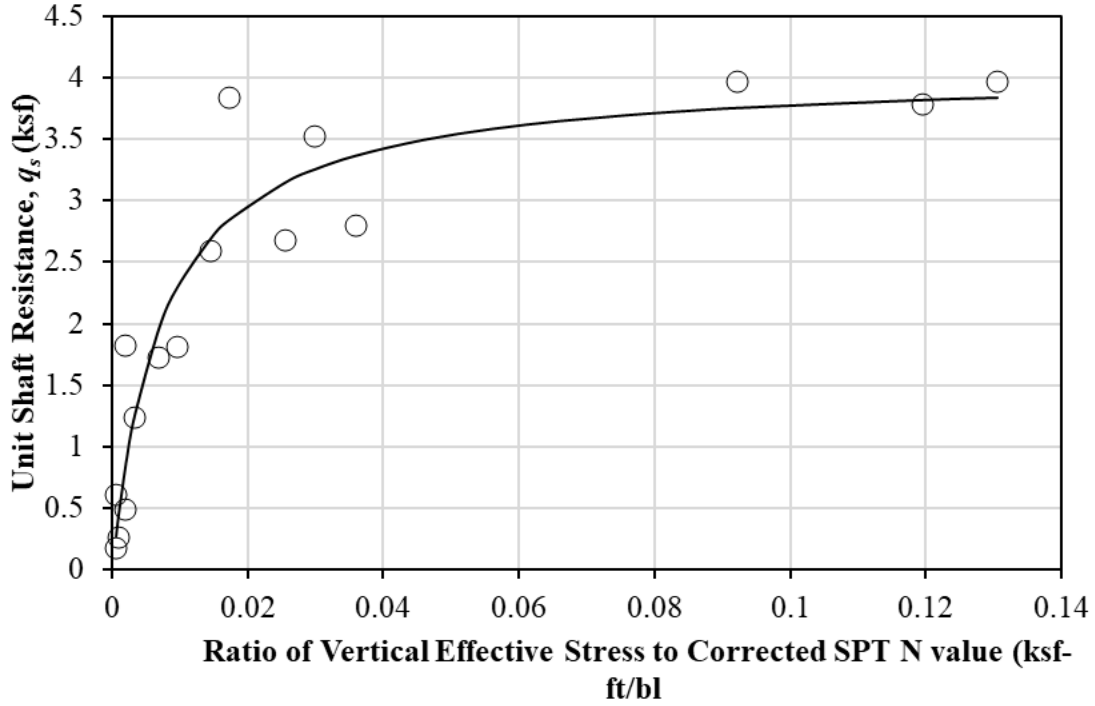


**Figure 5.4. Relationship Between Unit Shaft Resistance from CAPWAP and  $\sigma'_v/(N_1)_{60}$  for a) H-piles in CG-IGM b) Pipe Piles in CG-IGM.**

#### **5.4.2 Prediction of Unit End Bearing for Coarse-Grained Soil-Based IGM**

The SA method was developed to predict  $q_b$  of CG-IGM for both steel H and pipe piles. Three nonlinear models: power, YD, and logistic were evaluated according to the methodology described in Masud et al. (2022). The power model was selected to obtain the prediction equation for  $q_b$  given in Figure 5.5. Because of the training pile data used in this study, it was important to note that Eq. (3.3) was applicable for  $q_b$  values ranging from 123.23 ksf to 270.29 ksf and  $(N_1)_{60}/\sigma'_v$  ranging from 10.66 blows/ft-ksf to 114.3 blows/ft-ksf. Figure 5.5 shows that  $q_b$  increases nonlinearly with the increase in  $N/\sigma'_v$  at a gradually decreasing rate.

$$\hat{q}_b = 93.76P_a \left[ \frac{p_a (N_1)_{60}}{\sigma'_v 58} \right]^{0.22}$$

**Figure 5.5. Equation. Unit end bearing prediction equation for CG-IGM.**

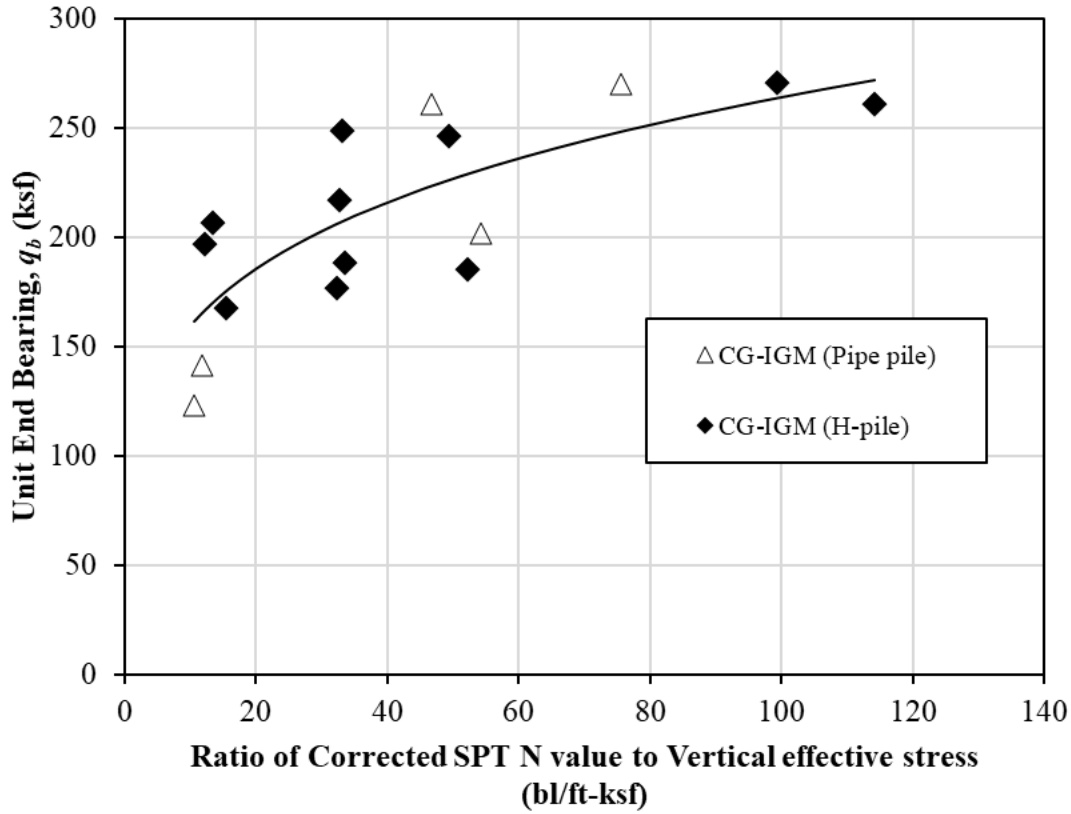


**Figure 5.6. Relationship Between Unit End Bearing from CAPWAP and ratio of  $(N_1)_{60}$  to  $\sigma'_v$  for Coarse-Grained Soil-Based IGMs.**

## 5.5 Validation of Proposed Static Analysis Methods

### 5.5.1 Unit Shaft Resistance

Validation of the proposed SA methods was conducted by comparing predicted  $q_s$  with the  $q_s$  determined at the EOD from CAPWAP based on separate test pile data consisting of 19 test piles from Illinois (Long and Anderson 2012) and two steel H-piles from Wyoming summarized in Table 5.2. From the 21 test piles, a total of 26 CG-IGM layers with  $q_s$  values ranging from 0.21 ksf to 4.38 ksf were used in this study. The performances of the proposed SA methods and existing  $\beta$ -method were compared in Figure 5.7a and Figure 5.7b, respectively. The statistical summaries (mean and COV of resistance biases) were inserted in Figure 5.7 assert that the prediction equation for H-piles in CG-IGM overpredicts  $q_s$  by about 6 percent on average while the  $\beta$ -method underpredicts the  $q_s$  by about 20 percent. For CEP piles in CG-IGM, the prediction equation overpredicts the  $q_s$  by about 14 percent on average while the  $\beta$ -method underpredicts the  $q_s$  by about 213 percent. The lower COV values suggest

that the proposed SA methods have smaller uncertainties and more consistent prediction of  $q_s$  than that by the  $\beta$ -method.

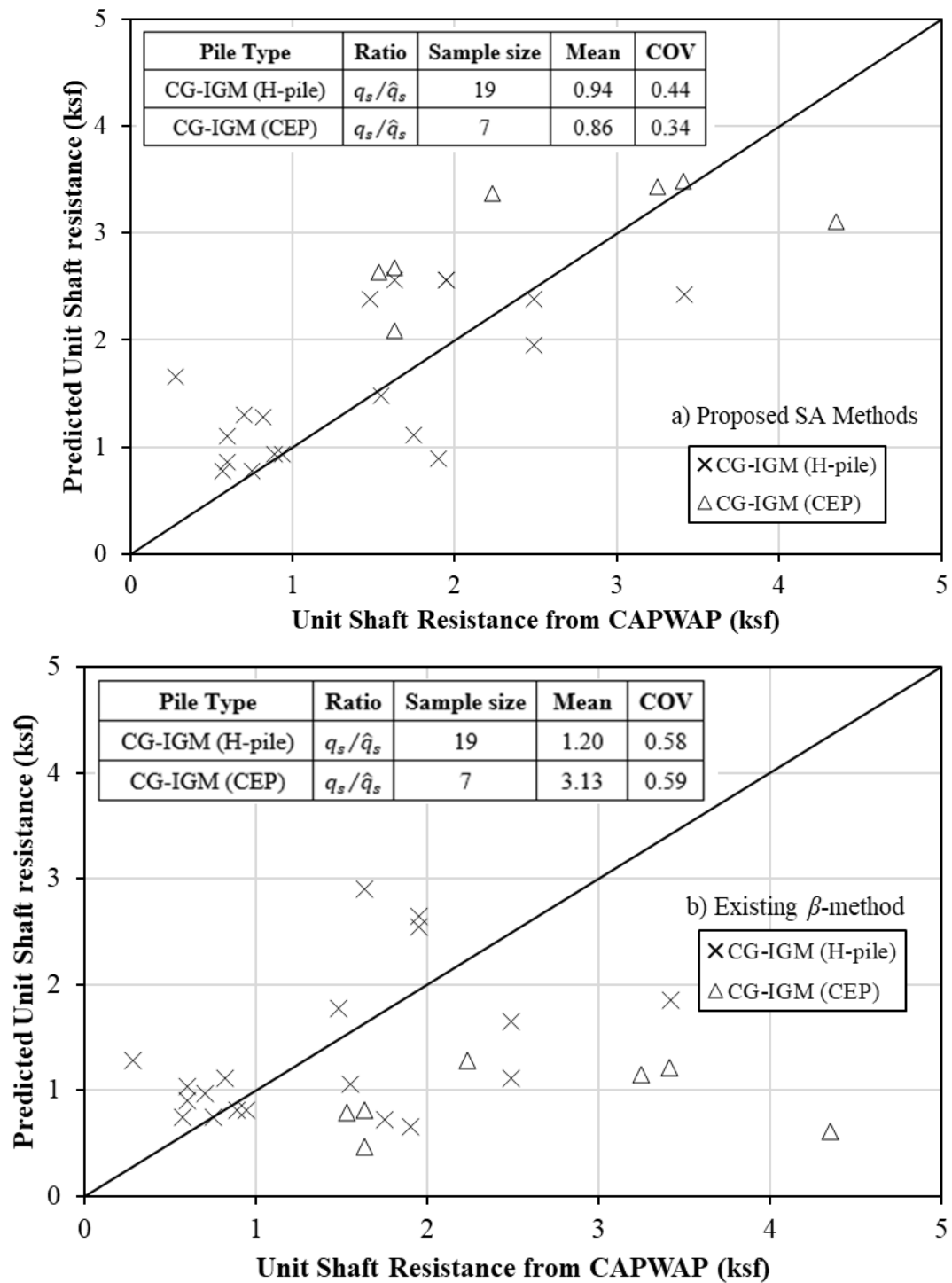


**Figure 5.7. Comparison Between Unit Shaft Resistances from CAPWAP and Predicted Unit Shaft Resistances using (a) the Proposed SA Methods and (b) the Existing  $\beta$ -Method.**

**Table 5.2. Summary of 24 Separate Test Piles Driven into Coarse Grained Soil-Based IGM.**

State	Project	Pile Loc./ID	Pile	$D_B$ (ft)	Subsurface	CG-IGM	$\sigma'_v/(N_1)_{60}$ (ksf-ft/bl)	$q_s$ (ksf)	$q_b$ (ksf)	Hammer	BC
IL	Mahomet	Pi at NA	HP 14×73	67	SBM	Gravel-IGM	0.02-0.03 <sup>#</sup>	0.28-0.82*	372.67	Del. D30-32	85
IL	Mahomet	Pi at P-2	HP 14×73	49	SBM	Sand-IGM	0.02-0.08 <sup>#</sup>	0.31-2.49*	313.3	Del. D30-32	69
IL	Bloomington	H pile	HP 12×63	101	SBM	S & G-IGM	0.04-0.09 <sup>#</sup>	1.09-1.48*	NA	APE D19-42	121
IL	Panther Creek	Pi at SA	HP 12×57	39	SBM	S & G-IGM	0.02-0.05 <sup>#</sup>	0.7-1.81*	230.1	ICE 42-S	25
IL	Stronghurst	Pi at P-1	14-in CEP	64.5	SBM	S-IGM	0.06-0.07 <sup>#</sup>	1.44-1.51*	NA	Del. D19-42	38
IL	Stronghurst	Pi at P-2	14-in CEP	51	SBM	S-IGM	0.04-0.05 <sup>#</sup>	1.53-1.63*	136.40	Del. D19-43	113
IL	Stronghurst	Pi at SA	14-in CEP	70	SBM	S-IGM	0.06	1.53	222.54	Del. D12-43	43
IL	Greenville	Pi-13 at P-1	14-in CEP	50	SBM	S-IGM	0.02-0.04	1.63-3.41	NA	Del. D25-32	37
IL	Greenville	Pi-12 at P-1	14-in CEP	23	SBM	S-IGM	0.02	0.77	118.05	Del. D25-32	19
IL	Plymouth	Pi at P-2	HP 14×102	43.2	SBM	G-IGM	0.016-0.02	0.21-0.6	448.4	Del. D19-32	403
IL	RCS Godfrey	Pi at SP	14-in CEP	19	SBM	S-IGM	0.01-0.017 <sup>#</sup>	0.89-0.93*	303.46	Del. D19-32	75
IL	RCS Godfrey	Pi at NA	14-in CEP	38	SBM	S-IGM	0.05-0.07 <sup>#</sup>	0.84-1.54*	255.19	Del. D19-32	128
IL	RCS Godfrey	Pi at SA	14-in CEP	40	SBM	S-IGM	0.02-0.04 <sup>#</sup>	1.53-2.23*	NA	Del. D19-32	80
IL	RCS Godfrey	Pi at NP	14-in CEP	29	SBM	S-IGM	0.04-0.08 <sup>#</sup>	3.25-4.35*	74.92	Del. D19-32	58
IL	Rockford	H pile-1	HP 12×53	49	SBM	S-IGM	0.02	0.25	NA	APE D19-32	49
IL	Rockford	H pile-2	HP 12×53	50	SBM	S-IGM	0.02	0.23	NA	APE D19-32	55
IL	Jacksonville	Pi at P-1	HP 12×53	55	SBM	S-IGM	0.021	2.45	NA	Del. D19-42	194
IL	Deer Creek	Pi at P-1	14-in CEP	35	SBM	S-IGM	0.02	0.56	225.82	Pil. D30-32	3048
IL	Freeport	Pi at P-5	14-in CEP	53	SBM	S-IGM	0.04	0.48	250.51	Pil. D30-32	98
MT	4230 Bridger Cr.	Pi at B-3	24-in OEP	28.1	SBM	G-IGM	0.03	NA	160.71	Del. D46-32	45
MT	4230 Bridger Cr.	Pi at B-4	16-in CEP	23.7	SBM	G-IGM	0.05	NA	423.6	Del. D46-32	53
MT	4226 Goat Cr.	Pi at B-1	16-in CEP	30.51	SBM	G-IGM	0.03	NA	235.22	ICE 42-S	96
WY	Hillsdale Int.	Pi at A-1	HP 12×53	60.9	SBM	SM-IGM	0.07	2.16	171.09	APE D19-42	73
WY	Hillsdale Int.	Pi at A-2	HP 12×53	55	SBM	SC-IGM	0.08	1.56	90.87	APE D19-42	51

IL=Illinois; MT=Montana; WY=Wyoming; Int.=Interchange; Cr.=Creek A=Abutment; Pi=Pile; P=Pier; B=Bent; Pi=Pile; EA=East abutment; WA=West abutment; NA=North abutment; SA=South abutment;  $D_B$ =Total pile penetration; S=Sand; G=Gravel; SM=Silty sand; SC=Clayey sand; CEP=Close ended pipe pile; SBM=Soil based (both coarse and fine) geomaterials; SBM & RB=Soil- and rock-based geomaterials;  $q_s$ =Unit shaft resistance from signal matching technique; <sup>#</sup>=Range of  $\sigma'_v/(N_1)_{60}$ ; \*=Range of  $q_s$ ;  $q_b$ =Unit end bearing from signal matching technique; NA=Not applicable; Del.=Delmeg; Pil.=Pileco; BC=Hammer blow count at end of driving (bl/ft).

**Table 5.3. Normality Results of the Proposed Static Analysis Methods and Existing  $\beta$ -method for the Estimation of Unit Shaft Resistance and Unit End Bearing in Coarse-Grained Soil-Based IGM**

For unit shaft resistance biases									
Steel pile type	SA method	Geo-material	Sample size	P-value for normality test		P-value for lognormality test		Loglikelihood	
				SW test	AD test	SW test	AD test	Normal	Lognormal
H-pile	Fig. (5.3a)	CG-IGM	73	0.001	0.002	0.73	0.57	-41.01	-34.89
Pipe pile	Fig. (5.3b)	CG-IGM	23	0.0004	0.0005	0.10	0.15	-12.34	-7.16
H- & Pipe pile	$\beta$ -method	CG-IGM	96	0.000	0.000	0.48	0.36	-155.39	-109.46
For unit end bearing resistance biases									
H- & pipe pile	Fig. (5.3)	CG-IGM	25	0.56	0.72	0.24	0.46	10.06	9.10
H- & pipe pile	$\beta$ -method	CG-IGM	25	0.001	0.006	0.21	0.16	-10.52	-4.82

SW=Shapiro-Wilk normality test; AD=Anderson-Darling normality test; S-IGM=Sand-based IGM; G-IGM=Gravel-based IGM; CG-IGM=Coarse-grained soil-based IGM.



**Table 5.4. LRFD Resistance Factors and Efficiency Factors of The Proposed Static Analysis Methods and Existing  $\beta$ -Method for the Estimation of Unit Shaft Resistance and Unit End Bearing in Coarse-Grained Soil-Based IGM.**

SA Method	IGM	Sample size (n)	Mean bias ( $\bar{x}$ )	COV bias (COV)	FOSM				FORM				MCS			
					$\beta_T=2.33$		$\beta_T=3.0$		$\beta_T=2.33$		$\beta_T=3.0$		$\beta_T=2.33$		$\beta_T=3.0$	
					$\varphi$	$\varphi/\bar{x}$	$\varphi$	$\varphi/\bar{x}$	$\varphi$	$\varphi/\bar{x}$	$\varphi$	$\varphi/\bar{x}$	$\varphi$	$\varphi/\bar{x}$	$\varphi$	$\varphi/\bar{x}$
Unit shaft resistance																
Fig. (5.3a)	CG-IGM	73	0.99	0.44	0.40	0.40	0.29	0.29	0.44	0.44	0.31	0.31	0.44	0.44	0.31	0.31
Fig. (5.3b)	CG-IGM	23	0.99	0.43	0.41	0.41	0.30	0.30	0.45	0.45	0.32	0.32	0.45	0.45	0.32	0.32
Figs. (5.3a) & (5.3b)	CG-IGM	96	0.99	0.43	0.41	0.41	0.30	0.30	0.45	0.45	0.32	0.32	0.45	0.45	0.32	0.32
$\beta$ -method	CG-IGM	96	1.43	0.86	0.24	0.17	0.13	0.10	0.25	0.17	0.14	0.10	0.25	0.17	0.14	0.10
Unit end bearing																
Fig. (5.3)	CG-IGM	25	0.99	0.17	0.69	0.69	0.57	0.57	0.82	0.82	0.70	0.70	0.82	0.82	0.70	0.70
$\beta$ -method	CG-IGM	25	0.56	0.67	0.14	0.25	0.09	0.16	0.15	0.26	0.10	0.17	0.15	0.26	0.10	0.17

COV=Coefficient of variation;  $\phi$ =Resistance factor;  $\phi/\bar{x}$ =Efficiency factor;  $\beta_T$ =Target reliability index; FOSM=First order second moment; FORM=First order reliability method; MCS=Monte Carlo simulation; S-IGM=Sand-based IGM; G-IGM=Gravel-based IGM; CG-IGM=Coarse-grained soil-based

### 5.5.2 Unit End Bearing

The performance of the proposed SA method for  $q_b$  was similarly conducted using an independent separate test pile dataset consisting of 12 test piles in Illinois (Long and Anderson 2012), three test piles in Montana (Mokwa and Brooks 2008) and two test piles in Wyoming as summarized in Table 5.2. The 12 test piles from Illinois were three HP 14 piles, one HP 12 pile, and eight 14 in CEP piles. The  $q_b$  values determined from CAPWAP range from 74.95 ksf to 448.43 ksf. The comparisons of  $q_b$  values for the proposed SA method and the existing  $\beta$ -method were illustrated in Figure 5.8a and Figure 5.8b, respectively. Figure 5.8a reveals that the proposed SA method provides a more accurate and consistent  $q_b$  prediction for nine data within the applicable  $q_b$  range represented by the dotted rectangle. The proposed SA method generally overpredicts  $q_b$  for  $q_b < 123.23$  ksf and underpredicts  $q_b$  for  $q_b > 270.29$  ksf. Considering all 17 data including 8 data outside and 9 data within the applicable  $q_b$  range, the mean bias of 1.08 suggests that the proposed SA method underpredicts  $q_b$  by about 8 percent on average. Considering only 9 data within the applicable  $q_b$  range indicated by the dotted rectangle in Figure 5.8a, the proposed SA method improves the  $q_b$  prediction with a mean bias of 0.97. Although the  $\beta$ -method possesses a comparable mean bias, the higher COV of 0.66 than that of the proposed SA method suggests that the  $\beta$ -method will yield a higher uncertainty in the  $q_b$  prediction while the proposed SA method provides a more consistent  $q_b$  prediction of piles driven in CG-IGM. In particular, the lowest COV of 0.20 confirms the adequacy of the proposed SA method in the  $q_b$  prediction.

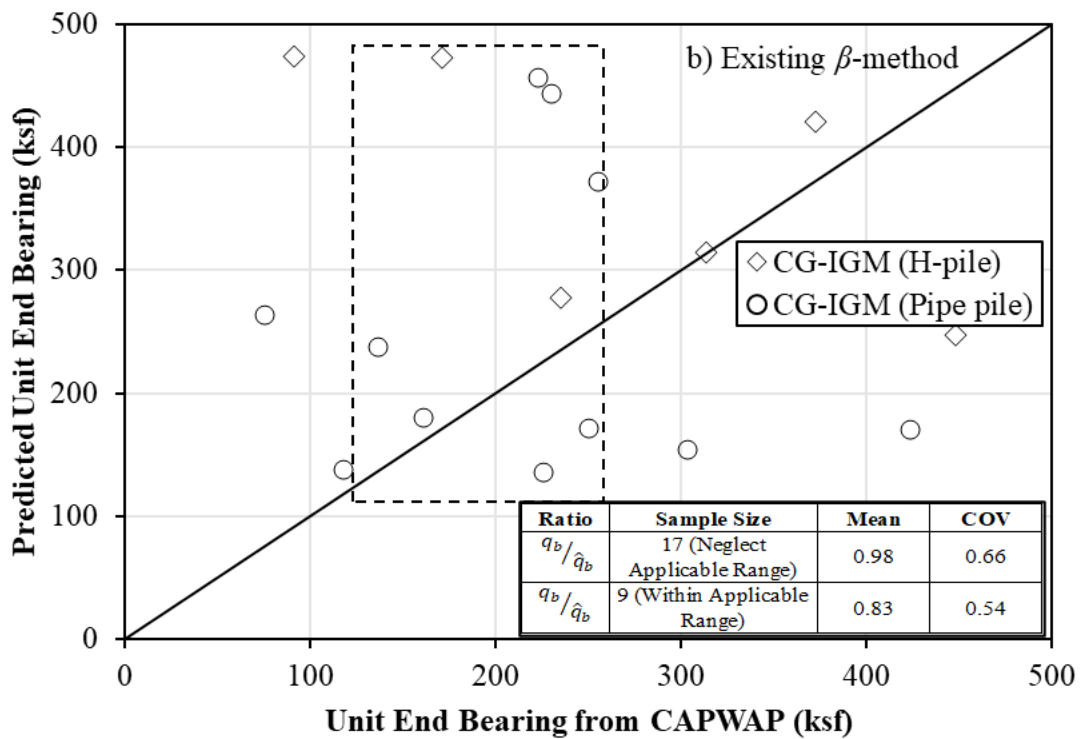
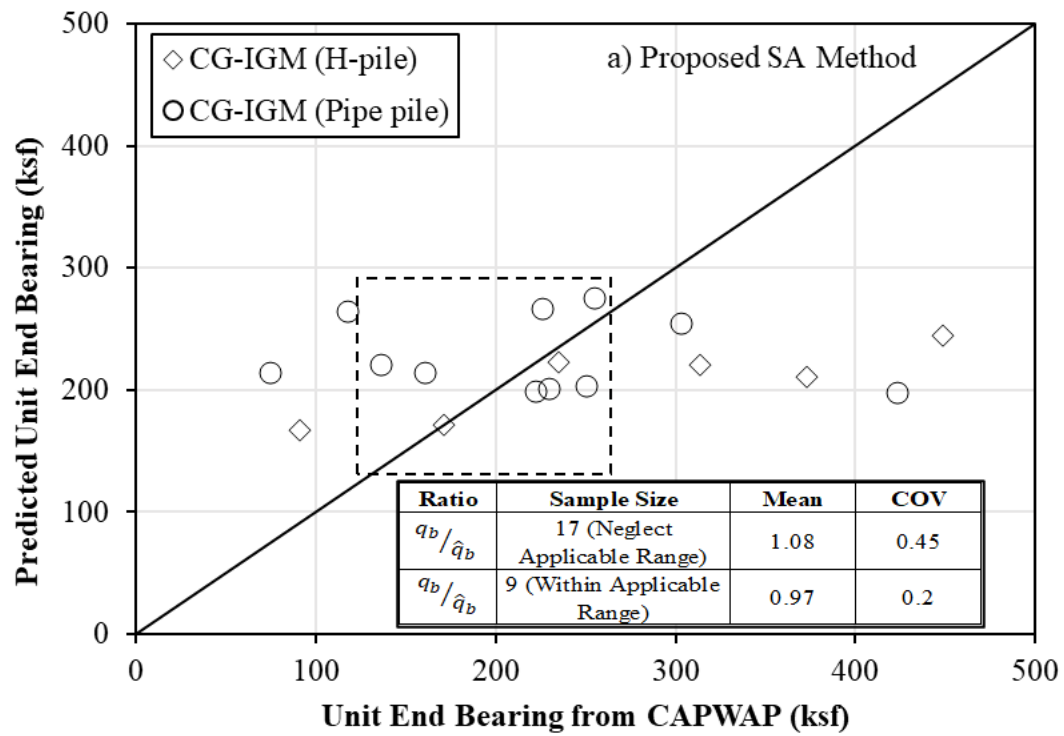


**Figure 5.8. Comparison Between Unit End Bearing from CAPWAP and Predicted Unit End Bearing using the (a) Proposed SA Method and (b) Existing  $\beta$ -Method.**

## 5.6 Change in Pile Resistances

### 5.6.1 Change in Unit Shaft Resistance

A total of 63 CG-IGM layers from 28 test piles and three states: Wyoming, North Dakota, and Illinois were included in this study to investigate the change in  $q_{s-t}$  over time. Among these 28 test piles, 19 were steel H-piles, and nine were 14-in CEP piles. The elapsed times ( $t$ ) from the EOD to BOR range from 0.125 day to 18 days. Figure 5.9 presents the percent change in  $q_{s-t}$  at a time  $t$  after the EOD with respect to the  $q_{s-t_0}$  at the EOD determined from CAPWAP for sand and gravel based IGM. The average ratios of maximum pile hammer energy (EMX) at BOR to EMX at EOD from PDA testing were calculated as shown in the table of Figure 5.9. The average EMX ratios of 1.1 for H-piles and 1.2 for CEP piles suggest that the hammer performance has minimal effect on the change in pile resistances with time. A setup factor ( $A$ ) given by the equation shown in Figure 4.10. was determined by assuming the initial time ( $t_0$ ) at 1 minute (Skov and Denver 1988; Ng et al. 2013a; Ng et al. 2013b). CEP piles exhibit a slightly higher pile setup rate of  $A=0.27$  than steel H-piles with  $A=0.26$ , because CEP piles induce a greater displacement of CG-IGM. Pipe piles create higher excess pore pressure than H-piles during installation (Finno et al. 1999). However, no clear difference in setup between low and high displacement piles was found in the study by Long et al. (1999). If a 1-day pile restrrike was performed based on the average  $A$  factors, the  $q_s$  of H-piles and CEP piles in CG-IGM will increase 67 percent and 86 percent on average, respectively (Figure 5.9). The short-term pile setup for less than one day could be attributed to the dissipation of excess pore water pressure built-up in dense or cemented CG-IGMs that were similarly observed in very dense sand by Finno et al. (1989) and Koutsiftas (2002).

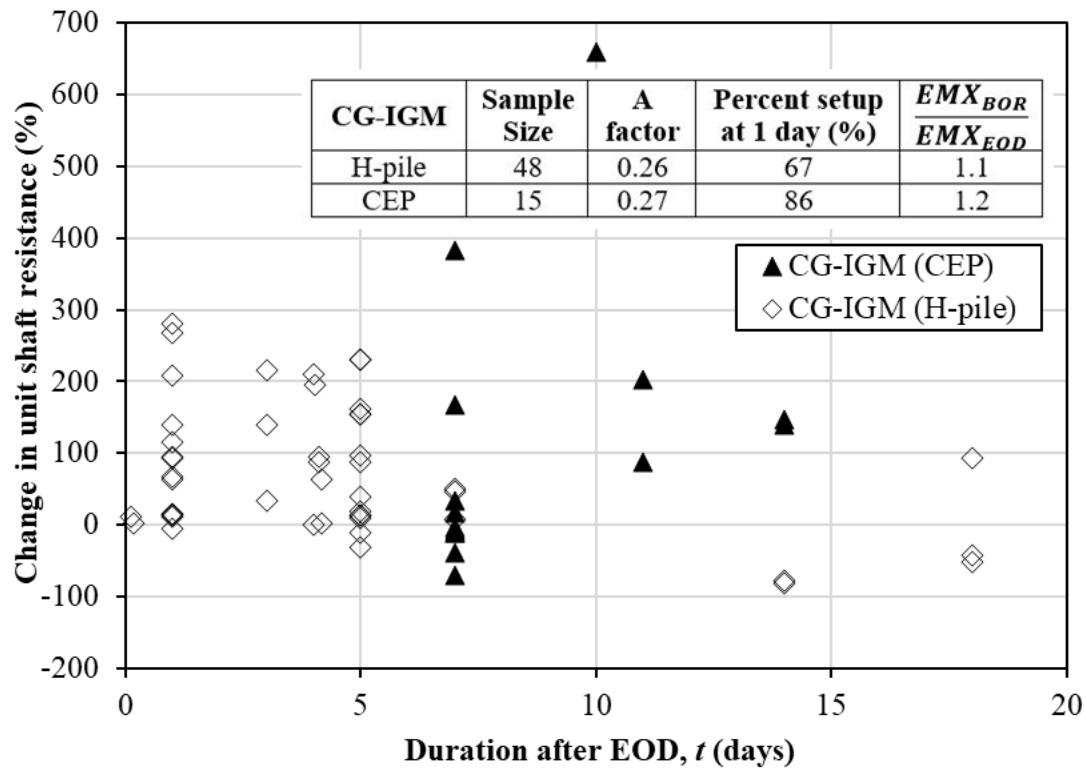


Figure 5.9. A Plot of Percent Change in Unit Shaft Resistance in CG-IGMs Against a Duration After The EOD.

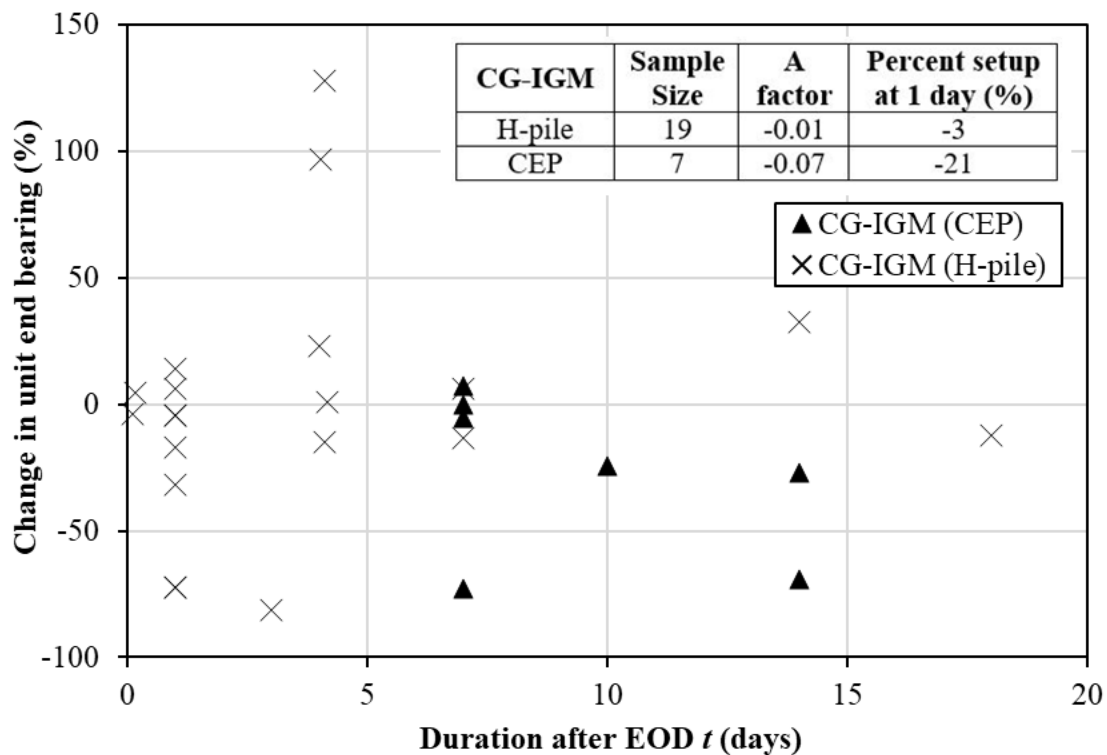


Figure 5.10. Plot of Percent Change in Unit End Bearing in CG-IGMs Against a Duration After the EOD.

### 5.6.2 Change in Unit End Bearing

A total of 23 test piles with 27 pile restrrike data from three states: Wyoming, North Dakota, and Illinois, with both  $q_b$  determined at the EOD and BOR from CAPWAP, were used to investigate the change in  $q_b$  over time. Among these 23 test piles, 16 were steel H-piles and seven were 14-in CEP. The elapsed times between the EOD and BOR range from 0.125 days to 18 days. Figure 5.10 shows that one closed ended pipe pile (CEP) in CG-IGM experience  $q_b$  setup at 6.28 percent. The other six CEP test piles in sand-based IGM experience  $q_b$  relaxation from -0.4 percent to -73.2 percent while H-piles experience both setup and relaxation. The inserted table in Figure 5.9 indicates that CEP piles in CG-IGM exhibit a higher  $q_b$  relaxation with an average  $A = -0.07$  than H-piles with an average  $A = -0.01$ . If a 1-day pile restrrike was performed based on the average  $A$  factors, the  $q_b$  of H-piles and CEP piles in CG-IGM will decrease 3 percent and 21 percent on average, respectively. A study conducted by Hannigan et al. (2019) concluded that H and CEP piles driven into very dense sand experience  $q_b$  relaxation of 17 percent and 38 percent, respectively. Figure 5.10 shows that relaxation mostly occurs in the end bearing than the shaft resistance. This phenomenon could be attributed to the result of negative pore water pressure in dense geomaterials like CG-IGM (Hannigan et al. 1997; Sawant et al. 2013). The compression of CG-IGM below pile toe causes a relief in the surrounding geomaterial at the pile toe elevation which eventually reduces  $q_b$ . When a pile was driven into dense CG-IGM stratum, crushing and breakage of cemented CG-IGM generates negative pore water pressure. Negative pore water pressure leads to a transient increase in the end bearing immediately after driving but relaxes with time as the negative pore water pressure dissipates to a hydrostatic condition. This effect of soil particle crushing leading to  $q_b$  relaxation was similarly observed on displacement piles driven into dense Florida granular soils (Herrera et al. 2018). Past studies have shown  $q_b$  relaxation in dense to very dense sand that resembles the behavior of the CG-IGM (Long et al. 1999, Svinkin 1994, 2002; Titi and Wathugala 1999; Yang 1956; Yang 1970).

### 5.7 LRFD Recommendations

To facilitate the implementation of design recommendations for piles in CG-IGMs, LRFD resistance factors ( $\phi$ ) for the proposed SA methods were calibrated using the FOSM (Adhikari 2019; Ng et al. 2012), FORM (Ng et al. 2019), and MCS (Allen et al. 2005). The  $\phi$  values were calculated based on target reliability indices ( $\beta_T$ ) of 2.33 for a redundant pile

group and 3.00 for a non-redundant pile group (Paikowsky et al. 2004; AASHTO 2020). The SW (1965) and AD (1952) tests were conducted to assess the normality of the resistance bias distribution. Detailed description of the  $\phi$  calibration can be found in Masud et al. (2022) and Islam et al. (2022b).

## 5.8 Resistance and Efficiency Factors

The training pile data used in the development of new SA methods and the testing pile data (within the applicable range) used in the validation were combined to determine the normality results of the proposed SA methods as summarized in Table 5.3. The resistance biases were modeled with the log-normal distribution as the p-values for this distribution were greater than 0.05 and this distribution has larger or comparable log-likelihood values. Table 5.4 summarizes the  $\phi$  and  $\phi/\bar{x}$  of the proposed SA methods for the prediction of  $q_s$  and  $q_b$  in CG-IGM for target  $\beta_T$  of 2.33 and 3.0. The more stringent FORM and MCS approaches lead to higher  $\phi$  and  $\phi/\bar{x}$  factors than the FOSM approach. The  $\phi$  values for the proposed SA methods based on the MCS and  $\beta_T$  of 2.33 range from 0.44 for H-piles in CG-IGM to 0.45 for pipe piles in CG-IGM while a relatively high  $\phi$  value of 0.82 was calibrated for the  $q_b$  prediction in CG-IGM. All  $\phi$  values reduce by about 30 percent on average when increasing the  $\beta_T$  from 2.33 to 3.00. The average  $\phi/\bar{x}$  factor of 0.45 for the proposed SA methods based on the MCS and  $\beta_T=2.33$  was higher than the average  $\phi/\bar{x}$  factors of 0.39 and 0.32 for the  $\beta$ -method and steel H and pipe piles driven in sandy soil, respectively (Paikowsky et al. 2004). Considering the total 96 CG-IGM layers, and comparing with the  $\beta$ -method, the  $\bar{x}$  value of 0.99 was closer to unity and has a lower COV of 0.43 which suggested that the proposed SA methods generally provide more accurate and consistent  $q_s$  prediction. The comparison of the  $\phi/\bar{x}$  factors also confirmed that the proposed SA methods were more efficient than the  $\beta$ -method in  $q_s$  prediction. Likewise, the  $\bar{x}$  value of 0.99 was closer to unity, a lower COV of 0.17, and higher  $\phi/\bar{x}$  factors indicate that the proposed equation provides a more accurate and consistent prediction of  $q_b$  of steel H and pipe piles in CG-IGM.

## 5.9 Summary and Conclusions

This chapter improves the understanding of pile resistance responses in CG-IGM and leads to the development of design recommendations for driven piles in CG-IGM based on 30 test

piles from 15 bridge projects in five U.S. states. The following conclusions and recommendations from this study were described as follows.

- A classification method was proposed to distinguish CG-IGM. Coarse-grained soil-based geomaterials with SPT N-values  $\geq 58$  blows/ft were classified as CG-IGM so that the uncertainties associated with the proposed SA methods in predicting pile resistances could be reduced and accounted for during pile design, and pile responses in CG-IGM could be better understood.
- New SA methods were developed for H and pipe piles driven in sand and gravel-based IGMs to improve the accuracy and reduce uncertainties associated with  $q_s$  predictions. All CG-IGMs and pile types were included in the training dataset to develop a new SA method for the  $q_b$  prediction. The validation of the proposed SA methods using separate pile data confirms the performance of the proposed SA methods in predicting  $q_s$  and  $q_b$ .
- Pile setup can be considered in the prediction of  $q_s$  in CG-IGMs. Close ended pipe pile (CEP) exhibits a slightly higher pile setup rate of  $A=0.27$  than steel H-piles with  $A=0.26$  because CEP piles induce a greater displacement of sand-based IGMs. If a 1-day pile restrike was performed based on the average A factors, the  $q_s$  of H-piles and CEP piles in CG-IGM will increase, on average, 67 percent and 86 percent on average, respectively.
- Pile relaxation should be accounted in the determination of  $q_b$  of piles in CG-IGM through a construction control method such as dynamic pile load testing. CEP piles in CG-IGM, with an average  $A=-0.07$ , experience a higher pile relaxation rate than H-piles in CG-IGM with an average  $A=-0.01$ . If a 1-day pile restrike was performed, the  $q_b$  of H and CEP piles in CG-IGM will decrease by 3 percent and 21 percent on average, respectively, based on the average A factors.



## CHAPTER 6: DRIVEN PILE RESISTANCES IN ROCK BASED INTERMEDIATE GEOMATERIALS

### 6.1 Introduction

Due to economic viability and durability, driven steel piles were now the most prevalent in regions where weak rocks or rock-based Intermediate GeoMaterials (R-IGM) such as mudstone, sandstone, claystone, and siltstone exist at shallow depths. Several different classification criteria for weak rocks or R-IGM have been proposed. For example, O'Neil and Reese (1999) included shale and mudstone as cohesive IGM that they classified as having unconfined compressive strength ( $q_u$ ) between 5 ksf to 50 ksf. However, Clarke and Smith (1993) classified weak rocks with  $q_u$  less than 10.4 ksf. Gannon et al. (1999) characterized weak rocks as having  $q_u$  between 12.5 ksf to 261 ksf that is much higher than O'Neil and Reese (1999) and Clarke and Smith (1993). A study conducted by Islam et al. (2022) proposed classification criteria for shales based on weathering conditions, mechanical properties, and measured pile resistances and divided them into rock-based shales and soil-based shales. These differences were attributed to the type of rocks, geographical locations used in the weak rock classification, and engineering applications. The weak sedimentary bedrock where penetration  $\geq 3$  ft of H-piles can be achieved and was classified as a weak rock by CDOT (2018). MDT (2008) establishes a criterion for IGM with  $q_u$  falling between 12.5 ksf and 260 ksf and stiffness modulus between 2.1 ksf and 21,000 ksf. Description of weak rocks is provided in Masterton et al. (1999) based on weathering grades and discontinuity pattern expressed as RQD and  $q_u$ . The rating-based classification is proposed based on RMR by Bieniawski (1987) and the Norwegian Geotechnical Institute (NGI) as well as Q-system by Barton (1987). Adhikari et al. (2020c) developed a classification criterion to separate R-IGMs or weak rocks governed by a geotechnical resistance from hard rocks governed by the pile structural capacity. This design philosophy was utilized in developing a criterion to differentiate R-IGM from hard rock based on limiting  $q_u$  values for intact and fractured rocks described in Adhikari et al. (2020c). Intact rocks and fractured rock masses contributing different geotechnical resistances were differentiated using RMR. This classification method was adopted in this study to differentiate R-IGM from hard rock.

Pile foundations were often driven into R-IGM to support civil infrastructures like bridges due to shallow bedrock stratigraphy in the Rocky Mountain and Appalachian regions of USA

and Canada. Thus, pile foundations in these regions rely on the resistance contributed from the R-IGM layers. Treating R-IGM as soils and applying existing SA methods developed for soils on piles in R-IGM could result in several construction challenges, such as early pile refusal and pile damage (Ng et al. 2015). A study by Ng and Sullivan (2017a) on 15 steel H-piles driven into IGM in Wyoming concluded that existing SA methods developed for soils resulted in an inconsistent and conservative prediction of geotechnical resistances.

Particularly, significant discrepancies were reported between resistances determined from dynamic load tests and predicted from existing SA methods for piles in IGM (Ng et al. 2015; Ng and Sullivan 2017a; Ng and Sullivan 2017b). Likewise, Mokwa and Brooks (2008) reported considerable variation between the predicted resistances from the SA methods and measured resistances in IGM determined from the signal matching technique using the CAPWAP. Additionally, the 20 static pile load tests did not result in any definite prediction equations to improve the prediction of pile resistances in R-IGM (Mokwa and Brooks 2008).

Piles driven into rocks have conventionally been treated as end-bearing piles. The primary reasons to neglect the shaft resistances in rocks were due to the 1) uncertainty associated with the amount of rock damage from pile driving (Barret and Prendergast 2020), and 2) the challenges with predicting these shaft resistances in damaged rocks (Fleming et al. 2008). Few methodologies have been proposed for the prediction of shaft resistances in rock that have been discussed in the next section. DLTs conducted on 50 steel H-piles in Winnipeg, Canada concluded that on average 25 percent, of the total pile capacity driven to limestone and mudstone was taken by the pile shaft (Belbes 2014). The tension test on steel tube piles driven into carbonate sandstone and siltstone in the Arabian Gulf, with  $q_u$  ranging from 36.55 ksf to 67.88 ksf, resulted in unit shaft resistance ( $q_s$ ) values ranging from 3.12 ksf to 5.01 ksf (Beake and Sutcliffe 1980). The study conducted by Matsumoto (1995) on two steel pipe piles driven into diatomaceous mudstone found that 100 percent applied load is supported by the shaft resistance on one pile and 90 percent by shaft resistance on another pile. Beaumont and Thomas (2007) conducted a test on tubular steel piles in conglomerate and Breccia, and the ultimate  $q_s$  was determined to be 10.44 ksf. The uplift tests on tubular piles driven into variable cemented extremely weak to weak sedimentary rock with variable calcium carbonate concentration and  $q_u$  from 6.26 ksf to 83.54 ksf resulted in a total uplift capacity of 1,036 kips and an average  $q_s$  of 1.82 ksf (Thomas et al. 2011). Studies performed by these researchers confirm the large percentage of total resistance was taken by the shaft resistance and the

incorrect assumption of neglecting the shaft resistance in R-IGM. Hence, an additional research study is required to develop SA methods for predicting the shaft resistance of piles driven in R-IGM.

The time-dependent pile responses in R-IGM have not been explicitly investigated, especially for piles driven in siltstone, sandstone, mudstone, claystone, and granite. Most literature reports both the increase and decrease in pile resistances driven into shale (Hannigan et al. 2020; Morgano and White 2004; Thompson and Thompson 1985; Likins and Husain 1984; Long and Anderson 2014; Islam et al. 2022). The study conducted by Hannigan et al. (2020) reported 14 percent loss in end bearing on a steel H-pile driven into siltstone. Compressive static and dynamic load tests were conducted on two 16-in open-ended pipe (OEP) piles driven into mudstone in Japan (Matsumoto 2015). The SLTs on test pile 1 and test pile 2 conducted 29 days and 11 days after the EOD, respectively, indicated significant pile setup of about twice the initial driving resistance. This setup was attributed to geomaterial strength recovery as pore pressure generation during SLT was small.

Recognizing these current limitations and challenges, this paper presents load test results to better understand pile responses in R-IGM and to develop recommendations to improve the current pile design and construction practices in R-IGM. Thirty-nine historical pile load test data from 28 bridge projects and 19 separate pile load test data from the literature were used to 1) develop and validate new SA methods for predicting the  $q_s$  and unit end bearing ( $q_b$ ) of piles driven in different R-IGM, 2) evaluate the changes in pile resistances in R-IGM, and 3) establish newly calibrated LRFD resistance factors using three probability-based methods to attain the target design reliability.

## **6.2 Existing SA Methods for Prediction of Driven Pile Resistances in R-IGMs**

Limited research has been conducted on piles driven into weak rocks or R-IGM, and existing SA methods for piles driven into weak rocks reported in literature were summarized in Table 6.1. Although many research works have been conducted on drilled piles in R-IGM, it has been found that the distribution of shear stress (unit shaft resistance) along driven piles differs largely from that of drilled piles with rock-sockets (Barret and Prendergast 2020). Vesic (1970) noticed that the  $q_s$  along driven piles increased with depth. On the other hand, large displacements were warranted to mobilize the shaft resistance at the bottom of drilled shafts

in rock (Williams et al. 1980). Most of the studies shown in Table 6.1 treated driven piles into rocks as end bearing piles. Rahman and Broms (1971) developed equations to predict  $q_b$  in terms of  $q_u$  based on only three SLTs. A linear relationship for  $q_b$  of piles driven in sandstone, mudstone, and shale was developed based on  $q_u$  (Morton 2012). Belbes (2014) suggested the equation  $q_b = 2.5 q_u$  proposed by Prakoso and Kulhaway (2002) based on only six  $q_u$  tests from 6 test sites in Canada. Tomlinson and Woodward (2014) provided a unit end bearing equation based on results of two SLTs and a dynamic test on 8-inch to 31-inch diameter pipe piles driven into mudstone and sandstone. All these studies treated driven piles into rocks as end bearing piles and no validation or LRFD recommendations were provided.

However, Belbes (2014) shows that 25 percent total capacity on average was by the shaft for piles driven into limestone and mudstone. In terms of evaluating the shaft resistance, Terente et al. (2015) used the total stress method or  $\alpha$ -method (Tomlinson 1980) and effective stress method or  $\beta$ -method (Esrig and Kirby 1979) that underpredicted the unit shaft resistance compared to unit shaft resistance from CAPWAP for driven piles in Mercia mudstone. Although Long (2016) proposed the modified SPT to predict the pile resistance in IGM with substantial scatter, LRFD guidelines were not developed since these prediction equations were not assessed or validated using a separate testing pile dataset. Existing  $\alpha$  and  $\beta$  methods originally developed for soils were calibrated for predicting pile resistance in weak rocks (Adhikari et. al 2020b; Solimon et al. 2018). Barret and Prendergast (2020) proposed an empirical equation for predicting  $q_s$  of piles driven into weak rocks and the dimensionless scaling factors shown in Table 6.1 ( $\alpha_0$  and  $\beta$ ) were calibrated using an iterative process for seven SLT data. Due to lack of data, no statistical approach was implemented to calibrate  $\alpha_0$  and  $\beta$ . Using  $\alpha_0=0.71$  and  $\beta=0.45$ , the equation was applied to check the unit shaft resistance using three pile tests that were not used in the calibration. The results revealed that the proposed model provides a better fit to measure data than existing models based on total stress and effective stress methods. No LRFD recommendation was provided for the proposed prediction equation. Previously, no studies have been conducted to develop SA methods for prediction of driven pile shaft resistance for a particular R-IGM. Based on the discussion in this section, it can be said that proper SA methods with LRFD recommendation for driven piles in R-IGM were warranted for better prediction of unit shaft resistance and unit end bearing.

### 6.3 Overview of Pile Load Test Data

New SA methods for estimating  $q_s$  and  $q_b$  of driven piles in various R-IGMs were developed in this study using 39 dynamic pile load test results from 28 bridge projects in 3 states: Montana, Wyoming, and Idaho. The bridge location, pile location, pile type, total pile penetration ( $D_B$ ), driving hammer, hammer blow counts, CAPWAP resistances,  $q_u$ , RQD, and SPT N-value (granite) or corrected SPT N-value ( $(N_1)_{60}$  (siltstone, sandstone, mudstone, and claystone) were summarized in Table 6.2. Among the 39 test piles, 20 were steel pipe piles (2 close-ended and 17 open-ended) and 19 were steel H-piles. The dynamic pile load tests were conducted using PDA with subsequent CAPWAP analysis. Previous studies have shown that pile resistances from CAPWAP were comparable to those from the SLTs (Likins and Rausche 2004; Sakr 2013). Based on load test results of 25 piles in IGM by Adhikari et al. (2020a) and 3 recently completed SLTs on steel H-piles in shale and siltstone (Islam 2021), the mean resistance bias (a ratio of pile resistance from SLT to resistance from CAPWAP) of 1.077 was closer to unity and the coefficient of variation (COV) of the resistance biases of 0.121 was relatively small. A comparison of 17 total pile resistances from seven operators using CAPWAP with the final pile resistance of 226.6 kips from an SLT yields a resistance bias of 0.971 that was closer to 1.0 and has a relatively low COV of 0.121 (Verbeek et al. 2015). Similarly, research based on 19 predictions yielded a similar resistance bias of 1.06 and a comparatively low COV of 0.107. (Fellenius 1988). These comparisons support the use of pile resistances from CAPWAP in this study.

### 6.4 New Static Analysis Methods for Resistance Prediction

The new SA methods for predicting  $q_s$  and  $q_b$  in R-IGM were developed for siltstone, claystone, granite, sandstone, and mudstone. Proposing prediction equations for specific R-IGM types will reduce the uncertainties associated with different geological characteristics and result in more reliable pile resistance predictions. Different nonlinear models were evaluated to predict  $q_s$  and  $q_b$  as response variables using R-studio statistical software (R Core Team 2016). Model selection criteria were used to choose from among different nonlinear models (Gu et al. 2018). The same methodology to choose the best model from among candidate models is described in Masud et al. (2022).

**Table 6.1. Existing Static Analysis Methods for the Estimation of Pile Resistances in Weak Rocks or Rock-Based IGM.**

Source	Resistance Estimation	Remarks
Rehnman and Broms (1971)	$q_b = 6.2 q_u$ (ksf) (Granite) $q_b = 5.2 q_u$ (ksf) (Limestone) $q_b = 4.8 q_u$ (ksf) (Sandstone)	Load test was conducted to evaluate the bearing capacity of three different rock materials (granite, limestone, and sandstone) using laboratory load tests on rock samples encased in concrete. The end bearing obtained from load test results were compared with Mohr-Coulomb theory, Griffith theory. Limestone and granite resembled Griffith theory, but underpredicted capacity by 50 percent. Sandstone resembled with the Mohr-Coulomb theory
Morton (2012)	Unit end bearing $q_b = 7.5 q_u$ $9.1 \text{ ksf} \leq q_b \leq 41.6 \text{ ksf}$ $112.8 \text{ ksf} \leq q_u \leq 376 \text{ ksf}$	Provided a linear relationship between $q_b$ of piles driven in sandstone, mudstone, and shale. The measured $q_p$ was obtained from the dynamic tests performed using PDA and CAPWAP from 15 small displacement piles from 10 bridge projects in Halifax, Canada. No LRFD recommendation was provided. No shaft resistance prediction was provided.
Belbas (2014)	Unit end bearing $q_b = 2.5 q_u$ (ksf) Prakoso and Kulhaway (2002) $1858 \text{ ksf} \leq q_p \leq 4574 \text{ ksf}$ and $480 \text{ ksf} \leq q_u \leq 1754.4 \text{ ksf}$	Fifty CAPWAP analysis of steel H piles driven to limestone and mudstone were conducted from 12 bridge sites in Winnipeg, Canada. Only 6 UCS test from 6 test sites was done. Suggest the Prakoso and Kulhaway (2002) equation for use. No correlation was developed for shaft resistance with $q_u$ .
Tomlinson and Woodward (2014)	Unit end bearing $q_b = 1.2 q_u$ to $1.75 q_u$ (ksf)	This recommendation was based on results of two SLTs and a dynamic test on 8-inch to 31-inch diameter pipe piles driven into mudstone, siltstone, and sandstone. Test Piles were treated as end bearing piles.
Terente et al. (2015)	Effective stress method for shaft resistance: $q_s = K \sigma'_v \tan \delta$ ; $K = 0.25 + 7 E_h \left( 0.001 + \frac{1}{z} \right)$ Total stress method for shaft resistance: $q_s = \alpha q_u$ ; $\alpha = 0.11 q_u^{-0.5}$	Offshore jacked pile driven into Mercia mudstone. Existing methods underpredicted the shaft resistance compared to resistance from CAPWAP. The conclusion was drawn based on only one case study.

Long (2016)	Unit shaft resistance Fine-grained IGM: $q_s = 0.021N_{MSPT}; \leq 2 \text{ ksf}$ Coarse-grained IGM: $q_s = 0.9N_{MSPT}^{0.25}; \leq 3 \text{ ksf}$ Unit end bearing Fine-grained IGM: $q_b = 0.935N_{MSPT}; \leq 200 \text{ ksf}$ Coarse-grained IGM: $q_b = 65N_{MSPT}^{0.3}; \leq 300 \text{ ksf}$	Used modified SPT method to predict the resistances of driven piles in IGMs consisting of very dense sand to gravels, very hard tills, weak sandstones and weathered granite, and limestone. Substantial dispersion was observed between pile resistances and $N_{MSPT}$ for different IGM types when exceeded the respective limits.
Soliman et al. (2018)	Unit shaft resistance $0.35 \leq \alpha \leq 0.62$ $0.1 \leq \beta \leq 1$ Unit end bearing $21 \leq N_c \leq 30; 8 \leq N_t \leq 50$	Calibrated the coefficients of $\alpha$ and $\beta$ -methods using 19 dynamic load test results of pile driven into clay shale, sandstone and siltstone from bridge projects in Edmonton, Canada. For bedrock the back-calculated calibrated factors were greater than the Canadian Foundation Engineering Manual (2006)
Adhikari et al. (2020b)	Calibrated $\alpha$ and $\beta$ factors for unit shaft resistance prediction $\hat{\alpha}(10^{-2}) = 64.63 \times q_u^{-0.656}$ $\hat{\beta} = 0.0098\phi^2 - 0.75\phi + 14.63$ Calibrated $N_c$ and $N_t$ factors for unit end bearing prediction $\widehat{N}_c = 39.8 \times q_u^{-0.635}$ $\widehat{N}_t = 0.907\phi^2 - 71.399\phi + 1428.55$	Used 28 driven steel H-piles from Wyoming. Calibrated $\alpha$ and $N_c$ factors were established for piles driven into claystone and siltstone. Calibrated $\beta$ and $N_t$ factors were established for piles driven into sandstone and siltstone.
Barret and Prendergast (2020)	Unit shaft resistance: $q_s = \sigma'_{rf} \tan \delta_f$ $\sigma'_{rf} = \alpha_0 q_u \left(\frac{h}{D}\right)^{-\beta} \left(\frac{1}{1+A_R}\right)$ for $0 < h/D < 1$ ; $\alpha_0=0.71; \beta=0.45$	Used 44 load test results of pile penetrating in weak rocks (calcareous siltstone, sandstone, calcareous sandstone, diatomaceous mudstone, conglomerate, and basalt) with the $17 \text{ ksf} \leq \text{average } q_u \leq 1,232 \text{ ksf}$ . Introduced the fiction fatigue phenomena. Applicable to sedimentary rocks except chalk. The variability of UCS of different rock types remains uncertain. A statistical approach was not adopted to calibrate the dimensionless factor.

$K$ =coefficient of lateral earth pressure;  $A_s$ =surface area of pile shaft;  $q_u$ =uniaxial compressive strength;  $q_s$ =unit shaft resistance;  $\sigma'_{rf}$ = effective radial stress at failure;  $\delta_f$ =interface friction angle;  $\alpha_0$  and  $\beta$ =dimensionless scaling factors;  $h, z$ =depth;  $D$ =pile diameter;  $A_R$ =area ratio of an open-ended pipe pile;  $N_{MSPT}$ =modified SPT N-value;  $E_h$ =average deformation modulus.

**Table 6.2. Summary of 39 Driven Piles in Rock Based IGM.**

St.	Bridge Project	Pile location	Pile	$D_B$ (ft)	Number of Layer R-IGM	$q_u$ (ksf)	$N$ or $(N_f)_{60}$ (blows/ft)	$q_s$ (ksf)	$q_b$ (ksf)	Hammer	RQD (percent)	BC
ID	SH-55 NF PR	P-4 at A-1	HP 12x74	56	7Granite	-	48-150'	0.71-4.92*	40.82	APE D30-42	13	60
ID	SH-55 NF PR	P-7 at A-2	HP 12x74	38	2Granite	-	43-100'	0.83-1.73*	314.38	APE D30-42	13	60
ID	SH-55 NF PR	P-1 at CPi	30-in OEP	61	2Granite	-	100-120'	1.31-2.55*	99.20	APE D70-52	13-15	52
ID	SH-55 NF PR	P-4 at CPi	30-in OEP	51.8	3Granite	-	96-125'	2.27-2.52*	50.52	APE D70-52	15-18	61
ID	US-95S SR bridge	P-2 at A-1	HP14x117	37	2Siltstone	15.84-44.06 <sup>#</sup>	37-47'	1.24-2.51*	81.63	Del D19-42	15-90	58
ID	US-95S SR bridge	P-1 at A-2	HP14x117	36	2Siltstone	-	114-150'	2.47-3.67*	95.24	Del D19-42	60-100	187
ID	US-95S SR bridge	P-32 at A-2	HP14x117	36	2Siltstone	54.14-67.7 <sup>#</sup>	108-120'	3.17-3.24*	68.03	Del D19-42	60-100	118
ID	SH-31 PC bridge	P-10 at A-2	HP12x74	32.4	2Siltstone	-	58-69'	1.18-1.57*	609.13	APE 30-42	NA	64
ID	SH-28-436 LR	P-1 at A-2	HP14x89	38.7	1Siltstone	-	70'	1.23	706.96	Diesel 30-32	NA	1451
ID	SH-28 LR bridge	P-2 at A-2	HP 12x74	64	8Mudstone 4Siltstone	-	32-264'	0.20-5.03*	123.7	ICE I30 V2	40-90	64
ID	SH-28 LR bridge	P-2 at A-1	HP 12x74	71	7Mudstone 5Siltstone 1Sandstone	7.34-63.79 <sup>#</sup>	16-75'	0.44-2.53*	358.23 (Mudstone)	ICE I30 V2	38-93	61
WY	PB-Parson Street	P-5 at A-1	HP 12x53	87.9	1Siltstone	45.2	66	1.65	55.92	Del D16-32	NA	164
WY	PB-MuddyCreek	P-10 at B-3	HP 12x53	38	1Siltstone	-	120	3.9	314.6	Del D16-32	68	240
WY	PB-Beech Street	P-1 at A-1	HP 12x53	46.7	1Siltstone	19	43	1.54	122.28	Del D16-32	21	55
WY	PB-Beech Street	P-5 at A-1	HP 12x53	46.9	1Siltstone	19	43	1.86	106.56	Del D16-32	21	66



WY	Woods Wardell	P-1 at Pi2	HP 12×53	23	2Claystone	1.4-76 <sup>#</sup>	29-65'	1.89-3.3*	243.9	APE D19-42	72	128
WY	Burns South	P-1 at Pi3	HP 14×73	37.6	1Sandstone	1.2	66	1.43	162.5	Del D16-32	NA	100
WY	Casper street	P-17 at Pi1	HP 14×73	20.5	1Sandstone	459	579	5.00	106.3	MVE M-19	NA	118
WY	Cedar street	P-5 at A-2	HP 12×53	41.2	1Sandstone	6.5	22	1.62	130	MVE M-19	54	60
MT	Bridge over CC	P-4 at B-3	24-in OEP	57.8	2Siltstone	-	41-44'	1.91-2.41*	18.87	Del D16-32	NA	72
MT	Bridge over RR	P at B-1	20-in OEP	36	4Siltstone	-	32-67'	1.27-3.56*	137.49	Del D16-32	NA	84
MT	M FK Porcupine	P-2 at B-3	20-in OEP	46.2	2Siltstone	11.37-26.35 <sup>#</sup>	27-29'	1.68	27.54	Del D19-42	NA	56
MT	Bridge over CoC	P-2 at B-2	16-in OEP	36.8	3Siltstone	-	31-59'	1.54-3.34*	284.7	ICE I30 V2	NA	83
MT	Bridge over BC	P-4 at B-1	16-in OEP	28.3	2Claystone	10.66-15.84 <sup>#</sup>	96-103'	1.15-1.27*	264.23	Del D19-32	NA	238
MT	MR - W Zurich	P-1 at B-1	16-in OEP	82.2	2Claystone	56.34-163.1 <sup>#</sup>	89-139'	2.28-3.60*	263.58	ICE I30	NA	74
MT	Bridge over Rock creek	P-1 at B2	20- OEP	45	1Claystone	3.6	37	0.35	44.59	ICE I30	NA	73
MT	Bridge over Rock creek	P-1 at B3	20- OEP	41	1Claystone	11.23	20	1.73	66.36	ICE I30	47	42
MT	Bridge Musselshel River	P-1 at B-1	16-in OEP	25	1Claystone	17.93	180	2.65	NA	APE D30-42	88	120
MT	Bridge Musselshel River	P-7 at B-2	24-in OEP	38.6	1Claystone	19.152	220	2.40	NA	APE D30-42	67-100	120
MT	Bridge BNSF	P-1 at A-4	HP 14×118	69.4	1Claystone	40.70	63	1.65	53.5	ICE I30v2	85-95	96
MT	12 km-E Jordan	P-8 at B-2	24-in OEP	27.8	1Claystone	7.06	50	3.73	105.92	ICE I 36	71-83	39
MT	Musselshell RV	P-4 at B-3	16-in CEP	36.5	1Sandstone	161.3	148	1.68	NA	APE D30-32	NA	112

MT	Bridge over BPR	P at B-2	24-in OEP	33	1Sandstone	15.6	75	0.9	388	Del D62-22	NA	960
MT	Bridge over WS	P at B-2	24-in CEP	35.3	1Claystone	15.84	NA	1.69	263.38	ICE I 62	NA	120
MT	Bridge over MR	P-3 at B-4	20-in OEP	28.6	3Mudstone	-	35-68'	2.66-4.98*	113.65	ICE I 36	NA	189
MT	Bridge over MR	P-1 at B-1	20-in OEP	28.0	3Mudstone	-	34-36'	2.89-4.17*	127.6	ICE I 36	90	172
MT	Bridge over Cr.	P16 at B1	16-in OEP	20.7	1Mudstone	-	197	4.04	1424	ICE I 36	NA	74
MT	Bridge over Cr.	P2 at B4	16-in OEP	20	1Mudstone	-	282	5.28	1046.5	ICE I 36	NA	44
MT	Bridge over LG creek	P4 at B2	HP14×89	30	2Sandstone	39.02	275-307'	2.23	275.9	Del D 19-42	25-52	100

St.=State; B=Bridge; st.=Street; ID=Idaho; WY=Wyoming; MT=Montana; BC=Butte Creek; MR=Milk River; PC=Pine Creek; WSC=Warm Spring Creek; CC=Crooked Creek; W=West; BPR=Big Powder River; LG=Lodge Grass Creek; WR=Weiser River; SR= Snake River; RP=Robinson Park; BC=Butte Creek; MR=Milk River; CC=Cherry Creek; RR=Rock creek; LR=Lemhi River; BPR=Big Powder River; SC=Sharpy Creek; BI=Broadus interchange; Cr.=Crooked Creek; Co.=Coral Creek; A=Abutment; Pi=Pile; P=Pier; B=Bent;  $D_B$ =Total pile penetration; CEP=Close ended pipe pile; OEP=Open ended pipe pile; R-IGM=Rock based IGM;  $q_u$ =Unconfined compressive strength;  $q_s$ =Unit shaft resistance; #=Range of  $q_u$  for multiple R-IGM layers; \*=Range of  $q_s$  for multiple R-IGM layers; '=Range of  $N$  or  $(N_f)_{60}$  for multiple R-IGM layers;  $q_b$ =Unit end bearing; NA=Not applicable; Del.=Delmeg; ICE=International Construction Equipment; APE=American Pile Driving Equipment; BC=Hammer blow count at end of driving (bl/ft).

### 6.4.1 Siltstone

Fifteen dynamic pile load tests from 11 bridge projects in Montana, Wyoming, and Idaho were utilized to develop new SA methods for predicting  $q_s$  and  $q_b$  of driven piles in siltstone. Among 15 test piles, 4 were open-ended pipe piles and the remaining 11 were steel H-piles. The relevant information for these piles is provided in Table 6.2. The prediction equations for  $q_s$  in siltstone were developed based on laboratory measured  $q_u$  and corrected SPT N-values  $(N_1)_{60}$ . The positive relationships between  $q_s$  from CAPWAP and  $q_u$  of siltstone is illustrated in Figure 6.4a, indicating a higher  $q_s$  resulted from a higher  $q_u$ . The power model is selected, and the resulting prediction equation is shown in Figure 6.1.

$$\hat{q}_s = 0.45q_u^{0.44}$$

**Figure 6.1. Equation. Unit Shaft Resistance Prediction Equation for Siltstone Based on Unconfined Compressive Strength.**

Figure 6.4b depicts a nonlinear and positive relationship between  $q_s$  from CAPWAP and  $(N_1)_{60}$ , indicating siltstone with a higher SPT blow count tends to have a higher shear strength and more resistance to pile penetration. To predict the  $q_s$  (ksf) of driven piles in siltstone in terms of  $(N_1)_{60}$  and atmospheric pressure ( $P_a=2.12$  ksf), the power model was selected, and the resulting prediction equation is shown in Figure 6.2.

$$\hat{q}_s = 0.42P_a \left[ \frac{(N_1)_{60}}{16} \right]^{0.63}$$

**Figure 6.2. Equation. Unit Shaft Resistance Prediction Equation for Siltstone Based on Corrected SPT N Value.**

Using the 14 test piles with pile tips embedded in siltstone, the nonlinear relationship between  $q_b$  from CAPWAP and the ratio of the SPT N-value to total pile penetration ( $D_B$ ) is shown in Figure 4.3. The  $q_b$  increases nonlinearly and at an increasing rate as the ratio of SPT N-value to  $D_B$  increases. A modified power model was selected, and the resulting prediction equation was given by Figure 6.3 in terms of SPT N-value,  $D_B$ , and  $P_a$ .

$$\hat{q}_b = 12.9P_a \left[ 2.43^{\left( \frac{32.4 N}{30 D_B} \right)} \right]$$

**Figure 6.3. Equation. Unit End Bearing Prediction Equation for siltstone.**

These suggested prediction equations for piles driven into siltstone should be applied accordingly with  $q_u$  of siltstone ranging from 7.34 to 67.7 ksf,  $(N_1)_{60}$  of siltstone ranging from 16 to 150 blows/ft, and  $N/D_B$  varying from 0.65 to 3.41 blows/ft-ft.

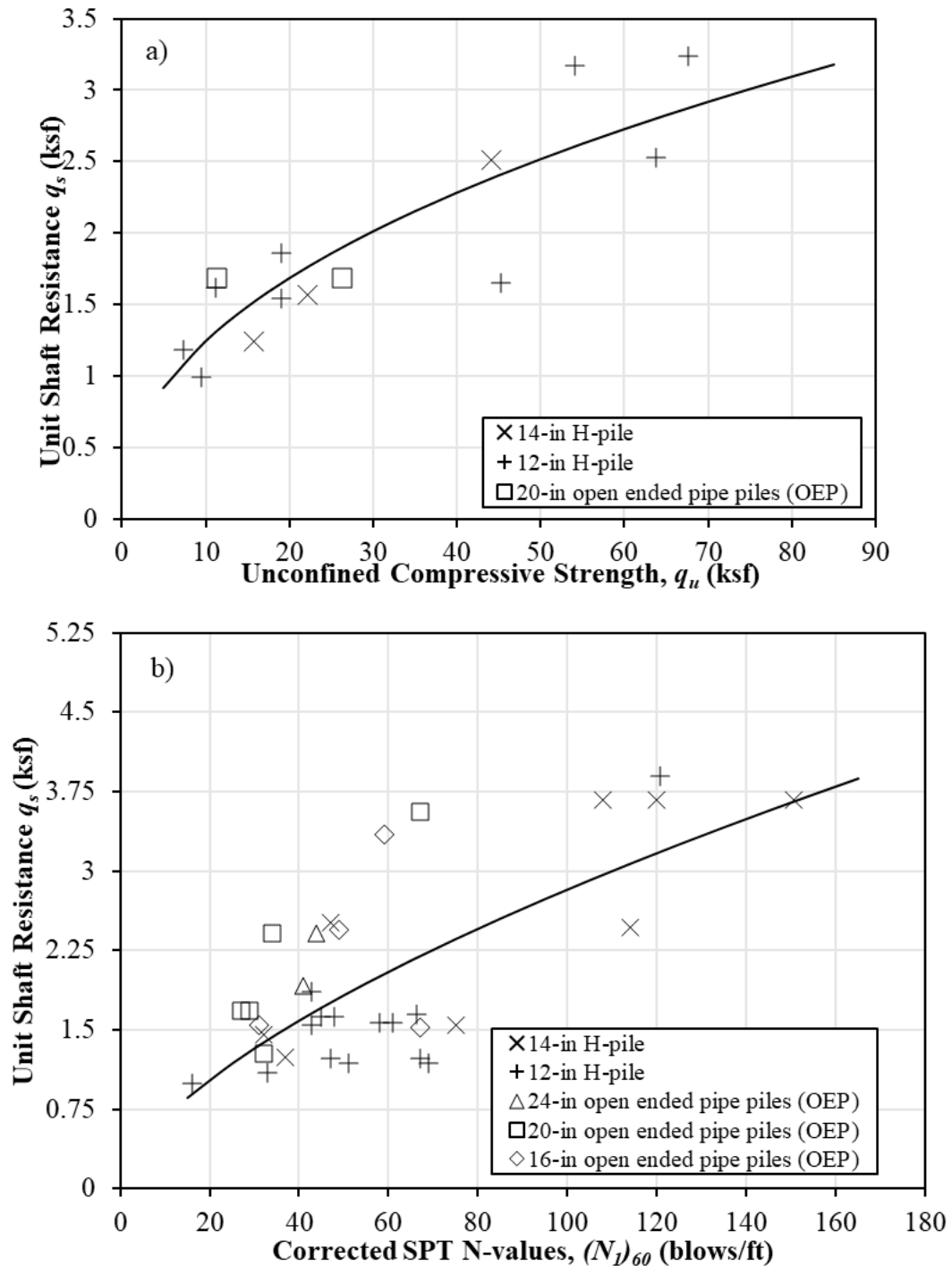


**Figure 6.4. Relationship Between Unit Shaft Resistance from CAPWAP and a) Unconfined Compressive Strength and b) Corrected SPT N-Value of Siltstone.**

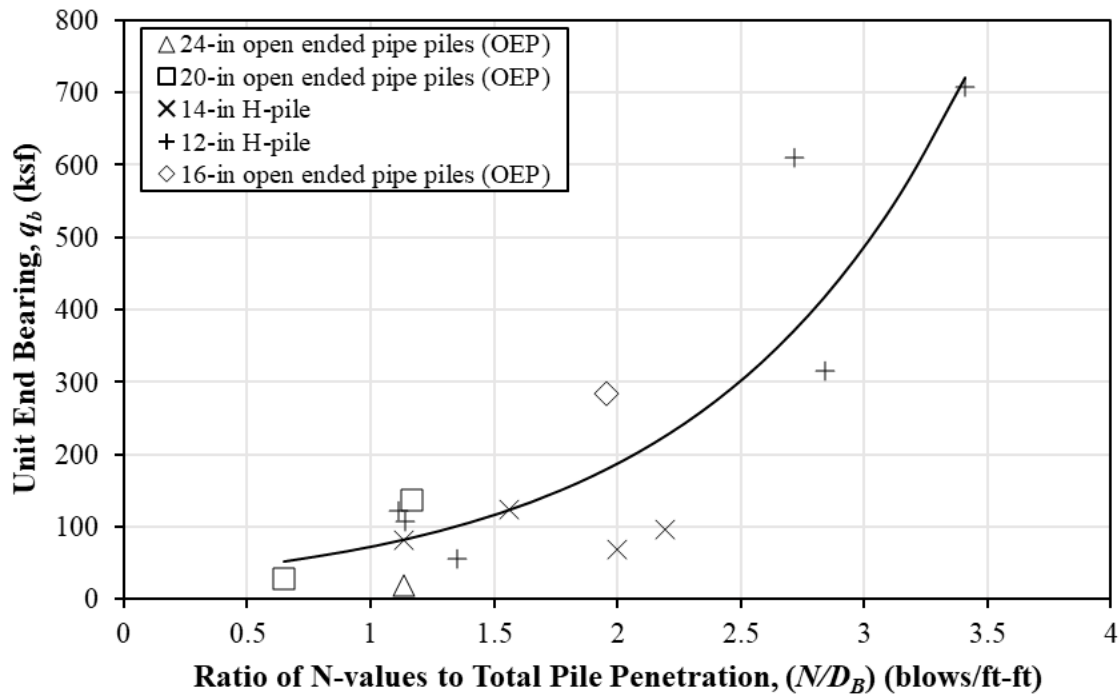


**Figure 6.5. Relationship Between Unit End Bearing from CAPWAP and the ratio of SPT N-value to Total Pile Penetration to Siltstone.**

#### 6.4.2 Claystone

The new SA methods for predicting  $q_s$  and  $q_b$  of driven steel H and pipe piles into homogenous claystone without any interbedded rock layers were developed using eight test pile results from five different bridge projects in Wyoming and Montana (Table 6.2). The relationship between the  $q_s$  from CAPWAP and laboratory measured  $q_u$  is shown in Figure 6.8. The power model given was selected as the best nonlinear model in terms of  $q_u$  for  $1.4 \text{ ksf} \leq q_u \leq 163.1 \text{ ksf}$  and  $0.35 \text{ ksf} \leq q_s \leq 3.6 \text{ ksf}$ . The associated prediction equation is given in Figure 6.6.

$$\hat{q}_s = 0.74q_u^{0.31}$$

**Figure 6.6. Equation. Unit Shaft Resistance Prediction Equation for Claystone.**

Figure 6.9 shows the relationship between  $q_b$  from CAPWAP for both H and pipe piles and  $q_u$  of the bearing claystone layers. The 16-in pipe pile with a conical point exhibits a higher  $q_b$ , which was attributed to the use of the conical point at the pile toe facilitating the embedment into the bearing layer. The saturation growth rate model was selected as the best model. The resulting prediction equation is shown in Figure 6.7.

$$\hat{q}_b = \frac{313.27q_u}{20.96 + q_u}$$

Figure 6.7. Equation. Unit End Bearing Prediction Equation for Claystone.

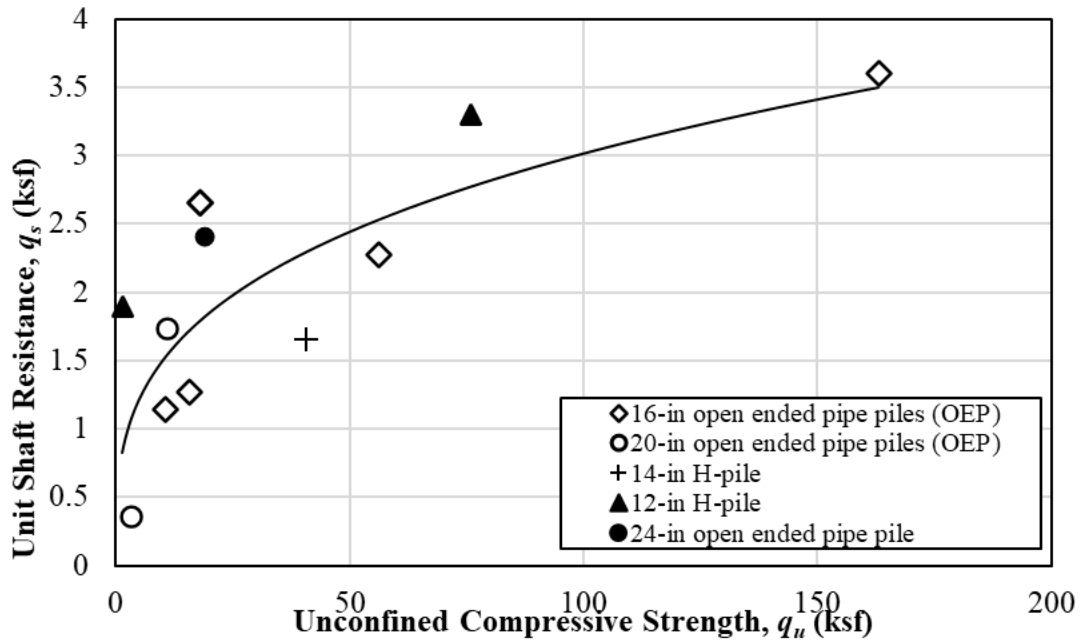


Figure 6.8. Relationship Between Unit Shaft Resistance from CAPWAP and Unconfined Compressive Strength of Claystone.

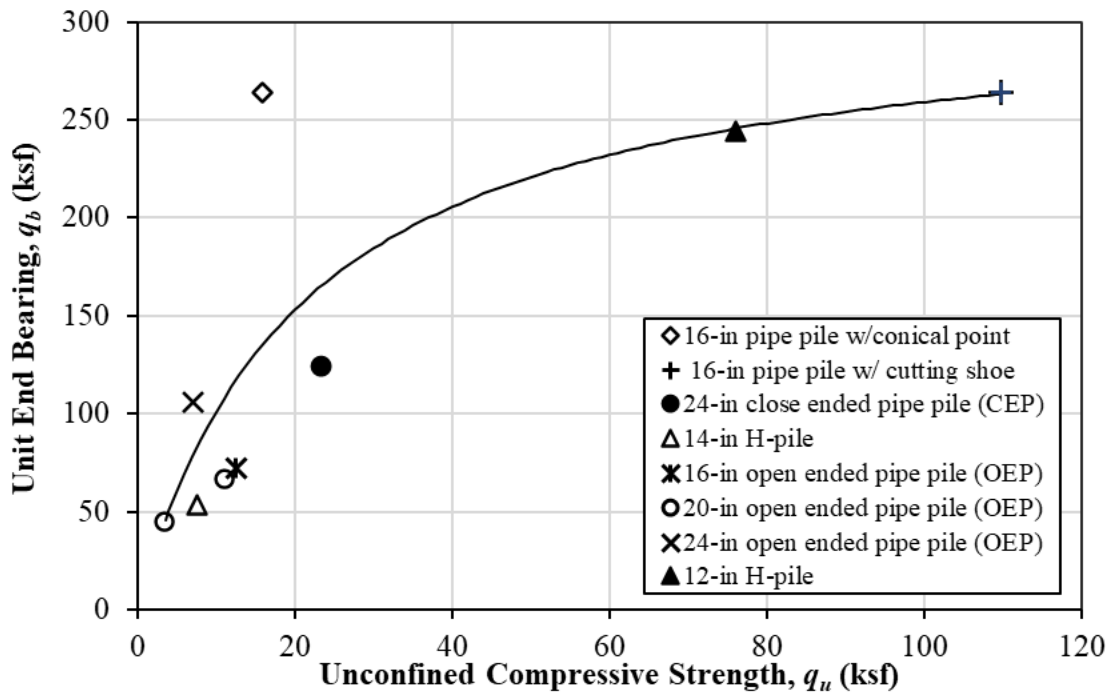


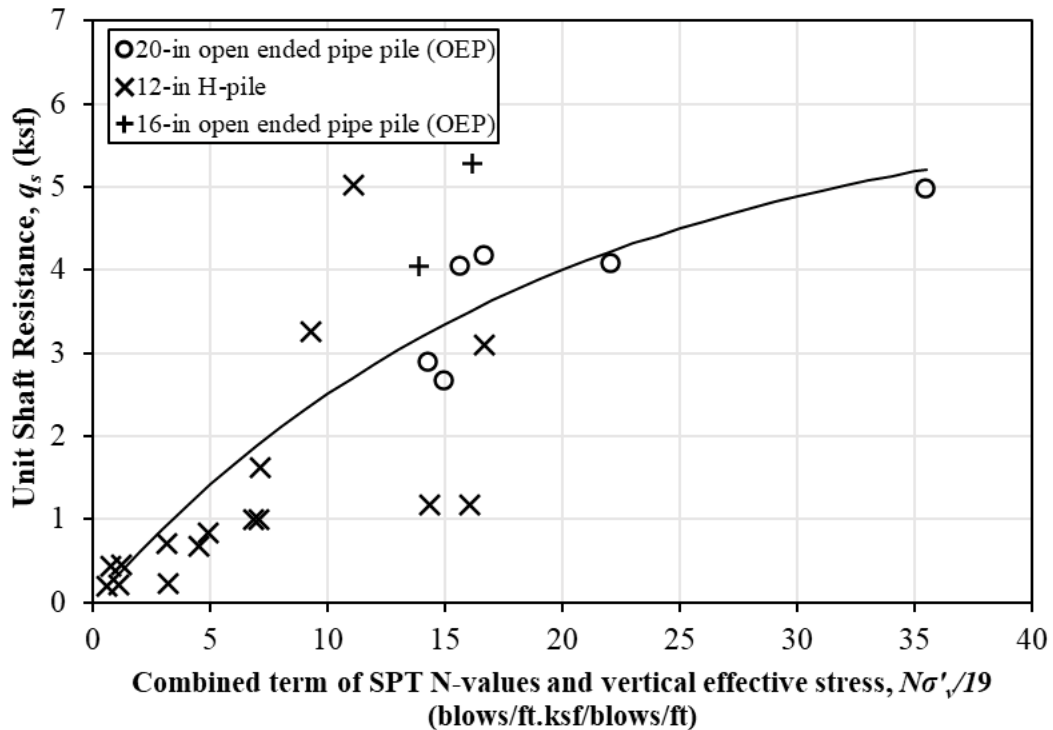
Figure 6.9. Unit End Bearing from CAPWAP Versus Unconfined Compressive Strength.

### 6.4.3 Mudstone

Figure 6.11 shows the relationship between  $q_s$  from CAPWAP and the combined term  $\frac{N \times \sigma'_v}{19}$  for 12-in H-piles, 16-inch open ended pipe pile, and 20-inch open ended pipe piles. The  $q_s$  increases at a higher SPT N-value. To account for the effective vertical stress along a pile shaft in a mudstone layer, the  $\sigma'_v$  value at the midpoint of the mudstone layer was selected in the combined term ( $N \times \sigma'_v$ ), which was normalized by the minimum  $N$  value of 19 to eliminate the unit associated with N-value. The  $q_s$  of the mudstone layer increases with the increasing  $\sigma'_v$  for 12-in H-pile and 20-in OEP piles. The exponential model was selected as the best model for predicting  $q_s$  of driven pipe and H piles in homogenous mudstone layers for  $0.2 \text{ ksf} \leq q_s \leq 5.3 \text{ ksf}$ ,  $19 \text{ blows/ft} \leq N \leq 168 \text{ blows/ft}$ , and  $0.19 \text{ ksf} \leq \sigma'_v \leq 8.12 \text{ ksf}$ . The associated prediction equation is given in Figure 6.10.

$$\hat{q}_s = 6.19 \left[ 1 - e^{\left( -0.05 \frac{N \times \sigma'_v}{19} \right)} \right]$$

**Figure 6.10. Equation. Unit Shaft Resistance Prediction Equation for Mudstone.**



#### 6.4.4 Sandstone

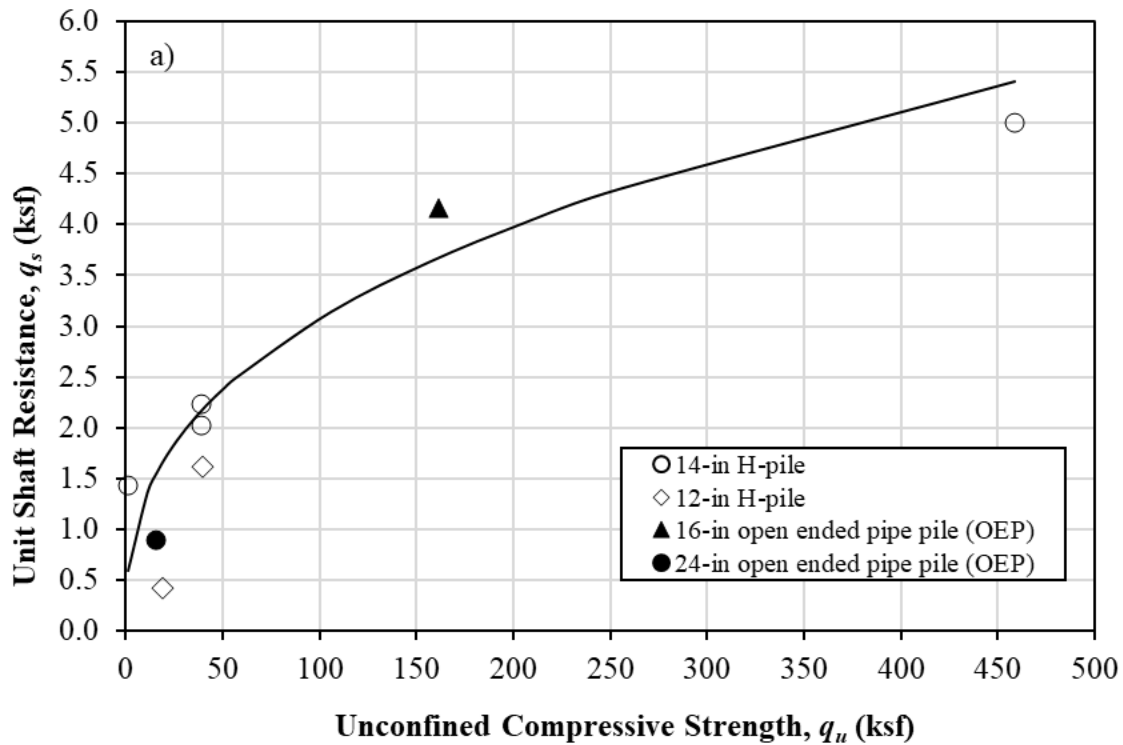
Figures 6.14(a) and 6.14(b) show the comparison of  $q_s$  with  $q_u$ , and the combined term  $\frac{q_u \times (N_1)_{60}}{579}$  for H-piles in homogenous sandstone layers, respectively. A positive relationship was observed in each comparison, suggesting the positive effect of  $q_u$  and  $(N_1)_{60}$  on  $q_s$ . Two different prediction equations given by Figure 6.12 and Figure 6.13 were developed for  $q_s$  in terms of the  $q_u$ , and  $\frac{q_u \times (N_1)_{60}}{579}$ , respectively. These prediction equations were applicable for H-piles and open-ended pipe piles driven in homogenous sandstone layers with  $0.43 \text{ ksf} \leq q_s \leq 5 \text{ ksf}$ ,  $1.2 \text{ ksf} \leq q_u \leq 459 \text{ ksf}$ , and  $18 \text{ blows/ft} \leq (N_1)_{60} \leq 579 \text{ blows/ft}$ .

$$\hat{q}_s = 0.56q_u^{0.37}$$

**Figure 6.12. Equation. Unit Shaft Resistance Prediction Equation for Sandstone based on Unconfined Compressive Strength.**

$$\hat{q}_s = 1.25 \left( \frac{q_u \times (N_1)_{60}}{579} \right)^{0.23}$$

**Figure 6.13. Equation. Unit Shaft Resistance Prediction Equation for Sandstone based on Unconfined Compressive Strength and Corrected SPT N-values.**





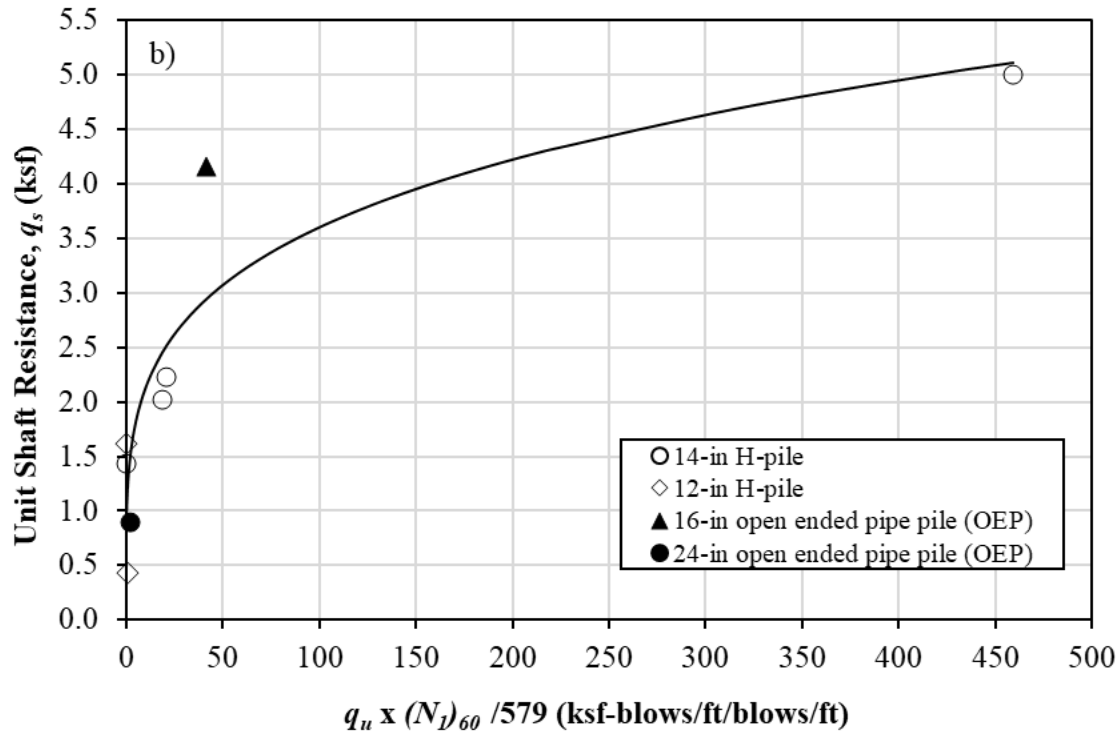


**Figure 6.14. Relationship Between Unit Shaft Resistance from CAPWAP and (a) Unconfined Compressive Strength for Sandstone Layers, (b) Product of Average Unconfined Compressive Strength and Corrected SPT N-value  $(N_1)_{60}$ .**

#### 6.4.5 Granite

The development of a new SA method for the prediction of  $q_s$  of driven piles in granite was accomplished using four dynamic load test results from a bridge project in Idaho. Figure 6.16 shows that the  $q_s$  from CAPWAP increases linearly with the SPT N-values. It is expected that granite with a higher SPT N-value will exhibit a higher shear strength and resistance to pile penetration. Compared to other candidate models: natural logarithm, modified exponential, a linear model in terms of N-value and the atmospheric pressure ( $P_a$ ) was selected for predicting  $q_s$  of driven piles in granite. The prediction equation is shown in Figure 6.15 and was applicable for driven H-pile and pipe piles driven into granite layers with  $0.83 \text{ ksf} \leq q_s \leq 4.92 \text{ ksf}$ , and  $43 \text{ blows/ft} \leq N \leq 150 \text{ blows/ft}$ .

$$\hat{q}_s = \left[ 0.7 \frac{N}{43} - 0.5 \right] P_a$$

**Figure 6.15. Equation. Unit Shaft Resistance Prediction Equation for granite.**

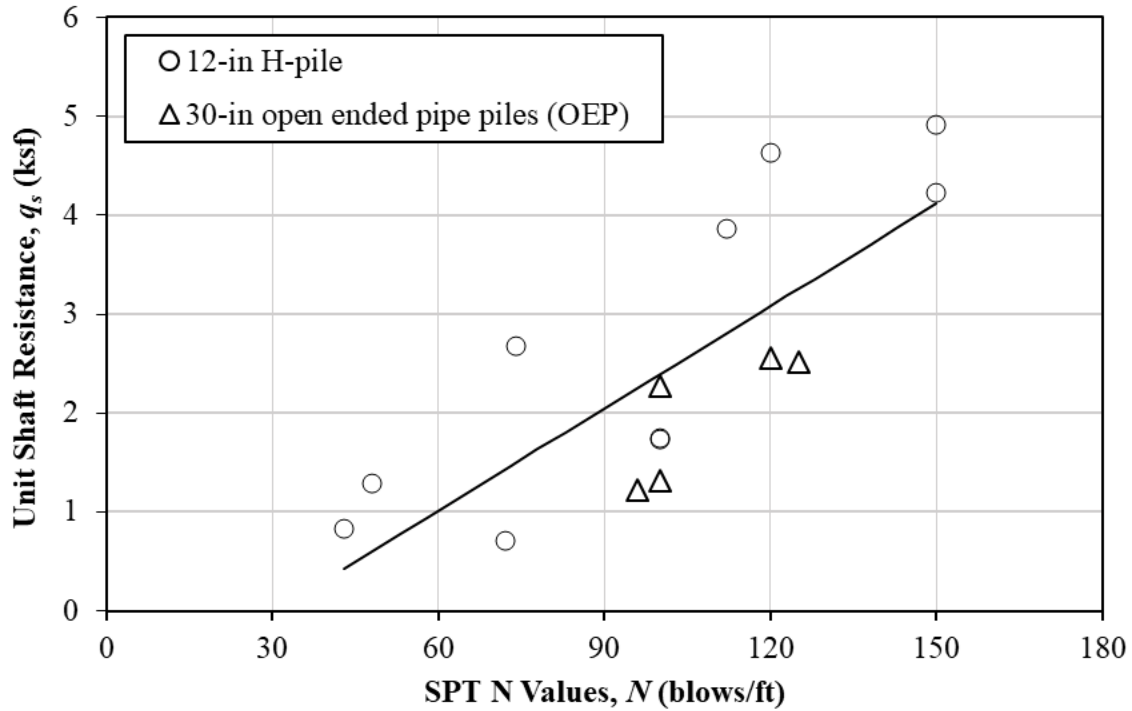


**Figure 6.16. Relationship Between Unit Shaft Resistances from CAPWAP and SPT N-Values of Granite.**

## 6.5 Validation of Proposed SA Methods

### 6.5.1 Unit Shaft Resistance

The validation of the proposed SA methods for  $q_s$  was conducted using 19 separate pile load data from Wyoming (ten steel H-piles), North Dakota (one 12-in steel H-piles), Idaho (one 14-in steel H-piles), Hongkong (two 12-in steel H-piles described in Yang 2006); Canada (three 14-in steel H-piles and one 20-in OEP in (Mortan 2012), and United of Arab Emirates (one 34-in OEP in Thomas et al. 2011). The relevant information of the pile load test data is summarized in Table 6.3. A total of 17 siltstone layers, 9 sandstone layers, 5 granite layers, and one claystone layer were identified along the 19 test piles. Figure 4.9 compares the  $q_s$  from the static and dynamic load tests with the predicted  $q_s$  for R-IGM. The table inserted in Figure 6.17 summarizes the sample size ( $n$ ), mean resistance bias ( $\bar{x}$ ), and COV of biases for different proposed SA methods and rock based IGM. The prediction of  $q_s$  in siltstone shown in Figure 6.1 yields a mean bias of 1.08 closer to 1 and a COV of 0.38. The mean bias was close to 1, which suggests the better prediction of  $q_s$  using the equation shown in Figure 6.2. Among the two proposed prediction equations for sandstone, statistical summaries were

determined for the prediction equation in Figure 6.13 considering nine applicable sandstone layers, while the prediction equation shown in Figure 6.14 can only be compared for two sandstone layers from the Cherry Creek Bridge project in North Dakota. With a mean bias of 0.99 and a COV of 0.33, the prediction equation shown in Figure 6.13 overestimates  $q_s$  on average by about 1 percent. For granite based on five steel H pile data points from Hongkong (Yang 2006), the mean bias of 1.14, which was close to 1, and COV of 0.39 indicate that the prediction equation shown in Figure 6.15, developed based on the test pile data in US can be also implemented to predict the  $q_s$  of piles driven in granite in Hong Kong.

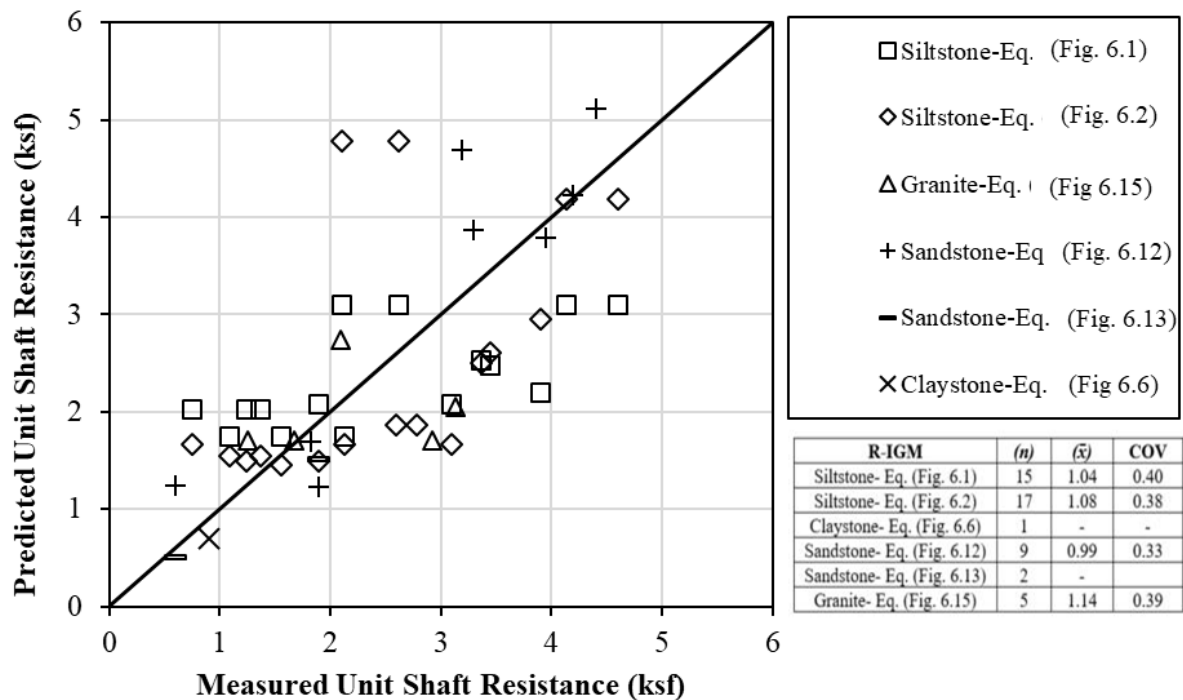


**Figure 6.17. Comparison of  $q_s$  from CAPWAP and Predicted  $q_s$  based on Separate Test Piles Driven into Siltstone, Sandstone, Claystone, and Granite.**

### 6.5.2 Unit End Bearing

The performance of the proposed prediction equation shown in Figure 6.3 and the prediction equation shown in Figure 6.7 of  $q_b$  was evaluated using separate test pile data in siltstone from the Lodgepole Creek bridge project and I-80 interchange bridge project in Wyoming and test pile data in claystone from the Cherry Creek bridge project in North Dakota (Table 6.3). The Lodgepole Creek project includes DLT on four HP 14×89 (P-1 to P-4) production piles and SLT on the HP 10×42 test pile (TP-5), while SLT was conducted on HP 12×53 test pile (TP-1) at the I-80 interchanges bridge project. For North Dakota, DLT was conducted on

HP 12×53 test pile at the Cherry creek bridge project. The data points close to the one-to-one line and inserted table in Figure 6.18 indicate that the proposed SA equations accurately predict the  $q_b$  of piles in siltstone with a mean of 1.01 and COV of 0.17. The proposed SA methods underpredicts the  $q_b$  by about 1 percent on average for siltstone based on these separate pile load test data.

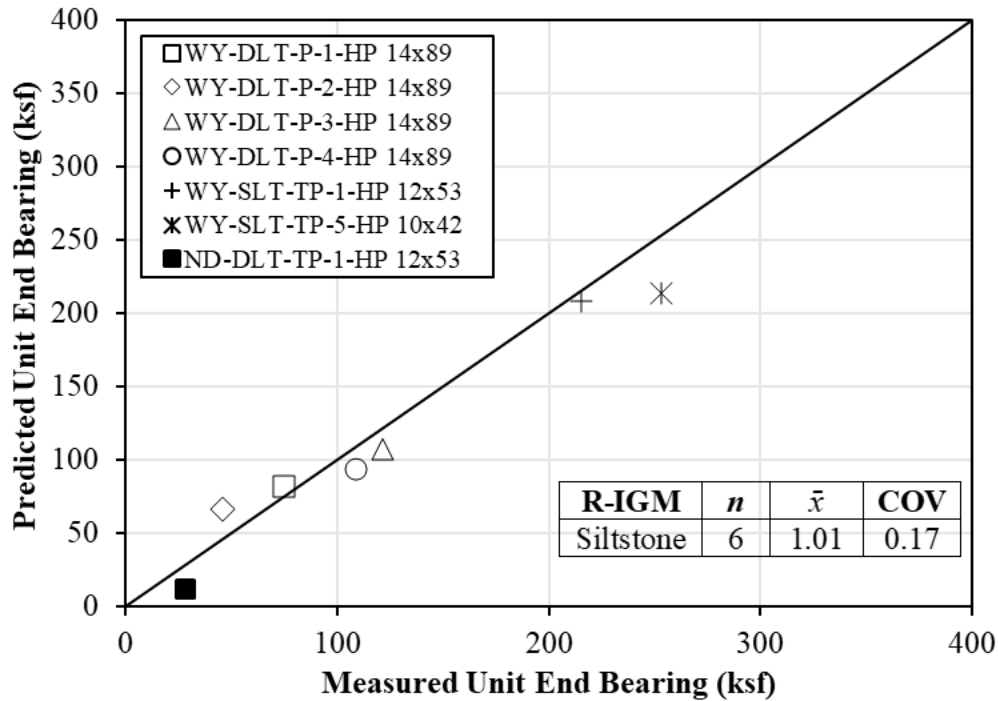


**Figure 6.18 Comparison of  $q_b$  from CAPWAP and Predicted  $q_b$  based on Separate Test Piles Driven into Siltstone and Claystone.**

## 6.6 Calibration of LRFD Resistance Factors

FOSM, FORM, and MCS were used to calibrate LRFD resistance factors ( $\phi$ ) of piles driven into R-IGM. The  $\phi$  values were calculated using target reliability indices ( $\beta_T$ ) of 2.33 for redundant piles and 3.00 for non-redundant piles (Paikowsky et al. 2004; AASHTO 2020). The resistance bias defined as a ratio of measured resistance to predicted response is determined for each prediction and R-IGM using the proposed SA equation (Masud et al. 2022). Next, statistical summaries in terms of mean and coefficient of variation (COV) of those resistance biases as well as a best-fit distribution were determined (Allen et al. 2005). The Shapiro-Wilk (SW) (1965) and Anderson-Darling (AD) (1952) tests were used to assess the normality of the population of biases. Because of its ability to detect non-normality, the SW test was preferred over other normality test methods (Mendes and Pala 2003). Both tests

evaluate the null hypothesis that a sample (resistance bias) was drawn from a normally distributed population. If the response of the sample originates from a log-normal distribution, then the logarithm of the response follows a normal distribution. The level of significance for both the SW and AD normality tests were set at 0.05. The null hypothesis was not rejected if the p-value exceeds the level of significance which indicates no evidence against the assertion of normality of the samples. The prediction equation shown in Figure 4.11 was used to derive mean biases ( $R$ ,  $D$ , and  $L$ ), load factors ( $D$  and  $L$ ), and COV values for  $R$ ,  $Q_D$ , and  $Q_L$  using the FOSM technique (Barker et al. 1991). The Rackwitz and Flessler (1978) technique was used to create the 192 stepwise FORM using the statistical computing tool R (R Core Team 2013). Similarly, MCS was carried out using the R programming language as explained by Adhikari (2019).

## 6.7 Resistance and Efficiency factor

The normality results of the proposed SA methods as summarized in Table 6.4 were determined using both the training pile dataset used in the development of new SA methods and the separate testing pile dataset used in the validation. The normality results with p-values greater than 0.05 and comparable log-likelihood values indicate that the resistance biases were better fit with a log-normal distribution. The resistance and efficiency factors of the proposed SA methods for the  $q_s$  and  $q_b$  predictions in different R-IGMs for target  $\beta_T$  values of 2.33 and 3.0 were calculated using both training and testing datasets and summarized in Table 6.5. Resistance and efficiency factors determined from FORM and MCS methods were higher than that from FOSM. The  $\phi$  values for the  $q_s$  prediction based on the MCS and  $\beta_T$  of 2.33 range from 0.43 for mudstone to 0.61 for siltstone. For sandstone, the prediction equation shown in Figure 6.13 yields higher efficiency factors compared to the prediction equation shown Figure 6.14 and was recommended for the prediction of  $q_s$  in sandstone. Similarly, the calibration yields  $\phi$  values of 0.43 and 0.42 for the prediction of  $q_b$  in claystone and siltstone, respectively. Compared with the calibrated  $\phi$  values for  $\beta_T=2.33$ , all  $\phi$  values for  $\beta_T=3.00$  are reduced on average by about 22 percent, which agrees with the 20 percent reduction recommended in AASHTO (2020).

## 6.8 Changes in Driven Pile Resistances

Pile resistances at the EOD and 24-hour BOR from CAPWAP for ten HP12 piles in Wyoming were compared to determine the change in pile resistances in claystone, sandstone,

and siltstone. Pile setup occurs when the pile resistance increases with time, whereas pile relaxation occurs when the pile resistance decreases with time. The short-term change (24 hours) in  $q_s$  and  $q_b$  corresponding to these three types of R-IGM were presented in Figure 6.19a and Figure 6.19b, respectively.

### ***6.8.1 Unit Shaft Resistance***

The inserted table in Figure 6.19a shows 5.9 to 87 percent increase in  $q_s$  or pile setup in claystone and 9.7 to 400 percent increase in  $q_s$  in siltstone. Since siltstone and claystone contain more than 50 percent silt and clay, respectively (Picard 1971), pile setup in both fine-grain claystone and siltstone was likely attributed to the dissipation of excess pore pressure, consolidation of claystone and siltstone, and increase in effective stress resulting from pile installation. A similar phenomenon was observed in fine-grained geomaterials (Long et al. 1999; Masud et al. 2022; Ng et al. 2013 a; b). For piles in sandstone, one pile shows a minimum pile relaxation of -1.4 percent, and the other three piles exhibit pile setup up to 59.7 percent. Generally, sandstone contains more than 50 percent percent of sand particles and behaves like coarse grained geomaterials (Picard 1971). Sandstone was denoted by Barrett and Prendergast (2020) as coarse-grained arenaceous rock. Axelsson (2002) stated that pile setup in coarse grained geomaterials was attributed to two strongly interconnected mechanisms creep (stress relaxation) and aging (increasing dilation and stiffness). Since short-term time effects were considered in this study, it is believed that pile setup in sandstone is attributed to the rapid dissipation of pore pressure in sandstone.

**Table 6.3. Summary of 19 Independent Test Piles Driven into Rock-Based IGM.**

Source	Country	Geomaterial	PL or PI Pile type	N	(N1)60 (blows/ft)	$\sigma'_v$ (ksf)	qu (ksf)	qs (ksf)	qb (ksf)
Thomas et al. (2011)	UAE	Sandstone	34-in OEP	NA	NA	NA	18.8	1.82	NA
Morton (2012)	Halifax, Canada	Sandstone	HP 14×102	NA	NA	NA	177.53-375.94#	3.3-4.4*	NA
Morton (2012)	Halifax, Canada	Sandstone	20-in OEP	NA	NA	NA	298.66	3.19-6.41*	NA
Morton (2012)	Halifax, Canada	Sandstone	HP 14×102	NA	NA	NA	167.08	3.95	NA
Morton (2012)	Halifax, Canada	Sandstone	HP 12×53	NA	NA	NA	225.56	4.19	NA
Lodgepole Creek Bridge	Wyoming, USA	Siltstone	P-5 at A-2 (HP 10×42)	110-150'	82-107'	NA	36.8-50.6#	3.36-3.9*	253.42
Lodgepole Creek Bridge	Wyoming, USA	Siltstone	P-4 at A-2 (HP 14×89)	48	34-38'	NA	22-30.6#	1.09-1.55*	74.48
Lodgepole Creek Bridge	Wyoming, USA	Siltstone	P-3 at A-2 (HP 14×89)	48-60'	36-43'	NA	30.6-32.4#	1.37-3.1*	46.10
Lodgepole Creek Bridge	Wyoming, USA	Siltstone	P-1 at A-2 (HP 14×89)	60	43	NA	30.6#	0.75	121.3
Lodgepole Creek Bridge	Wyoming, USA	Siltstone	P-2 at A-2 (HP 14×89)	60	43	NA	22#	2.13	108.5
I-80 Interchange bridge	Wyoming, USA	Siltstone	P at A-1 (HP 14×89)	125	NA	NA	NA	NA	215.1
Laramie Streets Adhikari (2020)	Wyoming, USA	Siltstone	122N (HP 12×53)	266	230	NA	80.6	2.62	NA
Laramie Streets Adhikari (2020)	Wyoming, USA	Siltstone	119O (HP 12×53)	266	230	NA	80.6	2.11	NA
Laramie Streets Adhikari (2020)	Wyoming, USA	Siltstone	9S (HP 12×53)	171	186	NA	80.6	4.6	NA
Laramie Streets Adhikari (2020)	Wyoming, USA	Siltstone	11S (HP 12×53)	171	187	NA	80.6	4.14	NA

Yang (2006)	Hongkong	Granite	PD2 HP 12×154	80-90'	NA	NA	NA	1.67-3.13*	NA
Yang (2006)	Hongkong	Granite	PD8 HP 12×154	80-100'	NA	NA	NA	1.25-2.08*	NA
Cherry Creek Bridge	North Dakota	Sandstone	HP 12×53	19-35'	18-29'	3.6-4.5"	7.98-8.11#	0.6-1.9*	NA
Cherry Creek Bridge	North Dakota	Claystone	HP 12×53	35	30	4.6	0.84	0.9	28.4
US-95 Pine Creek bridge	Idaho	Siltstone	P-1 at A-1; HP 14×117	53	52	NA	NA	2.6-2.78	NA

St.=State; A=Abutment; PL=Pile Location; PI=Pile Information; Pi=Pile; P=Pier; B=Bent; PD=Driven Pile; TP=Test pile;  $q_u$ =Unconfined compressive strength;  $q_s$ =Unit shaft resistance; " =Range of  $\sigma'_v$  for multiple R-IGM layers; # =Range of  $q_u$  for multiple R-IGM layers; \* =Range of  $q_s$  for multiple R-IGM layers; ' =Range of  $N/(N_1)_{60}$  for multiple R-IGM layers;  $q_b$ =Unit end bearing; NA=Not applicable.



**Table 6.4. Summary of Normality Results of the Resistance Biases Associated with Proposed Static Analysis Methods for Prediction of Unit Shaft Resistance and Unit End Bearing in Rock Based IGM.**

Geomaterial	Prediction Equation	Sample size ( <i>n</i> )	Mean Bias ( $\bar{x}$ )	COV of Bias	Normal		Log-Normal		Log-likelihood	
					SW	AD	SW	AD		
					P-value				Normal	Log-Normal
Unit shaft resistance ( <i>q<sub>s</sub></i> )										
Siltstone	$\hat{q}_s = 0.45q_u^{0.44}$ ; Eq. (4.1)	29	1.02	0.31	0.88	0.66	0.32	0.45	-7.5	-8.35
	$\hat{q}_s = 0.42P_a \left[ \frac{(N_1)_{60}}{16} \right]^{0.63}$ ; Eq. (4.2)	50	1.05	0.32	0.72	0.88	0.17	0.19	-16.71	-17.80
Claystone	$\hat{q}_s = 0.74q_u^{0.305}$ ; Eq. (4.4)	12	1.09	0.45	0.32	0.32	0.49	0.38	-8.16	-7.82
Mudstone	$\hat{q}_s = 6.19 \left( 1 - e^{(-0.052 \frac{N}{19} + \sigma_v')} \right)$ ; Eq. (4.6)	24	0.97	0.44	0.67	0.82	0.34	0.35	-13.03	-13.59
Sandstone	$\hat{q}_s = 0.56q_u^{0.37}$ ; Eq. (4.7)	17	1.03	0.45	0.09	0.15	0.55	0.24	-11.43	-10.18
	$\hat{q}_s = 1.25 \left( \frac{q_u \times (N_1)_{60}}{579} \right)^{0.23}$ ; Eq. (4.8)	10	1.08	0.47	0.55	0.54	0.76	0.83	-6.92	-6.66
Granite	$\hat{q}_s = \left[ 0.7 \frac{N}{43} - 0.5 \right] P_a$ ; Eq (4.9)	20	1.11	0.45	0.06	0.06	0.34	0.37	-14.27	-12.2
Unit end bearing ( <i>q<sub>b</sub></i> )										
Claystone	$\hat{q}_b = \frac{313.27q_u}{20.96 + q_u}$ ; Eq. (4.5)	9	0.99	0.44	0.04	0.07	0.28	0.33	-4.80	-3.06
Siltstone	$\hat{q}_b = 12.9P_a \left[ 2.43 \left( \frac{32.4 N}{30 D_B} \right) \right]$ ; Eq. (4.3)	20	1.00	0.46	0.82	0.81	0.23	0.21	-12.51	-13.53

SW=Shapiro-Wilk normality test; AD=Anderson-Darling normality test; COV=Coefficient of variation  $\bar{x}$ =Mean of ratio of CAPWAP measured resistance to predicted resistance.

**Table 6.5. LRFD Resistance Factors and Efficiency Factors of the Proposed Static Analysis Methods for the Prediction of Unit Shaft Resistance and Unit End Bearing in Rock Based IGM.**

R-IGM	Prediction Equation	FOSM				FORM				MCS			
		$\beta_T=2.33$		$\beta_T=3.00$		$\beta_T=2.33$		$\beta_T=3.00$		$\beta_T=2.33$		$\beta_T=3.00$	
		$\varphi$	$\varphi/\bar{x}$	$\varphi$	$\varphi/\bar{x}$	$\varphi$	$\varphi/\bar{x}$	$\varphi$	$\varphi/\bar{x}$	$\varphi$	$\varphi/\bar{x}$	$\varphi$	$\varphi/\bar{x}$
Unit shaft resistance ( $q_s$ )													
Siltstone	$\hat{q}_s = 0.45q_u^{0.44}$ ; Eq. (4.1)	0.55	0.53	0.42	0.41	0.62	0.61	0.49	0.48	0.61	0.60	0.48	0.47
	$\hat{q}_s = 0.42P_\alpha \left[ \frac{(N_1)_{60}}{16} \right]^{0.63}$ ; Eq. (4.2)	0.55	0.52	0.42	0.39	0.61	0.58	0.48	0.46	0.61	0.58	0.48	0.46
Claystone	$\hat{q}_s = 0.74q_u^{0.305}$ ; Eq. (4.4)	0.43	0.39	0.31	0.28	0.47	0.43	0.34	0.31	0.47	0.43	0.34	0.31
Mudstone	$\hat{q}_s = 6.19 \left( 1 - e^{(-0.052 \frac{N}{19} + \sigma_v')} \right)$ ; Eq. (4.6)	0.39	0.40	0.29	0.30	0.43	0.44	0.32	0.33	0.43	0.44	0.31	0.32
Sandstone	$\hat{q}_s = 0.56q_u^{0.37}$ ; Eq. (4.7)	0.41	0.40	0.29	0.28	0.44	0.43	0.31	0.30	0.44	0.43	0.31	0.30
	$\hat{q}_s = 1.25 \left( \frac{q_u \times (N_1)_{60}}{579} \right)^{0.23}$ ; Eq. (4.8)	0.41	0.38	0.29	0.27	0.44	0.41	0.31	0.29	0.44	0.41	0.31	0.29
Granite	$\hat{q}_s = \left[ 0.7 \frac{N}{43} - 0.5 \right] P_\alpha$ ; Eq (4.9)	0.44	0.39	0.32	0.29	0.48	0.43	0.43	0.30	0.48	0.43	0.34	0.30
Unit end bearing ( $q_b$ )													
Claystone	$\hat{q}_b = \frac{313.27q_u}{20.96+q_u}$ ; Eq. (4.5)	0.40	0.40	0.29	0.29	0.44	0.44	0.33	0.33	0.43	0.43	0.31	0.31
Siltstone	$\hat{q}_b = 12.9P_\alpha \left[ 2.43 \left( \frac{32.4 N}{30 D_B} \right) \right]$ ; Eq. (4.3)	0.39	0.39	0.28	0.28	0.42	0.42	0.31	0.31	0.42	0.42	0.31	0.31

$\varphi$ =Resistance factor;  $\varphi/\bar{x}$ =Efficiency factor;  $\beta_T$ =Target reliability index; FOSM=First order second moment; FORM=First order reliability method; MCS=Monte Carlo simulation.

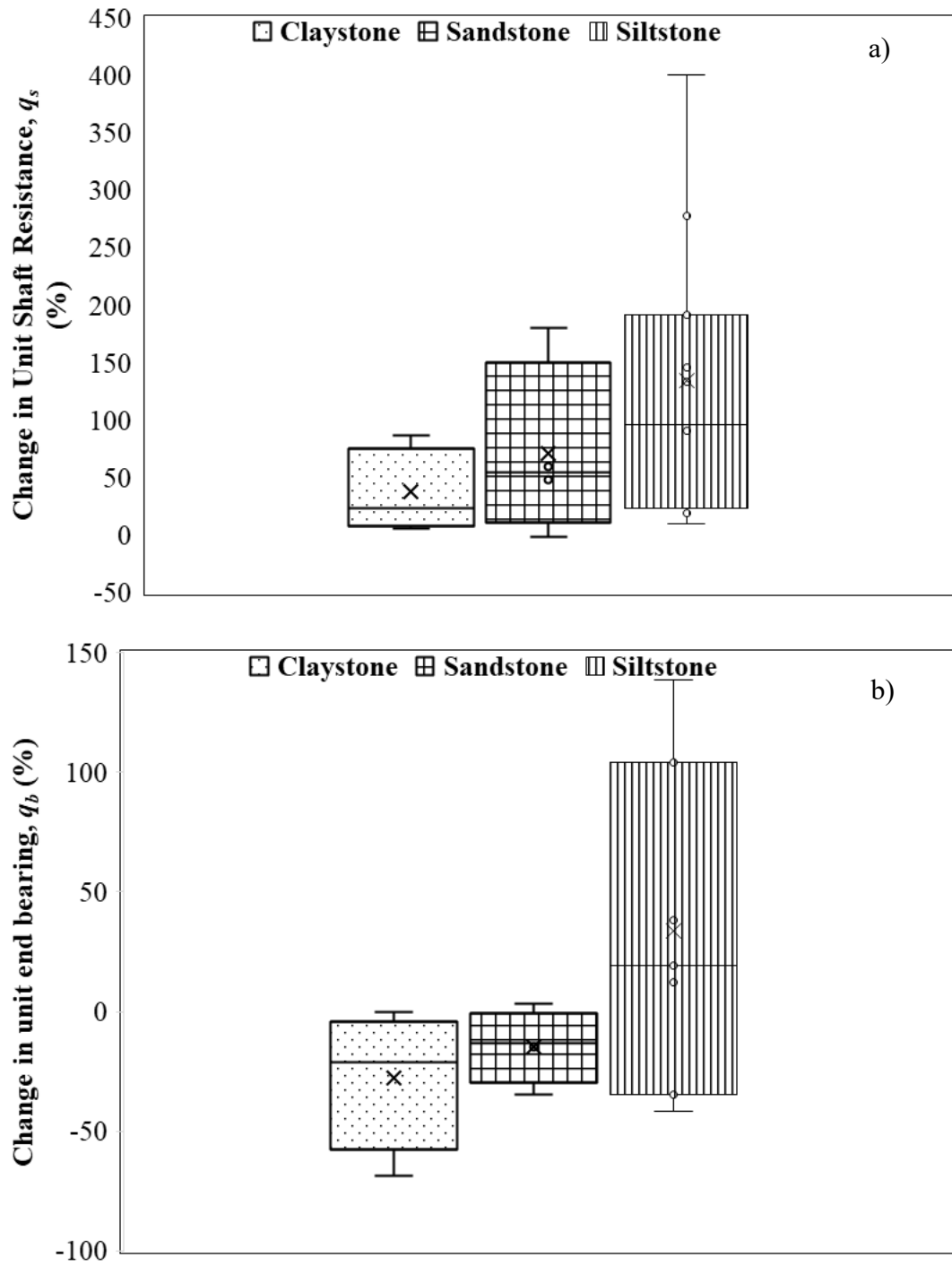


**Figure 6.19. Change in a) unit shaft resistance, and b) unit end bearing observed in different geomaterials 24 hours after the EOD.**

### 6.8.2 Unit End Bearing

Figure 6.19b and the inserted table show that pile relaxation occurs in sandstone with the change in  $q_b$  varying from -34.8 to 3.1 percent. Pile relaxation in end bearing is more likely to occur than in shaft resistance due to the generation of negative pore pressure in a dilatant sandstone (Sawant et al. 2013). This phenomenon is like the pile relaxation observed in dense to very dense fine sands (Long et al. 1999; Yang 1956; Yang, 1970). Figure 6.19b shows that all four test piles in claystone experience pile relaxation with the percent decrease in  $q_b$  varying from -0.13 percent to -68.6 percent. Among seven test piles driven into siltstone, five test piles experience pile setup with the percent increase in  $q_b$  varying from 12.2 percent to 138.6 percent while two H-piles experience a decrease in  $q_b$  with the percent change in  $q_b$  varying from -34.5 percent to -41.5 percent. The hard driving on siltstone and claystone, as well as the development of negative excess pore water pressure due to fracturing of both claystone and siltstone during driving were thought to be the causes of pile relaxation.

### 6.9 Summary and Conclusions

This chapter provides improvements on the design of driven steel H and pipe piles in R-IGM through the development of new SA methods for five different types of R-IGM or weak rock, newly calibrated LRFD resistance factors, and better understanding of time-dependent pile resistances in R-IGM. This study results in the following conclusions and recommendations.

- New SA methods for the prediction of  $q_s$  in R-IGM or weak rock were developed for five different rock types (siltstone, claystone, mudstone, sandstone, and granite). New SA methods were developed for the prediction of  $q_b$  in siltstone and claystone, respectively. The purpose of different SA methods for their respective rock types was to reduce uncertainties associated with R-IGM and to improve the accuracy of  $q_s$  and  $q_b$  predictions.
- The best model was chosen among the candidate models based on the lowest AICc, BIC, and RSE values. The power model and modified power model (Eq. 4.3) were selected for the prediction of  $q_s$  and  $q_b$  for piles driven into siltstone. The power model and saturation growth rate model were selected for the prediction of  $q_s$  and  $q_b$  for piles driven into claystone. The exponential association model, power model, and linear model were

selected for the prediction of  $q_s$  for piles driven into mudstone, sandstone, and granite, respectively.

- The comparisons of  $q_s$  and  $q_u$  for siltstone and claystone show that  $q_s$  increases with the increase in  $q_u$ . This increasing trend suggests that higher  $q_u$  results in higher  $q_s$ . The positive relationship of  $q_s$  and  $(N_1)_{60}$  for siltstone was observed because siltstone with a higher SPT blow count indicates a higher shear strength and exhibits a higher resistance to pile penetration. In addition, a positive linear relationship was observed between  $q_s$  and SPT N-value for granite, and an increasing trend was observed between  $q_s$  and the product of  $q_u$  and  $(N_1)_{60}$  for sandstone.
- The validation of the proposed SA methods using separate pile data obtained from the literature, WYDOT, and NDDOT confirms the performance of the proposed SA methods in the prediction of  $q_s$  and  $q_b$ . The performance of proposed SA methods for the  $q_s$  prediction in terms of  $q_u$  only for piles in siltstone, sandstone, and claystone was compared against existing SA methods from the literature. The mean biases closer to unity, smaller COV values of resistance biases, and higher efficiency factors confirm more accurate and consistent prediction of  $q_s$  and  $q_b$  by the proposed SA methods. However, it was important to note that the proposed SA methods and the calibrated LRFD resistance factors were developed based mostly on dynamic pile load test results and two static pile load tests. These recommendations should be cautiously implemented and further validated when more SLT load test results on weak rocks become available in the future.
- Short-term pile setup can be considered in the prediction of  $q_s$  for piles in claystone and siltstone. The ranges of pile setup in  $q_s$  at 1 day after the EOD for claystone and siltstone were 5.9 percent to 87 percent and 9.7 percent to 400 percent, respectively. It was believed the dissipation of excess pore pressure induced by pile installation in fine-grained R-IGM resulting in pile setup. The pile installation causes the consolidation of weak rocks along with the pile, thus increasing the effective stress with time. Pile relaxation in end bearing was more likely to occur in R-IGM due to the negative pore pressure near pile toe.

## CHAPTER 7: DRIVEN PILES IN ROCK-BASED SHALES

### 7.1 Introduction

Among soft rocks, shale has been considered a problematic material due to its degradation of shear strength and shrink-swell potential (Yagiz 2001). Shale is a fine-grained, clastic sedimentary rock formed by the deposition and compaction of silt and clay-size mineral particles over time. Shale is considered a transitional material due to having wide range of strength properties. The lacking pile load test data has delayed understanding of driven piles in shales, particularly with respect to pile resistance. Currently, there are no specific guidelines and design methods in existing foundation design manuals to predict unit shaft resistance ( $q_s$ ) and unit end bearing ( $q_b$ ) of piles driven in shale. Instead, the existing empirical static analysis (SA) methods developed for soils were being used to design the driven piles in shale.

Several empirical design methodologies have been described in the literature that focused on steel H-piles on soft rock types other than shale described in Chapter 6. The challenge with pile design and construction in shale is further exacerbated by the change in pile resistance with time, particularly the decrease in pile resistance known as pile relaxation reported in literature (Hannigan et al. 2020; Morgano and White 2004; Thompson and Thompson 1985). From a study of H-piles in shale from four project sites, Likins and Hussein (1984) reported pile relaxation of 10 to 50 percent on weathered shale within two weeks after pile driving. Thompson and Thompson (1985) suggested a range of 11 to 25 percent decrease in pile capacity determined from the dynamic measurement of close-ended pipe (CEP) piles in shale. An average 35 percent relaxation on end bearing was reported on piles driven into shales, and OEP piles experienced a greater average relaxation of 44 percent compared to 34 percent for H-piles (Hannigan et al. 2020). On the other hand, based on the 17 H-piles tested in shale, Long and Anderson (2014) found almost constant total pile capacity with time with a maximum total setup and relaxation of 19 percent and 14 percent, respectively. The limited past studies indicate different setup and relaxation in shale materials. Hence, the time-dependent pile responses due to shale weathering deserves further investigation. It is believed that pile relaxation in shale is caused by 1) the development of negative pore water pressure resulting from shale fracture and dilation, 2) change

in rock mineralogy and fractures resulting from pile driving, 3) relaxation of stresses in the rock around the pile, 4) shale shattering beneath a pile toe caused by driving adjacent piles to a deeper depth, and 5) shale softening from water migration to the pile toe resulted from negative pore pressure development (Hannigan et al. 2020).

Due to the limited research on driven piles in shale and the absence of reliable design methods, the performance of piles in shale is currently determined based on driving observation, local experience, and load demand through construction control approaches. Considering these shortcomings and challenges, this paper presents a shale classification system, relationships for predicting engineering properties of shale, new SA methods for predicting  $q_s$  and  $q_b$  for four different shale types and weathering conditions, Load and Resistance Factor Design (LRFD) recommendations for the proposed SA methods, and time-dependent pile responses in different shales.

## 7.2 Usable Pile Data

Seventy-one historical pile load test data from eight counties in Kansas were collected from the Kansas Department of Transportation (KDOT). These test pile data contained all relevant information, including PDA with the CAPWAP analysis from 16 bridges in 9 projects constructed between 2010 to 2017. Among the 71 test piles, 49 test piles with complete information were considered usable in this study. The relevant information of 49 usable test piles with 40 steel H-piles and nine 12.75 in steel shell driven piles were summarized in Table 7.1. The overburden soil layers included sand, clay, silt, and mixed soil, while the bearing layers were shale. These shale layers were categorized as soil-based shales and rock-based shales. The pile embedment lengths ranged from 22 to 105 ft, and the penetration lengths in shale varied from 33 to 30.1 ft. The  $q_s$  and  $q_b$  summarized in Table 7.1 were determined from CAPWAP at the end of driving (EOD). These piles were driven using diesel hammers with blow counts (bl) varying from 17 to 640 bl/ft.

Comparing pile resistances in IGMs determined from 19 SLTs and PDA/CAPWAP (Mokwa and Brooks 2008; Long 2016), a mean resistance bias ( $\lambda$ )=1.08 closer to unity and a relatively low coefficient of variation (COV) of resistance bias=0.121 suggested reliability in the CAPWAP

results (Adhikari et al. 2020b). Furthermore, past research studies have concluded that pile resistances predicted from CAPWAP were comparable to the measured resistances from SLT (Likins and Rausche 2004). Due to the current design and construction practices as well as high cost, SLT is rarely conducted on driven piles in shale. Hence, to advance the current knowledge and to improve pile resistance predictions, it is reasonable to use CAPWAP results in this study. However, it is recommended to use available SLT results in future studies.

### **7.3 Shale Classification and Properties**

#### ***7.3.1 Shale Classification***

A shale classification system based on texture, strength, grain size, plasticity, chemical or mineralogical characteristics, and bonding has been proposed by several investigators (Coduto 1999; Eid 2006; Underwood 1967). In addition, a shale classification system has been established based on Atterberg limits, slake durability, and the jar slake test (Deo 1972; Erguler and Shakoor 2009; Gamble 1971; Hopkins and Deen 1984). These shale classification systems were developed over time for different applications. Considerable discrepancies in the shale categorization and properties suggested the need for a more comprehensive classification system. The classification system by Underwood (1967) has been widely used to distinguish problematic shales from stronger shales for engineering design purposes (Yagiz 2001). This study adopted recommendations from Underwood (1967) and classified the shales into two broad types: ‘soil-like or soil-based shale’ and ‘rock-based shale’ from the field identification system. The soil-based shales were defined as compacted shales that contained soil particles without having intergranular cement such as calcareous, siliceous, and carbonaceous. The rock-based shales were defined as cemented or bonded shale having intergranular cement (Underwood 1967). Generally, soil-based shales are easily separated while rock-based shales are harder and more durable and cannot be easily separated into smaller pieces.

Depending on the presence of clay, silt, and sand-sized particles, KDOT classified soil-based shales into three subgroups: clayey shale, silty shale, and sandy shale. The proposed classification system was to first distinguish the soil-based shales from the rock-based shales using the field identification system. Furthermore, the ‘soil-based’ (SS) shale included clayey



shale and silty shale, with hardness defined as soft, moderately hard, and hard. The swell potential was used to distinguish clayey from silty shale as clayey shale swells in a barrel or core box. Five degrees of weathering (fresh, slightly weathered, moderately weathered, weathered, and highly weathered) were used by KDOT to describe the rock-based shale weathering. The fresh rock-based shale does not contain decomposition of the parent material and microcracks, and the slightly weathered rock-based shale showed a slight decomposition of parent material in joints with hair line cracks. On the other hand, moderately and weathered rock-based shale contained well-developed and decomposed joints with visible microcracks. The highly weathered rock-based shale was highly decomposed and extremely broken. Using those descriptions, the rock-based shale was classified into three different subgroups: soft & highly weathered shale (HW), moderately hard & moderately weathered to weathered shale (MW), and hard fresh & slightly weathered shale (SW) as indicated in Table 7.1.

**Table 7.1. Summary of Usable Driven Piles in Shales from Kansas.**

Pile ID	County of Kansas	Pile	LEMB (ft)	LIGM (ft)	Overburden Geomaterial	End bearing shale layer at pile toe	Shale	qua (ksf)	RQDa ( percent )	qsa (ksf)	qb (ksf)	Pile Hammer	BC
1	Clark	HP 14×73	94	19.26	sand	clayey, maroon shale	SS	9.6	73	1.4	59.9	Del. D19-42	87
2	Finney	HP 12×63	50	6.5	mixed	dark gray, calcareous, slightly w. shale	SW	124.1	100	3.8	302.0	Del. D19-42	120
3	Finney	HP 10×42	58	6.1	mixed	dark gray, calcareous, slightly w. shale	SW	124.1	100	2.9	326.4	Del. D19-42	59
4	Finney	HP 12×63	50	4.4	mixed	gray, calcareous, slightly w. shale	SW	125.9	84	2.8	332.1	Del. D19-42	160
5	Sedgwick	HP 12×63	81	12.1	sand	gray, calcareous, hard slightly w. shale	SW	39.3	76	3.4	305.1	Pil. D30-32	87
6	Sedgwick	HP 10×42	80	6.3	mixed	dark gray, clayey shale	SS	4.6	92	1.1	71.0	Del. D19-32	28
7	Sedgwick	HP 12×53	73	9.8	sand	shades of gray, silty shale	SS	4.8	91	1.0	96.3	Del. D30-02	18
8	Sedgwick	HP 12×74	68	8.5	sand	green, gray, highly w. shale	HW	5.8	88	0.6	157.7	Del. D30-02	27
9	Sedgwick	HP 12×74	69	10.2	sand	dark gray to gray, clayey shale	SS	5.8	88	NA	102.1	Del. D30-02	20
10	Sedgwick	HP 12×53	87	20.8	mixed	gray to dark gray, silty shale	SS	10.2	75	2.3	134.9	Pil. D30-32	40
11	Sedgwick	HP 10×42	80	4.96	clayey sand	Moderately hard, silty shale	SS	8.1	86	1.5	138.7	Del. D16-32	53
12	Sedgwick	HP 12×84	33	11.1	sand	hard, silty, gray shale	SS	24.9	57	2.2	162.5	Pil. D30-32	25
13	Sedgwick	HP 12×63	68	6.4	mixed	dark gray, banded, w. shale	MW	5.0	86	1.3	175.6	Del. D30-02	36
14	Sedgwick	HP 10×42	105	18.2	sand	dark gray to gray, w. shale	MW	11.1	85	1.6	190.7	Del. D19-32	60
15	Sedgwick	HP 12×53	73	3.4	clayey sand	dark gray, w. shale	MW	6.9	86	1.8	200.7	Del. D30-02	30
16	Sedgwick	HP 10×42	105	10.2	mixed	gray, calcareous shale, slightly w.	SW	17.1	87	2.5	197.8	Del. D19-32	192
17	Sedgwick	HP 12×63	68	16.2	sand	gray, generally w. shale	MW	4.2	92	1.4	226.2	Del. D30-02	24

18	Sedgwick	HP 10×42	84	11	sand	gray to dark gray, w. shale	MW	17.1	87	1.2	292.0	Del. D19-32	51
19	Sedgwick	HP 12×74	70	11.8	sand	dark gray to gray, w. shale	MW	21.9	86	1.3	384.5	Del. D30-02	80
20	Sedgwick	HP 12×74	47	26.8	sand	gray, hard, slightly w. shale	SW	33.2	80	3.3	35.1	Pil. D30-32	34
21	Sedgwick	HP 12×63	59	12.03	sand	gray, soft, highly w. shale	HW	7.7	85	0.8	50.8	Pil. D30-32	17
22	Sedgwick	HP 12×63	58	16.5	mixed	dark gray, silty shale	SS	4.4	22	0.9	129.9	Pil. D30-32	25
23	Sedgwick	HP 12×74	46	18.9	sand	gray, soft, highly w. shale	HW	6.3	66	0.8	135.5	Pil. D30-32	27
24	Sedgwick	HP 12×74	45	16.7	sand	gray, soft, highly w. shale	HW	8.1	90	2.0	87.3	Pil. D30-32	23
25	Sedgwick	HP 12×74	53	8.66	mixed	gray, soft, highly w. to w. shale	HW	8.6	35	0.9	99.8	Pil. D30-32	27
26	Sedgwick	HP 12×74	61	19.76	sand	gray, soft, highly w. shale	HW	4.6	68	1.5	39.7	Pil. D30-32	26
27	Sedgwick	HP 12×63	47	15.8	sand	clayey shale, firm	SS	8.1	84	2.4	84.8	Pil. D19-42	28
28	Sedgwick	HP 12×74	50	16.6	mixed	gray, moderately hard, w. shale	MW	3.8	50	1.7	48.2	Pil. D19-42	32
29	Sedgwick	HP 12×74	35	14.9	sand	gray, soft, highly w. shale	HW	20.7	87	2.0	143.7	Pil. D30-32	52
30	Sedgwick	HP 12×63	50	11.5	mixed	gray, moderately hard, w., thin bedded shale	MW	4.0	89	2.1	163.1	Pil. D30-32	34
31	Sedgwick	HP 12×63	52	25.9	mixed	gray, hard, slightly w., gypsum shale	SW	8.8	95	1.5	195.9	Pil. D30-32	26
32	Sedgwick	HP 12×74	61	20.5	mixed	gray, moderately hard, highly w. shale	MW	7.5	NA	2.4	262.5	Pil. D30-32	34
33	Sedgwick	HP 12×74	61	19	sand	gray, hard, slightly w. shale	SW	2.9	82	1.6	262.5	Pil. D30-32	34
34	Sedgwick	HP 12×74	54	20.7	mixed	gray, soft, highly w. shale	HW	5.0	79	1.0	158.7	Pil. D30-32	28
35	Clay	HP 12×74	29.9	30.1	mixed	clayey, gray, stiff to moderately hard shale	SS	51.6	83	2.6	182.7	Del. D19-42	62
36	Sheridan	12.75"D shell	41	6.9	sand	very dark gray, w. shale	MW	5.2	65	1.4	171.7	Del. D16-32	60
37	Sheridan	12.75"D shell	24	3.4	sand	very dark gray, w. shale	MW	13.6	79	NA	206.6	Del. D16-32	28
38	Sheridan	12.75"D shell	24	3.5	sand	very dark gray, w. shale	MW	5.2	83	1.3	282.2	Del. D16-32	40
39	Sheridan	12.75"D shell	24	6.9	sand	very dark gray, w. shale	MW	22.6	89	2.1	326.9	Del. D16-32	60
40	Sheridan	12.75"D shell	22	4	sand	very dark gray, w. shale	MW	5.2	88	1.5	334.8	Del. D16-32	60
41	Sheridan	12.75"D shell	23	3.3	sand	very dark gray, w. shale	MW	10.0	80	1.4	260.6	Del. D16-32	40

42	Sheridan	12.75"D shell	55	14.5	sand	very dark gray, w. shale	MW	7.1	94	1.6	221.4	Del. D16-32	90
43	Sheridan	12.75"D shell	36	29.4	sand	very dark gray, w. shale	MW	2.5	80	1.1	218.7	Del. D16-32	34
44	Sheridan	12.75"D shell	38	6.7	sand	very dark gray, w. shale	MW	10.0	80	1.4	221.4	Del. D16-32	41
45	Barton	HP 12×63	72	25.24	silty clay	clayey, gray with maroon mottling shale	SS	12.3	96	1.4	87.3	Del. D19-42	102
46	Barton	HP 10×42	82	17.3	mixed	clayey, greenish-gray, maroon shale	SS	9.2	36	1.5	98.0	Del. D19-42	46
47	Franklin	HP 12×53	26	5.45	silty clay	firm, non-weathered shale	SW	30.3	72	2.9	293.6	Del. D19-42	48
48	Geary	HP 12×63	47	21.8	silty clay	gray to blue gray, very hard shale	SW	41.6	69	2.3	236.2	Del. 16-32	640
49	Geary	HP 12×63	60	16.37	silty clay	tan to light gray, vuggy, hard shale	SW	55.3	67	2.7	283.2	Del. 16-32	128

$q_u$ —Unconfined compressive strength;  $q_s$ —Unit skin friction at EOD from CAPWAP;  $q_b$ —Unit end bearing at EOD from CAPWAP; RQD—Rock quality designation;  $L_{EMB}$ —Embedded pile length;  $L_{IGM}$ —Embedded pile length in IGM; soil based shale (SS); bl—Pile hammer blow; w.—Weathered; Del.—Delmag; Pil.—Pileco; HW—Soft & highly weathered shale; MW—Moderately hard & weathered shale; SW—Hard & slightly weathered shale; <sup>a</sup>—Average value of all shale layers; and BC—Hammer blow count at EOD per ft of penetration.

**Table 7.2. Range, Mean, and Standard Deviation of Mechanical Properties of Shales.**

Shale type	Qualitative description	N	$q_u$ (ksf)	E (ksf)	$\gamma$ (lb/ft <sup>3</sup> )	$\omega$ (percent)	RQD (percent)	Recovery (percent)	$q_s$ (ksf)
Soil-Based Shale (SS)	Clayey shale, silty shale, soft to hard	80	2.1-60 12.7±12.1	77.2-7660.8 877±1368	88.5-140.7 110.8±10.2	7.6-27.9 18.8±5.2	8-100 77±22	27-100 96±12	0.75-2.76 1.65 ± 0.65 <sup>a</sup>
Highly Weathered Shale (HW)	Soft, highly weathered	42	2.1-3.47 9.2±7.7	48-3968 490.8±620	93.6-131.8 103.1±8.3	12.7-35.3 24.7±4.4	10-92 70±21	33-100 91±17	0.19-1.1 0.58 ± 0.27 <sup>b</sup>
Moderately Hard & Weathered Shale (MW)	Moderately hard, weathered, and moderately weathered	43	2.1-155 24.6±37	52.2-11487 1754.4±2822	78.9-138.1 110.1±13.4	7.6-27.9 18.8±5.2	30-100 81±17	58-100 96±8	1.1-2.4 1.61 ± 0.33 <sup>c</sup>
Hard & Slightly Weathered Shale (SW)	Hard, slightly weathered, and fresh	56	3.13-247 73.5±66	85.6-30699 5998±7107	96.8-143 122.9±12.1	7.2-21 14.5±3.3	45-100 86±18	55-100 95±11	2.4-3.78 2.97 ± 0.4 <sup>d</sup>

N–Sample size;  $q_u$ –Unconfined compressive strength; E–Modulus of elasticity;  $\gamma$ –Dry unit weight;  $\omega$  –Water content; RQD–Rock Quality Designation;  $q_s$ –Unit skin friction; <sup>a</sup>–Sample size 25; <sup>b</sup>–Sample size 16; <sup>c</sup>–Sample size 27 and <sup>d</sup>–Sample size 28

### 7.3.2 Shale Properties

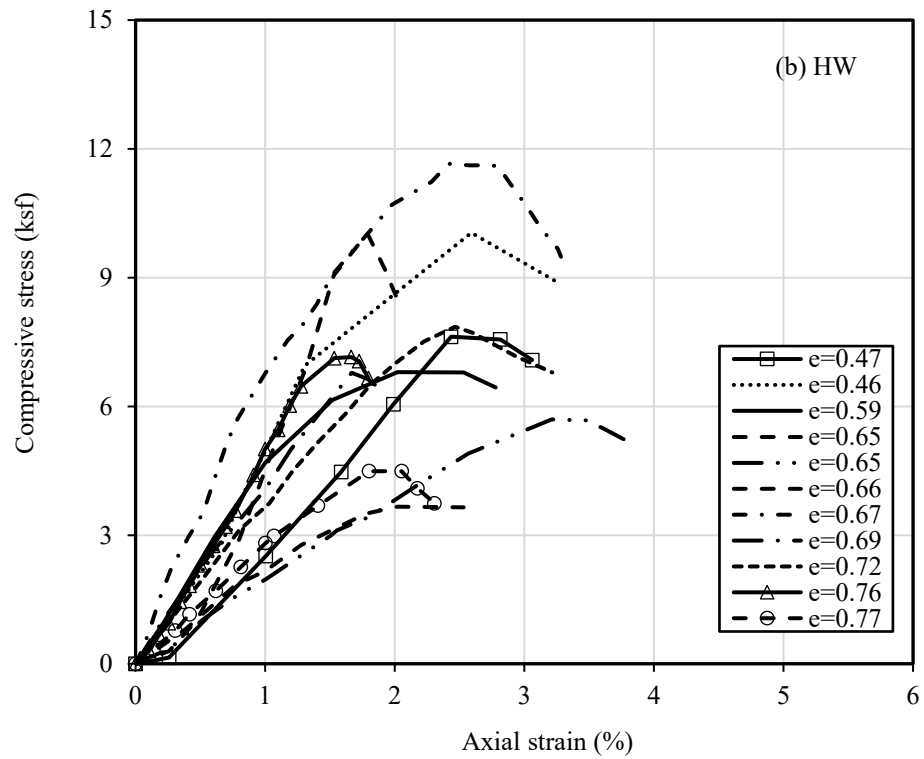
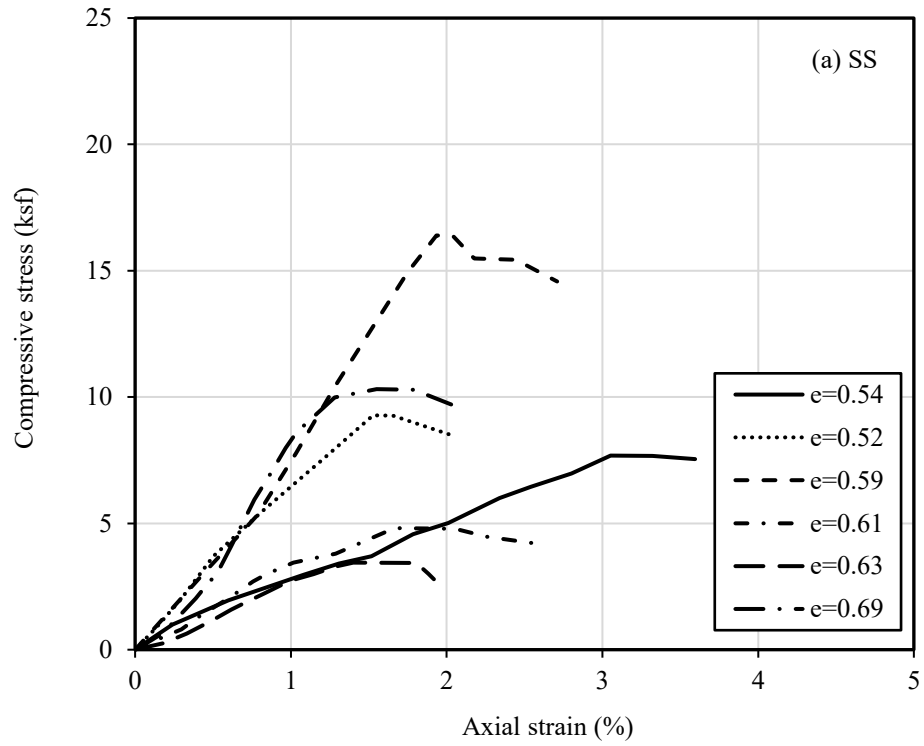
Extensive laboratory tests have been conducted by KDOT to measure  $q_u$ , Young's modulus ( $E$ ), unit weight ( $\gamma$ ), and water content ( $\omega$ ) of shales following the ASTM standard methods (2005). Similarly, Rock Quality Designation (RQD) of rock cores was determined according to the ASTM (2002). Table 7.2 shows that the mean and standard deviation of  $q_u$ ,  $\gamma$ , and  $E$  of rock-based shales decreased from slightly to highly weathered conditions (i.e., SW shales exhibit higher mean  $q_u$ ,  $\gamma$ , and  $E$  than that of MW and HW shales). This trend of properties was expected because the degree of weathering defined the decomposition of parent material in joints and presence of crack in shale materials. The higher degree of weathering meant the shale materials could be more porous and softer due to the weakening of grain-to-grain bonding. The growing microcracks led to rupture and produced local tensile stress in the shale material under compression. The mean shale properties decreased with the degree of weathering. The natural water content of rock-based shales increased from slightly to highly weathered conditions, and HW shales had the highest mean water content of 24.7 percent. Similarly, the mean RQD values of rock-based shales decreased from 86 percent of SW shales to 70 percent of HW shales, while the mean percent recovery did not show dependency on the weathering conditions. The upper and lower limits of  $q_s$  suggest that the  $q_s$  of HW shales should be less than 1.1 ksf, the  $q_s$  of MW shales should be between 1.1 ksf and 2.4 ksf, and the  $q_s$  of SW should be greater than 2.4 ksf. Hence, the rock-based shales can be objectively classified using the suggested  $q_s$  ranges, mean RQD,  $q_u$ , and  $E$  values (Table 7.2).

The mean  $q_u$ ,  $\gamma$ , and  $E$  of SS shales were higher than that of HW, but lower than the MW and SW shales. The SS shale group contained soft to hard shales, which could be a possible reason for having higher  $q_u$  than the HW shales. Furthermore, the SS shales were heavily over consolidated and hardened during geologic history through overlaying sediments (Bjerrum 1967; Mohamadi 2015). From an extensive study of 121 samples of soil-based shales (geologic group Eagle Ford Shale), Hsu and Nelson (2002) reported that the  $q_u$  of shales ranged from 9 to 120 ksf with an average 43 ksf. Another study on slightly weathered clayey shale reported a wide range of  $q_u$  from 42 to 167 ksf (Agung et al. 2017). There were several factors, such as mineral constituents, formation, geologic history, that can influence the properties of SS shales.

### **7.3.3 Stress Strain Behaviors**

The available stress-strain behaviors of SS, HW, MW, and SW shales under uniaxial compression were plotted in Figure 7.1. A total of 31 samples of various shale groups were tested at a 0.5mm/min strain rate. The Young's modulus, drop modulus (M), and failure strain, along with the pre-failure and post-failure responses, were determined for each sample. The drop modulus described the post-failure behavior was estimated as the slope of a linear fit line in that region (Kivi et al. 2018; Tutluoğlu et al. 2015). In the pre-failure region, some stress-strain curves of both SS and HW shales exhibited a nonlinear response initially followed by a linear-elastic region (Figure 7.1a and 7.1b). In the post-failure region, these two shale groups behaved either almost elastic, perfectly plastic for small strain or more ductile failure with very low drop modulus. The drop modulus was compared with the Young's modulus with a M/E ratio for each sample to evaluate brittle to ductile behaviors. A M/E value greater than one indicates a more brittle failure behavior, equals to one means elastic-perfectly plastic failure, and less than one indicates a more ductile failure behavior. The M/E ratios were always less than one for both SS and HW shales, which indicate less brittle and more ductile behavior. The mean void ratio ( $e$ ) of 0.6 for SS shales was comparable to the mean  $e$  of 0.64 for HW shales.

The stress-strain response of MW and SW shales were shown in Figures 7.1c and 7.1d, respectively. The stress-strain curves exhibited nonlinear responses initially followed by linear elastically at a higher stress level. Immediately after reaching the peak stress, instantaneous stress drop occurred, which indicates more brittle failure behavior. The M/E ratios for all MW and SW shales were more than one, with average ratios of 1.9 and 2.1, respectively. The comparison of stress-strain results concluded that MW and SW shales exhibited brittle failures while the SS and HW shales exhibited more ductile failure behavior. The average  $e$  values of MW and SW shales were 0.47 and 0.43, respectively. The lower  $e$  values indicated that the MW and SW shales were stiffer and could fracture more easily than the SS and HW shales that were more flexible, deformable and cannot easily fracture.





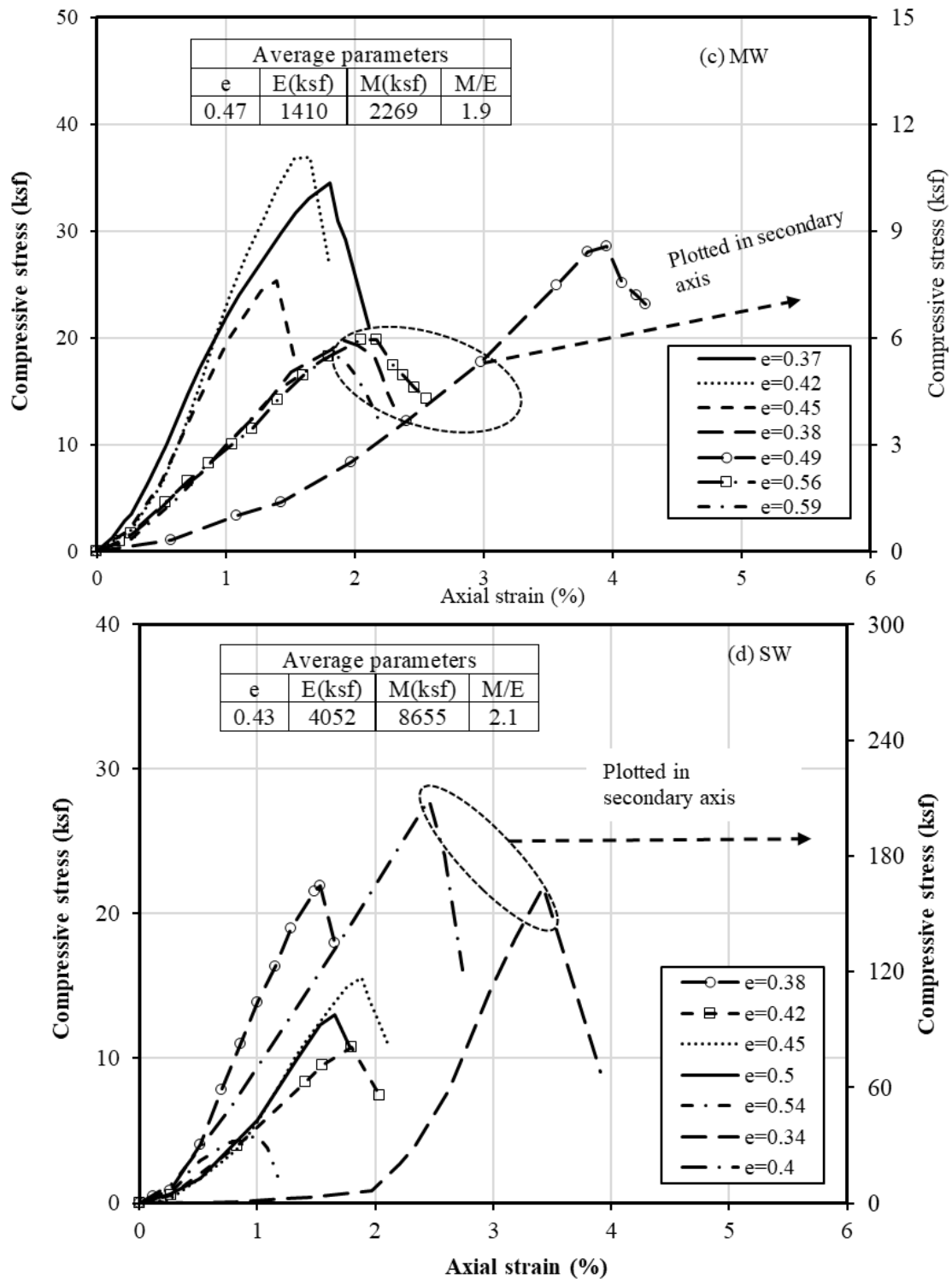


**Figure 7.1. Stress–Strain Curves of (a) Soil-Based Shale, (b) Soft & Highly Weathered Shale, (c) Moderately Hard & Weathered shale, (d) Hard & Slightly Weathered Shale at their respective void ratios,  $e$ .**

### 7.3.4 Young's Modulus of Shale

The logarithmic relationship given by Figure 7.2 between  $E$  and a ratio of  $q_u$  to  $\omega$  (percent) is shown in Figure 7.3a for  $1.7 \text{ ksf} \leq q_u \leq 272 \text{ ksf}$  and  $7.5 \leq \omega \leq 35.3$  percent. Statistical indices based on Akaike Information Criteria (AIC) and relative standard error (RSE) were included for comparison. This relationship suggested that a shale with a higher  $q_u$  is stiffer, and that the stiffness will be softened by the presence of water. The adverse effect of water content on the value of  $E$  for shale was attributed to weakening of intermolecular bonds, reduction of cemented quality, porosity, and grain size distribution (Cherblanc et al. 2016; Wang et al. 2017). The effect of  $q_u$  and  $\omega$  on  $E$  was similarly observed on shales considered as the bearing layer for drilled shafts (Stark et al. 2013).

$$\hat{E} = 1173 \left( \frac{q_u}{\omega} \right)^{0.86}$$

**Figure 7.2. Equation. Prediction Equation of Young's Modulus for Shale.**

### 7.3.5 Unconfined Compressive Strength of Shale

Figure 7.3b shows a logarithmic relationship between  $q_u$  and  $\omega$ , whereby the  $q_u$  decreases with increase in  $\omega$ . This relationship was expected because water changes the mineralogy and structure of shales, weakens cementing bonds, alters shale fabric, increases pore water pressure, and serves like a lubricant during shearing that reduces both stiffness and strength (Talal 2013). Furthermore, softening and expansion of clay minerals in the presence of water contributed to the reduction in  $q_u$  (Hawkins and McConnell 1992). In the absence of laboratory strength tests,  $\omega$  (percent) can be used as an index property to predict  $q_u$  (ksf) by the equation shown by Figure 7.4. Figure 7.3b also shows the upper and lower bound of the 95 percent prediction band.

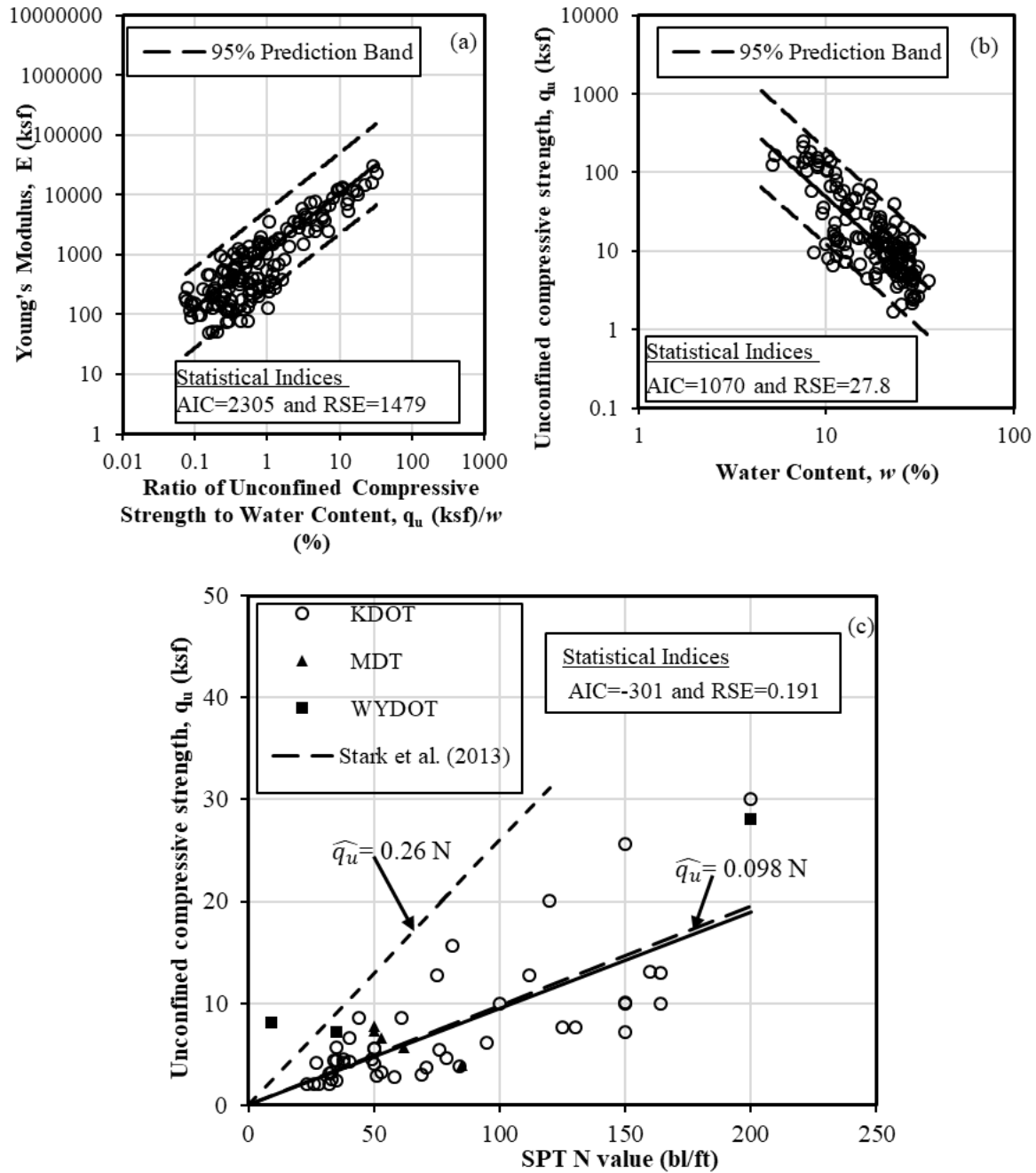


Figure 7.3. Relationships for (a) Young's Modulus Based on the Ratio of Unconfined Compressive Strength  $q_u$  to water content  $w$ , (b)  $q_u$  based on  $w$ , and (c)  $q_u$  based on SPT N-value.

$$\hat{q}_u = 670e^{-w/4.56}$$

Figure 7.4. Equation. Prediction Equation of Unconfined Compressive strength for shale.

Figure 7.2c shows a positive relationship between  $q_u$  and SPT N-value of shales obtained from KDOT, Montana Department of Transportation (MDT), and WYDOT. A linear relationship between  $q_u$  and N-value of IGMs had been suggested by researchers. Abu-Hejleh et al. (2005) proposed a linear equation (i.e.,  $q_u=0.26 N$ ) for claystone using four data points collected from two boreholes at two bridge projects on drilled shafts in Colorado. Using 20 load test data on drilled shafts in shales from five bridge projects in Illinois, Stark et al. (2013) developed a linear equation ( $q_u=0.078 N_{MSPT}$ ) to predict  $q_u$  (ksf) using the N-value obtained from a modified standard penetration test (MSPT) that was explicitly described in Long (2016). Based upon compiled shale data, Equation shown by Figure 7.5 is proposed for  $q_u$ , ranging from 2 to 30 ksf for N-values from 23 to 200.

$$\hat{q}_u = 0.094 N$$

**Figure 7.5. Equation. Prediction Equation of Unconfined Compressive Strength Based on SPT N Value.**

The equation shown in Figure 7.5 can be applied to predict  $q_u$  when intact and high-quality shales were difficult to sample for laboratory strength testing. Sampling challenges were exacerbated during a site investigation when the shale was highly weathered, moist, and disturbed by sampling.

## **7.4 Development of Static Analysis Methods**

### **7.4.1 Unit Shaft Resistance Prediction**

The  $q_s$  in each shale layer, along with a test pile and determined from CAPWAP (Table 7.1), were compared with the measured  $q_u$ , which is the most widely measured shale property in current practice. Figure 7.6 shows the nonlinear and increasing relationship between  $q_s$  and  $q_u$  for four shale types based on the classification criteria. The  $q_s$  for SS increased rapidly with  $q_u$  up to about 15 ksf and levels off thereafter (Figure 7.6a). This behavior indicated the minimal effect of  $q_u \geq 15$  ksf on  $q_s$ . Similar behavior was observed in SW shales where  $q_s$  increased rapidly with  $q_u$  up to about 37 ksf (Figure 7.6d). The value of  $q_s$  leveled off after a particular  $q_u$  value was due to the relative deformation between pile and shale along the pile-shale interface. A softer shale (SS

and HW shales) was more ductile or deformable and will experience a higher deformation, which caused full shaft resistance mobilization. A harder shale will have a higher strength for shaft resistance, but less deformability and will dilate and fracture during the relative movement leading to pile-shale slippage. Additionally, localized shear failure may occur at the pile-shale interface at higher  $q_u$ . This behavior supported the findings of decreasing shear strength in steel-rock interface with increasing  $q_u$  and decreasing steel roughness from the direct shear test of sandstone samples (Ziogos 2020). Similar observations in all shales suggested that  $q_s$  will not increase indefinitely with  $q_u$  and plastic behavior of shale that eventually governs the ultimate  $q_s$ . Figure 7.6 also shows that the  $q_s$  of rock-based shales decreased with an increase in weathering conditions (i.e., from slightly to highly weathered). This behavior was attributed to the decrease in  $q_u$  and E of shales at higher weathering conditions (Table 7.2). A higher E reduced shale deformation, resulting in an increase in the lateral stress along the pile-shale interface. The maximum  $q_s$  values from CAPWAP were 1.1, 2.3, and 3.78 ksf for HW, MW, and SW shales, respectively. The scatter of the measured  $q_s$  values in all shale types (Figure 7.6) could be attributed to the heterogeneous nature and intrinsic variability of shale properties from weathering, joint conditions, and sampling disturbance. These heterogeneities were assessed using the power, reciprocal, logarithmic, and exponential models to develop predictions for  $q_s$  (ksf) based on  $q_u$  (ksf) for 4 shale types. The best model was selected based on the smallest RSE and AIC. It is important to note that these proposed prediction SA equations (Figure 7.7a through 7.7d) were applicable for  $0.19 \text{ ksf} \leq q_s \leq 3.78 \text{ ksf}$  and  $2.18 \text{ ksf} \leq q_u \leq 126 \text{ ksf}$  and developed for a homogenous shale with no interbedded rock layers along a pile.

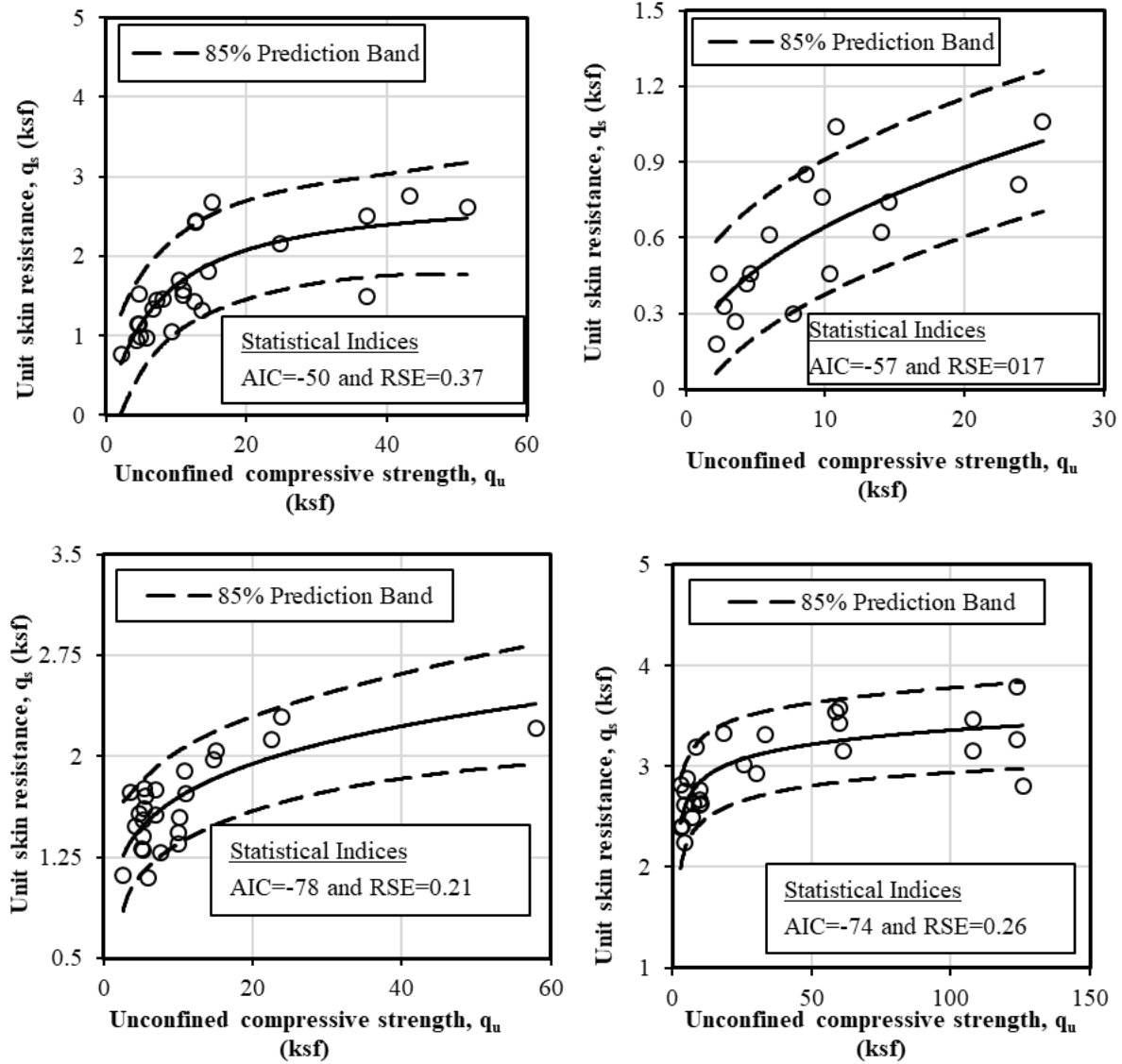


**Figure 7.6. The Unit Shaft Resistance of Piles Driven in: (a) Soil-Based Shale, (b) Soft & Highly Weathered Shale, (c) Moderately Hard & Weathered Shale, (d) Hard & Slightly Weathered Shale.**

$$a) \hat{q}_s(SS) = \frac{3.523 q_u}{(8.6 + q_u)^{.05}}$$

$$b) \hat{q}_s(HW) = 0.23 q_u^{0.45}$$

$$c) \hat{q}_s(MW) = \frac{1.196 q_u}{(0.5 + q_u)^{0.83}}$$

$$d) \hat{q}_s(SW) = \frac{2.62 q_u}{(0.467 + q_u)^{0.945}}$$

**Figure 7.7. Equation. Unit Shaft Resistance Prediction for a) SS Shale, b) HW Shale, c) MW Shale, and d) SW Shale.**

#### **7.4.2 Unit End Bearing Prediction**

The measured  $q_b$  used in this study was calculated by dividing CAPWAP end bearing with a box area of H-pile and a close-ended area of 12.75-in diameter shell pile using the CAPWAP estimated weight of test piles. The test piles data provided by KDOT suggested that MW and SW shales have higher  $q_b$  than that of SS and HW shales due to having higher  $q_u$  and E as shown in the Table 7.2. Moreover, the stress-strain behavior of MW and SW shales were similar in both the pre-failure and post-failure region (Figures 7.1c and 7.1d). Additionally, these two shale groups exhibited high drop modulus in the post-failure region that is an indication of brittle failure of these materials. On the other hand, SS and HW shales showed more ductile response in the post-failure region (Figures 7.1a and 7.1b). Table 7.2 indicate that the SS and HW shales were softer than the MW and SW shales. It would be expected that a punching shear failure may occur in SS and HW shales due to lower stiffness. However, a general shear failure may be expected in MW and SW shales due to higher stiffness. Considering the strength and stress-strain response, shales were categorized into two types in the  $q_b$  predictions: soil-based, soft & highly weathered (SS-HW) shales with most  $q_b \leq 150$  ksf, and moderately hard to hard & weathered to slightly weathered (MW-SW) shales with most  $q_b$  values greater than or equal to 150 ksf.

The relationships between  $q_b$  and  $q_u$  were shown in Figure 7.9 for 20 test piles in SS-HW shales and 29 test piles in MW-SW shales. Figure 7.9a shows a nonlinear and increasing relationship between  $q_b$  and  $q_u$  for SS-HW shales with 3  $q_b$  values slightly larger than 150 ksf. These 3  $q_b$  values were for harder and more-intact soil-based shale with  $q_u$  and RQD greater than 24 ksf and 83 percent, respectively. Figure 7.9b shows that the  $q_b$  of MW-SW shales increased rapidly with  $q_u$  up to 37 ksf, and then the increase in  $q_b$  reduced thereafter. These rapidly decreasing trends in

$q_b$  associated with  $q_u$  suggested that either local failure or punching failure is more likely to occur in the shale beneath a pile tip. Table 7.1 shows that among 49 test piles, 5 test piles resting on the SW shale reached refusal (blow count greater than 120). This may cause partial mobilization of end bearing due to inadequate energy transferred during the dynamic tests. Consequently, the overall relationship in  $q_b$  associated with  $q_u$  showed a decreasing trend at higher  $q_u$ . The ratios of  $q_b$  to  $q_u$  of SS-HW and MW-SW shales ranged from 3.55 to 21.76 and 2.44 to 80, respectively. The relatively high  $q_b$  of MW-SW shales were due to the higher E and  $q_u$  against shale deformation. The following prediction equations were proposed to predict  $q_b$  (ksf) in terms of  $q_u$  (ksf) for the two shale types. The equation shown in Figure 7.8a is applicable for  $39 \text{ ksf} \leq q_b \leq 182 \text{ ksf}$  and  $3.23 \text{ ksf} \leq q_u \leq 52 \text{ ksf}$ , and the equation shown in Figure 7.8b is applicable for  $35 \text{ ksf} \leq q_b \leq 384 \text{ ksf}$  and  $3.23 \text{ ksf} \leq q_u \leq 124 \text{ ksf}$ . These prediction equations were developed for a homogenous shale layer without any other interbedded rock layers within a distance of 3 times of pile dimension below a pile tip.

$$a) \hat{q}_b(SS - HW) = 45.72 q_u^{0.35}$$

$$b) \hat{q}_b(MW - SW) = \frac{190.64 q_u}{(1 + q_u)^{0.88}}$$

**Figure 7.8. Equation. Unit End Bearing Prediction Equation for a) SS-HW Shale and b) MW-SW Shale.**

Although  $q_b$  was influenced by  $q_u$ , other factors can influence the endearing of the pile in shale, such as frequency and inclination of fissures and joints and the nature of discontinuity. The  $q_b$  of a pile could be high if the shale is strong with closely spaced joints. However, shale with an open joint may fail by splitting due to the nonexistence of confining pressure, thus reducing  $q_b$ . Consequently, it is recommended to perform a pile restrike to confirm the target resistance if a pile is driven into a heavily jointed or steeply dipping shale formation (Tomlinson and Woodward 2014).



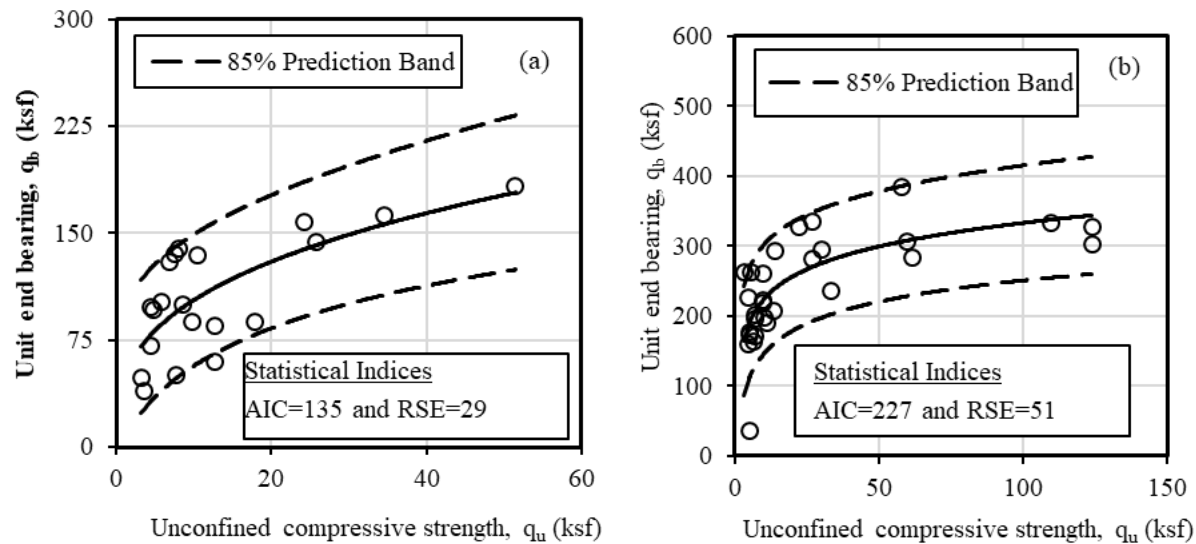


**Figure 7.9. Relationship between unconfined compressive strength and unit end bearing of piles driven into: (a) soil based, soft & highly weathered shale, (b) moderately hard to hard & weathered to slightly weathered shale.**

## 7.5 Validation of Proposed Static Analysis Methods

### 7.5.1 Unit Shaft Resistance Prediction

The performance of the proposed SA methods were evaluated by comparing the predicted resistances with the resistances determined from CAPWAP on 27 separate test piles and one static load test (pile ID 56) from 4 other Departments of Transportation and the literature (Long and Anderson 2012; Morton 2012). The pile, geomaterial, driving, hammer information, average shale properties, and average measured pile resistances of the 28 separate test piles were summarized in Table 7.3. Among 28 piles, 27 piles were tested in 16 counties and 5 states, and 1 was tested in Canada. The bearing layers included soil-based and highly weathered to slightly weathered shale, while the overburden layers consisted of sand and mixed soil. The 28 test piles comprised 18 H-piles, 8 OEP, and 2 CEP piles.

Figure 7.10a compares the predicted  $q_s$  from the equations shown in Figure 7.7 and measured  $q_s$  from CAPWAP and SLT of 39 shale layers and highlights the applicable  $q_s$  range between 0.19

and 3.78 ksf. The comparison showed that the proposed SA methods underpredicted  $q_s$  for  $q_s > 3.78$  ksf. Considering all 39 shale layers, the SA methods underpredicted  $q_s$  by about 26 percent on average (i.e., mean bias=1.36) and yielded a relatively high COV of 0.86 where the underprediction was worse at higher  $q_s$ . If the SA methods were applied to the applicable  $q_s$  range, the  $q_s$  prediction improved with only an average 3 percent underprediction (mean bias=1.03) and a much lower COV of 0.36. The SA methods provided better  $q_s$  predictions on H-piles than pipe piles with about an average 6 percent overprediction on H-piles and 19 percent underprediction on pipe piles. Figure 7.10a compares the predicted  $q_s$  of 2.46 ksf with the measured  $q_s$  of 2.53 ksf from the static load test on pile ID 56 of the Cerro Gordo 63 bridge in Adair County, Iowa. The subsurface profile consisted of silty clay, sand, glacial till, and a MW shale layer. The proposed method underpredicted the measured  $q_s$  value by about 2.5 percent.

### ***7.5.2 Unit End Bearing Prediction***

The performance of the proposed SA method prediction equations shown in Figure 7.8 for  $q_b$  prediction were evaluated by comparing the predicted  $q_b$  with the  $q_b$  from CAPWAP analysis on 25 separate test piles and one SLT on shale layers from three state DOTs and the literature (Long and Anderson 2012; Morton 2012). Figure 7.10b compares the predicted and measured  $q_b$  and highlighted the applicable  $q_b$  range between 35 and 384 ksf. The proposed SA methods overpredicted  $q_b$  by about 14 percent on average for all 26 data and 20 percent for 24 data within the applicable  $q_b$  range. The mean bias of 0.97 was closer to unity and a smaller COV of 0.31 suggested that the SA methods provided better prediction of  $q_b$  for H-piles than for pipe piles. In fact, the SA methods overpredicted  $q_b$  for pipe piles by about 69 percent. Comparing to  $q_b$  prediction on SS-HW and MW-SW shales, Equation 4.8 yields better prediction on SS-HW shales with a mean bias of 1.03 and a smaller COV of 0.33 compared to that for MW-SW shales. The predicted  $q_b$  of 85 ksf from the proposed equation was close to the measured  $q_b$  of 62 ksf from SLT. The difference was attributed to the full mobilization of  $q_b$  during the dynamic testing. The proposed SA method for steel H-pile provided a reasonable prediction for  $q_s$  and  $q_b$  compared with that from CAPWAP and SLT.

**Table 7.3. Summary of Separate Test Pile Data Used in the Validation Study.**

Pile ID	Source	County, State or Country	Pile	LEMB	LIGM	Overburden	End bearing shale layer	Shale Group	qua	RQDa	qsa	qb	Pile	BC
50	IADOT	Franklin	HP 10×57	20.0	3.5	sand	light gray, hard, slightly w. shale	SW	491*	86	6.22	221.80	Del. D19-42	120
51	WYDOT	Franklin	HP 10×57	20.0	3.5	sand	light gray, hard, slightly w. shale	SW	11.5*	86	7.21	298.24	Del. D19-42	120
52	WYDOT	Cerro Gordo	HP 14×73	11.1	9.0	sand	gray, slightly w. shale	SW	4.39*	NA	2.15	135.76	Del. D19-42	84
53	WYDOT	Cerro Gordo	HP 10×42	28.5	6.7	sand	gray, slightly w. shale	SW	8.14*	NA	NA	342.10	Del. D19-42	74
54	WYDOT	Ottumwa	HP 10×42	36.0	2.0	mixed	gray, slightly w. shale	SW	34.3*	NA	2.28	526.10	Del. D19-42	151
55	WYDOT	Adair	HP 10×57	56.0	6.5	mixed	Moderately w. shale	MW	4.59	NA	3.11	54.72	Del. D22	156
56	WYDOT	Adair	HP 10×57	56.0	6.5	mixed	Moderately w. shale	MW	4.59	NA	NA	NA	NA	NA
57	WYDOT	Plymouth	HP 10×57	44.0	10.2	mixed	dark gray firm to hard shale	SW	14.2*	NA	1.96	284.88	APE D19-42	53
58	WYDOT	Warren	HP 10×42	49.0	6.9	mixed	Highly w. shale	HW	14.2*	NA	0.31	85.63	Del. D19-32	18
59	WYDOT	Davis	HP 14×88	21.7	3.4	mixed	soft, clayey shale	SS	1.04	NA	2.84	119.46	Del. D19-42	53
60	WYDOT	Davis	HP 14×117	26.0	5.0	mixed	soft, maroon clayey shale	SS	1.25	NA	1.82	148.91	Del. D19-42	160
61	WYDOT	Hot Springs	HP 14×73	27.0	13.5	sand	hard slightly w. shale	SW	170.63	72	3.59	293.02	ICE 42-S	263
62	ITD	Natrona	HP 14×117	20.0	0.5	mixed	soft, highly w. shale	HW	8.15	11	0.50	149.33	MVE D-19	120
63	ITD	Lemhi	HP 12×74	71.0	70.4	mixed	moderately hard, w. shale	MW	5.22*	NA	0.54	NA	ICE I-30-V2	61
64	MDT	Lemhi	HP 12×74	64.0	61.9	mixed	dark, very soft-soft shale	HW	7.31*	NA	0.92	NA	ICE I-30-V3	64
65	MDT	Carbon	HP 14×117	32.6	18.2	mixed	moderately w. shale	MW	8.56	NA	1.63	377.19	ICE 80S	156
66	Morton (2012)	Teton	16"×0.75" OEP	26.6	13.0	gravel	slightly w. shale	SW	195.28	90	4.89	444.23	ICE I-36	240
67	Morton (2012)	Roosevelt	16"×0.5" OEP	95.0	2.5	mixed	gray, laminated, hard shale	SW	6.06*	86	2.07	134.08	APE D36-26	74

68	Morton (2012)	Roosevelt	16"×0.5" OEP	97.9	10.7	mixed	gray, laminated, hard shale	SW	6.06*	86	4.59	138.26	APE D36-26	192
69	Morton (2012)	Roosevelt	16"×0.5" OEP	81.0	5.2	mixed	gray, laminated, hard shale	SW	7.31*	89	3.78	141.39	APE D36-26	109
70	Morton (2012)	Musselshell	16"×0.5" OEP	32.7	21.3	mixed	dark grey to grey, hard shale	SW	13.16	70	3.45	139.10	Del. D19-32	160
71	Morton (2012)	Valley	20"×0.5" OEP	93.8	8.9	mixed	slightly w. shale	SW	3.97	100	3.76	61.40	Del.D-46-42	31
72	Morton (2012)	Valley	20"×0.5" OEP	91.8	7.2	mixed	moderately w. shale	MW	5.64	100	1.92	113.20	Del.D-46-32	29
73	Morton (2012)	Phillips	20"×0.5" OEP	136.5	2.1	mixed	dark gray, very hard shale	SW	11.7*	NA	3.34	57.43	ICE I-36	47
74	Morton (2012)	Treasure	16" CEP	32.5	21.5	mixed	dark grey to grey shale	SW	6.26*	NA	2.84	160.82	Del. D19-32	109
75	Morton (2012)	Golden Valley	16" CEP	27.5	12.0	mixed	dark grey, hard shale	SW	13.78	55	2.51	238.72	ICE 42S	160
76	Morton (2012)	Canada	HP 14×117	NA	NA	NA	dark shale, severely fractured	HW	208.85	13	NA	279.86	NA	108
77	L&A (2012)	Illinois	HP 14×117	15.0	2.0	mixed	moderately w. shale	MW	6.27	NA	0.84	169.59	NA	NA
50	IADOT	Franklin	HP 10×57	20.0	3.5	sand	light gray, hard, slightly w. shale	SW	491*	86	6.22	221.80	Del. D19-42	120

$q_u$ —Unconfined compressive strength; \*—estimated;  $q_s$ —Unit skin friction;  $q_b$ —Unit end bearing; RQD—Rock quality designation;  $L_{EMB}$ —Embedded pile length;  $L_{IGM}$ —Embedded pile length in IGM; bl—Pile hammer blow; L&A—Long and Anderson; w.—Weathered; Del.—Delmag; Pil.—Pileco; SS—Soil based shale; HW—Soft & highly weathered shale; MW—Moderately hard & weathered shale; SW—Hard & slightly weathered shale; NA—not available; <sup>a</sup>—Average value of all shale layers; and BC—Hammer blow count at EOD.

## 7.6 Validation of Proposed Static Analysis Methods

Uncertainties in pile design and construction were incurred from geomaterial sampling, material property estimation, soil disturbance, pile resistance estimation, and field verification.

Accounting for these uncertainties and ensuring prescribed reliability, probability-based theory has been used to calibrate LRFD resistance factor ( $\phi$ ) for a target reliability. FOSM, FORM and MCS were applied in this study to develop calibrated LRFD  $\phi$  for the proposed SA methods on the  $q_s$  and  $q_b$  predictions for driven piles in shale. A complete description of these reliability methods can be found in Adhikari (2019). The required statistical values of dead load and live load were adopted based on the recommendations by Paikowsky et al. (2004). It was assumed that the bridge spans were less than 36m, a dead to live load ratio of 2 was chosen for the LRFD calibration (Ng and Sritharan 2016; Haque and Abu-Farsakh 2018).

The Shapiro-Wilk (S) and Anderson-Darling (AD) normality tests were conducted to determine the most appropriate distribution for modeling resistance biases ( $\lambda$ ), defined as a ratio of measured pile resistance to predicted pile resistance (Table 7.4). The SW test was more robust and preferred over the other normality tests because of its capacity to detect non-normality (Mendes and Pala 2003). A 5 percent significance level was assumed so that a  $p$ -value below a threshold of 0.05 would indicate that the assumed distribution was not appropriate for modeling  $\lambda$ . The decision of best-fit distribution was made based on a higher log-likelihood value when both normal and log-normal distributions were not rejected. Table 7.4 shows that neither normal nor log-normal distribution were rejected except  $q_s$  for SS shale at which only log-normal was not rejected, and the comparable log-likelihood values led to the selection of log-normal distribution following the typical LRFD calibration procedure.

The mean ( $\bar{x}$ ) and COV of  $\lambda$  for each proposed SA equation were calculated and summarized in Table 7.5. Resistance factors and efficiency factors ( $\phi/\bar{x}$ ) were determined for a target reliability index ( $\beta_T$ ), denoted as the safety associated with a particular probability of failure ( $p_f$ ). A  $\beta_T$  value of 2.33 (i.e.,  $p_f=1$  percent) for a redundant pile group and  $\beta_T$  value of 3.0 (i.e.,  $p_f=0.1$  percent) for a nonredundant pile group were adopted (Paikowsky et al. 2004). Table 7.5 shows that the  $\bar{x}$  values ranging from 0.97 to 1.06 were close to unity, and the COV values from 0.23 to 0.38 were

relatively low. The prediction equation for  $q_s$  in MW shales has the best  $\bar{x}$  of 1.02 and smallest COV of 0.23, which yield the highest  $\phi$  and  $\phi/\bar{x}$  for all three reliability methods and indexes. Furthermore, Table 7.5 shows that the  $\phi$  estimated by the FOSM method was on average 10 percent and 13 percent lower than that by the FORM and MCS methods for  $\beta_T=2.33$  and  $\beta_T=3.00$ , respectively. The FORM and MCS methods yield almost identical  $\phi$  to the nearest 0.05 for both reliability indexes. The  $\phi$  values for  $\beta_T=3.00$  were on average 23 percent, 19 percent, and 21 percent lower than that for  $\beta_T=2.33$  based on FOSM, FORM, and MCS, respectively. These differences agree with the 20 percent reduction in  $\phi$  values for  $\beta_T=3.00$  recommended in AASHTO (2020). The  $\phi$  values based on the MCS and  $\beta_T=2.33$  vary from 0.45 to 0.74, which were higher than the 0.35 for the  $\alpha$ -method and 0.45 for the Canadian Geotechnical Society (1985) method (AASHTO 2020). The average  $\phi/\bar{x}$  values based on MCS were 0.6 and 0.47 for  $\beta_T$  values of 2.33 and 3.00, respectively. The average  $\phi/\bar{x}$  of the SA methods for  $q_s$  was slightly higher than that for  $q_b$ . The  $\phi/\bar{x}$  values of our proposed SA methods were higher than the average  $\phi/\bar{x}$  of 0.45 and 0.33 calculated for the  $\alpha$ -method for soils and both steel H-piles and pipe piles, respectively (Paikowsky et al. 2004). A sample calculation of factored pile resistance in shale is provided in the appendix.

## **7.7 Change in Pile Resistance in Shale**

### **7.7.1 Change in Unit Shaft Resistance**

CAPWAP results at EOD and beginning of restrike (BOR) of 39 test piles conducted in Kansas, Wyoming, and Iowa were used to investigate the change in pile resistances in shales. The 39 test piles consisted of 33 H-piles, and 6 12.75-in diameter shells driven into 76 shale layers. The percent change in  $q_{s-t}$  at an elapsed time (t) after EOD with respect to  $q_{s-t_0}$  at EOD was plotted against t ranging from 0.25 hours to 25 hours on a logarithmic scale (Figure 7.11). Logarithmic time was selected following the pile response in fine-grained soil determined from past studies (Abu-Farsakh and Haque 2020; Haque et al. 2017; Ng et al. 2013b). To compare the change in  $q_s$ , a rate of change in  $q_s$  with respect to t, known as the A factor, was determined using Equation shown in Figure 4.10 considering the initial time ( $t_0$ ) at hour 0.01 (Skov and Denver 1988) as shown in Table 7.4. A positive A factor indicated an increase in pile resistance with time known

as pile setup, while a negative A factor indicated a decrease in pile resistance with time known as pile relaxation. A ratio of maximum pile hammer energy (EMX) at BOR to EMX at EOD was calculated for each event to evaluate the effect of hammer performance on the pile resistances determined from PDA testing. The EMX ratios, ranging from 0.94 to 1.23 at one standard deviation with an average ratio of 1.07 (Table 7.4), suggested that the hammer performance had little to no effect on the time-dependent pile resistances, so that apparent pile setup or relaxation was not a concern in this study.

Figure 7.11a indicated that the SS shale always exhibited a positive change in pile resistance or pile setup with an average A factor of 0.76. This was attributed to the presence of fine-grained soils in the SS shale, described as clayey shale and silty shale. Pile setup in SS shale was attributed to the dissipation of excess pore water pressure induced from pile installation that caused consolidation of SS shale along the pile and increased the effective stress with time. This phenomenon was similarly observed in fine-grained soils (Long et al. 1999; Ng et al. 2013a; b). The  $q_s$  in the SS shale after the EOD increased on average by about 75 percent and 89 percent within 15 minutes and 24 hours, respectively. The broad range of A factors summarized in Table 7.4, which changed in  $q_s$  (Figure 7.11a) could be attributed to the range of permeability of SS shales resulting from geological processes (Neuzil 1994) that influenced the rate of pore water pressure dissipation and consolidation.

**Table 7.4. Summary of Setup Factors for Driven Piles in Shales.**

Pile ID	Pile	End bearing layer	Shale Group	EOD		BOR		Setup factor, A	
				BC	E <sub>max</sub> (kip-ft)	BC <sup>a</sup>	E <sub>max</sub> (kip-ft)	Shaft <sup>a</sup>	End bearing
4	HP 12×63	gray, calcareous, slightly w. shale	SW	160	22.90	480	22.09	0.06	-0.04
6	HP 10×42	dark gray, clayey shale	SS	28	16.20	32	17.66	0.21	0.89
7	HP 12×53	shades of gray, silty shale	SS	18	31.90	24	30.55	0.07	0.58
8	HP 12×74	green gray, highly w. shale	HW	27	31.20	34	37.46	0.39	0.35
11	HP 10×42	moderately hard, silty shale	SS	53	20.70	80	22.08	0.59	0.08
12	HP 12×84	hard, silty, gray shale	SS	25	22.30	48	21.01	0.11	0.95
13	HP 12×63	dark gray, banded, w. shale	MW	36	18.60	80	20.88	1.87	0.15
14	HP 10×42	dark gray to gray, w. shale	MW	60	21.10	69	19.82	1.32	-0.01
15	HP 12×53	dark gray, w. shale	MW	30	22.40	53	20.97	0.16	0.47
16	HP 10×42	gray, calcareous shale, slightly w.	SW	192	19.20	240	20.56	0.1	0
17	HP 12×63	gray, generally w. shale	MW	24	35.20	30	38.06	0.11	0.88
18	HP 10×42	gray to dark gray, w. shale	MW	51	19.20	63	19.69	0.63	-0.28
19	HP 12×74	dark gray to gray, w. shale	MW	80	35.90	60	36.49	0.83	-0.16
21	HP 12×63	gray, soft, highly w. shale	HW	17	30.50	32	37.05	0.32	0.57
22	HP 12×63	dark gray, silty, shale	SS	25	34.70	32	37.30	0.11	0.63
23	HP 12×74	gray, soft, highly w. shale	HW	27	31.50	37	35.11	0.1	0.07
24	HP 12×74	gray, soft, highly w. shake	HW	23	22.30	37	25.18	0.03	0.22
25	HP 12×74	gray, soft, highly w. to w. shale	HW	27	27.00	33	26.68	-0.06	0.53
26	HP 12×74	gray, soft, highly w. shale	HW	26	26.70	46	29.09	0.17	0.31
27	HP 12×63	clayey shale, firm	SS	28	21.70	38	22.24	0.45	0.32
29	HP 12×74	gray, soft, highly w. shale	HW	52	24.50	960	30.10	0.15	0.23
31	HP 12×63	gray, hard, slightly w., gypsum shale	SW	26	29.70	35	29.30	0.93	-0.28
34	HP 12×74	gray, soft, highly w. shale	HW	28	26.40	44	25.45	0.75	0.15
35	HP 12×74	clayey, gray, stiff to moderately hard shale	SS	62	15.90	68	18.09	0.14	0.48
36	12.75"D shell	very dark gray, w. shale	MW	60	14.30	96	17.07	0.34	0.11
38	12.75"D shell	very dark gray, w. shale	MW	40	19.50	40	21.92	1.28	-0.06
39	12.75"D shell	very dark gray, w. shale	MW	60	21.40	67	22.30	0.47	-0.15
40	12.75"D shell	very dark gray, w. shale	MW	60	19.40	69	20.66	-0.56	0.07
41	12.75"D shell	very dark gray, w. shale	MW	40	19.31	60	20.46	0.15	0.19
42	12.75"D shell	very dark gray, w. shale	MW	90	14.90	160	17.86	0.19	0.1
45	HP 12×63	clayey, gray with maroon mottling shale	SS	102	18.30	120	17.20	0.36	0.76
54	HP 10×42	gray, slightly w. shale	SW	151	23.03	160	22.06	0.01	-0.02
55	HP 10×57	moderately w. shale	MW	156	12.50	173	13.96	0.08	0.22



56	HP 10×57	moderately w. shale	MW	68	15.80	120	19.00	0.39	-0.1
57	HP 10×57	dark gray firm to hard shale	SW	53	18.40	60	20.20	0.04	-0.04
58	HP 10×42	highly w. shale	HW	18	15.77	120	19.32	1.59	1.71
59	HP 14×117	soft, clayey shale	SS	53	16.10	40	18.00	1.42	0.57
60	HP 14×117	soft, maroon clayey shale	SS	160	15.80	156	15.63	1.35	0.08
61	HP 14×73	hard slightly w. shale	SW	263	23.10	240	23.01	-0.1	-0.07

SS–Soil based shale; HW–Soft & highly weathered shale; MW–Moderately hard & weathered shale; SW–Hard & slightly weathered shale; NA–not available; <sup>a</sup>–Average value of all shale layers; and BC–Hammer blow count and E<sub>max</sub>– maximum hammer energy

**Table 7.5. Normality Test Results for the Proposed Static Analysis Methods for the Estimation of Unit Shaft Resistance and Unit End Bearing in Shales.**

For unit shaft resistance biases									
Steel pile type	SA method	Geo-material	Sample size	P-value for normality test		P-value for lognormality test		Loglikelihood	
				SW test	AD test	SW test	AD test	Normal	Lognormal
H-pile & 12 <sup>3</sup> / <sub>4</sub> shell	Figure (7.7a)	SS	27	0.02	0.05	0.18	0.08	NA	-7
H-pile & 12 <sup>3</sup> / <sub>4</sub> shell	Figure (7.7b)	HW	23	0.36	0.48	0.38	0.58	-9.1	-8.4
H-pile & 12 <sup>3</sup> / <sub>4</sub> shell	Figure (7.7c)	MW	31	0.16	0.23	0.55	0.37	11.1	11.9
H-pile & 12 <sup>3</sup> / <sub>4</sub> shell	Figure (7.7d)	SW	35	0.19	0.32	0.21	0.37	27.1	27.9
For unit end bearing resistance biases									
H-pile & 12 <sup>3</sup> / <sub>4</sub> shell	Figure (7.8a)	SS-HW	28	0.15	0.23	0.24	0.43	-6.82	-6.8
H-pile & 12 <sup>3</sup> / <sub>4</sub> shell	Figure (7.8b)	MW-SW	36	0.16	0.1	0.38	0.23	1.8	4.3

N–Sample size; SS–IGM soil-based shale; HW–Soft & highly weathered shale; MW–Moderately hard & weathered shale; SW–Hard & slightly weathered shale; SS-HW–Soil based, soft & highly weathered shale; MW-SW–Moderately hard to hard & weathered to slightly weathered shale; SW–Shapiro-Wilk normality test; AD–Anderson-Darling normality test; and NA–Not applicable.

**Table 7.6. LRFD Resistance Factors and Efficiency Factors of the Proposed Static Analysis Methods for the Estimation of Unit Shaft Resistance and Unit End Bearing in Shales.**

SA Method	IGM	Sample size (n)	Mean bias ( $\bar{x}$ )	COV bias (COV)	FOSM				FORM				MCS			
					$\beta_T=2.33$		$\beta_T=3.0$		$\beta_T=2.33$		$\beta_T=3.0$		$\beta_T=2.33$		$\beta_T=3.0$	
					$\varphi$	$\varphi/\bar{x}$	$\varphi$	$\varphi/\bar{x}$	$\varphi$	$\varphi/\bar{x}$	$\varphi$	$\varphi/\bar{x}$	$\varphi$	$\varphi/\bar{x}$	$\varphi$	$\varphi/\bar{x}$
Unit shaft resistance																
Figure (7.7a)	SS	27	1.01	0.33	0.51	0.51	0.39	0.39	0.57	0.57	0.45	0.45	0.57	0.57	0.44	0.44
Figure (7.7b)	HW	23	0.97	0.38	0.45	0.46	0.34	0.35	0.49	0.51	0.38	0.39	0.49	0.51	0.37	0.38
Figure (7.7c)	MW	31	1.02	0.23	0.64	0.63	0.50	0.49	0.73	0.72	0.62	0.61	0.74	0.73	0.61	0.60
Figure (7.7d)	SW	34	1.06	0.32	0.56	0.53	0.43	0.41	0.62	0.58	0.50	0.47	0.62	0.58	0.49	0.46
Unit end bearing																
Figure (7.8a)	SS-HW	28	0.98	0.32	0.52	0.53	0.4	0.41	0.57	0.58	0.46	0.47	0.57	0.58	0.45	0.46
Figure (7.8b)	MW-SW	36	1.02	0.29	0.57	0.56	0.45	0.44	0.64	0.63	0.52	0.51	0.64	0.63	0.51	0.50

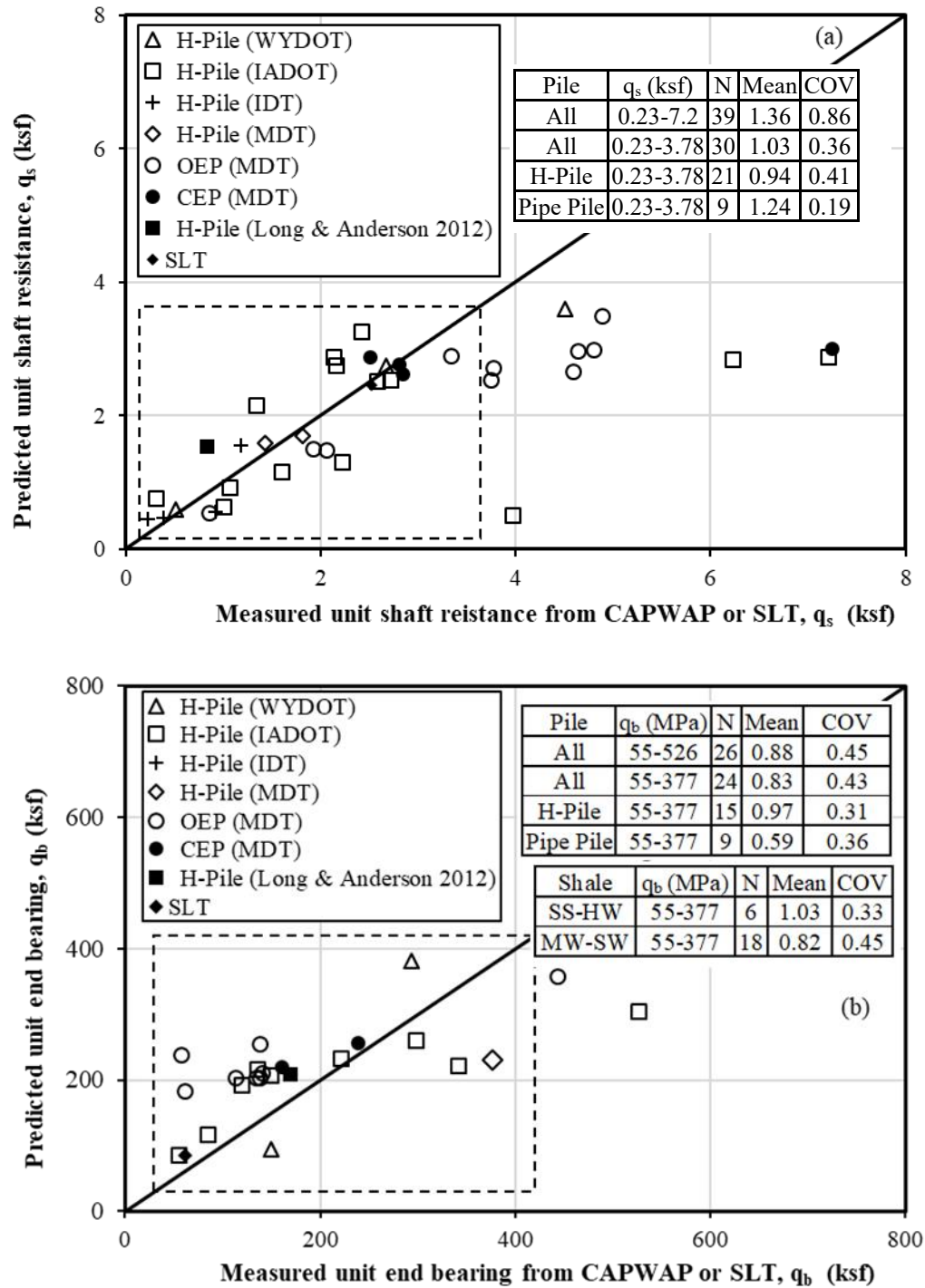


Figure 7.10. Comparison of Unit Pile Resistances from CAPWAP with (a) Predicted Unit Shaft Resistances, and (b) Unit End Bearing.

On the other hand, rock-based shales exhibited both pile setup and relaxation. Among the three rock-based shales, piles in the HW shale exhibited the highest pile setup with an average A factor of 0.36 (Figure 7.11b). Additionally, the  $q_s$  in HW shale increased on average by 32 percent and 52 percent in 15 minutes and 24 hours, respectively. A slightly lower average A value of 0.22 (Figure 7.11c) was found on piles driven in MW shales due to more relaxation in MW shales. In contrast, piles driven in SW shales exhibited mostly relaxation with an average A factor of -0.004 and an average 6.5 percent decrease of  $q_s$  in 24 hours (Figure 7.11d). Figures 7.11b through 7.11d indicated that the average time-dependent  $q_s$  changed from setup to relaxation from high to low degree of weathering (i.e., from HW to SW shales). This was likely due to the excess pore pressure dissipation and consolidation of HW shales leading to pile setup and shattering of some softer HW shales from pile driving leading to pile relaxation. The dilation of less weathered and stiffer MW and SW shales resulted in negative pore water pressure generation. The negative water pressure collected water toward the pile and softened the shales leading to pile relaxation. Furthermore, the high lateral stress possibly relieved around the disturbed zone that resulted from displacement and dilation of less weathered and stiffer shales along the pile shaft due to pile driving (Hannigan et al. 2020; Samson and Authier 1986). Higher dilation and relief of lateral stress in SW and MW shales were attributed to higher stiffness (Table 7.2 and Figure 7.1). Therefore, relaxation and setup should be cautiously considered during pile design in rock-based shales, and pile construction control should be performed to evaluate the time-dependent pile shaft resistances in rock-based shales.

### ***7.7.2 Change in Unit End Bearing***

The percent change in  $q_b$  with  $t$  in a logarithmic scale is shown in Figure 7.12. Piles driven in the SS and HW shales exhibited setup in all cases due to higher compressibility and lower stiffness that caused less pile rebound during driving. Additionally, the pile driving created instantaneous excess pore water pressure followed by dissipation that led to consolidation and increase in effective shale strength. The SS shale exhibited more setup than HW shale for 15 minutes and 24 hours (Figure 7.12a and 7.12b), and the average A factor 0.53 of SS shales was slightly higher than 0.46 of HW shales. However, according to the four steel H-piles driven in HW shales reported by Hannigan et al. (2020),  $q_b$  relaxation was reported with an average A factor of -0.08.

Although the magnitude of this relaxation A factor was relatively small, considering that  $q_b$  setup in pile design should be accompanied with construction control to evaluate the time-dependent  $q_b$  during construction.

Piles driven in the MW and SW shale experience both setup and relaxation in  $q_b$  (Figure 7.12 c and d). An average setup factor of 0.11 was determined for piles in MW shales with an average 34 percent increase in  $q_b$  at 24 hours after the EOD. However, an average relaxation factor of 0.07 was determined for piles in SW shales with an average 14 percent relaxation in  $q_b$  at 24 hours after the EOD. Figure 7.12c and 7.12d clearly indicated that SW shale exhibited more prominent relaxation than MW shales. This behavior was attributed to higher stiffness of SW shales that led to pile rebound during driving and created a gap between the pile toe and SW shale. From the case study of the pile in weak rock, Peiris et al. (2010) and Samson and Authier (1986) reported that piles driven through lower shaft resistance grounds into higher end bearing layer were more susceptible to relaxation, which could be a possible reason for relaxation in MW and SW shales. Furthermore, relaxation could result from shale softening from water migrating to pile toe resulted from the development of negative pore water pressure induced by the fracturing of shale, possible disturbance of weak planes such as joints and steep bedding plane, and foliation angle (Hannigan et al. 2020; Poon et al. 2017). The relaxation A factors of -0.07 for SW shale for H-piles match well with that determined for H-piles from Hannigan et al. (2020). This agreement suggested that piles driven in SW shales likely experience relaxation in  $q_b$  and construction control should be included to determine the relaxation in end bearing.

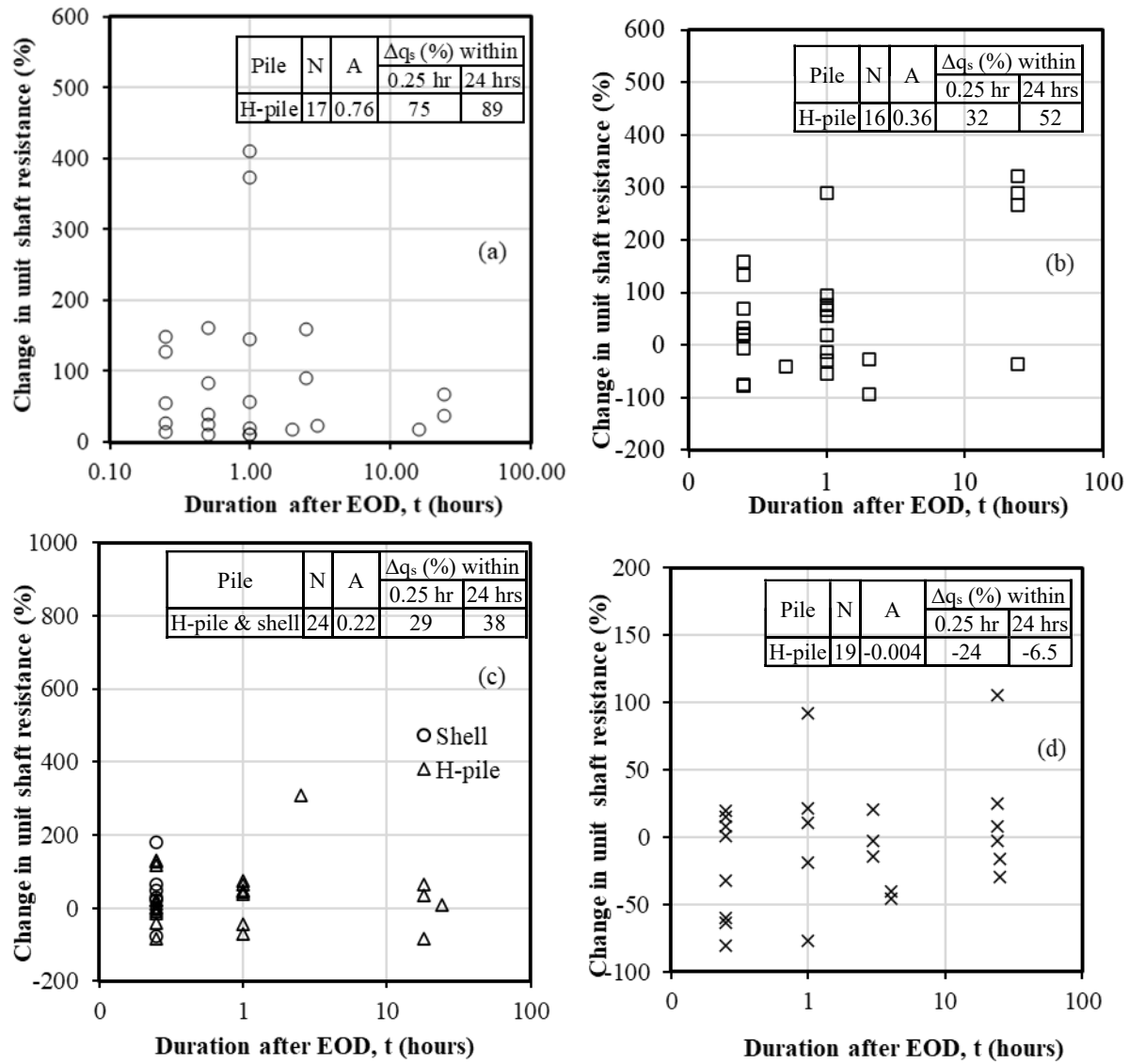


**Figure 7.11. Percent change in the unit shaft resistance with time in logarithmic scale: (a) SS shale, (b) HW shale, (c) MW shale, (d) SW shale.**

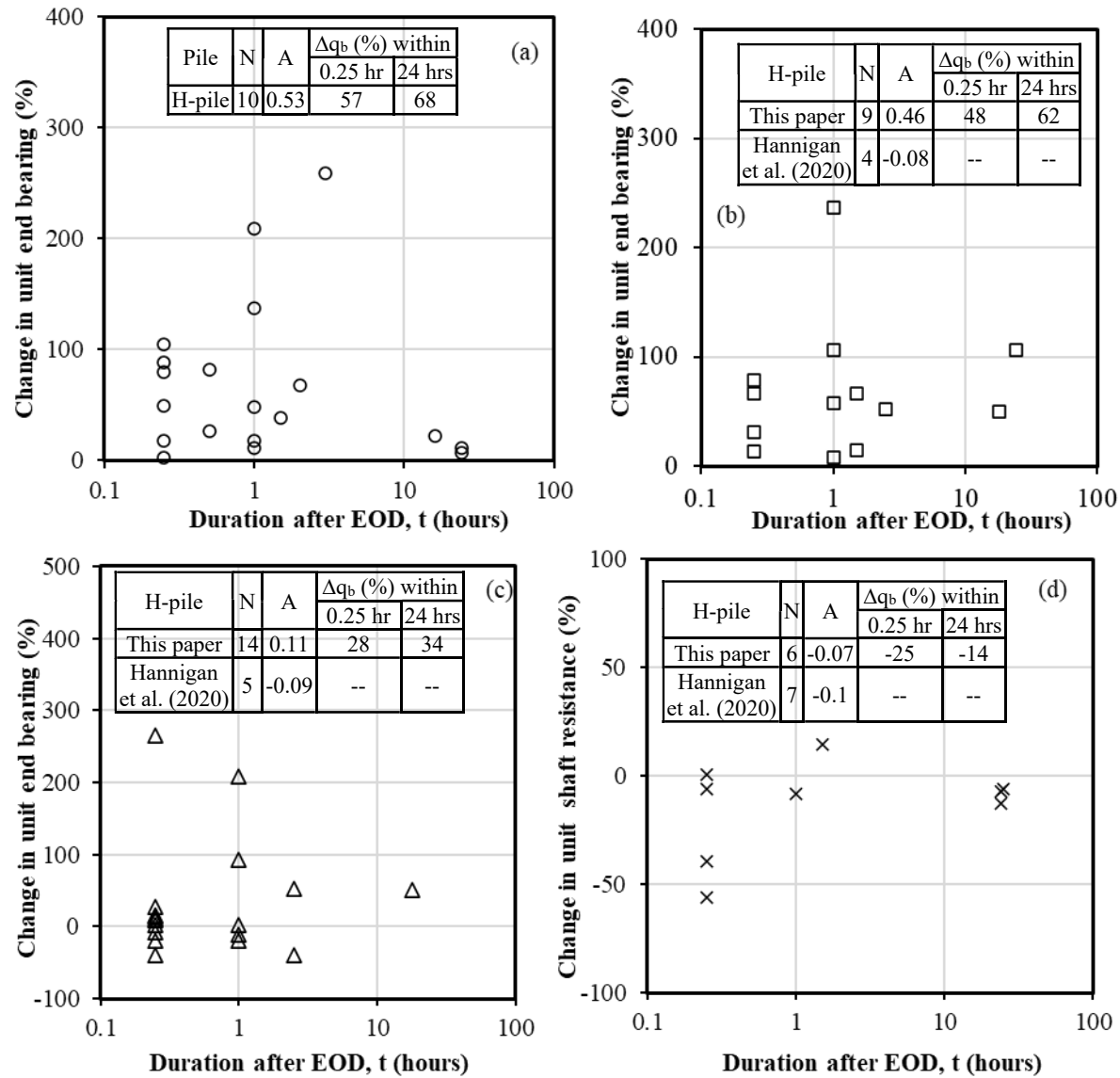


**Figure 7.12. Percent change in the unit end bearing with time in logarithmic scale: (a) SS shale, (b) HW shale, (c) MW shale, (d) SW shale.**

## 7.8 Summary and conclusions

The study presents the effect of shale weathering on the driven pile resistance predictions and the investigation of time-dependent pile responses in shales. A total of 49 usable test piles driven in soil-based and rock-based shale layers were analyzed to develop prediction equations for  $E$  and  $q_u$ , and new static analysis equations for predicting  $q_s$  and  $q_b$  in shales. These proposed SA equations were validated using 28 separate test pile data. Using both the training and separate



pile data, LRFD resistance factors for the proposed SA methods were calibrated. Lastly, the change in  $q_s$  and  $q_b$  with time was compared for different weathered shales in terms of  $A$  factors. The following conclusions were drawn from this study.

- Shales were classified into soil-based shale and rock-based shale based on the field description. The SS shale includes soft to hard clayey shale and silty shale. Depending on the weathering conditions and engineering properties, rock-based shales were further classified into soft & highly weathered shale (HW), moderately hard & weathered shale (MW), and hard & slightly weathered shale (SW). Due to geological processes, heavily over consolidated SS shales could show slightly higher mean  $q_u$ ,  $\gamma$ , and  $E$  than that of HW, but lower mean for MW and SW shales. The mean  $q_u$ ,  $\gamma$ ,  $E$ , and  $RQD$  values of rock-based shales decrease from low to high degree of weathering. The rock-based shales can be objectively classified using the suggested  $q_s$  ranges: less than 11 ksf for the HW shale, between 1.1 ksf and 2.4 ksf for the MW shale, and greater than 2.4 ksf for the SW shale. Furthermore, HW shales were more ductile while MW and SW shales were more brittle.
- The  $q_u$  and  $E$  of rock-based shales decrease with increasing water content and weathered conditions. A shale was stiffer with a higher  $q_u$ , and the stiffness will be softened by the presence of water. A logarithmic relationship was established between  $E$  and a ratio of  $q_u$  to  $\omega$ . The  $q_u$  of shale decreases with an exponential increase in  $\omega$ . Alternatively, the  $q_u$  of shale can be predicted using SPT N-values.
- The stress-strain behaviors of SS, HW, MW, and SW shales under uniaxial compression indicate unique characteristics in the post-failure region. In the post-failure region, these SS-HW shale groups behave either perfectly elastic-plastic for small strain or more ductile failure with a M/E ratio of less than one. However, the M/E ratios for all MW-SW shales were more than one, which indicates these shales exhibit more brittle failures than the SS- HW shales.
- The  $q_s$  of driven piles increases rapidly with  $q_u$  and levels off at a critical  $q_u$  due to slippage along the pile-shale interface and plastic behavior of shale. The  $q_s$  of rock-based shales decreases with the increase in weathering conditions. New SA methods given by

prediction equations were proposed for  $q_s$  for  $0.19 \text{ ksf} \leq q_s \leq 3.78 \text{ ksf}$  and  $2.18 \text{ ksf} \leq q_u$  of shales  $\leq 126 \text{ ksf}$  and for shales with no interbedded rock layers.

- New SA methods characterized prediction equations were proposed for  $q_b$  of SS-HW and MW-SW shales, respectively. The prediction equation for SS-HW shale was applicable for  $39 \text{ ksf} \leq q_b \leq 182 \text{ ksf}$  and  $3.23 \text{ ksf} \leq q_u \leq 52 \text{ ksf}$ , and the prediction equation for MW-SW shale is applicable for  $35 \text{ ksf} \leq q_b \leq 384 \text{ ksf}$  and  $3.23 \text{ ksf} \leq q_u \leq 124 \text{ ksf}$ .
- Using 28 separate test piles, the proposed prediction equations underpredict  $q_s$  by about 3 percent on average. These equations provide better  $q_s$  prediction on H-piles (6 percent overprediction) than pipe piles (19 percent underprediction). The proposed Eq. (8) and (9) overpredict the  $q_b$  on average by about 20 percent and provide better  $q_b$  prediction for H-piles than pipe piles.
- The LRFD calibration yields mean biases (0.97 to 1.06) closer to unity and relatively low COV values (0.23 to 0.38) for the proposed SA methods. The calibrated  $\phi$  values of 0.45 to 0.74 based on the MCS and  $\beta_T=2.33$  were higher than those recommended in AASHTO (2020). Furthermore, the proposed SA methods have higher efficiencies than those determined by Paikowsky et al. (2004).
- The SS shale exhibits setup while the rock-based shales exhibit both setup and relaxation in  $q_s$ . The average setup  $A$  factor of 0.76 was determined for steel H-piles in SS shales. Piles in HW shale exhibit a higher setup in  $q_s$  with average  $A$  factor of 0.36 and a lower setup factor of 0.22 in MW. Piles in SW exhibit relaxation in  $q_s$  with an average  $A$  factor of -0.004. Pile construction control methods should be included during the construction to evaluate the time-dependent  $q_s$  response in rock-based shales.
- Our study shows that piles in the SS and HW shale exhibit setup in  $q_b$  with average  $A$  factors of 0.53 and 0.48, respectively. However, data from the literature suggests that  $q_b$  relaxation could be encountered in HW shales with a lower  $A$  factor of -0.08. Piles in the MW and SW shale exhibit both setup and relaxation in  $q_b$ . The MW shale exhibits an average setup factor of 0.11, and SW shale exhibits an average relaxation factor of -0.07. Due to the variability of the natural shale materials and time-dependent responses, the calculated average  $A$  factors for  $q_s$  and  $q_b$  were for comparison purposes but were not recommended for design implementation.

## **CHAPTER 8: IMPROVED WAVE EQUATION ANALYSIS OF DRIVEN STEEL PILES IN INTERMEDIATE GEOMATERIALS**

### **8.1 Introduction**

Dynamic test methods, such as the PDA and signal matching analysis using the CAPWAP, were widely used throughout the construction stage to evaluate pile performance in IGM (Long, 2016; Masud et al., 2022c; Masud et al., 2023b). However, the signal matching analysis cannot be conducted until a test or production pile was outfitted with PDA sensors and driven by a pile hammer during construction to define pile driving acceptance criteria and to determine the proper penetration depth that would achieve the desired pile resistance. In contrast, a pile driving study utilizing 1D Wave Equation Analysis Program (WEAP) can be conducted before construction. In addition, WEAP has frequently been used as a low-cost construction control method.

WEAP was frequently used to evaluate pile drivability, predict static resistance, and maintain the integrity of piles in soils. However, assigning static and dynamic properties of IGM in WEAP can be challenging, particularly for IGM that exhibit SPT N-values greater than the WEAP maximum allowable input of 60 blows/ft. In addition, the default Smith parameters were developed using pile load test data in soils, and there were no guidelines to input the smith parameters for driven piles in intermediate geomaterials (IGMs) in the default WEAP method. Previous studies have investigated pile drivability in soil to predict geotechnical resistance and distribution, pile stress, hammer blow count, and hammer performance during installation (Doherty & Iggoe, 2013; Rausche et al., 2009; Schneider & Harmon, 2010). In those studies, the total pile resistance from WEAP was matched with the observed pile resistance from static load testing (Coyle et al., 1973; Raines et al., 1992; Rausche et al., 1997) or dynamic load tests (Iskander & Stachula, 2002; Ta & Hammann, 2013). However, studies have yet to be conducted for driven piles in IGM due to lack of data. As a result, adequate WEAP analysis procedures were needed.

This study aims to develop WEAP analysis procedures and Load and Resistance Factor Design (LRFD) guidelines for piles driven in IGM. Four WEAP methods, based on static analysis

methods and dynamic parameters for IGM, were evaluated in this study to determine pile resistances. New static analysis techniques and classification of IGM have been established by the authors (Islam et al., 2022a; Islam et al., 2022b; Masud et al., 2022a; Masud et al., 2022b; Masud et al., 2022c; Masud et al., 2023a; Masud et al., 2023b; Masud et al., 2023c; Masud 2024; Masud et al. 2024a, Masud et al. 2024b, Kalauni et al. 2024, Kalauni 2021). Those newly developed classification criteria and static analysis methods were implemented in the newly proposed WEAP methods for driven piles in IGM. This study also presents dynamic parameters of both soil based IGM (S-IGM) and rock based IGM (R-IGM) for application in various proposed WEAP methods. A total of 129 test piles (34 for S-IGMs and 95 for R-IGMs) were gathered from 7 seven different states to evaluate the WEAP methods, and 46 separate test piles (22 for S-IGMs and 24 for R-IGMs) were used to assess the performance of the WEAP methods. In order to obtain the desired reliability, the calibrated LRFD resistance factors ( $\phi$ ) were recommended for four WEAP methods utilizing three probability-based methods: the Factor of Safety Method FOSM, the FORM, and Monte Carlo Simulation (MCS). Thus, 129 historical pile load test data from 45 bridge projects completed in five states were used to 1) evaluate the performance of the four WEAP methods, 2) propose new damping parameters for driven piles in R-IGM, and 3) establish LRFD recommendations for R-IGM for different WEAP methods

## 8.2 Existing Wave Equation Analysis of Pile Driving

WEAP was developed based on a numerical solution of the one-dimensional wave equation (Smith, 1960; Goble & Rausche, 1976). WEAP has been widely used to determine drivability, static and ultimate pile resistances, and integrity of piles in soils. WEAP has been recognized as a reliable and economical construction control method that analyzes the compatibility of driving equipment with pile and soil conditions (Lawton et al., 1986). WEAP uses a series of lumped masses, springs, and dashpots to simulate the pile driving system and geomaterials. The Smith model accounts for the static and dynamic soil behaviors using the Smith parameters: shaft quake ( $Q_s$ ), toe quake ( $Q_t$ ), shaft damping ( $J_s$ ), and toe damping ( $J_t$ ). Smith parameters can be determined using the results of Static Load Tests (SLTs) and dynamic load tests with PDA and CAPWAP. However, this indeterminate problem in WEAP results in many combinations of  $Q_s$ ,  $Q_t$ ,  $J_s$ , and  $J_t$  to match a target pile resistance (Forehand & Reese, 1964).

Several studies have been performed to determine the Smith parameters, primarily for soils (Table 8.1). Liang and Sheng (1993) provided theoretical expressions for the Smith soil parameters regarding pile penetration velocities, accelerations, pile size, and soil properties. McVay and Kuo (1999) expressed the Smith parameters for piles in soil and limestone in terms of the Standard Penetration Test (SPT) N-value and rated hammer energy. A back-calculation analysis performed by Thendean et al. (1996) showed scattered back-calculated dynamic parameters and a relatively large average value of  $J_t=0.2$  s/ft for piles driven onto soft, weathered rock, or shale.

The SPT N-value based (SA) method is widely used as a geomaterial input procedure in WEAP. The SA method allows the user to input the SPT N-value of the geomaterial and uses prediction equations to determine other soil parameters in the calculation of the unit shaft resistance ( $q_s$ ) and unit end bearing ( $q_b$ ). Assigning an IGM in the SA method poses a challenge as there is no option for selecting IGM as a geomaterial. In addition, the WEAP SA method limits the maximum  $q_s$  (1.57 ksf for clay, 1.57 ksf for non-cohesive silt, 5.22 ksf for cohesive silt and 5.22 ksf for sand/gravel) and  $q_b$  (67.67 ksf for clay, 125.31 ksf for silt and 250.63 ksf for sand/gravel) to soils. However, the unit resistances of IGM could exceed these limits (Islam et al. 2022a, Islam et al. 2022b, Masud et al. 2023a). Treating the IGM as soil can underpredict pile resistance and create several construction challenges, such as early pile refusal and pile damage (Ng et al. 2019). Alternatively, the “Rock” input option in WEAP can be used for R-IGM. However, static analysis methods were not readily available to determine the  $q_s$  and  $q_b$  for R-IGM that can be manually input into the WEAP analysis. The challenge is further exacerbated when Smith parameters, originally developed for soils, were adopted for IGM. The WEAP program adopts the recommendations by Hannigan et al. (1998) (Table 8.1) and  $Q_t=0.04$  in for hard rock. The IGM can be treated as a cohesive geomaterial if  $q_u$  is inputted and a non-cohesive geomaterial if  $\phi$  is inputted. Despite these challenges, dynamic parameters for IGM have yet to be recommended.

**Table 8.1. Summary of Smith Parameters for Soils and Rocks from Previous Studies.**

Source	Smith (1962)	Coyle and Gibson (1970)	Coyle <i>et al.</i> (1973)	Hannigan <i>et.al</i> (1998)	Liang and Sheng (1993)	McVay and Kuo (1999)
$Q_s$	0.10 in	NA	0.10 in	0.10 in	$\frac{f_s r_0}{G} \ln \left( \frac{r_m}{r_0} \right)$	$e^{\left( \frac{B}{A \frac{E_r}{N_s} - 1} \right)}$
$Q_t$	0.10 in	NA	0.10 in	D/120 (very dense/hard soil); D/60 (soft soils); 0.04 in (hard rock)	$\frac{1 + \nu}{2E} p_y \left( \frac{D}{2} \right)$	$e^{\left( \frac{B}{A \frac{E_r D}{N_t^{12}} - 1} \right)}$
$J_s$	0.05 s/ft	NA	0.2 s/ft (clay); 0.05 s/ft (sand); 0.10 s/ft (silt)	0.20 s/ft (cohesive soil); 0.05 s/ft (non-cohesive soil)	1/3 of toe damping	$e^{\left( \frac{B}{A \frac{E}{N_s} - 1} \right)}$
$J_t$	0.15 s/ft	$\frac{1}{V^N} \left( \frac{P_d}{P_s} - 1 \right)$	0.01 s/ft (clay); 0.15 s/ft (sand and silt)	0.15 s/ft for all soils	$\frac{\rho}{3f_t} \left( 2r_0 \frac{\dot{v}_p}{v_p} + 3v_p \right)$	$e^{\left( \frac{B}{A \frac{E D}{N_t^{12}} - 1} \right)}$

$Q_s$  = Shaft quake;  $Q_t$  = Toe quake;  $J_s$  = Shaft damping;  $J_t$  = Toe damping; NA = Not Available;  $V$  = Velocity of soil deformation;  $P_d$  = Peak dynamic load;  $P_s$  = Peak static load;  $N$  = Exponential power modification (0.2 for sand and 0.18 for clay);  $f_s$  = Unit shaft resistance;  $r_0$  = Radius of pile;  $r_m$  = Radius of influence zone;  $G$  = Average shear modulus in the influence zone;  $\nu$  = Soil Poisson's ratio;  $E$  = Elastic modulus of soil;  $p_y$  = Yielding stress on cavity;  $D$  = Pile diameter (mm);  $\rho$  = Soil density;  $f_t$  = Unit toe resistance;  $\dot{v}_p$  = Pile penetration acceleration;  $v_p$  = Pile penetration velocity;  $A, B$  = Regression constants (McVay and Kuo, 1999);  $N_s$  = Weighted average skin SPT N-value;  $N_t$  = Weighted average toe SPT N- value; and  $E_r$  = Rated energy of SPT hammer.

### 8.3 Test Pile Data

This study uses 129 usable historical test pile data collected from Wyoming, Montana, Idaho, Iowa, Kansas, North Dakota, and Colorado. All piles were driven through overburden soils and soil-based IGM (S-IGM) onto R-IGM. This dataset is usable because it contains relevant subsurface, PDA, CAPWAP, pile, hammer, and driving information. The respective boring logs and geotechnical reports have the relevant geomaterial properties including N-value, unit weight ( $\gamma$ ),  $s_u$ ,  $\phi$ , and  $q_u$ . These usable test piles were used in the back-calculation of damping factors and calibration of LRFD resistance factors. Table 8.2 shows 34 test piles driven into soil based IGM only and Table 8.3 shows the 95 test piles driven to rock based IGM.

### 8.4 WEAP Procedures for Bearing Graph Analysis

Bearing graph studies were carried out on all usable 129 test piles using the WEAP SAD, WEAP UWD, WEAP SAR, and WEAP UWR methods. The abbreviations "SA" and "UW" were denoted as the standard SPT N-value based approach and the proposed static analysis methods, respectively. The "R" stands for recommended smith parameters derived from the back-calculation technique, whereas the "D" stands for the WEAP recommended Smith parameters. The subsections explicitly describe the four WEAP methods, which were illustrated in Figure 8.1.

#### 8.4.1 WEAP SAD Method

The default SA input procedure was used for inputting soil properties and predicting shaft resistance of overburden soils along each test pile. For the S-IGM and R-IGM, the following geomaterial input procedures were proposed and adopted.

##### 8.4.1.1 Soil Based IGM

- SPT N-value  $\leq 60$ : N-value and  $\gamma$  were used to define the geomaterial.
- SPT N-value  $> 60$  for coarse-grained soil-based IGM:  $\phi$  and  $\gamma$  define the geomaterial.
- SPT N-value  $> 60$  for fine-grained soil-based IGM:  $q_u$  and  $\gamma$  were used to define the geomaterial.

**Table 8.2. Summary of Historical Test Pile Data and Relevant Information for Soil Based IGM.**

St.	Project	Location	Pile Type	<i>L</i> (ft)	Bearing IGM	<i>S</i> (ft)	<i>B</i>	<i>R<sub>m</sub></i>	Hammer	WEAP SAD	WEAP UWD	WEAP UWR	WEAP SAR
WY	PB-Muddy Creek	P-1 at A-2	HP 12×53	53.6	ML*	7.4	109	381	Del D16-32	349.65	325.48	375.65	378.53
WY	PB-Muddy Creek	P-1 at B-2	HP 12×53	35.3	ML*	7.9	108	451	Del D16-32	365.21	351.22	428.87	420.44
WY	PB-Beech Street	P-1 at A-2	HP 12×53	44.7	ML*	6.8	62	286	Del D16-32	278.60	269.58	293.4	283.8
WY	PB-Beech Street	P-3 at A-2	HP 12×53	46.4	ML*	7.6	82	305	Del D16-32	323.76	306.28	342.78	328.83
WY	PBME (Parson Street)	PS P-4 at A-1	HP 12×53	73.2	ML*	6.3	32	333	APE D 30-32	342.86	333.45	295.92	300.25
WY	PBME (Parson Street)	PS P-3 at A-2	HP 12×53	70	ML*	6.7	35	325	APE D 30-32	371.13	367.6	315.06	322.24
WY	PBME (Beech Street)	BS P-2 at A-2	HP 12×53	41	ML*	5.8	35	332	APE D 30-32	365.28	357.47	345.12	347.62
WY	Hunter Creek	P-3 at A-2	HP 12×53	19.5	Sand <sup>#</sup>	5.5	850	245	MKT DE 40	295.47	288.81	402.7	402.7
WY	Hunter Creek	P-2 at A-1	HP 12×53	36	Sand <sup>#</sup>	6.3	63	227	MKT DE 40	211.35	225.10	230.51	230.99
WY	Elk Fork Creek	P-5 at A-2	HP 14×73	40	Sand <sup>#</sup>	8.2	49	405	ICE 42S	200.31	211.83	402.7	402.7
MT	Clark's Fork	P-1 at A-2	HP 14×73	45	Sand, G <sup>#</sup>	7	119	440	Del. D 19-42	472.83	362.9	445.96	460.5
MT	M FK Porcupine CK	P-4 at B-1	OEP 16"	47.3	MH*	8	23	318.3	ICE I-30	274.3	274.30	334.92	334.92
MT	Cottonwood Creek	P-3 at B-1	OEP 20"	136.5	CH*	9.5	313	649.3	ICE I-36	726.91	737.12	644.11	636.55



MT	Capitol Interchange	P-47 at B-4	CEP 16"	32.2	SC, G <sup>#</sup>	8.8	37	650.9	ICE I-36	527.30	552.60	650.95	653.82
MT	Capitol Interchange	P-8 at B-5	CEP 16"	48.5	SC, G <sup>#</sup>	8.8	32	506.4	ICE I-36	514.43	515.60	518.82	526.02
MT	Capitol Interchange	P-8 at B-1	CEP 16"	29	SC <sup>#</sup>	8.7	48	482.9	ICE I-30	381.00	381.47	526.87	545.4
MT	Capitol Interchange	P-2 at B-1	CEP 16"	27.9	SC <sup>#</sup>	10	60	668.4	ICE I-30	457.71	454.34	600.26	598.26
MT	Capitol Interchange	P-11 at B-5	CEP 16"	48.2	SC <sup>#</sup>	9.5	74	549	ICE I-30	644.12	678.97	527.26	528.2
MT	Capitol Interchange	P-11 at B-5	CEP 16"	48.2	SC <sup>#</sup>	9.5	74	549	ICE I-30	644.12	678.97	527.26	528.2
MT	Capitol Interchange	P-1 at B-1	CEP 16"	29.5	SC, G <sup>#</sup>	9.4	30	522.2	ICE I-36	478.20	484.30	472.71	475
MT	Capitol Interchange	P-38 at B-4	CEP 16"	27.5	SC, G <sup>#</sup>	8.8	44	570.5	ICE I-30	469.38	479.70	535.08	537.92
MT	Capitol Interchange	P-1 at B-1	CEP 16"	29.5	SC, G <sup>#</sup>	9.4	30	522.2	ICE I-36	478.20	484.30	472.71	475
MT	Capitol Interchange	P-38 at B-4	CEP 16"	27.5	SC, G <sup>#</sup>	8.8	44	570.5	ICE I-30	469.38	479.70	535.08	537.92
ID	US-95 WR Bridge	P-10 at Pi-1	HP 14×117	41.6	CH <sup>*</sup>	9.4	590	948	ICE I-30	800.25	778.63	905.84	929.54
ID	SH-55 SR bridge	P-3 at Pi-1	HP 14×117	56.2	CL <sup>*</sup>	8.2	1158	937.1	Del D 36-32	827.68	907.74	968.47	944.82
ID	SH-55 SR bridge	P-1 at Pi-4	HP 14×117	20	CL <sup>*</sup>	8	333	942.2	Del D 36-32	988.06	990.3	1199.05	1199.77
ID	SH-55 SR bridge	P-1 at Pi-5	HP 14×117	34	CL <sup>*</sup>	7.6	144	791.7	Del D 36-32	614.5	605.7	702.03	703.59
ID	SH-55 SR bridge	P-10 at A-2	HP 14×117	33.2	ML <sup>*</sup>	7.7	105	939.3	Del D 36-32	675.84	675.46	830.85	828.2

ID	SH-55 SR bridge	P-4 at A-1	HP 14×117	56.4	CH*	6.4	420	1001.5	Del D 36-32	657.35	700.73	733.27	721.18
ID	SH-55 SR bridge	P-1 at Pi-2	HP 14×117	48	CH*	7.9	71	765.1	Del D 36-32	607.76	606.50	678.02	668.17
ID	SH-55 SR bridge	P-2 at Pi-3	HP 14×117	35	SM <sup>#</sup>	7.7	72	717.1	Del D 36-32	634.91	630.95	684.81	709.15
ID	SH-51 SR Bridge	P-1 at A-1	HP 14×117	68.9	ML*	8.4	73	635	ICE I-30 V2	700.76	648.5	698.16	698.26
ID	SH-51 SR Bridge	P at A-2	HP 14×117	68.9	ML*	9	52	579.6	ICE I-30 V2	639.46	649.06	667.27	646.71
ID	SH-28 Lemhi River	P-2 at A-1	HP 14×89	41	GP-GM <sup>#</sup>	7.5	16	386.8	Pileco 30-32	246.33	231.48	251.30	251.28
ID	SH-52 UPPR Bridge	P-4 at A-1	HP 14×117	42.9	SP-SM <sup>^</sup>	8.5	31	502.2	ICE I-30 V2	682.13	588.56	608.62	586.06

PBME = Pine Bluffs Marginal EBL; SR = Snake river; *L* = Penetration length; Del = Delmag; A = Abutment; B = Bent; Pi = Pier; P = Test pile; *S* = Stroke height; *B* = Blow count (b/ft); EOD = End of Driving; *R<sub>m</sub>* = CAPWAP measured pile capacity at EOD; HP = H pile; CEP = Closed end pile; OEP = Open ended pile; CL = Lean clay; CH = Fat clay; MH = High plasticity silt; ML = Low plasticity silt; SC = Clayey sand; SM = Silty sand; Sand, G = Sand with gravel; SC, G = Clayey sand with gravel; GP-GM = Poorly graded gravel with silt; SP-SM = Poorly graded sand with silt; \* = Fine-grained soil-based IGM; <sup>#</sup> = Coarse-grained soil-based IGM; and <sup>^</sup> = Coarse-grained soil.

**Table 8.3. Summary of Historical Test Pile Data and Relevant Information for Rock Based IGM.**

St.	Project	Location	Pile Type	L(ft)	Bearing IGM	S (ft)	B	Rm	Hammer	WEAP SAD	WEAP UWD	WEAP UWR	WEAP SAR
CO	Interstate Highway No. 70	TP1 at A4	HP 12×74	35	Claystone	7.5	40	499.5	APE D30-32	366.22	362.98	446.06	452.55
ID	US-95S Snake River Bridge	P2 at A1	HP 14×117	37	Siltstone	6.9	58	360	Delmag D 19-42	253.97	249.1	319.78	319.56
ID	US-95S Snake River Bridge	P1 at A2	HP 14×117	36	Siltstone	7.5	187	550	Delmag D 19-42	512.99	444.74	675.52	675.22
ID	US-95S Snake River Bridge	P32 at A2	HP 14×117	37	Siltstone	8	118	520	Delmag D 19-42	381.85	321.5	608.36	606.26
ID	SH-31 Pine Creek Bridge	P1 at A1	HP 12×74	25.5	Sandstone	9	751	898.4	APE D30-42	907.3	804.1	912.14	917.4
ID	SH-31 Pine Creek Bridge	P10 at A2	HP 12×74	32.2	Siltstone	7.4	64	730.8	APE D30-42	546.64	533.5	574.6	566.67
ID	SH-28 13416 LR Bridge	P1 at A2	HP 14×89	45.5	Mudstone	7.5	25	324.9	Diesel 30-32	309.17	284.63	301.8	308.31
ID	SH-28 LR Bridge	P2 at A2	HP 14×89	64	Siltstone	9	64	536.6	ICE I30 v2	476.52	476.5	543.08	542.93
ID	SH-28 13416 LR Bridge	P1 at A1	HP 14×89	48	Claystone	7.5	26	459.9	Diesel 30-32	330.84	310.1	317.01	322.7
ID	SH-28 13436 LR Bridge	P1 at A2	HP 14×89	38.7	Siltstone	10.0	1451	1139.1	Diesel 30-32	997.92	997.92	1084.11	1090.69
KS	Maple Street over I-135	Pi 2-SB	HP 10×42	80	Shale	5.5	28	190.2	Delmag D 19-32	204	181.16	186.46	185.85
KS	US 24 over Huntress creek	Pi 2	HP 12×74	59.9	Shale	9	62	354.6	Delmag D 19-42	320.42	333.72	393.65	346.6

KS	K-4 over Cow Creek Drainage	Pi 2	HP 12×63	72	Shale	8	102	264.2	Delmag D 19-42	322.3	321.53	355.48	352.92
KS	Ramp B-NB-I-235 to EB US54/400	Pi 1	HP 12×53	73	Shale	7	30	279.4	Delmag D 30-02	305.6	275.03	293.28	321.68
KS	Ramp H-NB & SB I-235 to EB US54/400	Pi 3	HP 12×53	73	Shale	8.7	18	285.8	Delmag D 30-02	253.02	276.74	296.47	280
KS	Ramp H-NB & SB I-235 to EB US54/400	Pi 6	HP 12×63	68	Shale	8.75	24	411	Delmag D 30-02	273.53	265.16	319.15	315.22
KS	Ramp H-NB & SB I-235 to EB US54/400	Pi 6A	HP 12×74	69	Shale	8.5	20	311.3	Delmag D 30-02	253.48	274.4	302.67	266.47
KS	Ramp H-NB & SB I-235 to EB US54/400	Pi 6B	HP 12×74	70	Shale	8.75	80	543.7	Delmag D 30-02	510.1	489.56	523.4	531.3
KS	Ramp D-I-235 to EB US54/400	Pi 2	HP 12×74	47	Shale	7.75	34	530.7	Delmag D 30-02	328.2	329.74	396.8	397.17
KS	Ramp D-I-235 to EB US54/400	Pi 3	HP 12×84	33.7	Shale	6.5	25	342.3	Delmag D 30-02	253.98	228	263.97	277.41
KS	Ramp D-I-235 to EB US54/400	A1	HP 12×63	81	Shale	7.5	87	478.5	Delmag D 30-32	513.25	444.23	476.55	520.58
KS	Maple Street over I-135	Pi 1-NB	HP 10×42	84	Shale	6.5	51	280.1	Delmag D 30-32	399.22	213.3	257.11	280.23
KS	I-235 Floodway Crossing/13th st Interchange	Pi 1	HP 12x74	53	Shale	6.5	27	332.5	Pileco D30-32	322.86	313.62	328.3	352.28
KS	I-235 Floodway Crossing/13th st Interchange	Pi 3	HP 12x74	61	Shale	7.3	26	337.2	Pileco D30-32	288.33	295.26	363.16	332.65
KS	I-235 Floodway Crossing/13th st Interchange	Pi 4	HP 12x63	50	Shale	7.2	34	390.7	Pileco D30-32	326.04	335.94	376.5	401.3
KS	I-235 Floodway Crossing/13th st Interchange	Pi 5	HP 12x74	46	Shale	7.8	27	329.7	Pileco D30-32	291.78	293.77	335.34	326.96

KS	I-235 Floodway Crossing/13th st Interchange	Pi 10	HP 12x63	47	Shale	8.25	28	337.8	Pileco D30-32	338.1	324.07	387.68	369.4
KS	I-235 Floodway Crossing/13th st Interchange	Pi 11	HP 12x74	50	Shale	8.5	32	325.7	Pileco D30-32	247.12	284.83	313.8	298.38
KS	I-235 Floodway Crossing/13th st Interchange	Pi 6	HP 12x74	35	Shale	7	54	447	Pileco D30-32	419.56	399.59	445.46	473.96
KS	K-18 over US-77	A1	HP 12x63	60	Shale	9	128	412.9	Delmag D 16-32	398.67	398.67	436.7	410.78
KS	K-18 over US-77	Pi 1	HP 12x63	47	Shale	7.25	640	448.4	Delmag D 16-32	378.22	405.52	450.16	436.23
KS	Ramp B-NB-I-235 to EB US54/400	Pi 4A	HP 10x42	68	Shale	8	36	341.4	Delmag D 16-32	338.35	348.52	364.7	360.8
KS	Ramp B-NB-I-235 to EB US54/400	A1	HP 12x63	80	Shale	8	53	284.9	Delmag D 30-02	300	277.07	283.61	294.44
KS	Ramp D-I-235 to EB US54/400	A2	HP 12x53	87	Shale	7	40	324.9	Delmag D 30-02	370.21	344.11	374.71	399.63
KS	Maple Street over I-135	A1- NB	HP 10x42	105	Shale	7.25	60	249	Delmag D 30-32	290.32	227.27	274.16	273.81
KS	I-235 Floodway Crossing/13th st Interchange	Pi 7	HP 12x74	45	Shale	7.2	23	318	Pileco D30-32	243.62	249.18	296.88	291.43
KS	I-235 Floodway Crossing/13th st Interchange	Pi 8	HP 12x74	61	Shale	8	34	512.7	Pileco D30-32	365.41	363.59	425.82	430.74
KS	I-235 Floodway Crossing/13th st Interchange	Pi 2	HP 12x63	59	Shale	8.3	17	269.9	Pileco D30-32	278.1	292.22	328.9	298.68
KS	I-235 Floodway Crossing/13th st Interchange	Pi 4	HP 12x63	52	Shale	7.2	26	348.8	Pileco D30-32	265.07	281.65	324.05	319.86

KS	I-235 Floodway Crossing/13th st Interchange	Pi 5	HP 12x74	54	Shale	8.2	28	347.7	Pileco D30-32	299.15	314	348.65	338.51
KS	I-235 Floodway Crossing/13th st Interchange	Pi 9	HP 12x63	58	Shale	7.2	25	420.5	Pileco D30-32	292.98	287.68	323.57	334.48
KS	K-23 over Pawnee River	A2	HP 10x42	58	Shale	7.75	59	329.4	Delmag D 19-42	235.71	228.21	249.44	235.76
KS	K-23 over Pawnee River	Pi 1	HP 12x63	50	Shale	8	160	483	Delmag D 12-42	319.56	246.5	353	327.97
KS	K-23 over Pawnee River	Pi 3	HP 12x63	50	Shale	9.5	120	475.4	Delmag D 12-42	324.78	352	369.9	353.34
KS	US-183 over Day creek	Pi 1 (43)	HP 14x73	94	Shale	8	87	310.5	APE 19-42	456.46	455.12	465	456.33
KS	Ramp H-NB and SB-I-235 to EB US54/400	Pi 2	HP 12x74	68	Shale	8.25	27	412.5	Delmag D 30-02	312.26	320.97	344.8	342.67
KS	Maple Street over I-135	A1 - SB	HP 10x42	105	Shale	5.5	192	335.5	Delmag D 19-32	298.74	252.36	255.17	281.6
KS	I-235 Floodway Crossing/13th st Interchange	P8	HP 12x74	61	Shale	6.5	16	372.2	Pileco D30-32	198	191.56	223.65	213.7
KS	K-4 over Cow Creek Drainage	A1	HP 10x42	79	Shale	7	46	245	Delmag D 19-42	237.33	252.8	225.76	224.91
KS	HP 10x42	A1	HP 12x53	26	Shale	5.5	48	340.5	Delmag D 19-42	193.79	181.89	236.15	212.93
MT	Bridge over Rock reek	P1 at B3	20" OEP	41	Claystone	8.9	42	498.8	ICE I-30	408.6	426.94	495.74	499.2
MT	Milk River - 4 KM West Of Zurich	P1 at B3	16" OEP w/ CS	76.2	Claystone	10.5	106	568.6	ICE I-30	598.2	614.46	580.02	580.87
MT	Bridge Over Home Creek	P1 at B1	16" PP w/ CP	42.2	Claystone	8.3	120	650	ICE I-30	666.46	620.43	653.43	663.46

MT	Bridge over Crooked Creek	P16 at B1	16" OEP w/ CS	20.7	Mudstone	7.6	74	677.4	ICE I-36	557.4	559.01	666.58	657.3
MT	Bridge over Crooked Creek	P2 at B4	16" OEP w/ CS	20	Mudstone	6.5	44	560	ICE I-36	384.35	384.6	495.45	491.69
MT	12 KM East of Jordan - East	P1 at B1	16" CEP	36.5	Claystone	9.5	192	699.6	ICE I-36	704.64	699.97	662.74	723.7
MT	12 KM East of Jordan - East	P8 at B2	24" OEP	27.8	Claystone	9.5	39	713	ICE I-36	580.52	578.88	697.21	693.08
MT	Bridge over Rock reek	P1 at B2	20" OEP	45	Claystone	10	73	666.9	ICE I-30	583.08	586.74	611.43	643.46
MT	Bridge Over Musselshell River	P7 at B2	24" OEP w/ CS	38.6	Claystone	9	120	913.6	APE D30-42	678.97	679.96	905.6	904.72
MT	Bridge over Butte Creek	P4 at B1	16" PP w/ CP	28.34	Claystone	7.5	238	451.5	Delmag D19-42	479.44	480.01	593.01	581.45
MT	Bridge Over BNSF	P5 at A1	HP 14×117	68	Claystone	9.3	96	496.5	ICE I 30-V2	610.48	603.79	609.75	603.4
MT	Bridge Over BNSF	P1 at A4	HP 14×117	69.4	Claystone	9.3	96	498.4	ICE I 30-V2	546.92	583.21	632.67	576.2
MT	Milk River - 4 KM West Of Zurich	P6 at B2	16" OEP w/ CS	50.3	Claystone	10.5	87	617.9	ICE I-30	636.75	639.77	686.34	671.23
MT	M FK Porcupine CK-11M S Opheim	P2 at B3	20" OEP	46.2	Siltstone	8.2	35	315.1	ICE I-30	378.23	367.45	428.73	438.96
MT	Bridge over Milk River	P3 at B4	20" OEP w/ CS	93.5	Mudstone	10.6	189	793.57	ICE I-36	787.36	824.53	914.23	836.28
MT	Bridge over Milk River	P1 at B1	20" OEP w/ CS	91.54	Mudstone	10.8	172	808	ICE I-36	796.97	817.44	925.11	885.77
MT	Milk River - 4 KM West Of Zurich	P1 at B1	16" OEP	82.2	Claystone	10	74	552.20	ICE I-30	506.64	502.44	531.11	536.11
MT	Bridge Over Warm Spring Creek	B2	24" CEP	35.3	Claystone	11.2	120	1176.92	ICE I-62	1370.85	1399.58	1594.5	1609.65

MT	Bridge Over Musselshell River	P1 at B1	16 OEP w/CS	25	Claystone	9.8	120	652.90	APE D30-42	731.60	732.86	834.9	848.26
MT	Bridge over cherry creek	P4 at B3	24" OEP	57.97	Siltstone	11.5	135	866.78	ICE I-36	876.13	829.34	921.21	888.75
MT	Bridge over Lodge Grass Creek	P4 at B2	HP 14×89	30	Sandstone	8.8	100	525.6	Delmag D19-32	377.27	397.61	497.9	501.96
MT	Bridge Over Big Powder River	B2	24" OEP	33	Sandstone	9.8	960	1707.9	Delmag D62-22	1805.07	1805.24	2100.3	2108.4
MT	Bridge over Clarks Fork of Yellowstone River	B1	HP 14×89	32.61	Shale	9.5	315	674.4	ICE 80S	700.47	748.06	846.13	878.21
MT	Musselshell RV-7 M NE Roundup	P4 at B3	16" OEP	24.5	Clayey Sandstone	10.75	112	562.8	APE D 30-42	678.49	678.49	934.8	940.91
MT	Bridge Over Red Bank Creek	P3 at B2	16" OEP	36.1	Interbedded Mudstone/Sand stone	7.9	50	506	ICE I-36	499.95	499.95	611.6	616.32
MT	Bridge over Big Muddy Creek	P3 at B6	16" OEP	26.6	Shale	10.9	240	1274.8	ICE I-36	855.97	865.65	937.03	935.4
MT	Bridge over Sharpy Creek	P4 at B2	16" CEP	32.5	Sandy Shale	8.15	109	444.8	Delmag D19-32	381.6	381.6	493.65	491.57
WY	Woods Wardel	P1 at Pi2	HP 12×53	23	Claystone	7.5	128	450	APE D19-42	284.56	324.8	455.34	560.68
WY	Cedar Street	P5 at A2	HP 12×53	41.2	Sandstone	8.3	60	279	MVE M-19	302.27	304.81	291.81	303.58
WY	Laramie Streets (UPRR Overpass Section)	122N	HP 12×53	28.7	Siltstone	10.9	160	665	APE D19-52	604.34	618.04	668.96	672.58
WY	Laramie Streets (UPRR Overpass Section)	119O	HP 12×53	27.8	Siltstone	10.4	131	640	APE D19-52	562.32	586.83	628.75	633.47
WY	Laramie Streets (UPRR Overpass Section)	9S	HP 12×53	15.3	Siltstone	9.7	144	525.4	APE D19-52	579.32	583.92	666.32	669.52



WY	Laramie Streets (UPRR Overpass Section)	11S	HP 12×53	15.3	Siltstone	9.4	168	534.4	APE D19-52	590.64	644.48	675.9	680.04
WY	Burns South	P1 at Pi3	HP 14×73	37.6	Sandstone	6.2	100	370	Delmag D 16-32	319.97	320.03	372.27	373.11
WY	PB-Parson Street	P5 at A1	HP 12×53	87.9	Siltstone	7.5	164	310	Delmag D 16-32	360.15	340.66	318.47	345.11
WY	PB-Beech Street	P1 at A1	HP 12×53	46.7	Siltstone	7.1	55	266	Delmag D 16-32	283.2	275.42	271.63	271.48
WY	PB-Beech Street	P5 at A1	HP 12×53	46.9	Siltstone	7.1	66	286	Delmag D 16-32	300.88	292.4	289.41	288.34
WY	Casper Street	P1 at A2	HP 14×73	24.3	Sandstone	10.2	84	340.00	MVE M-19	431.57	430.85	443.22	448.16
WY	PB-Muddy Creek	P10 at B3	HP 12×53	38	Siltstone	10.1	240	671.00	Delmag D16-32	479.68	450.52	511.9	500.95
WY	N. Fork Shoshone River, Pahaska	P3 at A1	HP 14×73	41	Sandstone	8.4	114	514.00	ICE 42-S	317.14	332.45	366.7	346.56
WY	Woods Wardell Road Bridge	P1 at Pi2	HP 12×53	23	Claystone	7.5	128	450	APE D19-42	284.56	324.8	455.34	560.68
WY	Burns South	P1 at A1	HP 14×73	68.3	Sandstone	8	452	505.00	Delmag D16-32	551.86	551.86	550.75	541.02
WY	N. Fork Shoshone River, Pahaska	P3 at A2	HP 14×73	32	Sandstone	8.7	1125	385.00	ICE 42-S	481.33	481.33	570.23	595.66
WY	Owl Creek	P5 at B2	HP 14×73	27	Shale	7.68	263	337	ICE 42-S	308.3	308.34	381.62	341.81
WY	Casper Street	P17 at Pi1	HP 14×89	20.5	Shale	9.8	118	500	MVE M-19	383.24	468.55	468.16	470.86

St. = State; PBME = Pine Bluffs Marginal EBL; SR = Snake river;  $L$  = Penetration length; Del = Delmag; A = Abutment; B = Bent; Pi = Pier; P = Test pile;  $S$  = Stroke height;  $B$  = Blow count (b/ft); EOD = End of Driving;  $R_m$  = CAPWAP measured pile capacity at EOD; HP = H pile; CEP = Closed end pile; OEP = Open ended pile;

#### *8.4.1.2 Rock based IGM:*

- If  $q_u$  was available:  $q_u$  and  $\gamma$  is used to define the geomaterial.
- If  $q_u$  is not available and SPT N-value  $\leq 60$ : the rock-based IGM is simulated as its constituent geomaterial, and SPT N-value and  $\gamma$  were used to define the geomaterial.
- If  $q_u$  is not available and SPT N-value  $> 60$ : the rock-based IGM is simulated as its constituent geomaterial. The  $\phi$  and  $\gamma$  values were used to define the geomaterial for the R-IGM with major constituents of coarse-grained geomaterials (sandstone). The  $q_u$  and  $\gamma$  were used to define the geomaterial for the R-IGM with major constituents of fine-grained geomaterials (mudstone, claystone, siltstone, and shale).

The WEAP recommended unit resistances and Smith parameters were assigned to the respective IGM. The percentage shaft resistance determined from a drivability analysis was used as an input in the bearing graph analysis.

#### ***8.4.2 WEAP UWD Method***

The default SA input procedure was used for inputting soil properties and predicting shaft resistance of overburden soils along each test pile. For both S-IGM and R-IGM, the unit resistances determined using the proposed prediction equations (Table 8.4) were manually inputted via the “SA input form” for individual IGM layers. The WEAP recommended Smith parameters (Table 8.1) were assigned to the soil and IGM based on the description of IGM and pile type. The new percentage shaft resistance determined from a drivability analysis was used as an input in a bearing graph analysis.

#### ***8.4.3 WEAP SAR Method***

The default SA input procedure was used for inputting soil properties and predicting shaft resistance of overburden soils along each test pile. For both S-IGM and R-IGM, the geomaterial input procedures explained in the WEAP SAD method were used. The major difference between the WEAP SAR and WEAP SAD methods was that WEAP SAR uses the back-calculated dynamic parameters discussed in the following section. The back-calculated dynamic parameters

were manually inputted for each geomaterial layer using the “pile segment” and “soil segment damping/quake” options in the WEAP analysis.

**Table 8.4. Proposed Static Analysis Methods for Predicting Unit Resistances in IGM.**

IGM	Prediction Equation
ML-IGM	$\hat{q}_s = \left[ \frac{1.80}{1 + 44e^{-0.89 \frac{s_u}{P_a}}} \right] P_a$
CL-IGM	$\hat{q}_s = \left[ \frac{1.58}{1 + 47.6e^{-1.34 \frac{s_u}{P_a}}} \right] P_a$
CH-IGM	$\hat{q}_s = \left[ \frac{2}{1 + 50.4e^{-1.4 \frac{s_u}{P_a}}} \right] P_a$
CG-IGM	$\hat{q}_s = \left[ \frac{1.21}{1 + 12.62e^{-4.06 \left( \frac{\sigma'_v}{P_a} \frac{58}{(N_1)_{60}} \right)}} \right] P_a$
CG-IGM	$\hat{q}_s = \left[ \frac{\frac{\sigma'_v}{P_a} \frac{58}{(N_1)_{60}}}{0.105 + 0.52 \frac{\sigma'_v}{P_a} \frac{58}{(N_1)_{60}}} \right] P_a$
SS-shale	$\hat{q}_s = \frac{3.523 q_u}{(8.6 + q_u)^{1.05}}$
HW-shale	$\hat{q}_s = 0.23 q_u^{0.45}$
MW-shale	$\hat{q}_s = \frac{1.196 q_u}{(0.5 + q_u)^{0.83}}$
SW-shale	$\hat{q}_s = \frac{2.62 q_u}{(0.467 + q_u)^{0.945}}$
Siltstone	$\hat{q}_s = 0.45 q_u^{0.44}$
	$\hat{q}_s = 0.42 P_a \left[ \frac{(N_1)_{60}}{16} \right]^{0.63}$
Claystone	$\hat{q}_s = 0.74 q_u^{0.305}$
Mudstone	$\hat{q}_s = 6.19 \left[ 1 - e^{(-0.052 \frac{N}{19} \times \sigma'_v)} \right]$
Sandstone	$\hat{q}_s = 0.56 q_u^{0.37}$
Sandstone (for layers without $q_u$ )	$\hat{\beta} = 0.0098\phi^2 - 0.75\phi + 14.63; \hat{q}_s = \hat{\beta} \sigma'_v$
FG-IGM	$\hat{q}_b = \left[ \frac{\frac{s_u}{P_a} \times \frac{D}{D_B}}{0.001 + 0.0027 \frac{s_u}{P_a} \times \frac{D}{D_B}} \right] P_a$
CG-IGM	$\hat{q}_b = 93.76 P_a \left[ \frac{p_a}{\sigma'_v} \frac{(N_1)_{60}}{58} \right]^{0.22}$
SS-HW Shale	$\hat{q}_b = 45.72 q_u^{0.35}$
MW-SW Shale	$\hat{q}_b = \frac{190.64 q_u}{(1 + q_u)^{0.88}}$
Siltstone	$\hat{q}_b = 12.9 P_a \left[ 2.43 \left( \frac{32.4 N}{30 D_B} \right) \right]$
Claystone	$\hat{q}_b = \frac{313.27 q_u}{20.96 + q_u}$
Sandstone	$\hat{N}_t = 0.907\phi^2 - 71.399\phi + 1428.55; \hat{q}_b = \hat{N}_t \sigma'_v$

ML=silt with low plasticity; CL=clay with low plasticity; CH=clay with high plasticity; CG=coarse grained soil based IGM; SS=soil-based shale; HW=highly weathered shale; MW=moderately weathered shale; SW=slightly weathered shale;  $q_u$ =unconfined compressive strength;  $(N_1)_{60}$ =corrected SPT N values;  $\hat{\alpha}$ ,  $\hat{N}_c$ =calibrated coefficients for  $\alpha$  method;  $\hat{\beta}$ ,  $\hat{N}_t$ = calibrated coefficients for  $\beta$  method;  $\phi$ = friction angle.  $s_u$ =undrained shear strength;  $P_a$ =atmospheric pressure=2.12 ksf;  $D$ =pile dimension or diameter;  $D_B$ =total pile penetration;  $\hat{q}_s$ =predicted unit shaft resistance; and  $\hat{q}_b$ =predicted unit end bearing.

#### **8.4.4 WEAP UWR Method**

The default SA method was used to predict the  $q_s$  of overburden soils. The proposed static analysis methods were used to predict the  $q_s$  of the overburden S-IGM and the  $q_s$  and  $q_b$  of R-IGM. These predicted values of  $q_s$  and  $q_b$  for IGM were manually inputted into the WEAP. The recommended dynamic parameters determined from the back-calculation procedure, which were discussed in the following section, were manually inputted for each geomaterial layer using the “pile segment” and “soil segment damping/quake” options in the WEAP analysis. The bearing graph analysis was used to predict the ultimate pile resistance based on field measured hammer blow count for all the WEAP methods as illustrated in the flowchart (Figure 8.1).

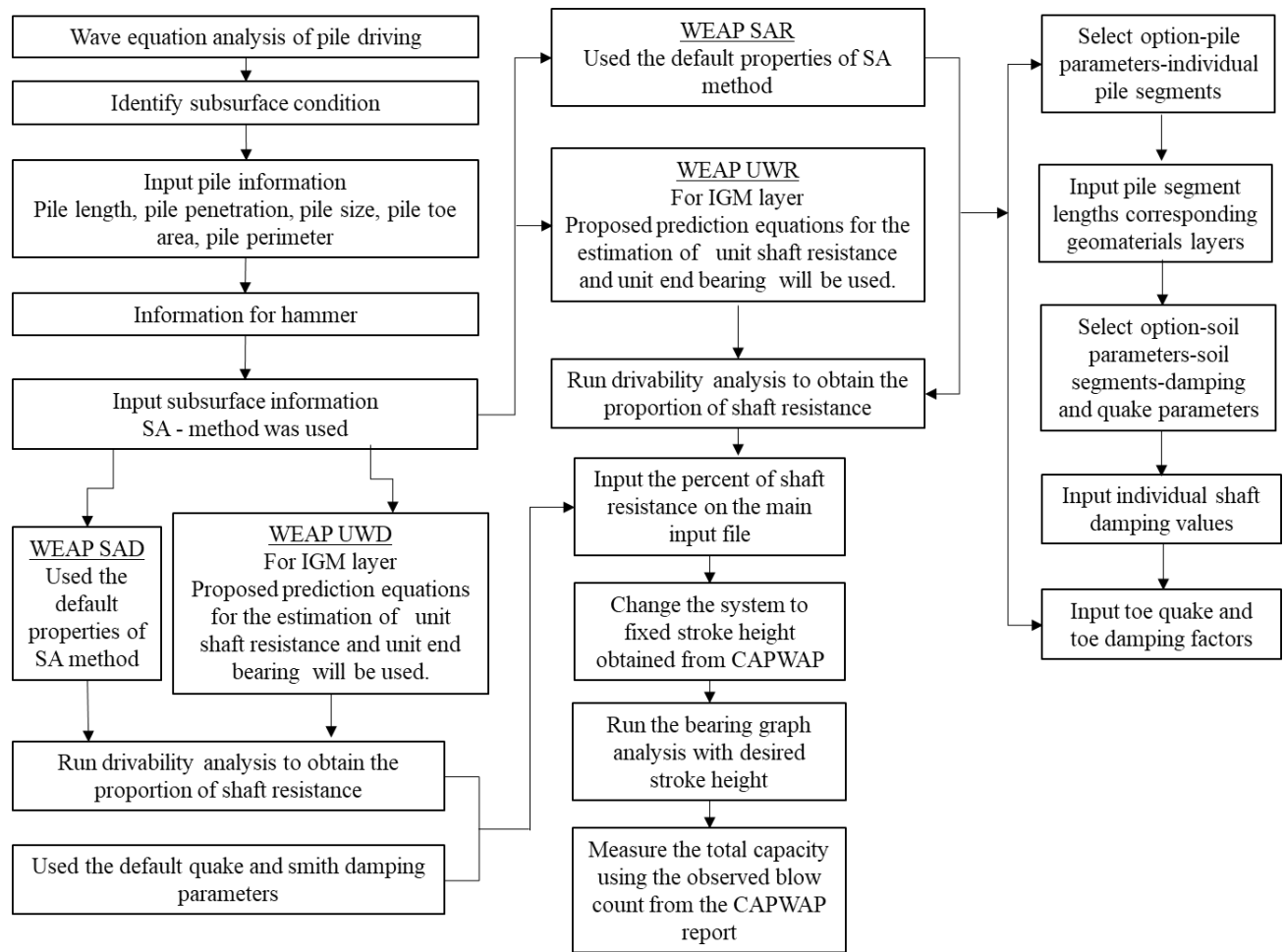


**Figure 8.1. A Flowchart Showing the Input Procedures for Four WEAP Methods.**

## 8.5 Back-Calculation Procedure

### 8.5.1 Soil Based IGM

Pile resistance prediction from WEAP depends on the selection of the quake values and damping factors. However, matching the pile resistance from CAPWAP with the predicted resistance from WEAP can yield a combination of quake and damping parameters. Thus, back-calculation becomes an indeterminate problem that requires the reduction of unknown quake and damping parameters. A parametric study has been performed to determine the effect of the quake and damping parameters on the bearing graph (Islam 2021). The study found that the  $J_s$  has the most effect on the bearing graph. On the other hand, the  $Q_s$  value has little effect on the bearing graph,

and thus the default  $Q_s$  value of 0.1 inch recommended in WEAP was adopted in this study. Since IGM is harder and stiffer than soil, it is reasonable to assume the WEAP recommended  $Q_t$  value of  $D/120$  (hard and stiff soils) for the soil-based IGMs. For the damping factors, a  $J_s$  to  $J_t$  ratio of one was assumed to create a determinate problem as pile resistance from WEAP depends on the relative effect of both damping factors. The parametric study showed that smaller Smith parameters increase the static pile resistance because the shaft resistance and end bearing were better mobilized at lower Smith parameters. The IGM was inputted through the SA method using the predicted unit resistances (Table 8.4). The bearing graph was generated by changing  $J_s$  and  $J_t$  for the individual IGM layers while considering the WEAP recommended values for the overburden soil layers. The predicted resistance from WEAP was determined using the stoke height and blow count at the End of Driving (EOD) given in the CAPWAP reports. The best back-calculated damping factors were determined by matching the WEAP predicted resistance with the resistance from CAPWAP at EOD until the difference was less than 0.1 percent. After analyzing the results from the back-calculation, it was found that the back-calculated damping parameters depend upon the type of bearing geomaterial and the overburden subsurface condition. Three different subsurface conditions were proposed along with the recommended damping factors.

#### *8.5.1.1 Subsurface Condition I (Fine-grained Soil-based IGM as Bearing Layer)*

Out of the 34 test piles, 15 test piles were driven onto fine-grained soil-based IGMs as the bearing layer. Subsurface condition I can be identified having fine-grained soil-based IGM as the bearing IGM layer and overlying with one or more of either soil layers or fine-grained soil-based IGM. Out of these 15 test piles, one test pile was excluded in the back-calculation as the WEAP predicted pile resistance could not be matched with the pile resistance from CAPWAP within a difference of 0.1 percent for a range of  $J_s$  and  $J_t$ . The average back-calculated damping factor of 0.18 s/ft for the fine-grained soil-based IGM was higher than the  $J_t$  of 0.15 s/ft, but lower than the  $J_s$  of 0.20 s/ft for cohesive soils. The higher average back-calculated  $J_t$  and lower average back-calculated  $J_s$  indicate that the current WEAP recommended  $J_t$  and  $J_s$  for cohesive soils will underpredict the shaft resistance and overpredict the end bearing of fine-grained soil-based IGM. A relationship for the back-calculated damping factor was established based on the  $s_u$  (ksf) of

fine-grained soil-based IGM at the pile tip and slenderness ratio (i.e., ratio of pile penetration  $L$  (ft) to pile dimension  $D_p$  (ft)) (Figure 8.3). The fitted linear regression function for predicting  $\hat{f}_t$  (s/ft) and  $\hat{f}_s$  (s/ft) was given by the equation shown in Figure 8.2 with a relatively high coefficient of determination ( $R^2$ ) of 0.74.

$$\hat{f}_t = \hat{f}_s = 0.0007 \frac{s_u \times L}{D_p} - 0.008$$

**Figure 8.2. Equation. Predicting Damping Value for FG-IGM as Bearing Layer.**

The equation shown by Figure 8.2 infers that the piles having a deeper bearing fine-grained soil-based IGM layer will demand higher damping factors, but the damping factors will decrease with increasing pile size. The equation shown in Figure 8.2 covers  $20 \text{ ft} \leq L \leq 136.5 \text{ ft}$ ,  $2.7 \text{ ksf} \leq s_u \leq 14.03 \text{ ksf}$ , and a wide range of pile sizes. However, a maximum damping factor of 0.375 s/ft was recommended for pile driving conditions with  $\frac{s_u \cdot L}{D_p} > 565 \text{ ksf}$ .

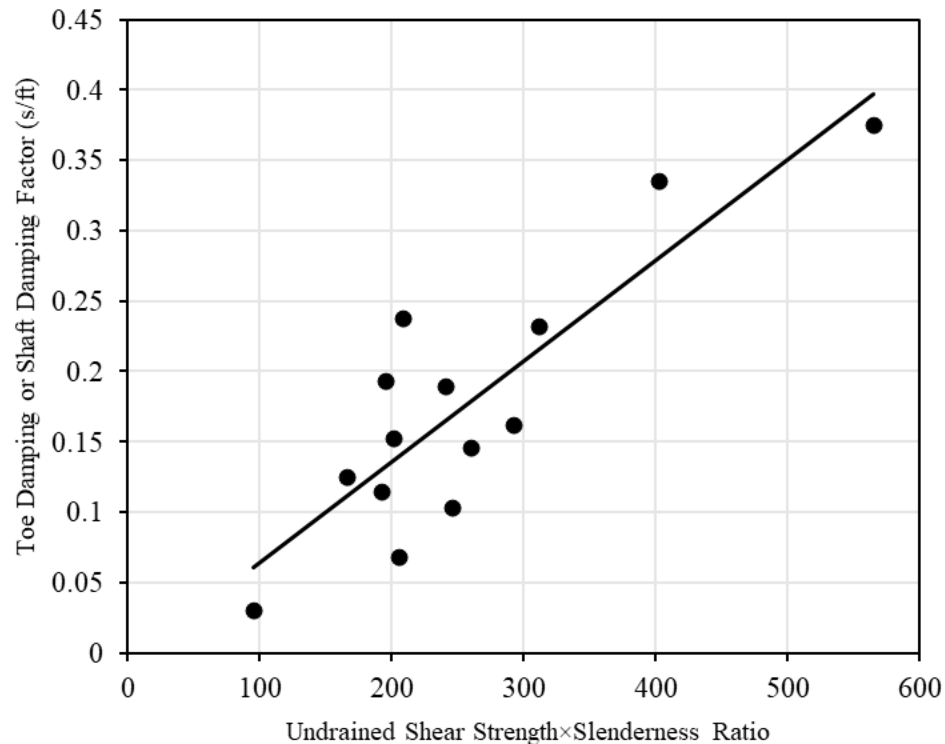


**Figure 8.3. Relationship Between Back-Calculated Damping Factor and the Product of Undrained Shear Strength and Slenderness Ratio.**



### 8.5.1.2 Subsurface Condition II (Coarse-grained Soil-based IGM as Bearing Layer)

Nine test piles were driven onto coarse-grained soil-based IGMs as the bearing layer. Subsurface condition II can be identified having coarse-grained soil-based IGM as the bearing IGM layer and overlying with one or more of either soil layers or coarse-grained soil-based IGM. Out of these nine test piles, two piles were excluded in the back-calculation as the WEAP predicted pile resistance could not be matched with the pile resistance from CAPWAP within a difference of 0.1 percent for a range of  $J_s$  and  $J_t$ . The average back-calculated damping factor for the coarse-grained soil-based IGM layers was 0.10 s/m. The average back-calculated damping was lower than the  $J_t$ , but higher than the  $J_s$  recommended in WEAP for non-cohesive soils. This comparison indicates that the current WEAP recommendations will underpredict the end bearing and overpredict the shaft resistance in coarse-grained soil-based IGM. Figure 8.5 shows a non-linear relationship between the back-calculated damping and the combined term of pile penetration length,  $L$  (ft), and corrected  $N$ ,  $(N_1)_{60}$  (blows/ft) below the pile tip. The nonlinear trend can be best described by an exponential relationship given by the equation shown in Figure 8.4.

$$\hat{J}_t = \hat{J}_s = 0.02e^{2.84 \frac{L}{(N_1)_{60}}}$$

**Figure 8.4. Equation. Predicting Damping Value for CG-IGM as Bearing Layer.**

The predicted  $\hat{J}_t$  (s/ft) and  $\hat{J}_s$  (s/ft) from the equation show that the damping factor decreases with the increasing  $(N_1)_{60}$  of coarse-grained soil-based IGM below the pile toe. Because of limited data with  $27.9 \text{ ft} \leq L \leq 48.5 \text{ ft}$ ,  $55 \text{ blows/ft} \leq (N_1)_{60} \leq 151 \text{ blows/ft}$ , a maximum value of 0.25 s/ft was recommended for  $\frac{L}{(N_1)_{60}} > 0.88$ . The pile sizes used in the development of the prediction equation include HP 12×53, HP 14×73, and 16-inch OEP. Future studies were recommended to improve the prediction equation for damping factors by including data with longer pile lengths and variable pile types (CEP) and sizes.

### 8.5.1.3 Subsurface Condition III (Either Soil or Soil-based IGM as Bearing Layer)

Out of the 34 test piles, 10 test piles fall under subsurface condition III with the bearing layer identified as either a fine-grained soil-based IGM, coarse-grained soil-based IGM, or soil. For the test piles with the fine-grained or coarse-grained soil-based IGM as the bearing layer, the subsurface condition was different from the subsurface conditions I and II due to the presence of both fine-grained and coarse-grained soil-based IGMs along the pile shaft. For piles with soil as the bearing layer, subsurface condition III was identified when either fine-grained soil-based IGM or coarse-grained soil-based IGM or both were present as overburden layers. The damping parameters were not found for this subsurface condition. The average back-calculated damping factors of 0.10 s/ft and 0.18 s/m were recommended for the coarse-grained and fine-grained soil-based IGM layers, respectively, to facilitate the proposed WEAP method. A flowchart to determine the subsurface conditions based on geotechnical and boring log information was provided in Figure 8.6. The recommended Smith dynamic parameters from the back-calculation were summarized in Table 8.5.

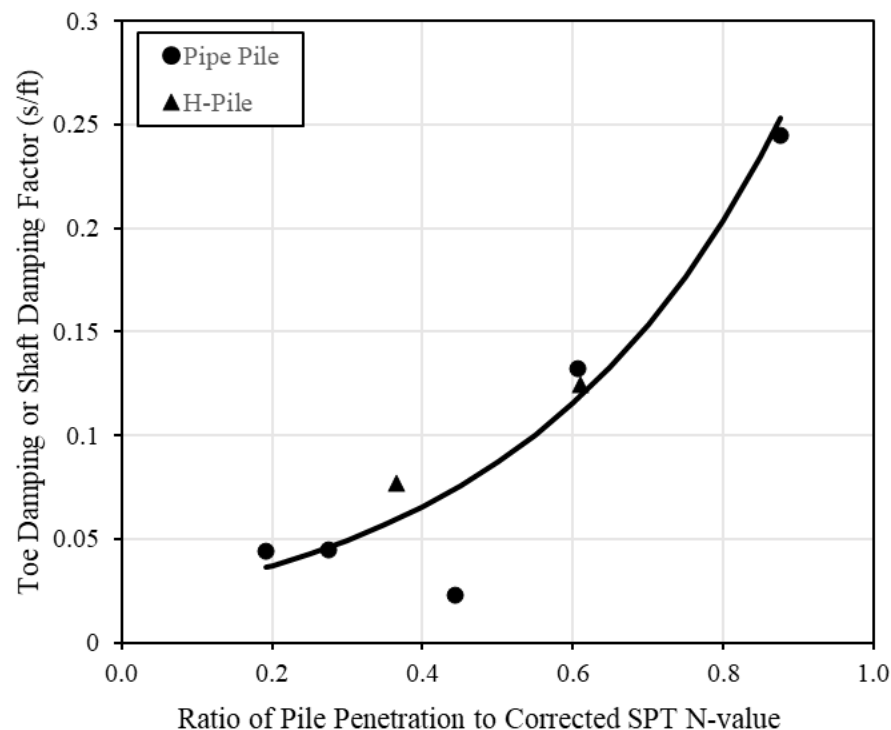


**Figure 8.5. Relationship Between Back-Calculated Damping Factor the Ratio of Pile Penetration to Corrected SPT N- Value.**

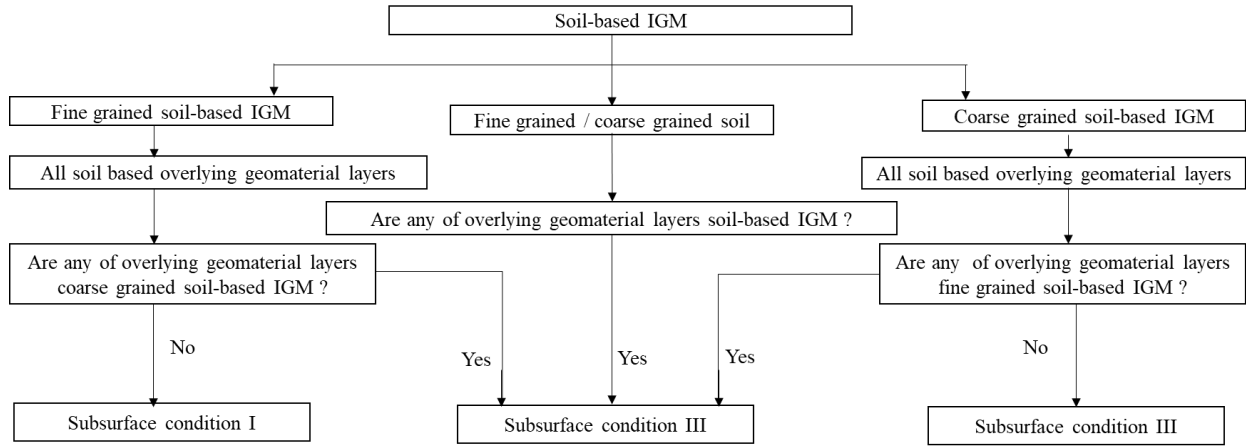


**Figure 8.6. Flowchart to Classify the Subsurface Conditions I, II, and III.**

### 8.5.2 Rock Based IGM

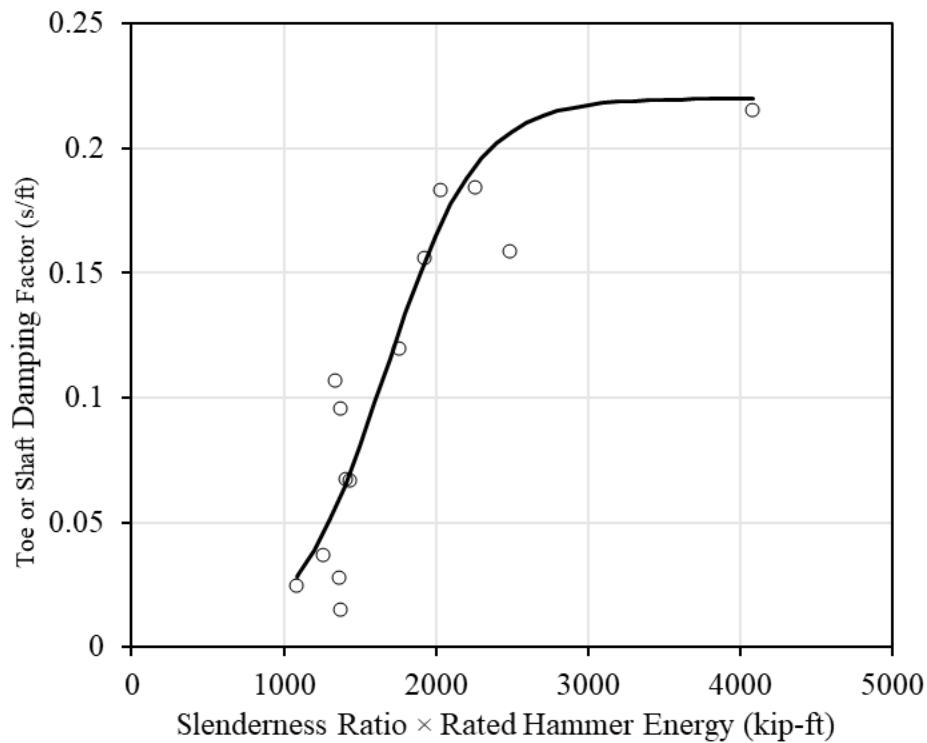
#### 8.5.2.1 Subsurface Condition IV & V: Rock-based IGM except Shale as the Bearing Layer

Table 8.5 shows the summary of the test piles identified under the subsurface condition IV and the back-calculated damping factors. Figure 8.8 shows a positive relationship between back-calculated damping factors of all rock-based IGMs except shale and the interaction term of slenderness ratio ( $L/D_p$ ) and rated hammer energy ( $E_r$ ). The damping factor reaches a maximum value of about 0.22 s/ft when the interactive term exceeds about 2,500 kip-ft. Several nonlinear models (exponential, logarithmic, rational, and modified exponential) were evaluated on fitting the back-calculated damping factors based on the corrected Akaike Information Criterion (AICc) and Bayesian Information Criterion (BIC). The nonlinear trend with the smallest AICc and BIC given by the equation shown in Figure 8.7 was proposed to predict the damping factors for the following rock-based IGM: claystone, sandstone, mudstone, and siltstone.

$$\hat{J}_t = \hat{J}_s = \frac{0.2}{1 + e^{\left(5.8 - 0.004 \times \frac{L}{D_p} \times E_r\right)}}$$

**Figure 8.7. Equation. Back Calculated Damping Factors for All R-IGM Except Shale for Subsurface Condition IV.**

where  $\hat{J}_t$  = predicted toe damping (s/ft),  $\hat{J}_s$  = predicted shaft damping (s/ft),  $L$  = pile penetration length (ft),  $D_p$  = pile dimension (ft), and  $E_r$  = rated hammer energy (kip-ft). The equation shown in Figure 8.7 considers  $20 \text{ ft} \leq L \leq 76.2 \text{ ft}$  and a wide range of rated hammer energies ( $43.24 \text{ kip-ft} \leq E_r \leq 90.67 \text{ kip-ft}$ ). Furthermore, this equation accounts for pile sizes ranging from HP 12×53 to 24-inch open-ended pipe piles. This equation was only applicable for damping factors ranging from 0.015 s/ft to 0.22 s/ft and the interaction term  $L/D_p \times E_r$  from 1,084 to 4,083 kip-ft. Particularly, the back-calculated damping factors for sandstone and siltstone ranged from 0.015 s/ft to 0.18 s/ft and for claystone and mudstone ranged from 0.03 s/ft to 0.16 s/ft.



**Figure 8.8. Back-Calculated Damping Factors for Rock-Based IGMs Except Shale for Subsurface Condition IV with Respect to Slenderness Ratio and Rated Hammer Energy.**

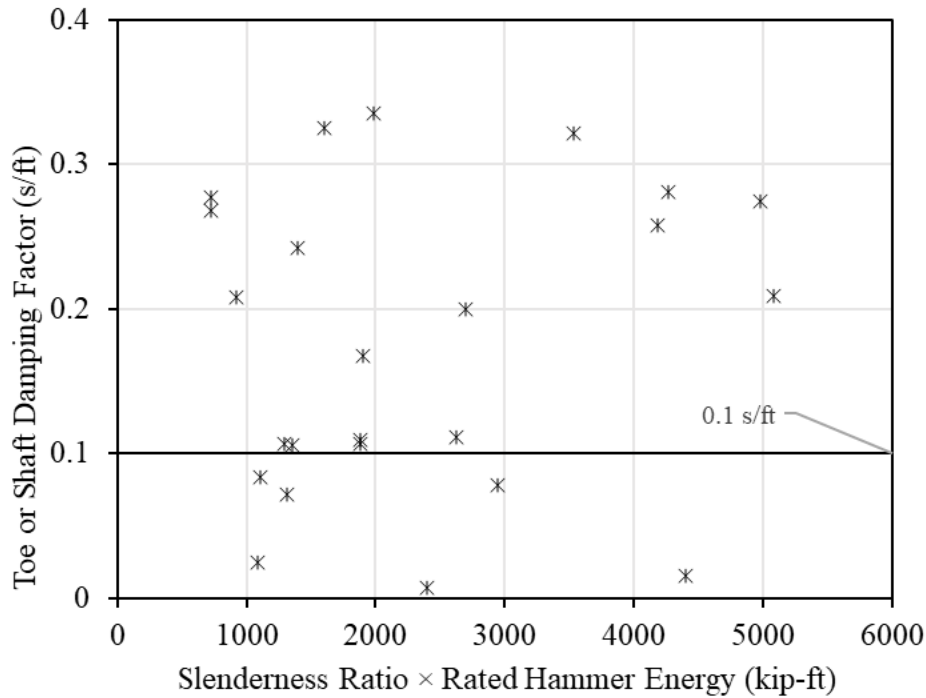


**Figure 8.9. Back-Calculated Damping Factors for Rock-Based IGMs Except Shale for Subsurface Condition V with Respect to Slenderness Ratio and Rated hammer energy.**

Figure 8.9 shows a high variation in the back-calculated damping factors and no relationship with the interactive term  $L/D_P \times E_r$ . This could be due to the presence of different S-IGM at different depths that affect the pile resistance prediction in WEAP. Instead of applying the default damping factors developed for piles in soils (Table 8.2), average back-calculated damping factors of 0.1 s/ft for rock-based IGMs (claystone, sandstone, mudstone, and siltstone) were recommended for the proposed WEAP methods for subsurface condition V. A flowchart to determine the subsurface conditions based on geotechnical and boring log information was provided in Figure 8.10. The recommended Smith dynamic parameters from the back-calculation study were summarized in Table 8.6.

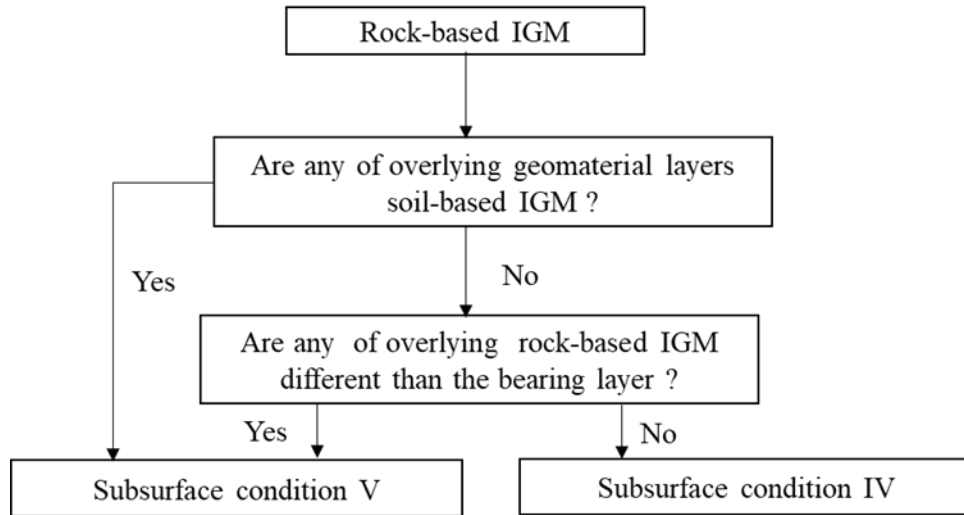


**Figure 8.10. A flowchart to determine subsurface conditions IV and V.**

#### 8.5.2.2 Subsurface Condition IV & V: Shale as the Bearing Layer

Figures 8.11 and 8.12 show the back-calculated damping factors for piles driven onto shale with respect to  $q_u$  and  $L$ , respectively for both subsurface conditions IV and V. The data points and back-calculated damping factors for piles bearing on shale layers were summarized in Table 8.5. The difference between these two subsurface conditions cannot be determined due to the lack of data for piles driven in subsurface condition V. Figures 8.11 and 8.12 shows that the back-calculated damping factors ranged from 0.04 s/ft to 0.43 s/ft for the soil-based and soft and highly weathered rock-based (SS-HW) shales and 0.03 s/ft to 0.18 s/ft for moderately hard to hard & slightly weathered (MW-SW) shales. The variation in the damping factors for shales was similarly observed in Thendean et al. (1996) for piles driven onto soft weathered rock including shale that exhibits relaxation and was suggested with an average  $J_r=0.2$  s/ft. Two different average back-calculated damping factors were found to be suitable for SS-HW and MW-SW shales. Most of the test piles were found to be scattered along an average damping factor with increasing  $q_u$  and pile penetration length. In fact, only a few test piles exhibit very high damping factors. Thus, an average back-calculated damping factor of 0.15 s/ft and 0.09 s/ft were recommended for SS-HW and MW-SW shale, respectively.

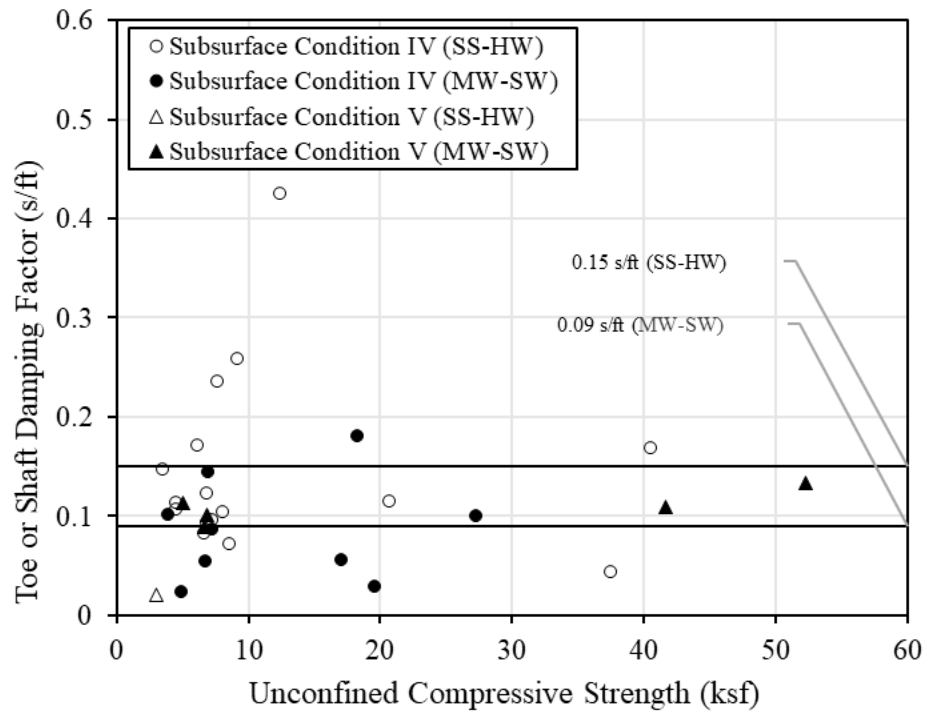


**Figure 8.11. Relationship of Back-Calculated Damping Factors for Shale with Unconfined Compressive Strength.**

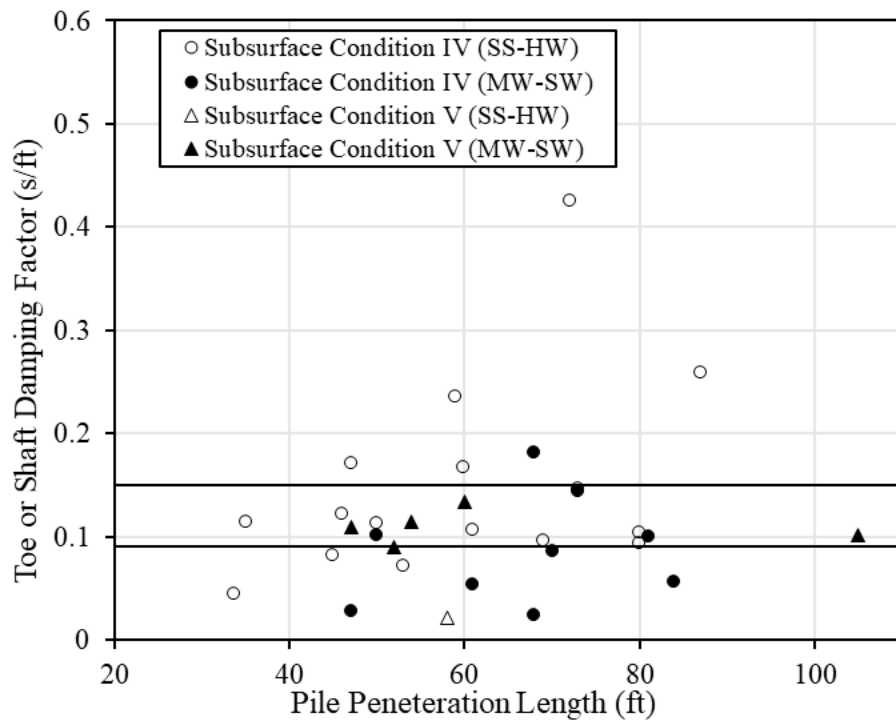


**Figure 8.12. Relationship of Back-Calculated Damping Factors for Shale with Pile Penetration Length.**

## 8.6 Bearing Graph Analysis Results

### 8.6.1 Soil Based IGM

Bearing graph analyses were conducted to determine the pile resistances considering all WEAP methods and subsurface conditions. The bearing graph analysis procedure for both WEAP-SAD, WEAP-UWD, WEAP-SAR and WEAP-UWR was illustrated in a flowchart in Figure 8.1. The pile resistance predicted using the different WEAP methods were summarized in Table 8.1.

Each predicted pile resistance from WEAP was compared with the measured pile resistance from CAPWAP at EOD in terms of a resistance bias ( $\lambda$ ) where  $\lambda > 1$  indicates that WEAP underpredicts the pile resistance and vice-versa. The comparison of the WEAP predicted resistance and CAPWAP measured resistance was shown in Figure 8.13 for WEAP-SAD, WEAP-UWD, WEAP-UWR, and WEAP-SAR based on different pile types and subsurface conditions, respectively. Figure 8.13 shows that WEAP-SAD, WEAP-UWD, WEAP-UWR, and WEAP-SAR with a mean resistance bias ( $\mu$ ) of 1.14, 1.15, 1.04 and 1.03, respectively, underpredict the pile resistances, on average, by about 12 percent, 13 percent, 4 percent, and 3 percent, respectively. Similarly, the Coefficient of Variation (COV) for the WEAP-SAD, WEAP-UWD, WEAP-UWR, and WEAP-SAR methods were 0.24, 0.22, 0.17, and 0.18, respectively. The WEAP-UW-R method has the lowest COV reflecting the lowest uncertainty associated with the pile resistance prediction. Compared with default WEAP-SAD, WEAP-UWR reduces the underprediction of pile resistances by about 8 percent on average and the uncertainty associated with the pile resistance prediction by 29.2 percent (i.e., a reduction in COV from 0.24 to 0.17).



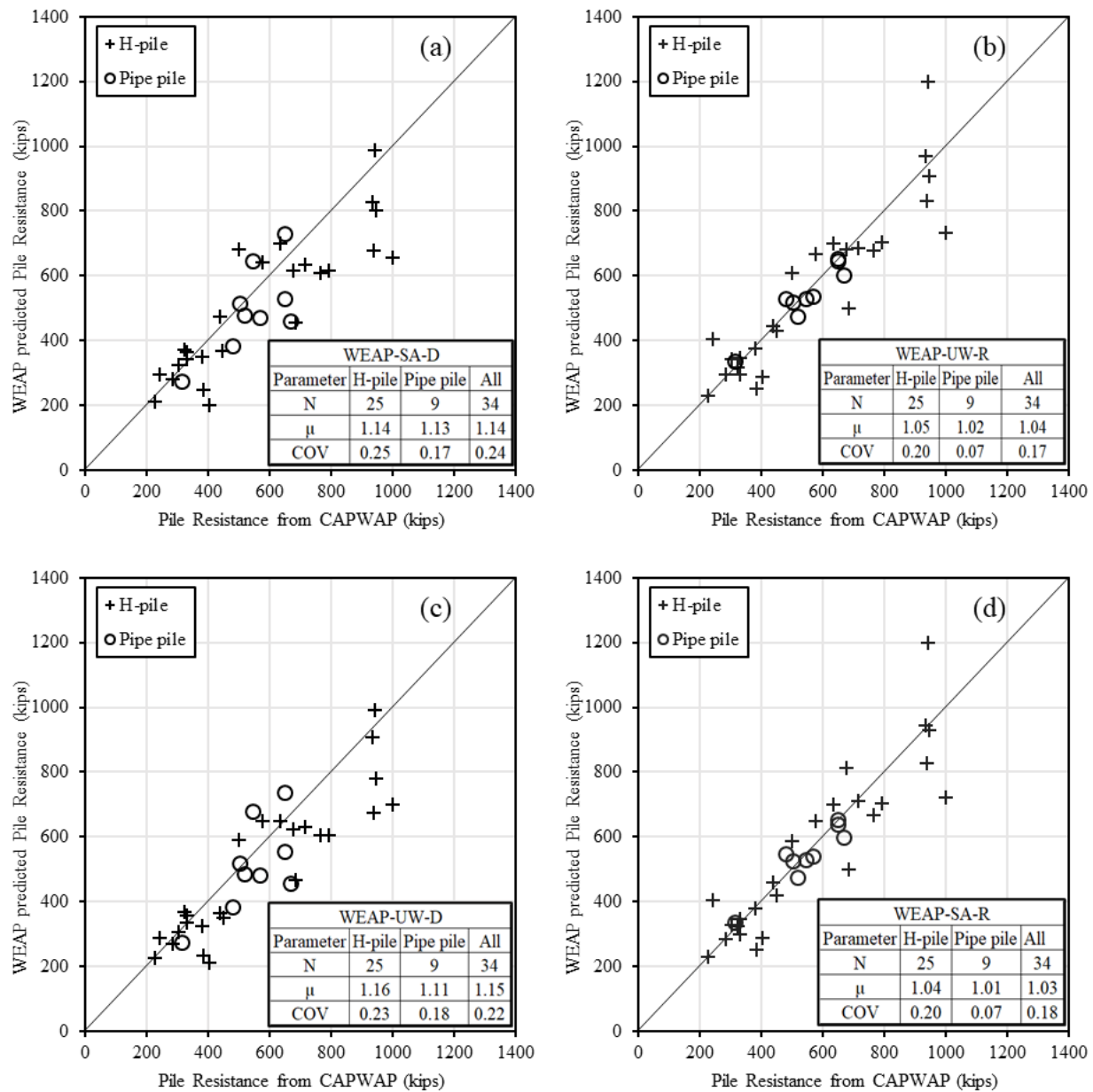


**Figure 8.13. Comparison of Measured Pile Resistances from CAPWAP and Predicted Pile Resistance from WEAP for the 25 H- and 9 Pipe piles as Training Data Using (a) WEAP-SA-D method, (b) WEAP-UWR method, (c) WEAP-UWD method, and (d) WEAP-SAR method.**

### **8.6.2 Rock based IGM**

Using the 95 usable test piles driven onto rock-based IGMs, ultimate pile resistances were predicted using the WEAP-SAD, WEAP-UWD, WEAP-UWR, and WEAP-SAR methods. The procedure of the bearing graph analysis for the four methods was shown in Figure 8.1. The predicted pile resistances from WEAP were compared with the pile resistances from CAPWAP at EOD in Figure 8.14 as well as in terms of resistance biases. A mean resistance bias ( $\mu$ ) greater than 1.00 indicates that WEAP underpredicts the pile resistance and vice-versa. The WEAP-SA-D method underpredicts most of the pile resistances of H and pipe piles. The incorporation of the newly developed static analysis methods does not affect the bearing graph analysis shown by the similar  $\mu$  (1.13 and 1.15) and COV (0.22 and 0.22) from WEAP-SA-D and WEAP-UW-D method, respectively. The WEAP-UW-R method improves the prediction of pile resistance in H-piles by reducing the COV from 0.22 to 0.18 and  $\mu$  from 1.16 to 1.03 in comparison to WEAP-SA-D method. The pile resistances in pipe pile were overestimated by the WEAP-UW-R method in comparison to the WEAP-SA-D and WEAP-UW-D methods yield a  $\mu$  value of 0.93 and no change in the COV. For the WEAP-SA-R method, the result for all piles was pretty similar to that of the WEAP-UW-R method. However, there was slightly higher COV (0.20 in comparison to 0.18) and  $\mu$  (1.01 in comparison to 1.0) from the WEAP-SA-R method. Overall, the WEAP-UW-R method has the best performance among the 4 methods as shown by the lowest COV and  $\mu$  closest to unity.

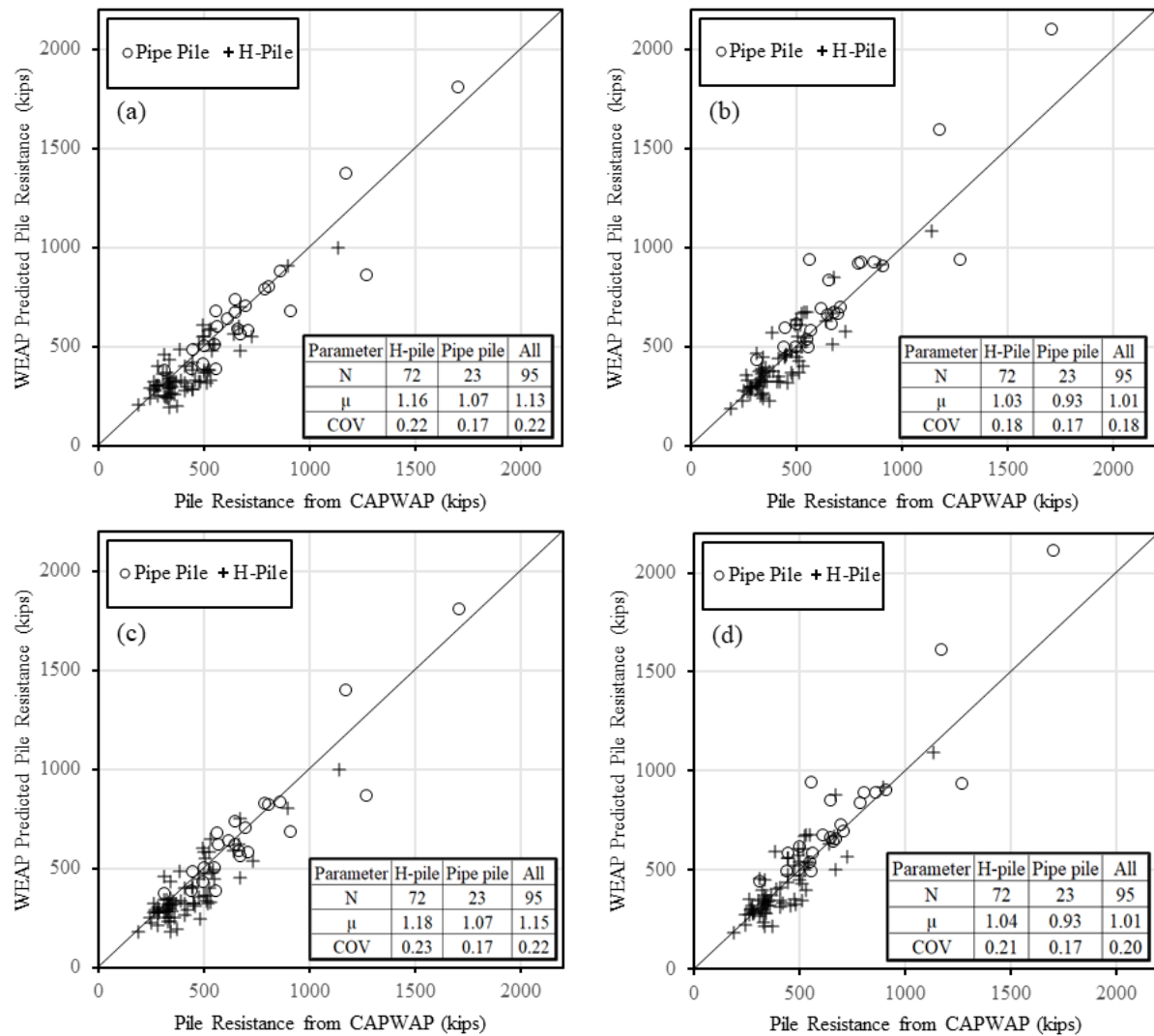


**Figure 8.14. Comparison of WEAP Predicted Pile Resistance with that from CAPWAP for 72 H and 23 Pipe Training Pile Data (a) WEAP-SAD, (b) WEAP-UWR, (c) WEAP-UWD, and (d) WEAP-SAR method.**

**Table 8.5. Back-Calculated Quake and Damping Parameters for Subsurface Conditions I, II, and III.**

Subsurface Condition	Geomaterial	$Q_s$ (in)	$Q_t$ (in)	$J_s$ (s/ft)	$J_t$ (s/ft)
I	Soil	0.1	$D/120$ (very dense/hard soil); $D/60$ (soft soil)	0.20 (Fine-grained); 0.05 (coarse-grained); 0.10 (silts)	0.15
I	Fine-Grained SB-IGM	0.1	$D/120$	$\hat{J}_t = \hat{J}_s = 0.0007 \frac{S_u \times L}{D_p} - 0.008$	$\hat{J}_t = \hat{J}_s = 0.0007 \frac{S_u \times L}{D_p} - 0.008$
II	Soil	0.1	$D/120$ (very dense/hard soil); $D/60$ (soft soil)	0.20 (Fine-grained); 0.05 (coarse-grained); 0.10 (silts)	0.15
II	Coarse-grained SB-IGM	0.1	$D/120$	$\hat{J}_t = \hat{J}_s = 0.02e^{2.84 \frac{L}{(N_1)_{60}}}$	$\hat{J}_t = \hat{J}_s = 0.02e^{2.84 \frac{L}{(N_1)_{60}}}$
III	Soil	0.1	$D/120$ (very dense/hard soil); $D/60$ (soft soil)	0.20 (Fine-grained); 0.05 (coarse-grained); 0.10 (silts)	0.15
III	Fine-Grained SB-IGM	0.1	$D/120$	0.18	0.18
III	Coarse-grained SB-IGM	0.1	$D/120$	0.10	0.10

$Q_s$  = Shaft quake;  $Q_t$  = Toe quake;  $J_s$  = Shaft damping;  $J_t$  = Toe damping;  $D_p$  = Pile Dimension (ft);  $D$  = Pile Diameter (ft);  $S_u$  = Undrained shear strength of the bearing layer at the bottom of pile tip (ksf);  $L$  = Embedded pile length (ft);  $(N_1)_{60}$  = Corrected  $N$  (blows/ft) of the bearing layer at bottom of pile tip; and SB-IGM = Soil-based Intermediate Geomaterial.

**Table 8.6. Back-Calculated Quake and Damping Parameters for Subsurface Conditions IV and V.**

SC	Geo-material	Geomaterial Type	$Q_s$ (in)	$Q_t$ (in)	$J_s$ (s/ft)	$J_t$ (s/ft)	
IV	Soil	Fine-grained and Coarse-grained	0.1	$D/120$ (very dense/hard soil); $D/60$ (soft soils)	0.2 (Fine-grained soil); 0.05 (coarse-grained soil)		0.15
	Rock-based IGM	Claystone, Sandstone, Mudstone, Siltstone		$D/120$	$\hat{J}_t = \hat{J}_s = \frac{0.2}{1 + e^{\left(5.8 - 0.004 \times \frac{L}{D_p} \times E_r\right)}}$		
		SS-HW shale			0.15		
		MW-SW shale			0.09		
V	<del>Soil</del>	Fine-grained and Coarse-grained		$D/120$ (very dense/hard soil); $D/60$ (soft soils)	0.2 (fine-grained soil); 0.05 (coarse-grained soil)		0.15
	<del>Soil-based IGM</del>	<del>Fine-grained</del>		$D/120$	0.18		
		<del>Coarse-grained</del>			0.10		
	Rock-based IGM	Claystone, Sandstone, Mudstone and Siltstone			0.10		
		SS-HW shale			0.15		
		MW-SW shale			0.09		

SC=Subsurface condition;  $Q_s$ =Shaft quake;  $Q_t$ =Toe quake;  $J_s$ =Shaft damping factor;  $J_t$ =toe damping factor;  $D_p$ =Pile dimension (ft);  $D$ =Pile diameter (in);  $E_r$ =Rated hammer energy (kip-ft); and  $L$ =Total embedded pile length (ft); SS-HW=Soil based, soft & highly weathered shale; MW-SW=Moderately hard to hard & slightly weathered shale.

## 8.7 Validation

### 8.7.1 Soil Based IGM

Forty-five separate pile data obtained from the pile load test program in Illinois by Long and Anderson (2012) were examined. Of the 45 test piles, 22 test piles driven in soil-based IGM were identified for the validation study. Of the 22 test piles, 5 piles were HP 310×79 piles and the remaining 17 test piles were 14” diameter shells with 0.25” and 0.312” wall thicknesses. Shell piles were described as pipe piles with a metal plate welded at the tip to form a close-ended pile (Long and Anderson 2012). The majority of the fine-grained soil-based IGM were found to be clay, and the majority of the coarse-grained soil-based IGM were hard till. Based on the description provided in the report, the clay was treated as clay-based IGM with low plasticity, and hard till was treated as sand-based IGM. Since the corrected  $N(N_{60})$  was reported, the classification for coarse-grained geomaterials was conducted based on  $N_{60} \geq 58$  blows/ft and the classification of fine-grained soil-based IGM was based on the reported  $s_u$  values (Figure 4.1). Bearing graph analyses were performed using the stoke height and blow count at the EOD. The summary of the test pile data collected from the Long and Anderson (2012) report along with the results of the bearing graph analysis using the 4 different WEAP methods were presented in Table 8.7. The  $\mu$  and COV of resistance biases for both WEAP methods were compared in Figure 8.15.

The test piles from Illinois were underpredicted by the WEAP-SA-D by only about 4 percent on average. This could be due to the use of the  $N_{60}$  values in the SA method and the possible prediction of relevant soil parameters. The WEAP-UW-R shows improvement over the WEAP-SA-D by reducing the underprediction of pile resistances by 5 percent and the COV by 20 percent (from 0.25 to 0.20). The results were comparable to those based on the 34 training test pile data (Figure 8.14). The three test piles denoted by the triangular markers were found to be in subsurface condition III with soil as the bearing layer. The resistance predictions of these three test piles improve using the WEAP-UW-R.

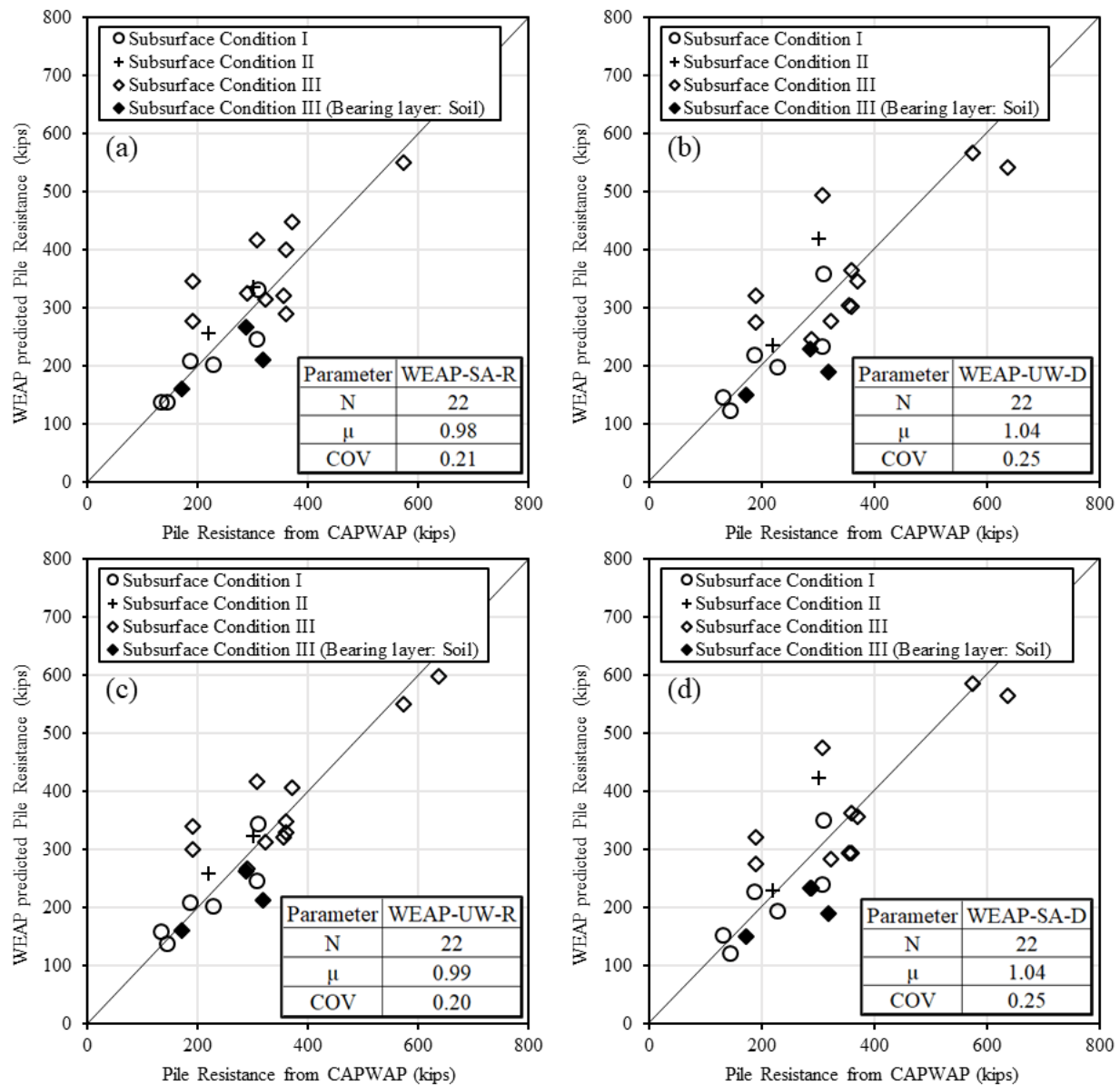


**Figure 8.15. Comparison of measured pile resistances from CAPWAP and predicted pile resistances for the 22 separate pile data from (a) WEAP-SA-R, (b) WEAP-UW-R, (c) WEAP-UW-D, and (d) WEAP-SA-D method.**

**Table 8.7. Summary of Independent Separate Test Pile Data and Relevant End of Driving (EOD) Information for Validation.**

Site	Location	Pile type	$L$ (ft)	Bearing geo-material	$S$ (ft)	$B$	$R_m$	Hammer	$R_{wp}^1$	$R_{wp}^2$	$R_{wp}^3$	$R_{wp}^4$
Jules <sup>5</sup>	SW wing, Pile 1	HP 12×53	25.5	Clay <sup>#</sup>	8.3	48	132.5	Delmag D 8-32	150.95	145.24	157.53	137.05
I-78 Over sangmon <sup>6</sup>	HP	HP 14×89	64	Sand*	6	30	300.6	Delmag D 36-32	422.61	417.67	323.47	334.44
Greenville <sup>7</sup>	Pile 3	PP 14"	28	Hard till*	6.2	42	189.6	Delmag D 25-32	320	320.32	339.81	345.86
Greenville <sup>7</sup>	Pile 12	PP 14"	22	Hard Till*	7.1	17	190.1	Delmag D 36-32	275.77	274.28	300.57	276.52
Greenville <sup>7</sup>	Pile 13	PP14"	50	Clay <sup>#</sup>	7.1	33	323.3	Delmag D 25-32	282.78	276	311.26	314.30
Mahomet <sup>7</sup>	North Abt.	HP 14×73	67.8	SG*	7	126	573.9	Delmag D 30-32	584.75	567.18	549.31	548.75
Mahomet <sup>7</sup>	South Abt.	HP 14×73	41.5	Sand <sup>^</sup>	7.2	42	286.8	Pileco D 19-42	232.1	227.94	262.87	265.44
Mahomet <sup>7</sup>	Pier 2	HP 14×73	50	SG*	8.3	81	636.7	Delmag D 30-32	563.79	540.43	596.92	656.61
Godfrey <sup>5</sup>	West Abt.	PP 14"	41	Clay <sup>#</sup>	8.5	52	227.5	Delmag D 12 -32	193.56	196.65	202.36	202.36
Bloomington <sup>7</sup>	K-pile	HP 12 ×63	101	SG*	7.8	115	307.4	APE D 19-42	473.9	494.44	417.41	416.94
Panther creek <sup>7</sup>	South Abt.	HP 10 ×57	39.5	SG*	9	144	359.5	ICE 42-S	362.62	363.62	346.82	398.84
Oquawka <sup>7</sup>	East Abt.	PP 14"	58	Sand <sup>^</sup>	6.8	37	171.6	MKT DE 42	149.24	149.8	160.93	160.75
Oquawka <sup>7</sup>	Pier	PP 14"	52.5	Sand <sup>^</sup>	8.2	49	318.4	MKT DE 42	189.8	189.57	212.16	210.25
Oquawaka <sup>5</sup>	West Abt.	PP 14"	66	Clay <sup>#</sup>	7.5	22	145	MKT DE 42	120.71	122.38	136.64	136.84
Stronghurst <sup>5</sup>	North Abt.	PP 14"	54.3	Clay <sup>#</sup>	9	40	307.4	Delmag D 19-42	238.56	233.95	246.5	244.82
Stronghurst <sup>5</sup>	Pier 1	PP 14"	69	Clay <sup>#</sup>	9.5	34	187.2	Delmag D 19-42	227.32	217.7	208.67	208.44
Stronghurst <sup>7</sup>	Pier 2	PP 14"	56.5	Sand*	9	38	289.6	Delmag D 19-42	232.13	245.56	265.42	323.81



Jacksonville <sup>7</sup>	Pier 1	HP 12 ×53	39	Clay <sup>#</sup>	8	120	371.2	Delmag D 19-32	355.13	346.16	406.33	446.96
Jacksonville <sup>5</sup>	Pier 2	HP 12 ×53	62.2	Clay <sup>#</sup>	7	200	309.4	Delmag D 19-32	349	358.07	342.94	331.55
RCS Godfrey <sup>7</sup>	North Abt.	PP 14"	39	SM <sup>*</sup>	7.3	90	358.8	Delmag D 19-32	293.6	301	329.75	290.18
RCS Godfrey <sup>6</sup>	North pier	PP 14"	29.5	Hard Till <sup>*</sup>	6	72	219.7	Delmag D 19-32	229.24	236.07	258.73	256.40
RCS Godfrey <sup>7</sup>	South pier	PP 14"	19.5	SM <sup>*</sup>	7	81	355	Delmag D 19-32	292.93	304	320.72	321.19

$L$  = Penetration length; Abt. = Abutment;  $S$  = Stroke height;  $B$  = Blow count (blows/ft); EOD = End of Driving;  $R_m$  = CAPWAP measured pile capacity at EOD; HP = H-pile; PP = Pipe pile; SG = Sandy gravel; SM = Silty sand; \* = Coarse-grained soil-based IGM; # = Fine-grained soil-based IGM; and ^ = Coarse-grained soil;  $R_{wp}$  = Pile capacity predicted from WEAP bearing graph analysis; <sup>1</sup> = Pile capacity predicted from WEAP-SA-D method; <sup>2</sup> = Pile capacity predicted from WEAP-UW-D method; <sup>3</sup> = Pile capacity predicted from WEAP-UW-R method; <sup>4</sup> = Pile capacity predicted from WEAP-SA-R method; <sup>5</sup> = Piles driven in subsurface condition I; <sup>6</sup> = Piles driven in subsurface condition II; <sup>7</sup> = Piles driven in subsurface condition III; SW = South-west.

### **8.7.2 Rock Based IGM**

Twenty-four separate pile data from 16 test piles were obtained for the validation of the WEAP methods described previously. Four steel H-piles were obtained as a part of our pile load test program consisting of dynamic load tests at the EOD using PDA/CAPWAP as well as SLTs. A SLT was performed 4 days after the EOD at the Lodgepole Creek bridge project in Laramie County, WY. SLTs were performed at 2 days and 3 days after the EOD at the bridge projects in Adair County and Wapello County, IA, respectively. Similarly, one SLT was performed in North Dakota one day after EOD. For the remaining twelve test piles, four production test piles at the Lodgepole creek bridge project, WY, two steel H-piles each in Cerro Gordo and Franklin Counties, IA, two H-piles in Plymouth County, IA, one each at Warren County and Davis County, IA were dynamically tested. The SLT performed in H-pile in North Dakota was bearing on the lignite layer, thus not useful for this study. However, CAPWAP analysis at different blow numbers proved useful for this study. Also, CAPWAP analysis at different blow numbers were performed on piles driven in Iowa. A summary of those results and respective blow counts have been provided in Table 8.8. Bearing graph analyses were performed using the WEAP-SA-D, WEAP-UW-D, WEAP-UW-R, and WEAP-SA-R methods based on the measured hammer stroke heights and blow counts at the EOD or respective initial blows. Figure 8.16 compares the pile resistances from the WEAP methods against those from CAPWAP and SLTs for  $\mu$  and COV.

Compared with the WEAP-SA-D method, the WEAP-UW-D method for all data points does not changes in  $\mu$ , but the COV increases from 0.21 to 0.23. Compared with the WEAP-SA-D method, the WEAP-UW-R method provides better prediction of pile resistances at the EOD and initial blows with  $\mu = 1.04$  closer to unity and smaller COV = 0.13. For the test pile in Adair County, IA, pile resistances from the WEAP-SA-D method (309 kips) and WEAP-UW-R method (340 kips) were comparable to the measured pile resistance from the SLT (309 kips). However, both WEAP methods underpredict the resistances of test piles in Laramie County WY and Wapello County IA. The underprediction increases with the increasing delay in the SLTs from 3 days in Wapello County IA to 4 days in Laramie County WY. The underprediction was attributed to the development of the WEAP-UW-R method based on test results at the EOD and the potential increase in pile resistance or pile setup in fine-grained geomaterials. From these 21

data points, the WEAP-UW-R and WEAP-SA-R method improve the pile resistance prediction over the WEAP-SA-D and WEAP-UW-D method by reducing the COV and having  $\mu$  closer to unity. For the SLTs (3 data points), the improvement was not that significant. In fact, the WEAP-UW-R method increases in COV (0.31 to 0.34) compared to the WEAP-SA-D method despite having  $\mu$  closer to unity. Based on these 24 test pile data, the WEAP-UWR method improves the accuracy and reliability of pile resistance predictions on average by 12 percent (i.e.,  $\mu$  from 1.21 to 1.08) and 5 percent (i.e., COV from 0.21 to 0.20) in comparison to the WEAP-SA-D method.

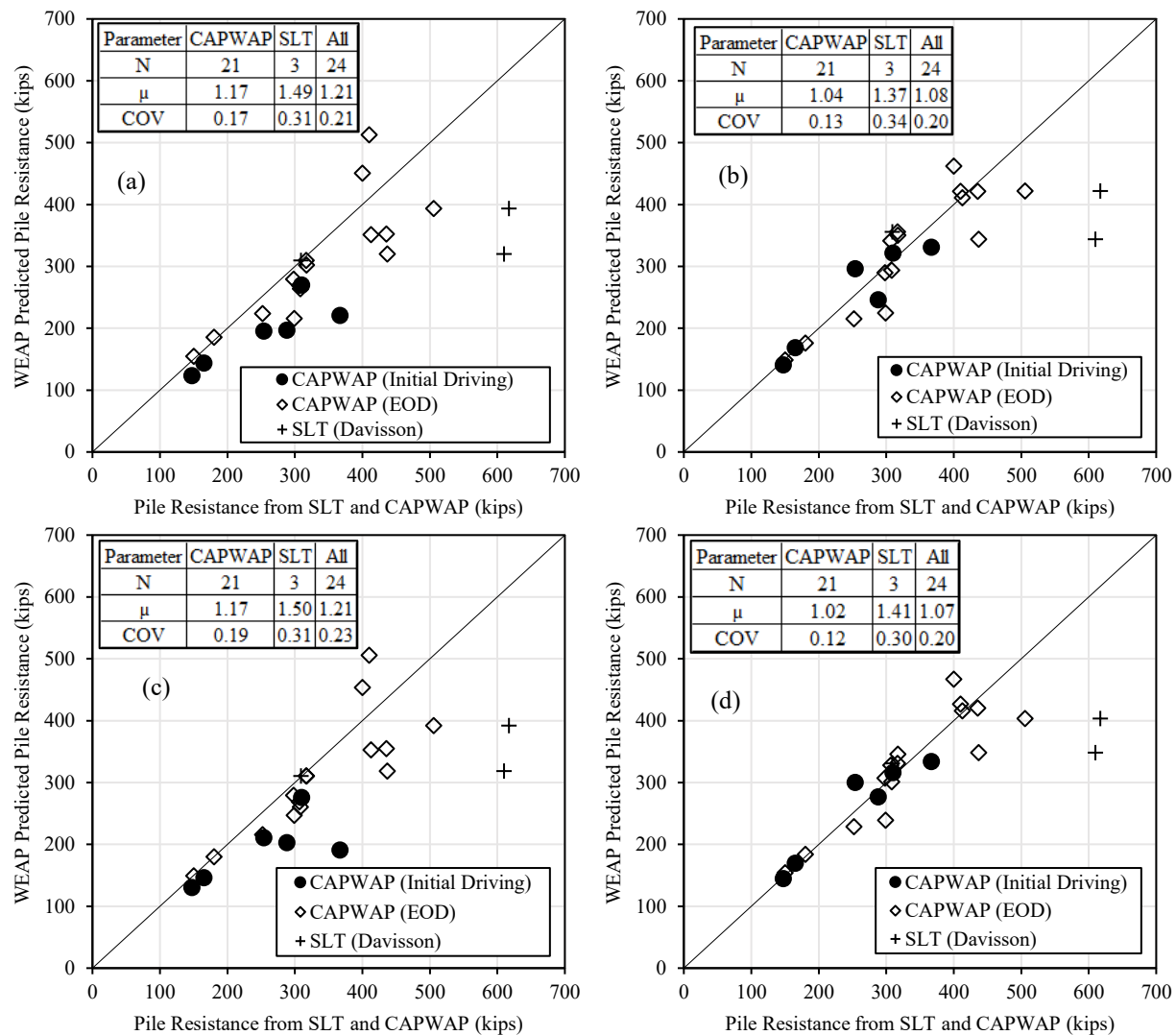


**Figure 8.16. Comparison of Pile Resistances from Static Load Tests and CAPWAP with the Predicted Pile Resistances from WEAP Methods for the 16 Validation Test Piles Using (a) WEAP-SAD, (b) WEAP-UWR, (c) WEAP-UWD, and (d) WEAP-SAR method.**

**Table 8.8. Summary of Independent Test Pile Data and Relevant Information for Validation of WEAP methods.**

State	Project	Test Type	Location	Pile type	L(ft)	Bearing geo- material	S (ft)	B	Rm	Hamme r	Rwp1	Rwp2	Rwp3	Rwp 4
ND	Cherry Creek Bridge Replacement	CAPWAP (blow number = 130)	TP	HP 12×53	50	Sandstone	7.5	10	165	Delmag D 30-32	144	143	146	146
ND	Cherry Creek Bridge Replacement	CAPWAP (blow number = 275)	TP	HP 12×53	60	Sandstone	7.5	19	288	Delmag D 30-32	197	197	203	203
ND	Cherry Creek Bridge Replacement	CAPWAP (blow number = 409)	TP	HP 12×53	66	Claystone	7.5	25	366.6	Delmag D 30-32	221	221	191	191
IA	Filmore Street over I- 35	CAPWAP (blow number = 282)	P2 at East A	HP 10×57	49	Shale	6.1	18	147.6	Delmag D 19-32	123	123	130	131
IA	Filmore Street over I- 35	CAPWAP EOD	P2 at East A	HP 10×57	56	Shale	7.2	40	306.9	Delmag D 19-32	269	269	269	269
IA	Highway 12 Over Indian Creek	CAPWAP blow number = 287	Pile 4 at N-A	HP 10×57	45	Shale	6.5	50	253.7	APE D 19-42	195	195	211	211
IA	Highway 12 Over Indian Creek	CAPWAP EOD	Pile 4 at N-A	HP 10×57	45.5	Shale	6.8	53	317.1	APE D 19-42	302	302	310	311
IA	Highway 12 Over Indian Creek	CAPWAP blow number = 160	P17 at Pi2	HP 10×57	23	Shale	6.5	41	310.1	APE D 19-42	270	270	275	274
IA	Highway 12 Over Indian Creek	CAPWAP EOD	P17 at Pi2	HP 10×57	26	Shale	7.3	68	400.1	APE D 19-42	451	450	453	455
IA	US 63 over Soap Creek	CAPWAP EOD	TP1	HP 14×117	21.7	Shale	7.3	53	410	Delmag D 19-42	513	513	506	506

WY	Bridge over Lodgepole Creek	CAPWAP EOD	P1 at A2	HP 14×89	54.9	Siltstone	6.8	21	150	Delmag D 19-42	154	155	149	149
WY	Bridge over Lodgepole Creek	CAPWAP EOD	P2 at A2	HP 14×89	54.9	Siltstone	7.1	28	180	Delmag D 19-42	186	186	180	180
WY	Bridge over Lodgepole Creek	CAPWAP EOD	P3 at A2	HP 14×89	55	Siltstone	7.9	38	299	Delmag D 19-42	215	215	247	247
WY	Bridge over Lodgepole Creek	CAPWAP EOD	P4 at A2	HP 14×89	54.9	Siltstone	7.8	35	252	Delmag D 19-42	223	223	216	215
IA	US 65 over Spring creek	CAPWAP EOD	P4 at South A	HP 10×57	20.1 6	Shale	6.6	120	412.9	Delmag D 19-42	351	350	353	353
IA	US 65 over Spring creek	CAPWAP EOD	P5 at South A	HP 10×57	20.0 8	Shale	6.95	120	435.7	Delmag D 19-42	352	351	354	354
IA	US 65 over East Beaver Dam Creek	CAPWAP EOD	P10 at North Pi	HP 14×73	11.5 4	Shale	6.6	84	298	Delmag D 19-42	279	279	279	279
IA	US 65 over East Beaver Dam Creek	CAPWAP EOD	P10 at North A	HP 10×42	28.5	Shale	6.25	74	308.1	Delmag D 19-42	264	263	260	261
IA	IA 92 over Marvel Creek	CAPWAP EOD	TP	HP 10×57	56	Shale	5.2	108	316.8	Delmag D 22	310	310	356	331
IA	IA 92 over Marvel Creek	SLT	TP	HP 10×57	56	Shale	NA	NA	309	NA	310	310	356	331
IA	Wapello US 63 Bridges	CAPWAP EOD	TP	HP 10×42	35.8	Shale	7.8	151	505.6	Delmag D 19-42	393	392	422	403
IA	Wapello US 63 Bridges	SLT	TP	HP 10×42	35.8	Shale	NA	NA	617	NA	393	392	422	403
WY	Bridge over Lodgepole Creek	CAPWAP EOD	TP	HP 10×42	55.5	Siltstone	8	96	437	Delmag D 19-42	320	318	344	348

WY	Bridge over Lodgepole Creek	SLT	TP	HP 10×42	55.5	Siltstone	NA	NA	610	NA	319.7	318.4	343.5	3478
----	-----------------------------------	-----	----	-------------	------	-----------	----	----	-----	----	-------	-------	-------	------

*L* = Penetration length; *A* = Abutment; *B* = Bent; *Pi* = Pier; *P* = Test pile; *N-A* = North-abutment; *S* = Stroke height; *B* = Blow count (b/ft); EOD = End of Driving; *R<sub>m</sub>* = CAPWAP measured pile capacity at EOD; HP = H pile; *R<sub>wp</sub>* = Pile capacity predicted from WEAP bearing graph analysis; <sup>1</sup> = Pile capacity predicted from WEAP-SA-D method; <sup>2</sup> = Pile capacity predicted from WEAP-UW-D method; <sup>3</sup> = Pile capacity predicted from WEAP-UW-R method; <sup>4</sup> = Pile capacity predicted from WEAP-SA-R method; NA = Not Available; EOD = End of Driving; CAPWAP = CAsE Pile Wave Analysis Program

**Table 8.9. Results from the Shapiro-Wilk and Anderson-Darling Tests for Soil Based IGM.**

Method	$n$	$\mu$	COV	Normal	Normal	Log-Normal	Log-Normal	Log-likelihood	Log-likelihood
				SW	AD	SW	AD		
				$p$	$p$	$p$	$p$	Normal	Log- Normal
WEAP-SAD	56	1.10	0.24	0.08	0.22	0.90	0.62	-4.99	-2.86
WEAP-UWD	56	1.11	0.23	0.10	0.13	0.46	0.24	-2.21	-1.05
WEAP-UWR	56	1.02	0.18	0.007	0.003	0.001	0.0008	NA	NA
WEAP-SAR	56	1.01	0.19	0.005	0.03	0.03	0.02	NA	NA
WEAP-SAD (No Outliers)	54	1.08	0.21	0.76	0.70	0.32	0.33	3.28	4.23
WEAP-UWD (No Outliers)	54	1.08	0.21	0.08	0.25	0.19	0.11	2.58	2.90
WEAP-UWR (No Outliers)	50	1.02	0.12	0.08	0.13	0.26	0.15	33.49	34.04
WEAP-SAR (No Outliers)	51	1.00	0.14	0.23	0.28	0.65	0.52	29.07	29.80

$n$  = Sample size;  $\mu$  = Mean resistance bias; COV = Coefficient of Variation; SW = Shapiro Wilk's test; AD = Anderson Darling test;  $p$  = p-value of normality test; NA = Not applicable.

**Table 8.10. Calibrated Resistance Factors for WEAP Analysis on driven piles in Soil-Based IGM.**

Method	FOSM				FORM				MCS			
	$\beta_T=2.33$	$\beta_T=2.33$	$\beta_T=3.00$		$\beta_T=2.33$	$\beta_T=2.33$	$\beta_T=3.00$		$\beta_T=2.33$	$\beta_T=2.33$	$\beta_T=3.00$	
	$\varphi$	$\frac{\varphi}{\mu}$	$\varphi$	$\frac{\varphi}{\mu}$	$\varphi$	$\frac{\varphi}{\mu}$	$\varphi$	$\frac{\varphi}{\mu}$	$\varphi$	$\frac{\varphi}{\mu}$	$\varphi$	$\frac{\varphi}{\mu}$
WEAP-SAD	0.70	0.64	0.57	0.52	0.82	0.75	0.70	0.64	0.82	0.75	0.69	0.63
WEAP-UWD	0.70	0.64	0.57	0.52	0.82	0.75	0.70	0.64	0.82	0.75	0.69	0.63
WEAP-UWR*	0.75	0.74	0.64	0.63	0.94	0.92	0.84	0.82	0.93	0.91	0.83	0.81
WEAP-SAR	0.72	0.72	0.61	0.61	0.88	0.88	0.79	0.79	0.88	0.88	0.77	0.77

FOSM = Factor of Safety Method; FORM = First Order Reliability Method; MCS = Monte Carlo Simulation;  $\beta_T$  = Reliability index;  $\varphi$  = Resistance factor;  $\frac{\varphi}{\mu}$  = Efficiency factor; \* = Most efficient method.



## 8.8 LRFD Resistance Factors

The resistance factors ( $\phi$ ) for WEAP, as recommended by the AASHTO (2020), were originally developed for piles driven in soils. To ascertain the reliability of WEAP on pile resistance predictions, the LRFD  $\phi$  was calibrated to reflect the uncertainty associated with the resistance prediction of driven piles in IGM. Improved pile design reliability was obtained by limiting the database to a particular geologic region and corresponding construction practices (Bougataya and Stuedlein 2016). The LRFD  $\phi$  was calibrated using FOSM, FORM, and MCS. The efficiency of the WEAP methods was assessed using efficiency factors ( $\phi/\mu$ ), which were established at reliability indexes ( $\beta_T$ ) of 2.33 and 3.0 for a redundant pile group and a non-redundant pile group, respectively (Paikowsky et al. 2004). The calibration of resistance factors using FOSM, FORM, and MCS required three statistical summaries:  $\mu$ , standard deviation and COV of resistance biases. The details of the calibration procedure were discussed in the literature (Paikowsky et al. 2004; Ng et al. 2018).

### 8.8.1 Soil Based IGM

The  $\phi$  values were calibrated using both the 34 training piles and 22 separate test piles used in the validation. The Shapiro-Wilk (SW) test and Anderson-Darling (AD) test were performed to assess whether the resistance biases violated the assumptions of Normality or Log-Normality. A significance level of 0.05 was used for these normality tests. The results of the normality tests were summarized in Table 8.9. For the WEAP-SAD and WEAP-UWD, no violation of the Normal and Log-Normal distribution assumptions was detected because the  $p$ -value were greater than 0.05. However, for the WEAP-UWR and WEAP-SAR, both the Normal and the Log-Normal distribution assumptions were rejected by the SW and AD tests as their  $p$ -values were less than 0.05. Test piles were identified as outliers if the difference between  $\lambda$  and  $\mu$  exceeds twice the standard deviation. These outliers were then excluded to improve the quality of the calibrated  $\phi$  (Paikowsky et al. 2004). The normality test results after removing the outliers (Table 8.9) showed that both the Normal and Log-Normal distribution assumptions were not violated for the WEAP-SA-D, WEAP-UWD, WEAP-UWR, and WEAP-SAR. Thus, the Log-Normal

distribution was selected in the LRFD  $\phi$  calibration based on the higher Log-likelihood value for all WEAP methods.

Table 8.10 shows that the  $\phi$  values of WEAP-SAD and WEAP-UW-D vary from 0.70 to 0.82 while higher  $\phi$  values ranging from 0.75 to 0.94 were calibrated for WEAPUWR at  $\beta_T = 2.33$ . Similarly, the  $\phi$  values of WEAP-SAR vary from 0.72 to 0.88 at  $\beta_T = 2.33$ . Lower  $\phi$  values ranging from 0.57 to 0.70, 0.57 to 0.70, 0.64 to 0.84, and 0.61 to 0.79 were calibrated for WEAP-SAD, WEAP-UWD, WEAP-UWR, and WEAP-SAR, respectively, at  $\beta_T = 3.00$ . These higher calibrated  $\phi$  values were attributed to  $\mu$  closer to one and lower COV values. In this study,  $\phi$  values based on FORM and MCS were on average 19.5 percent, 19.5 percent, 27.6 percent, and 25 percent higher than that from FOSM for WEAP-SAD, WEAP-UWD, WEAP-UWR, and WEAP-SAR, respectively. The  $\phi$  values for the WEAP-UWR and WEAP-SAR were only slightly higher than those for the WEAP-SAD and WEAP-UWD. In addition, the  $\phi/\mu$  values of the WEAP-UWR and WEAP-SAR were, on average, 22.9 percent and 18.4 percent higher than the  $\phi/\mu$  of the WEAP-SAD.

### **8.8.2 Rock Based IGM**

The calibrated resistance factors were developed using both the 95 training and 24 separate test pile data. The Shapiro-Wilk (SW) test and Anderson-Darling (AD) test were performed to test if the resistance biases violate the assumptions of the Normal or Log-Normal distributions (Table 8.11). A significance level of 0.05 was used for these normality tests. The Normal distribution assumption was rejected by the SW and AD tests for all WEAP methods as the p-values were less than 0.05 (Table 8.12). Since the p-values based on the SW test were greater than 0.05, for the WEAP-SA-D and WEAP-UW-R methods, no violation of the Log-Normal distribution assumption could be detected. However, for WEAP-UW-D and WEAP-SA-R methods, assumptions of Log-normal distribution were rejected by both SW and AD tests. Test piles were identified as outliers if the difference between  $\lambda$  and  $\mu$  exceeds twice the standard deviation. These outliers were then excluded to improve the quality of the calibrated  $\phi$  (Paikowsky et al. 2004). After removing the outliers, the assumption of Normal distribution was rejected by SW and AD tests for all WEAP methods. However, the assumptions of Log-normal distribution were

accepted by SW tests for all WEAP methods with  $p$  value greater than 0.05. Thus, the Log-normal distribution was selected for the  $\phi$  calibration.

The calibrated  $\phi$  and  $\phi/\mu$  values for both WEAP methods were calculated and summarized in Table 8.12. For the WEAP-SAD method, the  $\phi$  values range from 0.72 to 0.84 for  $\beta_T=2.33$  and 0.58 to 0.72 for  $\beta_T=3.00$ . For the WEAP-UWD method, the  $\phi$  values range from 0.73 to 0.86 for  $\beta_T=2.33$  and 0.60 to 0.74 for  $\beta_T=3.00$ . For the WEAP-UWR method, the  $\phi$  values range from 0.71 to 0.86 for  $\beta_T=2.33$  and 0.59 to 0.75 for  $\beta_T=3.00$ . For the WEAP-SAR method, the  $\phi$  values range from 0.69 to 0.84 for  $\beta_T=2.33$  and 0.58 to 0.74 for  $\beta_T=3.00$ . The calibrated LRFD  $\phi$  of all the WEAP methods for FOSM at  $\beta_T=2.33$  and  $\beta_T=3.00$  were similar and can be rounded up to the nearest 0.05 to be 0.7 and 0.6, respectively. Although the  $\phi$  values of the WEAP methods were similar, the efficiency factor ( $\phi/\mu$ ) values show that the WEAP-UW-R or WEAP-SA-R methods were the most efficient. Compared to WEAP-SA-D method, the average  $\phi/\mu$  values of the WEAP-UW-R method were on average 15.9 percent and 19 percent higher than the  $\phi/\mu$  of the WEAP-SA-D method for  $\beta_T=2.33$  and  $\beta_T=3.00$ , respectively. Also, the  $\phi/\mu$  values for the WEAP-UW-R and WEAP-SA-R were similar for all methods at all reliability indices. The  $\phi/\mu$  values show that the WEAP-UW-D method was slightly more efficient than the WEAP-SA-D method.

Comparing with the  $\phi$  of 0.40 at  $\beta_T=2.33$  recommended for WEAP at EOD using a database of 99 test piles in soils (Paikowsky et al. 2004), the proposed calibrated  $\phi$  values (0.72, 0.73, 0.71, and 0.69) using FOSM at  $\beta_T=2.33$  for piles driven in rock-based IGMs were 80 percent, 82.5 percent, 77.5 percent, and 72.5 percent higher for the WEAP-SA-D, WEAP-UW-D, WEAP-UW-R, and WEAP-SA-R methods, respectively. Furthermore, the proposed calibrated  $\phi$  values were higher than the  $\phi=0.50$  recommended in the AASHTO (2020). The proposed higher calibrated  $\phi$  values were attributed to the mean biases closer to 1.00 and lower COV values. Similarly, the  $\phi/\mu$  of the WEAP-SA-D, WEAP-UW-D, WEAP-UW-R, and WEAP-SA-R methods for  $\beta_T=2.33$  using FOSM (i.e., 0.62, 0.63, 0.7, and 0.7 respectively) were about 158.3 percent, 162.5 percent, 191.7 percent, and 191.7 percent higher than the  $\phi/\mu$  of 0.24 developed for piles in soils (Paikowsky et al. 2004).

**Table 8.11. Results from the Shapiro-Wilk Test and Anderson-Darling Test.**

WEAP Method	$N$	$\mu$	$COV$	Normal		Log-Normal		Log likelihood	
				SW	AD	SW	AD	Normal	Log-Normal
				$p$	$p$	$p$	$p$		
WEAP-SAD	119	1.15	0.25	0.002	0.002	0.51	0.27	-2.44	-2.44
WEAP-UWD	119	1.16	0.26	0.000005	0.000005	0.04	0.04	-7.04	2.40
WEAP-UWR	119	1.03	0.20	0.000006	0.000006	0.07	0.004	23.89	30.40
WEAP-SAR	119	1.02	0.21	0.000002	0.0000002	0.006	0.0002	18.80	27.26
WEAP-SAD (No Outliers)	115	1.13	0.22	0.02	0.01	0.20	0.20	12.08	14.26
WEAP-UWD (No Outliers)	114	1.13	0.21	0.015	0.007	0.31	0.30	18.46	21.05
WEAP-UWR (No Outliers)	113	1.01	0.16	0.003	0.0006	0.05	0.01	46.11	48.28
WEAP-SAR (No Outliers)	113	0.99	0.16	0.007	0.0004	0.05	0.003	45.71	46.86

$N$  = Sample size;  $\mu$  = Mean resistance bias;  $COV$  = Coefficient of variation; SW = Shapiro Wilk's test; AD = Anderson Darling test;  $p$  = p-value of normality test.

**Table 8.12. Calibrated Resistance Factors for WEAP Analysis on Piles in Rock-Based IGM.**

Method	FOSM				FORM				MCS			
	2.33		3.00		2.33		3.00		2.33		3.00	
	$\varphi$	$\frac{\varphi}{\mu}$	$\varphi$	$\frac{\varphi}{\mu}$	$\varphi$	$\frac{\varphi}{\mu}$	$\varphi$	$\frac{\varphi}{\mu}$	$\varphi$	$\frac{\varphi}{\mu}$	$\varphi$	$\frac{\varphi}{\mu}$
WEAP-SAD	0.72	0.62	0.58	0.50	0.84	0.72	0.72	0.62	0.83	0.72	0.7	0.60
WEAP-UWD	0.73	0.63	0.6	0.52	0.86	0.74	0.74	0.64	0.85	0.73	0.72	0.62
WEAP-UWR*	0.71	0.70	0.59	0.58	0.86	0.85	0.75	0.74	0.85	0.84	0.74	0.73
WEAP-SAR	0.69	0.70	0.58	0.59	0.84	0.85	0.74	0.75	0.83	0.84	0.72	0.73

FOSM = First Order Second Method; FORM = First Order Reliability Method; MCS = Monte Carlo Simulation;  $\varphi$  = Resistance factor; and  $\frac{\varphi}{\mu}$  = Efficiency factor.

## 8.9 Summary and Conclusions

A total of 129 test piles consisting of thirty-four test piles driven into soil based IGM from four states and ninety-five test piles driven into rock based IGM from seven states were used in this study to develop a new procedure for WEAP analysis to improve the prediction of pile resistances. The back-calculation of the Smith dynamic parameters for the soil-based IGM was performed by matching the WEAP predicted pile resistance with the measured resistance from CAPWAP at the EOD.

- A value of 0.1 inch and  $D/120$  for  $Q_s$  and  $Q_t$ , respectively, were found to be adequate for both soil-based IGMs and rock based IGMs.
- The Smith damping factors were found to depend on the pile driving and subsurface conditions. Single values of Smith damping factors were inadequate in satisfying different pile and driving conditions. Three subsurface conditions were identified based on overburden and bearing geomaterials. Prediction equations to reflect different pile conditions and driving conditions were proposed to predict the damping factors. For the subsurface condition I with a fine-grained soil-based IGM as the bearing layer, the proposed equation was recommended for  $J_s$  and  $J_t$ .
- For the subsurface condition II with a coarse-grained soil-based IGM as the bearing layer, the proposed equation was recommended for  $J_s$  and  $J_t$ . However, for subsurface condition III, the average back-calculated damping factors of 0.10 s/ft and 0.18 s/ft were recommended for coarse-grained soil-based IGM and fine-grained soil-based IGM, respectively.
- The  $J_s$  and  $J_t$  values were found to be highly dependent on the pile driving and subsurface conditions. For subsurface condition IV, a prediction equation to reflect different pile and driving conditions was proposed to predict  $J_s$  and  $J_t$  for rock-based IGMs, except for shale. Average damping factors of 0.09 s/ft, 0.15 s/ft were recommended for MW-SW shale and SS-HW shale, respectively.
- For subsurface condition V, average back-calculated  $J_s$  and  $J_t$  values of 0.10 s/ft, 0.18 s/ft, 0.10 s/ft, 0.09 s/ft, 0.15 s/ft were recommended for coarse-grained soil-based IGM, fine-

grained soil-based IGM, rock-based IGM except shale, MW-SW shale, and SS-HW shale, respectively.

- A  $\phi$  value of 0.70, 0.70, 0.75, and 0.72 for WEAP-SA-D, WEAP-UW-D, WEAP-UW-R, and WEAP-SA-R, respectively, calibrated based on FOSM at  $\beta_T=2.33$  for piles driven in soil-based IGMs were higher than the  $\phi$  value of 0.5 recommended in AASHTO (2020) for piles in soils. Comparing with  $\phi = 0.4$  calibrated for piles in soils by Paikowsky et al. (2004), the calibrated  $\phi$  values increase 75 percent, 75 percent, 87.5 percent, and 80 percent for WEAP-SA-D, WEAP-UW-D, WEAP-UW-R, and WEAP-SA-R, respectively. In addition to having slightly higher  $\phi$  values, WEAP-UWR was found to be the most efficient for Soil Based IGM.
- The  $\phi$  values of 0.72, 0.73, 0.71, and 0.69 calibrated for WEAP-SA-D, WEAP-UW-D, WEAP-UW-R, and WEAP-SA-R methods based on FOSM for  $\beta_T=2.33$  were higher than the current AASHTO (2020) recommended  $\phi$  value of 0.5. Compared with the  $\phi$  value calibrated for WEAP on piles in soils by Paikowsky et al. (2004), the proposed calibrated  $\phi$  values increase by 80 percent, 82.5 percent, 77.5 percent, and 72.5 percent for WEAP-SA-D, WEAP-UW-D, WEAP-UW-R, and WEAP-SA-R methods, respectively. The  $\phi/\mu$  values of the WEAP-SA-D, WEAP-UW-D, WEAP-UW-R, and WEAP-SA-R methods for piles in IGMs based on  $\beta_T=2.33$  and FOSM were about 158.3 percent, 162.5 percent, 191.7 percent and 191.7 percent higher than the  $\phi/\mu$  values developed for piles in soil by Paikowsky et al. (2004). The WEAP-UW-R method was found to be most efficient among the four WEAP methods.

## **CHAPTER 9: MACHINE LEARNING BASED ECONOMIC IMPACT ANALYSIS FOR STEEL PILES DRIVEN IN INTERMEDIATE GEOMATERIALS**

### **9.1 Introduction**

This chapter presents an economic impact assessment of steel piles driven in IGM by comparing the performance of newly developed SA methods and existing SA methods using 149 dynamic pile load test (DLT) results from seven US states. The economic impact assessment considers the number of piles required for each bridge abutment, bent, or pier. The factored total resistance determined from the PDA with subsequent signal matching using the CAPWAP for each of the 149 test piles was taken as the baseline in each comparison. The respective total number of piles required for each abutment, pier, or bent was calculated by dividing the total structural load with the total factored resistance obtained either from DLT, existing SA method, or proposed SA method. The difference in the number of piles was calculated by subtracting the number of piles predicted using the existing SA method or proposed SA method from the number of piles based on the DLT. The difference in number of piles was converted to an equivalent steel weight that was then normalized by the respective structural load demand. The positive and negative steel weights per load indicate the underestimation and overestimation of number of piles from the SA method resulting from the overestimation and underestimation of the pile resistance, respectively.

A comparative study was conducted based on different states, pile types, and bearing IGM layers to evaluate the differences in steel pile weight per load for the proposed and existing SA methods. Three Machine Learning (ML) algorithms: Random Forest (RF), Support Vector Machine (SVM) and Neural Network (NNET) were used to predict the difference in steel weight based on the proposed SA method. To predict the difference in steel weight, three percentage-based variables were employed as inputs: total pile penetration, total shaft resistance, and total end bearing in IGM. Among the 149 test piles, 118 test piles were used to train the ML algorithms, and 31 test piles were used to validate the ML algorithms. The predicted difference in steel weight from a selected ML Algorithm was optimized to achieve zero difference in steel weight using a novel application of the Genetic Algorithm (GA) to minimize the discrepancy



resulting from pile design during construction. The best ML algorithm, in this case SVM, was used to produce contour maps of the predicted difference in steel pile weight at the optimized value based upon the training data. These contour maps were then validated with this test data. The validation indicates that these contour plots can be used as a guide to enhance the pile performance in IGMs for future bridge projects.

## **9.2 Historical Pile Load Test Data**

In this study, a pile load test database was created to compile bridge project construction plans, pile load test results, site investigation bore logs, pile driving records, hammer information, and other relevant technical reports from seven state transportation agencies. The total number of test piles, depending on pile types and bearing IGM layers, and pile penetration ranges were shown in Figures 9.1 and 9.2. The number of test piles ranges from 3 in North Dakota to 38 in Kansas. All states use steel H-piles while only Montana uses steel pipe piles. Figure 9.1 shows that the pile penetration ranges from 11.5 ft of the H-pile in Kansas to 139 ft of the H-pile in Wyoming. Figure 9.2 shows that Montana has the most difference in bearing IGM layers while Kansas has only shale as the bearing IGM layer. Figure 9.2 shows a wide range of pile penetrations in IGM for different states from 1 ft to 69 ft. Among the total 149 test piles, 117 driven piles were H10 to HP14 piles while the remaining 32 test piles were 16-in to 24-in diameter steel pipe piles (3 close-ended and 29 open-ended). Among the 149 test piles, 48 test piles were in shale, 24 in fine-grained soil-based IGM (FG-IGM), 23 in coarse-grain soil-based IGM (CG-IGM), 21 in claystone, 19 in siltstone, 10 in sandstone, and 4 in mudstone. The proposed classification criteria and static analysis methods have been used for economic impact assessment.

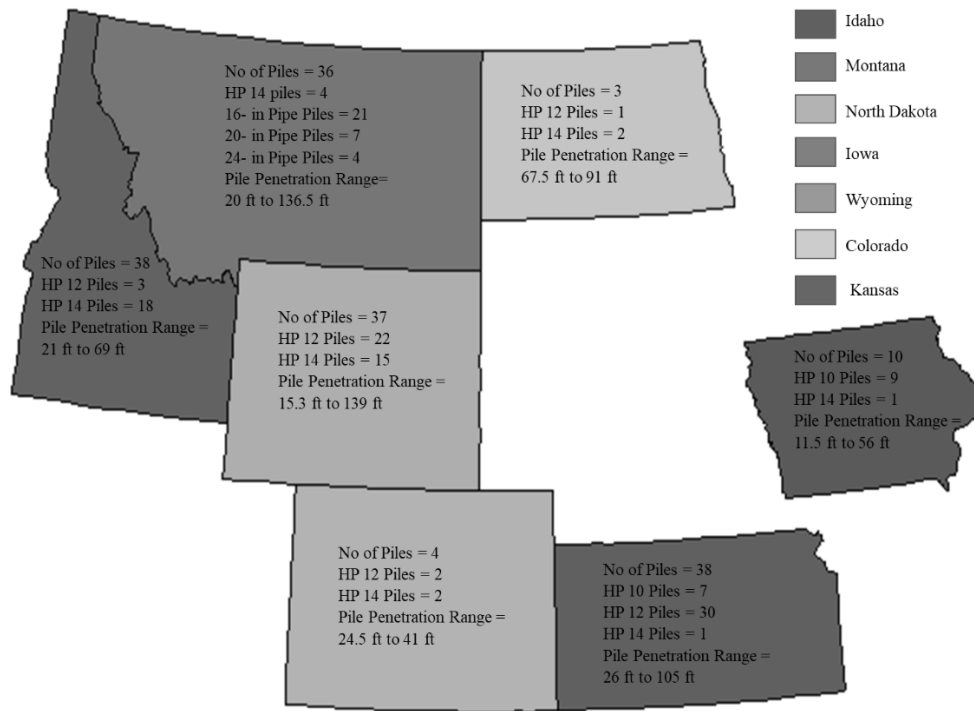


**Figure 9.1. Map of the Total Number of Test Piles and Total Pile Penetration Ranges in Seven US States.**

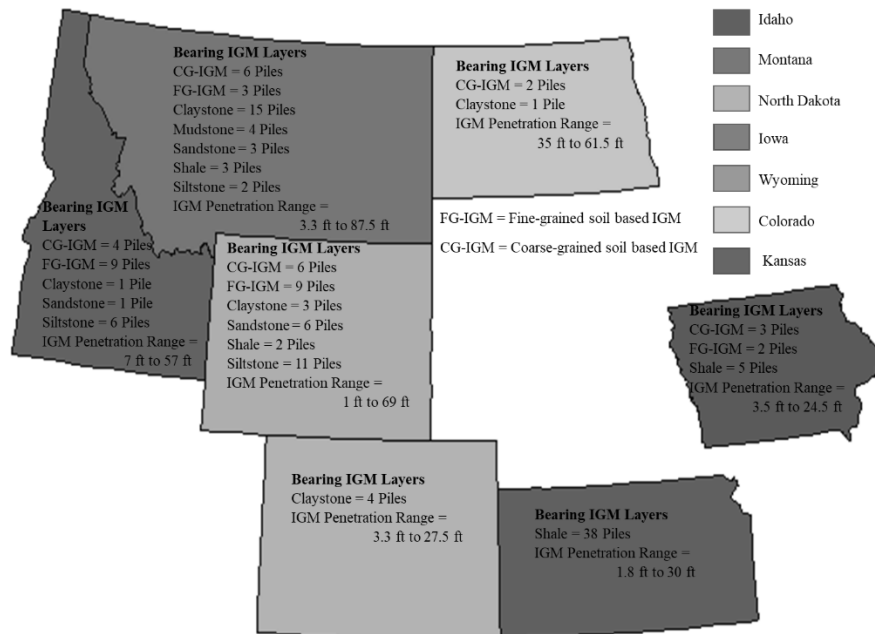


**Figure 9.2. Map Showing the Bearing IGM Layers for Different Test Piles and Range Of Pile Penetration in IGM in Seven US States.**

## 9.3 Economic Impact Assessment

### 9.3.1 Methodology and Test Pile Example

An economic impact assessment was carried out to examine the effectiveness of the proposed SA methods and LRFD recommendations in terms of quantities for cost estimation with respect to the results from the pile load test during bridge construction, such as number of piles and steel weights. The methodology for economic impact assessment has the following seven steps:

Step 1. The total load demand at each pier or abutment location was calculated by multiplying the factored load per pile ( $\gamma Q$ ) with the number of piles per pier or abutment.

Step 2. The total factored resistance per pile from CAPWAP ( $\phi R_C$ ) was determined using the AASHTO (2020) recommended  $\phi$  of 0.65. The total pile resistance determined from CAPWAP was considered as the field “measured” resistance, which was used to determine the required number of production piles installed on site in the study.

Step 3. Using the total pile penetration length in the geomaterial, total resistance per pile was calculated using the existing SA methods. The  $\beta$ -method with  $\phi$  of 0.25 was used for coarse-grained soil and CG-IGMs, and the  $\alpha$ -method with  $\phi$  of 0.35 was used for fine-grained soil and FG-IGMs. For R-IGMs, siltstone, claystone, and mudstone were denoted as fine-grained rock as they contain more than 50 percent silt and clay. Sandstone was denoted as coarse-grained rock as it contains more 50 percent sand sized particles (Picard 1971). Finally, the total factored resistance using existing SA methods ( $\phi R_E$ ) for each test pile was calculated by adding the total shaft resistances and end bearing.

Step 4. Using the total pile penetration, the  $\phi R$  per pile was calculated using a combination of existing SA methods for soil and the proposed SA methods for IGM along with their corresponding  $\phi$  values based on  $\beta_T$  of 2.33 for Monte Carlo Simulations. Finally, the total factored resistance ( $\phi R_P$ ) for each test pile was calculated using the proposed SA method for IGM by adding the total shaft resistances and end bearing.

Step 5. The required number of piles to satisfy the LRFD strength limit state ( $\gamma Q \leq \phi R$ ) was determined by dividing the total load demand from Step 1 with the  $\phi R$  from Step 2 ( $\phi R_C$ ), Step 3 ( $\phi R_E$ ), and Step 4 ( $\phi R_P$ ) depending on the design and construction control methods.

Step 6. The difference in the number of piles was calculated by subtracting the number of piles for the existing SA method from the number of piles based on the pile load test. Similar calculation of the difference in the number of piles was calculated for the proposed SA method. A negative difference indicates the underprediction of pile resistance by the SA method resulting in a higher number of piles than that from the pile load test. A positive difference indicates the overprediction of pile resistance by the SA method resulting in a lower number of piles than that from the pile load test.

Step 7. The difference in number of piles was converted to an equivalent steel weight by calculating the plug weight (difference in number of piles  $\times$  pile penetration length  $\times$  unit weight of pile), which was then normalized by the respective load demand determined from Step 1. The positive and negative steel weights per load indicate underestimation and overestimation of numbers of piles, respectively. A flow chart describing the methodology was shown in Figure 9.3.

To demonstrate this methodology, a sample calculation was performed on the HP 12 $\times$ 53 test pile from the Cherry Creek Bridge on Highway 1806 in North Dakota. This project was selected as an example because the subsurface profile consists of multiple different geomaterial layers (Figure 9.4). Table 9.1 shows that the  $\phi R_C$ ,  $\phi R_E$  and  $\phi R_P$  values were 278.9 kips, 140.33 kips, 209.9 kips, respectively. The number of test piles were calculated as  $N_C=4.66$ ,  $N_E=9.26$ , and  $N_P=6.19$  for the CAPWAP, existing SA method, and proposed SA method, respectively, by dividing the total factored structural load of 1,300 kips with total factored resistance obtained from respective methods. Next, the differences in number of piles were calculated as -4.60 ( $N_C - N_E$ ) for the existing SA method and -1.53 ( $N_C - N_P$ ) for the proposed SA method. The next step was to convert the difference in number of piles to an equivalent steel weight, which was -16334.60 lbs for the existing SA method and -5433.03 lbs for the proposed SA method. Finally, the difference in steel weight was normalized by the total factored structural load, which was -

12.57 lbs/kip for the existing SA method and -4.18 lbs/kip for the proposed SA method. The differences in number of piles or differences in steel weight based on the existing and proposed SA methods were negative, indicating underestimation of the pile resistance and overestimation of the number of piles than that of CAPWAP. The proposed SA method yields a smaller difference in steel weight of -4.18 lbs/kip compared to -12.57 lbs/kip of the existing SA method.

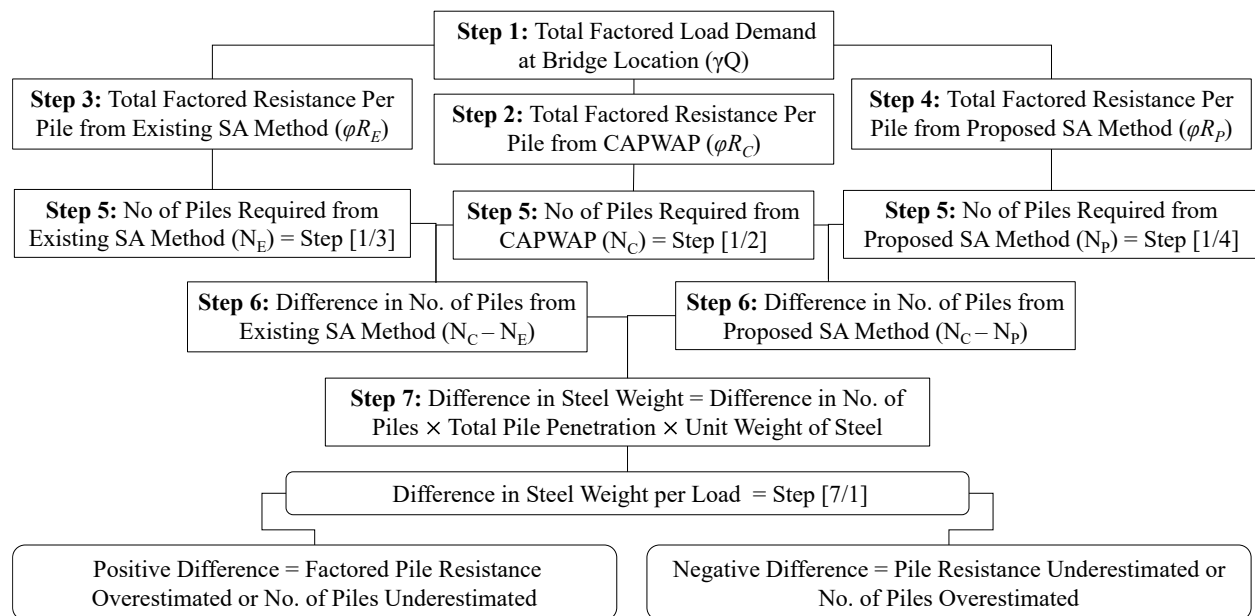


**Figure 9.3. A Flow Chart Showing the Methodology for Economic Impact Assessment.**

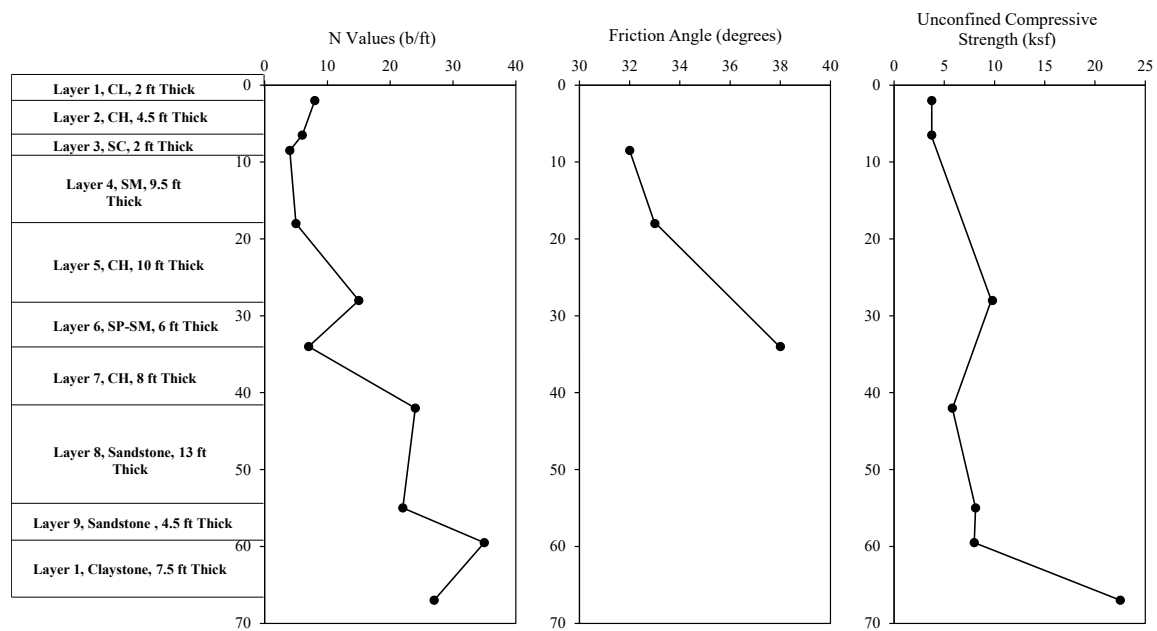


**Figure 9.4. Subsurface Profile and Geomaterial Properties for the Test Pile from the Cherry Creek Bridge on Highway 1806 in North Dakota.**

**Table 9.1. Calculation of Difference in Steel Weight for a HP12×53 Test Pile in ND.**

<b>Step 1 - Total Structural Load (kips)</b>	1300	
<b>Step 2 - Total Resistance from CAPWAP (kips)</b>	429.1	
<b>Step 2 - Factored Resistance from CAPWAP, <math>\phi R_C</math> (kips)</b>	278.9	
<b>Shaft resistance (kips)</b>	<b>Existing SA Methods</b>	<b>Proposed SA Methods</b>
Layer 1 (FG-soil)	4.16	4.16
Layer 2 (FG- soil)	9.35	9.35
Layer 3 (CG- soil)	0.55	0.55
Layer 4 (CG-soil)	4.90	4.90
Layer 5 (FG-IGM)	17.06	45.1
Layer 6 (CG-soil)	7.38	7.38
Layer 7 (FG-IGM)	12.68	5.17
Layer 8 (R-IGM)	18.65	27.33
Layer 9 (R-IGM)	6.25	9.47
Layer 10 (R-IGM)	29.45	26.77
<b>Steps 3 &amp; 4 - Total Factored Shaft Resistance (kips)</b>	110.43	140.18
<b>Steps 3 &amp; 4 - End Bearing (kips)</b>	29.90	69.8
<b>Steps 3 &amp; 4 - Total Factored Resistance (kips)</b>	<del><math>\phi R_E</math></del> = 140.33	<del><math>\phi R_E</math></del> = 209.9
Total Pile Penetration (ft)	67	
Total Penetration in IGM (ft)	43	
Total Penetration in IGM (%)	64	
Percent Shaft Resistance in IGM (%)	59.9	54.2
Percent End Bearing in IGM (%)	21.3	33.3
<b>Step 5 - No of Piles (CAPWAP), <math>N_C</math></b>	4.66	
<b>Step 5 - No of Piles from SA Methods</b>	$N_E = 9.26$	$N_P = 6.19$
<b>Step 6 - <math>N_C - N_E</math> or <math>N_C - N_P</math></b>	-4.60	-1.53
<b>Step 7 - Equivalent difference in Steel Weight (lbs)</b>	-16334.60	-5433.03
<b>Difference in Steel Weight (lbs/kip)</b>	-12.57	-4.18

### 9.3.2 Comparative Study of the Difference in Steel Pile Weight

A comparative study was conducted to determine the average difference in steel weight for both the proposed and existing SA methods based on different states, pile types, and bearing IGM types (Figure 9.5). All states, except North Dakota, yield negative differences in steel weight ranging from -4.93 lbs/kip to -12.67 lbs/kip based on pile resistances predicted using the existing SA method. This indicates the underestimation of total factored pile resistance from the existing SA method for all states, which leads to overestimation of the number of piles. The negative differences in steel weight from the proposed SA method were also observed in Kansas, Idaho, Wyoming, Montana, and Colorado. However, the more efficient proposed SA method yields a smaller average difference in steel weight. Figure 9.5 shows that for all pile types, the existing

SA method yields -1.21 lbs/kip to -16.47 lbs/kip. Except for the HP10 and 20-in pipe piles, the proposed SA method yields -1.27 lbs/kip to -5.55 lbs/kip that were smaller than that of the existing SA method. The proposed SA method yields 0.78 lbs/kip only in CG-IGM while existing SA method yields -1.23 lbs/kip. For the other six IGM bearing layers, both the proposed SA methods and existing SA methods yield -0.99 lbs/kip to -9.07 lbs/kip and -1.57 lbs/kip to -13.38 lbs/kip, respectively.

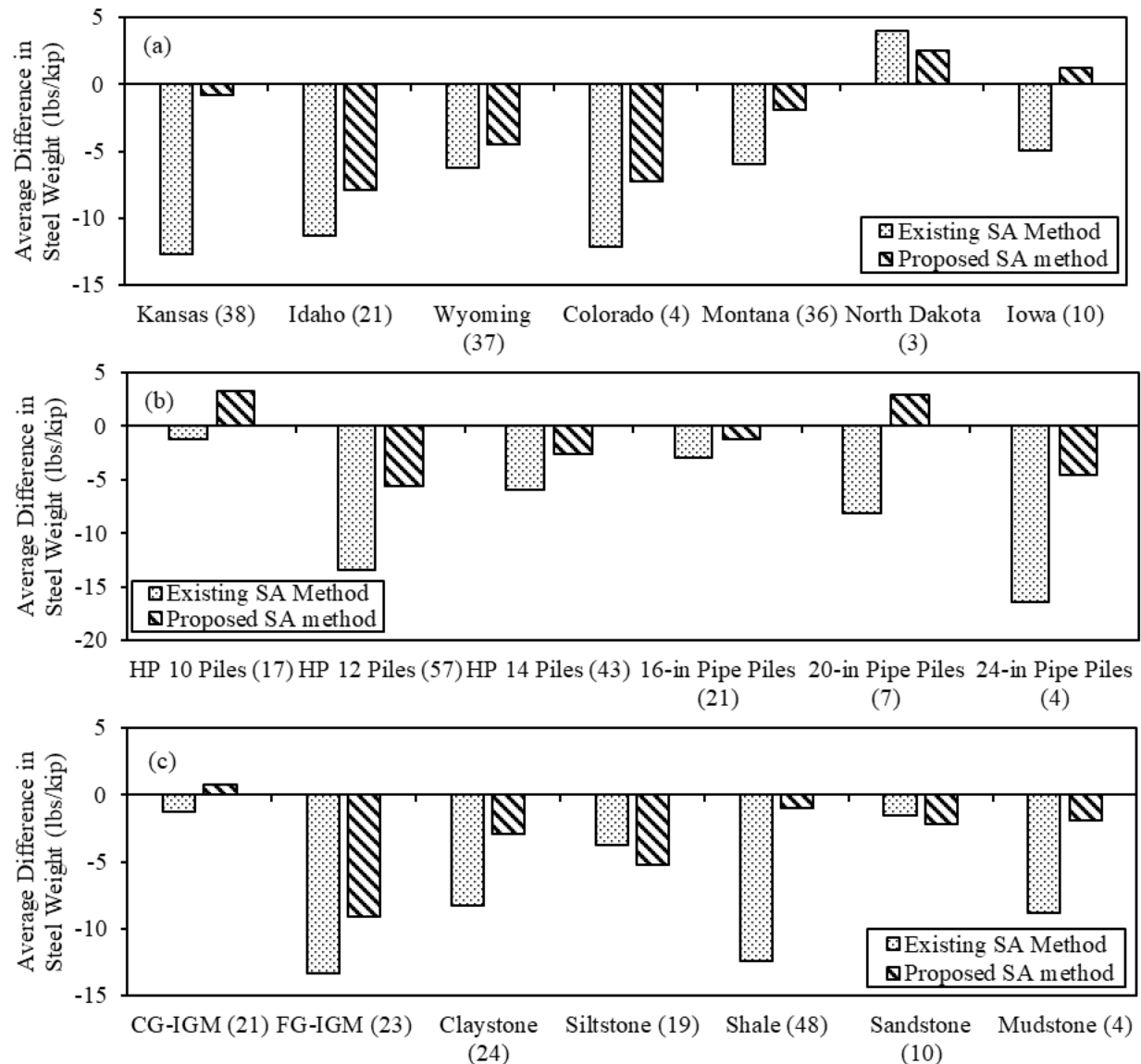


**Figure 9.5. Plots of Average Difference in Steel Weight based on (a) States, (b) Pile Types, and (c) Bearing IGM types with No. of Piles in Each Parenthesis.**



#### 9.4 Prediction of Difference in Steel Weight with Machine Learning Algorithms

The difference in steel weight for the proposed SA method was predicted using Machine Learning (ML) algorithms. Three independent variables used in this study were pile penetration in IGM layers (ft), total shaft resistance from IGM layers (kips), and end bearing from an IGM layer (kips). These variables were used to predict the difference in steel weight (lbs/kip). To make the analysis more interpretable, these independent variables were converted into percentages denoted as percent length, percent shaft, and percent end in IGM as given by Equations shown in Figure 9.6a, 9.6b, and 9.6c respectively.

$$\text{a) \% length in IGM} = \frac{\text{Total Penetration in IGMs (ft)}}{\text{Total Pile Penetration (ft)}} \times 100$$

$$\text{b) \%shaft in IGM} = \frac{\text{Total Factored Shaft Resistance Contributed from IGMs (kip)}}{\text{Total Factored Pile Resistance (kip)}} \times 100$$

$$\text{c) \% end in IGM} = \frac{\text{Total Factored End Bearing from IGM (kip)}}{\text{Total Factored Pile resistance (kip)}} \times 100$$

**Figure 9.6. Equations. Predictors of the Difference in Steel Weight Involving Percentage of IGM a) Length, b) Shaft, and c) End**

Figure 9.7 illustrates the pairwise relationships and sample correlations of the response variable (the difference in steel weight) and the independent variables (percent length, percent shaft, and percent end in IGM) based on 149 test piles. These sample correlations do not demonstrate any simple linear relationships between the independent variables and the difference in steel weight as the correlation values of -0.088, -0.089, and -0.1567 were relatively close to zero. Thus, ML algorithms were used in this study, rather than attempting to model possible complex relationships that also require model-based assumptions. The goal of ML was to generate predictions by learning from previous (training) data to adequately predict future (test) data.

Among the 149 test piles, a sample of 118 observations was used for training and the remaining 31 observations were used for testing. The ML algorithms of interest include Random Forest (RF), Neural Network (NNET), and Support Vector Machine (SVM). The next section provides a short methodology describing the ML algorithms, and how they were applied in this study. The ML algorithms were implemented using the R program (R Core Team 2006) where specific details of this implementation were described below.

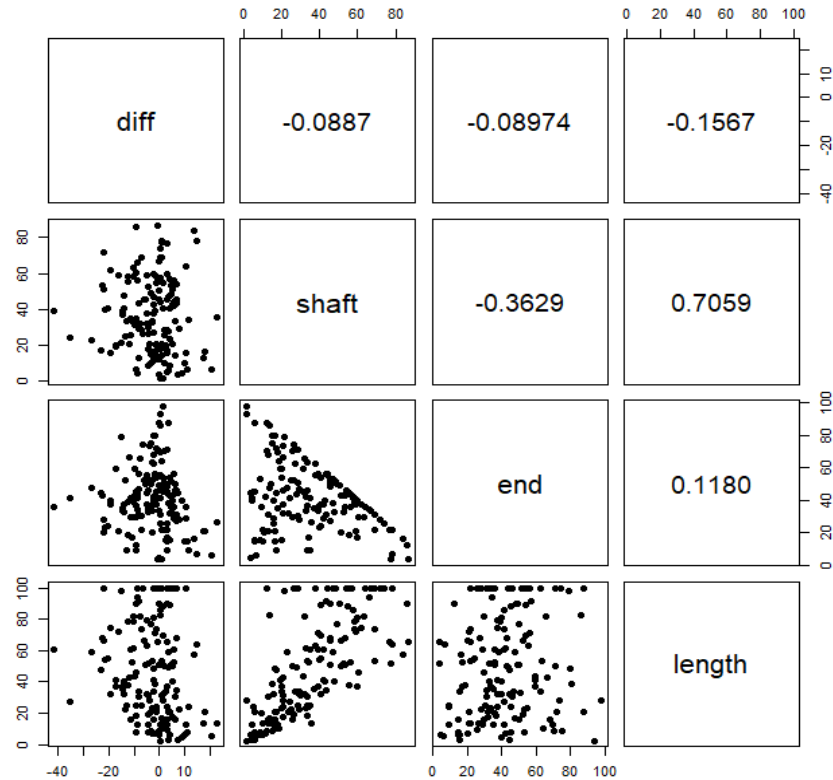


**Figure 9.7. Pairwise Relationships Among the Variables Based on 149 Test Piles.**

#### **9.4.1 Random Forest (RF)**

Random Forest (RF) improves performance and accuracy by combining decision trees. It was a bagging ensemble method, which means that a subset of the data was used to train each individual tree in parallel, and the predicted value was the average from the decision trees.

Preliminary analyses were conducted using simple regression trees (Izenman 2008, James et al. 2013). However, this approach proves to be too simplistic to provide good predictive results for

this study. Thus, RF was used to accommodate the additional complexity. RF, as used here, was a collection of 500 hundred decision trees that vary due to bootstrap samples of the observations (James et al. 2013, Breiman 2001). A subset of the predictor variables was also used to decorrelate the trees. The number of variables in which to build these trees (mtry) serves as a hyperparameter for RF (James et al. 2013).

#### ***9.4.2 Neural Network (NNET)***

The Neural Network (NNET) was a commonly used ML algorithm in engineering applications. NNET was designed to automatically mimic the intelligence of the human brain and so consists of three layers of neurons associated with inputs, hidden layers, and the output (Izenman 2008, Ripley 1996, Venables et al. 2002). A single hidden layer was used here, and the number of neurons for this hidden layer (size) was the hyperparameter. The activation functions relating the response and the predictors to the hidden layer were chosen to be linear, which was associated with better predictive performance in this application (Kutner et al.2004).

#### ***9.4.3 Support Vector Machine (SVM)***

The Support Vector Machine (SVM) was a complicated ML algorithm, yet it provides a flexible approach. The SVM has been adapted for regression problems in which the response variable was continuous as in this study (Chang et al. 2011). The objective of SVM was to identify a function, described as an epsilon hypertube, that closely tracks the response variable. In this study, epsilon was taken to be 0.01 and the cost of misprediction was taken to be 1. The key that makes SVM so powerful was the 'kernel trick', which enables SVM to perform better with respect to the multi-dimensional predictor space. The radial kernel was a commonly used kernel for SVM to account for nonlinearity, and this kernel depends upon the specification of the hyperparameter for scaling (scale) (Ripley 1996).

#### ***9.4.4 Hyperparameter Tuning***

The ML algorithms depend upon hyperparameter values that must be optimally set for this application. This includes 'mtry' for RF, 'size' for NNET, and 'scale' for SVM. The optimal

setting of these hyperparameter values was dictated by the predictive ability of these algorithms. Thus, to prevent overfitting, these hyperparameter values were determined using Leave-One-Out Cross Validation (LOOCV) from the training data set (Kutner et al. 2004). Thus, the hyperparameter values were chosen to minimize the Root Mean Square Error (RMSE) given below based upon LOOCV as shown in Figure 9.8 where  $y_{(i)}$  was the difference in steel weight that was not fit by the algorithm, and  $\hat{y}_{(i)}$  was the corresponding predicted value for this new value for  $y_{(i)}$ . In this manner, the hyperparameters of the ML algorithms were chosen to be optimized for predicting new observations. The LOOCV evaluation was conducted using the train function in the R package ‘caret’ (Kuhn 2008).

$$\text{LOOCV RMSE} = \frac{1}{n} \sum_{i=1}^n (y_{(i)} - \hat{y}_{(i)})^2$$

**Figure 9.8. Equation. Computation of LOOCV RMSE.**

This function was also able to evaluate the variable importance (VI) of the predictors in each of the ML algorithms based upon LOOCV. A high VI measure for a predictor indicates that predictor variable was more important to the predictive ability of the ML algorithm. Table 9.2 shows the LOOCV RMSE values and variable importance for three different ML algorithms. The prediction performance results show that SVM has lower LOOCV RMSE value and that the most important variable was percent length for SVM

**Table 9.2. Different Factors for the Exploration of Machine Learning Algorithms.**

Hyperparameter Tuning					
ML Algorithms	Hyperparameter values	LOOCV RMSE	Variable Importance		
			% shaft	% end	%length
RF	mtry = 1	9.58	3423.74	3166.98	3358.79
NNET	size = 5, decay=0	9.82	29.89	29.32	40.78
SVM	sigma = 0.3	9.41	0.09	0.07	0.16
Prediction Performance					
ML Algorithms		RMSE	MAD	R2	
RF		8.17	6.84	0.13	
NNET		8.01	7.03	0.16	
SVM		7.91	6.56	0.18	
Optimization					
ML Algorithms	% shaft	% end	% length	Predicted steel weight difference (lbs/kips)	
RF	51.78	54.64	21.49	0.000319	
NNET	65.22	48.28	15.07	0.000356	
SVM	43.01	36.32	31.47	0.000314	

#### 9.4.5 Prediction Performance

The data in this study utilizes a validation set approach in which the data was randomly split into a training set and a testing set (James et al. 2013). The ML algorithms with the tuned hyperparameters were applied to the test data to evaluate predictive performance. The performance metrics for the test data include the Root Mean Square (RMSE), Mean Absolute Deviation (MAD), and Pseudo-R<sup>2</sup> (R2) were given below in Figure 9.9. R2 should not be confused with the usual coefficient of variation, but it provides a crude measure of predictive ability of the ML algorithm relative to using the mean of the testing data for prediction (Kutner 2004). The best ML algorithm should minimize RMSE and MAD and maximize R2 for the testing data. The criteria values were shown in Table 7.3. The R2 values here were not very high but do demonstrate predictive ability in the ML algorithms. The best predictive performance on the test data was SVM according to all three criteria.

$$\text{a) RMSE} = \frac{1}{n} \sum_{i=1}^n (y_i - \hat{y}_i)^2$$

$$\text{b) MAD} = \frac{1}{n} \sum_{i=1}^n |y_i - \hat{y}_i|$$

$$\text{c) R2} = 1 - \sum_{i=1}^n (y_i - \hat{y}_i)^2 / \sum_{i=1}^n (y_i - \bar{y}_i)^2$$

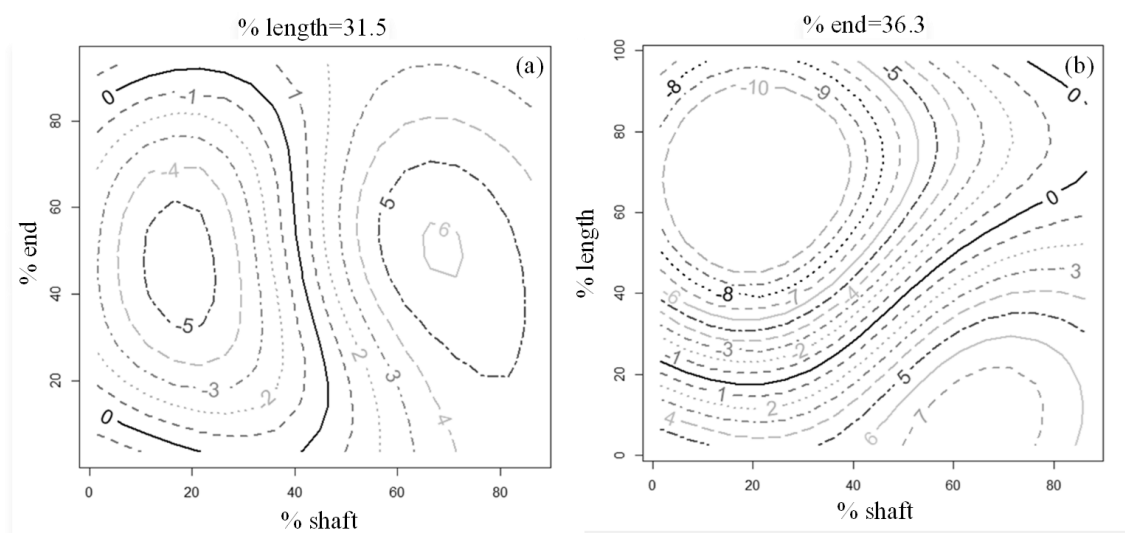
**Figure 9.9. Equations. Prediction accuracy measures given by a) RMSE, b) MAD and c) Pseudo R2.**

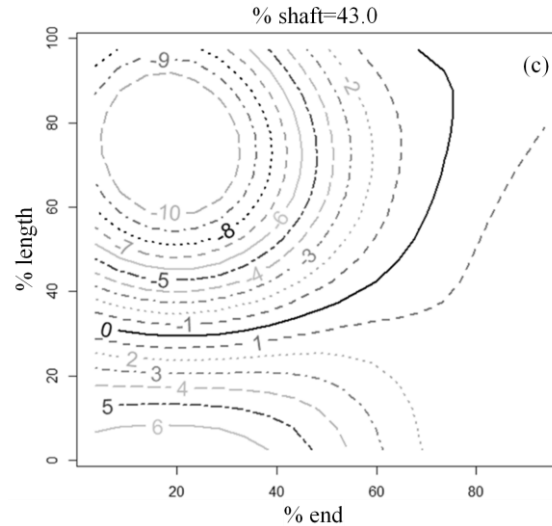
#### 9.4.6 Optimization

In this study, it was desirable to optimize the predicted difference in steel weight to be 0. However, the ML algorithms do not provide explicit prediction equations that can be directly optimized. In addition, it was likely that the prediction surface of the difference in steel weight from the ML algorithms could be highly irregular. Thus, a Genetic Algorithm (GA) was used to find the optimal values of the regressors: percent shaft, percent end and percent length in which

the predicted difference in steel weight for the test data was close to 0. The GA was an evolutionary search strategy based on simplified rules of biological population genetics and theories of evolution (Goldberg 1989). A potential solution to the optimization problem was viewed as an organism with a chromosome, gene, allele, locus, genotype, and phenotype. The keys to the GA were the selection, crossover, and mutation operators (Sivanandam et al. 2008). The GA was implemented in the GA package in the R program for regression problems using the lsSelection operator (probability of selection was determined to be proportional to the objective function with linear scaling), the laCrossover operator (local arithmetic crossover as a mixture of two parents with weight equal to the specified probability of crossover), and the raMutation operator (uniform random mutation over the given range with specified probability of mutation) (Yu et al. 2010). The probability of crossover of 0.8 and probability of mutation of 0.1 were set for this study (Scrucca 2013). Thus, the GA was used in a novel manner here to explicitly solve the values of predictors that satisfy the optimization problem as shown in Table 9.2 (i.e., percent shaft of 43.01 percent, percent end of 36.32 percent, and percent length of 31.47 percent).

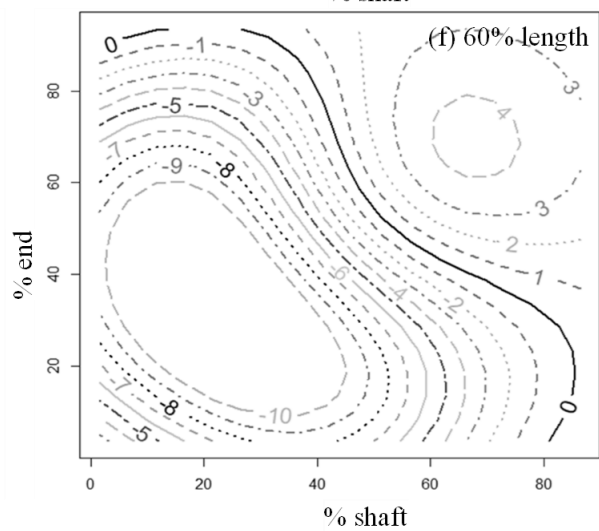
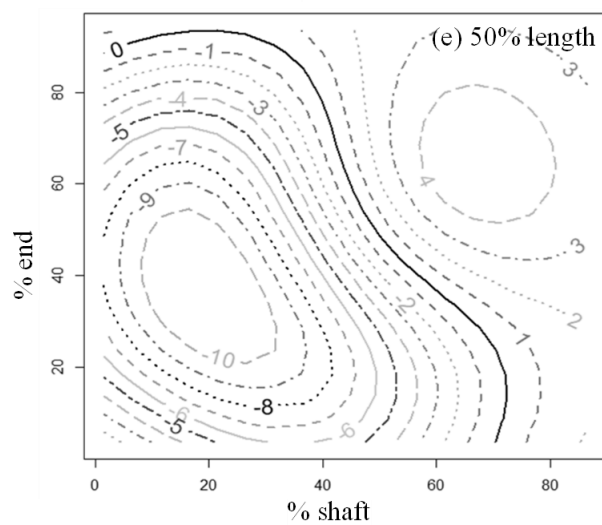
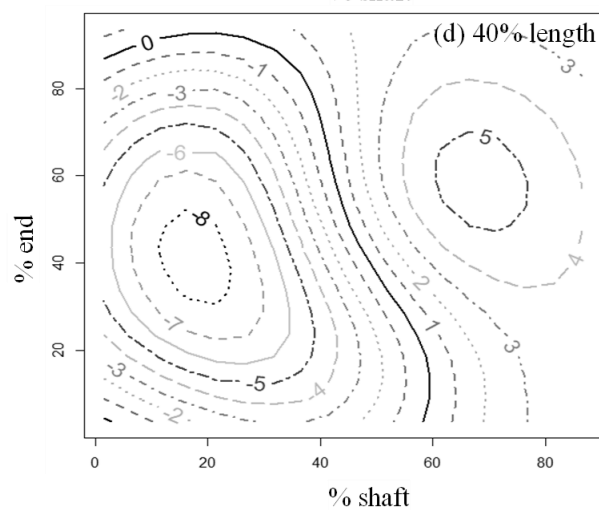
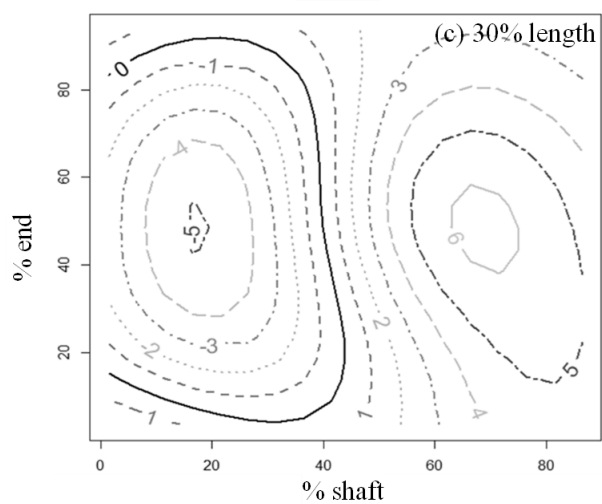
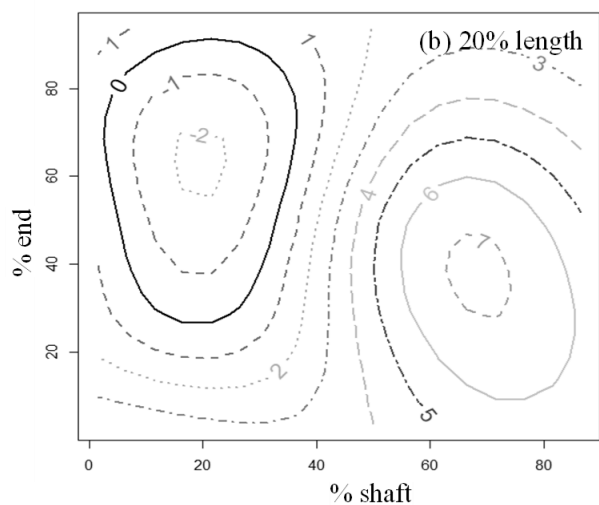
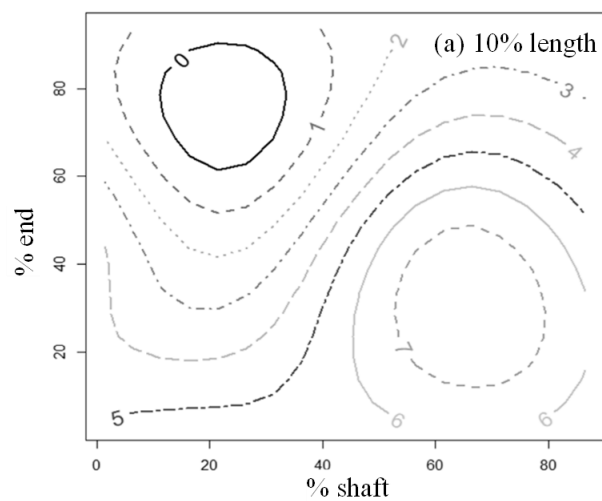
The SVM algorithm was selected for this further analysis given its better predictive ability on the test data. The contour plots in Figure 9.10 show the regions of the predicted difference (from -10 to 10) in steel weight for the predictive surface obtained from SVM using the training data. These contour plots have been adjusted to be centered near the optimum value of the SVM predictive surface that was identified by GA.





**Figure 9.10. Contour Plots for the Optimized Values Using SVM a) percent Length was Optimized and Fixed at 31.5 percent, b) percent End was Optimized and Fixed at 36.3 percent, and c) percent Shaft was Optimized and Fixed at 43 percent.**

The percent length in IGM was the most important variable for SVM since it has the highest VI in Table 9.2. Thus, another set of contour plots was provided in Figure 9.11 to predict the difference in steel weight based upon the training data with various percent length values. Figure 9.11a to Figure 9.11j show just percent shaft and percent end with respect to 10, 20, 30, 40, 50, 60, 70, 80, 90, 100 percent length in IGM for the prediction of the difference in steel weight. These plots will be beneficial and convenient for engineers in predicting the difference in steel weight based on the proposed SA methods to alleviate construction challenges encountered in current practice.





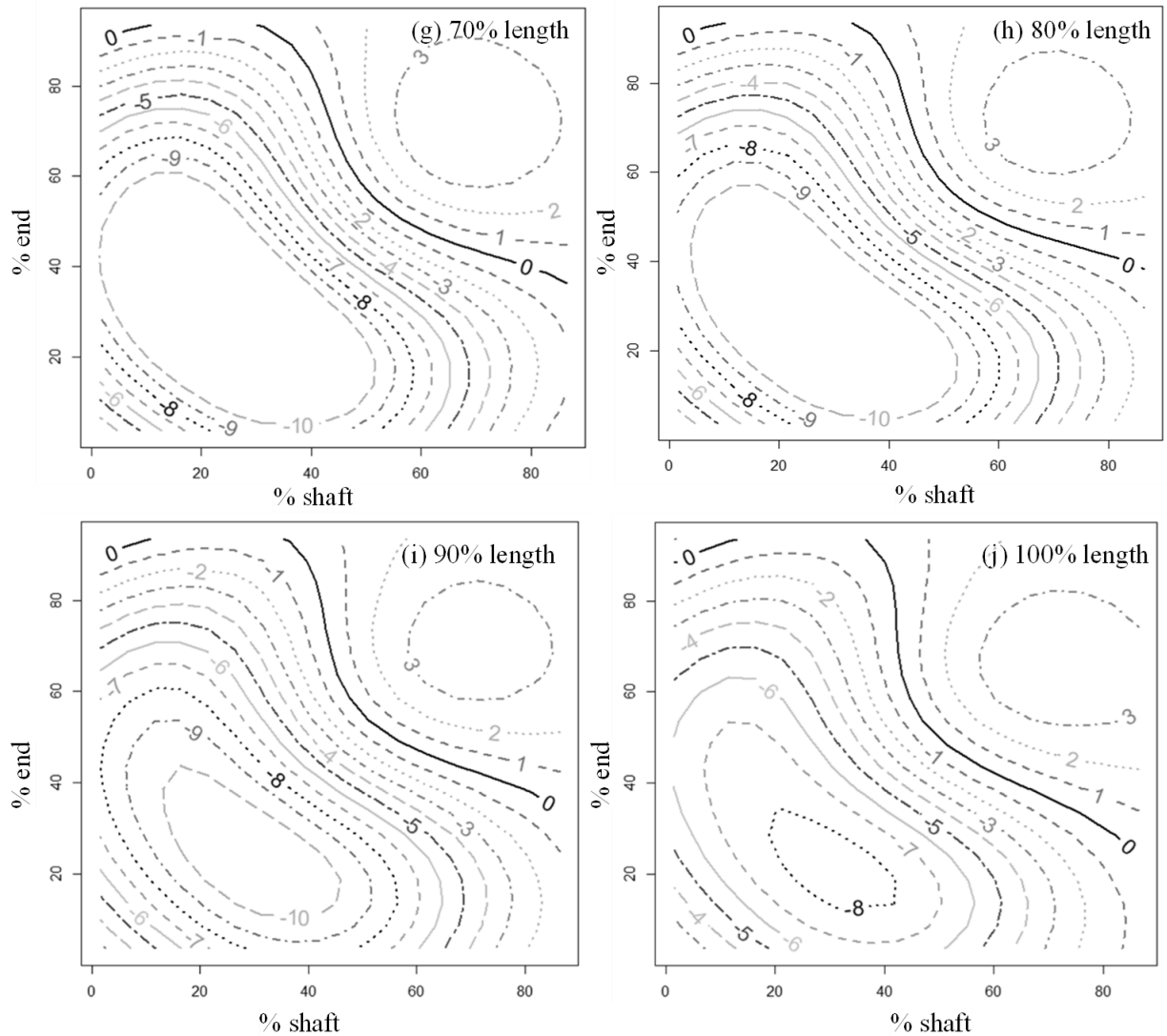


**Figure 9.11. Contour Plot to predict the Difference in Steel Weight in Terms of percent Shaft, percent End and a) 10 percent Length, b) 20 percent Length c) 30 percent Length d) 40 percent Length e) 50 percent Length f) 60 percent Length g) 70 percent Length h) 80 percent Length i) 90 percent Length, and j) 100 percent Length in IGM.**

The contour plots illustrate the prediction surface for SVM that was obtained from the training data in terms of percent shaft, percent end, and percent length. The contour plots can be validated using the test data. This involves comparing the predicted values of the difference in steel weight for the test data obtained from SVM with those predictive values obtained from the contour plots based upon the training data given the values of percent shaft, percent end, and percent length.

Figure 9.12 illustrates the plot comparing the relationship between these predicted values. Figure 9.12 shows that predicted values for the test data from SVM agree closely with the predicted values from the contour plots that were based on the training data. The fitted regression line has an estimated slope of 0.990 and estimated intercept of 0.175. These values were quite close to the 1-1 reference line that has a slope of 1 and intercept 0. In addition, the error sum of squares for the fitted regression line was 11.45 while the error sum of squares for the 1-1 reference line was only slightly larger with a value of 12.56, which amounts to a difference of 8.78 percent. Also, recall that exact predicted values cannot be obtained from the contour plots that can also create some differences between these predicted values. Nevertheless, this validation indicates that these contour plots can be used as a convenient and easy to use guide to enhance the pile performance in IGMs for future bridge projects.

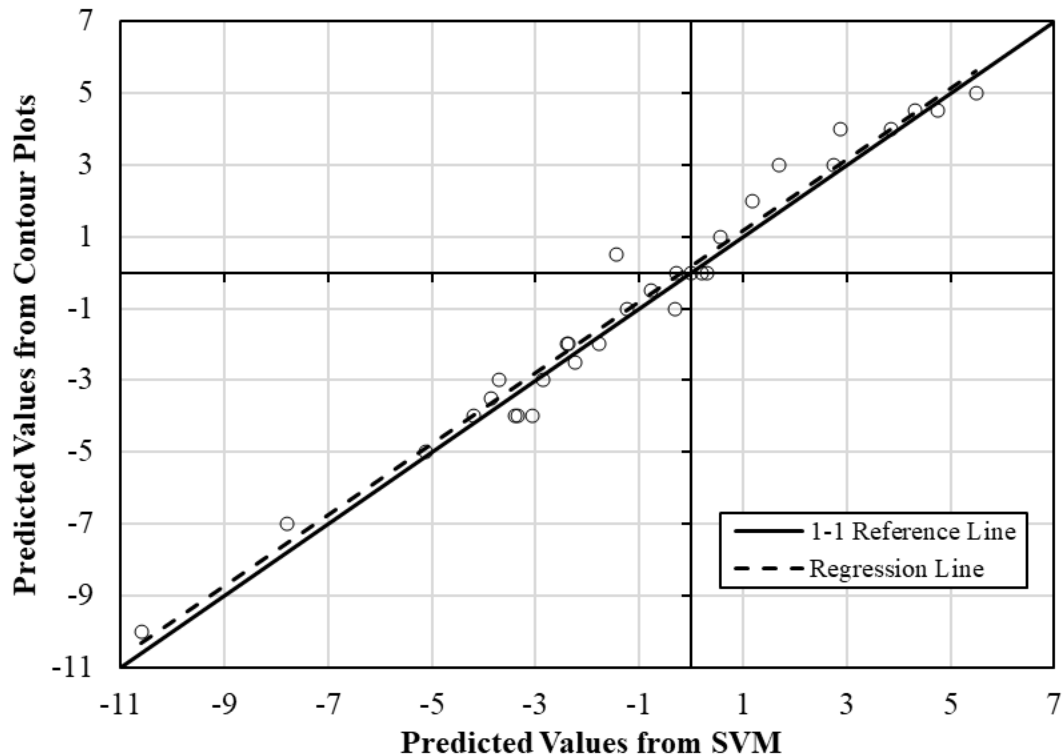


**Figure 9.12. Plot of the Predicted Values for SVM Based on the Test Data Versus the Observed Predicted Values from the Contour Plot which was Originally Developed from the Training Data.**

## 9.5 Summary and Conclusions

This study presents the economic impact assessment for steel piles driven in IGMs by comparing the proposed and existing SA methods based on 149 pile load test results from seven US states. Three ML algorithms: RF, SVM, and NNET were used to predict the differences in steel weight for the proposed SA method based on percent length, percent shaft and percent end in IGM. This study yields the following conclusions:

- All states, except North Dakota, yield negative differences in steel weight ranging from -4.93 lbs/kip to -12.67 lbs/kip based on the existing SA method. A negative difference indicates the underestimation of total factored pile resistance from the existing SA method that results in overestimation of the number of piles. The negative differences in steel weight ranging from -0.78 lbs/kip to -7.29 lbs/kip based on the proposed SA method were also observed in Kansas, Idaho, Wyoming, Montana, and Colorado. However, the proposed SA method yields a smaller average difference in steel weight for the states.
- For all pile types, the existing SA method yields negative differences in steel weight ranging from -1.21 lbs/kip to -16.47 lbs/kip. Except HP10 and 20-in pipe piles, the proposed SA method also yields negative differences in steel weight ranging from -1.27 lbs/kip to -5.55 lbs/kip, which were smaller than that of the existing SA method.
- For CG-IGM, the proposed SA method yields a positive 0.78 lbs/kip while the existing SA method yields -1.23 lbs/kip. For the other six IGM bearing IGM types, both the proposed and existing SA methods yield -0.99 lbs/kip to -9.07 lbs/kip and -1.57 lbs/kip to -13.38 lbs/kip, respectively.
- Analysis of the ML algorithm results reveals that SVM yields the lowest LOOCV RMSE of 9.41 compared to 9.58 for RF and 9.82 for NNET. The percent length was the most important variable in terms of predicting the difference in steel weight. SVM was the best ML algorithm for this application as it has the lowest RMSE, MAD, and highest pseudo-Rsquare of 7.91, 6.56, and 0.18, respectively.
- The optimal values to produce a predicted difference in steel weight close to zero were 43.0 percent shaft, 36.3 percent end and 31.5 percent length based on SVM.

- The generated contour plots based on SVM utilizing the GA optimization can be used to predict the difference in steel weight according to the validation results using the test data.
- The proposed contour plots show just percent shaft and percent end with respect to 10, 20, 30, 40, 50, 60, 70, 80, 90, 100 percent length in IGM so that engineers can predict the difference in steel weight based on the proposed SA method for future driven piles in IGM to reduce construction challenges encountered in current practice.

It was important to note that ML algorithms were also conducted in this study based on different pile and IGM types as additional independent variables. However, the LOOCV RMSE in Equation (7.4) did not substantially decrease with the addition of these predictors. Future research should be conducted to investigate their differences when more information was available to be incorporated into the database for test piles in IGMs.

## CHAPTER 10: VARIABILITY ANALYSIS

### 10.1 Introduction

Understanding the variability of soil and intermediate geomaterials (IGM) was crucial for the design and performance of driven piles in geotechnical engineering, particularly in the Rocky Mountain region of the United States, where geological conditions can be highly variable and complex. This chapter focuses on the analysis of variability and its impact on pile capacity and performance, emphasizing inherent variability and geological uncertainty in geomaterials.

Inherent variability refers to the natural differences in geomaterial properties from one point to another in space. These differences can be attributed to various factors such as mineral composition, moisture content, and compaction history. Inherent variability was an intrinsic characteristic of geomaterials, reflecting the natural heterogeneity within a given geomaterial type. For example, the shear strength or density of soil can vary significantly over short distances due to these inherent differences (Oluwatuyi et al. 2024).

Geological uncertainty, on the other hand, arises from the unpredictability in the spatial distribution and composition of different geomaterials. This type of uncertainty was often due to complex geological processes that result in the intermingling of different soil and rock types or the presence of inclusions within a more uniform geomaterial mass. Geological uncertainty can manifest as variations in layer thickness, the presence of unexpected geomaterial types, or abrupt changes in geomaterial properties at boundaries (Oluwatuyi et al. 2023).

Both inherent variability and geological uncertainty contribute to the overall uncertainty in geotechnical design and must be considered together to ensure reliable predictions of pile performance. To address these challenges, this chapter employs geostatistical methods to incorporate both inherent variability and geological uncertainty using data from multiple boreholes and load tests (Oluwatuyi et al. 2023). By doing so, it aims to improve the reliability of pile resistance estimations and optimize site investigation plans.

In the Rocky Mountain region, geotechnical engineers face unique challenges due to diverse geological conditions. The geomaterials of the region include various types of soils and

intermediate geomaterials such as mudstone, shale, gravel, and sandstone. These materials exhibit different mechanical properties and behaviors, which can significantly affect pile design and performance (Oluwatuyi et al. 2023). The presence of residual layers and the variability in geomaterial properties necessitate a detailed understanding of both inherent variability and geological uncertainty to ensure the safety and reliability of infrastructure projects.

Recent studies have shown that incorporating both types of variability into the design process can lead to more accurate predictions and safer designs. For instance, the use of geostatistical methods allows for the direct incorporation of borehole data, even when the number of boreholes was limited, and provides a probabilistic representation of the geomaterial distribution (Li et al. 2016). This approach, combined with the simulation of random fields to account for inherent variability, enhances the ability to estimate pile resistance accurately (Oluwatuyi et al. 2023).

Furthermore, the application of geostatistical methods, such as universal kriging and conditional simulation, has proven effective in predicting geomaterial properties at unsampled locations. These methods help quantify the uncertainties associated with geotechnical predictions and improve the reliability of pile design (Oluwatuyi et al. 2022). The integration of these modeling techniques into geotechnical engineering practices was crucial for addressing the complex geological conditions in the Rocky Mountain region and other similar areas.

In summary, inherent variability was related to the natural differences within the same type of geomaterial, whereas geological uncertainty involves the unpredictability in the spatial arrangement of different geomaterials. Both types of variability can impact geotechnical design and must be addressed comprehensively to enhance the accuracy and reliability of engineering predictions. This chapter will delve into the methods and findings related to the variability analysis from various project sites, providing insights and recommendations for future geotechnical investigations.

## **10.2 Geological Uncertainty and Inherent Variability in Site Investigation**

Site investigation was a crucial aspect of geotechnical design, providing essential geomaterial-related information. To obtain an optimal site investigation plan (OSIP), it was essential to reduce both inherent variability and geological uncertainty. An OSIP that addresses both types of uncertainties can lead to better predictions of geomaterial properties for pile foundation design. By integrating both inherent variability and geological uncertainty into the site investigation and design process, geotechnical engineers can develop more accurate models of subsurface conditions. This integration leads to improved reliability in pile resistance estimations and other geotechnical design outcomes, ultimately enhancing the safety and performance of infrastructure projects.

### ***10.2.1 Geological Uncertainty in Site Investigation***

The performance and reliability of geotechnical structures, such as pile foundations, were largely dependent on the supporting geomaterial categories and layers present at a project site. Borehole exploration, a common site investigation technique, provides geomaterial and subsurface information, but it was practically infeasible to collect observations across the whole site with a borehole scheme due to limitations in SI techniques, budget constraints, and unforeseen problems during drilling. This results in sparse borehole data and introduces uncertainty at unobserved locations concerning geomaterial categories, transitions, and combinations. Geological uncertainty refers to the variability due to one geomaterial layer being embedded in another or the introduction of portions of different geomaterial categories within a homogenous geomaterial mass (Qi et al. 2016). Unlike inherent variability of geomaterial properties, geological uncertainty requires careful consideration during pile design, as the variability of geomaterial properties across different categories was more distinct than within the same soil category (Oluwatuyi et al. 2022).

In geotechnical engineering, geological uncertainty in layered profiles was challenging to study due to sparse subsurface data, creating difficulties in design and construction. To address this limitation, a hybrid approach involving various spatial Markov chain prediction models and Monte Carlo simulation was used. This method estimates transition rates, predicts geomaterial

categories at unobserved locations, simulates multiple realizations to propagate uncertainty, and quantifies subsurface stratigraphy uncertainty using information entropy. The hybrid approach accommodates sparse borehole data by reporting categorical data at thin depth intervals, improving computational efficiency and flexibility in borehole locations. This method was demonstrated to provide accurate estimation even in the presence of thin geomaterial layers and allows for computationally efficient extensions to three-dimensional applications, providing more realistic and comprehensive site information. This approach enhances the design reliability and safety of pile foundations by accurately determining spatial geomaterial boundaries and reducing geological uncertainties.

### ***10.2.2 Inherent Variability in Site Investigation***

Inherent variability, also referred to as property uncertainty, was the most influential type of uncertainty in geotechnical engineering and was typically assessed using random field methods (Phoon and Kulhawy 1999). Random field modeling generates a spatial representation of geomaterial properties to simulate the subsurface region, while variogram analysis provides insights into the degree of spatial correlation and fluctuation scales of geomaterial properties (Christakos 2012). Advanced geostatistical techniques such as Bayesian compressive sampling, Karhunen–Loève expansion, and conditional random fields have been employed to quantify inherent variability (Wang et al. 2019). These methods allow for accurate predictions of geomaterial properties at unsampled locations by incorporating statistical uncertainty into the models.

Assessing inherent variability was crucial for constructing an effective site investigation plan. Property uncertainty can be reduced by determining an adequate number of well-placed boreholes (Crisp et al. 2020). In regions like the Rocky Mountains, deep foundations for bridges often encounter shallow bedrock stratigraphy known as intermediate geomaterials (IGM), which exhibit properties between soil and rock. This chapter of the report aims to predict geomaterial properties using sparse borehole data, assess inherent variability by quantifying property uncertainty of multilayered geomaterials, and develop a site investigation plan with a low degree of property uncertainty. Universal kriging was employed to analyze all geomaterial layers with



different means for the geomaterial property to improve prediction accuracy at unsampled locations. By integrating these advanced methods, geotechnical engineers can develop more accurate models of subsurface conditions, leading to improved reliability in pile resistance estimations and enhanced safety and performance of infrastructure projects.

### 10.3 Methodology

#### 10.3.1 Geological Uncertainty

The methodology for assessing geological uncertainty in this report utilizes a hybrid approach combining various spatial Markov Chain (spMC) models and Monte Carlo simulation to predict three-dimensional geomaterial categories and to assess geological uncertainties. This approach was designed to handle the limitations posed by sparse borehole data, providing a comprehensive and realistic depiction of subsurface conditions. The key steps in this methodology were described below:

##### 10.3.1.1 Data Collection and Preparation

Sparse borehole data from the site investigation were used as the primary source of information. The categorical data from boreholes, representing different geomaterial layers, were collected and reported at every thin depth interval of 3 inches. This granularity helps in accurately capturing the transition rates between different geomaterial categories.

##### 10.3.1.2 Estimation of Transition Rate Matrices

The transition rate matrices were estimated to understand the probability of transitioning from one geomaterial category to another across spatial locations. For a spatial location  $\mathbf{s}$ , let  $Z(\mathbf{s})$  denote the categorical random variable representing the geomaterial category at that location. The transition probability  $t_{ij}(\mathbf{h})$  of going from categorical state  $z_i$  to categorical state  $z_j$  was shown in Figure 10.1

$$t_{ij}(\mathbf{h}) = \Pr(Z(\mathbf{s} + \mathbf{h}) = z_j \mid Z(\mathbf{s}) = z_i)$$

**Figure 10.1. Equation. The Transition Probability.**

where  $i, j = 1, 2, \dots, n_s$  with  $n_s$  as the number of geomaterial states. The collection of transition probabilities  $t_{ij}(\mathbf{h})$  in Figure 10.1 across all  $i, j$  was given by the  $n_s \times n_s$  transition probability matrix,  $\mathbf{T}(\mathbf{h})$  as shown in Figure 10.2

$$\mathbf{T}(\mathbf{h}) = \exp(\|\mathbf{h}\| \mathbf{R}_h)$$

**Figure 10.2. Equation. Transition Probability Matrix.**

where  $R_h$  was the transition rate matrix that depends on the direction given by the lag  $\mathbf{h}$  (Sartore et al. 2016). This relationship allows for the conversion of observed transition probabilities into transition rates, which were essential for modeling geological uncertainty. The transition rate illustrates the immediate rate at which the Markov chain transitions between geomaterial categories. These transition rates aid in understanding the subsurface stratigraphy and in obtaining the corresponding predictions for a site.

#### 10.3.1.3 Subsurface Prediction

Geological modeling was conducted to predict the geomaterial categories at unobserved locations. The conditional probability  $q_j(\mathbf{s}_0)$  of category  $j$  at an unobserved location ( $\mathbf{s}_0$ ) was approximated using algorithms such as Multinomial Categorical Prediction (MCP). The MCP method, based on Bayesian maximum entropy, was particularly effective in reproducing complex patterns. The conditional probability was given by equation shown in Figure 10.3.

$$q_j(\mathbf{s}_0) \approx \frac{p_i \prod_{l=1}^n t_{ik_l}(\mathbf{s}_0 - \mathbf{s}_l)}{\sum_{i=1}^{n_s} p_i \prod_{l=1}^n t_{ik_l}(\mathbf{s}_0 - \mathbf{s}_l)}$$

**Figure 10.3. Equation. Conditional Probability Matrix.**

where  $p_i$  was the proportion in category  $i$  and  $t_{ik_l}(\mathbf{s}_0 - \mathbf{s}_l)$  represents the transition probability as defined in Equation (1) from the state  $z_i$  to state  $z_k$  for observation with index  $l$ .

#### 10.3.1.4 Subsurface Simulation

Monte Carlo simulations were performed to propagate uncertainty in the predictions. Multiple realizations of the subsurface model were generated by repeating the prediction method  $n_M$  times to approximate the conditional probabilities,  $q_j(\mathbf{s}_0)$  in Equation (3). These simulations help in quantifying the uncertainty associated with the predicted geomaterial categories. For each realization, a different set of random values was used to simulate the spatial distribution of geomaterial categories.

#### 10.3.1.5. Quantification of Uncertainty using Information Entropy

Information entropy was used to quantify geological uncertainty. The entropy  $H$  at a location  $\mathbf{s}_0$  was calculated based on the conditional probabilities from the simulations to provide a measure of uncertainty. The entropy was defined by the equation shown in Figure 10.4

$$H_m(\mathbf{s}_0) = - \sum_{j=1}^{n_s} q_{j,m}(\mathbf{s}_0) \log_{n_s} q_{j,m}(\mathbf{s}_0)$$

**Figure 10.4. Equation. Information Entropy to Quantify Geological Uncertainty.**

Lower entropy values indicate lower uncertainty in the predictions, while higher entropy values indicate higher uncertainty. These values will be used in delineating and characterizing the stratigraphic boundaries between geomaterials. Cross-validation was also performed to evaluate the accuracy of the geomaterial predictions. The data from each borehole were used alternately as validation data while the rest serve as training data. The percentage match between observed and predicted geomaterial categories provides an index of prediction accuracy (Oluwatuyi et al. 2023; Oluwatuyi 2023).

#### 10.3.2 Inherent Variability

The methodology for assessing inherent variability, also known as property uncertainty, uses random field (RF) approaches and geostatistical techniques to predict geomaterial properties at unsampled locations and quantify the associated uncertainties. The key steps in this methodology were outlined below.

### 10.3.2.1. Data Collection and Preparation

Sparse borehole data from site investigations serves as the primary data source. These data provide information about geomaterial properties from the field or laboratory test. The collected data were reported at specific depth intervals and log-transformed, providing a basis for subsequent geostatistical analysis.

### 10.3.2.2. Random Field Generation

Random field modeling was employed to generate a spatial representation of geomaterial properties. This involves defining a random vector for a geomaterial property, ( $\mathbf{Y}$ ), where the covariance matrix  $\Sigma$  shown in Figure 10.5 represents the spatial correlation structure. The spatial correlation function  $H(\rho)$  was specified via:

$$\Sigma = \sigma^2 H(\rho)$$

**Figure 10.5. Equation. Covariance Matrix.**

where  $\sigma^2$  was the partial sill and  $\rho$  was the range parameter. The exponential correlation function shown in Figure 10.6, where  $h$  was the separation distance between spatial locations, was often used due to its simplicity and suitability for geotechnical data:

$$H(\rho) = \exp(-h/\rho)$$

**Figure 10.6. Equation. Exponential Correlation Matrix.**

### 10.3.2.3. Variogram Analysis

The spatial correlation structure shown in Figure 10.7 was represented by the variogram, which models the semi-variance as a function of lag distance  $h$ :

$$\gamma(h) = \frac{1}{2} E \left[ (Z(s) - Z(s + h))^2 \right]$$

**Figure 10.7. Equation. Spatial Correlation Structure.**

where  $\mathbf{s}$  and  $\mathbf{s} + \mathbf{h}$  were spatial locations separated by distance  $\mathbf{h}$ . Variogram modeling helps in understanding the spatial dependence of geomaterial properties.

#### 10.3.2.4. Geomaterial Property Prediction

Universal kriging (UK) was used to predict geomaterial properties at unsampled locations. UK provides the best linear unbiased prediction by incorporating both the mean and covariance structure of the data. The prediction at an unsampled location ( $\mathbf{s}_0$ ) was given by:

$$\hat{y}(\mathbf{s}_0) = \mathbf{x}(\mathbf{s}_0)' \hat{\boldsymbol{\beta}} + \hat{\mathbf{v}}' \hat{\boldsymbol{\Sigma}}^{-1} (\mathbf{y}(\mathbf{s}) - \mathbf{X} \hat{\boldsymbol{\beta}}),$$

**Figure 10.8. Equation. Unsampled Location Prediction Equation.**

where  $\mathbf{s}$  contains the observed spatial locations,  $\hat{\boldsymbol{\beta}}$  was the estimate of the regression coefficient vector  $\boldsymbol{\beta}$  obtained from generalized least squares,  $\hat{\boldsymbol{\Sigma}} = \hat{\sigma}^2 \mathbf{H}(\hat{\rho})$  was the restricted maximum likelihood estimate of the covariance matrix  $\boldsymbol{\Sigma}$ ,  $\mathbf{x}(\mathbf{s}_0)$  was the value of the design matrix at  $\mathbf{s}_0$ ,  $\mathbf{y}(\mathbf{s})$  was the vector of the geomaterial property values at  $\mathbf{s}$ , and  $\hat{\mathbf{v}}$  was a vector of covariances with entries  $\widehat{\text{cov}}(Y(\mathbf{s}_0), Y(\mathbf{s}_i))$  for  $i = 1, \dots, n$ .

#### 10.3.2.5. Conditional Simulation

Conditional simulation was conducted to account for uncertainties associated with the plug-in estimates used in the UK. This involves generating multiple realizations of the geomaterial properties that match the observed data and the spatial correlation structure. The simulation process produces realizations that match the observed values at sampled locations.

#### 10.3.2.6. Quantification of Uncertainty

The uncertainty associated with the predicted geomaterial properties was quantified using the standard deviation (SD). The SD of the predictions provides a measure of variability:

$$SD_l = \frac{1}{n_s - 1} \sum_{i=1}^{n_s} (\hat{y}_{i,l} - \bar{y}_l)^2$$

**Figure 10.9. Equation. Standard Deviation Prediction Equation.**

where  $l$  indexes the layer,  $i$  indexes the simulation,  $n_s$  was the total number of simulations,  $\hat{y}_{i,l}$  was the predicted geomaterial property value for layer  $l$  and simulation  $i$ , and  $\bar{\hat{y}}_l$  was the sample mean of the predicted geomaterial property value for layer  $l$  and simulation  $i$ . Lower SD values indicate lower uncertainty in the predictions, while higher SD values indicate higher uncertainty. Cross-validation was performed to evaluate the accuracy of the predictions. Leave-one-out cross-validation (LOOCV) was used, where each borehole was alternately used as validation data while the rest serve as training data. The prediction accuracy was assessed by comparing the predicted geomaterial properties to the observed values using root mean square error (RMSE) and bias.

### ***10.3.3 Optimal Site Investigation Plan***

To optimize the site investigation plan, subsequent borehole locations were selected based on their potential to reduce the combined uncertainties. The procedure for determining the OSIP for bridge design through the combined analysis of geological and property uncertainties was summarized in Figure 10.10. A heatmap (Figure 10.11 to Figure 10.12) of uncertainty was generated for the site, indicating areas where additional boreholes would most effectively reduce uncertainty. The process involves:

- Initial Boreholes: Data from initial boreholes were used to establish a baseline uncertainty.
- Uncertainty Heatmap: A heatmap was generated to visualize the uncertainty across the site.
- Selection Criteria: Boreholes were selected at locations with the highest potential for reducing uncertainty.
- Iterative Process: The process was repeated iteratively, updating the uncertainty heatmap with each new borehole until further reductions in uncertainty were no longer cost-effective.
- Finalizing the site investigation plan: The final site investigation plan was established by balancing the reduction in uncertainty with the cost of additional boreholes. The optimal

number and locations of boreholes were determined to achieve a reliable subsurface characterization for the design of geotechnical structures.

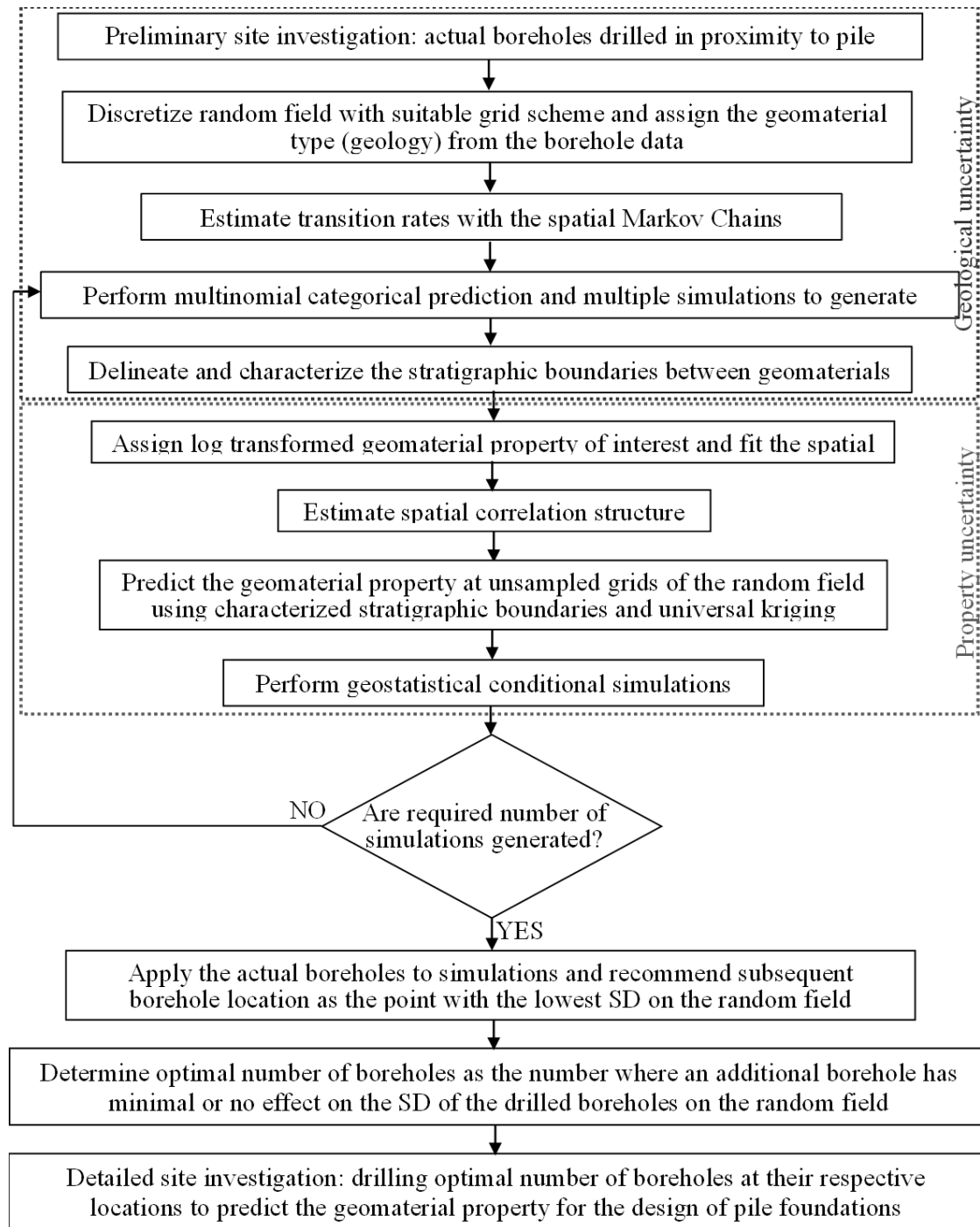


**Figure 10.10. Flowchart of An Optimal Site Investigation Plan for Pile Design Considering Both Geological and Property Uncertainties.**

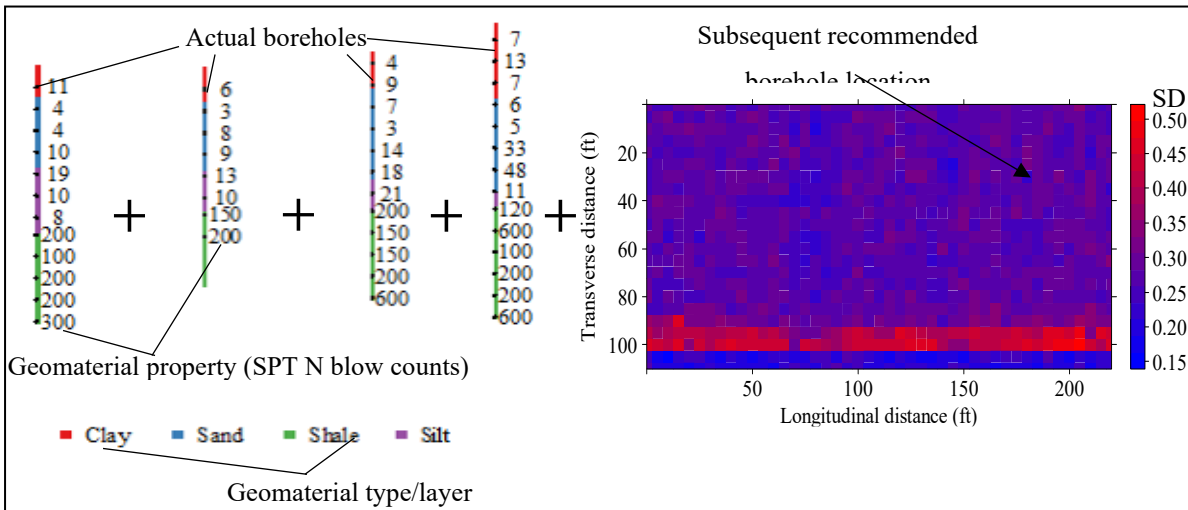


**Figure 10.11. Pictorial Explanation of Subsequent Recommended Borehole Selection for OSIP (Plus Sign Implies Combination and Not Summation).**

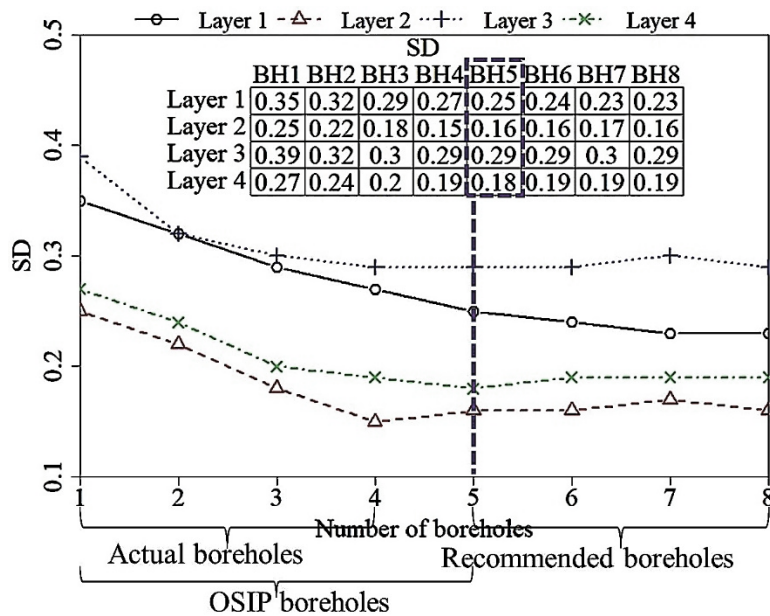


**Figure 10.12. Pictorial Explanation of Actual and Recommended Boreholes that Determine the Optimal Number of Boreholes.**



## 10.4 Site Investigation Plans

Site investigation plans (SIPs) present the fundamental site-specific data and understanding that inform structural design. The information gathered during the site investigation helps engineers make informed decisions about the type and configuration of the necessary piles. Based on the knowledge of uncertainty, three forms of SIPs were discussed in this chapter of the report. A summary of the differences in the three forms of SIPs used in this study was presented in **Table 10.1** and described in the next subsections.

**Table 10.1. The Three Forms of Sips Used in Pile Design.**

SIP	Borehole for design	Additional borehole needed	Geostatistical simulation	Static analysis method	Estimation of uncertainties in pile resistance	Resistance factor developed
CSIP	Proximity to pile	No	No	Yes	Linear	Yes
ASIP	All usable	No	Yes	Yes	Linear or nonlinear	Yes
OSIP	All usable	Yes	Yes	Yes	Linear or nonlinear	Yes

### 10.4.1 Current Site Investigation Plan

The Current Site Investigation Plan (CSIP) was widely accepted as the primary approach to pile design in current practice due to its proven track record of success, practicality, and cost-effectiveness. The resistance of a pile driven through the subsurface was predicted based on the geomaterial properties obtained from the borehole closest to the pile as illustrated in Figure 10.13. While the CSIP does not explicitly specify a required number of boreholes for pile design, engineers typically select borehole locations close to the structural component (pile) and determine the number of boreholes based on factors such as site complexity, requirements, and expert judgment. The selection of borehole locations and the quality of data obtained were crucial factors influencing the pile resistance prediction. The SA methods used to predict pile resistance in this study were tailored to the specific geomaterial and pile type with the aim of reducing transformation uncertainties. Specialized SA methods have been developed in this report for IGM due to the unique characteristics and validated with diverse data. These methods consistently outperformed conventional SA methods, such as the alpha method, demonstrating improved accuracy and reduced uncertainty (Masud et al. 2022; Islam et al. 2022). Empirical

validation further strengthens the reliability of these SA methods that were tailored for IGM. The evaluation of the overall pile load-bearing capacity, or total resistance, using the SA method was expressed as follows shown in Figure 10.15

$$\text{Total resistance } (R_T) = \text{Side resistance } (R_s) + \text{Base resistance } (R_b)$$

**Figure 10.13. Equation. Total resistance Prediction Equation.**

where  $R_s = (A_s)_{total} \sum_{i=1}^n (f_s)_i$ ,  $R_b = A_b f_b$ ,  $n$  was the number of geomaterial layers providing side resistance,  $A_s$  was the total area of the pile portion providing side resistance (pile perimeter  $\times$  pile length),  $f_s$  was the unit side resistance of the pile in a geomaterial layer indexed  $i$ ,  $A_b$  was the cross-sectional area of the pile toe, and  $f_b$  was the base resistance on a unit toe area of the pile (measured to a depth of  $5D$  above the toe and  $3.5D$  below the toe,  $D$  was the pile diameter or width). The quantities  $f_s$  and  $f_b$  were determined using the SA method selected based on the geomaterial and pile type at the site. The alpha method was chosen for cohesive soil, the beta method for cohesionless soil, and the newly developed SA methods for IGM. These selections were backed by empirical validation, historical success, and ongoing research to ensure accuracy and reliability. The CSIP, while practical, has limitations concerning geomaterial variability, uncertainties, and its reliance on empirical models. Previous research has focused on addressing these limitations, including techniques for quantifying subsurface variability, refining empirical models, and integrating diverse data sources to enhance accuracy and reliability in pile design. Ongoing efforts were directed toward optimizing decision-making processes that consider environmental impacts as areas for potential improvement in the field.

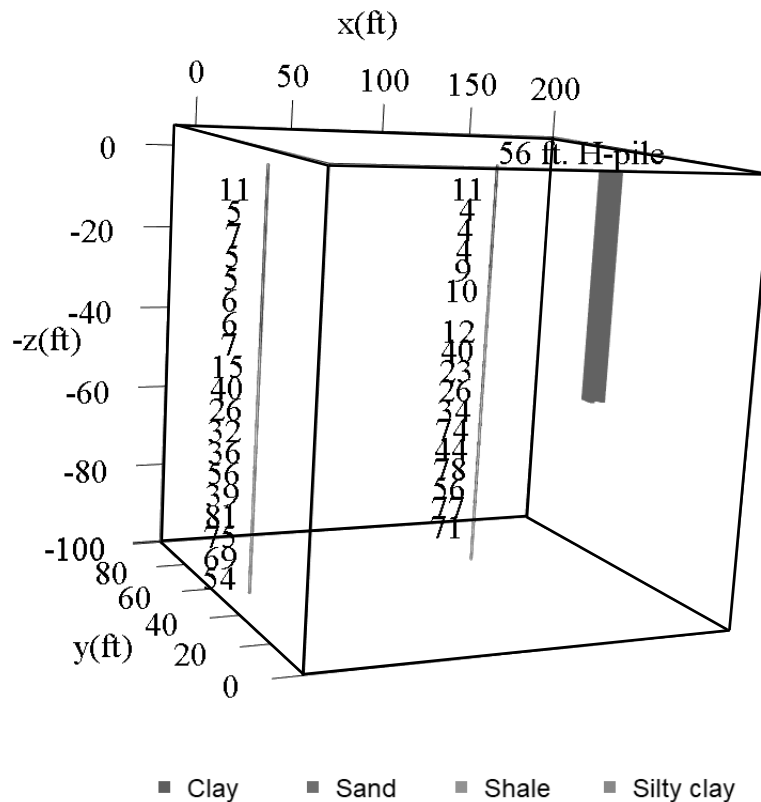


**Figure 10.14. Current Site Investigation Plan used in pile design for a bridge site in Kansas, USA.**

#### ***10.4.2 Actual Site Investigation Plan***

The Actual Site Investigation Plan (ASIP) represents an advancement in the field of pile design as it aims at addressing the challenges posed by subsurface variability and uncertainties. In the initial stages of pile design, it was crucial to conduct SI to gather essential subsurface information, including geomaterial types and properties. This information was collected through the drilling of boreholes on the site, as depicted in Figure 10.13. However, SI was inherently limited by the number of boreholes available for data collection, leading to uncertainties in subsurface characterization. ASIP was developed to explicitly account for these uncertainties and enhance the prediction of pile resistance through the following steps:

- Prediction of geomaterial type: ASIP begins by analyzing the data obtained from all available boreholes drilled across the site. Geostatistical methods, such as multinomial

categorical prediction (MCP), were used to predict the distribution of geomaterial types across unsampled portions of the site. These predictions were iteratively simulated to establish a geological profile of the subsurface structure of the site (see Figure 10.15). The geological profile allows for the division of the subsurface into distinct geomaterial layers, which was a crucial step in subsequent analysis.

- Prediction of geomaterial property: Geostatistical methods, like Universal Kriging, were then applied to predict geomaterial properties at unsampled locations. These predictions were conditioned on the geological profile established in Step 1. Consequently, the predicted geomaterial property value was obtained based on the mean value associated with the respective geomaterial layer, thereby reducing the prediction errors (Oluwatuyi et al. 2023). To quantify uncertainty, the predicted geomaterial properties were conditionally simulated multiple times and the standard deviation was calculated. The average value across these simulations was taken as the simulated geomaterial property of the subsurface (refer to Figure 10.16). The geomaterial property was obtained from the average value associated with the respective geomaterial layer. This does not imply uniformity of geomaterial property for each geomaterial layer. Instead, the average value was an estimate for the geomaterial property within each geomaterial layer to account for heterogeneity.
- Pile resistance prediction: The final step involves the evaluation of the total resistance of the pile using the static analysis methods discussed in this report. Notably, this step diverges from CSIP. Instead of relying solely on the geomaterial properties revealed by the nearest borehole, ASIP employs the simulated geomaterial property from Step 2 at the exact pile location (as illustrated in Figure 10.17).

ASIP offers several key advantages over CSIP. It was adaptable to diverse geological conditions and can enhance accuracy through improved borehole data quality. Thus, ASIP can be effective in addressing the challenges posed by subsurface variability and uncertainties (Oluwatuyi et al. 2023). Ongoing research aims to explore its broader applications and refinements, thereby aligning with evolving construction engineering practices.

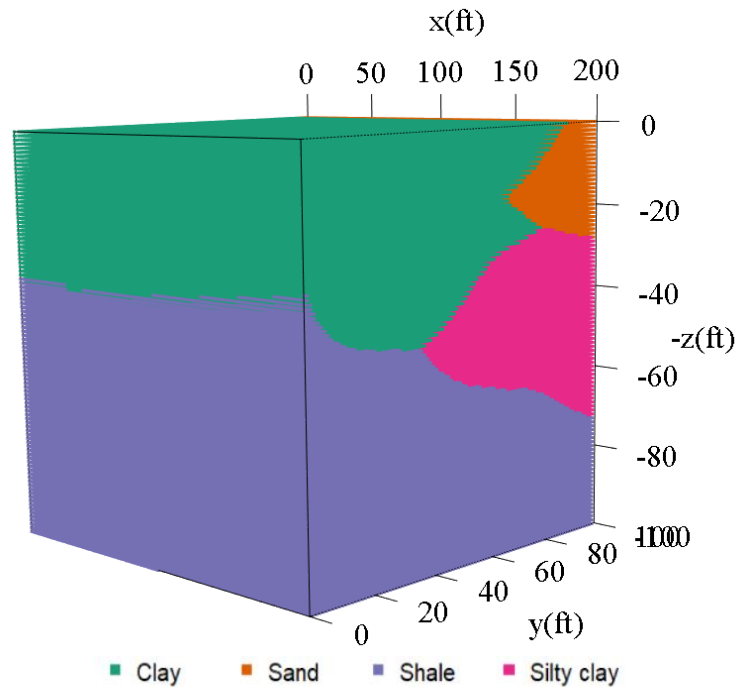


**Figure 10.15. Simulated geological profile for the bridge site in Kansas, USA.**

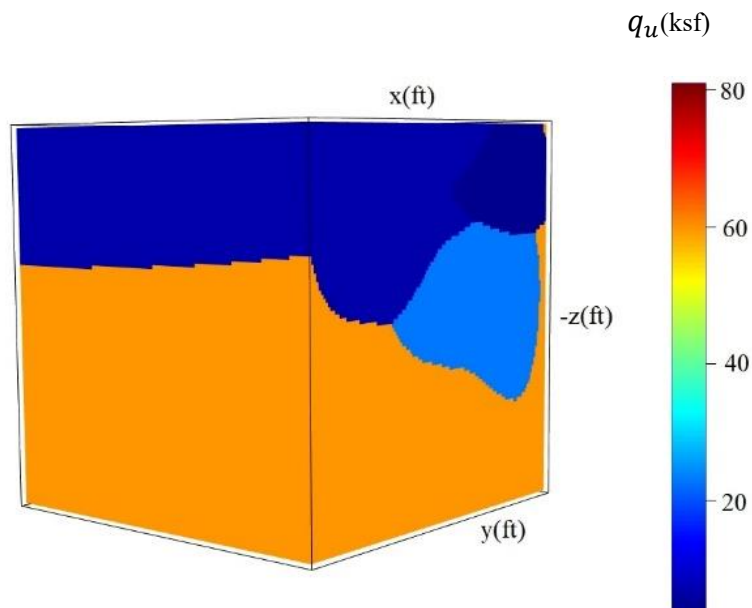


**Figure 10.16. Simulated geomaterial property for the bridge site in Kansas, USA.**

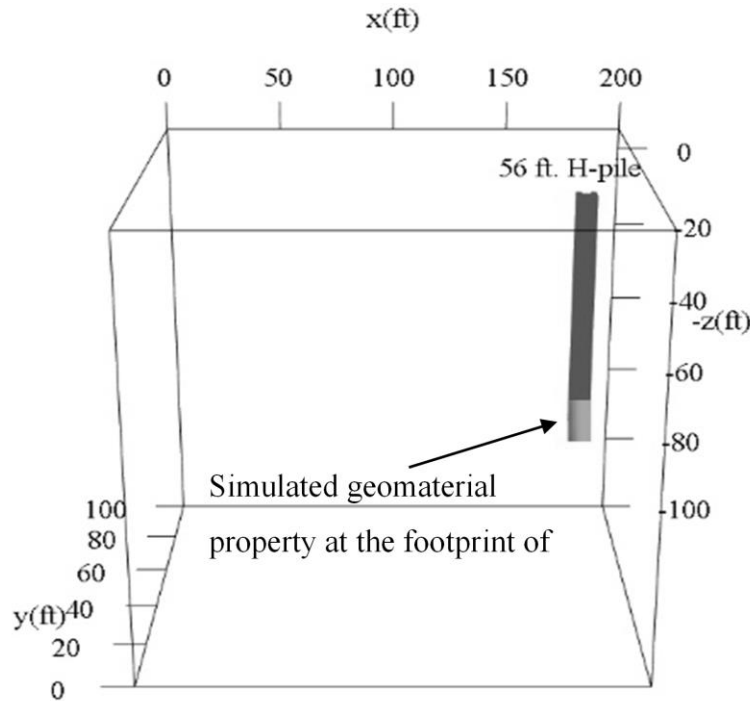


**Figure 10.17. Geostatistical Simulation of Geomaternal Property at the Pile Location for the Design.**

#### ***10.4.3 Optimal Site Investigation Plan***

The Optimal Site Investigation Plan (OSIP) was introduced to further mitigate subsurface uncertainties, which was a challenge for its substantial impact on project safety, cost-effectiveness, and structural integrity. OSIP offers a valuable enhancement to the existing ASIP methodology by gathering additional site information through strategically positioned boreholes (Zhang and Wang 2023). The motivation behind introducing OSIP lies in its potential to enhance the accuracy and reliability of pile design. As ASIP paved the way for improved subsurface characterization, OSIP takes the next step by reducing uncertainties. These uncertainties can lead to unforeseen complications and increased costs if not properly addressed. Apart from the additional boreholes, the OSIP procedure closely aligns with ASIP, building upon the foundational steps outlined. Steps 1 and 2 used in ASIP were replicated, incorporating data from both the original and additional boreholes. This combined dataset enhances the validity of the

simulated subsurface, ultimately leading to more accurate pile design (Oluwatuyi et al. 2023). Finally, the total resistance of the pile was predicted following the methods detailed in Step 3. Thus, OSIP represents an advancement to elevate the accuracy, reliability, and cost-effectiveness of pile design while addressing the challenges posed by subsurface uncertainties.

## ***10.5 Pile foundation design***

### ***10.5.1 End-bearing resistance prediction (Geotechnical-structural uncertainties)***

A static analysis method has been developed to predict the end-bearing resistances of H-piles driven into weathered shales (Islam et al. 2022). To reduce geotechnical-structural uncertainties, regional data and site-specific observations were collected to develop a resistance prediction equation or static analysis method (Zhang et al. 2004). The unit end-bearing or toe resistance  $\hat{q}_b$  in *ksf* was estimated using the uniaxial compressive strength ( $q_u$ ) of the shale in *ksf*, as shown Figure 10.18.

$$\hat{q}_b(ksf) = 45.72q_u^{0.35}$$

**Figure 10.18. Equation. Unit End Bearing Prediction for Shale.**

The developed prediction equation for end-bearing resistance was applicable within a range of  $q_u$  values from 3.24 *ksf* to 124 *ksf*. The equation was determined using the dynamic load test. The predicted end-bearing (*kips*) was obtained by multiplying the unit end-bearing  $\hat{q}_p(ksf)$  by the pile toe area ( $ft^2$ ). Other geotechnical structural uncertainties were addressed through the probabilistic method used to calibrate the LRFD resistance factor for a target reliability index. In semi-empirical methods for predicting pile end bearing, the depth of the pile plays a role in estimating end resistance. The effects of depth in predicting pile toe resistance using semi-empirical methods include geomaterial properties, overburden pressure, pile displacement, and load transfer mechanisms. The depth factor was considered an input variable in these semi-empirical methods to account for its influence on geomaterial behavior and model uncertainty. To prevent punching shear failure in weathered shale caused by its shear strength, the unit end-

bearing  $\hat{q}_p$  ( $ksf$ ) depends on the geomaterial properties to a depth of 3.5D below the pile toe and 5D above the pile toe where D represents the pile diameter or width.

### ***10.5.2 Pile design using CSIP***

Figure 10.13 illustrates a 56 ft. long H-pile driven through overburden clay, sand, and silty clay into the weathered shale bedrock. As previously stated, the current practice in bridge pile foundation design involves using information from the borehole (actual boreholes or CSIP) that was closest to the pile. The closest borehole to the pile has a depth of 100 ft. and  $q_u$  values in  $ksf$ , with an approximate distance of 46 ft. between the borehole and the pile. To estimate the end-bearing of the H-pile using CSIP, the average of the  $q_u$  values within the marked rectangular portion (i.e., 26  $ksf$ , 34  $ksf$ , and 74  $ksf$ ), as shown in Figure 10.13, was substituted into the Equation shown in Figure 10.4 and multiplied by the pile toe area. The average  $q_u$  value used in the end-bearing prediction takes uncertainty into account. However, the CSIP used in pile design was limited due to the noticeable distance of approximately 46 ft. between the borehole and the test pile. Consequently, an error in end-bearing prediction may occur due to variations in the  $q_u$  values measured at this borehole region and the  $q_u$  values that will be measured at the same region of the pile toe. Furthermore, the engineer still needs to address the geomaterial uncertainties present on the project site since piles were constructed in groups.

### ***10.5.3 Pile design using OSIP***

The end-bearing resistance prediction of CSIP can be improved by utilizing the proposed OSIP and geostatistical simulation. The design process involves predicting the geomaterial properties, specifically at the location of the test pile. The uncertainties related to the geology and ground predictions for the site were also reduced by incorporating boreholes from the OSIP.

Geostatistical methods were used to acquire additional high-quality data that will reduce uncertainties and improve resistance prediction accuracy. For CSIP, it was recommended to use geomaterial information from boreholes drilled near the pile (Crisp et al. 2020). However, despite the proximity, there may still be spatial variation in the geomaterial properties between the pile and the borehole. Furthermore, the subsurface information from a single borehole cannot



fully capture the subsurface condition of all piles within a group. Therefore, it was necessary to consider uncertainties across the entire site rather than focusing on specific borehole locations. The predictions from the five OSIP boreholes (two actual boreholes and three recommended additional boreholes) were used as the new input data. The new data were used to re-simulate the geology and ground properties at the unsampled locations of the random field. The average of the  $q_u$  values in  $ksf$  from the 100 re-simulated sub surfaces for each of the grid locations on the random field was shown in Figure 10.18a. The average of the  $q_u$  values from the re-simulated random field were selected in the region of 5D above the pile toe and 3.5D below the pile toe. The average of the  $q_u$  values selected along the pile toe, as shown in Figure 8b, was substituted into Equation (11) and multiplied by the pile toe area to estimate the end-bearing resistance.

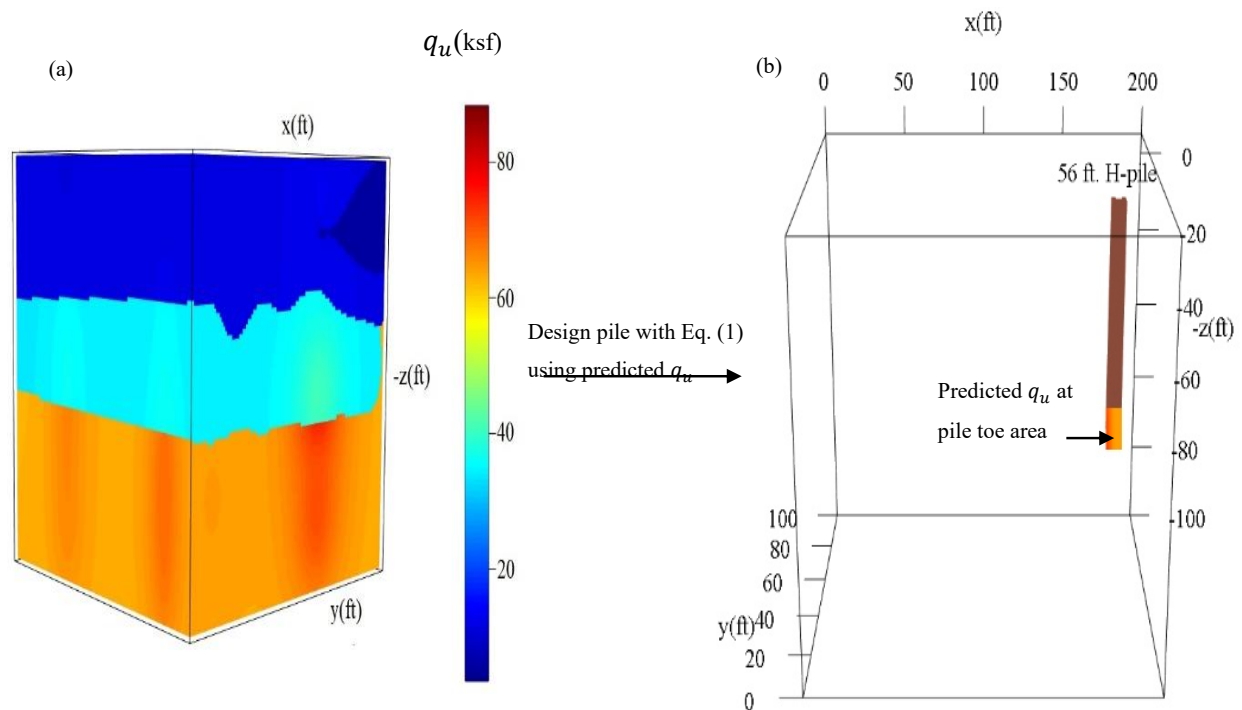


**Figure 10.19. Incorporating OSIP and Geostatistical Simulation into Pile Design.**

#### ***10.5.4 Load and resistance factor design (LRFD) calibration***

The objective of the reliability-based LRFD calibration was to select appropriate load and resistance factors for design, ensuring that the computed probability of failure remains below the target probability of failure. By implementing LRFD, the critical components of the structure were assessed independently, resulting in a more cost-effective design. The predicted end-bearing resistances for weathered shale bedrock obtained from different foundation sites were used in the calibration of the resistance factor ( $\phi$ ). A summary of the data from the pile load test conducted in Kansas, Iowa, and Wyoming was presented in Table 10.2. Since static load test data was not available for these sites, dynamic load test was used as a reference for comparing pile resistances. Previous studies have demonstrated that pile resistances determined from dynamic load test agree relatively well with the measured resistance in IGM from static load tests (Adhikari et al. 2020; Masud et al. 2022). Table 10.2 also presents the number of actual boreholes (CSIP) and the number of OSIP boreholes for each test pile foundation. It was important to note that the OSIP boreholes consist of a combination of actual boreholes from CSIP and recommended boreholes from the geostatistical analysis. Both CSIP and OSIP resistances were predicted for each test pile.

**Table 10.2. Summary of Test Pile Data and End-Bearing in Weathered Shale.**

State	County	Bridge project	Actual number of boreholes (CSIP)	Number of boreholes in OSIP	Pile type	Depth of pile penetration (ft.)	Toe area (ft <sup>2</sup> )	Resistance from dynamic load test (kips)	CSIP predicted resistance (kips)	OSIP predicted resistance (kips)
Kansas	Clay	US 24 over Huntress Creek	1	5	HP 12x74	59	1.028	182.7	181.6	332.2
Kansas	Clark	US-183 over Day Creek	2	5	HP 14x73	94	1.383	82.8	111.8	107.8
Kansas	Sedgwick	Ramp B (NB I-235 to EB US-54/400)	2	6	HP 10x42	80	0.694	94.1	66.0	75.9
Kansas	Sedgwick	Ramp H (SB I-235 to EB US-54/400)	2	6	HP 12x53	73	1.000	96.3	79.4	82.1
Kansas	Sedgwick	Ramp H (SB I-235 to EB US-54/400)	2	6	HP 12x74	68	1.028	162.5	143.4	155.8
Kansas	Sedgwick	Ramp H (SB I-235 to EB US-54/400)	2	6	HP 12x74	60	1.028	105.0	86.9	108.9
Kansas	Sedgwick	Ramp D SB I-235 to US-54/400	2	6	HP 12x53	87	1.000	132.8	103.8	95.8
Kansas	Sedgwick	Ramp D SB I-235 to US-54/400	2	6	HP 12x84	33	1.048	30.1	71.5	43.8
Kansas	Sedgwick	Maple Street over I-135	2	6	HP 10x42	80	0.694	48.2	53.8	75.6
Kansas	Sedgwick	I-235 Floodway crossing	8	12	HP 12x74	46	1.028	139.4	95.2	140.2
Kansas	Sedgwick	I-235 Floodway crossing	8	12	HP 12x74	45	1.028	89.8	104.6	101.2
Kansas	Sedgwick	I-235 Floodway crossing	8	12	HP 12x74	53	1.028	102.8	99.9	99.8
Kansas	Sedgwick	I-235 Floodway crossing	8	12	HP 12x74	61	1.028	40.8	63.9	41.5
Kansas	Sedgwick	I-235 Floodway crossing	8	12	HP 12x63	59	1.005	50.9	69.1	55.2
Kansas	Sedgwick	I-235 Floodway crossing	8	12	HP 12x63	58	1.005	133.7	90.0	103.8

Kansas	Sedgwick	I-235 Floodway crossing	8	12	HP 12x63	47	1.005	61.3	75.3	69.6
Kansas	Sedgwick	I-235 Floodway crossing	8	12	HP 12x74	50	1.028	48.2	71.0	48.9
Kansas	Sedgwick	I-235 Floodway crossing	8	12	HP 12x74	35	1.028	147.8	146.9	158.1
Kansas	Barton	K-4 over Cow Creek Drainage	2	5	HP 12x63	72	1.005	87.8	94.8	77.4
Kansas	Barton		2	5	HP 10x42	79	0.694	66.5	53.7	57.9
Iowa	Adair	Adair Highway 92	2	5	HP 10x57	56	0.709	38.0	60.6	47.8
Wyoming	Natrona	Casper West Belt loop	2	6	HP 14x89	21	1.411	217.0	134.0	142.3

To calculate the resistance factor ( $\phi$ ), the resistance bias for each test pile foundation was calculated as shown in Figure 10.19

$$bias_{(i)} = \frac{y_{(i)}}{\hat{y}_{(i)}}$$

**Figure 10.20. Equation. Bias Prediction Equation.**

where  $i = 1, \dots, 22$  indexes the test pile foundation,  $y_{(i)}$  was the resistance determined from dynamic load test for test pile  $i$ , and  $\hat{y}_{(i)}$  was the predicted resistance from the CSIP and OSIP incorporated into the SA pile design method for test pile  $i$ . The mean and COV of the resistance bias for the twenty-two test piles were also calculated and shown in Figure 10.20. The bias distribution indicates that the OSIP, with a COV of 0.24, performs comparatively better in predicting the end-bearing resistance of the pile than the CSIP, with a COV of 0.31. The incorporation of OSIP and simulation decreases the prediction error associated with CSIP by 25.6 percent.

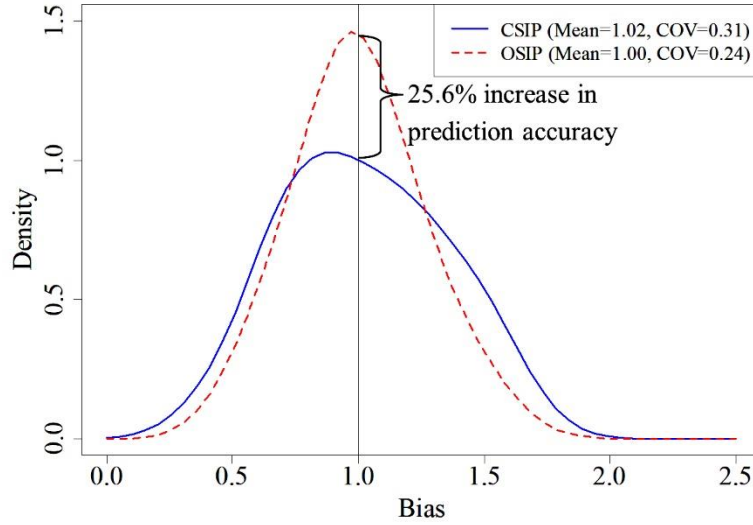


**Figure 10.21. Resistance bias distribution comparing CSIP and OSIP incorporated into pile design.**

Monte Carlo simulation for a log-normal distribution was used to calibrate the LRFD resistance factors. The procedure for MC involves generating random resistance bias using statistical summaries (e.g., mean, standard deviation) to specify the log-normal distribution. The number of simulations ( $N$ ) was dependent on the desired accuracy level, COV of resistance bias, and target reliability index ( $\beta_T$ ). For this study, the value  $N$  was set to 1,000,000. The limit state function with the generated random resistance bias was evaluated and a trial resistance factor  $\phi$  was assumed. The number of failures ( $N_f$ ) where the load was equal to or greater than the resistance was recorded. The probability of failure ( $P_f$ ) and the reliability index ( $\beta$ ) were estimated as shown in Figure 10.22 and 10.23.

$$P_f = \frac{N_f}{N}$$

**Figure 10.22 Equation. The Probability of Failure.**

$$\beta = \Phi^{-1}(1 - P_f)$$

**Figure 10.23. Equation. The reliability Index.**

where  $\Phi^{-1}$  was the inverse cumulative distribution function for the standard normal distribution. If the estimated  $\beta$  from Equation (14) was different from the target  $\beta_T$ , a new trial resistance

factor  $\phi$  was assumed and the process was repeated until the target  $\beta_T$  was achieved. In this study, the target  $\beta_T$  values were set as 2.33 and 3.00 for redundant and nonredundant pile groups, respectively (Paikowsky 2004). The calibrated resistance factors ( $\phi$ ) and efficiency factors ( $\phi/\lambda_R$ ) for the target  $\beta_T$  values were summarized in Table 10.3 for the CSIP and OSIP. The resistance factor ( $\phi$ ) and the efficiency ( $\phi/\lambda_R$ ) of the OSIP were approximately 20 percent higher than that of the CSIP at a target reliability index of 2.33.

**Table 10.3. LRFD Calibration for End-Bearing H-Piles Driven into Weathered Shale.**

Site investigation plan	Sample Size ( $N$ )	Mean bias ( $\lambda_R$ )	$COV_R$	$\beta_T=2.33$ $\phi$	$\beta_T=2.33$ $\phi/\lambda_R$	$\beta_T=3.00$ $\phi$	$\beta_T=2.33$ $\phi/\lambda_R$
CSIP	22	1.02	0.31	0.59	0.58	0.47	0.47
OSIP	22	1.00	0.24	0.71	0.71	0.60	0.60

$N$ =Sample size;  $\lambda_R$ =Mean resistance bias;  $\beta_T$ =Reliability index;  $\phi$  = Resistance factor;  $\phi/\lambda_R$  = Efficiency factor.

## 10.6 Cost-Benefit and Break-Even Analysis

### 10.6.1 Cost-Benefit Analysis

The cost-benefit analysis combines the potential savings expected from an action subtracted from the total cost of taking that action. The action referred as the additional boreholes to improve the reliability of the bridge pile foundation. In this study, cost-benefit analysis was performed on a series of test piles to assess the savings of using OSIP instead of CSIP for pile design. The analysis was systematically conducted to compare and determine which site investigation option for pile design ensures safety while preserving savings. The procedure for the cost-benefit analysis includes the following steps:

- obtain the factored load demand per structure in kips,
- estimate the factored end-bearing pile resistance by multiplying the predicted end-bearing resistance (in Table 10.2) with the LRFD calibrated end-bearing resistance factor ( $\phi$ ) for each site investigation plan (CSIP and OSIP) at a target reliability index of 2.33 (in Table 3),
- determine the number of piles per structure for each site investigation plan by dividing the factored load demand per structure obtained in step 1 with the factored resistance per pile estimated in step 2,

- the number of piles in saving (*PS*) based on the OSIP was calculated by subtracting the number of piles per structure obtained using OSIP from the number of piles obtained using CSIP.

The negative value in the number of piles saved (*PS*) was an indication of underpredicted end-bearing obtained from incorporating OSIP compared to that of CSIP that leads to an overestimation in the number of piles per structure. The positive *PS* value indicates overprediction of end-bearing obtained from incorporating OSIP compared to that of CSIP that leads to an underestimation of the number of piles per structure. The saving in dollars was calculated as follows by subtracting the cost of additional or recommended boreholes from the cost of the number of piles saved:

$$Savings(\$) = (PS \times PL \times PC) - ((CD + CT) \times NR)$$

**Figure 10.24. Equation. The Reliability Index.**

where *PS* was the saving in the number of piles, *PL* was the length of the pile that was assumed as the depth of pile penetration for the cost-benefit analysis, *PC* was the cost of fabricating and installing the pile per ft. pile length, *CD* was the cost of drilling the borehole, *CT* was the cost of geomaterial property testing, and *NR* was the number of recommended boreholes. Cost components such as mobilization and transportation were omitted but could be added to Equation (15) if they were known.

The price list to compute the savings in dollars was obtained from the Wyoming Department of Transportation weighted average bid price and presented below:

- The average bid price for a HP14 pile was \$93.00 per ft. run.
- The average bid price for a HP12 pile was \$77.84 per ft. run.
- The average bid price for a HP10 pile was \$76.79 per ft. run.

The drilling of a borehole was terminated at a minimum of 15 ft. of continuous bedrock layer, and sampling for the geomaterial property testing in each borehole was taken at every 5 ft. depth

(Oluwatuyi et al., 2022). The cost of drilling a recommended OSIP borehole and  $q_u$  testing the collected sample per 5 ft. run depth at \$153.60 will result in a calculated average savings of \$39,410 per test pile foundation as presented in Table 10.4.

**Table 10.4. Cost-Benefit Analysis of Using OSIP and Geostatistical Simulation in Pile Design.**

Pile	No of OSIP recommended boreholes	Depth of pile penetration (ft)	Factored load demand per structure (kips)	Factored resistance per pile (kips)		Estimated number of piles per structure		Saving in number of piles using OSIP over CSIP (PS)	Cost-saving (\$)
				CSIP	OSIP	CSIP	OSIP		
HP 12x74	4	59	6480	107.1	235.9	60	27	33	144,304.56
HP 14x73	3	94	3632	66.0	76.5	55	47	8	61,272.96
HP 10x42	4	80	1782	38.9	53.9	46	33	13	70,031.20
HP 12x53	4	73	7104	46.8	58.3	152	122	30	161,499.36
HP 12x74	4	68	6048	84.6	110.6	71	55	16	76,334.08
HP 12x74	4	60	4032	51.3	77.3	79	52	27	118,728.00
HP 12x53	4	87	1854	61.2	68.0	30	27	3	9,625.68
HP 12x84	4	33	8200	42.2	31.1	194	264	-70	- 183,865.44
HP 10x42	4	80	1824	31.7	53.7	57	34	23	131,463.20
HP 12x74	4	46	7640	56.2	99.6	136	77	59	205,605.28
HP 12x74	4	45	7080	61.7	71.9	115	99	16	50,515.20
HP 12x74	4	53	7400	58.9	70.9	126	104	22	84,248.80
HP 12x74	4	61	7600	37.7	29.5	202	258	-56	- 273,397.12
HP 12x63	4	59	6840	40.8	39.2	168	175	-7	-39,397.84
HP 12x63	4	58	5980	53.1	73.7	113	81	32	137,344.00
HP 12x63	4	47	4896	44.4	49.4	110	99	11	34,467.92
HP 12x74	4	50	4824	41.9	34.7	115	139	-24	-99,552.00
HP 12x74	4	35	7760	86.7	112.3	90	69	21	52,911.60
HP 12x63	3	72	3480	55.9	55.0	62	63	-1	-12,240.00
HP 10x42	3	79	2444.8	31.7	41.1	77	60	18	101,914.74
HP 10x57	3	56	180	35.8	33.9	5	5	0	-5,160.96
HP 14x89	4	21	7812	79.1	101.0	99	77	22	40,385.52
Average Saving per foundation									39,410.85

### 10.6.2 Break-even analysis

Break-even analysis was a financial tool to assess the highest amount a client could invest in a recommended borehole that will result in no loss. It was used in measuring the cost viability of increasing SI from CSIP to OSIP or rather the cost viability of adding the recommended



boreholes to SI that may vary with projects, locations, and sites. A relationship was developed for this study between the average savings per foundation and the cost of SI per 5 ft run depth as follows:

$$\text{Average savings (\$)} = 46341 - 46.14 \times \text{cost of SI}$$

**Figure 10.25. Equation. The Reliability Index.**

The relationship indicates that the average saving reduces with an increase in the SI price as shown in Figure 10.25 A break-even cost (BEC) of \$1004.36 per 5 ft deep run was calculated for SI.

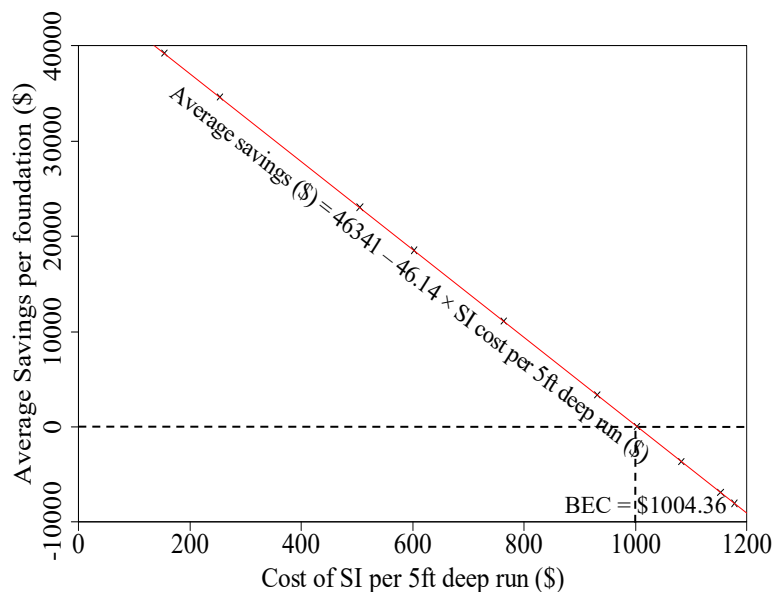


**Figure 10.26. Relationship Between Average Savings and Cost of Additional Site Investigation Based Upon The 22 Test Piles Driven into Weathered Shale.**

## 10.7 Practical Recommendations for Future Projects

Based on the findings and methodologies discussed in this report, several practical recommendations can be made to improve the design and performance of pile foundations in geotechnical engineering projects, particularly in regions with complex geological conditions such as the Rocky Mountain region of the United States. These recommendations aim to enhance

the reliability of site investigations, optimize borehole placements, improve the accuracy of pile resistance predictions, and ensure cost effectiveness and efficiency in project execution.

- **Comprehensive Site Investigations:** Future projects should prioritize comprehensive site investigations to gather detailed subsurface information. This involves increasing the number of boreholes and ensuring they were strategically placed to capture significant variations in geomaterial properties and layers.
- **Use of Advanced Geostatistical Methods:** Incorporating advanced geostatistical methods, such as universal kriging and conditional simulation, into site investigation and design processes can improve the prediction accuracy of geomaterial properties at unsampled locations. These methods allow for the integration of sparse borehole data and provide a probabilistic representation of geomaterial distribution.
- **Optimization of Borehole Placement:** An optimal site investigation plan (OSIP) should be employed to determine the best locations for additional boreholes. Generating uncertainty heatmaps to identify areas with the highest potential for reducing uncertainty ensures that subsequent boreholes were strategically placed, improving the overall accuracy of subsurface characterization and pile resistance predictions.
- **Iterative Site Investigation Process:** Adopt an iterative approach to site investigation and design. Initial boreholes from preliminary site investigation provide a baseline understanding, while subsequent boreholes and updated simulations refine the subsurface model. This process should continue until the reduction in uncertainty was no longer cost-effective, balancing accuracy and budget constraints.
- **Integration of Geological and Property Uncertainties:** Quantify and incorporate both geological and property uncertainties into site investigation plans. Addressing these uncertainties together can lead to more accurate models of subsurface conditions, enhancing the reliability of pile resistance estimations and overall design safety.

## **CHAPTER 11: SUMMARY, CONCLUSIONS AND RECOMMENDATIONS**

### **11.1 Summary**

This report considers the comprehensive field load, geotechnical investigation, and LRFD design and recommendations for driven piles in intermediate geomaterials (IGM). For this purpose, seven electronic databases were created for seven transportation agencies using Microsoft Access. The database will help to manage the historical test pile data obtained from the transportation agencies. The user manual for this database was provided in Chapter 2. Chapter 3 evaluates three types of static pile load systems for 11 driven steel piles design in intermediate geomaterials for engineers to apply in future bridge and construction projects. Classification of fine-grained soil-based intermediate geomaterials, new static analysis methods for design, LRFD recommendations, and changes in driven pile resistance were presented in Chapter 4.

Classification of coarse-grained soil-based IGM, including newly developed static analysis methods, and changes in pile resistances, and LRFD recommendation were provided in Chapter 5. Chapter 6 gives reliability-based driven pile designs for the rock-based intermediate geomaterials, which focuses on the new static analysis methods for different rock-based intermediate geomaterials. Chapter 7 focuses on driven pile resistances for shales considering weathering effects. Chapter 8 evaluates improved WEAP procedures for predicting pile resistance in soil-based IGMs and rock-based IGMs including LRFD resistance factors. The recommendations were based on the back-calculated Smith parameters and static analysis methods. Chapter 9 describes the economic impact assessment for steel piles driven in intermediate geomaterials based on newly proposed static analysis methods. It also shows the improvement in predicting the financial performance of piles using machine learning to mitigate the existing challenges with piles driven in intermediate geomaterials. Finally, Chapter 10 describes variability analysis for driven steel piles in intermediate geomaterials

### **11.2 Conclusions**

The report yields the following conclusions.

- This study improves understanding of driven pile resistance responses in both soil-based intermediate geomaterials and rock-based intermediate geomaterials. The research offers

important insights into the behavior of driven piles through in-depth testing and analysis under a range of geologic conditions thereby assisting in the creation of more precise design recommendations.

- The study provides insight into the viability and performance of many static load test systems, such as IndeSPLS, InteSPLS, and InnoSPLS, under various geological circumstances. It outlines the benefits and drawbacks of each method in terms of labor intensity, cost-effectiveness, and suitability for bridge building schedules. To ascertain ultimate pile resistances, a variety of failure criteria were utilized, which provide valuable information on the load-displacement response and residual forces during pile driving.
- New static analysis methods were developed for the prediction of unit shaft resistance and unit end bearing for different pile types and different IGM types. These newly developed static analysis methods, which were customized for particular soil and rock types, were meant to lower uncertainty and raise the accuracy of predictions about pile resistance, increasing the dependability of pile design in a range of geological conditions. Effectiveness in predicting pile resistances was confirmed by validation of the proposed static analysis methods utilizing distinct pile datasets.
- The improved WEAP analysis and newly proposed damping parameters will help engineers for driven pile design in IGM compared to default WEAP methods.
- The utilization of machine learning (ML) methods in the economic evaluation of steel piles inside intermediate geomaterials (IGMs) has noteworthy advantages. A comparative study reveals areas where money may be saved. Overall, ML-driven economic assessment changes pile design methods and facilitates the construction of robust and affordable infrastructure.
- The variability analysis will enhance the reliability of site investigations, optimize borehole placements, improve the accuracy of pile resistance predictions, and ensure cost effectiveness and efficiency in project execution.

### 11.3 Recommendations

This research advances the understanding of driven pile behavior in intermediate geomaterials to provide engineers with more reliable design recommendations, to give better prediction methods in different geologic conditions, and to improve efficiency and safety of bridge construction projects.

#### 11.3.1 Classification of IGM

The following flow chart shown in Figure 11.1 should be used to classify the different types of IGM for driven pile design.

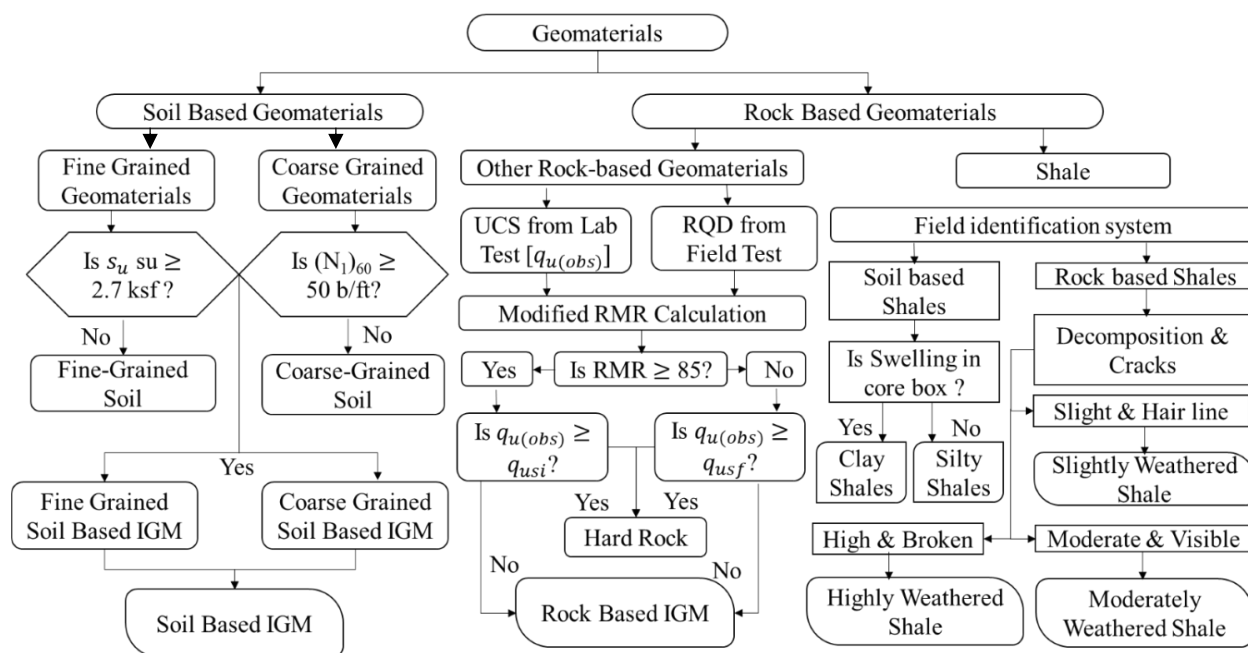


**Figure 11.1. Flowchart for Classification of Different IGM for Driven Pile Design.**

#### 11.3.2 Proposed Prediction Equations and LRFD recommendations

Table 11.1 and Table 11.2 show the prediction equations and LRFD recommendations for design of driven piles in soil based and rock based intermediate geomaterials, respectively.

**Table 11.1. Proposed Prediction Equations and LRFD Recommendations for Driven Piles  
in Soil Based IGM**

IGM	Prediction Equation	Applicable range	Application	$\beta_T=2.33$ $\phi$	$\beta_T=3.00$ $\phi$
ML-IGM (Shaft)	$\hat{q}_s = \left[ \frac{1.80}{1 + 44e^{-0.89\frac{s_u}{P_a}}} \right] P_a$	$3.22 \text{ ksf} \leq s_u \leq 16.07 \text{ ksf}$ $0.27 \text{ ksf} \leq q_s \leq 4.35 \text{ ksf}$	Steel H piles Pipe piles	0.44	0.31
CL-IGM (Shaft)	$\hat{q}_s = \left[ \frac{1.58}{1 + 47.6e^{-1.34\frac{s_u}{P_a}}} \right] P_a$	$3.46 \text{ ksf} \leq s_u \leq 15.31 \text{ ksf}$ $0.17 \text{ ksf} \leq q_s \leq 4.24 \text{ ksf}$	Steel H piles Pipe piles	0.43	0.32
CH-IGM (Shaft)	$\hat{q}_s = \left[ \frac{2}{1 + 50.4e^{-1.4\frac{s_u}{P_a}}} \right] P_a$	$2.75 \text{ ksf} \leq s_u \leq 15.94 \text{ ksf}$ $0.28 \text{ ksf} \leq q_s \leq 4.68 \text{ ksf}$	Steel H piles Pipe piles	0.80	0.66
CG-IGM (Shaft)	$\hat{q}_s = \left[ \frac{1.21}{1 + 12.62e^{-4.06\left(\frac{\sigma'_v}{P_a} \frac{58}{(N_1)_{60}}\right)}} \right] P_a$	$0.0006 \text{ ksf-ft/bl} \leq \frac{\sigma'_v}{(N_1)_{60}} \leq 0.08 \text{ ksf-ft/bl}$ $0.06 \text{ ksf} \leq q_s \leq 3.04 \text{ ksf}$	Steel H piles	0.44	0.31
CG-IGM (Shaft)	$\hat{q}_s = \left[ \frac{\frac{\sigma'_v}{P_a} \frac{58}{(N_1)_{60}}}{0.105 + 0.52 \frac{\sigma'_v}{P_a} \frac{58}{(N_1)_{60}}} \right] P_a$	$0.0005 \text{ ksf-ft/bl} \leq \frac{\sigma'_v}{(N_1)_{60}} \leq 0.13 \text{ ksf-ft/bl}$ $0.17 \text{ ksf} \leq q_s \leq 3.96 \text{ ksf}$	Pipe piles	0.45	0.32
FG-IGM (End)	$\hat{q}_b = \left[ \frac{\frac{s_u}{P_a} \times \frac{D}{D_B}}{0.001 + 0.0027 \frac{s_u}{P_a} \times \frac{D}{D_B}} \right] P_a$	$0.08 \text{ ksf-ft/ft} \leq s_u \frac{D}{D_B} \leq 0.89 \text{ ksf-ft/ft}$ $27.71 \text{ ksf} \leq q_b \leq 399.16 \text{ ksf}$	Steel H piles Pipe piles	0.57	0.43
CG-IGM (Shaft)	$\hat{q}_b = 93.76 P_a \left[ \frac{p_a (N_1)_{60}}{\sigma'_v 58} \right]^{0.22}$	$10.7 \text{ bl/ft-ksf} \leq \frac{(N_1)_{60}}{\sigma'_v} \leq 114.3 \text{ bl/(ft-ksf)}$ $123.2 \text{ ksf} \leq q_b \leq 270.3 \text{ ksf}$	Steel H piles, Pipe piles	0.82	0.70

FG-IGM=fine grained soil based IGM; CG-IGM=coarse grained soil based IGM; CL-IGM=low plasticity clay (lean clay) IGM; CH-IGM=high plasticity clay (fat clay) IGM; ML=low plasticity silt (IGM);  $s_u$ =undrained shear strength (ksf);  $P_a$ =atmospheric pressure=2.12 ksf;  $D$ =pile dimension or diameter (ft);  $D_B$ =total pile penetration (ft);  $\sigma'_v$ =vertical effective overburden stress (ksf);  $(N_1)_{60}$ =corrected SPT N values (blow/ft);  $\hat{q}_s$ =predicted unit shaft resistance (ksf);  $\hat{q}_b$ =predicted unit end bearing (ksf); Shaft= unit shaft resistance; End=unit end bearing; ksf-ft/bl=kip per square foot  $\times$  foot per SPT hammer blow; bl=SPT blow count.

**Table 11.2. Proposed Prediction Equations and LRFD Recommendations for Driven Piles  
in Rock Based IGM.**

IGM	Prediction Equation	Applicable range	Application	$\beta_T=2.33$ $\phi$	$\beta_T=3.00$ $\phi$
SS-shale (Shaft)	$\hat{q}_s = \frac{3.523 q_u}{(8.6 + q_u)^{1.05}}$	2.18 ksf $\leq q_u \leq 51.5$ ksf 0.76 ksf $\leq q_s \leq 2.68$ ksf	Steel H piles Steel Shell	0.57	0.44
HW-shale (Shaft)	$\hat{q}_s = 0.23 q_u^{0.45}$	2.18 ksf $\leq q_u \leq 25.6$ ksf 0.18 ksf $\leq q_s \leq 1.06$ ksf	Steel H piles Steel Shell	0.49	0.37
MW-shale (Shaft)	$\hat{q}_s = \frac{1.196 q_u}{(0.5 + q_u)^{0.83}}$	2.6 ksf $\leq q_u \leq 58$ ksf 1.12 ksf $\leq q_s \leq 2.29$ ksf	Steel H piles Steel Shell	0.74	0.61
SW-shale (Shaft)	$\hat{q}_s = \frac{2.62 q_u}{(0.467 + q_u)^{0.945}}$	4.54 ksf $\leq q_u \leq 126$ ksf 2.24 ksf $\leq q_s \leq 3.78$ ksf	Steel H piles Steel Shell	0.62	0.49
Siltstone (Shaft)	$\hat{q}_s = 0.45 q_u^{0.44}$	7.34 ksf $\leq q_u \leq 67.7$ ksf 0.99 ksf $\leq q_s \leq 3.24$ ksf	Steel H piles Open ended pipe piles	0.61	0.48
Siltstone (Shaft)	$\hat{q}_s = 0.42 P_a \left[ \frac{(N_1)_{60}}{16} \right]^{0.63}$	16 b/ft $\leq (N_1)_{60}$ $\leq 151$ bl/ft 0.89 ksf $\leq q_s \leq 3.90$ ksf	Steel H piles Open ended pipe piles	0.61	0.48
Claystone (Shaft)	$\hat{q}_s = 0.74 q_u^{0.305}$	3.6 ksf $\leq q_u \leq 163$ ksf 0.35 ksf $\leq q_s \leq 3.6$ ksf	Steel H piles Pipe piles	0.47	0.34
Mudstone (Shaft)	$\hat{q}_s = 6.19 \left[ 1 - e^{(-0.052 \frac{N}{19} \times \sigma'_v)} \right]$	0.6 ksf $\leq \frac{N}{19} \times \sigma'_v$ $\leq 35.5$ ksf 0.20 ksf $\leq q_s \leq 5.3$ ksf	Steel H piles Pipe piles	0.43	0.31
Sandstone (Shaft)	$\hat{q}_s = 0.56 q_u^{0.37}$	19 ksf $\leq q_u \leq 459$ ksf 0.43 ksf $\leq q_s \leq 5$ ksf	Steel H piles Pipe piles	0.44	0.31
Sandstone (for layers without $q_u$ ) (Shaft)	$\hat{\beta} = 0.0098 \phi^2 - 0.75 \phi$ $+ 14.63$ $\hat{q}_s = \hat{\beta} \sigma'_v$	37 deg. $\leq \phi \leq 45$ deg. $0.10 \leq \hat{\beta} \leq 1.35$	Steel H piles	0.37	0.26
SS-HW Shale (End)	$\hat{q}_b = 45.72 q_u^{0.35}$	3.61 ksf $\leq q_u \leq 51.5$ ksf 39.7 ksf $\leq q_b \leq 182.7$ ksf	Steel H piles Steel Shell	0.57	0.45

MW-SW Shale (End)	$\hat{q}_b = \frac{190.64 q_u}{(1 + q_u)^{0.88}}$	5.4 ksf $\leq q_b \leq$ 124 ksf 35.1 ksf $\leq q_b \leq$ 384.5 ksf	Steel H piles Steel Shell	0.64	0.51
Siltstone (End)	$\hat{q}_b = 12.9 P_a \left[ 2.43^{\left( \frac{32.4 N}{30 D_B} \right)} \right]$	0.65 bl/ft-ft $\leq \frac{N}{D_B}$ $\leq$ 3.41 bl/ft-ft 18.9 ksf $\leq q_b \leq$ 720.1 ksf	Steel H piles Pipe piles	0.47	0.31
Claystone (End)	$\hat{q}_b = \frac{313.27 q_u}{20.96 + q_u}$	3.6 ksf $\leq q_u \leq$ 109.7 ksf 44.5 ksf $\leq q_b \leq$ 263.6 ksf	Steel H piles	0.43	0.31
Sandstone (End)	$\hat{N}_t = 0.907 \phi^2 - 71.399 \phi + 1428.55$ $\hat{q}_b = \hat{N}_t \sigma'_v$	37 deg. $\leq \phi \leq$ 45 deg. $6 \leq \hat{N}_t \leq$ 107	Steel H piles	0.41	0.35

SS=soil-based shale; HW=highly weathered shale; MW=moderately weathered shale; SW=slightly weathered shale;  $q_u$ =unconfined compressive strength (ksf);  $(N_1)_{60}$ =corrected SPT N values (blow/ft);  $\hat{\alpha}$ ,  $\hat{N}_c$ =calibrated coefficients for  $\alpha$  method;  $\hat{\beta}$ ,  $\hat{N}_t$ = calibrated coefficients for  $\beta$  method;  $\phi$ = friction angle (degrees);  $D_B$ =total pile penetration (ft);  $\sigma'_v$ = vertical effective overburden stress (ksf);  $N$ = field SPT N values (blow/ft); Shaft=unit shaft resistance; End=unit end bearing; bl=SPT hammer blow count.



### 11.3.3 Improved WEAP analysis and LRFD resistance factors

Table 11.3 shows the recommended damping parameters for WEAP analysis for five different subsurface conditions for WEAP analysis. Table 11.4 shows the recommended resistance and efficiency factors for WEAP analysis for driven pile design in IGM.

**Table 11.3. Back calculated quake and damping parameters for subsurface conditions I, II, III, IV, and V.**

SC	Geomaterial	$Q_s$ (in)	$Q_t$ (in)	$J_s$ (s/ft)	$J_t$ (s/ft)
I	Soil	0.1	$D/120$ (very dense/hard soil); $D/60$ (soft soil)	0.20 (Fine-grained); 0.05 (coarse-grained); 0.10 (silts)	0.15
	FG-IGM		$D/120$	$\hat{J}_t = \hat{J}_s = 0.0007 \frac{S_u \times L}{D_B} - 0.008$	
II	Soil		$D/120$ (very dense/hard soil); $D/60$ (soft soil)	0.20 (Fine-grained); 0.05 (coarse-grained); 0.10 (silts)	0.15
	CG-IGM		$D/120$	$\hat{J}_t = \hat{J}_s = 0.02 e^{\frac{2.84 L}{(N_1)_{60}}}$	
III	Soil		$D/120$ (very dense/hard soil); $D/60$ (soft soil)	0.20 (Fine-grained); 0.05 (coarse-grained); 0.10 (silts)	0.15
	FG-IGM			0.18	
	CG-IGM		$D/120$	0.10	
IV	Soil		$D/120$ (very dense/hard soil); $D/60$ (soft soils)	0.2 (Fine-grained soil); 0.05 (coarse-grained soil)	0.15
	Claystone, Sandstone, Mudstone, Siltstone		$D/120$	$\hat{J}_t = \hat{J}_s = \frac{0.2}{1 + e^{(5.8 - 0.004 \times \frac{L}{D_B} \times E_r)}}$	
	SS-HW shale			0.15	
	MW-SW shale			0.09	
V	Soil		$D/120$ (very dense/hard soil); $D/60$ (soft soils)	0.2 (fine-grained soil); 0.05 (coarse-grained soil)	0.15
	FG-IGM		$D/120$	0.18	
	CG-IGM			0.10	
	Claystone, Sandstone, Mudstone, Siltstone			0.10	
	SS-HW shale			0.15	
	MW-SW shale			0.09	

ML=silt with low plasticity; CL=clay with low plasticity; CH=clay with high plasticity; CG=coarse grained soil based IGM; SS=soil-based shale; HW=highly weathered shale; MW=moderately weathered shale; SW=slightly weathered shale;  $Q_s$  = shaft quake;  $Q_t$  = toe quake;  $J_s$  = shaft damping;  $J_t$  = toe damping;  $D_B$  = pile dimension (ft);  $D$  = pile diameter (ft);  $s_u$  = undrained shear strength of the bearing layer at the bottom of pile tip (ksf);  $L$  = embedded pile length (ft);  $(N_1)_{60}$  = corrected  $N$  (blows/ft) of the bearing layer at bottom of pile tip; and SB-IGM = Soil-based Intermediate Geomaterial. SC=Subsurface condition;  $E_r$ =Rated hammer energy (kip-ft).

**Table 11.4. Recommended Resistance and Efficiency Factors for WEAP analysis**

Method	Soil Based IGM				Rock Based IGM			
	$\beta_T=2.33$		$\beta_T=3.00$		$\beta_T=2.33$		$\beta_T=3.00$	
	$\varphi$	$\varphi/\bar{x}$	$\varphi$	$\varphi/\bar{x}$	$\varphi$	$\varphi/\bar{x}$	$\varphi$	$\varphi/\bar{x}$
WEAP-SAD (Default)	0.70	0.64	0.57	0.52	0.72	0.62	0.58	0.50
WEAP-UWD	0.70	0.64	0.57	0.52	0.73	0.63	0.6	0.52
WEAP-UWR	0.75	0.74	0.64	0.63	0.71	0.70	0.59	0.58
WEAP-SAR	0.72	0.72	0.61	0.61	0.69	0.70	0.58	0.59

$\varphi$  = Resistance factor; and  $\frac{\varphi}{\mu}$  = Efficiency factor. D–WEAP default damping; UW–University of Wyoming proposed static analysis methods for  $q_s$  and  $q_p$ ; R–Recommended damping factors

### 11.3.3 Economic Impact Analysis

The proposed contour plots in Chapter 9 can be used by the Engineers to predict the difference in steel weight based on the proposed SA methods for future driven piles in IGM to reduce construction challenges encountered in current practice.

## 11.4 Future Studies

- Future research should concentrate on confirming and refining the proposed SA methods using more data from static load testing on weak rocks and intermediate geomaterials. .
- Predictive models may be able to include more information about pile behavior and increase the precision of steel weight prediction with inclusion of other independent factors, such as pile and IGM types.
- It was important to conduct long-term monitoring and data collecting in order to compile thorough data on pile performance and behavior over time. This will enable the creation of more reliable prediction models and the improvement of design suggestions.

## REFERENCES

- AASHTO. (2020). AASHTO LRFD Bridge Design Specifications 9th Edition U.S. Customary Units. American Association of State Highway and Transportation Officials (AASHTO), Ishington, D.C.
- Abu-Farsakh, M. Y., and Haque, N. (2020). Modified Time Factor to Estimate the Duration of Pile Setup. *Geotechnical and Geological Engineering*, Springer, 38(6), 5787–5804.
- Abu-Hejleh, N. M., O'Neill, M. W., Hanneman, D., and Attwooll, W. J. (2005). Improvement of the geotechnical axial design methodology for Colorado's drilled shafts socketed in weak rocks. *Transportation research record*, SAGE Publications Sage CA: Los Angeles, CA, 1936(1), 100–107.
- Adhikari, P. (2019). Load and Resistance Factor Design and Construction Control of Driven Piles in Intermediate Geomaterials. Ph.D. Dissertation, Department of Civil and Architectural Engineering, University of Wyoming, Laramie, WY.
- Adhikari, P., Gebreslasie, Y. Z., Ng, K. W., and Wulff, S. S. (2019). Performance Assessment of Wave Equation Analysis for Driven Steel H-Piles in IGM. *DFI Journal*, 13(1).
- Adhikari, P., Ng, K. W., Gebreslasie, Y. Z., and Wulff, S. S. (2020a). Improved  $\alpha$ - and  $\beta$ -Methods for the Estimation of Shaft Resistance of Steel-H Piles Driven into Intermediate Geomaterials. *Geo-Congress 2020: Foundations, Soil Improvement, and Erosion*, Reston, VA: American Society of Civil Engineers, 114–123.
- Adhikari, P., Ng, K. W., Gebreslasie, Y. Z., and Wulff, S. S. (2020b). Static and Economic Analyses of Driven Steel H-Piles in IGM Using the WyoPile Database. *Journal of Bridge Engineering*, American Society of Civil Engineers, 25(5), 4020016.
- Adhikari, P., Ng, K. W., Gebreslasie, Z. Y., Wulff, S. S., and Sullivan, T. (2020c). Geomaterial Classification Criteria for Design and Construction of Driven Steel H-Piles. *Canadian Geotechnical Journal*, 57(4), 616–621.
- Agung, P., Pramusandi, S., and Damianto, B. (2017). Identification and classification of clayshale characteristic and some considerations for slope stability. *African Journal of Environmental Science and Technology*, Academic Journals, 11(4), 163–197.
- Akai, K. (1997) *Testing Methods for Indurated Soils and Soft Rocks-Interim Report*.

- Akaike, H. (1974). A new look at the statistical model identification. *IEEE transactions on automatic control*, Ieee, 19(6), 716–723.
- Allen, T.M. (2005). Development of Geotechnical Resistance Factors and Downdrag Load Factors for LRFD Foundation Strength Limit State Design. Final Report FHWA-NHI-05-052, Federal Highway Administration, U.S. Department of Transportation, Ishington, D.C.
- Anderson T.W. and Darling, D.A. (1952). “Asymptotic Theory of Certain ‘Goodness-of-fit Criteria based on Stochastic Processes.” *The Annals of Mathematical Statistics*, 23,193-212.
- Ashford, S. A., and Jakrapiyanun, W. (2001). “Drivability of glass FRP composite piling. *Journal of Composites for Construction*, American Society of Civil Engineers, 5(1), 58–60.
- ASTM. (2002). Standard test method for determining rock quality designation (RQD) of rock core. ASTM standard D6032-02. ASTM International.
- ASTM. (2005). Standard Test Methods for Laboratory Determination of Water (Moisture) Content of Soil and Rock by Mass: ASTM D 2216-05. ASTM International.
- ASTM (2007) D. 1143/D 1143M-07 Standard Test Methods for Deep Foundations under Static Axial Compressive Load. Annual Book of ASTM Standards.
- Authier, J., and Fellenius, B. H. (1980). “Quake values determined from dynamic measurements.” *Proceedings of the First International Seminar on Application of Stress-Wave Theory to Piles*, H. Bredenberg Editor, AA Balkema, Rotterdam, 197–216.
- Barker, R. M., Duncan, J. M., Rojiani, K. B., Ooi, P. S. K., Tan, C. K., and Kim, S. G. (1991). *Manuals for the Design of Bridge Foundations*. NCHRP Report 343, Transportation Research Board of the National Academics, Washington, D.C.
- Barton, N. (1976). Recent experiences with the Q-system. Johannesburg.
- Barrett, J. W., and Prendergast, L. J. (2020). Empirical shaft resistance of driven piles penetrating weak rock. *Rock Mechanics and Rock Engineering*, Springer, 53(12), 5531–5543.
- Bartoskewitz, R. E., and Coyle, H. M. (1970). Wave Equation Prediction of Pile Bearing Capacity Compared with Field Test Results. Research Report 125-5, Texas Transportation Institute, Texas A&M University, College Station, Texas.
- Beake, R. H., and Sutcliffe, G. (1980). Pipe pile drivability in the carbonate rocks of the southern Arabian Gulf. *Proceedings of Conference on Structural Foundations on Rock*,

- Sydney, Australia. Rotterdam, Netherlands: A.A. Balkema.
- Becker, D., and Moore, I. (2006). Canadian foundation engineering manual.
- Belbas, R. E. J. (2014). "The capacity of driven steel H-piles in lacustrine clay, till and karst bedrock: a Winnipeg case study." MS Thesis, Department of Civil Engineering, University of Manitoba, Winnipeg, Canada.
- Bica, A. V. D., M. Prezzi, H. Seo, R. Salgado, and D. Kim. (2014), Instrumentation and Axial Load Testing of Displacement Piles. Proceedings of the Institution of Civil Engineers-Geotechnical Engineering, Vol. 167, No. 3, pp. 238–252.
- Bieniawski, Z. (1988). The rock mass rating (RMR) system (geomechanics classification) in engineering practice. In Rock Classification Systems for Engineering Purposes. ASTM International.
- Burnham, K. P., and D. R. Anderson. 2003. Model selection and multimodel inference: A practical information-theoretic approach, 2nd ed. Springer-Verlag, New York.
- Bjerrum, L. (1967). "The third Terzaghi lectures; Progressive failure in slopes of overconsolidated plastic clay and clay shales." Journal of the Soil Mechanics and foundations Division, American Society of Civil Engineers, 93(5), 1–49.
- Breiman, L., 2001. Random Forests. Machine Learning, 45, pp. 5-32.
- Christakos, G. (2012). Random Field Models in Earth Sciences. Chelmsford: Courier Corporation.
- Clarke, B.G., Smith, A., (1993). Self-boring pressuremeter tests in weak rocks. In The Engineering Geology of Weak Rock: Proceedings of the 26th Annual Conference of the Engineering Group Geological Society, Leeds, UK, pp. 233–241. Clayton, C. R. I. (1995). The Standard Penetration Test (SPT): Methods and Use. CIRIA London.
- Colorado Department of Transportation (CDOT). (2018). CDOT Bridge Design Manual. Denver, CO.
- Chang, C.C, Lin, C.J., 2011. LIBSVM: A Library for Support Vector Machines. ACM Transactions on Intelligent Systems and Technology. 22(7), 1-27.  
<https://doi.org/10.1145/1961189.1961199>
- Cherblanc, F., Berthonneau, J., Bromblet, P., and Huon, V. (2016). "Influence of water content on the mechanical behaviour of limestone: Role of the clay minerals content." Rock

- Mechanics and Rock Engineering, Springer, 49(6), 2033–2042.
- Ching, J., and Phoon, K. K. (2012). Value of geotechnical site investigation in reliability-based design. *Advances in Structural Engineering*, 15(11), 1935–1945.
- CIRIA. (2002). C574 Engineering in chalk. Ciria, London.
- Coduto, D. P. (1999). *Geotechnical engineering: principles and practices*.
- Coyle, H. M., Foye Jr, R., and Bartoskewitz, R. E. (1973). Wave Equation Analysis Of Instrumented Test Pile. Offshore Technology Conference, Offshore Technology Conference, Houston, Texas.
- Crisp, M. P., M. B. Jaksa, and Y. L. Kuo. (2020). Effect of Borehole Location on Pile Performance. *Georisk*, 1–16. <https://doi.org/10.1080/17499518.2020.1757721>.
- Crisp, Michael, Mark Jaksa, Yien Kuo, Gordon A. Fenton, and Vaughan Griffiths. (2020). Characterizing Site Investigation Performance in a Two Layer Soil Profile. *Canadian Journal of Civil Engineering*, 1–9. <https://doi.org/10.1139/cjce-2019-0416>.
- Davisson, M. T. (1972) High Capacity Piles. *Proc. Innovations in Found. Const.*, Vol. 52.
- De Beer, E. E. (1968) Proefondervindelijke Bijdrage Tot de Studie van Het Grensdragvermogen van Zand Onder Funderingen Op Staal (Deel 2–3). *Annales des travaux publics de Belgique* (2nd series), Vol. 69, No. 1, pp. 44–88.
- De Freitas, H., (1993). Introduction to Session 1.2: Weak Arenaceous Rock. In *The Engineering Geology of Weak Rock: Proceedings of the 26th Annual Conference of the Engineering Group Geological Society*, Leeds, UK, pp. 115–123.
- Deo, P. (1972). *Shales as embankment materials*. Purdue University.
- Doherty, P., and Igoe, D. (2013). A Driveability Study of Precast Concrete Piles in Dense Sand. *DFI Journal-The Journal of the Deep Foundations Institute*, Taylor & Francis, 7(2), 3–16.
- Eid, H. T. (2006). Factors influencing determination of shale classification indices and their correlation to mechanical properties. *Geotechnical & Geological Engineering*, Springer, 24(6), 1695.
- Erguler, Z. A., and Shakoor, A. (2009). Quantification of fragment size distribution of clay-bearing rocks after slake durability testing. *Environmental & Engineering Geoscience*, Association of Environmental & Engineering Geologists, 15(2), 81–89.

- Esrig, M., Kirby, R.C., (1979). Advances in general effective stress method for the prediction of axial capacity for driven piles in clay. Offshore Technology Conference. Houston, TX, pp 437–449.
- Fellenius, B. H. (2015). Static Tests on Instrumented Piles Affected by Residual Load. DFI Journal-The Journal of the Deep Foundations Institute, Vol. 9, No. 1, pp. 11–20.
- Forehand, P. W., and Reese, J. L. (1964). Prediction of pile capacity by the wave equation. Journal of the Soil Mechanics and Foundations Division, ASCE, 90(2), 1–26.
- Fuller, F. M., and H. E. Hoy. (1970). Pile Load Tests Including Quick-Load Test Method, Conventional Methods, and Interpretations. Highway Research Record, No. 333.
- Gamble, J. C. (1971). Durability-plasticity classification of shales and other argillaceous rocks. Ph. D. thesis, University of Illinois.
- Goble, G. G., and Rausche, F. (1976). Wave equation analysis of pile driving: WEAP program. volume II. user's manual (No. FHWA/IP-76-14.2 Final Rpt.).
- Goldberg, D., (1989). Genetic Algorithms in Search, Optimization, and Machine Learning. Addison-Wesley Professional: Boston, MA.
- Gu, Y., Wei, H.-L., and Balikhin, M. M. (2018). Nonlinear predictive model selection and model averaging using information criteria. Systems Science & Control Engineering, Taylor & Francis, 6(1), 319–328.
- Hannigan, P. J., Goble, G. G., Likins, G. E., and Rausche, F. (2006). Design and Construction of Driven Pile Foundations Reference Manual–Volume II. Publication No. FHWA NHI-05-043. National Highway Institute. Federal Highway Administration.
- Hannigan, P., Ryberg, A., and Moghaddam, R. . (2020). Identification and quantification of pile relaxation. Proceedings of DFI 44th Annual Conference on Deep Foundations, Chicago, IL.
- Haque, M. N., Abu-Farsakh, M. Y., Tsai, C., and Zhang, Z. (2017). Load-testing program to evaluate pile-setup behavior for individual soil layers and correlation of setup with soil properties. Journal of Geotechnical and Geoenvironmental Engineering, American Society of Civil Engineers, 143(4), 4016109.
- Hawkins, A. B., and McConnell, B. J. (1992). Sensitivity of sandstone strength and deformability to changes in moisture content. Quarterly Journal of Engineering Geology and Hydrogeology, Geological Society of London, 25(2), 115–130.

- Hopkins, T. C., and Deen, R. C. (1984). Identification of shales. *Geotechnical Testing Journal*, ASTM International, 7(1), 10–18.
- Hsu, S.-C., and Nelson, P. P. (2002). Characterization of eagle ford shale.”*Engineering Geology*, Elsevier, 67(1–2), 169–183.
- Irvine, J., Terente, V., Lee, L. T., and Comrie, R. (2015). Driven pile design in weak rock. *Proc. Int. Symp. on Frontiers in Offshore Geotechnics III, ISFOG 2015*, 569–574.
- Iskander, M. G., and Stachula, A. (2002). Wave equation analyses of fiber-reinforced polymer composite piling. *Journal of Composites for Construction*, American Society of Civil Engineers, 6(2), 88–96.
- Islam, M. S. (2021). Pile behaviors in shales through full-scale static load testing, dynamic testing, and finite element analysis. MS thesis, Dept. of Civil and Architectural Engineering, Univ. of Wyoming.
- Islam, M. S., Ng, K. W., & Wulff, S. (2022a). Prediction of Driven Pile Resistances in Shales Considering Weathering and Time Effects. *Canadian Geotechnical Journal*.
- Islam, M. S., Ng, K., & Wulff, S. S. (2022b). Improved Wave Equation Analysis of Steel H-Piles in Shales Considering LRFD and Economic Impact Studies. *Journal of Bridge Engineering*, 27(6), 04022039.
- Izenman, A.J., (2008). *Modern Multivariate Statistical Techniques*. Springer: New York.
- James, G., Witten, D., Hastie, T., and Tibshirani, R. (2013). *An introduction to statistical learning*. Springer.
- Kalauni, H. K. (2021). New Static Analysis Methods and Improved Wave Equation Analysis Program for Driven Piles in Intermediate Geomaterials with Load and Resistance Factor Design Recommendations. MS thesis, Dept. of Civil and Architectural Engineering University of Wyoming.
- Kalauni, H. K., Masud, N. B., Ng, K., & Wulff, S. S. (2024). Improved Wave Equation Analysis for Piles in Soil-Based Intermediate Geomaterials with LRFD Recommendations and Economic Impact Assessment. *Geotechnics*, 4(2), 362-381.
- Kivi, I. R., Ameri, M., and Molladavoodi, H. (2018). Shale brittleness evaluation based on energy balance analysis of stress-strain curves. *Journal of Petroleum Science and Engineering*, Elsevier, 167, 1–19.



- Kodsy, A., Ozturk, B. and Iskander, M., (2023). Forecasting of pile plugging using machine learning. *Acta Geotechnica*, 1-18.
- Korb, K. W., and Coyle, H. M. (1969). Dynamic and Static Field Tests on a Small Instrumented Pile. Texas Transportation Institute, Texas A & M University.
- Kuhn, M., (2008). Caret Package. *Journal of Statistical Software*, 28, 1-26.  
<https://doi.org/10.18637/jss.v028.i05>
- Kulhawy, F. H., and Mayne, P. W. (1990). Manual on estimating soil properties for foundation design. Electric Power Research Inst., Palo Alto, CA (USA); Cornell University, Ithaca
- Kutner, M.H, Nachtsheim, C.J., Neter, J., (2004). *Applied Linear Regression Models*, fourth ed. McGraw-Hill Irwin: New York.
- Likins, G. E., and Hussein, M. (1984). Relaxation Of H Piles in Shale. Lecture notes, Pile Driving Analyser Users Days, Stockholm.
- Likins, G., and Rausche, F. (2004). Correlation of CAPWAP with static load tests. *Proceedings of the Seventh International Conference on the Application of Stresswave Theory to Piles*, Citeseer, 153–165.
- Li, Z, X Wang, Hui Wang, and Robert Y. Liang. (2016). Quantifying Stratigraphic Uncertainties by Stochastic Simulation Techniques Based on Markov Random Field. *Engineering Geology* 201:106–22. <https://doi.org/10.1016/j.enggeo.2015.12.017>.
- Long, J., and Anderson, A. (2012). Improved Design for Driven Piles on a Pile Load Test Program in Illinois.
- Long, J., and Anderson, A. (2014). Improved design for driven piles based on a pile load test program in Illinois: phase 2. Illinois Center for Transportation.
- Long, J. H. (2016). Static pile load tests on driven piles into Intermediate-Geo Materials. University of Illinois at Urbana-Champaign. Dept. of Civil Engineering.
- Long, J. and Horsfall, J. (2017). Static Pile Load Tests on Driven Piles in Intermediate Geo Materials.” Project 0092-12-08, Research Brief, Wisconsin Highway Research Program, February, Madison, WI.
- Long, J. H., Kerrigan, J. A., and Wysockey, M. H. (1999). Measured time effects for axial capacity of driven piling. *Transportation research record*, SAGE Publications Sage CA: Los Angeles, CA, 1663(1), 8–15.

- Marinos, P.G., (1997). Hard soils-soft rocks: Geological features with special emphasis to soft rocks. In *Geotechnical engineering of hard soils-soft rocks*, pp. 1807-1818.
- Martin, C. D. (2015). "Behaviour of shales in underground environments." 13th ISRM international congress of rock mechanics, Montreal, Canada.
- Masud, N.B., Ng, K.W., Wulff, S.S., Johnson, T., (2022a). Driven Piles in Fine-Grained Soil-Based Intermediate Geomaterials. *Journal of Bridge Engineering*. 27(6), 4022037. [https://doi.org/10.1061/\(ASCE\)BE.1943-5592.0001887](https://doi.org/10.1061/(ASCE)BE.1943-5592.0001887)
- Masud, N.B., Ng, K.W., Islam, M.S., Wulff, S.S., (2022b). Static and Dynamic Pile Load Tests on Steel H-Piles in Intermediate Geomaterials. *Geo-Congress 2022: Foundations, Soil Improvement, and Erosion*, American Society of Civil Engineers, Reston, VA, pp. 104-112.
- Masud, N.B., Ng, K.W., Wulff, S.S., (2022c). New Static Analysis Methods for the Prediction of Driven Pile Resistance in Siltstone. *Geo-Congress 2022: Foundations, Soil Improvement, and Erosion*, American Society of Civil Engineers, Reston, VA, pp. 93-103.
- Masud, N.B., Ng, K.W., Wulff, S.S., (2023a). Resistance responses and design recommendations for driven piles in coarse-grained soil-based intermediate geomaterials. *Soils and Foundations*. 63(6), 101381. <https://doi.org/10.1016/j.sandf.2023.101381>.
- Masud, N.B., Ng, K.W., Oluwatuyi, O.E., Islam, M.S., Kalauni, H.K., Wulff, S.S., (2023b). Evaluation of Static Load Test Systems for Driven Piles in Intermediate GeoMaterials. *Transportation Research Record: Journal of the Transportation Research Board*. 15, 03611981231163827. <https://doi.org/10.1177/03611981231163827>
- Masud, N.B., Ng, K.W., Kalauni, H.K., Wulff, S.S., (2023c). Reliability-based design improvement and prediction of steel driven pile resistances in rock-based intermediate geomaterials. *Acta Geotechnica*. 1-23. <https://doi.org/10.1007/s11440-023-01909-1>
- Masud, N.B., (2024). Comprehensive Field Load Test Program and Development of LRDF Recommendations for Driven Piles In Intermediate Geomaterials. Ph.D. Dissertation, Department of Civil and Architectural Engineering, University of Wyoming, Laramie, WY.
- Masud, N. B., Wulff, S. S., & Ng, K. (2024a). Economic impact analysis for steel piles driven in intermediate geomaterials using machine learning algorithms. *Acta Geotechnica*, 1-19.
- Masud, N. B., Ng, K., & Wulff, S. S. (2024b) A Case Study to Investigate Field Load Test of Driven Piles in Siltstone. In *Rocky Mountain Geo-Conference 2024* (pp. 43-57).

- McVay, M. C., and Kuo, C. L. (1999). Estimate damping and quake by using traditional soil testing. Department of Civil Engineering, University of Florida, Gainesville, FL, USA.
- Mohamadi, M. (2015). “Experimental and Constitutive Investigation of the Thermo-Hydro-Mechanical Behavior of Shales: A Case Study of the Colorado Clay Shale.” University of Calgary (Canada).
- Mokwa, R. L., and Brooks, H. (2008). Axial capacity of piles supported on intermediate geomaterials. Montana. Dept. of Transportation. Research Programs.
- Morgano, C. M., and White, B. A. (2004). “Identifying soil relaxation from dynamic testing.” Proceedings of the Seventh International Conference on the Application of Stresswave Theory to Piles, 415–421.
- Morton, T. S. (2012). Assessing Driven Steel Pile Capacity on Rock Using Empirical Approaches.
- Nie, R., W. Leng, Q. Yang, and Y. Frank Chen (2018). Effects of Pile Residual Loads on Skin Friction and Toe Resistance. *Soil Mechanics and Foundation Engineering*, Vol. 55, No. 2, pp. 76–81.
- Ng, K., Adhikari, P., and Gebreslasie, Y. Z. (2019). Development of load and resistance factor design procedures for driven piles on soft rocks in Wyoming. Wyoming. Dept. of Transportation.
- Ng, K., and Sullivan, T. (2017a). Challenges and recommendations for steel H-piles driven in soft rock. *Geotech. Eng.*, 48(3), 1–10.
- Ng, K. W., Roling, M., AbdelSalam, S. S., Suleiman, M. T., and Sritharan, S. (2013a). Pile setup in cohesive soil. I: experimental investigation. *Journal of Geotechnical and Geoenvironmental Engineering*, American Society of Civil Engineers, 139(2), 199–209.
- Ng, K. W., Suleiman, M. T., and Sritharan, S. (2013b). Pile setup in cohesive soil. II: Analytical quantifications and design recommendations. *Journal of Geotechnical and Geoenvironmental Engineering*, American Society of Civil Engineers, 139(2), 210–222.
- Ng, K. W., and Sullivan, T. (2017b). Recent development of load and resistance factor design (LRFD) for driven piles on soft rock. *Geo-Risk 2017*, 307–316.
- Ng, K. W., Yasrobi, S. Y., and Sullivan, T. A. (2015). Current Limitations and Challenges of Driven Piles in Rock as Demonstrated using Three Case Studies in Wyoming.” *IFCEE*

2015, 500–517.

O'Neill, M. W., and L. C. Reese (1999). Drilled Shafts: Construction Procedures and Design Methods, FHWA, Publication No. FHWA-IF-99-025, McLean, VA, Department of Transportation, Federal Highway Administration, Office of Implementation.

Oluwatuyi, O.E. (2023). Consideration of Uncertainties in Site Investigation Plans and LRFD Recommendations for Piles Driven into Intermediate Geomaterials. University of Wyoming ProQuest Dissertations. United States -- Wyoming: University of Wyoming.

Oluwatuyi, O.E., R Holt, R. Rajapakshage, S. S. Wulff, and K. W. Ng. (2022a). Inherent Variability Assessment from Sparse Property Data of Overburden Soils and Intermediate Geomaterials Using Random Field Approaches. *Georisk: Assessment and Management of Risk for Engineered Systems and Geohazards* 16 (4): 766–81.

<https://doi.org/10.1080/17499518.2022.2046783>.

Oluwatuyi, O.E., K. Ng, and S.S. Wulff. (2023a). Improved Resistance Prediction and Reliability for Bridge Pile Foundation in Shales through Optimal Site Investigation Plans. *Reliability Engineering & System Safety* 239:109476. <https://doi.org/10.1016/j.res.2023.109476>.

Oluwatuyi, O.E., K.W. Ng, S.S. Wulff, and N.B. Masud. (2023b). The Effect of Geological Uncertainty on the Shaft Resistance Prediction and Reliability of Piles Driven in Multi-Layered Geomaterials. *Transportation Research Record* 2677 (6): 687–96.

<https://doi.org/10.1177/03611981221149733>.

Oluwatuyi, O.E., K.W. Ng, S.S. Wulff, and R. Rajapakshage. (2023c). Optimal Site Investigation Through Combined Geological and Property Uncertainties Analysis. *Geotechnical and Geological Engineering* 41 (4): 2377–93. <https://doi.org/10.1007/s10706-023-02403-x>.

Oluwatuyi, O.E., Kam W Ng, Shaun S Wulff, and Taylor Ree. 2024. Uncertainty Reduction Strategies to Enhance Geotechnical Site Characterization: A Case Study of the Red Roof Landslide in Wyoming. *Discover Geoscience* 2 (1): 1–14. <https://doi.org/10.1007/s44288-024-00015-3>.

Oluwatuyi, O.E., R. Rajapakshage, S.S. Wulff, and K.W. Ng. (2022b). Quantifying Geological Uncertainty Using Conditioned Spatial Markov Chains. In *Geo-Congress 2022*, 436–45. <https://doi.org/10.1061/9780784484036.043>.

- Oluwatuyi, O.E., R. Rajapakshage, S.S. Wulff, and K.W. Ng. (2023d). Proposed Hybrid Approach for Three-Dimensional Subsurface Simulation to Improve Boundary Determination and Design of Optimum Site Investigation Plan for Pile Foundations. *Soils and Foundations* 63 (1): 101269. <https://doi.org/10.1016/J.SANDF.2022.101269>.
- Paikowsky, S. G. (2004). Load and resistance factor design (LRFD) for deep foundations. Transportation Research Board.
- Paikowsky, S. G., Birgisson, B., McVay, M., Nguyen, T., Kuo, C., Baecher, G., Ayyub, B., Stenersen, K., O'malley, K., and Chernauskas, L. (2004). Load and resistance factor design (LRFD) for deep foundations, NCHRP Report 507. Transportation Research Board, Ishington, DC, 76.
- Peiris, T. A., Morris, B., Kelly, R., and Chan, K. (2010). Methodology to demonstrate pile capacity In relaxing ground.
- Phoon, K. K., and F. H. Kulhawy. 1999. Characterization of Geotechnical Variability. *Canadian Geotechnical Journal* 36 (4): 612–24. <https://doi.org/10.1139/t99-038>
- Picard, M.D., (1971). Classification of fine-grained sedimentary rocks. *Journal of Sedimentary Research, SEPM Society for Sedimentary Geology*. 41(1), 179–195. <https://doi.org/10.1306/74D7221B-2B21-11D7-8648000102C1865>
- Pile Dynamics, I. (2010). GRLWEAP Manual for Windows. 30725 Aurora Road, Cleveland, OH 44139 USA: PDI.
- Poon, B., McKay, G., Chan, K., and Castañeda, L. R. (2017). Dynamic load testing of 2 meter steel tubular piles driven into foliated phyllite bedrock. *Proceedings of DFI-PFSFPiled Foundation and Ground Improvement Technology for the Modern Building and Infrastructure Sector*.
- Qi, Xiao Hui, Dian Qing Li, Zi Jun Cao, and Xiao Song Tang. 2016. Uncertainty Analysis of Slope Stability Considering Geological Uncertainty. In *Proceedings of 12th International Symposium on Landslides and Engineered Slopes—Experience, Theory and Practice*, 1685–93.
- R Core Team., (2016). R: A language and environment for statistical computing. R Foundation for Statistical Computing, Vienna, Austria. <http://www.R-project.org/>.

- Rackwitz, R., and Flessler, B. (1978). "Structural Reliability under Combined Random Load Sequences." *Computers & Structures*, Elsevier, 9, 489–494.
- Raines, R. D., Ugaz, O. G., and O'Neill, M. W. (1992). Driving characteristics of open-toe piles in dense sand. *Journal of geotechnical engineering*, American Society of Civil Engineers, 118(1), 72–88.
- Ramey, G. E., and Hudgins, A. P. (1977). Sensitivity and Accuracy of the Pile Wave Equation. *Ground Engineering*, 10(7), 45–47.
- Rehman, S., and Broms, B. B. (1971). Bearing capacity of piles driven into rock. *Canadian Geotechnical Journal*, NRC Research Press, 8(2), 151–162.
- Rausche, F., Nagy, M., and Likins, G. (2008). Mastering the art of pile testing. In *Proceedings of the 8th International Conference on the Application of Stress Wave Theory to Piles*, J. A. Santos, 1932, Lisbon, Portugal, September 8–10. Amsterdam, The Netherlands: IOS., 19–32.
- Rausche, F., Nagy, M., Webster, S., and Liang, L. (2009). CAPWAP and refined wave equation analyses for driveability predictions and capacity assessment of offshore pile installations. *International Conference on Offshore Mechanics and Arctic Engineering*, 375–383.
- Rausche, F., Thendean, G., Abou-matar, H., Likins, G. E., and Goble, G. G. (1997). Determination of pile driveability and capacity from penetration tests. Volume I. Report No. FHWA-RD-96-179, McLean, Va.: Federal Highway Administration.
- Ripley, B.D., (1996). *Pattern Recognition and Neural Networks*. Cambridge University Press, Cambridge, UK.
- Rehman, S., and Broms, B. B. (1971). Bearing capacity of piles driven into rock. *Canadian Geotechnical Journal*, NRC Research Press, 8(2), 151–162.
- Samson, L., and Authier, J. (1986). Change in pile capacity with time: case histories. *Canadian geotechnical journal*, NRC Research Press, 23(2), 174–180.
- Santi, P.M., Doyle, B.C., Shakoor, A., (1997). The locations and engineering characteristics of weak rock in the US. In *Characterization of weak and weathered rock masses*. Association of Engineering Geologists Special Publication, Denver, CO. 1–22.
- Sartore, Luca, Paolo Fabbri, and Carlo Gaetan. 2016. SpMC: An R-Package for 3D Lithological Reconstructions Based on Spatial Markov Chains. *Computers and Geosciences* 94:40–47. <https://doi.org/10.1016/j.cageo.2016.06.001>.

- Schneider, J. A., and Harmon, I. A. (2010). Analyzing drivability of open ended piles in very dense sands. DFI Journal-The Journal of the Deep Foundations Institute, Taylor & Francis, 4(1), 32–44.
- Schwarz, G. (1978). Estimating the dimension of a model The Annals of Statistics 6 (2), 461–464. URL: [http://dx. doi. org/10.1214/aos/1176344136](http://dx.doi.org/10.1214/aos/1176344136).
- Scrucca, L., (2013). GA: A Package for Genetic Algorithms in R. Journal of Statistical Software. 53,1-37.
- Shapiro, S. S., and Wilk, M. B. (1965). "An Analysis of Variance Test for Normality (Complete Samples)." Biometrika, JSTOR, 52(3/4), 591–611.
- Sivanandam, S.N., Deepa, S.N., (2008). Introduction to Genetic Algorithms. Springer, Berlin, Germany.
- Skov, R., and Denver, H. (1988). Time-dependence of bearing capacity of piles. Proc. Third International Conference on the Application of Stress-Wave Theory to Piles. Ottawa, 25–27.
- Smith, E. A. (1960). Pile-driving analysis by the wave equation. American Society of Civil Engineers Transactions, 86(4), 35–61.
- Smith, T., Banas, A., Gummer, M., and Jin, J. (2011). Recalibration of the GRLWEAP LRFD resistance factor for Oregon DOT.No. FHWA-OR-RD-11-08). Research Unit, Oregon Department of Transportation.
- Soliman, M., Walter, D., Crabtree, B., and Lee, A. (2018). Driven Steel Piles in Clay Shale on Northeast Anthony Henday Drive in Edmonton.” 71st Canadian Geotechnical Conference and the 13th Joint CGS/IAH-CNC Groundwater Conference, Edmonton, Alberta, Canada.
- Stark, T. D., Long, J. H., and Assem, P. (2013). Improvement for determining the axial capacity of drilled shafts in shale in Illinois. Illinois Center for Transportation.
- Stevens, R. F., Wiltsie, E. A., and Turton, T. H. (1982). Evaluating pile driveability for hard clay, very dense sand, and rock.” Proceedings of the 14th Annual Offshore Technology Conference, Houston, USA, 465–469.
- Ta, A.-N., and Hammann, M. (2013). Application Of Adjusted Wave Equation Analysis For Optimized Pile Acceptance Criteria. Advances in Soil Mechanics and Geotechnical Engineering, 230–233.

- Talal, A.-B. (2013). The impact of water content and ionic diffusion on the uniaxial compressive strength of shale. *Egyptian Journal of Petroleum, Elsevier*, 22(2), 249–260.
- Team, R. C. (2013). *R: A language and environment for statistical computing*. Vienna, Austria.
- Terente, V., Irvine, J., Comrie, R., and Crowley, J. (2015). Pile driving and pile installation risk in weak rock. *Proceedings of European Conference on Soil Mechanics & Geotechnical Engineering XVI*, September 2015, Edinburgh, UK, DOI:10.1201/b18442-73, 1187–1192.
- Thompson, C. D., and Thompson, D. E. (1985). Real and apparent relaxation of driven piles. *Journal of Geotechnical Engineering, American Society of Civil Engineers*, 111(2), 225–237.
- Tomlinson, M., and Woodward, J. (2014). *Pile design and construction practice*. CRC Press.
- Tutluoğlu, L., Öge, İ. F., and Karpuz, C. (2015). Relationship between pre-failure and post-failure mechanical properties of rock material of different origin. *Rock Mechanics and Rock Engineering, Springer*, 48(1), 121–141.
- Underwood, L. B. (1967). Classification and identification of shales. *Journal of the Soil Mechanics and Foundations division, ASCE*, 93(6), 97–116.
- Venables, W.N., Ripley, B.D., (2002). *Modern Applied Statistics with S*. Springer: New York.
- Wang, S. R., Hagan, P., Li, Y. C., Zhang, C. G., Liu, X. L., and Zou, Z. S. (2017). Experimental study on deformation and strength characteristics of sandstone with different water contents. *Journal of Engineering Science and Technology Review*, 10(4), 199–203.
- Wang, Yu, Zheng Guan, and Tengyuan Zhao. 2019. “Sample Size Determination in Geotechnical Site Investigation Considering Spatial Variation and Correlation.” *Canadian Geotechnical Journal* 56 (7): 992–1002. <https://doi.org/10.1139/cgj-2018-0474>.
- Yagiz, S. (2001). Overview of classification and engineering properties of shales for design considerations. *Construction and Materials Issues 2001*, 156–165.
- Yu, X., Gen, M., (2010). *Introduction to Evolutionary Algorithms*. Springer, London. UK.
- Zhang, Liang, and Lei Wang. 2023. Optimization of Site Investigation Program for Reliability Assessment of Undrained Slope Using Spearman Rank Correlation Coefficient. *Computers and Geotechnics* 155:105208. <https://doi.org/10.1016/j.compgeo.2022.105208>.
- Zhang, Limin, Wilson H. Tang, Lulu Zhang, and Jianguo Zheng. 2004. Reducing Uncertainty of Prediction from Empirical Correlations. *Journal of Geotechnical and Geoenvironmental*



Engineering 130 (5): 526–34. [https://doi.org/10.1061/\(asce\)1090-0241\(2004\)130:5\(526\)](https://doi.org/10.1061/(asce)1090-0241(2004)130:5(526)).

Ziogos, A. (2020). Investigation of the interface shearing resistance of steel and concrete on different rocks for renewable energy gravity foundation applications. University of Dundee Dundee, UK.

## APPENDIX

A HP 14×73 steel H-pile was to be driven at a site where soil and shale conditions were provided in Figure. The overburden soil was a 65.6 ft thick silty clay with an average undrain shear strength ( $s_u$ ) 1.17 ksf. The 58 ft thick underlying shale layer consists of SS, HW, MW and SW shales. The calculations of normal pile shaft resistances, nominal end bearing and factored pile resistance in the shale layers in accordance with the proposed LRFD recommendations were illustrated as follows:

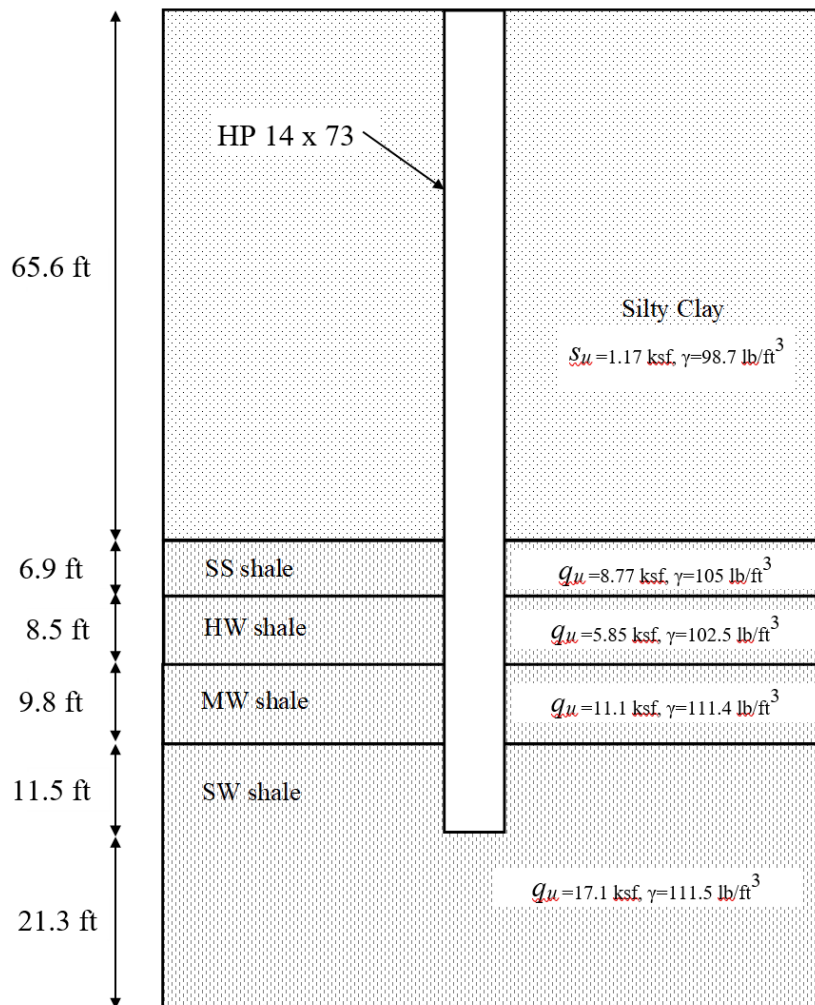


**Figure. Subsurface Profile and pile penetration.**

1) Pile width = 1.18 ft, Toe area ( $A_t$ ) = 1.4 ft<sup>2</sup> and pile perimeter (P) = 4.72 ft.

2) The  $q_s$  in 6.9-ft thick SS shale was predicted using Figure 7.7a

$$\hat{q}_s(SS) = \frac{3.52 \times 8.77}{(8.6 + 8.77)^{1.05}} = 1.55 \text{ ksf}$$

The shaft resistance in the SS layer ( $R_{SS}$ ) =  $1.55 \times 4.72 \times 6.9 = 50.2$  kips

3) The  $q_s$  in 8.5-ft thick HW shale was predicted using Figure 7.7b

$$\hat{q}_s(HW) = 0.23 \times 5.85^{0.45} = 0.51 \text{ ksf}$$

The shaft resistance in the HW layer ( $R_{HW}$ ) =  $0.51 \times 4.72 \times 8.5 = 20.5$  kips

4) The  $q_s$  in 9.8-ft thick MW shale was predicted using Figure 7.7c

$$\hat{q}_s(MW) = \frac{1.196 \times 11.1}{(0.5 + 11.1)^{0.83}} = 1.74 \text{ ksf}$$

The shaft resistance in the MW layer ( $R_{MW}$ ) =  $1.74 \times 4.72 \times 9.8 = 80.3$  kips

5) The  $q_s$  in 11.5-ft thick SW shale was predicted using Figure 7.7d

$$\hat{q}_s(SW) = \frac{2.62 \times 17.1}{(.467 + 17.1)^{0.945}} = 2.99 \text{ ksf}$$

The shaft in SW layer ( $R_{SW}$ ) =  $2.99 \times 4.72 \times 11.5 = 162.1$  kips

6) The  $q_b$  in SW shale was predicted using Figure 7.8b

$$\hat{q}_b(MW - SW) = \frac{190.64 \times 17.1}{(1 + 17.1)^{0.88}} = 254.8 \text{ ksf}$$

The end bearing in SW layer ( $R_t$ ) =  $254.8 \times 1.4 = 356.9$  kips

7) The total factored pile resistance in the shale layers using the proposed LRFD resistance factors based on FORM for  $\beta_T=3.0$  (non-redundant pile group) from Table 5 is

$$\phi R = 0.45 \times 50.2 + 0.38 \times 20.5 + 0.62 \times 80.3 + 0.5 \times 162.1 + 0.52 \times 356.9 = 346 \text{ kips}$$